frontiers | Research Topics

Faults and earthquakes viewed by networks, monitoring systems and by numerical modelling techniques

Edited by
Giovanni Martinelli, Fuqiong Huang, Caibo Hu, Yongsheng Zhou and Fabrizio Gherardi

Published in
Frontiers in Earth Science

ISSN 1664-8714
ISBN 978-2-8325-7322-8
DOI 10.3389/978-2-8325-7322-8

Generative AI statement
Any alternative text (Alt text) provided alongside figures in the articles in this ebook has been generated by Frontiers with the support of artificial intelligence and reasonable efforts have been made to ensure accuracy, including review by the authors wherever possible. If you identify any issues, please contact us.

About Frontiers

Frontiers is more than just an open access publisher of scholarly articles: it is a pioneering approach to the world of academia, radically improving the way scholarly research is managed. The grand vision of Frontiers is a world where all people have an equal opportunity to seek, share and generate knowledge. Frontiers provides immediate and permanent online open access to all its publications, but this alone is not enough to realize our grand goals.

Frontiers journal series

The Frontiers journal series is a multi-tier and interdisciplinary set of open-access, online journals, promising a paradigm shift from the current review, selection and dissemination processes in academic publishing. All Frontiers journals are driven by researchers for researchers; therefore, they constitute a service to the scholarly community. At the same time, the *Frontiers journal series* operates on a revolutionary invention, the tiered publishing system, initially addressing specific communities of scholars, and gradually climbing up to broader public understanding, thus serving the interests of the lay society, too.

Dedication to quality

Each Frontiers article is a landmark of the highest quality, thanks to genuinely collaborative interactions between authors and review editors, who include some of the world's best academicians. Research must be certified by peers before entering a stream of knowledge that may eventually reach the public - and shape society; therefore, Frontiers only applies the most rigorous and unbiased reviews. Frontiers revolutionizes research publishing by freely delivering the most outstanding research, evaluated with no bias from both the academic and social point of view. By applying the most advanced information technologies, Frontiers is catapulting scholarly publishing into a new generation.

What are Frontiers Research Topics?

Frontiers Research Topics are very popular trademarks of the *Frontiers journals series*: they are collections of at least ten articles, all centered on a particular subject. With their unique mix of varied contributions from Original Research to Review Articles, Frontiers Research Topics unify the most influential researchers, the latest key findings and historical advances in a hot research area.

Find out more on how to host your own Frontiers Research Topic or contribute to one as an author by contacting the Frontiers editorial office: frontiersin.org/about/contact

Faults and earthquakes viewed by networks, monitoring systems and by numerical modelling techniques

Topic editors

Giovanni Martinelli — National Institute of Geophysics and Volcanology, Section of Palermo, Italy

Fuqiong Huang — China Earthquake Networks Center, China

Caibo Hu — University of Chinese Academy of Sciences, China

Yongsheng Zhou — Institute of Geology, China Earthquake Administration, China

Fabrizio Gherardi — Institute of Geosciences and Georesources, Department of Earth System Sciences and Technologies for the Environment, National Research Council (CNR), Italy

Citation

Martinelli, G., Huang, F., Hu, C., Zhou, Y., Gherardi, F., eds. (2026). *Faults and earthquakes viewed by networks, monitoring systems and by numerical modelling techniques*. Lausanne: Frontiers Media SA. doi: 10.3389/978-2-8325-7322-8

Table of contents

frontiers | Frontiers in Earth Science

TYPE Editorial
PUBLISHED 15 December 2025
DOI 10.3389/feart.2025.1731996

OPEN ACCESS

EDITED AND REVIEWED BY
Jeroen van Hunen,
Durham University, United Kingdom

*CORRESPONDENCE
Giovanni Martinelli,
giovanni.martinelli15@gmail.com
Fuqiong Huang,
hfqiong126@126.com

RECEIVED 24 October 2025
REVISED 25 November 2025
ACCEPTED 25 November 2025
PUBLISHED 15 December 2025

CITATION
Martinelli G, Huang F, Hu C, Zhou Y and Gherardi F (2025) Editorial: Faults and earthquakes viewed by networks, monitoring systems and by numerical modelling techniques.
Front. Earth Sci. 13:1731996.
doi: 10.3389/feart.2025.1731996

Editorial: Faults and earthquakes viewed by networks, monitoring systems and by numerical modelling techniques

Giovanni Martinelli[1]*, Fuqiong Huang[2]*, Caibo Hu[3], Yongsheng Zhou[4] and Fabrizio Gherardi[5]

[1]National Institute of Geophysics and Volcanology, Section of Palermo, Palermo, Italy, [2]China Earthquake Networks Center, Beijing, China, [3]National Key Laboratory of Earth System Numerical Modeling and Application, College of Earth and Planetary Science, University of Chinese Academy of Sciences, Beijing, China, [4]State Key Laboratory of Earthquake Dynamics and Forecasting, Institute of Geology, China Earthquake Administration, Beijing, China, [5]Istituto di Geoscienze e Georisorse Consiglio Nazionale delle Ricerche, Pisa, Italy

KEYWORDS

rock rheology, earthquake precursors, geofluids, monitoring systems, numerical modeling techniques, networks

Editorial on the Research Topic
Faults and earthquakes viewed by networks, monitoring systems and by numerical modelling techniques

1 Introduction

Rock rheology controls rock deformation caused by Earth's internal forces. Rheology examines the relationships between stress (force per unit area) and strain rate (rate of deformation) in materials. Plate tectonics has shown that the complete explanation of the interaction of Earth's lithosphere with mantle convection and other driving factors requires considering several other interacting factors beyond plate movement. The complicated deformation patterns of plate boundary zones, which space geodetic tools can now properly map, demonstrate this. Mineralogy, geofluid composition and content, mineral grain size, melt content, temperature, pressure, and differential stress affect rock rheology. Rocks exhibit considerable variability in their mineralogical and chemical composition, and our expanding knowledge of regional heat transport and tectonic stresses is of paramount importance. The upper mantle convection pattern under tectonic plates is not directly related to plate borders. Using geophysical factors like topography, gravity, S-wave dispersion, and heat flow, geological structures can be discovered and analyzed. However, earthquakes are the primary way to observe sudden movements occurring a few kilometers below the Earth's surface. The link between earthquake depths and subduction speeds suggests the influence of temperature on seismic activity. This Research Topic seeks to understand what distinguishes seismic fault movement from creeping fault movement. Geofluid mapping has been utilized to identify areas of tectonic activity. Earthquakes persist in areas with significant tectonic activity,

and geofluids will continue to contribute to the genesis of earthquakes until affected by major global geodynamic events.

This Research Topic presents the findings obtained using the latest geophysical, geochemical, geodetic, and statistical methodologies. Understanding the entire process—from nucleation to earthquake—is the goal. Recent annual meetings of the China Earthquake Prediction Forum, the Asia Oceania Geosciences Society, the European Geosciences Union, the American Geophysical Union, and others stressed the importance of observatory networks of monitoring systems from space, ground, and subsurface based on multiple sensors for potential anomalies related to inter-seismic (pre-seismic), co-seismic, and post-seismic processes and their spatial and temporal scales of numerical modeling of the physical processes of nucleation, dynamic rupturing, and seismic wave propagating of earthquakes.

2 Aims and content of this research topic

Goals and contents of this Research Topic "*Faults and Earthquakes Viewed by Networks, Monitoring Systems, and Numerical Modeling Techniques*" refer to recent research on earthquake processes which uses multidisciplinary approaches from geophysical, geochemical, geodetic, and geological parameters. Enhancing risk appraisal and prediction abilities is the most relevant disaster mitigation approach in seismically active locations. Multidisciplinary investigations of small-scale cracks in the laboratory and seismogenic features in field test locations have contributed to our comprehensive understanding of earthquake processes from preparation to faulting in recent decades. Pre-earthquake observations, methods, and perspectives can elevate our understanding of the processes preceding earthquakes. Modeling, which can be used to set up earthquake forecasting experiments, verifies test site areas of all sizes that are found globally in seismically active locations.

3 Overview of published contributions

This Research Topic compiles a total of 13 articles, involving geochemical and hydrogeological parameters in tectonically active areas (4 articles), ground deformations (2 articles), stress modeling (2 articles), source modeling (1 article), apparent resistivity of rocks (1 article), microseismic location (1 article), teleseismic location (1 article), and ground motion measurements (1 article).

3.1 High-potential precursors of earthquakes from geochemical and hydrogeological parameters

Li et al. examined the geochemical characteristics of fault zone gases and their implications for understanding fault activity and seismic events. Their study underscores the importance of isotope tracing in deciphering fluid sources, migration pathways, and the evolution of fault zones. Chen et al. assessed the sensitivity and validity of various geochemical parameters as monitoring and precursory tools in Beijing, a key seismic monitoring area.

Zhang et al. examined eight wells situated near the Longmenshan–Anninghe fault zone, which exhibit significant disparities in groundwater-level changes. The authors quantified the observed changes using the Molchan diagram and investigated potential factors influencing the changes using correlation analyses. Yang et al. analyzed five soil gas continuous monitoring stations to carry out observations of fault gas concentrations within the Yanqing fault zone. The results show that the time series of the hydrogen (H_2) gas concentration has a close relationship with local seismic activity and far-field strong earthquakes.

3.2 Ground deformation of earthquakes inferred from InSAR and GNSS measurements

Chen et al. introduced a novel fault co-seismic dislocation inversion method based on parallel elastic finite element simulations. The authors conducted inversion tests using various idealized fault models to validate their approach. Combining geodetic and seismological analyses, Lin et al. deduced that afterslip is the dominant mechanism of near- to intermediate-field post-seismic deformation and also likely represents the driving force that controls aftershock productivity and the spatiotemporal migration of seismicity.

3.3 Approaches to stress modeling using the proposed model and stress state

Xu and Zeng proposed a model to reveal the relationships between differential stress, seismicity, brittle–ductile transition, and boundary depth of the upper and lower crust in the continental crust and linked the multiple observations from geophysics and geology in Southeastern Tibetan Plateau. Lei et al. suggested that the high load/unload response ratio value before its decline may mark the end of the rock medium's yielding phase, and Outgoing Longwave Radiation data can reflect, to some extent, the state of tectonic stress accumulating along active faults in a critical condition.

3.4 Favored model for source modeling

De Lorenzo and Michele proposed a new technique and applied it to a small-magnitude earthquake (ML3.3) that occurred in Central Italy. They identified the most likely rupture models and examined the issue of correlation among model parameters.

For the investigated event, a circular crack model was resulted favored over a heterogeneous rupture model.

3.5 Extracting the anomalies of apparent resistivity of rocks

Lei et al. provided a reference framework for earthquake precursor studies by demonstrating how to quantitatively remove environmental interference in anisotropy analyses and how to avoid areas with large local influences.

3.6 High-precision microseismic location

Wu et al. proposed a high-precision location algorithm for 3D Fast Sweeping Method seismic sources to develop a small-scale regional microseismic location model for coal mines.

3.7 Fast automatic determination of teleseismic location

Yuan et al. proposed a fully automatic approach by integrating the advantages of seismic scanning based on navigated automatic phase-picking, which can automatically detect and locate seismic events from continuous waveforms, and the depth-scanning algorithm, which can determine the precise focal depth of local and regional earthquakes by matching depth phases. This method can be used to establish high-quality teleseismic catalogs and depth-phase databases.

3.8 Ground motion measurements using a dense array

Zhou et al. deployed a seismic array in Gongquan Town to observe seismic activities and analyzed the amplification effects in the area. The research results from weak-motion seismograms of aftershocks indicate significant seismic ground motion amplification in Gongquan Town. The observed phenomenon highlights the need to pay special attention to the risk of significant damage caused by the combined effects of extreme amplification in future earthquake mitigation efforts.

4 Discussion and perspectives

The advancement of geosciences is built upon modern observational methodologies. Utilizing extensive laboratory experiments, several scientists have demonstrated that earthquakes may be preceded by potential precursors that might aid in forecasting. The prolonged accumulation of previous events has provided insights into the mechanisms underlying the preparation of significant earthquakes. This volume contains several unique concepts that can elevate the knowledge of earthquake mechanisms. This Research Topic emphasizes the complex nature of seismic activity and has favored submissions that employ geophysical, geochemical, and geodetic techniques to elucidate the earthquake process from nucleation to manifestation. The scope includes innovative research utilizing observation networks and sophisticated numerical modeling that synthesizes diverse data. A critical re-assessment of the suggested methodologies, along with cutting-edge and innovative insights, may clarify favored avenues for research. The primary objective is to present an updated overview of existing information about the processes that precede earthquake occurrence. This information may be utilized to design earthquake forecasting experiments aimed at evaluating their accuracy across various geophysical settings.

Author contributions

GM: Conceptualization, Investigation, Writing – original draft, Writing – review and editing. FH: Writing – original draft, Writing – review and editing. CH: Writing – original draft, Writing – review and editing. YZ: Writing – original draft, Writing – review and editing. FG: Writing – original draft, Writing – review and editing.

Funding

The authors declare that no financial support was received for the research and/or publication of this article.

Acknowledgements

This Research Topic originates from expanding the influence of the annual conference on the China Earthquake Prediction Forum which was co-sponsored by the Earthquake Prediction Committee of the Seismological Society of China and the Department of Monitoring and Prediction of the China Earthquake Administration. The editors wish to thank all the authors who contributed their manuscripts and reviewers who contributed their time and expertise to reviewing the manuscripts.

Conflict of interest

The authors declare that the research was conducted in the absence of any commercial or financial relationships that could be construed as a potential conflict of interest.

The authors declared that they were an editorial board member of Frontiers, at the time of submission. This had no impact on the peer review process and the final decision.

Generative AI statement

The authors declare that no Generative AI was used in the creation of this manuscript.

Any alternative text (alt text) provided alongside figures in this article has been generated by Frontiers with the support of artificial intelligence and reasonable efforts have been made to ensure accuracy, including review by the authors wherever possible. If you identify any issues, please contact us.

Publisher's note

frontiers | Frontiers in Earth Science

TYPE Original Research
PUBLISHED 16 July 2024
DOI 10.3389/feart.2024.1428167

OPEN ACCESS

EDITED BY
Caibo Hu,
University of Chinese Academy of Sciences, China

REVIEWED BY
Yong Zhang,
Peking University, China
Yujun Sun,
Chinese Academy of Geological Sciences, China

*CORRESPONDENCE
Salvatore de Lorenzo,
salvatore.delorenzo@uniba.it

RECEIVED 05 May 2024
ACCEPTED 17 June 2024
PUBLISHED 16 July 2024

CITATION
de Lorenzo S and Michele M (2024), An EGF technique to infer the source parameters of a circular crack growing at a variable rupture velocity.
Front. Earth Sci. 12:1428167.
doi: 10.3389/feart.2024.1428167

An EGF technique to infer the source parameters of a circular crack growing at a variable rupture velocity

Salvatore de Lorenzo [1]* and Maddalena Michele [2]

[1]Dipartimento di Scienze della Terra e Geoambientali, Università di Bari "Aldo Moro", Bari, Italy, [2]Istituto Nazionale di Geofisica e Vulcanologia, Roma, Italy

Circular crack models with a constant rupture velocity struggle to effectively model both the amplitude and duration of first P-wave pulses generated by small magnitude seismic events. Assuming a constant rupture velocity is unphysical, necessitating a deceleration phase in the rupture velocity to uphold the causality of the healing process. Moreover, a comprehensive failure model might encompass an initial nucleation phase, typically characterized by an increase of the initial rupture velocity. Studies have demonstrated that quasi-dynamic circular crack models featuring variable rupture velocities can accurately model the shape of the observed first P-wave pulse. Based on these principles, an Empirical Green's function (EGF) approach was previously formulated to estimate the source parameters of small magnitude earthquakes, called MAIN. In addition to determine the source radius and stress drop, this method also enables the inference of the temporal evolution of rupture velocity. However, this method encounters difficulties when the noise-to-signal ratio in the recordings of smaller earthquakes used as EGF exceeds 5%, a common situation when employing regional-scale recordings of small-magnitude earthquakes as EGF. Through synthetic tests, we demonstrated that, in such instances, the problem of this technique is that the alignment between the onset of P waves of EGF and MAIN is not rightly recovered after the initial inversion step. Consequently, a novel inversion method has been developed to address this issue, enabling the identification of the optimal alignment of P-wave arrivals in EGF and MAIN across all stations. A Bayesian statistical approach is proposed to meticulously investigate the solutions of model parameters and their correlations. Using the new technique on a small magnitude earthquake (M_L = 3.3) occurred in Central Italy enabled us to identify the most likely rupture models and examine the issue of correlation among model parameters. Application of Occam's Razor Principle suggests that, for the investigated event, a circular crack model should be favored over a heterogeneous rupture model.

KEYWORDS

circular crack, variable rupture velocity, empirical Green's function, nucleation and deceleration phase, Bayesian statistics

1 Introduction

When an earthquake occurs, the available energy is partitioned between the radiated energy and the fracture energy (i.e., the energy lost to the heating and plastic deformation

accompanying the rupture growth) (Madariaga, 1976). Depending primarily on the frictional forces along the fault, the rupture may then grow at low or high rupture velocity. The slower the rupture velocity V_r, the less available energy is radiated (Boatwright, 1980). Moreover, the changes in rupture velocity are responsible for the high-frequency damaging waves (Madariaga, 1977). Thus, rupture velocity and its evolution are crucial parameters for understanding earthquake physics and assessing seismic hazard in a tectonic region.

In studies aimed at inferring the source parameters from the inversion of seismic spectra, rupture velocity is generally assumed to be less than the shear wave velocity V_S. However, numerous recent studies suggest that assuming a sub-shear rupture velocity regime ($V_r < V_S$) may be incorrect. Indeed, many large magnitude earthquakes are characterized by a super-shear rupture velocity regime (e.g., Bouchon and Vallée, 2003; Wang et al., 2016; Chounet et al., 2018).

As concerns the small magnitude earthquakes, a minor number of studies have been dedicated to accurately estimating the rupture velocity. In these cases, in fact, the correlation among source parameters may strongly bias the obtained results (see Abercrombie, 2021 for an overview of the challenges related to source parameter estimation). Therefore, it is crucial to further develop methods aimed at precisely determining the rupture velocity of small magnitude earthquakes. Since a kinematic circular crack model rupturing at a constant velocity may yield biased estimates of rupture velocity, stress drop and source dimension, owing to their correlation (Deichmann, 1997; Chounet et al., 2018; Abercrombie, 2021), it is essential to investigate whether the use of quasi-dynamic circular crack models with variable rupture velocity can assist in better constraining these parameters. Including a variable rupture velocity has indeed been shown to be necessary to effectively model both the rupture duration and amplitude of the first P-pulses of small magnitude earthquakes, a task where constant rupture velocity models are insufficient (Deichmann, 1997). Furthermore, while correlations among model parameters may be inevitable when using earthquake recordings from only one or few stations, it is expected that these tradeoffs can be reasonably mitigated when a larger number of recordings, covering various azimuths and distances, are included. The worldwide increase in the availability of high-quality recordings of small earthquakes at a regional scale now provides the opportunity to assess whether quasi-dynamic circular crack models can accurately reproduce the main properties of the energy radiated by a small magnitude earthquake.

Based on these grounds, in this article we propose an improvement of a previously developed technique (de Lorenzo et al., 2008 in the next referred to as DFB) designed to deduce the source parameters of a small magnitude earthquake. The technique assumes that the rupture follows the quasi-dynamic behavior of the Sato (1994) model. The new formulation of the inverse method allows to use also seismic recordings characterized by a noise-to-signal ratio greater than 10%, as it is commonly observed on low-pass filtered traces of seismic recordings of small earthquakes ($M_L < 2$) recorded at a regional scale (source-to-receiver distances less than 100 km).

2 Materials and methods

In this section, we begin by outlining the theoretical basis of the circular crack model considered in this study. Subsequently, we provide a concise overview of the inversion method introduced by DFB, followed by an explanation, illustrated through a synthetic test, of the necessity for modifying this method. Finally, we describe the new technique for inferring source model parameters.

2.1 Kinematic and quasi-dynamic source models

The representation theorem (Aki and Richards, 2002) constitutes the general form of the equations describing the displacement at a point inside an elastic medium, due to the forces acting in a source volume. It shows that the content of a seismic recording is described by two tensors. The first one is the Green's tensor, i.e., the response of the medium to impulsive point forces located at the hypocenter of the earthquake. The second one is the seismic moment tensor, that describes the complex system of body forces acting in the source volume. The aim of seismic source studies is therefore reconducted to infer the shape of the source time function, i.e., the moment rate function $\dot{M}(r,t)$ of the couples of forces acting at the sides of the fault plane (e.g., Madariaga, 2007):

$$\dot{M}(r,t) = \mu \iint \Delta\dot{u}\left(t - \frac{r}{c}\right) dS \tag{1}$$

where the integral is computed on the ruptured surface Σ, $\Delta\dot{u}$ is the slip rate on the fault and μ is the rigidity of rocks on the fault plane. The integral of $\dot{M}(r,t)$ (Eq. 1) over the time is an invariant of the rupture process, representing the seismic moment of the forces acting in the source volume. Since the functional form of $\dot{M}(r,t)$ is known to depend on the take-off angle θ (i.e., the angle formed by the ray leaving the source with the normal to the fault plane), $\dot{M}(r,t)$ is sometimes called the apparent moment rate function (AMRF) or the apparent source time function (ASTF). The inverse problem of earthquake source mechanics consists therefore of analyzing seismograms to obtain the details of the earthquake rupture process, but this problem is known to be unstable and dependent on the adopted source model, often requiring additional constraints to stabilize it (Das, 2015).

In the kinematic rupture models the slip function is prescribed on the fault. Simple kinematic circular crack models with a constant stress on fault and rupturing at a constant rupture velocity (e.g., Brune, 1970) are considered unable to furnish reliable estimates of source parameters (Abercrombie, 2021). There are several possible explanations for this disagreement, such as the heterogeneity of the friction on the fault plane and/or the non-circular geometry of the final ruptured area. However, another less considered explanation is that the kinematic models do not account for the evolution of the rupture velocity during the rupture process (e.g., Deichmann, 1997; Madariaga and Ruiz, 2016).

The first simple but complete kinematic model, consisting of a circular crack rupturing at a constant velocity, was proposed by Sato and Hirasawa (1973). This model reproduces the general properties of the waves radiated during an earthquake, such as focusing, directivity and stopping phases (e.g., Madariaga, 2007). According

to Boatwright (1980), the Sato and Hirasawa (1973) circular crack is a quasi-dynamic model, in that the slip function complies at each time with the theoretical solution to the static problem of a circular crack (Eshelby, 1957). From a theoretical point of view, the main limit of this model is represented by the instantaneous non-causal freezing of the rupture once the rupture front reaches the border of the circular fault (Madariaga, 2007). To evaluate what happens in the interior of the fault when the rupture stops, it was then necessary to solve the dynamical problem. The solution to this problem was found by Madariaga (1976). He demonstrated that, when the rupture reaches the border, the rim of the fault generates P, S and Rayleigh healing waves that propagate inward from the border. The passage of these waves progressively reduces **to zero slip rate** in the interior of the fault allowing a causal healing of the rupture.

Based on these findings, Boatwright (1980) developed two quasi-dynamic models aimed at overcoming the limit of the Sato and Hirasawa (1973) model. These two models enclose into an analytical formulation the continuous decrease of the slip-rate on the fault. In the first one, known as the decelerating D-model, an initial constant rupture speed propagation phase is followed by a linear decrease to zero of rupture velocity, leading to a progressive decrease of slip rate on the fault (Figure 2 of Boatwright, 1980). The second one is the M-model, which is a simplified analytic representation of the slip rate evolution discovered by Madariaga (1976). The M-model exhibits a similar trend, with a more pronounced decrease in slip rate after the rupture stops (Figure 3 of Boatwright, 1980).

Quasi-dynamic analytical models that include variations in rupture velocity play a crucial role in formulating models for estimating source parameters from the inversion of P and/or S waveforms observed during seismic radiation. These models use closed analytical forms of the slip function, enabling simpler numerical schemes compared to the finite difference solutions used in dynamic problem simulations. The most complete analytical model of circular crack was proposed by Sato (1994), which incorporated the decelerating phase introduced by Boatwright (1980) into a three-stage rupture velocity history. In the Sato (1994) model, the rupture velocity initially increases to simulate the low moment rate nucleation phase (e.g., Ellsworth and Beroza, 1998). This acceleration phase is followed by a constant rupture velocity phase and then by a final linear decrease to zero of rupture velocity (Vr), according to Boatwright (1980) D-model (see Figure 1).

The analytical expressions of the AMRF found by Sato (1994) is:

$$\dot{M}_c(t) = \frac{12}{7}\Delta\sigma\frac{c}{\sin\theta}\left[L_a^2(t) - L_b^2(t)\right] \tag{2}$$

where $L_a(t)$ and $L_b(t)$ represent the distance, from the center of the fault, of the two points of the isochrone (Bernard and Madariaga, 1984) nearest and farthest from the receiver. This dependence of the AMRF on specific points of isochrone explains the reason why the quasi-dynamic models reproduce the ubiquitously observed stopping phases (for a discussion see Madariaga, 2007). In Eq. 2, c is the phase velocity of considered body waves, θ is the take-off angle between source and receiver. θ depends on dip and strike of the fault plane (e.g., Zollo and de Lorenzo, 2001). Assuming that fault plane orientation is known, as supposed in this study, calculating the AMRF requires assigning five model parameters, referred to as the model parameter vector:

$$\boldsymbol{m} = \left(L, \Delta\sigma, \frac{Vr_{max}}{V_S}, \frac{t_1}{T}, \frac{t_2}{T}\right) \tag{3}$$

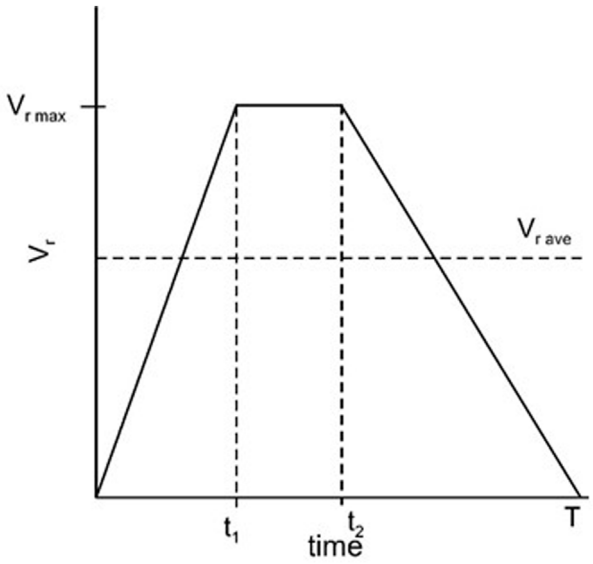

FIGURE 1
Plot of the rupture velocity history considered in this article. The nucleation phase corresponds to the initial accelerating phase from 0 and t_1; the decelerating phase occurs from t_2 and T.

In this expression, L is the radius of the final crack, $\Delta\sigma$ the dynamic stress drop, Vr_{max} the maximum value of rupture velocity, V_S the shear wave velocity at the source, t_1 the duration of acceleration phase, t_2 the starting time of the deceleration phase and T is the total duration of the rupture process (Figure 1). It can be easily shown that:

$$Vr_{ave} = \frac{Vr_{max}}{2}\left(1 + \frac{t_2}{T} - \frac{t_1}{T}\right) \tag{4}$$

In Eq. 4 Vr_{ave} is the average rupture velocity. As shown in DFB, the expression of AMRF for P-waves holds in all the subsonic regime, i.e., $Vr_{max} < V_P$, therefore including the super-shear regime, i.e., $V_s < Vr_{max} < V_P$.

2.2 The limits of the starting EGF technique

One of the most used methods for inferring the AMRF of an earthquake is the Empirical Green's Function (EGF) method (Hartzell, 1978). This method involves approximating the Green's function with the recording of a small magnitude earthquake, referred to as the EGF, which is co-located with the earthquake of interest and has the same focal mechanism. In the original EGF method the AMRF is estimated by dividing the spectrum of the MAIN by the spectrum of the EGF. To mitigate the numerical instability caused by spectral division, the first improvement to the original technique was the use of a water-level criterion (e.g., Mueller, 1985). Recent advancements in this technique (e.g., Bertero et al., 1997; Vallée, 2004) have introduced positivity constraints and the conservation of seismic moment, further reducing the instability associated **with spectral division**.

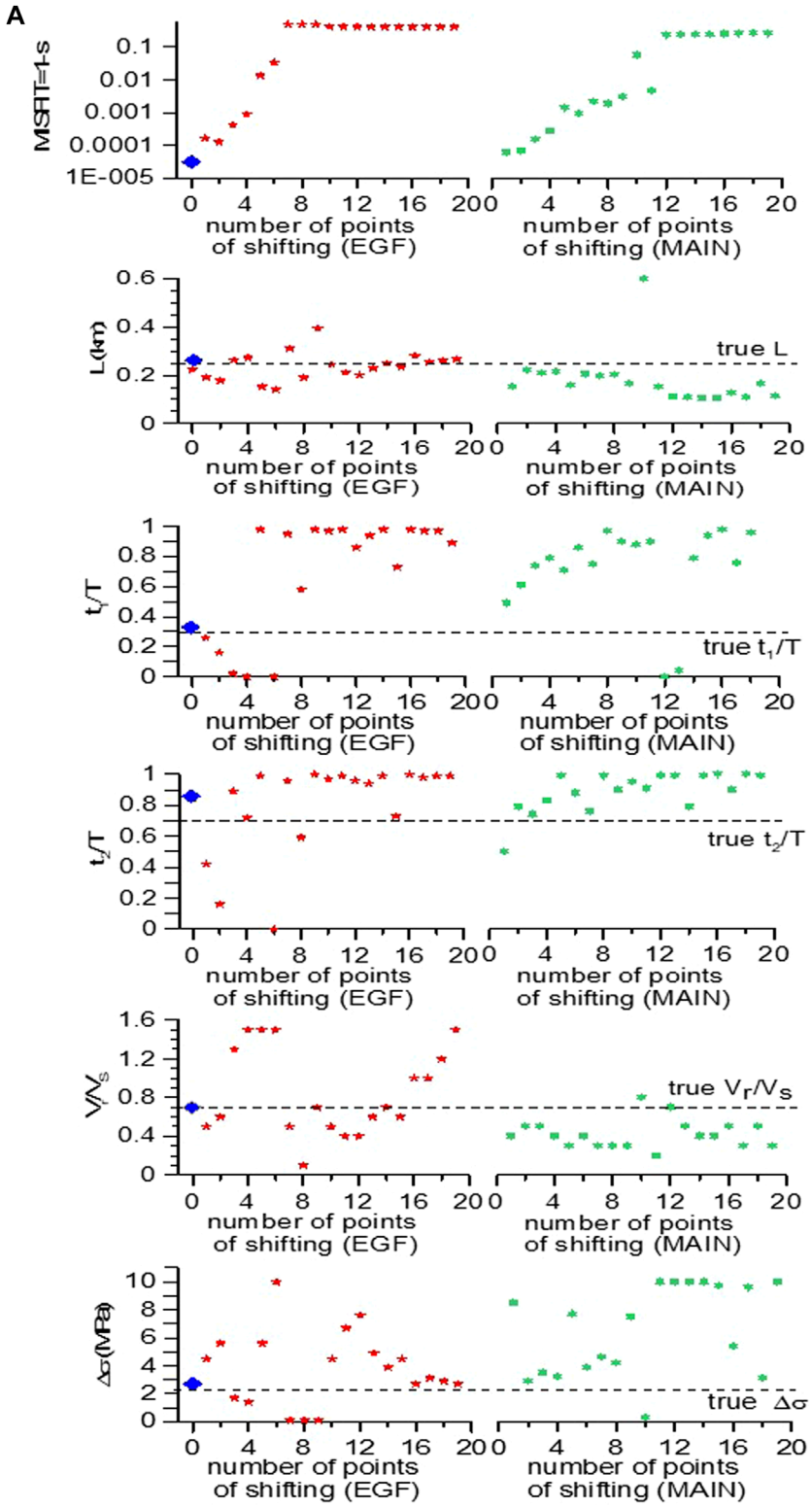

FIGURE 2
(Continued).

To address the instability issues associated with spectral deconvolution an alternative EGF approach, based on convolution rather than deconvolution, was also developed (e.g., Zollo et al., 1995; Shibazaki et al., 2002). This approach involves assuming the functional form of the AMRF and formulating an inverse problem for the inference of the AMRF model parameters.

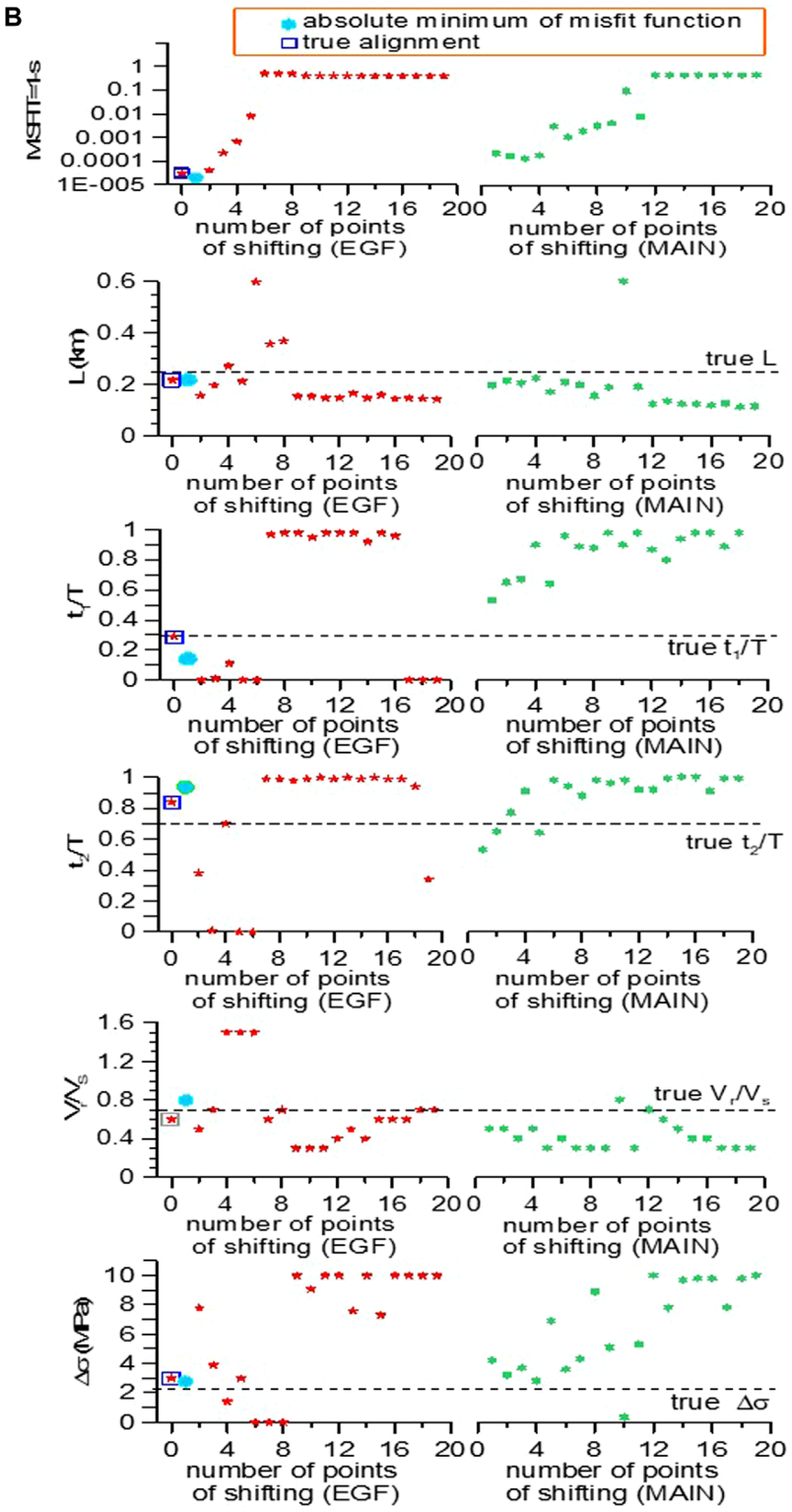

FIGURE 2
(Continued). **(A)** Inversion results for test1. Red points represent the inversion results obtained by back shifting the EGF with respect to the initial alignment. Green points represent the inversion results obtained by back shifting the MAIN with respect to the initial alignment. The blue rhombus represents the solutions for the true alignment between the onset of the MAIN and the EGF, that, in this case, coincides with the best fit solution. **(B)** Inversion results for test2. Red points represent the inversion results obtained by back shifting the EGF with respect to the initial alignment. Green points represent the inversion results obtained by back shifting the MAIN with respect to the initial alignment. The blue rectangles represent the solutions for the true alignment between the onset of the MAIN and the EGF, that do not coincide, in this case, with the best fit solutions, represented by the cyan circles.

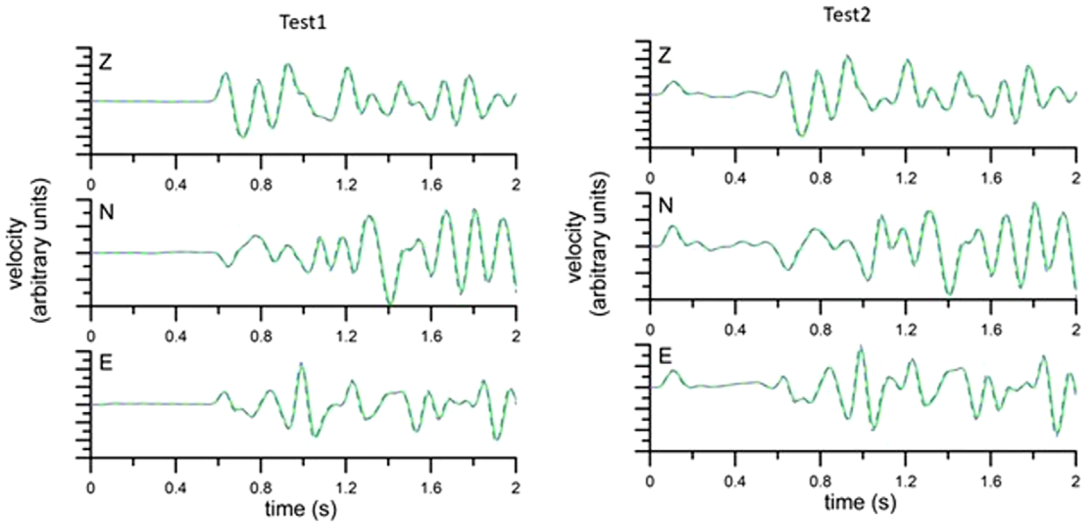

FIGURE 3
Matching between observed and theoretical synthetic waveforms for the two synthetic tests. Green lines represent the synthetic observed waveforms. Blue lines represent the synthetic retrieved waveforms.

As concerns small magnitude earthquakes, DFB developed a similar EGF technique, assuming the AMRF derived from the Sato (1994) model described earlier. They applied the technique to model the seismic radiation of some earthquakes of the 1997 Umbria-Marche seismic sequence, but using only high-quality recordings as EGF, i.e., seismograms of small magnitude earthquakes characterized by a noise-to-signal ratio less than 5%.

In this article, we aim to demonstrate how the inverse problem developed by DFB needs modification to enable the use of EGFs recorded at a regional scale (source-to-receiver distance less than 100 km), which typically have noise-to-signal ratios exceeding 10%. The new technique utilizes the same theoretical framework as the DFB method, which we will briefly summarize here.

Let us consider a mainshock (referred to as the MAIN) and a smaller magnitude earthquake recorded at M seismic stations: $S_1, \ldots, S_M$. We assume that all the assumptions of the EGF technique are met, meaning that the smaller earthquake is either co-located with the MAIN or is located at a short distance from it, and shares a similar focal mechanism with the MAIN. Under these hypotheses, we can consider the recordings of the smaller earthquake to be representative of the Green's function of the MAIN and can therefore be used as Empirical Green's functions (referred to as the EGF) (Hartzell, 1978). For a station located at a distance r from the MAIN, using the representation theorem, the theoretical seismogram is then computed as:

$$\boldsymbol{U_i^{teo}(r,t) = \dot{M}_c(t,m) * EGF_i(r,t) \quad i = x,y,z} \tag{5}$$

where the symbol $*$ indicates the time domain convolution and $\dot{M}_c(t,m)$ is computed using Eq. 2. The problem consists of searching the model vector, denoted as $\boldsymbol{m}$ in Eq. 3 that minimizes the misfit between the observed and the theoretical seismogram, computed using Eq. 5. The misfit M between the observed and the theoretical waveforms is computed in the time domain as $M = 1\text{-}s$, where s, known as the semblance, is an operator that quantifies the degree of similarity between two signals and ranges between 0 and 1. If $s = 1$ (ideal case) the two signals are coincident; if $s = 0$ the two signals are equal and opposite or very different (for details see DFB). Using time-domain data effectively doubles the amount of information available for spectral analysis.

The search for the optimal model parameters is performed using the Simplex Downhill method (Press et al., 1989), which is a highly efficient technique for exploring the model parameter space in nonlinear inverse problem, as shown also in other studies (e.g., Zollo and de Lorenzo, 2001 and references therein). The synthetic tests described in DFB suggest that the inversion method is robust and effective when dealing with data characterized by low noise N to signal S ratio (N/S less than 5%). The inversion scheme proposed by DFB is based on two steps:

In the initial step of the inversion process, a single-station inversion is performed at each available seismic station, allowing to estimate the best-fit model parameter vector for that station. Since the inversion is performed in the time domain, it is necessary to determine the optimal alignment between the onset of the first P-wave arrival of the Empirical Green's Function (EGF) and the mainshock (MAIN), after both signals are filtered below the corner frequency of the EGF, as prescribed by the technique (Hartzell, 1978). However, due to the application of **generally used** non-causal low-pass filter, the onset of the filtered P-waves from both MAIN and EGF may become misaligned. Additionally, the onset of the P-wave in the EGF could be masked by noise due to the small size of the EGF. Moreover, the P-wave onset in the MAIN, particularly during the nucleation phase of the rupture process, may be gradually emergent, making it challenging to identify.

To address these challenges, DFB proposed conducting 2 N_{sh} inversions, where N_{sh} represents the number of shifts considered. This involves testing each possible backward shift in time $E^j dt\left(E^j = 1, N_{sh}\right)$ of the EGF relative to the onset of the MAIN, and each possible backward shift in time $M^j dt\left(M^j = 1, N_{sh}\right)$ of

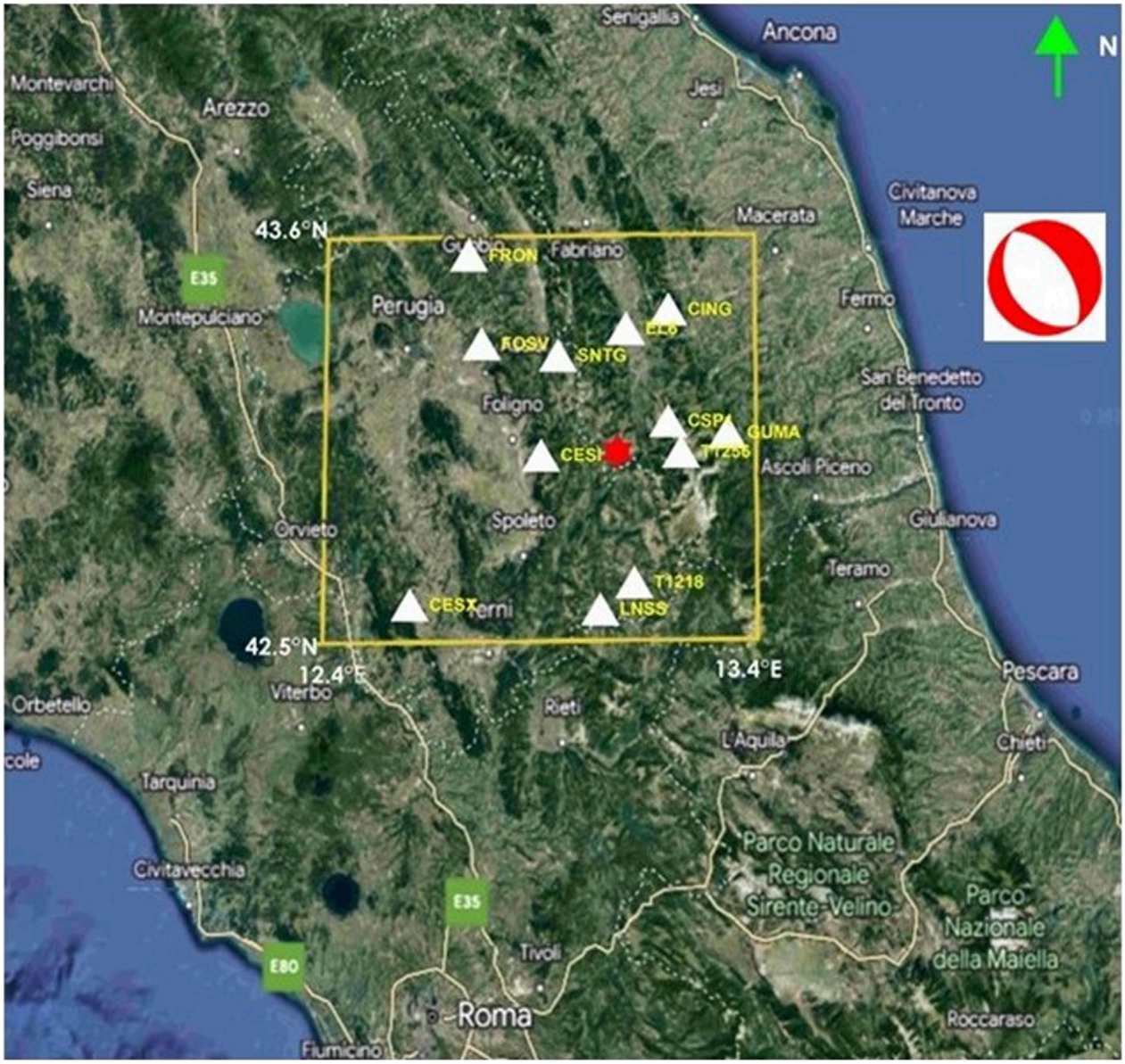

FIGURE 4
Location of the events and seismic stations considered in this study. The red star indicates the epicenters of MAIN and EGF. The white triangles indicate the seismic stations used in the inversion of source parameters. The station names are reported in yellow characters. The focal mechanism of the MAIN is also shown.

the MAIN relative to the onset of the EGF, with dt representing the sampling time. This approach aims to identify the optimal alignment within a time window equivalent to 2 $N_{sh}dt$, determined by minimizing the misfit among all the obtained 2 N_{sh} alignments. In our new inversion scheme, we retain this step from the DFB inversion method, using N_{sh} =20. This choice spans an overall range of alignments equal to 2 $N_{sh}dt$ = 0.4 s for signals sampled at dt = 0.01 s. This approach allows for a comprehensive search for the optimal alignment to improve the accuracy of the inversion results.

In the second step of the DFB inversion, the joint inversion of EGF-MAIN pairs from all seismic stations is conducted, with each pair's optimal alignment fixed at the value determined in the first step. Notably, the station estimates of model parameters obtained in the first step are disregarded in the second step of the DFB procedure. Due to the nonlinear nature of the equations linking model parameters and data, DFB employed the random deviates approach to estimate errors on model parameters. Through a robust analysis using synthetic and real EGF data, DFB demonstrated that the effectiveness of the inversion technique in recovering true model parameters is highly dependent on the level of noise in the data. When the noise-to-signal (N/S) ratio is less than 5%, stable estimates and reliable AMRF are obtained (Figure 5B of DFB). Conversely, when $N/S \geq 10\%$, multiple solutions are inferred (Figure 5C of DFB), resulting in a reduced resolution of the AMRF model parameters. The difficulties arise because, at higher noise levels ($N/S \geq 10\%$), the increased noise amplitude can introduce spurious oscillations

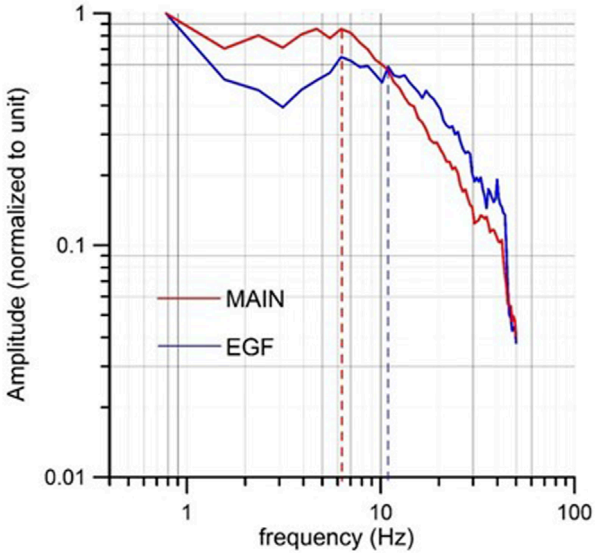

FIGURE 5
Average common spectrum of the MAIN and the EGF. The vertical shadow lines intercept, on the horizontal axis, the corner frequency of the two events.

TABLE 1 Noise to signal ratio of EGF and MAIN for the two synthetic tests.

Waveform	*N/S* (%) (Test1)	*N/S* (%) (Test2)
EGF (E)	3.5	18
EGF (N)	4.4	34
EGF (Z)	1.8	14

around the first P-wave pulse of the EGF. When convoluted with the AMRF, these oscillations may produce theoretical signals that incorrectly align with the observed P-wave pulses. Therefore, DFB limited the application of this method to a small number (two or three) of MAIN-EGF pairs from select seismic events to mitigate these issues.

2.3 A synthetic test with a real noisy EGF

A robust synthetic study to evaluate the reliability of the results for the single station inversion (first step) has been already conducted in DFB, where both the effect of a different location of MAIN and EGF, the uncertainty in focal mechanisms and many other aspects were analyzed through synthetic tests. Obviously, those results remain still valid.

To elucidate the necessity for modifying the DFB inversion strategy in the presence of noisy waveforms ($N/S \geq 10\%$), we present the results of its application in two synthetic tests, using three-component recordings at the seismic station CSP1 of a small earthquake (M_L = 1.9) occurred in Central Italy. The waveforms exhibit a low noise-to-signal ratio (N/S), as detailed in Table 1.

In test1, after the application of a low-pass filter to the EGF below the corner frequency (fc=10 Hz) we estimated a noise-to-signal ratio $N/S \leq 5\%$ (Table 1). The observed synthetic mainshock was computed using Eq. 5 with the following model parameters:

$$\mathbf{m} = \left(L, \Delta\sigma, \frac{V_{r_{max}}}{V_S}, \frac{t_1}{T}, \frac{t_2}{T}\right) = (.25\,\mathbf{km}, 2\,\mathbf{MPa}, 0.7, 0.3, 0.7) \quad (6)$$

The results of the first step of inversion are summarized in Figure 2A. All parameters are accurately recovered with minimal uncertainties, which could also be addressed using the random deviates technique, as discussed in DFB. It is worth to note that, in this case, the true alignment between the onset of P-waves of the MAIN and EGF is correctly identified after the inversion. In fact, the absolute minimum of the misfit function corresponds to this alignment (i.e., zero shift of the EGF relative to the MAIN).

In test2, to simulate a scenario with a noisiest EGF, we added to the EGF a random noise obtained as a linear combination of random sinusoidal waves with frequencies f_i lying inside the frequency band of the EGF:

$$N(t) = \sum_{i=1}^{N} A_i cos(2\pi f_i t) + B_i sin(2\pi f_i t) \quad (7)$$

Using Eq. 7, the noise-to-signal ratio of the EGF was increased above 10%, as detailed in Table 1. The same model parameters of test1 (Eq. 6) were used to compute the observed synthetic mainshock. The results of the first step of inversion are depicted in Figure 2B. The source parameters exhibit slightly higher uncertainty compared to test 1, which can be mitigated using the random deviates technique as discussed in DFB. However, the most significant issue arises from the erroneous alignment between the onset of P-waves of the EGF and MAIN inferred from the inversion. We discuss in the next section the reason why this problem may severely impede to find the optimal model parameter solution when using the recordings of the EGF and MAIN at several stations. The excellent waveform fitting in both tests is illustrated in Figure 3, highlighting a strong a correlation among the source parameters that enables accurate reproduction of the observed seismogram even with small differences of the model parameters from their true values.

2.4 The new formulation of the inverse problem

In the DFB inversion process, the second stage involves identifying the optimal model parameters by keeping the P-wave onset alignments of EGF and MAIN fixed at the values obtained in the first stage. However, when $N/S \geq 10\%$, the recovered alignments may be inaccurate, and combining these inaccuracies across multiple stations can hinder the search for the absolute minimum of the misfit function. This observation is not mere speculation; it derives from several trials we conducted using both synthetic and real data.

Therefore, the only feasible approach to proceed with the second stage of DFB inversion would be to conduct multiple inversions, each incorporating a different combination of alignments. Unfortunately,

this problem exhibits exponential complexity. In fact, if M_s represents the number of stations, exploring all the possible combinations of alignments requires an enormous number $N_{inv} = (2N_{sh})^{Ms}$ of inversions at the second step, one for each combination of alignments of EGF and MAIN of all the stations. The scale of this task becomes practically unmanageable when dealing with many stations, typically on the order of ten or several tens, even when leveraging parallel computing and/or reducing N_{sh} to a smaller value (e.g., from 40 to 10). For instance, if we have M_s = 12 stations, we should perform $N_{inv} = (2N_{sh})^{M_s} = 10^{12}$ inversions, which is computationally prohibitive.

Based on these new findings, we have opted to replace the second step of the inversion process of DFB with an alternative approach, which is inspired by techniques used to reconstruct slip functions on faults for cases involving heterogeneous ruptures (e.g., Festa and Zollo, 2006). In such cases, solutions obtained from the first step of single station inversion are used to construct the final solution, whereas they were ignored in the DFB scheme.

In the new approach, we aim to assess which solution from the first inversion step best represents the source process. To do this, for each of the station solutions found at the first step we must first evaluate the misfit at the remaining stations. Given our observation that the optimal alignment between MAIN and EGF is unreliable with noisy seismograms (Figure 2B), we must compute the misfit function for every possible alignment of EGF-MAIN pairs at all other stations. In this way we can select the station solution that gives rise to the overall minimum misfit. From a computational point of view, we observe that, for each of the M_S model parameter solutions inferred at the first step, we need to select, at the others M_S-1 stations and among the $2N_{sh}$ possible alignments, the optimal alignment of MAIN and EGF. This approach requires computing $2N_{sh}$ (M_S-1) values of the misfit function. This procedure has to be repeated for all the M_S model parameter solutions inferred at the first step. This implies that the number of forward models to be computed is now $2N_{sh}(M_S - 1)M_S$. The complexity of the problem is now quadratic relative to the number of stations and can be executed on a personal computed within a brief computation time. Therefore, this second step enables us to determine the optimal alignments of all MAIN-EGF pairs and also to infer an initial solution of the model parameters.

Owing to the nonlinear form of the inverse problem, the uniqueness of the solution is however not guaranteed. A further exploration of the whole model parameter space is then required to find the model parameter solution which corresponds to the absolute minimum of the misfit function. This third and final step, moreover, is required also to analyze the correlation among model parameters that can result in multiple solutions. Instead of using the empirical approach based on random deviates, this step is now realized through a grid-search method, based on a modified Bayesian formulation of the inverse problem as proposed by Hu et al. (2008). The probability density function (pdf) of a model m given the measured data d, $\sigma(m|d)$, is expressed as follows:

$$\boldsymbol{\sigma(m|d) = p(d|m)p(m)} \tag{8}$$

where $p(d|m)$ is the pdf of d for the given m and $p(m)$ is the *a priori* pdf for the model. In our case, the only available *a priori* information on model parameters can be derived from the magnitude and the corner frequency of the earthquake. From the corner frequency f_c of the mainshock, we can compute an initial estimate of the source dimension can be obtained, using, e.g., the Madariaga (1976) circular crack model:

$$\boldsymbol{L = \frac{0.32\, V_S}{f_c}} \tag{9}$$

Moreover, if a M_L vs. M_0 relationship is available, a preliminary estimate of M_0 can be obtained from M_L, and therefore a preliminary estimate of the stress drop can be inferred, using the relationship (Eshelby, 1957):

$$\boldsymbol{\Delta\sigma = \frac{7}{16}\frac{M_0}{L^3}} \tag{10}$$

The preliminary estimates are often derived from previous studies based on the assumption of a constant rupture velocity model. As a result, the preliminary information can be used only to define a range of admissible values for $\Delta\sigma$ and L. Regarding the geometry of the seismic source, because the fault plane orientation is fixed in the inversion process, there is no need to impose any *a priori* information on the takeoff angle of AMRF. We therefore assume an *a priori* uniform distribution of model parameters inside V_1, i.e.,:

$$\boldsymbol{p(m) = \begin{cases} 1\, if\, m \in V_1 \\ 0\, if\, m \notin V_1 \end{cases}} \tag{11}$$

where:

$$\boldsymbol{V_1: \begin{cases} \Delta\sigma_{min} \le \Delta\sigma \le \Delta\sigma_{max} \\ L_{min} \le L \le L_{max} \\ 0 < V_r \le V_P \end{cases}} \tag{12}$$

In Eq. 12 $[\Delta_{\sigma min}, \Delta_{\sigma max}]$ and $[L_{min}, L_{max}]$ are the ranges of *a priori* admissible values of stress drop and source radius.

As concerns the pdf, Hu et al. (2008) showed that $p(d|m)$ can be approximated with the following likelihood function $\theta(d|m)$:

$$\boldsymbol{p(d|m) = \theta(d_{obs}|m) = exp(-E(m))} \tag{13}$$

In Eq. 13 $E(m)$ is an error function, assumed to be coincident with M, the complementary value of the semblance: $E(m) = M = 1 - s$. In the single station inversion, we used the same error function $E(m)$. We note that, with this choice, $\theta(d_{obs}|m)$ is rightly equal to 1 for the ideal case of zero misfit (s = 1). However, when the signals u_i^{obs} and u_i^{teo} are equal and opposite, but also when $u_i^{obs} \gg u_i^{teo}$ or when $u_i^{obs} \ll u_i^{teo}$, it results s = 0 and M = 1, at which does not correspond $\theta(d_{obs}|m) = 0$ but $\theta = e^{-1}$. To normalize the likelihood function in order to obtain θ = 0 when s = 0, the following linear transformation has to be performed:

$$\boldsymbol{\theta(d_{obs}|m) = \frac{1}{1-e}(1 - \exp(1 - M))} \tag{14}$$

Using Eq. 14, the above expression Eq. 8 becomes:

$$\boldsymbol{\sigma(m|d) = \frac{\theta(d_{obs}|m)}{\int_{V_1}\theta(d|m)dm} = \frac{\frac{1}{1-e}(1 - \exp(1 - M))}{\int_{V_1}\left[\frac{1}{1-e}(1 - \exp(1 - M))\right]dm}} \tag{15}$$

TABLE 2 Local magnitude, origin time and geographic coordinates of the hypocenter of MAIN and EGF. The focal mechanism solutions of the mainshock are also reported.

	ML	Origin time (y-m-d h:m:sec)	Latitude (°)	Longitude (°)	Depth (km)	Dip (°)	Strike (°)	Rake (°)
MAIN	3.3	2016-11-19 01:12:37.981	43.01°	13.08°	7.9	35	145	−90
						325	55	270
EGF	1.9	2016-11-19 01:47:10.641	43.01°	13.08°	9.2			

To account for the different level of noise on data at each station, M is computed as the weighted sum of the complementary semblances M_i, with $i = 1,\ldots N_S$:

$$\boldsymbol{M_i = 1 - s_i} \tag{16}$$

through the equation:

$$\boldsymbol{M} = \frac{\sum_{i=1}^{N_s} \boldsymbol{w_i M_i}}{\sum_{i=1}^{N_s} \boldsymbol{w_i}} \tag{17}$$

In Eq. 16 *si* represent the single station semblances, whereas in Eq. 17 the weights are computed using the rule:

$$\boldsymbol{w_i} = \frac{\mathbf{1}}{\left[\left(\frac{N}{S}\right)_{EGF_i} + \left(\frac{N}{S}\right)_{MAIN_i}\right]^2} \tag{18}$$

In Eq. 18 (N/S) Main, i and (N/S)EGF, I represent, respectively the noise-to-signal-ratio of Main and EGF. After inferring the most probable solution, a final test, based on the Occam Razor principle (Akaike, 1973), will be conducted to determine whether the source model obtained from the inversion of all the data is preferable to the heterogeneous source model inferred in the initial step.

3 Application to a real case

To show how the method works, we will analyze a pair of EGF-MAIN events that were recorded during the seismic sequence that occurred in the Central Italy in 2016. This sequence was initiated by a $M_W = 6$ earthquake occurred on 24 August 2016 (Chiaraluce et al., 2017) and persisted for several months, generating over one hundred earthquakes daily (Michele et al., 2016; Chiaraluce et al., 2022). The MAIN **($M_L = 3.3$)** and EGF **($M_L = 1.9$)** events were located close to each other near the small town of Fiordimonte (MC). They represent a couple of double-difference relocated earthquakes (Waldhauser and Ellsworth, 2000) from the Michele et al. (2020) catalog. The absolute locations of the MAIN and the EGF were obtained from the CLASS catalog (Latorre et al., 2023), while the focal mechanism of MAIN, as reported by Malagnini and Munafò (2018), is summarized in Table 2 and shown in Figure 4. Both events exhibit similar focal mechanisms, which was evident from the coincidence of P-wave polarities observed at nearly all the stations.

In our data selection process, we focused on seismic stations located within 100 km of the event epicenters (Table 3). Among these stations, we selected twelve three-component recordings characterized by a clear onset of the first P-wave of the EGF and waveform similarities between EGF and MAIN, as required by the assumptions of the EGF technique.

To include the possibility that rupture occur in a supershear regime (Vs.≤Vr) the present method can be applied only to P-waves and their coda. DFB showed in fact that the range of applicability of the Sato (1994) is the subsonic regime (Vs.≤Vr≤Vp) only when using P-waveforms. This is because the apparent moment rate inferred by Sato (1994) holds for any seismic phase whose velocity c satisfies the relation Vr≤c. Therefore, the inclusion of S waves would limit the application of the technique to the subshear regime.

The spectra of EGF exhibit a corner frequency (f_c) ranging between 10 and 12 Hz, while the spectra of MAIN have a corner frequency of about 6 Hz. These corner frequencies are highlighted in the normalized average spectrum plots (Houston and Kanamori, 1986), shown in Figure 5. The scaling between the corner frequency and the inverse of pulse width implies that the source pulse width of EGF should be less than about one-half that of the MAIN, aligning with the assumption of the method proposed by DFB.

To prepare the seismic waveforms for analysis, we applied low-pass filtering below the corner frequency of EGF. The average level of noise (N) was calculated as the average absolute amplitude in a 0.5-s time window preceding the P-wave arrival, while the average level of signal (S) was computed as the average absolute amplitude in a 0.5-s time window following the P-wave arrival. As summarized in Table 3, recordings of MAIN exhibit a very low noise-to-signal ratio (N/S), **which is clearly correlated with the source to receiver distance**. Conversely, recordings of EGF show varying levels of noise, with N/S ratios ranging from a minimum of 0.8% to a maximum of 64.5%, indicating significant noise interference in some cases.

3.1 Inversion results

In the first inversion step, we considered different time windows (T_L) ranging from $T_L = 0.7$ s to $T_L = 1.3$ s. The starting time of T_L was set at 0.2 s before the picked P-wave arrival on non-filtered traces to accommodate potential misalignments in the P-wave onset between EGF and MAIN. At the end of our trials, the optimal time window ($T_L = 0.9$ s) was determined as the one that minimized the overall misfit function. It is important to note that, for $T_L = 0.9$ s, the overall window includes both the first P-waveform (having a pulse width of about 0.2 s) and a substantial part of its coda, lasting approximately 0.5 s. In this way not only the first P-pulse is considered, as done in DFB, but also the main part of the radiated P-wave energy. In the inversion, we considered a total number $2N_{sh}$

TABLE 3 Percentage noise-to-signal (N/S) ratio at the three components of MAIN and EGF and source (MAIN)-to receiver distance R. E indicates the East component, W indicates the West component and Z indicates the vertical component of waveforms.

			(N/S) ∗ 100				
		MAIN			EGF		
	E	N	Z	E	N	Z	R (km)
CESI	0.1	0.2	0.1	9.2	18.4	4.9	17.8
CESX	2.3	1.2	0.7	64.5	19.9	19.8	60.6
CING	2.2	0.3	0.3	50.7	25.6	4.5	43.4
CSP1	0.1	0.1	0.0	0.81	3.6	0.8	16.8
EL6	0.7	0.7	0.3	21.8	24.3	8.2	37.0
FOSV	0.7	1.6	0.2	42.5	44.2	10.2	41.8
FRON	0.6	0.8	0.8	26.28	19.9	16.6	64.2
GUMA	1.1	0.7	0.4	23.0	13.1	5.5	23.9
LNSS	0.4	0.4	0.5	20.6	13.2	18.2	46.8
SNTG	0.8	0.6	0.3	18.4	30.0	12.8	31.7
T1218	0.3	0.5	0.1	18.7	20.2	4.8	39.3

=40 of alignments. In this way, for signals sampled with a sampling time dt = 0.01 s, a time window of 0.2 s before the P-wave arrival of MAIN on unfiltered traces is spanned and a time window of 0.2 s before the P-wave arrival of EGF on unfiltered traces.

The model parameter estimates obtained for each station after the first inversion step are summarized in Table 5. These estimates typically exhibit variability among stations. The retrieved source radius can be categorized into two distinct ranges: (0.1 km ≤ L ≤ 0.22 km; $\Delta\sigma \geq 2$ MPa) and ($L \geq 0.30$ km; $\Delta\sigma \leq 1$ MPa). A smaller source radius is generally associated with a higher stress drop, indicative of the well-known correlation between these parameters.

The comparison between observed and theoretical seismograms (Figure 6) generally shows a very good match and, in some cases, an excellent match, as evidenced by the low values of the misfit function (reported in Table 4), despite the presence of significant noise affecting many EGF recordings. This robust result was also observed in the synthetic test with the noisiest EGF (Figure 3).

In the second step of the inversion process, we computed the optimal alignments of MAIN and EGF for each model parameter station solution obtained in the first step (refer to Table 4). This involved determining the combination of alignments that minimized the misfit function across all available stations, while keeping the model parameters fixed at the values obtained in the initial step. Once we identified the optimal alignments for each model parameter station solution, we selected the best combination corresponding to the absolute minimum of the inferred misfit functions (see Figure 7). For the event under study, the optimal combination of alignments was determined using the model parameter solution obtained for station GUMA in the first step.

After fixing the selected alignments, we employed the grid-search method to compute the values of the likelihood function $\theta(m,d)$ within the volume V_1 (refer to Eq. 15). The volume V_1 in Eq. 11 was selected using the scaling laws (Eqs 9, 10) of the source parameters found in a previous study for the same area (de Lorenzo et al., 2010). This third step enabled us to identify a primary maximum (A) and a secondary maximum (B) of the likelihood function, although these maxima are very close in value (θ~0.95). All the other secondary maxima are characterized by significantly smaller values of the likelihood function (θ<0.9). The presence of the two separated maxima (A and B) is evident from the map (Figure 8A), in the plane $[L,\Delta\sigma]$, of the cumulative probability distribution functions (CPDF) described by the equation:

$$\sigma\left(L_i,\Delta\sigma_j|\boldsymbol{d}\right)=\frac{1}{\mathrm{E}}\int_0^1 d\left(\frac{V_r}{V_p}\right)\int_0^1 d\left(\frac{t_2}{T}\right)\int_0^1 d\left(\frac{t_1}{T}\right)\theta\left(\boldsymbol{d}|L_i,\frac{V_r}{V_p},\Delta\sigma_j,\frac{t_1}{T},\frac{t_2}{T}\right) \tag{19}$$

where:

$$\boldsymbol{E}=\int_{V_1}\boldsymbol{\theta}(\boldsymbol{d}|\boldsymbol{m})\boldsymbol{dm} \tag{20}$$

Instead, by mapping (Figure 8B) in the $[L,V_r/V_S]$ plane the CPDF described by the equation:

$$\sigma\left(L_i,\frac{V_{r,j}}{V_p}|\boldsymbol{d}\right)=\frac{1}{\mathrm{E}}\int_0^{\Delta\sigma_{max}}\boldsymbol{d}(\Delta\sigma)\int_0^1 d\left(\frac{t_2}{T}\right)\int_0^1 d\left(\frac{t_1}{T}\right)\theta\left(\boldsymbol{d}|L_i,\frac{V_{r,j}}{V_p},\Delta\sigma,\frac{t_1}{T},\frac{t_2}{T}\right) \tag{21}$$

a larger correlation area, that includes only the solution B, is found.

Finally, a large correlation area, but enclosing only the solution A, is also found (Figure 8C) when mapping, in the $[\Delta\sigma,V_r/V_S]$ plane, the CPDF described by the equation:

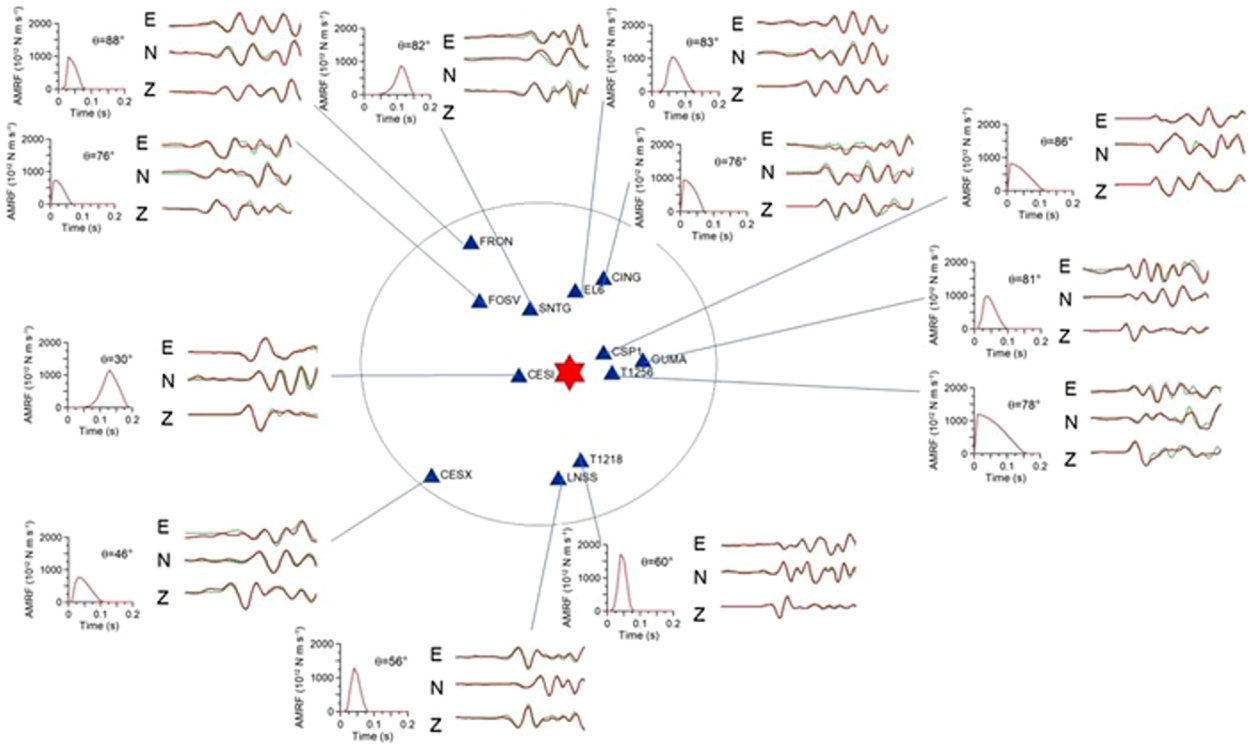

FIGURE 6
Comparison between observed (green) and theoretical (red) mainshock as a function of the source-to-receiver azimuth, after the first step of inversion. The lines connecting stations and seismograms are oriented approximately along the source-to-receiver azimuth. For each station the retrieved Sato (1994) AMRF is also shown.

TABLE 4 Results of the first step of inversion for the studied event.

Station	# Points of shifting	Shifted seismogram	L (km)	t_1/T	t_2/T	Ds (Mpa)	V_r/V_s	M = 1-s
CESI	15	M	0.35	0.69	0.96	0.7	0.58	0.021
CESX	2	E	0.30	0.24	0.45	0.7	1.04	0.049
CING	1	E	0.22	0.33	0.98	1.9	1.49	0.088
CSP1	1	E	0.35	0.00	0.30	0.6	1.5	0.018
EL6	3	M	0.18	0.63	0.66	3.7	0.48	0.026
FOSV	2	M	0.17	0.34	0.58	2.4	1.07	0.053
FRON	4	M	0.14	0.70	0.98	4.9	0.72	0.017
GUMA	5	M	0.18	0.48	0.48	3.2	0.67	0.036
LNSS	7	M	0.11	0.52	0.52	12.1	0.44	0.029
SNTG	16	M	0.10	0.80	0.95	14.7	0.200	0.072
T1218	1	E	0.12	0.43	0.84	19.3	0.443	0.011
T1256	3	M	0.52	0.000	0.30	0.4	1.584	0.077

TABLE 5 The two model parameter solutions for the event considered in this study.

Solution	L (km)	Δσ (Mpa)	t_1/T	t_2/T	V_r/V_s
A	0.28 ± 0.04	1.6 ± 1.1	0.26 ± 0.24	0.63 ± 0.25	0.90 ± 0.14
B	0.20 ± 0.04	3.1 ± 1.4	0.06 ± 0.24	0.33 ± 0.25	0.61 ± 0.14

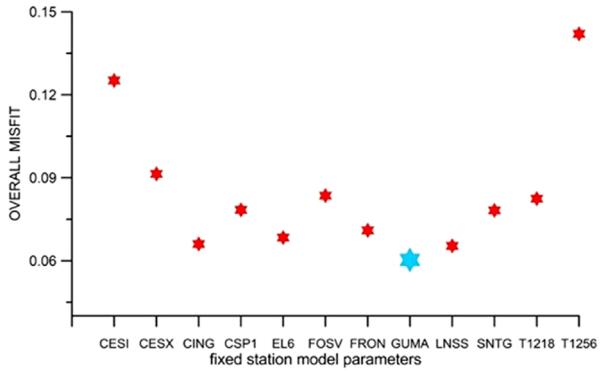

FIGURE 7
Plot of the minimum misfit M = 1-s (non-dimensional) vs. the station name at the second step of inversion (see the text). Each point represents the absolute minimum among the misfit values that are obtained by fixing the model parameters at the values obtained at the first step at that station and letting vary the alignments between MAIN and EGF at all the other stations. The absolute minimum among these is found when we consider the model parameters found for station GUMA (sky-blue star) at the first step of inversion.

$$\sigma\left(\Delta\sigma_i, \frac{V_{r,j}}{V_p}|\boldsymbol{d}\right) = \frac{1}{\mathrm{E}}\int_0^{L_{max}} d(\mathrm{L}) \int_0^1 d\left(\frac{t_2}{T}\right) \int_0^1 d\left(\frac{t_1}{T}\right) \theta\left(\boldsymbol{d}|L, \frac{V_{r,j}}{V_p}, \Delta\sigma_i, \frac{t_1}{T}, \frac{t_2}{T}\right) \tag{22}$$

Figure 9 illustrates the fit of synthetic waveforms to observed waveforms for solution B. A minor reduction in the quality of fitting compared to the single station inversion case (Figure 6) is observed. This reduction is statistically expected because the number of degrees of freedom decreases from $ndf = 12 \times 5 = 60$ for the single station inversion to $ndf = 5$ for the case of a single rupture model.

Model parameters and their associated errors (refer to Table 5) were computed as weighted averages, using the following relationships:

$$\langle m_{i_k} \rangle = \frac{\int_V \mathrm{m}_{i_k} \theta\left(\boldsymbol{d}|\mathrm{m}_{i_1}, \mathrm{m}_{i_2}, \mathrm{m}_{i_3}, \mathrm{m}_{i_4}, \mathrm{m}_{i_5}\right) \mathrm{dm}_{i_1} \mathrm{dm}_{i_2} \mathrm{dm}_{i_3} \mathrm{dm}_{i_4} \mathrm{dm}_{i_5}}{\int_V \theta\left(\boldsymbol{d}|\mathrm{m}_{i_1}, \mathrm{m}_{i_2}, \mathrm{m}_{i_3}, \mathrm{m}_{i_4}, \mathrm{m}_{i_5}\right) \mathrm{dm}_{i_1} \mathrm{dm}_{i_2} \mathrm{dm}_{i_3} \mathrm{dm}_{i_4} \mathrm{dm}_{i_5}} \tag{23}$$

$$\Delta m_{i_k} = \frac{\int_V \left(\mathrm{m}_{i_k} - \langle m_{i_k} \rangle\right)^2 \theta\left(\boldsymbol{d}|\mathrm{m}_{i_1}, \mathrm{m}_{i_2}, \mathrm{m}_{i_3}, \mathrm{m}_{i_4}, \mathrm{m}_{i_5}\right) \mathrm{dm}_{i_1} \mathrm{dm}_{i_2} \mathrm{dm}_{i_3} \mathrm{dm}_{i_4} \mathrm{dm}_{i_5}}{\int_V \theta\left(\boldsymbol{d}|\mathrm{m}_{i_1}, \mathrm{m}_{i_2}, \mathrm{m}_{i_3}, \mathrm{m}_{i_4}, \mathrm{m}_{i_5}\right) \mathrm{dm}_{i_1} \mathrm{dm}_{i_2} \mathrm{dm}_{i_3} \mathrm{dm}_{i_4} \mathrm{dm}_{i_5}} \tag{24}$$

In Eqs 23, 24, V represents the volume of a polyhedron, defined in the five-dimensional parameter space, centered on each maximum of the likelihood function, and excluding secondary maxima. The choice of V was performed by analyzing the shape of the correlation maps of the model parameter couples around the maximum (Figures 10, 11).

3.2 Heterogeneous rupture model vs. circular crack model

To determine whether the inferred circular crack models A and B are better representatives of the source process compared to the heterogeneous fault model inferred in the first step, we utilized the corrected Akaike information criterion (*AICc*), which summarizes the Occam's Razor principle. According to the *AICc* (also used in DFB), when comparing two models describing the data, the preferred model is the one that minimizes the quantity given by Akaike (1973):

$$\boldsymbol{AICc} = \boldsymbol{npt}\ln\left(\hat{\boldsymbol{\sigma}}^2\right) + \boldsymbol{2k} + \frac{\boldsymbol{2k(k+1)}}{\boldsymbol{npt-1}} \tag{25}$$

In Eq. 25 k is the number of model parameters, *npt* is the overall number of points of seismograms involved in the inversion and:

$$\hat{\boldsymbol{\sigma}}^2 = \frac{\sum_{m=1}^{nst}\sum_{j=1}^{3}\sum_{i=1}^{npt} \boldsymbol{w}_j \left(\boldsymbol{U}_{mji}^{obs} - \boldsymbol{U}_{mji}^{teo}\right)^2}{\sum_{m=1}^{nst}\sum_{j=1}^{3}\sum_{i=1}^{npt} \boldsymbol{w}_j} \tag{26}$$

Eq. 26 computes the weighted squared residual between data and data predicted by the model. For the heterogeneous model obtained after the first step of inversion and summarized in Table 4, we obtained *AICc* = 61749. Instead, for the circular crack models A and B summarized in Table 5, we obtained respectively *AICc* = 56900 and *AICc* = 56961. Therefore, for the studied event, a circular crack model with variable rupture velocity better represents the source model compared to the heterogeneous fault model that could be derived from the back-projection of the single station solutions.

4 Discussion and conclusion

Upon analyzing the results presented in Table 5 and examining the correlation maps depicted in Figures 10, 11, it is evident that the parameters most affected by uncertainty are the durations of both the nucleation (t_1) and deceleration (t_2) phases. Despite the significant percentage error associated with estimating these parameters, models A and B, which are considered most likely, demonstrate that rupture velocity varies during the rupture process. Specifically, for model

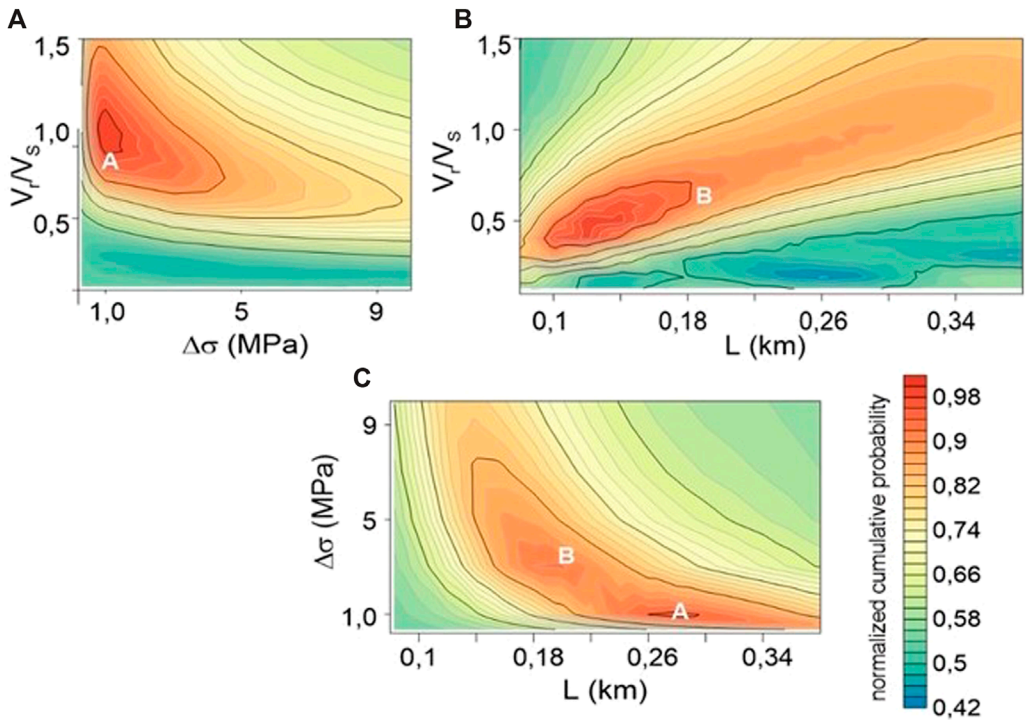

FIGURE 8
Plot of the normalized cumulative probability density functions (CPDF). In each map A and B indicate the position of the two inferred best fit solutions (A and B, Table 5) in the three planes. **(A)** CPDF in the plane [Δ_σ, V_r/V_S]; **(B)** CPDF in the plane [L,Vr/Vs]; **(C)** CPDF in the plane [L, Δ_σ].

A, the correlation maps in Figure 10 suggest the existence of a nucleation phase ($t_1/T \neq 0$), while the deceleration phase is less clear. Conversely, the correlation maps in Figure 11 suggest that for model B, a deceleration phase ($t_2/T<1$) is necessary, with the nucleation phase being less resolved. Thus, regardless of the preferred model choice, the rupture process must involve either a nucleation or a deceleration phase. Model B, characterized by a minimal nucleation phase, aligns closely with Boatwright's (1980) original causal decelerating model. These observations, coupled with the ability of the model to reproduce the initial P-wave pulse across all azimuths (Figure 9), indicate that circular crack models with variable rupture velocity overcome the limitations of simplified circular crack models with constant rupture velocity (Brune, 1970; Sato and Hirasawa, 1973) in accurately modeling P-waveform shapes.

The errors affecting source radius, rupture velocity, and stress drop are notably small, as indicated by the visual examination of the maps in Figures 10, 11, along with the error estimates provided in Table 5. Consequently, the inferred stress drops using this method are more constrained compared to those typically derived from seismic spectra inversion (e.g., de Lorenzo et al., 2010; Abercombie, 2021). This improvement arises because EGF techniques incorporate site effects in the empirical Green's function, whereas in seismic spectra inversions site effects are usually estimated as average residuals between observed and retrieved spectra.

As discussed in the introduction section, higher is the rupture velocity and higher is the fraction of the accumulated energy radiated by an earthquake. Interestingly, the two most probable V_r/V_S (rupture velocity to shear wave velocity) ratios identified in this study (0.61 and 0.9) lie at the edges of the previously reported range of variability ($0.65 < V_r/V_S < 0.85$) from earlier studies (Heaton, 1990), suggesting a potential sub-shear regime for the analyzed event. However, for solution A, the results do not entirely rule out a super-shear regime. Specifically, the correlation map in the [Vr/Vs, t_2/T] plane indicates that the maximum likelihood region [θ (d|m) ~ 0.95] corresponds to cases where $V_r/V_S > 1$, coupled with a shorter duration of the deceleration phase. Exploring rupture velocity in Central Italy could be critical for enhancing seismic hazard assessment in the region. Notably, recent research has highlighted the significant role of pore fluid-pressure effects in increasing rupture velocity (Pampillon et al., 2023). This phenomenon might also apply to Central Italy, where the local tectonic regime is influenced by fluid-filled crack systems parallel to thrust fronts (see de Lorenzo and Trabace, 2011, and references therein).

Whereas significant advances have been made in constraining the rupture velocity of great magnitude earthquakes (see Bouchon and Valle, 2003 and references therein), rupture velocity of a small earthquakes remains one of the parameters less constrained by seismological methods, that are generally based on the assumption of a constant rupture velocity. Therefore, future studies should focus more deeply on this important parameter, using more realistic rupture models than a simple circular crack model rupturing at a constant velocity.

The correlation among the most constrained parameters ($\Delta\sigma$, V_r, and L) is clear from the cumulative probability distribution

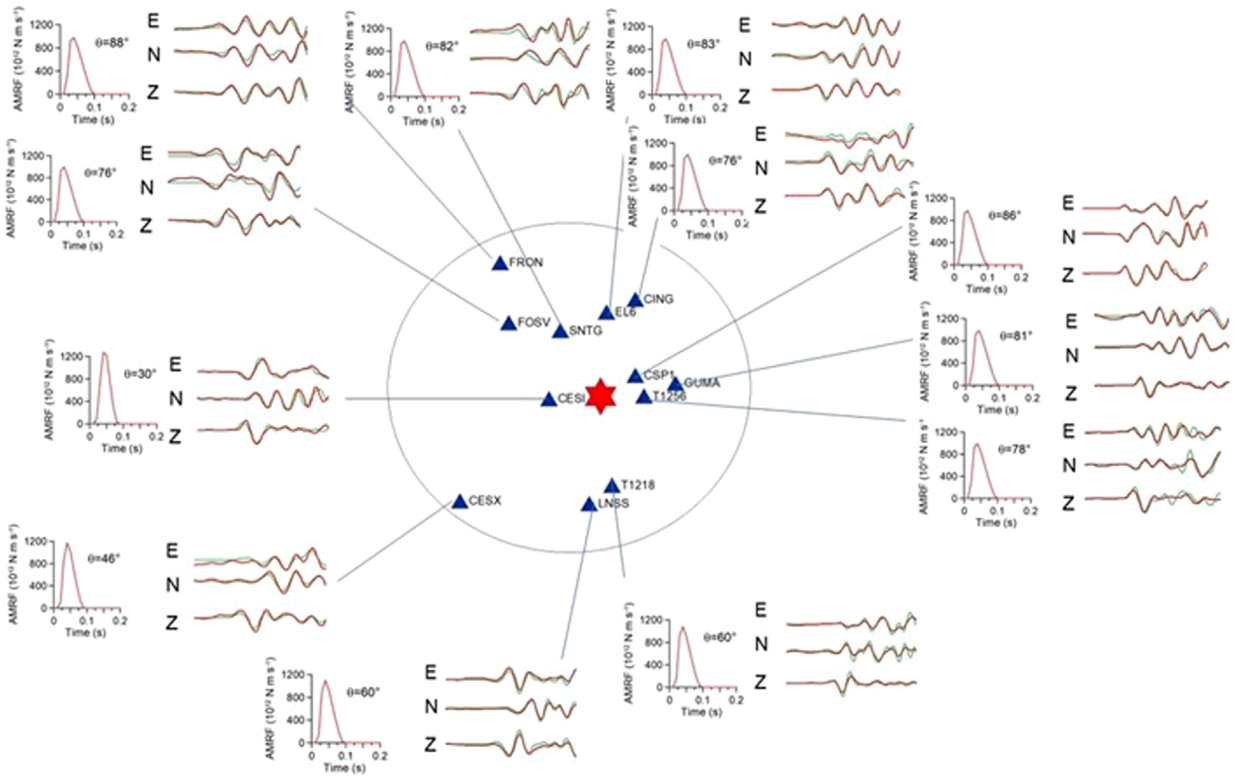

FIGURE 9
Comparison between observed (green) and theoretical (red) mainshock as a function of the source-to-receiver azimuth, for the preferred solution. The lines connecting stations and seismograms are oriented approximately along the source-to-receiver azimuth. For each station the retrieved Sato (1994) AMRF is also shown.

function (CPDF described by the Eqs 19-22) plots of Figure 8, where the effects of nucleation and deceleration phase are averaged out. When analyzing couple of parameters, the correlation becomes weaker (Figures 10, 11). This observation indicates that the introduction of a nucleation and deceleration phase in the rupture process can significantly reduce the correlation between stress drop, rupture velocity and source radius. The CPDF plots confirm the anticorrelation between $\Delta\sigma$ and L found in previous studies (Abercombie, 2021), indicating that an increase in $\Delta\sigma$ is typically associated with a decrease in L. This correlation aligns with the constraint provided by the Eshelby (1957) relationship (Eq. 10) applied to quasi-dynamic source models.

A more contentious issue arises regarding the potential anti-correlation between $\Delta\sigma$ and V_r (Chounet et al., 2018). The CPDF map in the [$\Delta\sigma$, V_r] plane (Figure 8) suggests that this correlation significantly impacts our findings. Theoretically, this correlation arises from the Eshelby (1957) relationship, particularly when considering the interaction between source rise time, source dimension, and rupture velocity inherent in all quasi-dynamic source models (as expressed in Eqs 18, 19 of Deichmann, 1997). Consequently, our results support the working hypothesis proposed by Causse and Song (2015), which postulates that this anti-correlation reduces the variability in predicted peak-ground acceleration (PGA), aligning it more closely with observed PGA values.

Furthermore, the evident correlation between L and V_r (Figure 8) can be readily explained by recalling that these two parameters are linked by the following equation: that arises from Eq. 6 of Deichmann (1997) for the case of a constant acceleration phase.

Between the two obtained solutions A and B, we opted for solution B as the preferred choice, despite its slightly lower likelihood value (0.95 vs. 0.954). This decision was based on two main reasons. Firstly, upon visually inspecting the waveform fitting, we observed that model B tends to reproduce the first P-pulse across all stations more accurately, whereas model A performs better in reproducing the P-wave coda. Notably, the results were obtained by using a sufficiently wide time window (T_L = 0.9 s), which includes several secondary arrivals following the first P-pulse. Secondly, considering scaling laws from seismic events in the same area during a prior 1997 seismic sequence, it was noted that source radii are consistently smaller than 250 m for M_L<3.5 (de Lorenzo et al., 2010). This information further supports the preference for solution B in our study.

The differences observed in the retrieved AMRFs after the initial inversion step (as shown in Table 4) suggest a heterogeneous rupture process that deviates from a simple circular crack model with variable rupture velocity. Typically, in such cases, researchers might consider using the estimates from the initial inversion step to infer the slip function on the fault plane through back-projection of station slip functions onto the fault plane, a technique also employed for small magnitude earthquakes (Festa and Zollo, 2006; Stabile et al., 2012).

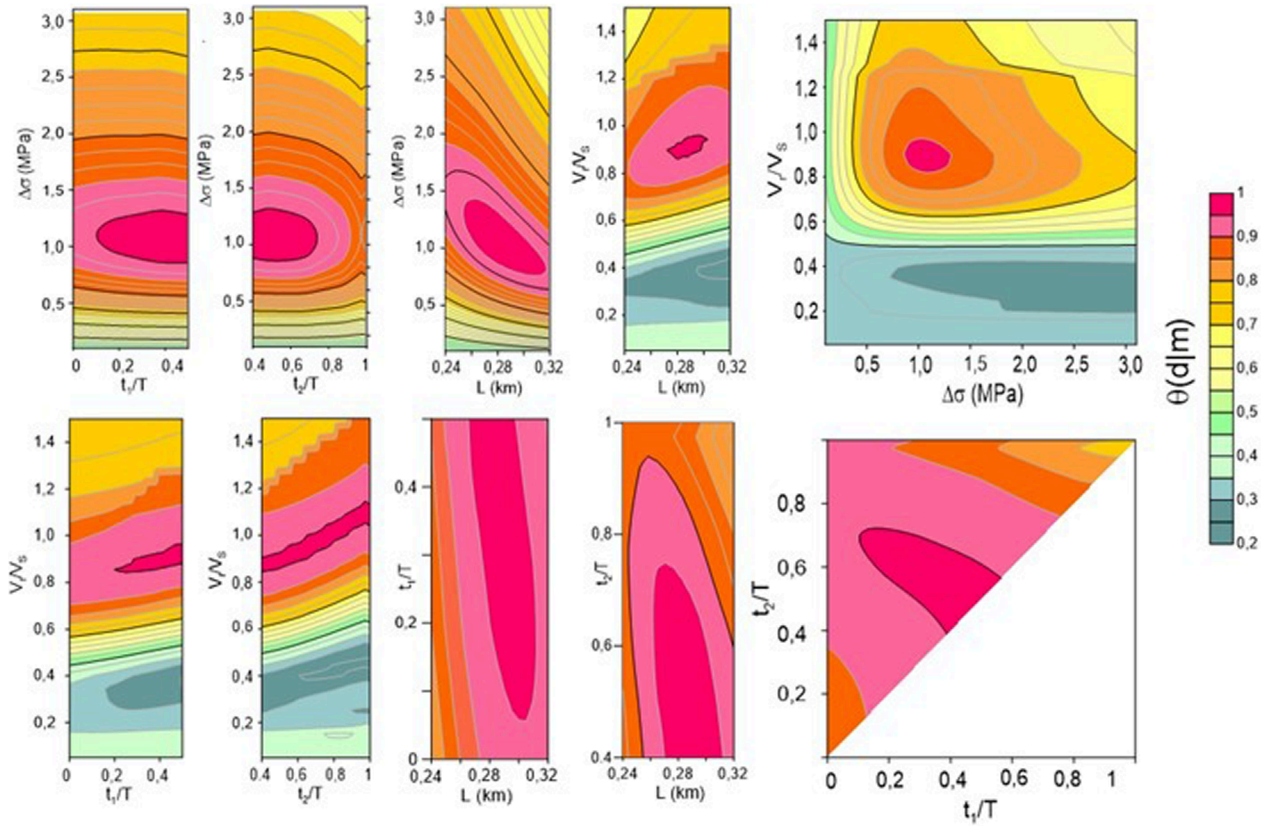

FIGURE 10
Correlation maps for the solution A. the values of the likelihood function are contoured as a function of each couple of model parameters $\left(L, \Delta\sigma, \frac{Vr_{max}}{V_S}, \frac{t_1}{T}, \frac{t_2}{T}\right)$. In the calculation of the likelihood function, three parameters are fixed to the best fit values of solution A and the other two are let to vary.

However, for the studied event, we ruled out this possibility by comparing the values of corrected *AICc* obtained after both inversion steps. This comparison led us to conclude that, in this case, a circular crack model with variable rupture velocity can better reproduce the main properties of P-wave seismic radiation observed at various azimuths and distances compared to a heterogeneous model. This finding is particularly intriguing given that the selected time window (T_L = 0.9 s) also includes a significant portion of the P-wave coda. Nevertheless, the non-uniqueness inherent in seismic source inversion (Das, 2015) and the determination of an optimal time window (T_L = 0.9 s) for our analysis suggest that other quasi-dynamic crack models (e.g., Dong and Papageorgiou, 2002; 2003) or techniques (e.g., Festa and Zollo, 2006; Cuius et al., 2023) may produce equivalent or superior results with different choices of T_L. Moving forward, one key challenge in future seismic source studies should involve comparing results obtained from different techniques and developing a multi-scale approach in the time domain to determine the optimal time extent at which a circular crack model truly represents the optimal source model for small magnitude earthquakes.

A further test has been made by considering only the stations characterized by a high noise-to signal ratio (Cesx, Cing, Fosv, Fron, Sntg, see Table 3) but we obtained, as expected, a reduction of the quality of fitting (the maximum of likelihood function at the second step reduces to 0.87). Therefore, the optimal configuration for this method would consist of using both waveforms having a smaller noise-to signal ratio, which constrain the alignment between MAIN and EGF at the second step, and waveforms having a higher noise-to-signal ratio, which allow to reduce the correlation between model parameters.

One limit of the present model is its non-applicability to the case of unilateral faults. In these cases, it is in-fact expected that observed waveforms will exhibit a clear dependence of the pulse width and/or amplitude variations with the source-to-receiver azimuth, and the present formulation, based on the directivity function of a circular crack, cannot be adopted to retrieve the corresponding source parameters. However, the structure of the inversion method presented in this article will remain valid also in this case, by adopting the appropriate source model for this situation.

The method presented in this article addresses challenges associated with using noisy EGF, as described in DFB, to evaluate whether a circular crack model with variable rupture velocity accurately represents the source process of a small magnitude earthquake. This technique enables the determination of whether such a model is representative of the source process by allowing for a quantitative assessment of the multiplicity of solutions and correlations among model parameters using the Bayesian formulation described. This approach overcomes the local analysis typically achievable with random deviates techniques, providing a more comprehensive and robust framework for seismic source characterization.

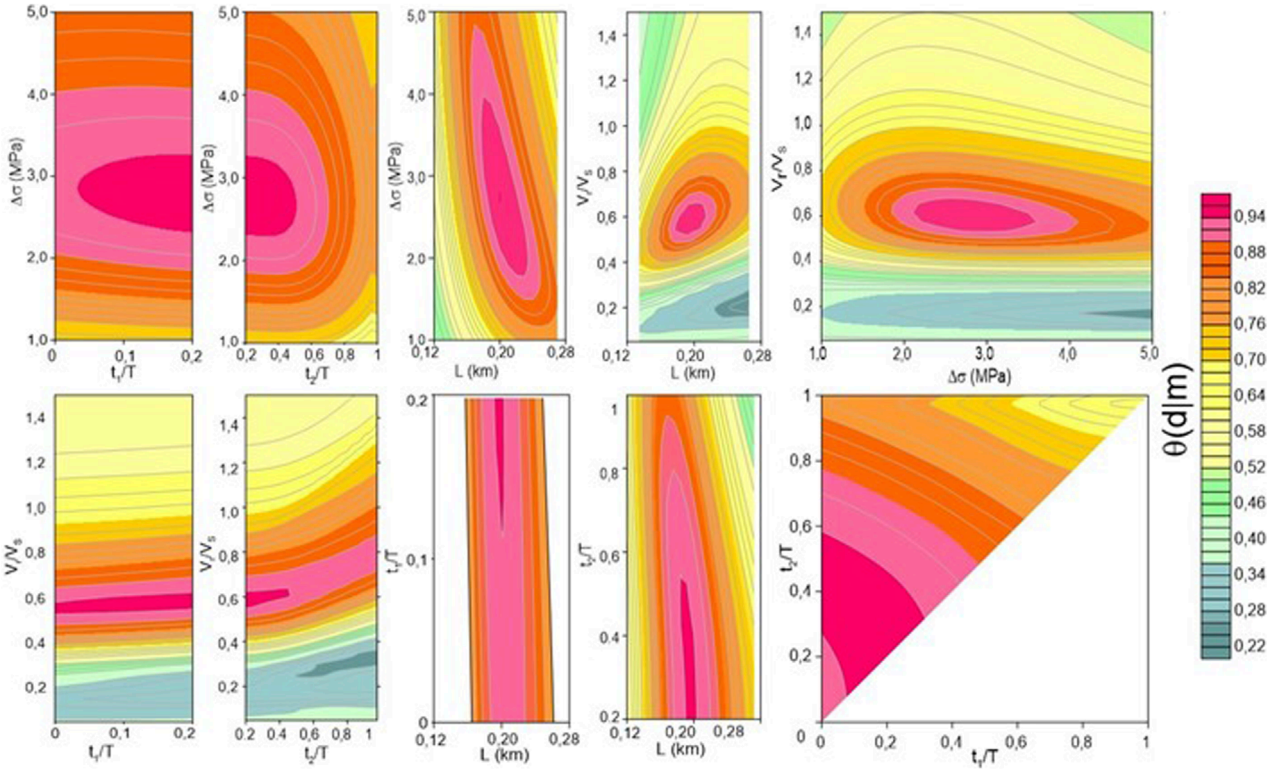

FIGURE 11
Correlation maps for the solution B. The values of the likelihood function are contoured as a function of each couple of model parameters $\left(L, \Delta\sigma, \frac{Vr_{max}}{V_s}, \frac{t_1}{T}, \frac{t_2}{T}\right)$. In the calculation of the likelihood function, three parameters are fixed to the best fit values of solution B and the other two are let to vary.

The method presented in this paper uses strike and dip fault inferred from fault mechanism solution. In a future study it has to be evaluated if strike and dip fault can be inferred from the joint inversion of P-waveforms and P polarities.

Data availability statement

Publicly available datasets were analyzed in this study. This data is available by request to corresponding author.

Author contributions

SdL: Writing–review and editing, Writing–original draft, Visualization, Validation, Supervision, Software, Resources, Project administration, Methodology, Investigation, Funding acquisition, Formal Analysis, Conceptualization. MM: Writing–review and editing, Visualization, Validation, Supervision, Investigation, Formal Analysis, Data curation.

Funding

The author(s) declare that financial support was received for the research, authorship, and/or publication of this article. This study was financially supported by PRIN-MIUR Italian research funds. It is also part of the European PNRR project "PE RETURN: Multi-risk science for resilient communities under a changing climate—Volcanoes and Earthquakes."

Acknowledgments

Marilena Filippucci is acknowledged for furnishing the Fortran codes used in the DFB article.

Conflict of interest

The authors declare that the research was conducted in the absence of any commercial or financial relationships that could be construed as a potential conflict of interest.

Publisher's note

References

Abercrombie, R. E. (2021). Resolution and uncertainties in estimates of earthquake stress drop and energy release. *Phil. Trans. R. Soc. A.* 379 (2196). doi:10.1098/rsta.2020.0131

Akaike, H. (1973). "Information theory as an extension of the maximum likelihood principle," in *Second international symposium on information theory*. Editors B. N. Petrov, and F. Csaki (Budapest: Akademiai Kiado), 267–281.

Aki, K., and Richards, P. G. (2002). *Quantitative seismology*. 2nd Edition. Sausalito, CA: Univ. Sci. Books, 700.

Bernard, P., and Madariaga, R. (1984). A new asymptotic method for the modeling of nearfield accelerograms. *Bull. Seismol. Soc. Am.* 74, 539–557. doi:10.1785/bssa0740020539

Bertero, M., Bindi, D., Boccacci, P., Cattaneo, M., Eva, C., and Lanza, V. (1997). Application of the projected Landweber method to the estimation of the source time function in seismology. *Inverse Probl.* 13, 465–486. doi:10.1088/0266-5611/13/2/017

Boatwright, J. (1980). A spectral theory for circular seismic sources: simple estimates of source dimension, dynamic stress drop and radiated seismic energy. *Bull. Seismol. Soc. Am.* 70, 1–28. doi:10.1785/BSSA0700010001

Bouchon, M., and Vallée, M. (2003). Observation of long supershear rupture during the magnitude 8.1 kunlunshan earthquake. *Science* 301, 824–826. doi:10.1126/science.1086832

Brune, J. N. (1970). Tectonic stress and the spectra of seismic shear waves from earthquakes. *J. Geophys. Res.* 75, 4997–5009. doi:10.1029/JB075i026p04997

Causse, M., and Song, S. G. (2015). Are stress drop and rupture velocity of earthquakes independent? Insight from observed ground motion variability. *Geophys. Res. Lett.* 42, 7383–7389. doi:10.1002/2015GL064793

Chiaraluce, L., Di Stefano, R., Tinti, E., Scognamiglio, L., Michele, M., Casarotti, E., et al. (2017). The 2016 central Italy seismic sequence: a first look at the mainshocks, aftershocks, and source models. *Seismol. Res. Lett.* 88 (3), 757–771. doi:10.1785/0220160221

Chiaraluce, L., Michele, M., Waldhauser, F., Tan, Y. J., Herrmann, M., Spallarossa, D., et al. (2022). A comprehensive suite of earthquake catalogues for the 2016-2017 Central Italy seismic sequence. *Sci. Data* 9 (1), 710. doi:10.1038/s41597-022-01827-z

Chounet, A., Vallée, M., Causse, M., and Courboulex, F. (2018). Global catalog of earthquake rupture velocities shows anticorrelation between stress drop and rupture velocity. *Tectonophysics* 733, 148–158. doi:10.1016/j.tecto.2017.11.005

Cuius, A., Meng, H., Saraò, A., and Costa, G. (2023). Sensitivity of the second seismic moments resolution to determine the fault parameters of moderate earthquakes. *Front. Earth Sci.* 11, 1198220. doi:10.3389/feart.2023.1198220

Das, S. (2015). "Supershear earthquake ruptures – theory, methods, laboratory experiments and fault superhighways: an update," in *Perspectives on European earthquake engineering and seismology. Vol. 2, geotechnical, geological and earthquake engineering*. Editor A. Ansal (Springer), 39, 1–20. doi:10.1007/978-3-319-16964-4

Deichmann, N. (1997). Far-field pulse shapes from circular sources with variable rupture velocities. *Bull. Seismol. Soc. Am.* 87 (5), 1288–1296. doi:10.1785/BSSA0870051288

de Lorenzo, S., Filippucci, M., and Boschi, E. (2008). An EGF technique to infer the rupture velocity history of a small magnitude earthquake. *J. Geophys. Res.* 113, B10314. doi:10.1029/2007JB005496

de Lorenzo, S., and Trabace, M. (2011). Seismic anisotropy of the shallow crust in the Umbria–Marche (Italy) region. *Phys. Earth Planet. Int.* 189, 34–46. doi:10.1016/j.pepi.2011.09.008

de Lorenzo, S., Zollo, A., and Zito, G. (2010). Source, attenuation, and site parameters of the 1997 Umbria-Marche seismic sequence from the inversion of *P* wave spectra: a comparison between constant Q_P and frequency-dependent Q_P models. *J. Geophys. Res.* 115, B09306. doi:10.1029/2009JB007004

Dong, G., and Papageorgiou, A. S. (2002). Seismic radiation from a unidirectional asymmetrical circular crack model, Part II: variable rupture velocity. *Bull. Seismol. Soc. Am.* 92 (3), 962–982. doi:10.1785/0120010209

Dong, G., and Papageorgiou, A. S. (2003). On a new class of kinematic models: symmetrical and asymmetrical circular and elliptical cracks. *Phys. Earth Planet. Int.* 137, 129–151. doi:10.1016/S0031-9201(03)00012-8

Ellsworth, W. L., and Beroza, G. C. (1998). Observation of the seismic nucleation phase in the Ridgecrest, California, earthquake sequence. *Geophys. Res. Lett.* 25 (2), 401–404. doi:10.1029/97GL53700

Eshelby, J. D. (1957). The determination of the elastic field of an ellipsoidal inclusion, and related problems. *Proc. R. Soc. Lond.* 241, 376–396. doi:10.1098/rspa.1957.0133

Festa, G., and Zollo, A. (2006). Fault slip and rupture velocity inversion by isochrone backprojection backprojection. *Geophys. J. Int.* 166 (2), 745–756. doi:10.1111/j.1365-246X.2006.03045.x

Hartzell, S. (1978). Earthquake aftershocks as Green's functions. *Geophys. Res. Lett.* 5 (1), 1–4. doi:10.1029/GL005I001P00001

Heaton, T. H. (1990). Evidence for and implications of self-healing pulses of slip in earthquake rupture. *Phys. Earth Planet. Inter.* 64, 1–20. doi:10.1016/0031-9201(90)90002-F

Houston, H., and Kanamori, H. (1986). Source spectra of great earthquakes: teleseismic constraints on rupture process and strong motion. *Bull. Seismol. Soc. Am.* 76 (1), 19–42. doi:10.1785/BSSA0760010019

Hu, C., Stoffa, P., and McIntosh, K. (2008). First arrival stochastic tomography: automatic background velocity estimation using beam semblances and VFSA. *Geoph. Res. Lett.* 35 (23), L23307. doi:10.1029/2008GL034776

Latorre, D., Di Stefano, R., Castello, B., Michele, M., and Chiaraluce, L. (2023). An updated view of the Italian seismicity from probabilistic location in 3D velocity models: the 1981–2018 Italian catalog of absolute earthquake locations (CLASS). *Tectonophysics* 846, 229664. doi:10.1016/j.tecto.2022.229664

Madariaga, R. (1976). Dynamics of an expanding circular fault. *Bull. Seismol. Soc. Am.* 66, 639–666. doi:10.1785/BSSA0660030639

Madariaga, R. (1977). High-frequency radiation from crack (stress drop) models of earthquake faulting. *Geophys. J. Int.* 51, 625–651. doi:10.1111/j.1365-246X.1977.tb04211.x

Madariaga, R. (2007). Seismic source theory. *Treatise Geophys.*, 59–82. doi:10.1016/b978-044452748-6.00061-4

Madariaga, R., and Ruiz, S. (2016). Earthquake dynamics on circular faults: a review 1970–2015. *J. Seismol.* 20, 1235–1252. doi:10.1007/s10950-016-9590-8

Malagnini, L., and Munafò, I. (2018). On the relationship between ML and Mw in a broad range: an example from the Apennines, Italy. *Bull. Seismol. Soc. Am.* 108 (2), 1018–1024. doi:10.1785/0120170303

Michele, M., Chiaraluce, L., Di Stefano, R., and Waldhauser, F. (2020). Fine-scale structure of the 2016–2017 Central Italy seismic sequence from data recorded at the Italian National Network. *J. Geophys. Res. Solid Earth* 125 (4), e2019JB018440. doi:10.1029/2019jb018440

Michele, M., Di Stefano, R., Chiaraluce, L., Cattaneo, M., De Gori, P., Monachesi, G., et al. (2016). The Amatrice 2016 seismic sequence: a preliminary look at the mainshock. *Ann. Geophys.* 59 (Fast Track 5)–2016. doi:10.4401/ag-7227

Mueller, C. S. (1985). Source pulse enhancement by deconvolution of an empirical Green's function. *Geophys. Res. Lett.* 12 (1), 33–36. doi:10.1029/GL012i001p00033

Pampillón, P., Santillán, D., Mosquera, J. C., and Cueto-Felgueroso, L. (2023). The role of pore fluids in supershear earthquake ruptures. *Sci. Rep.* 13, 398. doi:10.1038/s41598-022-27159-x

Press, W. H., Flannery, B. P., Teukolsky, S. A., and Vetterling, W. T. (1989). *Numerical Recipes, The Art of Scientific Computing (Fortran Version)*. Cambridge, U. K.: Cambridge Univ. Press.

Sato, T. (1994). Seismic radiation from circular cracks growing at variable rupture velocity. *Bull. Seismol. Soc. Am.* 84 (4), 1199–1215. doi:10.1785/BSSA0840041199

Sato, T., and Hirasawa, T. (1973). Body wave spectra from propagating shear cracks. *J. Phys. Earth* 21, 415–431. doi:10.4294/JPE1952.21.415

Shibazaki, B., Yoshida, Y., Nakamura, M., Nakamura, M., and Katao, K. (2002). Rupture nucleations in the 1995 Hyogo-ken Nanbu earthquake and its large aftershocks. *Geophys. J. Int.* 149 (3), 572–588. doi:10.1046/j.1365-246X.2002.01601.x

Stabile, T. A., Satriano, C., Orefice, A., Festa, G., and Zollo, A. (2012). Anatomy of a microearthquake sequence on an active normal fault. *Sci. Rep.* 2, 410. doi:10.1038/srep00410

Vallée, M. (2004). Stabilizing the empirical green function analysis: development of the projected landweber method. *Bull. Seismol. Soc. Am.* 94 (2), 394–409. doi:10.1785/0120030017

Waldhauser, F., and Ellsworth, W. L. (2000). A double-difference earthquake location algorithm: method and application to the northern hayward fault, California. *Bull. Seism. Soc. Am.* 90, 1353–1368. doi:10.1785/0120000006

Wang, D., Mori, J., and Koketsu, K. (2016). Fast rupture propagation for large strike-slip earthquakes. *Earth Planet. Sci. Lett.* 440, 115–126. doi:10.1016/j.epsl.2016.02.022

Zollo, A., Capuano, P., and Sing, S. K. (1995). Use of small earthquake records to determine the source time functions of larger earthquakes: an alternative method and an application. *Bull. Seismol. Soc. Am.* 85 (4), 1249–1256. doi:10.1785/BSSA0850041249

Zollo, A., and de Lorenzo, S. (2001). Source parameters and three-dimensional attenuation structure from the inversion of microearthquake pulse width data: method and synthetic tests. *J. Geophys. Res.* 106 (B8), 16,287–16,306. doi:10.1029/2000JB900463

frontiers | Frontiers in Earth Science

TYPE Original Research
PUBLISHED 06 September 2024
DOI 10.3389/feart.2024.1448035

OPEN ACCESS

EDITED BY
Pierpaolo Zuddas,
Sorbonne Universités, France

REVIEWED BY
Marcella Barbera,
University of Palermo, Italy
Fernando Lopes,
Muséum National d'Histoire Naturelle, France

*CORRESPONDENCE
Yuxuan Chen,
cyx630@163.com
Guiping Liu,
liuguiping@bjseis.gov.cn
Fuqiong Huang,
hfqiong126@126.com
Leyin Hu,
huleyin@bjseis.gov.cn

RECEIVED 12 June 2024
ACCEPTED 12 August 2024
PUBLISHED 06 September 2024

CITATION
Chen Y, Liu G, Huang F, Wang Z, Hu L, Yang M, Sun X, Hua P, Zhu S, Zhang Y, Wu X, Wang Z, Xu L, Han K, Cui B, Dong H and Zhou Y (2024) Multiple geochemical parameters of the Wuliying well of Beijing seismic monitoring networks probably responding to the small earthquake of Chaoyang, Beijing, in 2022. *Front. Earth Sci.* 12:1448035. doi: 10.3389/feart.2024.1448035

Multiple geochemical parameters of the Wuliying well of Beijing seismic monitoring networks probably responding to the small earthquake of Chaoyang, Beijing, in 2022

Yuxuan Chen[1]*, Guiping Liu[1]*, Fuqiong Huang[2]*, Zhiguo Wang[1], Leyin Hu[1]*, Mingbo Yang[1], Xiaoru Sun[1], Peixue Hua[1], Shijun Zhu[1], Yanan Zhang[1], Xiaodong Wu[1], Zhihui Wang[1], Lvqing Xu[1], Kongyan Han[1], Bowen Cui[1], Hongyan Dong[1] and Yonggang Zhou[3]

[1]Beijing Earthquake Agency, Beijing, China, [2]China Earthquake Networks Center, Beijing, China, [3]The Bureau of seismology of Yanqing District of Beijing, Beijing, China

Hydrological changes in groundwater coupled with earthquakes had been documented in previous studies by global researchers. Although few reports investigate multiple geochemical parameters that respond to earthquakes, trace elements received less attention, whereas they were suggested to be more sensitive to small earthquakes than the commonly used geochemical parameters. Beijing is located in the Zhangjiakou-Bohai (Zhang-Bo) seismic belt of North China, and although the occurrence of small earthquakes is frequent, the great historic earthquake in the Sanhe-Pinggu area M8 in 1679 in the adjoining southeast of Beijing gained widespread public attention. To find effective precursors that are significant for operational earthquake forecasting of the Beijing area, we carried out a one year test research project through weekly collection of groundwater samples during June 2021 to June 2022 from the seismic monitoring well of Wuliying in northwest Beijing. The 41 trace elements chemical compositions were analyzed for each sample. During the project ongoing period, the biggest earthquake with a magnitude of ML3.3 occurred in the Chaoyang District of Beijing on 3 February 2022. The content changes in these trace elements were systematically monitored before and after the earthquake. Through retrospective research, it was found that a few sensitive trace elements were anomalous to be coupled to the earthquake, including Li, Sc, Rb, Mo, Cs, Ba, W, U, Sr, Mn, Ni, and Zn. In addition to trace elements, we examined stable isotopes of hydrogen and oxygen and the existing hydrological data on groundwater level, temperature, major ions, and gases to assess the validity of geochemistry as a monitoring and predictive tool. We only found that F- (fluorine) ions and He (helium) gas had apparent shifts related to the earthquakes, while no shifts in the groundwater level were observed. Such characteristics of multiple geochemical parameters indicate that trace elements are likely to be more sensitive to crustal strain than the groundwater level and major ions. We assumed a most likely mechanism of the combination of mixing and water–rock interactions to explain the phenomenon. The probable

scenario was that minor stresses caused by the earthquakes might create micro-cracks in bedrocks, thereby leading to a small volume of chemically distinct water mixing with the original water of the aquifer, and finally, the earthquake-induced rock fractures enhance the water–rock interactions, resulting in the post-seismic recovery of trace elements and $\delta^{18}O$ value migration to the GWML. More testing works to find other sensitive sites to investigate multiple geochemical characteristics aiming at long-term to short-term earthquake prediction in the Beijing area and Zhang-Bo seismic belt are in progress.

KEYWORDS

Zhang-Bo (Zhangjiakou-Bohai) seismic belt, earthquake precursor, trace elements, hydrogen and oxygen stable isotopes, gases

1 Introduction

As part of the earthquake precursor detection program, changes in groundwater levels, temperatures, and chemical parameters related to earthquakes have been documented for decades (Toutain et al., 1997; Roeloffs, 1998; Montgomery and Manga, 2003; Wang and Manga, 2010; Skelton et al., 2014; Manga and Wang, 2015; De Luca et al., 2018; Martinelli, 2020). Because of the feasibility of using automated monitoring systems, earthquake-related changes in water levels, temperatures, and radon concentrations are the most commonly reported responses (King, 1981; Kitagawa et al., 1996; Manga and Wang, 2015; Martinelli, 2020). These monitoring methods of groundwater also play key roles for precursor detection in China, and a nationwide network of monitoring wells located along strain-sensitive locations has been constructed for this purpose.

Comparisons with conventional hydrological parameters such as water level and temperatures, geochemical changes induced by earthquakes have become increasingly important (Martinelli, 2020; Claesson et al., 2004) because geochemical changes are considered to be sensitive to crustal stress and beneficial for earthquake prediction (Thomas, 1988; Wakita, 1996; Poitrasson et al., 1999; Manga and Wang, 2015; Martinelli and Dadomo, 2017; Shi et al., 2020; Kopylova et al., 2022; Chen and Liu, 2023). For example, based in part on hundreds of hydrological anomalies including geochemical changes, an imminent prediction was made before the 1975 M7.3 Haicheng earthquake in China (Wang et al., 2006). Following the 1995 M7.2 Kobe earthquake, several papers reported precursory changes in the concentrations of radon, chlorine, and sulfate ions in the groundwater (Tsunogai and Wakita, 1995; Igarashi et al., 1995). Claesson et al. (2004) observed simultaneous changes in trace elements, major elements, and isotope before and after major earthquakes. Skelton et al. (2019) found pre-seismic changes in five parameters (Na, Si, K, $\delta^{18}O$, and $\delta^{2}H$) before three earthquakes and the post-seismic changes in eight parameters (Ca, Na, Si, Cl, F, SO_4, $\delta^{18}O$, and $\delta^{2}H$).

Among these geochemical parameters, trace elements were thought to be more sensitive to earthquakes. For example, Rosen et al. (2018) showed that trace elements (Al, Cu, Pb, Mn, and Sr) exhibited post-seismic peak changes in four hot springs but noted only small changes for the major ions. Barberio et al. (2017) documented another study on changes in trace elements (As, Fe, V, and Cr) that were associated with the seismic sequence, but the study showed no changes for the major ions (K, Na, Ca, Mg, and Cl). Shi et al. (2020) showed that trace element concentrations had significant decreases in response to the Tonghai earthquake but no significant changes in major ions and hydrogen and oxygen isotope concentrations. However, trace element changes induced by earthquakes have been documented relatively rarely (Martinelli, 2020; Claesson et al., 2004) because manual sampling and expensive and time-consuming laboratory analyses are required (Wang and Manga, 2010; Shi et al., 2020). Another problem is to understand which geochemical elements would be good candidates for monitoring and prediction. For this purpose, Chen and Liu (2023) continuously collected water samples for a whole year and found that Li, Sc, Ti, Pb, Cu, Nb, Th, Zn, Tl, U, and REEs responded to small earthquakes in Beijing, China.

Overall, most documented studies have used the major elements or single species geochemical indicators, and they respectively examined the major elements (Tsunogai and Wakita, 1995; Toutain et al., 1997; Kingsley et al., 2001; Woith et al., 2013), hydrogen and oxygen isotopes (Taran et al., 2005; Skelton et al., 2014), and trace elements (Chen and Liu, 2023) related to earthquakes. Few reports investigate the characteristics of multiple geochemical parameters' response to earthquakes.

In this paper, we continuously collected water samples of the Wuliying well and analyzed multiple geochemical parameters including trace elements and hydrogen and oxygen isotopes, combining existing data on the groundwater level, temperature, major ions, and gases, to examine comprehensive hydrological changes related to earthquakes, discuss the possible mechanisms, and assess the sensitivity and validity of multi-geochemistry as a predictive tool in the future.

2 Background of geological settings

2.1 Faults and earthquakes in and around Beijing

Beijing is the capital of China with a large population, and it is located in the intersection of the North China Plain and the Zhang-Bo (Zhangjiakou-Bohai) seismic belt. North China has experienced strong earthquakes frequently over the last few decades

(Chen and Liu, 2023), such as the Xingtai M7.2 earthquake in 1966, Bohai M7.4 earthquake in 1969, Haicheng M7.3 earthquake in 1975, Tangshan M7.8 earthquake in 1976, and Zhangbei M6.2 earthquake in 1998. The Zhang-Bo seismic belt is a group of NW–W orderly active fault zones, which starts from the northern margin of Taihang Mountain in the west and enters the Bohai Sea in the east. It is an important NW seismic activity zone with high seismic activity in North China (Yang et al., 2022). Hence, there is potential risk and danger of damaging earthquakes at Beijing in the following years.

Beijing also developed regional active faults, mainly including the NW orderly Nankou-Sunhe fault zone and two groups of NE orderly active fault zones named the Huangzhuang-Gaoliying fault zone and Shunyi-Liangxiang fault zone (Figure 1). All earthquakes occur along these fault zones or where they intersect (Figure 1), and almost all of these earthquakes were less than M3. Therefore, it is of great scientific and practical significance for small earthquakes monitoring and prediction in the Beijing area.

To better monitor the seismic activity in the capital area, the Chinese Earthquake Administration (CEA) started to deploy the Beijing metropolitan digital Seismic Network (BSN) in the late 90s. Currently, the network consists of broadband, borehole, and surface short-period stations that cover Beijing and the surrounding areas densely and uniformly (Jiang et al., 2008; Li and Huang, 2014). Since 2001, 107 stations have been installed in the Chinese capital region, which is the most advanced and densest digital seismic network in Mainland China. A large number of high quality waveforms have been recorded, which provides an opportunity to improve the location accuracy of small earthquakes in the region (Jiang et al., 2008).

Beijing hosted the 2022 Winter Olympic Games from February 4 to 20. For security purpose, continuous monitoring of possible earthquake areas had been strengthened, which provided an opportunity to investigate trace element variation during this time. There were approximately 400 earthquakes that were recorded in Beijing during the study period (Figure 1A), and only 22 of them were above M1.0. On 3 February 2022, one of the biggest earthquakes with a magnitude of ML3.3 occurred in the Chaoyang District of Beijing (Figure 1). Furthermore, there were 10 earthquakes above M1.5 that occurred densely during January to March 2022 (Figure 1B), but spatial distribution of these earthquakes was not clustered and spread along the NW orderly Nankou-Sunhe fault and NE orderly Huangzhuang-Gaoliying fault (Figure 1).

2.2 Hydrogeological condition of the Wuliying well and the monitoring techniques

The Wuliying well is located in the north of Wuliying village, Yanqing District, Beijing. The well is 2 km west of the Yanqing seismic monitoring station and has an epicentral distance of ~65 km from the Chaoyang earthquake (Figure 1). Geologically, the Wuliying well is located in the Yan-Huai (Yanqing-Huailai) sediment basin, where lies in the junction area of Yanshan Mountain and Zhang-Bo seismic belt. The northern marginal fault zone of the Yan-Huai Basin is 3 km northwest of the well, and pressure faults have developed around the well area, so the structural site of the well is sensitive to stress changes.

The Wuliying well was drilled in 1984 with a depth of 533 m, and the lithology consists of Quaternary sediment thickness of 330 m, including clay, sand, and gravel. Below the sediment are Jurassic basalt, then Sinian (Precambrian) limestone, and dolostone (Figure 2). The wellbore is open to Sinian dolostone from 505 m to the bottom of the well, and the only water inlet is at carbonate conditions, including dolomite and calcite. The well is a flowing artesian geothermal well with a flow rate 2.5 L/s, temperature 33.4°C, pH 7.3, and the water type is HCO_3–Na (Chen, 2023).

The Wuliying seismic monitoring well in Yanqing district, Beijing has established continuous and long-term monitoring systems on comprehensive hydrological parameters, including water level, temperature, Hg (mercury), Rn (radon), major ions, and gases (dissolved and degassing gases from water). Comprehensive monitoring methods have been measured daily in the Wuliying well for decades, including the water level, deep water temperature, four major ions (F^-, Cl^-, SO_4^-, and NO_3^-), five dissolved gases in water (Hg, H_2, He, N_2, and CH_4), and three degassing gases (Hg (gas), Rn (gas), and H_2 (gas)) (sample gathering device in Figure 2). The sufficient data provided an important foundation for earthquake monitoring and prediction in Beijing. In this research, we compare the seismic sensitivity of trace elements to all geochemical parameters already available of the Wuliying wells. Hence, the Wuliying well provided an opportunity to investigate multiple parameter variations coupled to earthquakes.

In addition, the Songshan hot spring is ~10 km from the Wuliying well. The spring is an artesian geothermal type, and the water comes from the granite rock body of Dahaituo Mountain that is also near the northern marginal fault of the Yan-Huai Basin (Figure 1). Investigation of trace elements in the Songshan spring had been first documented in detail by Chen and Liu, 2023.

3 Methodology

3.1 Data collection

The groundwater level and deep water temperature observation of the Wuliying well are usually recorded at 1 minute interval by an SWY-2 and SZW-2 digital instrument, respectively. The instruments were developed and produced by the Institute of Crustal Dynamics, China Earthquake Administration. The water-level sensor has a range of 0–50 m, resolution of 1 mm, sampling interval of 1 s, precision of 0.02 percent, and accuracy of 0.05 percent (Chen, 2023).

Daily geochemical observations are conducted by the staff working at Yanqing monitoring station every day, including four major anions (F^-, Cl^-, SO_4^-, and NO_3^-), five dissolved gases in water (Hg, H_2, He, N_2, and CH_4), and three degassing gases (Hg (gas), Rn (gas), and H_2 (gas)). Major anions were analyzed by ion chromatography (CIC-200), dissolved gases in water were analyzed by gas chromatography (SP-3400), dissolved Hg in water was measured by mercury-measuring instruments (RG-BS) using atomic absorption, Hg (gas) degassing from the well was measured

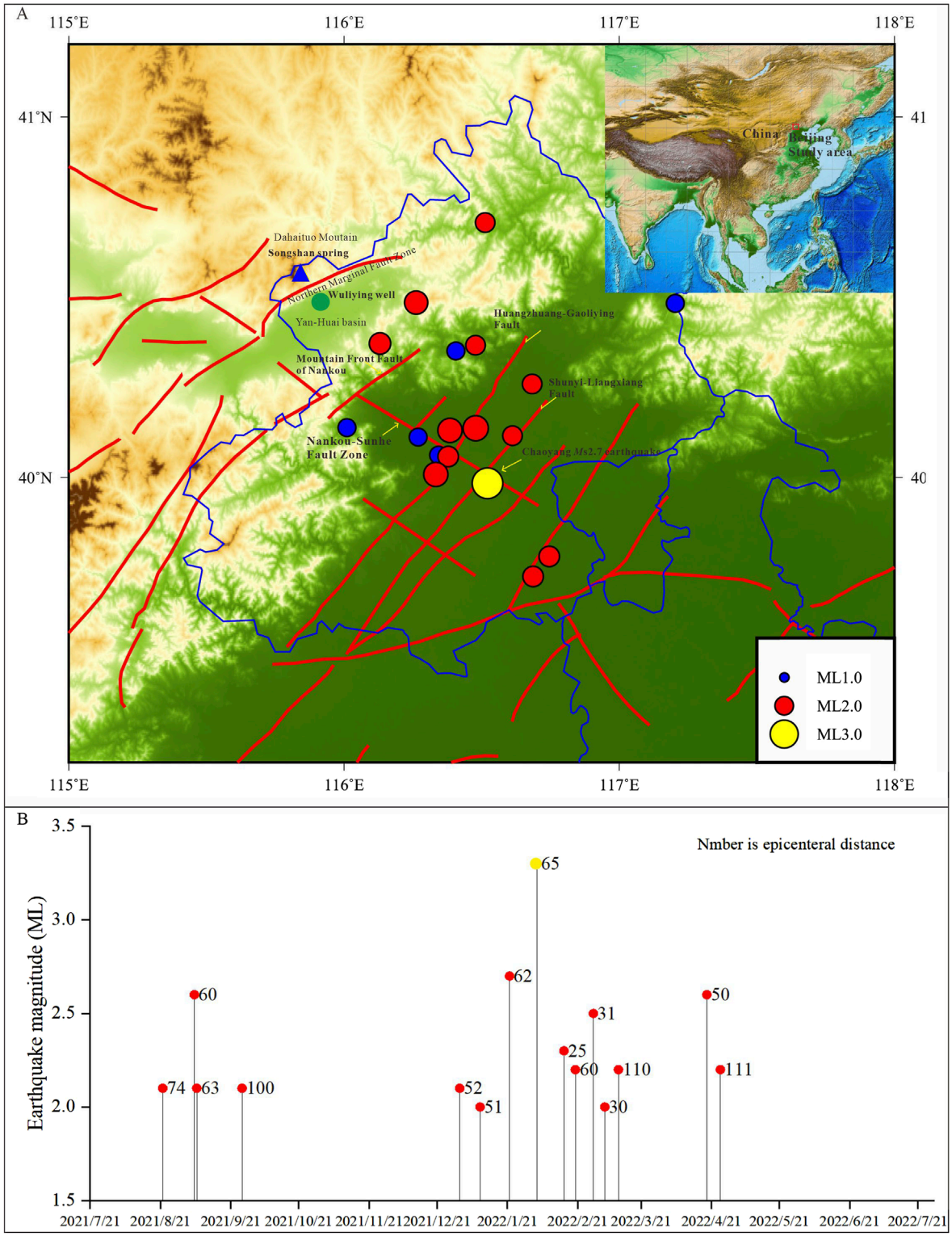

FIGURE 1
Earthquake distribution **(A)** of the Beijing area from June 2021 to June 2022 and the time sequence of earthquakes **(B)** above M1.0 (modified from Chen and Liu, 2023). The biggest yellow circle is Chaoyang M2.7 (ML3.3) earthquake, and the blue triangle and green circle were location of the Songshan hot spring and Wuliying monitoring well, respectively.

by a digital instrument (ATG-6138M), Rn (gas) was measured by a digital instrument (BG 2015R), and H_2 (gas) was measured by a digital instrument (ATG-6118H).

In addition to the above measurements, we collected water samples with relatively high sample rates for trace element analysis. The sampling and analytical procedures were described by Chen

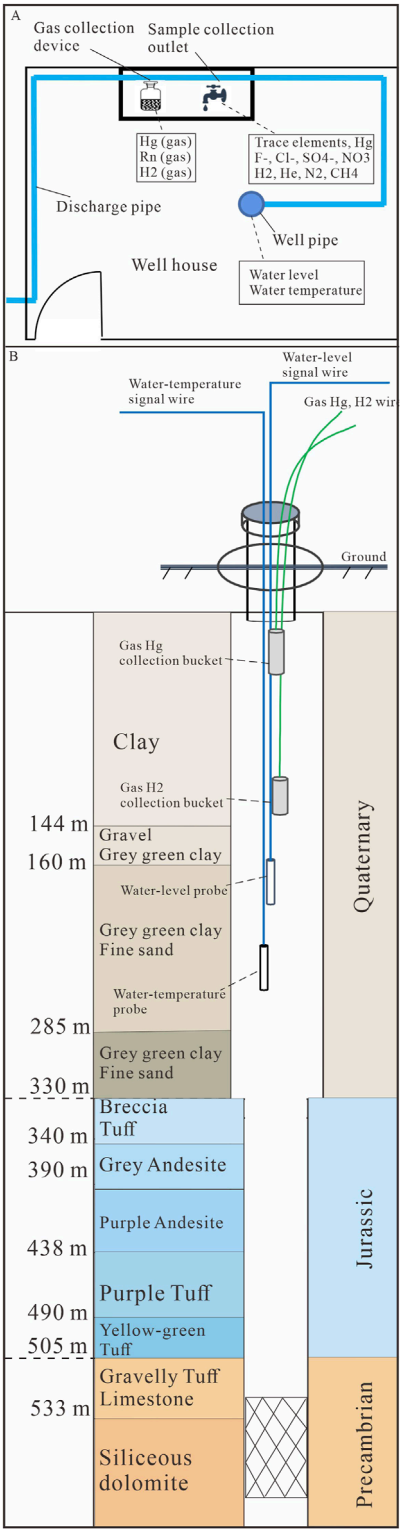

FIGURE 2
Distribution of gas and water sample gathering devices of the Wuliying well **(A)** and the lithology of the wellbore **(B)**. The grid-like section in **(B)** indicates the screen section in the well.

and Liu, 2023: water samples were collected in relatively high and regular sample rates every 7–10 days, from June 2021 to June 2022, and a total of 61 water samples were collected during the study period (almost 1 year). Each sample was stored in 200-mL polyethylene bottles. All samples were sent monthly to the Beijing Research Institute of Uranium Geology for 41 trace element constituent analysis, including Li, Ti, Pb, Sc, Ni, Cu, Nb, Th, Zn, Tl, U, Ga, Mo, Ba, Rb, Cs, Sr, Be, Mn, Cr, Co, Y, Bi, and rare earth elements (La, Ce, Pr, Nd, Sm, Eu, Gd, Tb, Dy, Y, Ho, Er, Tm, Yb, and Lu) (Supplement.xls). Each sample was filtered with 0.45-μm membranes and then acidified with 2% nitric acid before testing it on the machine (An ELEMENT XR mass spectrometer). Measurements were repeated four times for each sample and then averaged to get the results; relative standard deviation (RSD) of each sample was better than 5%. The concentration units were ug/L (ppb).

The stable isotopes of oxygen ($\delta^{18}O$) and deuterium ($\delta^{2}H$) were also analyzed at the Beijing Research Institute of Uranium Geology using a liquid-water isotope analyzer (MAT253) with an accuracy of 0.2‰ for $\delta^{18}O$ and δD.

3.2 Statistical analyses

We used data smoothing methods including LOWESS, rLOWESS, LOESS, and rLOESS (Chen and Liu, 2023). The LOWESS (locally weighted scatterplot smoothing) means local regression using weighted linear least squares and a first-degree polynomial model. The rLOWESS means a robust version of LOWESS that assigns lower weight to outliers in the regression. The LOESS means local regression using weighted linear least squares and a second-degree polynomial model. rLOESS means a robust version of LOESS. Hydrological variations and anomalies were considered apparent through smoothing.

We also calculate a Pearson correlation matrix (r values matrix) of 41 trace elemental compositions, and the r-values were considered statistically significant if $p < 0.05$. The significant r values can quantitatively indicate the correlation between each element. The correlation matrix was converted into a visual network by R program to check geochemical elemental clustering and grouping. In the network, each geochemical element is a node, and each correlation is an edge, in which the width of the edges according to the magnitude of the correlation and the placement of the nodes is a function of the pattern of correlations (Epskamp et al., 2012). This means that stronger correlations have shorter and wider edges and closer placement of nodes (Chen and Liu, 2023).

4 Results

The results of all samples are listed in Supplement.xls. The groundwater level in the Wuliying well continuously increased from 1.3 to 1.8 m during July 2021 to August 2022 (Figure 3A). The deep water temperature in the Wuliying well also consecutively increased

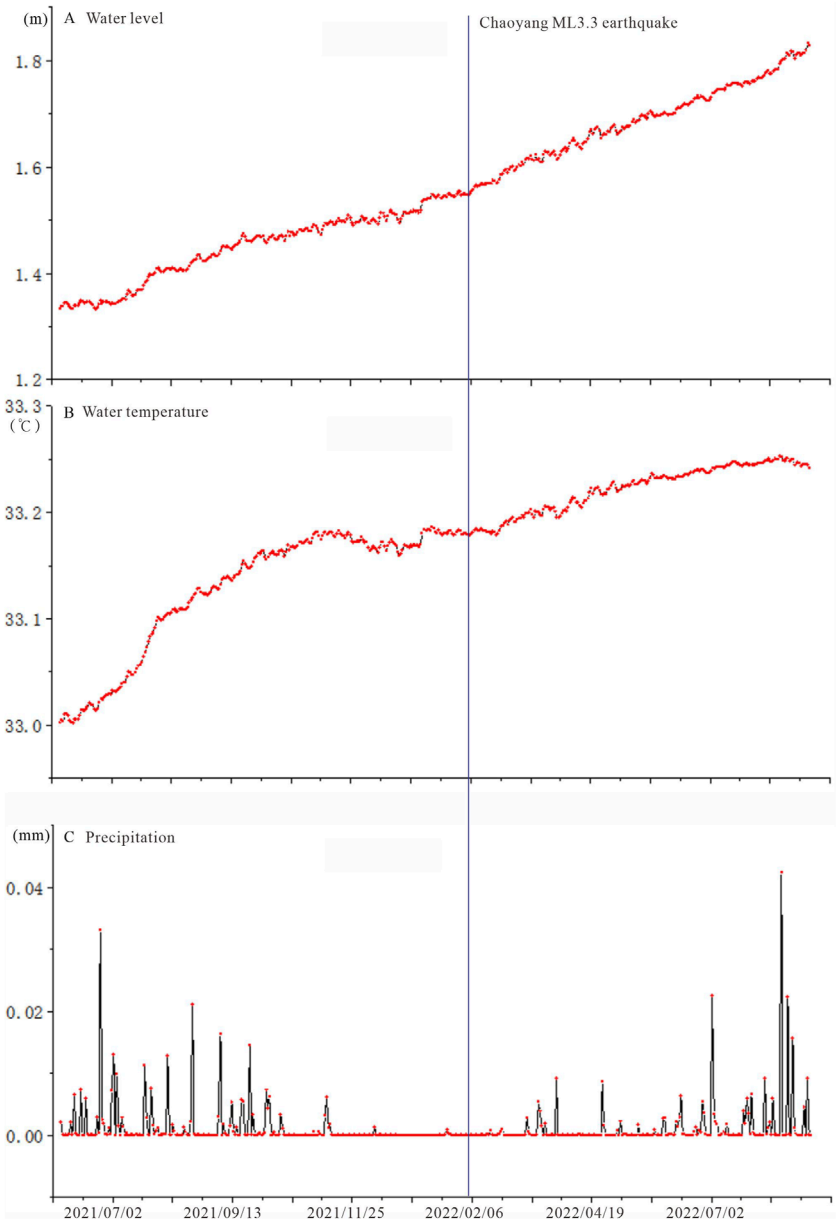

FIGURE 3
Water level and deep water temperature changes and precipitation during the study period (modified from Chen and Liu, 2023). The blue vertical line shows the time of the Chaoyang ML3.3 earthquake.

from 33.0°C to 33.22°C during the study period (Figure 3B). The changes in the water level and temperature have no relationship to precipitation as there is only large amount of precipitation during summer (from June to August every year) (Figure 3C). No abnormal changes for the groundwater level and temperature were found temporally related to earthquakes (Figure 3).

The trends of the major ions (F^-, Cl^-, SO_4, and NO_3^-) are different (Figure 4). F- had an obvious decrease from 3.6 mg/L to 2.9 mg/L (Figure 4) during October to December 2021 before the Chaoyang earthquake and then had stable concentrations from January to June 2022 during and after the earthquakes. Cl^- was stable for most of the year, but it declined rapidly in June 2022. SO_4^- was stable during the sampling period, and only some minor fluctuations in the months before and after the earthquake were observed. NO_3^- continued to rise during July 2021 to January 2022, but then it trends down. Changes in NO_3^- have a good temporal correlation with the earthquake, but NO_3^- is easily contaminated by organic matter, so this correlation is not certain.

Dissolved gases (Hg, H_2, He, N_2, and CH_4) in water also have different trends (Figure 4). Hg was stable for most of the year, but it increased rapidly in April–June 2022. H_2 had high values in July–August 2021 and then stabilized at low values from September 2021 to June 2022. Notably, He distinctly increased from 0.03% to 0.05% during November 2021 to February 2022 before the Chaoyang

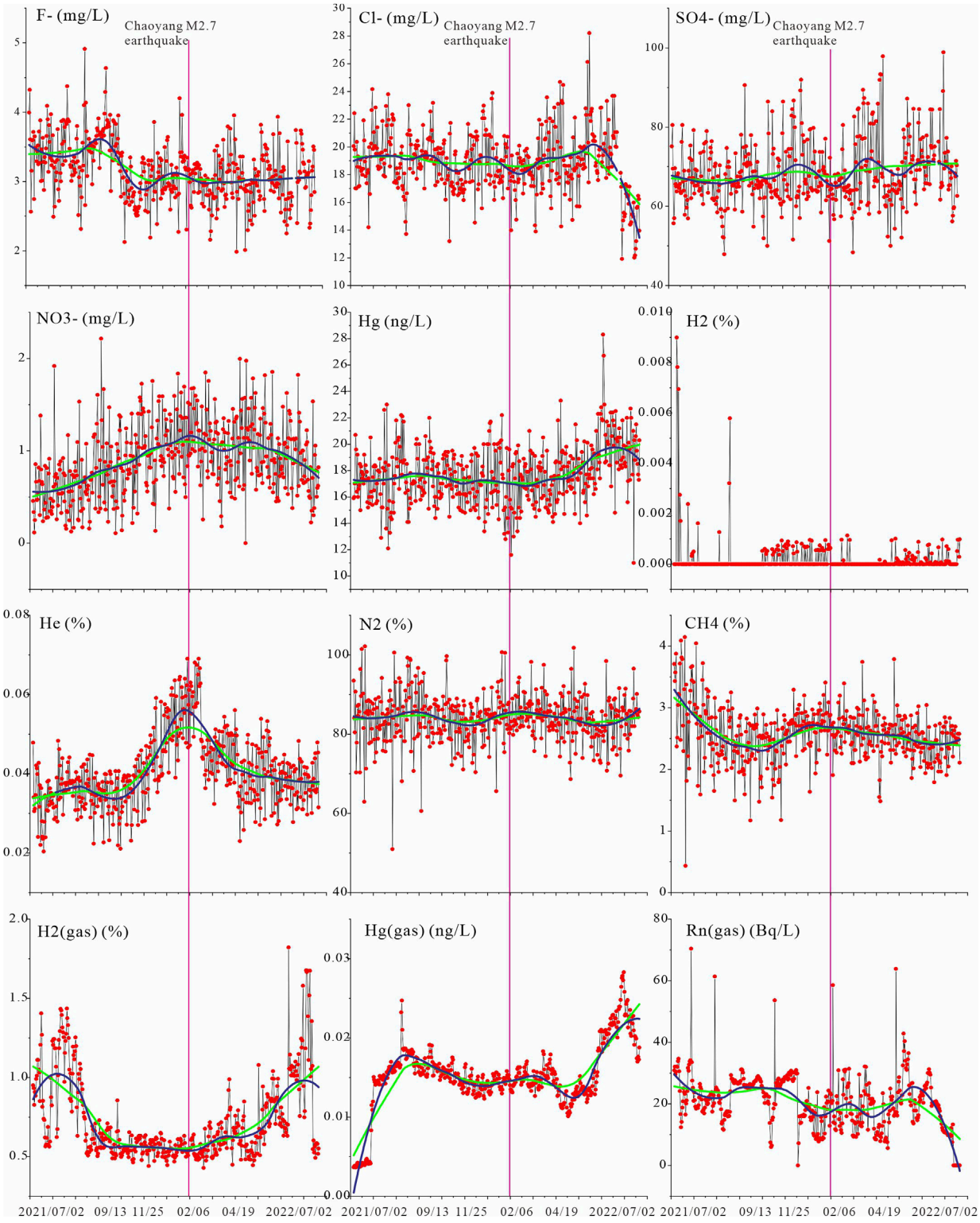

FIGURE 4
Content changes in 12 multiple parameters in the Wuliying well during the study period, including four major ions (F^-, Cl^-, SO_4^-, and NO_3^-), five dissolved gases in water (Hg, H_2, He, N_2, and CH_4), and three gases (H_2 (gas), Hg (gas), and Rn (gas)). The green line and blue line indicate the LOWESS and LOESS fitting methods, respectively. The pink vertical line shows the time of the Chaoyang ML3.3 earthquake. The *x*-axis of figures was a convenient conversion of actual dates to decimal for mathematical smoothing and fitting.

earthquake and decreased from 0.05%–0.03% from March 2022 to June 2022 (Figure 4) after the earthquake. N_2 was relatively stable during the study period. CH_4 declined rapidly from June to November 2021, and then, it was relatively stable from January to June 2022.

Three degassing/escaping gases (Hg (gas), Rn (gas), and H_2 (gas)) from water were relatively stable from October 2021 to March 2022. Notably, H_2 (gas) and Hg (gas) have peaks in July each year (Figure 4), which were likely to be related to the season but not to earthquakes. When the air temperature is high in summer, these gases' concentrations increased degassing, and when the air temperature is low in winter, these gas concentrations decreased.

The average concentration of rare earth elements (REE) is low at 0.001ug/L. The PAAS-normalized REE display remarkable positive Eu anomalies and LREE (light REE) depletion or HREE (heavy REE) enrichment distribution patterns (Figure 5A). Eu concentrations showed obvious periodic changes in the time series (Figure 5B), the period was more evident when data smoothing was done using the mathematic method (LOESS), and the Eu element concentration formed three convex peaks in September 2021, February 2022, and July 2022, respectively (Figure 5B).

Apart from REE, other 27 trace elements show different time series patterns. Based on the element correlation matrix (Figure 6A, gray box), these elements can be broadly classed into two groups (Figure 6B). The first group consists of Li, Sc, Rb, Mo, Cs, Ba, W, U, Sr, Mn, Ni, and Zn, which cluster each other in the correlation network, drawing pink circles in Figure 6B. These elements had a consistent trend: rapidly decreased from December 2021 to early February 2022 (Figure 7), before the earthquake, and then increased in later time. The decreased changes were marked when smoothing methods were used (Figure 7, LOWESS and LOESS methods). The small variations in the first group trace elements might be due to the measurement error of each sample; however, since the trends are clearly evident, the overall trend is more relevant than individual variations, so the variations are believable.

The second group consists of Pb, Cr, Ga, Cu, Be, Nb, Ti, V, Y, Cd, Tl, Th, Sb, Bi, and Co, which were dispersed among each other in the correlation network (gray circles in Figure 6B). These elements had no regular changes and no temporal coincidence with earthquakes.

For the hydrogen (δ^2H) and oxygen ($\delta^{18}O$) isotopes, we analyzed five samples (2 December 2021, 3 January, 3 February, 3 March, and 3 April 2022) of the Wuliying well and Songshan hot spring, respectively. The hydrogen and oxygen isotopes exhibited small fluctuations during the study period. At the Wuliying well, δ^2H and $\delta^{18}O$ values range from −89.0‰ to −90.5‰ and from −13.4‰ to −12.5‰, respectively. At Songshan spring, δ^2H and $\delta^{18}O$ values range from −89.7‰ to −91.0‰ and from −12.8‰ to −13.0‰, respectively. These values all plot to the left of the GMWL (the global meteoric water line from Craig, 1961) and LMWL (the local meteoric water line from Yu et al., 1987).

5 Discussions

5.1 Water level and temperature

During the study period, the Chaoyang ML3.3 earthquake occurred in the region, but the epicentral distance was ~65 km, and the seismic energy density produced by the earthquake at Wuliying well was $\sim 0.03 * 10^{-4}$ J/m3 (calculation according to the method from Wang, 2007), which is much smaller than the minimum energy density (10^{-4} J/m3) that was required for triggering hydrological responses based on global observations (Wang, 2007). The calculation of the above empirical formula was consistent with the actual observations, that is, no abnormal changes in the groundwater level and temperature to the earthquake, and they had no temporal relationship.

Many previous studies have documented co-seismic groundwater level changes, following earthquakes, and have proposed several mechanisms to explain the responses, such as co-seismic static strain-induced dilation and compaction (Ge and Stover, 2000), liquefaction or consolidation of sediments (Wang et al., 2001), and permeability changes caused by shaking (Brodsky et al., 2003). Among these mechanisms, the crustal strain dilation or aquifer permeability changes causing mixtures of different waters are usually considered to be the mechanism that explains these responses (Woith et al., 2013; Skelton et al., 2014). For our case, the absence of concomitant shifts in the water level excluded the previously proposed mechanisms in aquifer dilation/compaction and permeability changes, which would cause abundant groundwater movement and the massive addition of additional water into the wellbore, causing an increase in water levels.

5.2 Major ions and gases

In our data, three major ions (F^-, Cl^-, and NO_3^-) had changed during the study period; however, the change in Cl^- did not correspond to the time of the earthquake, NO_3^- is easily contaminated by organic matter, and the correlation is not certain, so only F- had an obvious decrease approximately one month before the Chaoyang earthquake, which were temporal-related, and the tendency is consistent with results of the previous studies. For example, Wei et al. (1991) also found that F- concentrations appeared clearly negative anomalies around the Sihai (northwest of Beijing) M3.0 earthquake in 1986 and Zhangjiawan (Xuanhua city near Beijing) M4.2 earthquake in 1987. They suggested that the probable mechanism is the aquifer mixing process, that is, large volumes of chemically distinct groundwater enter the well and mix with the original water, so that the mixing ratio is changed. Skelton et al. (2019) also found that F- from one site in northern Iceland had decreased response to the M5.3 earthquake in 2013. They also infer mixing of groundwater sources caused by the rupture of a hydrological barrier between sources.

The mechanism of major ions was suggested to be affected by many factors, and considerably larger changes in aquifer properties or large volumes of mixing would be needed (Rojstaczer and Wolf, 1992). Variation in major ion concentrations in groundwater can record mixing and/or switching between different groundwater sources (Skelton et al., 2019), water–rock interactions, or some combination of both the processes. This is because groundwater sources tend to be chemically distinct from one another and because water–rock interactions can cause species release into (or removal from) groundwater. Hence, in this study, F- ion had an obvious decrease, meaning a small mixing of

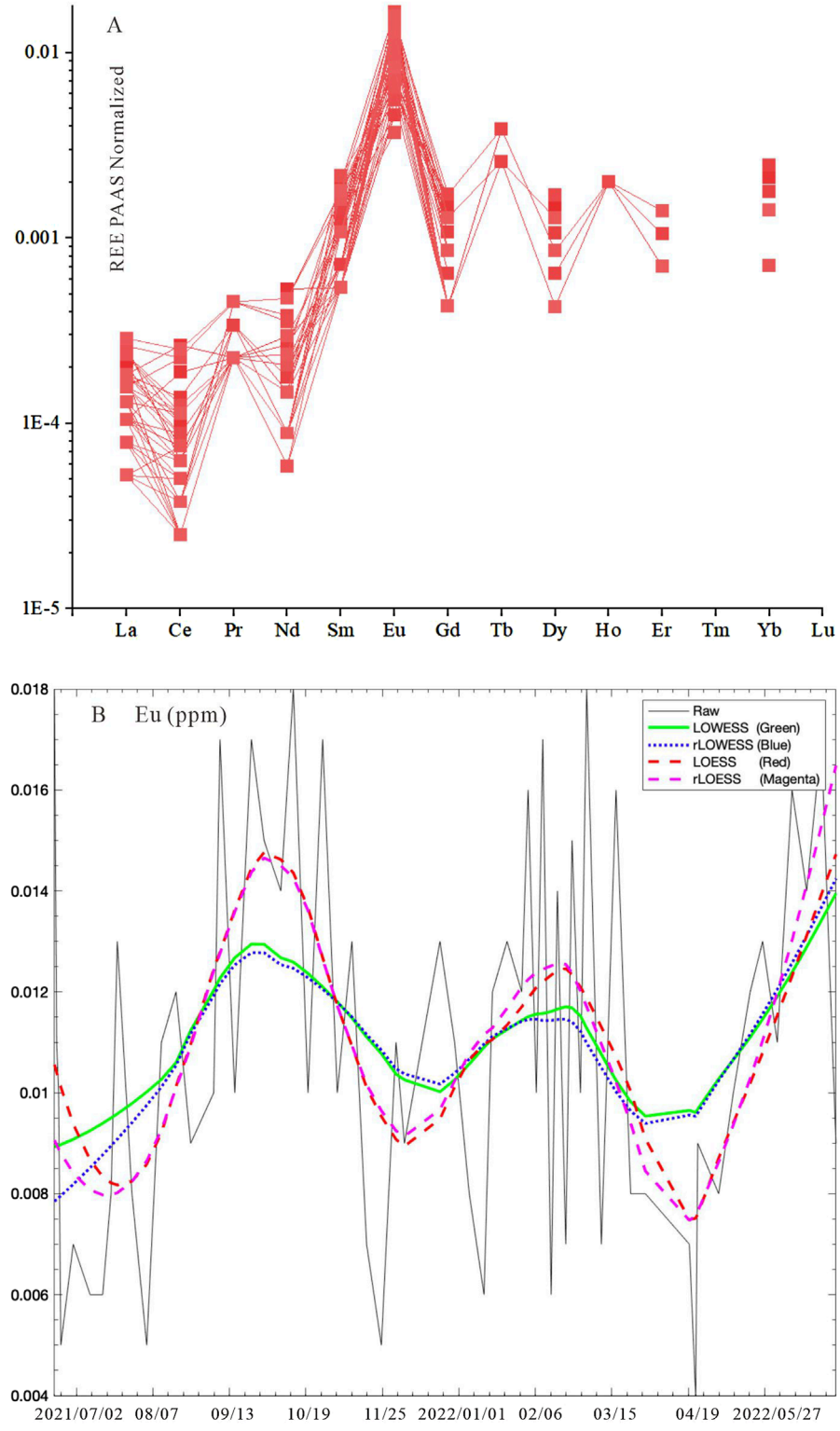

FIGURE 5
PAAS shale-normalized REE patterns **(A)** and variation in Eu **(B)** during the study period. The *x*-axis of figures was convenient conversion of actual dates to decimal for mathematical smoothing and fitting.

groundwater sources reflecting the leakage along a fracture system or a minor switching between sources reflecting the rupture of a hydrological barrier between sources.

Geochemical gases involved in the Earth's degassing activity are considered responsible for water-gas-rock interaction processes able to induce chemical variations in groundwater composition (King,

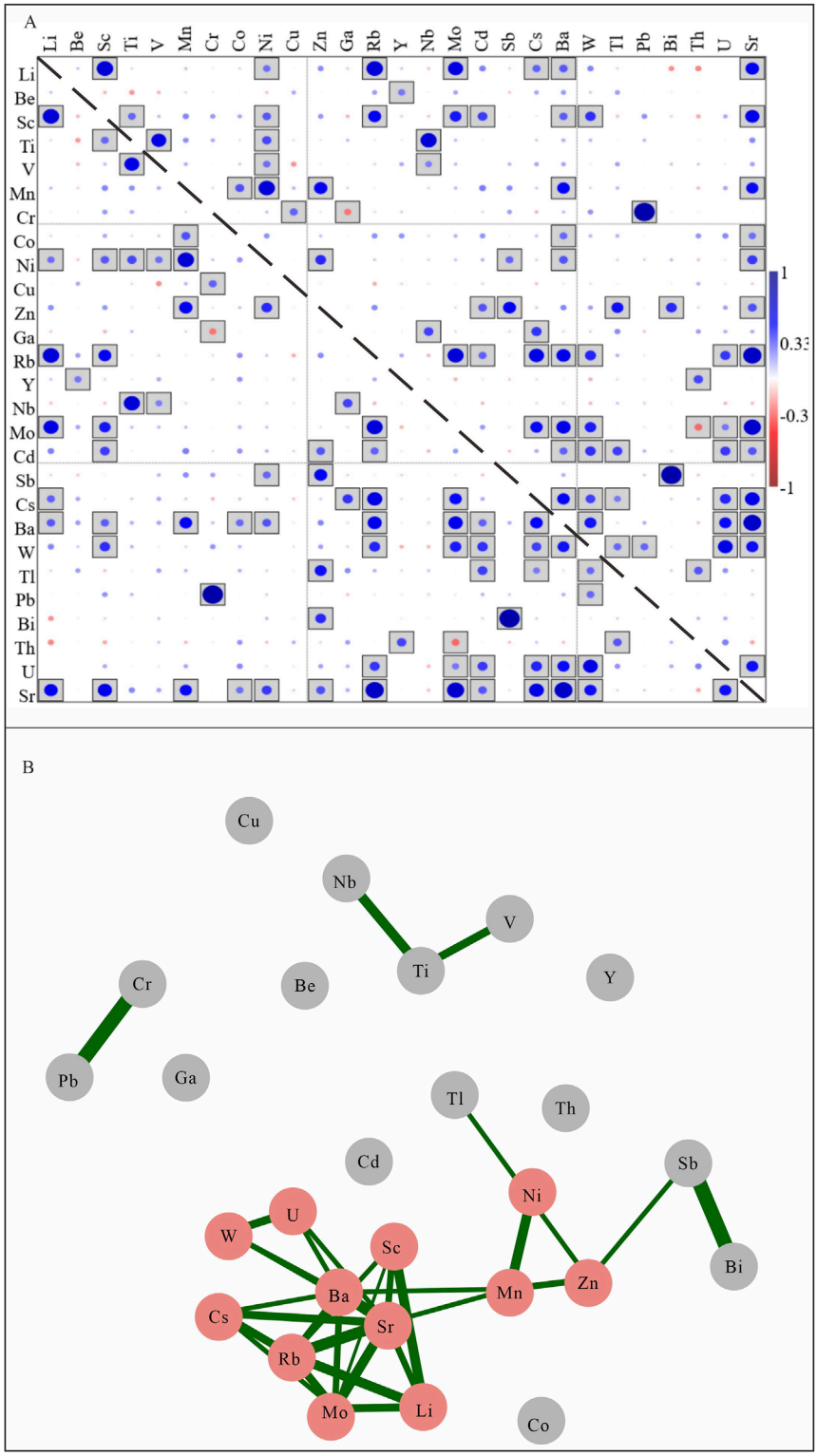

FIGURE 6
Trace element correlation matrix **(A)** and elemental correlation cluster **(B)**. Each circle in A represents the strength of the element correlation; the larger the circle, the stronger the correlation, and the box represents that the correlation has statistical significance. Network structures in B based on the correlation matrix of **(A)**. Each geochemical element is a node, and each correlation is an edge. Stronger correlations have shorter and wider edges and a closer placement of nodes.

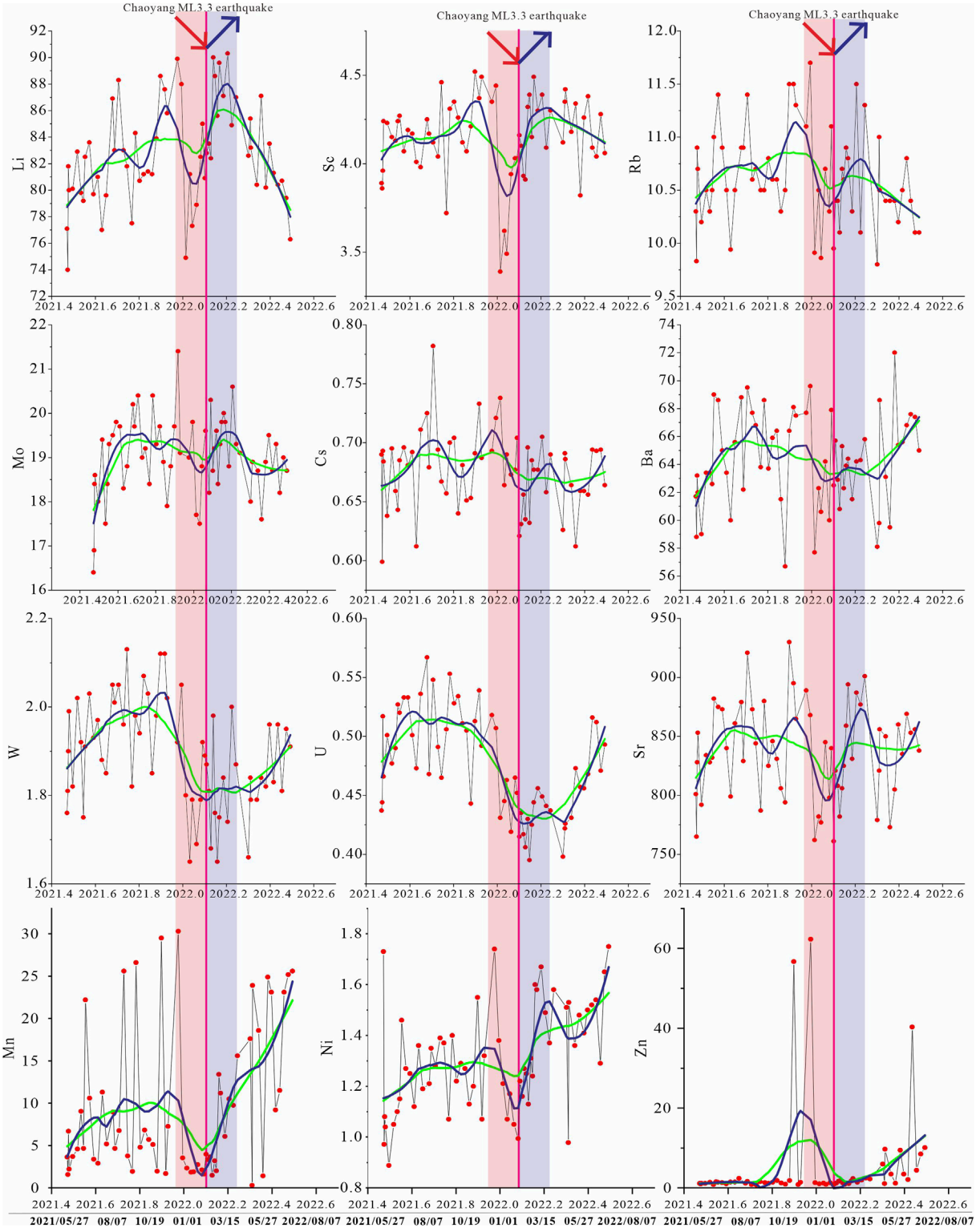

FIGURE 7
Time series of trace elements in the Wuliying well during the study period, including Li, Sc, Rb, Mo, Cs, Ba, W, U, Sr, Mn, Ni, and Zn (unit, in ug/L). The green line and blue line indicate the LOWESS and LOESS fitting methods, respectively. The pink shadow shows the time period of decline of trace elements. The blue shadows the show time period of increase of trace elements. The purple vertical line shows the time of the Chaoyang ML3.3 earthquake. The date of the *x*-axis is decimal for mathematical smoothing and fitting. The bolded font at the bottom is the actual date.

1986; Martinelli, 2015). About all geochemical anomalies have been directly or indirectly attributable to deep fluid pressure variations induced by crustal deformative processes since fluid pressure is proportional to stress and volumetric strain (Petrini et al., 2012). From the results (Figure 4), four dissolved gases (Hg, H_2, He, and CH_4) in water had changed during the study period, while the changes in Hg, H_2, and CH_4 did not correspond to the time of the earthquake, only He (helium) increased approximately two months before the Chaoyang earthquake and then decreased and returned to the original value a few months after the earthquake, so they had a strong temporal relationship. Due to its deep origin and characteristics, helium appears as a powerful indicator of deep and early demixing processes, and it appears as an exceptional marker of crustal discontinuities, using faults, tiny fractures, and paths to rise to the surface (Wakita et al., 1978; Toutain and Baubron, 1999). Note that Gao and Xing (2011) also found an abnormal increase of He in the Wuliying well before the Wenchuan M8.0 earthquake in 2008. In this study, He had an obvious increase, implying deep rooting of the fractures, and the fractures had occurred at the microscale, and gas leakage along fracture pathways formed because of crustal dilation associated with the stress build-up before the earthquake.

Three degassing/escaping gases (Hg (gas), Rn (gas), and H_2 (gas)) from water were relatively stable. The high values of these gases in summer may be related to air temperature and do not correspond to the time of the earthquakes.

5.3 Hydrogen and oxygen isotopes

Broadly speaking, the usefulness of using stable isotopes to predict earthquakes due to these responses is less likely to be site-specific. Specifically, variations in δ^2H in groundwater records mixing and/or switching between different groundwater sources, whereas variation in $\delta^{18}O$ in groundwater records the water–rock interaction (Skelton et al., 2019). This is because rocks, compared with water, contain proportionally more oxygen than hydrogen (Taylor, 1977). Hence, groundwater $\delta^{18}O$ values are strongly affected by water–rock interactions. δ^2H values are largely unaffected by the water–rock interaction, and can, therefore, provide a faithful record of mixing and/or switching between different groundwater sources (Skelton et al., 2019).

In our data, the $\delta^{18}O$ and δ^2H values of groundwater from both sites (Wuliying well and Songshan hot spring) plot to the left of the GMWL and LMWL (Figure 8A) and exhibited small variations. Furthermore, note that the variation in $\delta^{18}O$ of the Wuliying well had a small increasing trend, varied from −13.4‰ to −12.5‰ (Figure 8B), and shifted from a less negative $\delta^{18}O$ value toward GMWL, implying the strengthened degrees of the water–rock interaction. δ^2H had low values compared with values in rivers (~-85 to −65‰ in the Chaobai river (Song et al., 2007); −70 to −60‰ in the Yongding river (Liu et al., 2008)), meaning that there was no leakage of surface water (river) into the borehole. δ^2H had a small downward trend and varied from −89.0‰ to −90.5‰ (Figure 8C), indicating minor mixing between older (isotopically lighter) groundwater sources and original water. Hence, stable isotope data point to the combination of groundwater mixing and water–rock interaction processes.

5.4 Rare earth elements (REEs)

The REE content in the Wuliying site was very low (ug/L), which eliminated the influence of surface water and soil REE, because surface water and soil had a relatively high REE content (mg/L). The low REE content indicated that the confined water was sealed and was not affected by the surface environment.

In our case, the water of the Wuliying well displayed remarkable positive Eu anomalies and HREE (heavy REE) enrichment distribution patterns (Figure 5A), which indicated that REE in water came from feldspar and calcite minerals. Eu is a redox-sensitive REE, and in reducing settings, Eu (III) can be reduced to Eu(II), creating the potential for fractionation relative to the other REEs (Elderfield, 1988). However, this redox transformation requires both low redox potential and high temperature, a combination most commonly found in magmatic systems rather than in Earth-surface environments (Bau, 1991). Feldspar commonly becomes Eu-enriched during magmatic crystallization, owing to ready substitution of Eu^{2+} for Ca^{2+} (Taylor and McLennan, 1985; Chen et al., 2021). The calcite usually had an HREE-enriched pattern because of stronger carbonate complexation of HREEs (Webb and Kamber, 2000; Chen et al., 2021). The strength of REE-carbonate complexation increases from La to Lu as a result of a systematic increase in the stability constant of ligand complexes with increasing atomic number. The above REE results coincide with petrological evidence as the aquifer in the Wuliying well is made of limestone and dolostone containing a large amount of calcite. The overlying Jurassic basaltic rocks contain a lot of feldspar, so REE features indicated that groundwater in the Wuliying well was a mixture that came from different host rocks, implying that some fractures cut through both aquifers dominated by the limestone and overlying basaltic rocks.

The REE can trace the host rocks from which the water originated. The Eu concentrations showed obvious periodic changes with no response to the earthquake. The mechanism might be related to rock weathering rather than the earthquake. Because the concentration of Eu elements released by feldspar minerals was related to the strength of rock weathering caused by periodic temperature changes, it is most likely that weathering causes the periodic feldspar minerals to release REE to water.

5.5 Trace element characterization

Mechanism explanations for geochemical anomalies are relatively rare and based on co-seismic geochemical changes, following the earthquake (Claesson et al., 2007; Skelton et al., 2019). We considered the previously proposed mechanisms for changes in geochemical compositions. For example, Favara et al. (2001) collected geochemical composition (Ca, Cl, and SO_4) at three thermal springs in central Italy in the 1997–1998 seismic swarm. The authors suggested that the recorded variations actually seem to have been induced by permeability variations related to crustal deformation in the absence of elastic energy release. Rosen et al. (2018) proposed that the changes in trace elements were likely related to the release of groundwater of different residence times from pore spaces or fractures. Shi et al. (2020) suggested that the changes in trace elements were the combined result of the addition of

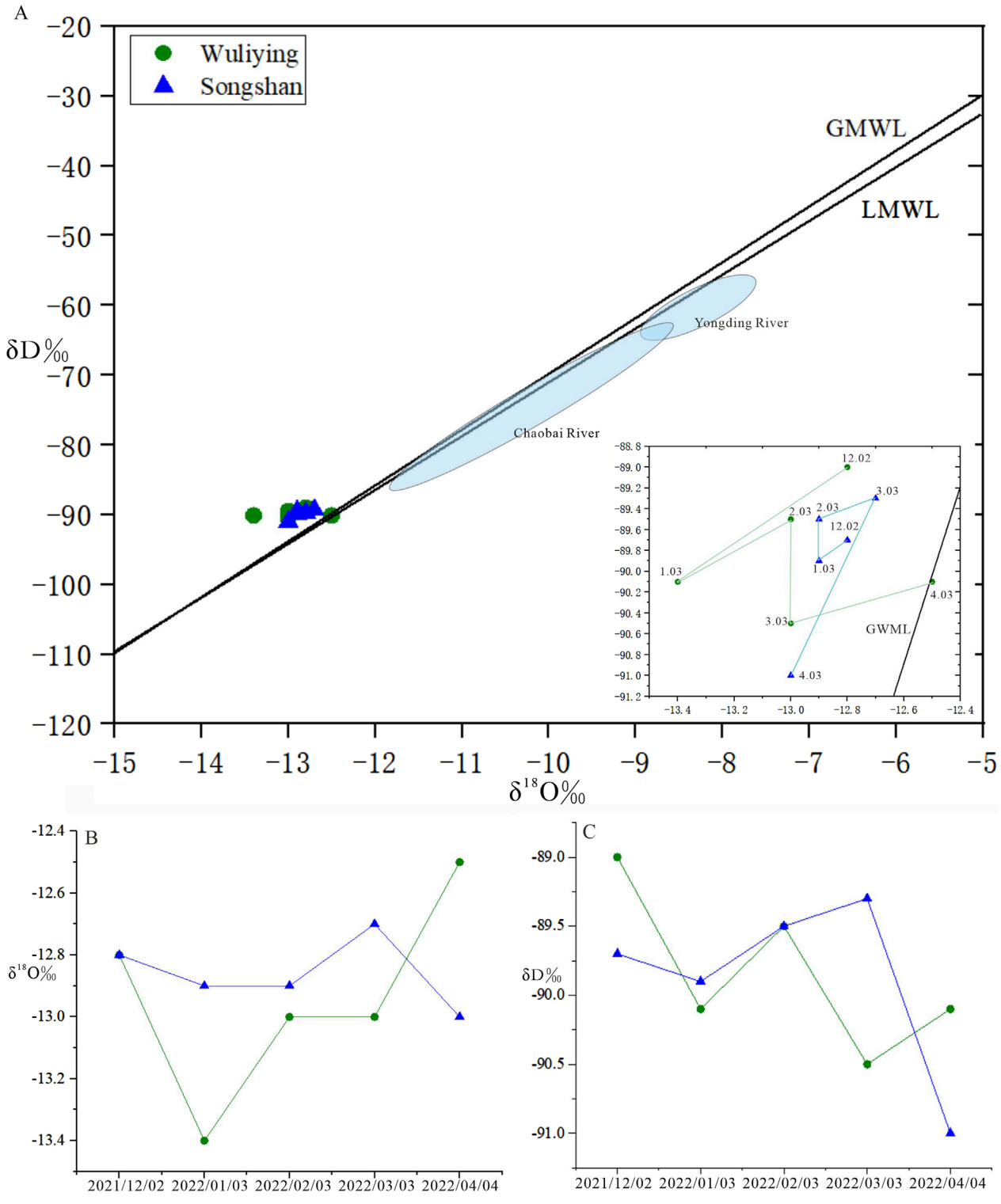

FIGURE 8
(A). Bi-variant plot of δD and $\delta^{18}O$ in the five samples (2 December 2021, 3 January, 3 February, 3 March, and 3 April 2022) in the Wuliying well and Songshan spring in Yanqing District, Beijing. The δD and $\delta^{18}O$ of the Chaobai River cited from Song et al. (2007). The δD and $\delta^{18}O$ of the Yongding River cited from Liu et al. (2008). The inset shows the enlarged δD and $\delta^{18}O$ variation. **(B)** Time series of $\delta^{18}O$. **(C)** Time series of δD.

small amounts of water from the reservoirs isolated by the hydraulic barrier and the changes in the physical–chemical environment, following the earthquake.

Most of above mechanisms were proposed based on studies of co-seismic changes. In our study, we investigate characteristics of trace elements on pre-seismic changes, and based on smoothing

methods, we can confirm probable associations between pre-seismic shifts of trace elements and the earthquake (Figure 7). These trace elements have pre-seismic downward changes, which were similar with the previous observations. For example, Claesson et al. (2004) reported pre-seismic rapidly decreased anomalies in the concentrations of Cr and Fe before the Mw 5.8 earthquake in 2002, and they interpreted that the earthquake ruptured a hydrological barrier, permitting a rapid influx of water of other aquifers. The pattern of the post-seismic recovery of chemical compositions could refer to Claesson et al. (2007); they proposed that the increase in the reactive surface area would shift the system out of chemical equilibrium and lead to a more extensive water–rock interaction, and increases in concentrations of some dissolved cations would be expected.

Furthermore, it is noteworthy that these sensitive trace elements originated from different rocks. For examples, Li and Sc probably came from basaltic rocks as Li is a typical lithophile and often enriched in mica and other silicate minerals, and Sc has a very high partition coefficient in granites (Mou, 1999). Rb, Cs, Ba, Sr, Mn, and Mo most likely came from carbonate of limestone and dolostone because these elements are closely located in the periodic table nearby the Ca element, indicating that these elements have very similar chemical properties as Ca. According to petrology, elements of Ba, Rb, Cs, and Sr often replace Ca in the calcite mineral with isomorphism (Mou, 1999). W, U, Ni, and Zn are transition elements in the periodic table, which were present in both basaltic rock and dolostone. The characteristics of different origins of the trace elements imply the ruptures cutting through strata, including different lithologies dominated by dolostone and basaltic rocks, which was consistent with REE features and the lithology of the Wuliying well.

Hence, the mechanism of trace element response in the Wuliying well may be explained as follows: the pre-seismic minor stress/strain changes caused by the Chaoyang earthquake led to small (micro) fractures cutting aquifers and overlying basaltic rocks, and maybe other nearby small isolated reservoirs, thereby leading to the mixing of chemically distinct water with the original water. The small amount of water with different trace element concentrations added, which diluted the element concentration, because the concentrations of trace elements were usually very low, and below the detection limits in many groundwater sources, the trace elements concentrations could change easily (Rosen et al., 2018). Finally, the increase in the reactive surface area caused by fractures would enhance the water–rock interactions, resulting in the post-seismic recovery of trace elements. After the earthquake, sawtooth patterns emerged in some trace elements, most likely caused by undulant changes in sealing off of the fracture with time. Thus, the mechanism of trace elements in the Wuliying well may have been the combined result of mixing and water–rock interaction processes.

We need to note that trace elements showed different responses in nearby sites. Trace elements in the Songshan hot spring near the Wuliying well had significantly upward or downward changes based on different groups in response to the Chaoyang earthquake (same earthquake in this paper), which are documented in detail by Chen and Liu, 2023, meaning that the sensitivity of trace elements in different sites may depend on many factors that could affect the fluid chemistry in a specific aquifer system. We infer that the site-specific behavior of species concentrations reflects, differing rock mineral assemblages. This is not surprising, given the differing groundwater source. For example, the aquifer of the Wuliying well came from dolomite and basaltic host rocks, while the aquifer of Songshan spring came from the granite host rocks. Furthermore, the two monitoring sites are on different structural locations; the Wuliying well is located in the sediment basin at the lower plate of the northern marginal fault, while the location of Songshan spring is on the bedrock at the upper plate of the northern marginal fault zone, implying different stress/strain sensitivities. So, trace element species were site-specific. More trace element data are needed to provide an additional understanding of the sensitivity of different trace elements to earthquake stress.

5.6 Mechanism of multiple geochemical parameters

In summary, most of those mechanisms were proposed based on studies related to springs with a single hydrological parameter, usually using the water level or major ions. Few studies have examined both groundwater levels and multiple geochemical constituents in response to earthquakes (Barberio et al., 2017; Rosen et al., 2018; Skelton et al., 2019; Shi et al., 2020). In our study, we investigate characteristics of multiple hydrological parameters. We found no shift in the water level and temperature related to earthquake, F- of major ions decreased and He gases increased before the earthquake, and some trace elements decreased before the earthquake and then returned to initial concentration, including Li, Sc, Rb, Mo, Cs, Ba, W, U, Sr, Mn, Ni, and Zn.

Hence, the mechanism for multiple hydrological parameters in this study most likely can be explained as a combination result of mixing and water–rock interactions. The mixing could be examined by no shift in the groundwater level, small decrease in the hydrogen isotopes (δ^2H) and major ion concentration (F-), and pre-seismic decrease in trace elements (including Li, Sc, Rb, Mo, Cs, Ba, W, U, Sr, Mn, Ni, and Zn). The probable scenario was that minor stresses caused by the Chaoyang earthquake might create micro-cracks in bedrocks, thereby leading to mixing between chemically distinct water and the original aquifer. Because the volume of water added to the system was small, there would be slight changes in the above hydrological parameters. Finally, the increase in the reactive surface area caused by fractures would enhance the water–rock interactions, resulting in the post-seismic recovery of trace elements. This interpretation is also supported by concomitant shifts of $\delta^{18}O$ values, and the shift from a less negative $\delta^{18}O$ value toward GMWL also indicates strengthening degrees of the water–rock interaction.

5.7 Coupling between geochemical changes and earthquakes

As mentioned above, a group of small earthquakes above M1.0, mainly the biggest Chaoyang M2.7 earthquake, had small magnitudes and longer epicenter distance, while the small earthquakes caused several abnormal shifts of multiple geochemical changes, such as, F-, He, hydrogen and oxygen isotopes, particularly trace element changes. The sensitive geochemical parameters of

the Wuliying well had strong temporal correspondence with the Chaoyang earthquake.

They also had a strong spatial correlation because these seismic activities in Beijing mainly occurred on one NW orderly fault zone orderly on a regional scale. The Wuliying well was also located in the northwest direction of the Chaoyang earthquake, and the direction was consistent with the NW orderly fault zone. Furthermore, the local fault zone was controlled by the large-scale NW orderly Zhang-Bo seismic belt in North China, so the associations indicated that the Zhang-Bo seismic zones were strongly active from January to March 2022.

Hence, the monitoring of trace element changes has temporal–spatial significance in the Beijing area, where small earthquakes occur frequently. Furthermore, we propose to find other sensitive sites to investigate continuous and long-term multiple geochemical characteristics in Beijing and the Zhang-Bo seismic belt that would be helpful for deepening the understanding of the mechanism of geochemistry changes in response to earthquake stress.

6 Wider implications

Overall, we can state that past earthquakes in our study area were probably associated with multiple pre-seismic and post-seismic geochemical shifts, and the Chaoyang earthquake had been recorded at two sites (Wuliying well and Songshan hot spring). A few trace elements are inferred to bound geochemical anomalies coupled to earthquakes, and trace elements offer the greatest potential as a precursor of M < 3 earthquakes in Beijing, confirming the findings of Chen and Liu, 2023. Trace elements might be more sensitive to small earthquake stress and would be good candidates to monitor small earthquake activities. Several other geochemical parameters for coupling with earthquakes could be shown and can offer valuable insights about the causes of coupling between geochemical changes and earthquakes. Hence, the monitoring of multiple geochemical compositions has great scientific and practical significance in the Beijing area, where small earthquakes occur frequently. Furthermore, it is possible that with further extension of our time series, trace element shifts can also be used to verify the association with other earthquakes; therefore, we suggest that the monitoring of multiple geochemical compositions should be sufficiently long so that random coincidences can be ruled out and the longevity of the time series permits statistical verification of coupling between geochemical changes and earthquakes.

7 Conclusion

In this study, we have examined the sensitivity of multiple geochemical constituents to earthquakes, including trace elements, four major anions (F^-, Cl^-, SO_4^-, and NO_3^-), five dissolved gases in water (Hg, H_2, He, N_2, and CH_4), and three degassing gases (Hg (gas), Rn (gas), and H_2 (gas)). Based on mathematical smoothing and fitting methods, we can better observe the association between geochemical shifts to the earthquakes. This study has the following three conclusions:

1. Although the Chaoyang earthquake had a small magnitude, long distance, and small energy density, the F-, He, and oxygen isotopes of the Wuliying well had strong temporal correspondence with the earthquakes. A few sensitive trace elements also are anomalies coupled to the earthquakes, including Li, Sc, Rb, Mo, Cs, Ba, W, U, Sr, Mn, Ni, and Zn. These trace elements are likely to be sensitive to a crustal minor strain by the small earthquakes, which offer the greatest potential as a precursor of M < 3 earthquakes in Beijing.
2. We attribute source mixing and the water–rock interaction caused by micro-scale fractures as the mechanism of coupling between changes in trace elements, oxygen isotopes, and earthquakes in this study. Our explanation provided the possibility of geochemical signals to small physical perturbations occurring at a depth.
3. This work assessed the sensitivity and validity of multi-geochemical parameters as monitoring and predictive tools in Beijing as a key seismic monitoring area. Trace elements might be more sensitive to small crustal strain and would be good candidates for short-term seismic precursor anomalies, which should be considered a priority for monitoring the tectonic activities and establishment of seismic monitoring networks along faults. Thus, the construction of continuous and long-term monitoring system for trace elements will be necessary in Beijing even on the Zhang-Bo seismic belt in the future. On the other hand, trace element monitoring could be used not only as a precursor before earthquakes but also as a good way to assess environmental changes caused by earthquakes, thus evaluating the magnitude of the disaster after earthquakes by changes in the water quality.

Data availability statement

The datasets presented in this study can be found in online repositories. The names of the repository/repositories and accession number(s) can be found in the article/supplementary material.

Author contributions

YC: formal analysis, funding acquisition, investigation, methodology, supervision, validation, visualization, writing–original draft, and writing–review and editing. GL: formal analysis, supervision, validation, and writing–review and editing. FH: formal analysis, supervision, validation, and writing–review and editing. ZW(4th author): funding acquisition, supervision, and writing–review and editing. LH: funding acquisition, supervision, and writing–review and editing. MY: supervision and writing–review and editing. XS: writing–review and editing. PH: writing–review and editing. SZ: writing–review and editing. YAZ: writing–review and editing. XW: investigation and writing–review and editing. ZW(12th Author): investigation and writing–review and editing. LX: investigation and writing–review and editing. KH: writing–review and editing. BC: writing–review and editing.

HD: writing– review and editing. YOZ: investigation and writing–review and editing.

Funding

The author(s) declare that financial support was received for the research, authorship, and/or publication of this article. This work was supported by grants from the Project of Technology Innovation of Beijing Earthquake Agency (BJWC-2022017), the Beijing Earthquake Short-Term Tracking and Anomaly Verification Program (ZQDL05), and the Science and Technology Project of Beijing Earthquake Agency (Grant No.BJMS-2024001).

Acknowledgments

The authors express their sincere thanks to editors and reviewers for valuable constructive comments on this manuscript that greatly enhanced the clarity and improved this work.

Conflict of interest

The authors declare that the research was conducted in the absence of any commercial or financial relationships that could be construed as a potential conflict of interest.

Publisher's note

Supplementary material

The Supplementary Material for this article can be found online at: https://www.frontiersin.org/articles/10.3389/feart.2024.1448035/full#supplementary-material

References

Barberio, M. D., Barbieri, M., Billi, A., Doglioni, C., and Petitta, M. (2017). Hydrogeochemical changes before and during the 2016 Amatrice-Norcia seismic sequence (central Italy). *Sci. Rep.* 7 (1), 11735. doi:10.1038/s41598-017-11990-8

Bau, M. (1991). Rare-earth element mobility during hydrothermal and metamorphic fluid-rock interaction and the significance of the oxidation state of europium. *Chem. Geol.* 93, 219–230. doi:10.1016/0009-2541(91)90115-8

Brodsky, E. E., Roeloffs, E., Woodcock, D., Gall, I., and Manga, M. (2003). A mechanism for sustained groundwater pressure changes induced by distant earthquakes. *J. Geophys. Res.* 108 (B8), 2390. doi:10.1029/2002JB002321

Chen, Y. X., and Liu, J. B. (2023). Groundwater trace element changes were probably induced by the ML3.3 earthquake in Chaoyang district, Beijing. *Front. Earth Sci.* 11, 1260559. doi:10.3389/feart.2023.1260559

Chen, Y. (2023). Time-frequency characteristics of groundwater in Wuliying monitoring well, Yanqing, Beijing and its relationship with regional seismic activity (in Chinese). *North China Earthq. Sci.* 41 (2), 58–68. doi:10.3969/j.issn.1003–1375.2023.02.000

Chen, Y., Jianbo ∗ , L., BingShen, Y. W., Wu, R., Zhan, R., and Zhan, R. (2021). Geochemistry of lower ordovician microbialites on the yangtze platform, south China: implications for oceanic oxygenation at the onset of the GOBE. *Palaeogeogr. Palaeoclimatol. Palaeoecol.* 578, 110564. doi:10.1016/j.palaeo.2021.110564

Claesson, L., Skelton, A., Graham, C., Dietl, C., Mörth, M., Torssander, P., et al. (2004). Hydrogeochemical changes before and after a major earthquake. *Geology* 32 (8), 641–644. doi:10.1130/g20542.1

Claesson, L., Skelton, A., Graham, C., and M, C. M. (2007). The timescale and mechanisms of fault sealing and water-rock interaction after an earthquake. *Geofluids* 7 (4), 427–440. doi:10.1111/j.1468-8123.2007.00197.x

Craig, H. (1961). Isotopic variations in meteoric waters. *Science* 133 (3465), 1702–1703. doi:10.1126/science.133.3465.1702

De Luca, G., Di Carlo, G., and Tallini, M. (2018). A record of changes in the Gran Sasso groundwater before, during and after the 2016 Amatrice earthquake, central Italy. *Sci. Rep.* 8, 15982. doi:10.1038/s41598-018-34444-1

Elderfield, H. (1988). The oceanic chemistry of the rare-earth elements. *Philos. Trans. R. Soc. Lond.* A325, 105–126. doi:10.1098/rsta.1988.0046

Epskamp, S., Cramer, A., Waldorp, L., Schmittmann, V., and Borsboom, D. (2012). Qgraph: network visualizations of relationships in psychometric data. *J. Stat. Softw.* 48, 1–18. doi:10.18637/jss.v048.i04

Favara, R., Italiano, F., and Martinelli, G. (2001). Earthquake-induced chemical changes in the thermal waters of the Umbria region during the 1997-1998 seismic swarm. *Terra nova.* 13 (3), 227–233. doi:10.1046/j.1365-3121.2001.00347.x

Gao, L., and Xing, C. Q. (2011). Two abnormalities in fluid precursor observation in beijing wuliying well and related discussion (in Chinese). *Northwest. Seismol. J.* 33 (3), 644–652. doi:10.3969/j.issn.0253-4967.2011.03.013

Ge, S., and Stover, S. C. (2000). Hydrodynamic response to strike-and dip-slip faulting in a halfspace. *J. Geophys. Res.* 105 (B11), 25513–25524. doi:10.1029/2000JB900233

Igarashi, G., Saeki, S., Takahata, N., Sumikawa, K., Tasaka, S., Sasaki, Y., et al. (1995). Groundwater radon anomaly before the Kobe earthquake in Japan. *Science* 269, 60–61. doi:10.1126/science.269.5220.60

Igarashi, G., and Wakita, H. (1995). Geochemical and hydrological observations for earthquake prediction in Japan. *J. Phys. Earth* 43, 585–598. doi:10.4294/jpe1952.43.585

Jiang, C.-sheng, Zhong-liang, Wu, and Li, Y.-T. (2008). Estimating the location accuracy of the Beijing Capital Digital Seismograph Network using repeating events. *Chin. J. Geophys.* 51 (3), 817–827. doi:10.3321/j.issn:0001-5733.2008.03.022

King, C. Y. (1981). Do radon anomalies predict earthquakes? *Nature* 262. doi:10.1038/293262a0

King, C. Y. (1986). Gas geochemistry applied to earthquake prediction: an overview. *J. Geophys. Res. Solid Earth* 91 (B12), 12269–12281. doi:10.1029/jb091ib12p12269

Kingsley, S., Biagi, P., Piccolo, R., Capozzi, V., Ermini, A., Khatkevich, Y., et al. (2001). Hydrogeochemical precursors of strong earthquakes: a realistic possibility in Kamchatka. *Part C. Sol. Terr. Planet. Sci.* 26, 769–774. doi:10.1016/s1464-1917(01)95023-8

Kitagawa, Y., Koizumi, N., and Tsukuda, T. (1996). Comparison of postseismic groundwater temperature changes with earthquake-induced volumetric strain release: yudani Hot Spring. Japan. *Geophys Res. Lett.* 23 (22), 3147–3150. doi:10.1029/96gl02517

Kopylova, G. N., Boldina, S. V., and Serafimova, Y. K. (2022). Earthquake precursors in the ionic and gas composition of groundwater: a review of world data. *Geochem. Int.* 60 (10), 928–946. doi:10.1134/s0016702922100056

Li, Z.-chao, and Huang, Q.-hua (2014). Assessment of detectability of the Capital circle Seismic Network by using the probability-based magnitude of completeness (PMC) method. *Chin. J. Geophys.* 57 (8), 2584–2593. doi:10.6038/cjg20140818

Liu, F., Li, Y. H., and Lin, J. (2008). A hydrogen and oxygen isotope study of groundwater in the Yongding River drainage of Beijing and its environmental significance (in Chinese). *Acta Geosci. Sin.* 29 (2), 161–166.

Manga, M., and Wang, C.-Y. (2015). *Earthquake hydrology, treatise on geophysics.* Amsterdam: Elsevier.

Martinelli, G. (2015). Hydrogeologic and geochemical precursors of earthquakes: an assessment for possible applications. *Boll. Geofis. Teor. Appl.* 56, 83–94. doi:10.4430/bgta0146

Martinelli, G. (2020). Previous, current, and future trends in research into earthquake precursors in geofluids. *Geosciences* 10, 189. doi:10.3390/geosciences10050189

Martinelli, G., and Dadomo, A. (2017). Factors constraining the geographic distribution of earthquake geochemical and fluid-related precursors. *Chem. Geol.* 469, 176–184. doi:10.1016/j.chemgeo.2017.01.006

Montgomery, D. R., and Manga, M. (2003). Streamflow and water well responses to earthquakes. *Science* 300, 2047–2049. doi:10.1126/science.1082980

Mou, B. -l. (1999). *Elements in geochmistry (in Chinese)* (Beijing: Peking University Press).

Petrini, R., Italiano, F., Riggio, A., Slejko, F. F., Santulin, M., Buccianti, A., et al. (2012). Coupling geochemical and geophysical signatures to constrain strain changes along thrust faults. *Boll. Geof. Teor. Appl.* 53, 113–134. doi:10.4430/bgta0017

Poitrasson, F., Dundas, S. H., Toutain, J.-P., Munoz, M., and Rigo, A. (1999). Earthquake-related elemental and isotopic lead anomaly in a springwater. *Earth. Planet. Sci. Lett.* 169 (3), 269–276. doi:10.1016/s0012-821x(99)00085-0

Roeloffs, E. A. (1998). Presistent water level changes in a well near Parkfield, California, due to lacal and distant earthquakes. *J. Geophys. Res.* 103 (B1), 868–889. doi:10.1029/97JB02335

Rojstaczer, S., and Wolf, S. (1992). Permeability changes associated with large earthquakes:An example from Loma Prieta, California. *Geology* 20 (3), 211–214. doi:10.1130/0091-7613(1992)020<0211:pcawle>2.3.co;2

Rosen, M. R., Binda, G., Archer, C., Pozzi, A., Michetti, A. M., and Noble, P. J. (2018). Mechanisms of earthquake-induced chemical and fluid transport to carbonate groundwater springs after earthquakes. *Resour. Res.* 54 (8), 5225–5244. doi:10.1029/2017wr022097

Shi, Z. M., Zhang, H., and Wang, G. C. (2020). Groundwater trace elements change induced by M5.0 earthquake in Yunnan. *J. Hydrology* 581 (2020), 124424. doi:10.1016/j.jhydrol.2019.124424

Skelton, A., Andrén, M., Kristmannsdóttir, H., Stockmann, G., Mörth, C. M., Sveinbjörnsdóttir, Á., et al. (2014). Changes in groundwater chemistry before two consecutive earthquakes in Iceland. *Nat. Geosci.* 7, 752–756. doi:10.1038/ngeo2250

Skelton, A., Liljedahl-Claesson, L., Wästeby, N., Andrén, M., Stockmann, G., Sturkell, E., et al. (2019). Hydrochemical changes before and after earthquakes based on long-term measurements of multiple parameters at two sites in northern Iceland—a review. *J. Geophys. Res.* 124, 2702–2720. SolidEarth(ja). doi:10.1029/2018JB016757

Song, X. F., Li, F. D., Yu, J. J., Tang, C. Y., Yang, C., Liu, X. C., et al. (2007). Characteristics of groundwater cycle using deuterium, oxygen-18 and hydrochemistry in Chaobai River Basin (in Chinese). *Geogr. Res.* 26 (1), 11–21.

Taran, Y. A., Ramirez-Guzman, A., Bernard, R., Cienfuegos, E., and Morales, P. (2005). Seismic-related variations in the chemical and isotopic composition of thermal springs near Acapulco, Guerrero, Mexico. *Geophys. Res. Lett.* 32 (14). doi:10.1029/2005gl022726

Taylor, H. P., Jr. (1977). Water/rock interactions and the origin of H2O in granitic batholiths: thirtieth WilliamSmith lecture. *J. Geol. Soc.* 133 (6), 509–558. doi:10.1144/gsjgs.133.6.0509

Taylor, S. R., and McLennan, S. M. (1985). *The continental crust: its composition and evolution*. Oxford: Blackwell.

Thomas, D. (1988). Geochemical precursors to seismic activity. *Pure. Appl. Geophys.* 126 (2–4), 241–266. doi:10.1007/bf00878998

Toutain, J., Munoz, M., Poitrasson, F., and Lienard, A. (1997). Springwater chloride ion anomaly prior to a M L = 5.2 Pyrenean earthquake. *Earth. Planet. Sci. Lett.* 149 (1), 113–119. doi:10.1016/s0012-821x(97)00066-6

Toutain, J.-P., and Baubron, J.-C. (1999). Gas geochemistry and seismotectonics: a review. *Tectonophysics* 304, 1–27. doi:10.1016/s0040-1951(98)00295-9

Tsunogai, U., and Wakita, H. (1995). Precursory chemical changes in ground water: Kobe earthquake, Japan. *Jpn. Sci.* 269, 61–63. doi:10.1126/science.269.5220.61

Wakita, H. (1996). Geochemical challenge to earthquake prediction. *PNAS* 93 (9), 3781–3786. doi:10.1073/pnas.93.9.3781

Wakita, H., Fujii, N., Matsuo, S., Notsu, K., Nagao, K., and Takaoka, N. (1978). 'Helium spots': caused by a diapiric magma from the upper mantle. *Science* 200, 430–432. doi:10.1126/science.200.4340.430

Wang, C.-Y. (2007). Liquefaction beyond the near field. *Seismol. Res. Lett.* 78, 512–517. doi:10.1785/gssrl.78.5.512

Wang, C.-Y., Cheng, L. H., Chin, C. V., and Yu, S. B. (2001). Coseismic hydrologic response of an alluvial fan to the 1999 Chi-Chi earthquake. Taiwan. *Geol* 29 (9), 831–834. doi:10.1130/0091-7613(2001)029<0831:chroaa>2.0.co;2

Wang, C. Y., and Manga, M. (2010). *Earthquakes and water*. Berlin Heidelberg: Springer-Verlag.

Wang, K., Chen, Q.-F., Sun, S., and Wong, A. (2006). Predicting the 1975 Haicheng earthquake. *Bull. Seism. Soc. Am.* 96, 757–795. doi:10.1785/0120050191

Webb, G. E., and Kamber, B. S. (2000). Rare earth elements in Holocene reefal microbialites: a new shallow seawater proxy. *Geochim. Cosmochim. Acta* 64, 1557–1565. doi:10.1016/s0016-7037(99)00400-7

Wei, J.-zhen, An-qi, J., and Si-yuan, F. (1991). Abnormal variation of F-, Cl-, SO4-inos in Wuliying well, Yanqing county, Beijing (in Chinese). *Earthquake*, 37–42.

Woith, H., Wang, R., Maiwald, U., Pekdeger, A., and Zschau, J. (2013). On the origin of geochemical anomalies in groundwaters induced by the Adana 1998 earthquake. *Chem. Geol.* 339, 177–186. doi:10.1016/j.chemgeo.2012.10.012

Yang, M., Liu, G., Liu, Z., Ma, J., Li, L., Wang, Z., et al. (2022). Geochemical characteristics of geothermal and hot spring gases in Beijing and Zhangjiakou Bohai fault zone. *Front. Earth Sci.* 10, 933066. doi:10.3389/feart.2022.933066

Yu, J. S., Yu, F. J., and Liu, D. P. (1987). The oxygen and hydrogen isotopic compositions of meteoric waters in the eastern part of China (in Chinese). *Geochemistry* (01), 22–26. doi:10.19700/j.0379-1726.1987.01.003

frontiers | Frontiers in Earth Science

TYPE Methods
PUBLISHED 11 September 2024
DOI 10.3389/feart.2024.1433395

OPEN ACCESS

EDITED BY
Giovanni Martinelli,
National Institute of Geophysics and Volcanology, Italy

REVIEWED BY
Vincenzo Lapenna,
National Research Council (CNR), Italy
Mita Uthaman,
Indian Institute of Technology Kharagpur, India

*CORRESPONDENCE
Li Jianyong,
jyli@seis.ac.cn
Yu Chen,
yuchen@seis.ac.cn

RECEIVED 15 May 2024
ACCEPTED 28 August 2024
PUBLISHED 11 September 2024

CITATION
Lei Y, Jianyong L, Chen Y, Haizhen Z, Dequan H and Weiyu M (2024) Determination of stress state based on coupling characteristics of load/unload response ratio and outgoing longwave radiation before large earthquakes.
Front. Earth Sci. 12:1433395.
doi: 10.3389/feart.2024.1433395

Determination of stress state based on coupling characteristics of load/unload response ratio and outgoing longwave radiation before large earthquakes

Yu Lei[1,2], Li Jianyong[3]*, Yu Chen[3]*, Zhang Haizhen[4], Hong Dequan[1] and Ma Weiyu[3]

[1]Anhui Earthquake Agency, Hefei, China, [2]University of Science and Technology of China, Hefei, China, [3]China Earthquake Network Center, Beijing, China, [4]National Satellite Meteorological Center, China Meteorological Administration, Beijing, China

The Load/Unload Response Ratio (LURR) is a seismic prediction method based on the dynamic evolution of the stress-strain relationship of rocks. By adopting Benioff strain as the response indicator, an in-depth analysis was conducted on the LURR anomalies within 400 km of the epicenter and its surrounding areas before the *Ms*7.4 earthquake in Madoi, Qinghai Province, on 22 May 2021. The analysis revealed that the LURR value peaked 1 month before the earthquake and then declined within half a month, indicating that the rock medium in the seismic gestation area was approaching the end of its yielding phase. Further investigation using the Outgoing Longwave Radiation (OLR) data from the National Oceanic and Atmospheric Administration (NOAA) satellite was conducted to study the short-term and imminent anomalous evolution of ground longwave radiation values after the high values declined (from May 14 to 25). The results showed that, spatially, significant and continuous OLR anomalies were observed only in the northern area of the epicenter before the earthquake, and these anomalies exhibited a trend of expanding towards the epicenter. Temporally, the entire anomalous evolution process can be divided into six phases: initial warming, anomaly expansion, peak intensity, anomaly weakening, earthquake occurrence, and anomaly disappearance. To validate this finding, the spatiotemporal evolution characteristics of LURR and OLR within 300 km of the epicenter and its surrounding areas before the *Ms*6.4 earthquake in Yangbi, Yunnan Province, on 21 May 2021, were analyzed, and similar patterns were found. These results suggest that the high LURR value before its decline may mark the end of the rock medium's yielding phase, and OLR data can reflect, to some extent, the state of tectonic stress accumulation along active faults in a critical condition. A comprehensive study of the anomalous evolution characteristics of these two physical parameters before the earthquake is

not only conducive to the continuity from long-term to short-term forecasts but also of great significance for more accurately assessing the trend of seismic activity.

KEYWORDS

LURR, OLR, NOAA, Madoi earthquake, stress state

1 Introduction

The study of Solid Earth-atmosphere interactions in the epicentral region, particularly through the analysis of thermal infrared anomalies on the Earth's surface in the short term preceding earthquakes, has garnered significant interest in seismic forecasting. Mogi (1984) pioneered this field, and subsequent research has furthered our understanding. For instance, Gorny (1988) observed a notable enhancement in the thermal infrared radiation over a large area approximately 10 days prior to several major earthquakes in the Gazli region in 1984. Ouzounov and Freund (2004), in their analysis of MODIS data, identified significa nt land surface temperature patterns preceding earthquakes, which they attributed to a positive hole-type charge.

Mechanism Saraf et al. (2008) examined 10 earthquakes in the Iranian region and reported an increase in land surface temperature (LST) of about 2°C–13°C at the epicenter and its vicinity 1–10 days before the main shock. Additionally, rock mechanics experiments, such as those conducted by Cui, C., et al. (1993) and Wu, L., et al. (2004), have demonstrated that the destabilization and fracturing of rocks are accompanied by the emission of infrared radiation. These experimental findings offer a mechanical rationale for the use of infrared remote sensing in seismic monitoring and prediction.

Currently, the identification and extraction of pre-earthquake thermal infrared anomalies predominantly rely on statistical methods, as discussed by Tramutoli (2007). Lisi et al. (2010) applied the Robust Satellite Technique (RST) to analyze thermal infrared observations associated with the Abruzzo earthquake on 6 April 2009. Yang and Guo (2010) introduced a novel subtraction method to investigate the thermal anomalies preceding the Zhangbei earthquake in China. However, due to the complexity of thermal infrared anomaly changes, these statistical methods have inherent limitations. They often result in issues such as the broad distribution of anomaly areas, high variability in the spatial distribution of anomalies, and an absence of clear temporal patterns (Qiang, Z., et al., 1997; Xu, X., et al., 1990; Yu, C., et al., 2023). Consequently, there is an urgent need to develop methods with a solid physical basis and mechanical underpinnings to more accurately and swiftly ascertain the background values of thermal infrared anomalies in the lead-up to strong earthquakes.

In recent years, the load-unload response ratio (LURR) has emerged as a valuable tool for analyzing the nonlinear mechanical processes preceding major earthquakes, as documented in the works of Yu and Zhu, 2010 and Zakupin et al. (2021). This approach aids in refining the selection of thermal infrared background values. The concept of LURR was introduced by Yin et al. (1995) and has since become a staple in retrospective seismic prediction studies, as referenced in Yu et al. (2015). Drawing from systematology, the dynamic evolution of constitutive relations within rock media in seismogenic regions is investigated. This is achieved by establishing a relationship between internal system dynamics and external factors, as depicted in Figure 1. During the elastic phase of rock media, the responses to loading and unloading are nearly identical, yielding a LURR value of approximately 1.0. However, as the rock mass transitions into the dilatancy phase due to stress accumulation, the responses to loading and unloading become markedly different, resulting in a LURR value exceeding 1.0. Consequently, LURR serves as a diagnostic tool to identify the critical state of the medium prior to catastrophic rupture, offering a robust reference for the determination of thermal infrared anomaly background values.

Earthquakes result from the rapid release of accumulated energy when stress within the rock medium reaches a critical state, leading to fault instability and rupture. Outgoing longwave radiation (OLR), an observable remote sensing parameter, theoretically concentrates at wavelengths between 8 and 12.5 μm, primarily determined by the temperature and emissivity of the emitting surface. Real-time OLR essentially reflects the surface temperature variations of the observed region, and recent studies have found a correlation between pre-earthquake dynamic evolution of OLR and changes in geostresses (Wu et al., 2006). Additionally, LURR, a physical quantity reflecting the stress state of the rock medium, often utilizes Benioff strain as a responsive measure for the loading-unloading process. Therefore, establishing a physical correlation between LURR and OLR could provide a mechanical basis for the selection of OLR background values, enhancing the reliability of this selection, reducing the uncertainty in conclusions due to the randomness of the calculation process, and narrowing the spatial range of anomalies, thereby excluding potentially interfering anomalous areas.

Thus, this paper attempts to integrate the LURR method into longwave radiation seismic observation techniques. By analyzing the coupling relationship between the pre-earthquake short-term evolution of LURR and OLR anomalies, we aim to determine the stress state of the seismogenic region prior to an earthquake. The Coulomb failure stress induced by the solid tide on the fault plane serves as the criterion for judging the loading-unloading process (Yin et al., 2008). To explore the correlation between these two, this study takes the *Ms*7.4 Madoi earthquake in China, which occurred in 2021, as a case study.

2 Methods

Over the past 2 decades since its introduction, the LURR has become a widely utilized tool in the practice of earthquake prediction (Yu and Zhu, 2010; Liu and Yin, 2017). Time series analyses have consistently demonstrated significant anomalies in the form of elevated values on a temporal scale ranging from months

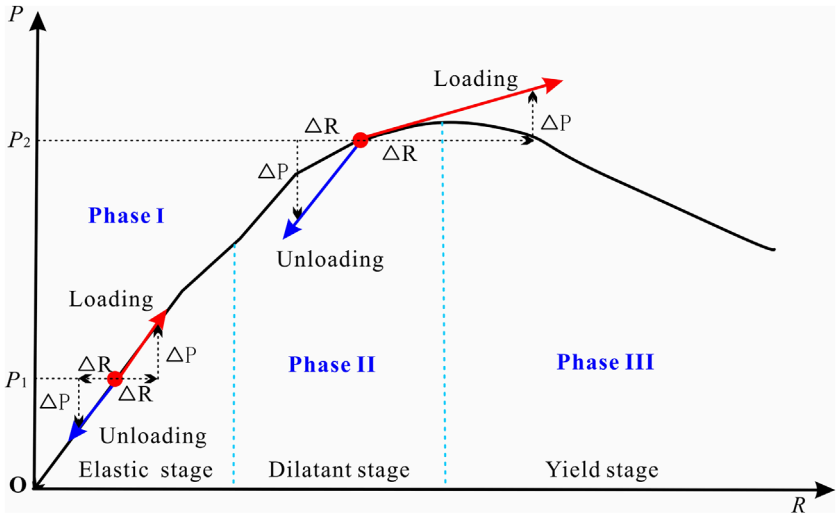

FIGURE 1
Schematic diagram of the rock constitutive relationship. *P* and *R* represent the load and response, respectively. At the point P_1 in phase I, the response (ΔR) to the small changes of ΔP in the loading and unloading are almost the same. At the phase II, the response to loading is significantly greater than unloading, and the phase III is characterized with macroscopic damage.

to years preceding major seismic events. These anomalies can be instrumental in identifying the prospective timing and epicentral regions of future earthquakes (Liu et al., 2012).

2.1 Judgment of loading and unloading process

The load-unload response ratio, denoted as Y (LURR), is formulated as $Y = X_+/X_-$, where the symbols "+" and "−" represent the loading and unloading processes, respectively, and x signifies the response rate.

In the field of earthquake prediction, the determination of loading and unloading phases hinges on the variations in coulomb fracture stress (ΔCFS), which are provoked by the tidal forces of the sun and moon acting upon the seismic fault surface.

$$CFS = \tau_n - f\sigma_n \tag{1}$$

f, τ_n, σ_n represent internal friction coefficient, shear stress and normal stress respectively。 $\tau_n - f\sigma_n$ in Formula 1 is also called effective shear stress τ_e. If $\vec{\mu}$ denotes the slip vector, the construction effective shear stress (Equation 2A) and the tidal effective shear stress (Equation 2B) can be expressed as:

$$\vec{\tau}_e^{\,T} = \vec{\tau}^{\,T} - f\sigma^T \frac{\vec{\mu}}{|\vec{\mu}|} \tag{2A}$$

$$\vec{\tau}_e^{\,t} = \vec{\tau}^{\,t} - f\sigma^t \frac{\vec{\mu}}{|\vec{\mu}|} \tag{2B}$$

Generally, the aggregate of tectonic and tidal shear stresses is indicative of the shear stress acting upon the fault plane, as illustrated in Figure 2, that is Equation 3:

$$\tau_e = \vec{\tau}_e^{\,T} + \vec{\tau}_e^{\,t} \tag{3}$$

Despite the fact that tectonic stress significantly exceeds tidal stress by several orders of magnitude, its rate of change is so gradual that it can be regarded as constant during practical computational procedures. The increase in effective shear stress attributable to tidal forces on the fault plane can be formulated as:

$$\Delta\tau_e = \vec{\tau}_e^{\,t} \cdot \frac{\vec{\mu}}{|\vec{\mu}|} \tag{4}$$

As illustrated in Figure 2B, when the angle θ is less than 90°, the forces are additive, signifying a rise in stress. Conversely, when θ exceeds 90°, they are subtractive, indicating a reduction in stress. Differential the Formula 4 in the time domain:

$$g = \frac{d}{dt}\left(\vec{\tau}_e^{\,t} \cdot \frac{\vec{\mu}}{|\vec{\mu}|}\right) \tag{5}$$

The criterion delineating loading and unloading is derived from Equation 5, where a positive value of "g" indicates loading, and a negative value signifies unloading.

2.2 The selection of response quantities

In the realm of earthquake prediction, theoretically, any geophysical variables capable of reflecting the instability process within the seismogenic region are viable candidates for response variables. Assuming "*P*" and "*R*" denote load and response, respectively, the response rate, X, can be reformulated as follows (Equation 6):

$$X = \lim_{\Delta P \to o} \frac{\Delta R}{\Delta P} \tag{6}$$

ΔR represents the alteration in response "R" that results from the variation in the load variable, ΔP. When the medium's strength substantially exceeds the load, X_+ is approximately equal to X_-,

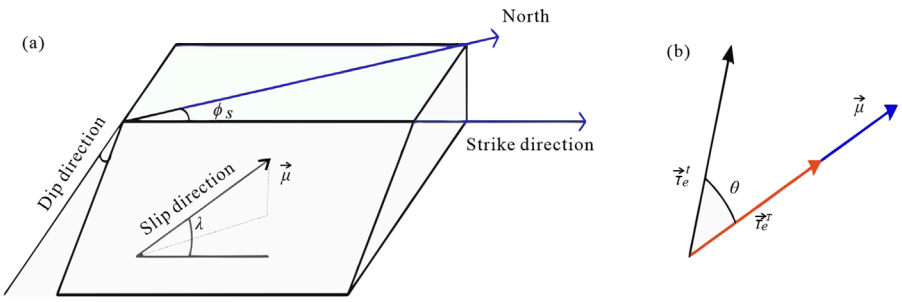

FIGURE 2
Determination of loading and unloading periods induced by tidal stress **(A)** the slip direction on the focal plane driven by the tectonic shear stress; **(B)** the relationship between the tectonic and tide effective shear stresses.

hence the LURR is approximately 1. As the medium approaches failure, X_+ exceeds X_-, resulting in a LURR greater than 1, which allows us to assess if the medium remains in a stable phase.

The loading-unloading response ratio is defined in terms of seismic energy, E, and its associated parameters, serving as the response quantity:

$$Y_m = \left(\sum_{i=1}^{N+} E_i^m\right)_+ / \left(\sum_{i=1}^{N+} E_i^m\right)_- \quad (7)$$

in Formula 7, E_i denotes seismic energy and "+""–" denotes loading and unloading respectively. M can be 0, 1/3, 1/2, 2/3 or 1. When M = 1, E^{m} is the earthquake energy. When M = 1/3 or 2/3, E^{m} denotes linear scale and surface scale of seismogenic region, respectively. When M = 1/2, E^{m} denotes the Benioff strain. When M = 0, the Y value corresponds to the number of earthquakes occurring during addition and unloading.

3 Applications and data

In this retrospective study, the LURR method is applied to long-wave radiation observations to analyze the dynamic evolution characteristics of the Madoi *Ms*7.4 earthquake that occurred on 22 May 2021, in the northwestern part of Qinghai Province, China (34.59° N, 98.34° E). Historical seismicity data reveal that there have been five earthquakes with a magnitude of seven or greater within a 300 km radius of the epicenter since 1900, indicating a region of active seismicity (Figure 3). Notably, the most significant of these was the Magnitude 7.7 earthquake on 17 March 1947, in Dari County, Guoluo Prefecture, Qinghai Province, which was approximately 179 km from the Madoi earthquake's epicenter. The most recent significant earthquake was a 7.1 magnitude event on 14 April 2010, approximately 224 km from Yushu City in Yushu Prefecture, Qinghai Province. The closest in terms of spatial proximity was the 7.5 magnitude earthquake on 7 January 1937, situated 122 km east of Aran Lake, Qinghai Province.

The Madoi County earthquake is situated within the interior of the Bayan Har block, with the closest fault being the Gande South Marginal Fault Zone. The Bayan Har block, located in the central-eastern region of the Tibetan Plateau, is bounded by significant left-lateral strike-slip fault zones: the East Kunlun Fault to the north and the Garze-Yushu-Xianshuihe fault system to the south, both of which trend nearly east-west. Its eastern boundary is marked by the Longmenshan thrust fault zone, which strikes in a NNE direction and plays a crucial role in accommodating the present-day crustal deformation of the Tibetan Plateau. The Bayan Har block is a significant tectonic unit that has been the most seismically active region in mainland China over the past 2 decades, experiencing several earthquakes with a magnitude of Ms ≥ 7.0 (Figure 3). In addition to the aforementioned fault zones, Figure 3 also marks several larger fault zones around the Madoi earthquake, such as the Madoi-Gande fault and the Dari fault zone, etc.

Perform a spatial evolution analysis on the LURR anomalies prior to the Madoi *Ms*7.4 earthquake with the following computational parameters: Spatially, a step size of 0.25° is used for sliding along the longitude and latitude directions. Within the scanning area, the Benioff strain of earthquakes ranging from 0 to 4.0 magnitudes (m = 1/2) is taken as the response quantity, and the ΔCFS with an internal fault friction coefficient f = 0.4 is calculated based on the rate-and-state-dependent friction model by Yin et al. (2000). The calculation time window is set to 6 months, with a sliding time window of 0.5 months. The calculation results represent the distribution of LURR anomalies at the end of the time window (Figure 4). Figure 4 displays the LURR time series computed by using earthquakes within 100, 200, and 400 km from the Madoi mainshock. The input data is retrieved from the CENC catalog (http://www.ceic.ac.cn).

The OLR data utilized in this study originates from the series of satellites operated by the United States National Oceanic and Atmospheric Administration (NOAA). This data is employed to analyze the pre-earthquake coupling relationship with LURR. The dataset is recognized for its good applicability and completeness, with a spatial resolution of 1°×1° and a temporal resolution of 1 day. Each data file comprises 360×181 grid points that cover the globe. To more accurately determine the timing of the LURR high-value drop and to avoid discrepancies in the final analysis due to variations in the length of the background date selection, we have plotted an enlarged version of the LURR time series curve from June 2020 to June 2021 (Figure 4C). Based on the outcomes from the 100 km and 200 km analyses, in conjunction with the focal mechanism solutions, May 13th has been preliminarily identified as the peak decline period for LURR. Consequently, the OLR data from this particular day have been chosen as the reference background values. The observational precision of the NOAA satellite sensor indicates

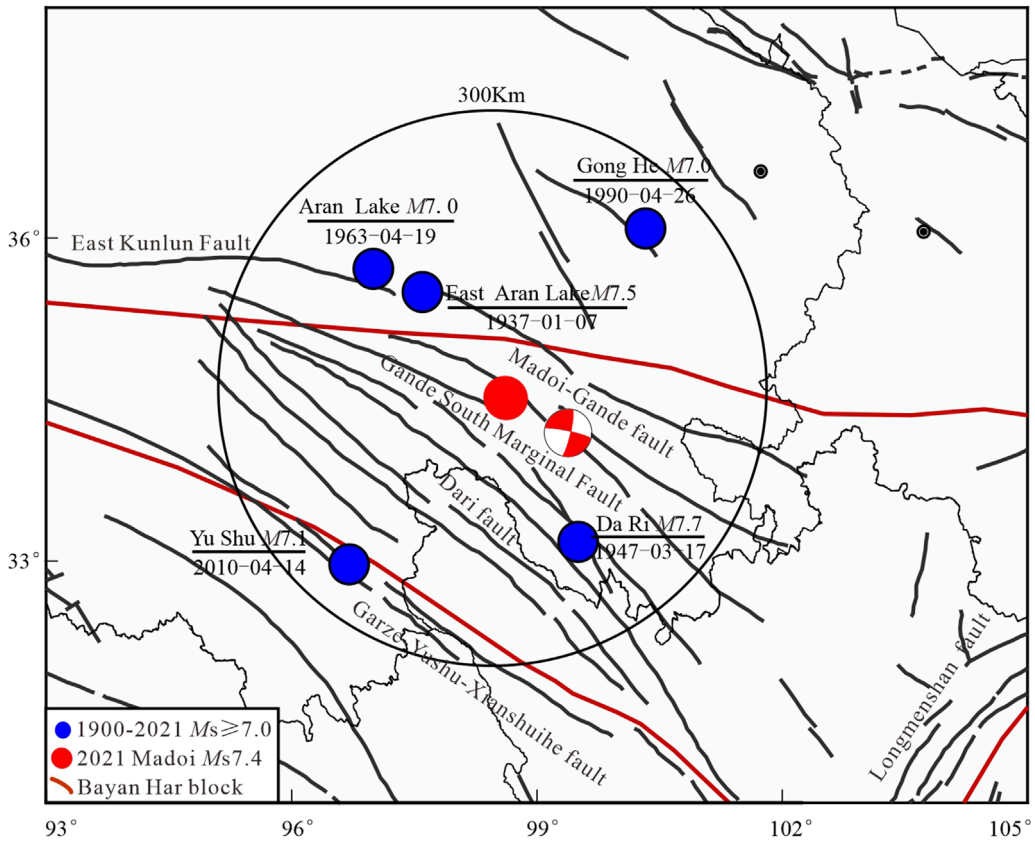

FIGURE 3
Active faults and historically earthquakes above 7.0 magnitude within 300 km of the epicenter The blue dots in the diagram represent historical earthquakes within 300 km of the epicenter from 1900–2021.

a data uncertainty of 0.5 W/m^2. Subtracting the background day's longwave radiation values from the nighttime terrestrial longwave radiation values for the period spanning May 14th to 25th, 2021, within the specified spatial bounds of (31~39°N, 88~105°E), yields the ΔOLR values. The calculation of ΔOLR is articulated by the following formula:

$$\triangle \mathrm{OLR} = \mathrm{OLR}_i - \mathrm{OLR}_b \tag{8}$$

in Equation 8, OLR_i represents the OLR value at a specific point in time on day i, while OLR_b denotes the OLR value of the reference background day.

Zhang, Y. et al. (2021) performed a statistical analysis on thermal infrared anomalies preceding earthquakes in China from 2011 to 2017, focusing on the magnitude range of M4.0 to M7.0. The findings indicated that the amplitude of variation in longwave radiation prior to these earthquakes ranged from 75 W/m^2 to 100 W/m^2. Given that the Madoi earthquake in 2021 had a magnitude of M_S7.4, the study selected an anomaly fluctuation range of 90 to 100 W/m^2 for detailed examination. The determination of the ΔOLR anomaly threshold is grounded in the following approach: identifying the maximum ΔOLR value across the entire study area for this seismic event, which is set at 100 W/m^2, and using this as the upper limit of the color scale. The scale then descends to the lowest value by decrements of 10 W/m^2, establishing the lower limit at 90 W/m^2. This results in a data variation range of 10 W/m^2. The findings are depicted in Figure 5.

4 Results and explanations

Overall, as depicted in Figure 4B, the LURR time series calculated at three different spatial scales generally remain below the threshold of 1.0 for the majority of the time. However, in the brief period preceding the Madoi mainshock, the LURR values rapidly increase to significantly high levels, far exceeding 1.0. These findings are supported by the research of Yin et al. (2000) and Yu et al. (2020), who observed that LURR values fluctuate around 1.0 for several months to 3 years prior to the mainshock. Subsequently, the LURR values ascend rapidly to abnormally high levels, reaching up to 2.0, and persist for several months before declining just before the earthquake, with the shortest duration being less than 2 months.

To rigorously and accurately examine the relationship between LURR anomalies and the stress state in the seismogenic region, it is necessary to conduct analyses using different critical area scales. We computed the LURR time series curves for three distinct radii centered on the mainshock epicenter. The amplitude of the LURR high-value decline prior to the mainshock decreases with the radius, and the results for the smallest radius of 100 km exhibit the most pronounced LURR anomaly peak. This may indicate that

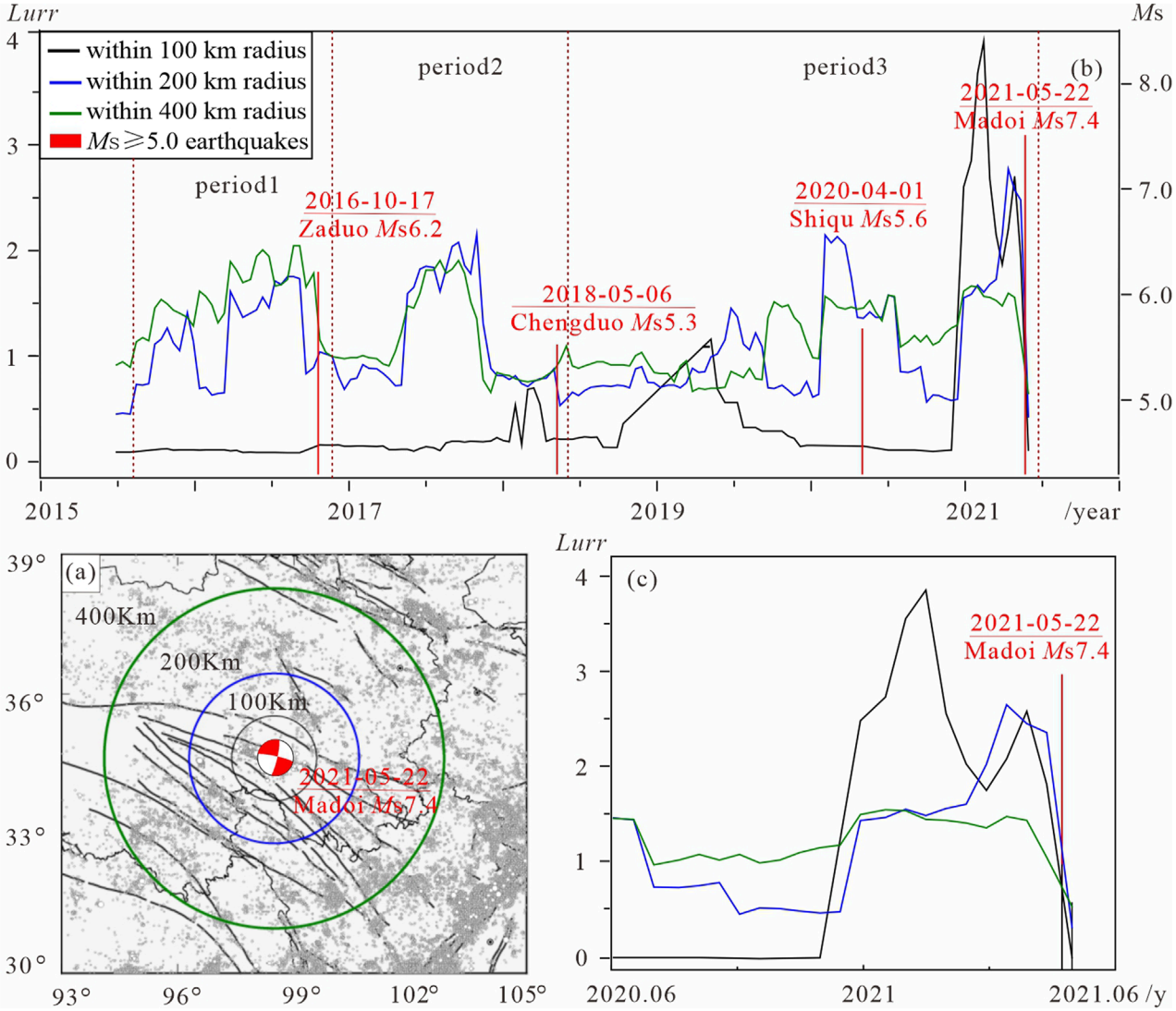

FIGURE 4
LURR time series of the Madoi *Ms*7.4 earthquake **(A)** different distance scales; **(B)** LURR time series with three different distance scales; **(C)** Magnification result of LURR timing curve.

the stress accumulation in the seismogenic region is primarily concentrated within a 100 km range. Furthermore, prior to several other earthquakes (M≥5.0) within a 400 km radius of the epicenter since 2015, similar LURR evolution patterns of rapid increase and sustained high values followed by a decline before the earthquake were observed with both 200 km and 400 km radii. In conjunction with the 100 km results, this suggests that the selection of different seismogenic areas for LURR calculation significantly influences the sensitivity of measuring the critical degree of stress accumulation before a major earthquake (Yu et al., 2006).

As shown in Figure 5, within the study area, a significant anomaly in OLR was observed before and after the earthquake following the decline of the high LURR values. On May 14, no significant radiation enhancement was observed near the epicenter. On the 15th, a slight radiation enhancement appeared north of the epicenter, with an increase of up to 94 W/m^2. On the 16th, the OLR anomaly showed a slight increase in both spatial extent and intensity. The anomaly diminished on the 17th, but from the 18th to the 19th, the OLR anomaly exhibited a significant enhancement in both spatial extent and intensity. The anomaly continued to expand in the northern region of the epicenter, with the affected area increasing and gradually shifting towards the epicenter, reaching an anomaly increase of 98 W/m^2. The increase then declined on the 20th and 21st. Following the earthquake on May 22, the OLR anomaly showed an explosive increase from the 22nd to the 23rd, with the maximum increase exceeding 100 W/m^2. The anomalous area continued to expand north of the epicenter, and the anomaly dissipated after the 24th. Statistical analysis of the anomaly amplitude and range is presented in Table 1. The specific numerical values of the anomaly amplitude and range also reveal the same phenomenon.

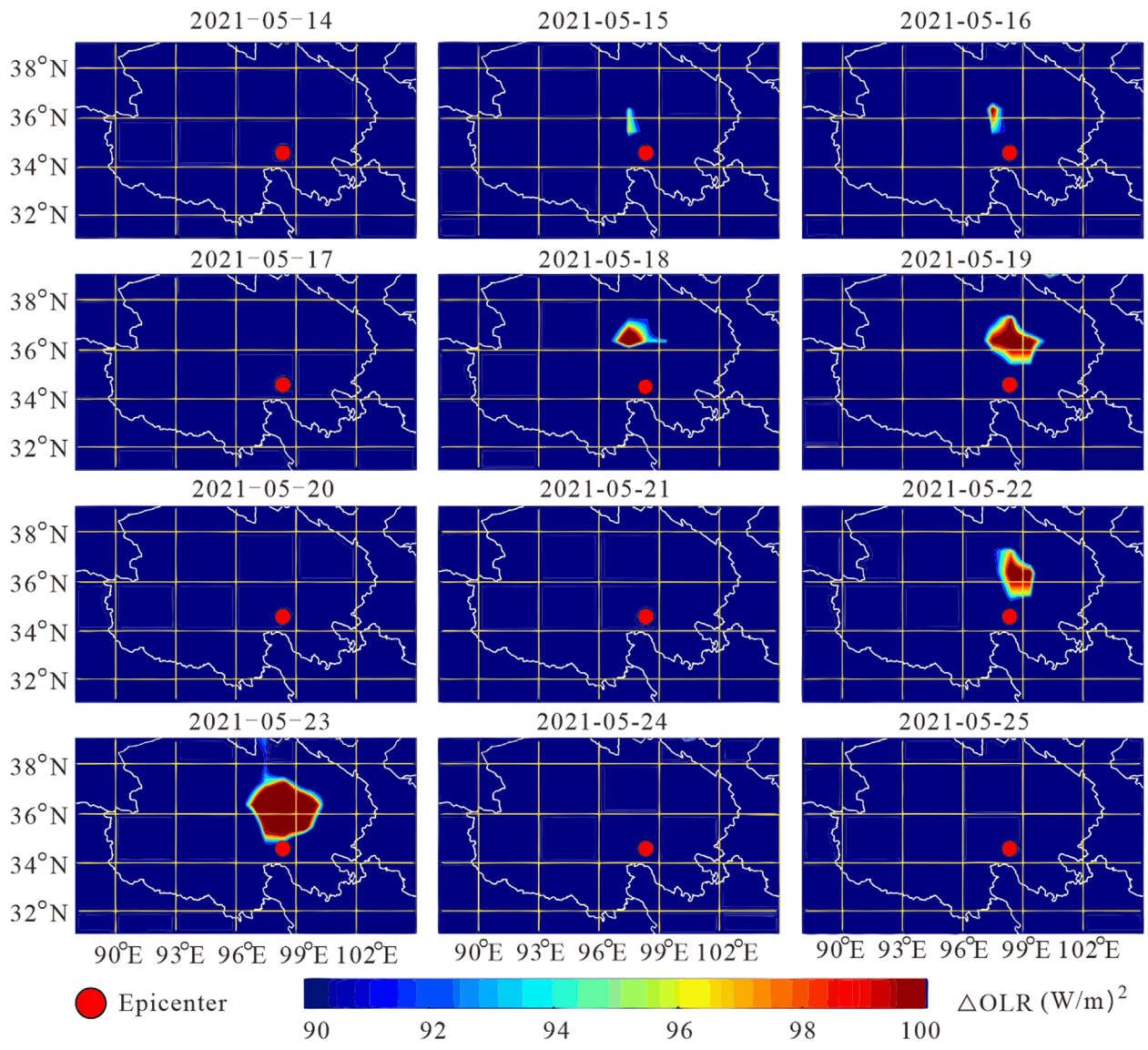

FIGURE 5
Spatio-temporal evolution of the OLR anomaly of the Madoi *Ms*7.4 earthquake the OLR data of May 13th is chosen as the reference background value.

5 Discussion

Earthquake prediction primarily encompasses long-term, mid-term, and short-term time scales. Taking China as an example, routine consultations are held annually, monthly, and weekly, with different durations of predictions adopting different approaches and tracking different anomalous features. In long-term forecasting, annual predictions include methods such as the R-score, exploration of seismic activity (e.g., seismic quiescence, seismic belts), and seismological parameters (e.g., b-value), where anomalies must generally exceed a certain threshold and persist for more than 3 months. By comparing existing anomalies with their related predictive indicators, a comprehensive probability analysis method is used to derive the final prediction results. The R-value test of the prediction results over the past 30 years shows an upward trend in effectiveness, with the value gradually rising from 0.1 in 1990 to the current level of 0.35 (Yu et al., 2022).

For mid-term and short-term forecasting, monthly and weekly consultations target areas based on annual results. Evidence supporting mid-term and short-term predictions is based on significant increases or cessations in seismic activity, as well as sudden changes in geochemical and geophysical observational data, with anomalies (exceeding the threshold) generally lasting no more than 3 months. Yu et al. (2022) analyzed the time series of monthly prediction R-values for earthquakes of magnitude 5.0 or above occurring in the following calendar month, using 2018 as a reference. The results indicate that before June 2018, due to the absence of earthquakes in the seismic hazard areas, the R-value was negative. However, after that, the R-value turned positive as some earthquakes were detected. The annual average R-value was 0.11, significantly lower than the annual R-score.

TABLE 1 Statistical table of OLR anomalies from May 14th to May 25th.

Date	Latitude of epicenter	Longitude of epicenter	Distance between the OLR anomalies and the epicenter/Km	The range of OLR anomalies (Km^2)	The maximum amplitude of OLR anomalies (W/m2)
2021-05-14	34.59°N	98.34°E	—	—	—
2021-05-15	34.59°N	98.34°E	98	3,000	94
2021-05-16	34.59°N	98.34°E	90	4,800	96.5
2021-05-17	34.59°N	98.34°E	—	—	—
2021-05-18	34.59°N	98.34°E	110	12,000	97
2021-05-19	34.59°N	98.34°E	48	41,000	98
2021-05-20	34.59°N	98.34°E	—	—	—
2021-05-21	34.59°N	98.34°E	—	—	—
2021-05-22	34.59°N	98.34°E	32	28,000	99.5
2021-05-23	34.59°N	98.34°E	10	62,000	100
2021-05-24	34.59°N	98.34°E	—	—	—
2021-05-25	34.59°N	98.34°E	—	—	—

Notes: "/" indicates no significant OLR (Outgoing Longwave Radiation) anomaly amplitude values on that day.

Currently, short-term earthquake prediction is more challenging than mid-term prediction because mid-term anomalies persist for a longer duration, usually several months or even years. Observed anomalies can be continuously used for multiple short-term predictions, making it difficult to link anomalies with the timing of earthquakes on a short time scale, which also reflects that short-term prediction remains a current challenge.

The LURR, based on the Benioff strain release from small earthquakes triggered by tidal stress, serves as an effective physical parameter to reflect the dynamic evolution of the constitutive relationship within rock media. When tectonic stress is at a low level, indicative of the elastic phase, minor stress variations, such as those due to tides, are insufficient to trigger seismic events. During this phase, the differences in Benioff strain response between loading and unloading are negligible, and the LURR is expected to fluctuate around 1.0. However, when the accumulated tectonic stress on a fault reaches a higher level, even the slightest stress change can be seismically significant. This perspective is validated by the pre-failure dilatancy model proposed by Brace and colleagues (Brace et al., 1966; Scholz et al., 1973). According to the Kaiser effect (Li and Nordlund, 1993), in this phase, earthquakes are often triggered by an increase in Coulomb failure stress, implying that under the periodic tidal shear stress, the Benioff strain release during loading exceeds that during unloading. Consequently, this differential strain release between loading and unloading can be detected by the LURR method, mathematically expressed as a LURR ratio significantly greater than 1.0 (as shown in Figure 4). This suggests that an anomalously high LURR value can indicate a high-stress state in the region, which can lead to changes in the elastic modulus of the rock media.

Further analysis indicates that the duration (T2) from the decline of LURR to the occurrence of an earthquake may correlate with the intensity of seismic activity in the region. We can divide the period from 2015 to 2021 into three phases, defining T3 as the time interval between the last earthquake of one phase and the first of the subsequent phase. The statistical results are as Table 2.

The results indicate that shorter intervals of T3 are associated with longer durations of T2. This finding can be interpreted as follows: when the medium's homogeneity is higher, such as in regions that have not experienced earthquakes for an extended period, ruptures may occur sooner. Conversely, areas characterized by a lower degree of medium uniformity, typically associated with regions of heightened seismic activity, may experience a protracted timeline for rupture occurrence. By considering the characteristics of regional seismic activity, the timing of future earthquakes might be more accurately determined by the moment when LURR values begin to decline.

We diligently endeavor to apply the LURR (load-unload response ratio) method to evaluate the post-earthquake aftershock scenarios. In response to the urgent requirement for swift determination following seismic events, we have fine-tuned the computational time frame to a 5-day window with a 1-day slide, while maintaining all other parameters constant. This adjustment facilitates the generation of the LURR time-series variations post the Madoi earthquake, as depicted in Figure 6, As illustrated in Figure 6, despite the intense aftershock activity in the immediate aftermath

TABLE 2 Time duration corresponding to each phase in Figure 4 and the and the T2 and T3 associated with the earthquakes.

Period	Duration	Earthquake	T2/months	T3/months
I	2015-10—2016-10	2016-10-17 Zaduo Ms 6.2	1	24
II	2016-10—2018-05	2018-05-06 Chengduo Ms5.3	6	19
III	2018-05—2021-05	2020-04-01 Shiqu Ms5.6	0	23
		2021-05-22 Madoi Ms7.4	0.5	36

Notes: T2-duration from the decline of LURR, to the occurrence of an earthquake; T3-the time interval between the last earthquake of one phase and the first of the subsequent phase.

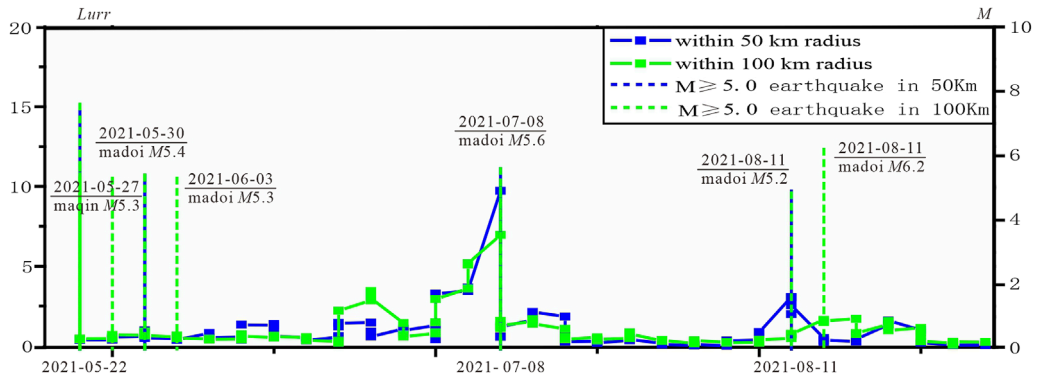

FIGURE 6
LURR Time-series curve following the *Ms* 7.4 Madoi earthquake in 2021.

of the earthquake, the LURR values are observed to be low. This phenomenon can be attributed to the main shock and the several strong aftershocks that transpired within a short time span, which were characterized by an unloading process, thus leading to the observed results. Later, in the months of July and August, two significant aftershocks occurred within the aftershock zone. Notably, the LURR results for both 50 km and 100 km distances exhibited a pronounced increase prior to the occurrence of these strong aftershocks. This suggests that the LURR method provides a certain degree of predictive insight into the analysis of post-earthquake aftershocks.

OLR, as a physical observation that reflects the surface temperature changes of the observed region, has been widely utilized in the field of earthquake prediction. Ma Jin and others have conducted extensive research on the evolution of the fault temperature field before earthquakes. Based on experimental results from rock samples, they divided the deformation phase of a single stick-slip event into two phases: the stress accumulation phase (LO) and the stress release phase (OP). The stress release phase can be further divided into four phases: OA represents the initial phase of sub-critical instability, AB the second phase of sub-critical instability, BE the instability phase, and EP the post-instability phase. Recent studies have shown that if the medium's stress change process is in the OB phase (sub-critical instability phase), the process leading to the medium's failure becomes irreversible, and an inevitable earthquake is imminent. According to the theoretical implications of LURR, the rapid rise and subsequent decline of the LURR time series curve before an earthquake can reflect the MO to OE phases of the sample's rupture process. The moment of the high-value return can be considered as an indication of the time when the sample enters the OE phase (Figure 7). The corresponding times for each moment in Figure 7 and the percentage distribution of time for each deformation phase are listed in Tables 3, 4.

Rock loading experiments have demonstrated that local temperatures near the fault plane, particularly at positions adjacent to the rupture point, increase following the peak stress moment, denoted as time O. Subsequently, at time A, the fault undergoes comprehensive cooling as it enters a phase of rapid stress release. Some measurement points located on either side of the fault experience a rapid temperature increase during the instability phase (BE), coincident with fault slip. Furthermore, a continued temperature rise is observed even after the slip has occurred (EP phase), as depicted in Figure 8. This phenomenon can be attributed to two primary factors. Firstly, the low thermal conductivity of rocks implies that the transfer of heat from the fault zone to the surface may be delayed. Secondly, the impact of post-seismic slip on temperature, while often overlooked, is a significant consideration. The continued temperature increase after fault slip underscores the complex thermal dynamics at play during seismic events.

The OLR evolution process in the epicentral area, processed in this study from the moment of the LURR high-value return to 2 days after the earthquake, appears to correlate well with the temperature changes observed in rock fracture experiments:

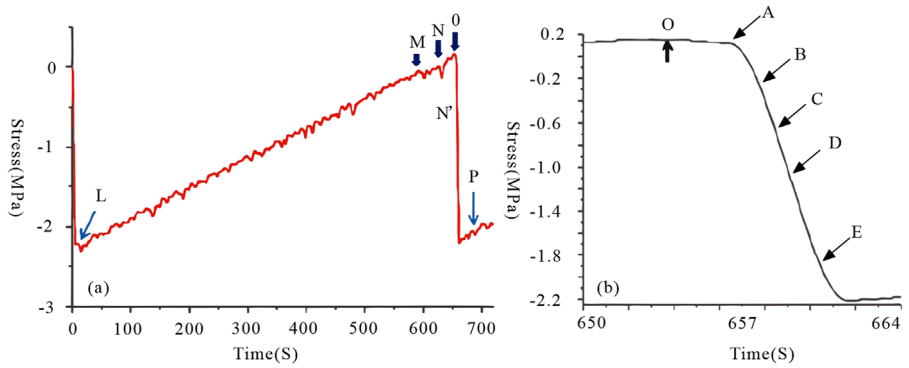

FIGURE 7
An enlarged diagram of the differential stress-time process **(A)** the instability time process **(B)** in a stick-slip event (From Ma and Guo, 2012).

TABLE 3 Corresponding times for each moment in Figure 7.

Point	L	M	N	O	A	B	C	D	E	P
Moment/s	0	593.36	627.45	654.77	656.66	657.59	658.47	658.91	660.3	684.51

TABLE 4 Percentage of time for each deformation phase in Figure 7.

Deformational phase	Elastic deformation	Yield deformation	Subcritical instability phase I	Subcritical instability phase II	Instability phase	Post-instability phase
Percentage of duration (%)	87	8.9	0.2	0.13	0.37	3.4

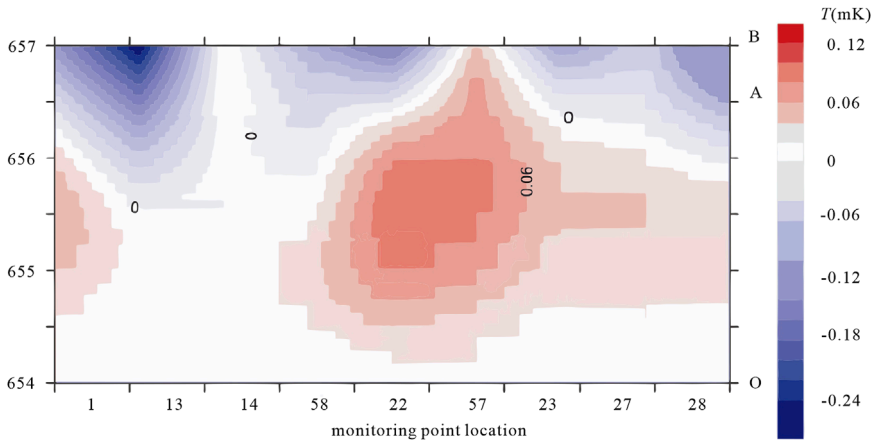

FIGURE 8
Sub-instability phase (O-A-B) along the fault temperature changes with time (From Ma et al., 2012). The temperature at time O is zero.

(1) From May 14th to 19th, an enhancement in OLR radiation near the fault was observed, with the intensity of the increase progressively strengthening, corresponding to the OA phase.

(2) On May 20th and 21st, a continuous decline in OLR radiation was noted for two consecutive days prior to the earthquake, aligning with the AB phase.

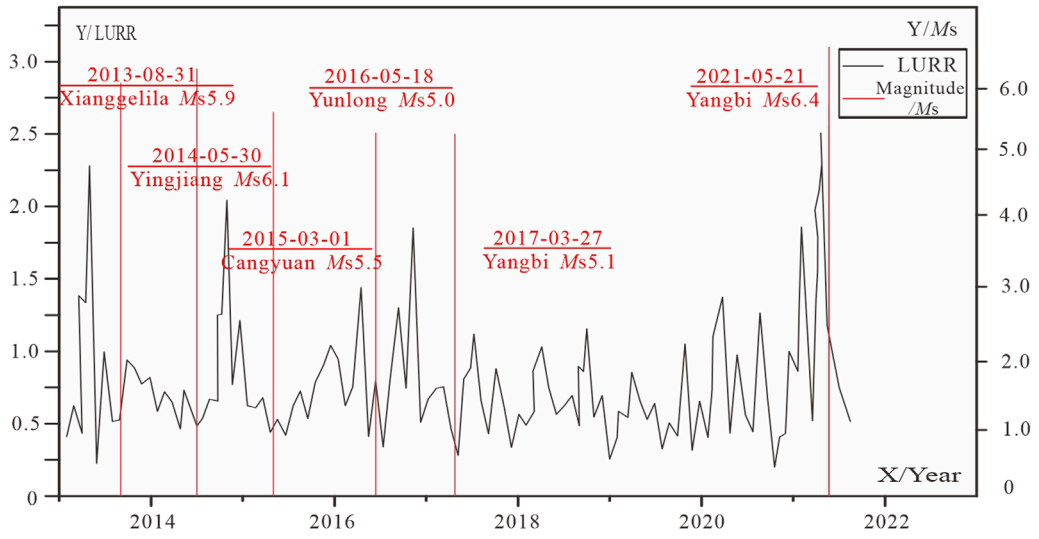

FIGURE 9
Time series of Yangbi M_S6.4 earthquake LURR (2013.01-2021.06).

TABLE 5 Time series table of the Yangbi M_S6.4 earthquake within 300 km from the epicenter.

Time of seismic event	Latitude of epicenter	Longitude of epicenter	Epicenter	Magnitude/*Ms*	LURR high-value time	T2/days
2013-8-31	28.20	99.40	xianggelila	5.9	2013-02-15	97
2014-5-30	25.03	97.82	yingjiang	6.1	2013-02-15	169
2015-3-1	23.46	98.91	cangyuan	5.5	2014-12-10	81
2016-5-18	26.10	99.53	yunlong	5.0	2016-03-30	49
2017-3-27	25.89	99.80	yangbi	5.1	2016-11-20	158
2021-5-21	25.67	99.87	yangbi	6.4	2021-5-10	11

Notes: T2-duration from the decline of LURR, to the occurrence of an earthquake.

(3) Following the mainshock on May 22nd (post the E point), an enhancement in OLR radiation was observed for two consecutive days in the northern part of the epicentral area, surpassing pre-shock levels in both extent and intensity, reflecting the EP phase.
(4) By May 24th to 25th, the enhancement in OLR radiation had dissipated.

In summary, temporally, the entire OLR anomaly evolution process preceding the Madoi earthquake, as indicated by LURR changes, experienced a sequence of initial warming, anomaly expansion, peak intensity, anomaly weakening, earthquake occurrence, and anomaly disappearance over a period of 8 days. This sequence corresponds to the evolutionary characteristics of radiation emitted during each phase observed in rock fracture experiments, essentially reflecting the process of stress accumulation in the rock medium to a critical state, post-seismic stress re-distribution, and the subsequent recovery of fault strength. Spatially, the area of enhanced OLR radiation is located to the north of the epicenter, where the temperature changes in the medium are generally proportional to the incremental strain accumulation. The mainshock is situated in a transition zone from a high strain value area to a low strain value area, with the high strain value area located to the north of the epicenter, roughly coinciding with the region of enhanced OLR radiation.

To verify the accuracy and universality of the aforementioned analysis method, the temporal and spatial evolution patterns of LURR and OLR for the *Ms*6.4 earthquake in Yangbi County, Yunnan Province (N25.67, E99.87) on 21 May 2021, were used for validation. Earthquakes within 300 km of the Yangbi earthquake epicenter (N25.67, E99.87) from 1 January 2013, to 30 June 2021, were selected for calculation. The Benioff strain of earthquakes with magnitudes Ml 0-4.0 in the region when m = 1/2 was scanned and used as the response variable. Multiple loading and unloading cycles were applied in the calculations to prevent strong fluctuations in the load/unload response ratio that might be caused by a small number of earthquakes. In this calculation, the fault friction coefficient of

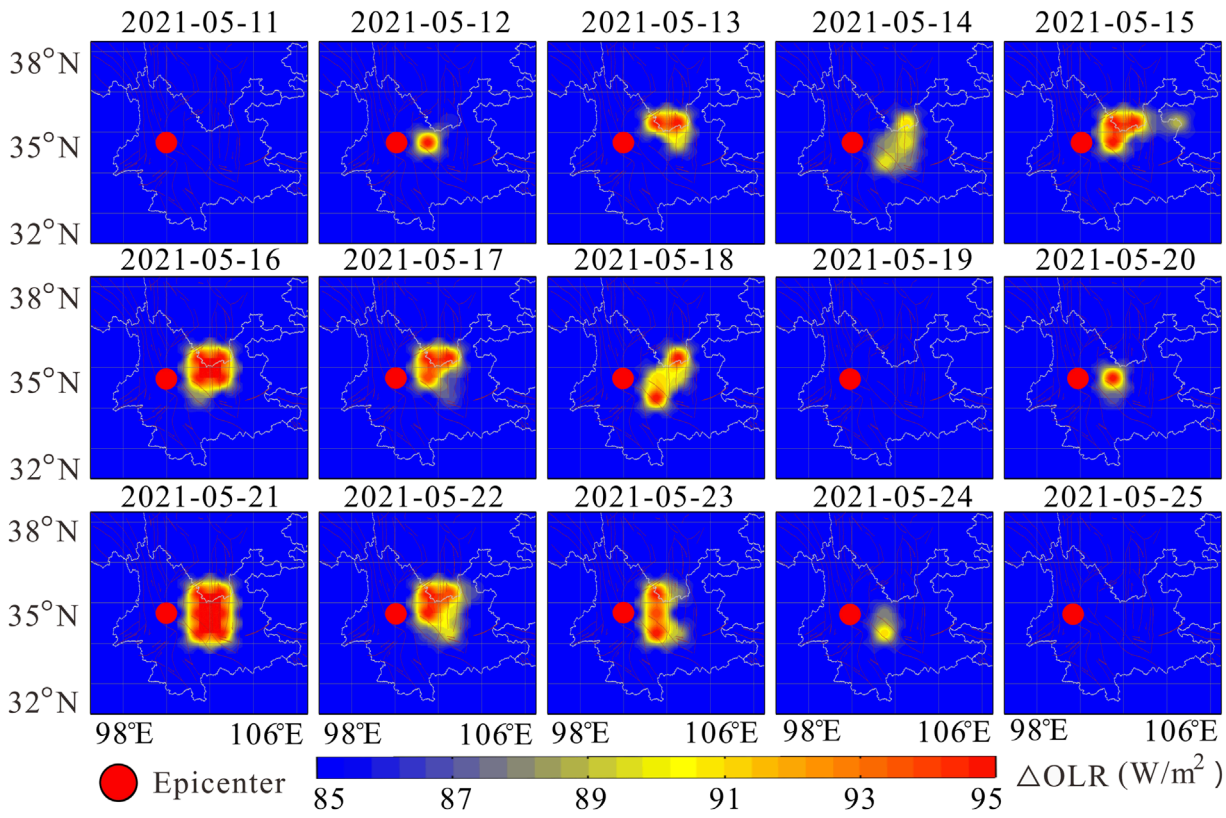

FIGURE 10
Spatial-temporal evolution of OLR of the Yangbi M_S6.4 earthquake (2021.05.11-2021.05.25).

CFS was taken as 0.4, with a window length of 1 month and a step length of 10 days.

Following the aforementioned method and selected data, the calculation results were plotted (Figure 9). It is evident from the figure that within the selected time period, within a 300 km radius of the Yangbi earthquake epicenter, several earthquakes above magnitude five exhibited significant high-value anomalies in LURR before occurring (Figure 9). Taking this Yangbi earthquake as an example, the LURR values gradually increased 6 months before the earthquake, reaching the maximum value half a month before the event, after which the LURR data began to decline, and the Yangbi *M*s6.4 earthquake occurred during this decline. Summarizing the process of this earthquake's occurrence, it was found that the LURR anomaly before this earthquake is consistent with the pre-earthquake LURR anomaly evolution pattern of the *M*s7.4 earthquake in Madoi, Qinghai Province. Combining with the high-value anomalies of LURR before the occurrence of five other earthquakes with magnitude *M*s5.0 or above in this region, it was found that the time from the high-value anomaly of LURR to the occurrence of the earthquake was no less than 1 month and no more than 15 months (Table 5). Therefore, to more accurately determine the time and location of the earthquake, this paper combines LURR with OLR, and follows the continuous daily changes of OLR after the high value of LURR has declined, in order to more accurately determine the three essential elements of the Yangbi earthquake.

In the specific analysis process, this paper selects a fixed date (10 May 2021) as the reference background for OLR data. The daily, same-time, and same-range ground longwave radiation values during the period from the fixed date to 4 days after the earthquake are subtracted from this background to obtain the continuous daily change images before and after this earthquake. These images serve as the basis for the analysis of the imminent anomalies before this earthquake (Figure 10).

From May 11 to 14, 2021, no significant radiation enhancement was observed in the area near the epicenter. On the 15th, a slight radiation enhancement began in the eastern part of the epicenter, with an increase of up to 10W/m^2. On the 16th, the OLR (Outgoing Longwave Radiation) anomaly continued to strengthen and spatially moved towards the epicenter. On the 17th, the OLR began to diminish, reaching its minimum value on the 19th. On the 20th, the OLR values increased again, leading up to the Yangbi *M*s6.4 earthquake on the 21st. Influenced by the stress changes on the fault after the earthquake, the OLR anomaly persisted on May 22-23, with the area of the anomaly continuously shrinking, and the anomaly disappeared after the 24th. Summarizing the entire process of the earthquake's gestation, occurrence, and development, within a relatively short period (from May 11 to May 24), the OLR anomaly went through six phases: initial warming, anomaly expansion, peak intensity, anomaly weakening, earthquake occurrence, and anomaly disappearance. The process of OLR anomaly change is consistent with the characteristics of stress accumulation in the rock medium

reaching a critical state, post-seismic stress redistribution, and the recovery of fault strength in rock fracture experiments. It also matches the seismic occurrence pattern of the *M*s7.4 earthquake in Madoi, Qinghai Province, as mentioned earlier in the text.

By integrating LURR with the OLR anomaly evolution, the moment of LURR's high-value decline may provide a physically meaningful indicator of the onset of anomalies for remote sensing earthquake monitoring. This integration also provides a mechanical basis for the evolution of pre-earthquake thermal anomalies. It not only enhances the reliability of selecting OLR background values and reduces the uncertainty in conclusions caused by the randomness of the calculation process but also narrows the spatial range of anomalies, excluding potentially interfering anomalous areas. Furthermore, it improves the temporal resolution of the LURR time series, allowing for a more refined analysis of the anomaly evolution process following the LURR high-value decline, thereby increasing the accuracy of predictions. This approach facilitates a natural transition in timing from medium to short-term forecasting.

6 Conclusion

The findings of this study reveal that 3 months prior to the 2021 Madoi M_S7.4 earthquake, there was a significant anomaly in the LURR values, which were based on Benioff strain as the responsive indicator. Notably, a pronounced high-value anomaly was observed. Following the decline of this abnormal peak, a significant short-term OLR anomaly emerged in the northern sector of the epicentral area. A parallel phenomenon was also identified in the 2021 Yangbi M_S6.4 earthquake.

The evolution of these anomalies aligns with the process observed in loading experiments, where rock media accumulate stress to a critical threshold, leading to destabilization and eventual rupture. By integrating these two seismic prediction parameters, which possess distinct physical implications, we can more accurately reflect the stress accumulation status in the epicentral region prior to an earthquake. Furthermore, it allows for a more nuanced portrayal of the stress level variations as the fault medium approaches the terminal phase of the yielding process.

This approach enhances our understanding of the temporal and spatial dynamics involved in the gestation, occurrence, and progression of earthquakes. It offers a viable methodology for the study of earthquake prediction, contributing to a more informed and scientific basis for seismic forecasting.

Data availability statement

The raw data supporting the conclusions of this article will be made available by the authors, without undue reservation.

Author contributions

YL: Conceptualization, Formal Analysis, Investigation, Software, Supervision, Writing–review and editing. LJ: Data curation, Methodology, Software, Supervision, Writing–original draft. YC: Data curation, Formal Analysis, Methodology, Writing–original draft. ZH: Conceptualization, Data curation, Methodology, Writing–original draft. HD: Data curation, Formal Analysis, Writing–review and editing. MW: Methodology, Software, Supervision, Writing–review and editing.

Funding

The author(s) declare that financial support was received for the research, authorship, and/or publication of this article. China-ASEAN Earthquake Disaster Monitoring and Defense Capability Improvement Project (No. 123999101), the third batch of Fengyun-3 meteorological satellite projects (No.FY-3(03)-AS-11.10-ZT), General Program of National Natural Science Foundation of China (42474116), the Earthquake Joint Funds of NSFC (Grant No. U2039205), Anhui Provincial Key Research and Development Project (2022m07020002), Spark Program of Earthquake Sciences (XH23021YB), Three Combined Project (3JH-202402004). These funding bodies have had a positive impact on expenses related to data acquisition, data analysis, and participation in academic exchanges.

Acknowledgments

This paper uses NOAA satellite data from the United States.

Conflict of interest

The authors declare that the research was conducted in the absence of any commercial or financial relationships that could be construed as a potential conflict of interest.

Publisher's note

References

Brace, W. B., Paulding, J. R., and Scholz, C. H. (1966). Dilatancy in the fracture of crystalline rocks. *J. Geophys. Res.* 71 (16), 3939–3953. doi:10.1029/jz071i016p03939

Cui, C., Deng, M., and Geng, N. (1993). Spectral radiation characteristics of rocks under different pressures. *Chin. Sci. Bull.* 38 (6), 538–541. (in Chinese). doi:10.1360/csb1993-38-6-538

Gorny, V. I. (1988). The earth outgoing IR radiation as an indicator of seismic activity. *Proc. Acad. Sci. USSR* 301 (1), 67–69.

Li, C., and Nordlund, E. (1993). Experimental verification of the Kaiser effect in rocks. *Rock Mech. Rock Eng.* 26 (4), 333–351. doi:10.1007/bf01027116

Lisi, M., Filizzola, C., Genzano, N., Grimaldi, C. S. L., Lacava, T., Marchese, F., et al. (2010). A study on the Abruzzo 6 April 2009 earthquake by applying the RST approach to 15 years of AVHRR TIR observations. *Nat. Hazards Earth Syst. Sci.* 10 (2), 395–406. doi:10.5194/nhess-10-395-2010

Liu, Y., and Yin, X. C. (2017). A dimensional analysis method for improved load-unload response ratio. *Pure Appl. Geophys.* 175 (Suppl. l), 633–645. doi:10.1007/s00024-017-1716-6

Liu, Y., Yin, X. C., and Yuan, S. (2012). Exploration study of dimension analysis applying to earthquake prediction. *Chin. J. Geophys.* 55 (9), 3043–3050. doi:10.6038/j.issn.0001-5733.2012.09.022

Ma, J., Sisherman, M., and Guo, Y. (2012). Identification of pre-earthquake sub-instability stress state-taking the evolution of temperature field of 5 ° bend fault as an example. *Earth Sci.* 42 (5), 633–645. (in Chinese).

Mogi, K. (1984). "Fundamental studies on earthquake prediction," in *A collection of papers of international symposium on continental seismicity and earthquake prediction (ISCSEP)*. Beijing: Seismological Press, 619–652.

Ouzounov, D., and Freund, F. (2004). Mid-infrared emission prior to strong earthquakes analyzed by remote sensing data. *Adv. Space Res.* 33 (3), 268–273. doi:10.1016/s0273-1177(03)00486-1

Qiang, Z., Kong, L., Guo, M., Wang, Y., Zheng, L., Lin, C., et al. (1997). Experimental study of satellite thermal infrared warming mechanism. *Acta Seismol. Sin.* 19 (2), 197–201. (in Chinese).

Saraf, A. K., Rawat, V., Banerjee, P., Choudhury, S., Panda, S. K., Dasgupta, S., et al. (2008). Satellite detection of earthquake thermal infrared precursors in Iran. *Nat. Hazards* 47 (1), 119–135. doi:10.1007/s11069-007-9201-7

Scholz, C. H., Sykes, L. R., and Aggarwal, Y. P. (1973). Earthquake prediction: a physical basis. *Science* 181, 803–810. doi:10.1126/science.181.4102.803

Tramutoli, V. (2007). "Robust satellite techniques (RST) for natural and environmental hazards monitoring and mitigation: theory and applications," in 2007 International Workshop on the Analysis of Multi-Temporal Remote Sensing Images. IEEE, 1–6. doi:10.1109/MULTITEMP.2007.4293057

Wu, L., Liu, S., Wu, Y., and Li, Y. (2004). Thermal infrared radiation law of discontinuous combination fault rupture and its significance of tectonic earthquake precursor. *Chin. J. Rock Mech. Eng.* 23 (1), 24–30. (in Chinese).

Wu, L. X., Liu, S. J., Wu, Y., and Wang, C. (2006). Precursors for rock fracturing and failure—part I: IRR image abnormalities. *Int. J. Rock Mech. Min. Sci.* 43 (3), 473–482. doi:10.1016/j.ijrmms.2005.09.002

Xu, X., Qiang, Z., and Lin, C. (1990). Sudden ground warming and impending earthquake precursor. *Seismol. Geol.* 12 (3), 243–249. (in Chinese).

Yang, Y. Z., and Guo, G. M. (2010). Studying the thermal anomaly before the Zhangbei earthquake with MTSAT and meteorological data. *Int. J. Remote Sens.* 31 (11), 2783–2791. doi:10.1080/01431160903095478

Yin, X. C., Chen, X., Song, Z., and Yin, C. (1995). A new approach to earthquake prediction: the Load/Unload Response Ratio (LURR) Theory. *Pure Appl. Geophys.* 145, 701–715. doi:10.1007/978-3-0348-9065-6_17

Yin, X. C., Wang, Y. C., Peng, K., Bai, Y. L., Wang, H., and Yin, X. F. (2000). Development of a new approach to earthquake prediction: load/unload response ratio (LURR) theory. *Pure Appl. Geophys.* 157, 2365–2383. doi:10.1007/978-3-0348-7695-7_29

Yin, X. C., Zhang, L. P., Zhang, Y. X., Peng, K. Y., Wang, H. T., Song, Z. P., et al. (2008). The newest developments of load-unload response ratio (LURR). *Pure Appl. Geophys.* 165, 711–722. doi:10.1007/s00024-008-0314-z

Yu, C., Cui, J., Zhang, W., Ma, W., Ren, J., Su, B., et al. (2023). Quasi-synchronous variations in the OLR of NOAA and ionospheric Ne of CSES of three earthquakes in xinjiang, january 2020. *Atmosphere* 14 (12), 1828. doi:10.3390/atmos14121828

Yu, H., Yu, C., Ma, Z., Zhang, X., Zhang, H., Yao, Q., et al. (2020). Temporal and spatial evolution of load/unload response ratio before the M 7.0 Jiuzhaigou Earthquake of Aug. 8, 2017 in Sichuan province. *Pure Appl. Geophys.* 177, 321–331. doi:10.1007/s00024-019-02101-x

Yu, H., Yuan, Z., Yu, C., Zhang, X., Gao, R., Chang, Y., et al. (2022). The medium-to-short-term earthquake predictions in China and their evaluations based on the R-score. *Seismol. Soc. Am.* 93 (2A), 840–852. doi:10.1785/0220210081

Yu, H. Z., Shen, Z. K., Wan, Y. G., Zhu, Q. y., and Yin, X. c. (2006). Increasing critical sensitivity of the Load/Unload Response Ratio before large earthquakes with identified stress accumulation pattern. *Tectonophysics* 428 (1), 87–94. doi:10.1016/j.tecto.2006.09.006

Yu, H. Z., Zhou, F. R., Cheng, J., and Wan, Y. G. (2015). The sensitivity of load/unload response ratio and critical region selection before large earthquakes. *Pure Appl. Geophys.* 172, 173–183. doi:10.1007/s00024-014-0903-y

Yu, H. Z., and Zhu, Q. Y. (2010). A probabilistic approach for earthquake potential evaluation based on the load/unload response ratio method. *Concurrency Comput. Pract. Exp.* 22 (12), 1520–1533. doi:10.1002/cpe.1509

Zakupin, A. S., Bogomolov, L. M., and Boginskaya, N. V. (2021). Using the load/unload response ratio and self-developing processes methods of analyzing seismic sequences to predict earthquakes in sakhalin. *Izvestiya, Atmos. Ocean. Phys.* 56 (7), 693–705. doi:10.1134/s0001433820070105

Zhang, Y., Meng, Q., Ouillon, G., Sornette, D., Ma, W., Zhang, L., et al. (2021). Spatially variable model for extracting TIR anomalies before earthquakes: application to Chinese Mainland. *Remote Sens. Environ.* 267, 112720. doi:10.1016/j.rse.2021.112720

frontiers | Frontiers in Earth Science

TYPE Methods
PUBLISHED 13 September 2024
DOI 10.3389/feart.2024.1423823

OPEN ACCESS

EDITED BY
Giovanni Martinelli,
Section of Palermo, Italy

REVIEWED BY
Vincenzo Lapenna,
National Research Council (CNR), Italy
Timangshu Chetia,
North East Institute of Science and Technology (CSIR), India

*CORRESPONDENCE
Li Jianyong,
jyli@seis.ac.cn

RECEIVED 26 April 2024
ACCEPTED 29 August 2024
PUBLISHED 13 September 2024

CITATION
Lei Y, Jianyong L, Junfeng C, Dequan H, Manfeng C, Wei J and Weiyu M (2024) Analysis of anisotropy anomalies identification in apparent resistivity observation. *Front. Earth Sci.* 12:1423823. doi: 10.3389/feart.2024.1423823

Analysis of anisotropy anomalies identification in apparent resistivity observation

Yu Lei[1,2], Li Jianyong[3]*, Cao Junfeng[1], Hong Dequan[1], Cui Manfeng[3], Ji Wei[4] and Ma Weiyu[3]

[1]Anhui Earthquake Agency, Hefei, China, [2]University of Science and Technology of China, Hefei, China, [3]China Earthquake Network Center, Beijing, China, [4]Geovis Environment Technology Co., Ltd., Beijing, China

Since 1966, China has been using apparent resistivity observation to forecast strong aftershocks of the Xingtai earthquake. Retrospective studies of subsequent strong earthquakes have shown that anomalies in apparent resistivity observation before earthquakes usually exhibit anisotropic characteristics. In addition to the anisotropic changes in apparent resistivity before earthquakes, factors such as subway operation near the observation area, metal pipeline networks, and changes in water levels have also been found to cause anisotropic changes. These factors are called environmental interference factors. Therefore, distinguishing between anisotropic changes before earthquakes and anisotropic changes caused by interference and eliminating the effects of interference is crucial for using apparent resistivity observations for forecasting. Taking the observation of Hefei seismic station in Anhui Province as an example, a model is constructed using the finite element method to try to establish a method for analyzing anisotropy in apparent resistivity before earthquakes, and the data from other provincial stations are used for verification. In the modeling process, the influence coefficient is a measure of the relationship between the variation in apparent resistivity and the changes in the medium of the measurement area. The following results are obtained by calculating the influence coefficient using the finite element method: the influence coefficient between the power supply electrode and the measuring electrode of the apparent resistivity observation is negative, and the rest are positive, and the distribution of the influence coefficient shows obvious symmetry, with the axis of symmetry being the line connecting the electrodes and its midline, and the absolute value of the influence coefficient is inversely proportional to the distance from the electrodes. In addition, according to the constructed finite element model, the amplitude of anisotropic changes caused by interference can be quantitatively calculated. Given that interference is ubiquitous in various regions of the world, this study can provide a reference for international earthquake forecasters to quantitatively remove environmental interference in anisotropy. Moreover, when building apparent resistivity stations in seismic areas for earthquake prediction, it is best to avoid areas with larger local influence coefficients to ensure that the anomalous data before the earthquake is true and reliable.

KEYWORDS

finite element, apparent resistivity, influence coefficient, layered medium, anisotropy

1 Introduction

The seismic method of apparent resistivity in seismology is employed to predict earthquakes by monitoring temporal variations in the electrical properties of the Earth's media. After the 1966 Xingtai earthquake, China initiated the use of apparent resistivity methods to forecast strong aftershocks of the earthquake. Subsequent retrospective studies on several major earthquakes have shown that anomalies in apparent resistivity observation before the earthquakes typically exhibit characteristics of anisotropy. Over the past 50 years, this network has grown to encompass over 90 stations. During the operation of the seismic network, the theory of anisotropic variations has evolved and played a role in earthquake monitoring and forecasting (Zhao et al., 1983; Ellis et al., 2010; Bachrach, 2011; North and Best, 2014; Sævik et al., 2014; Thongyoy et al., 2023). Moreover, observations of apparent resistivity changes have been utilized to predict certain moderate earthquakes (Du, 2010; Xu et al., 2014).

With ongoing societal development, various observation sites now confront varying degrees of interference. During the operation of subways, the presence of metal pipeline networks, and changes in water levels can cause local variations in the medium of the measurement area, thereby affecting the electrical structure of the area and resulting in anisotropic changes in the observation. However, these changes are not the pre-seismic anisotropic anomalies required for earthquake prediction. During routine observations, initial cracks in the medium may close or shift under increasing stress. Eventually, new cracks tend to form along the direction of maximum principal stress (Kemeny, 1991). To analyze the relationship between the apparent resistivity changes and variations in the geological medium, global geoelectric researchers have developed theories focusing on one-dimensional sensitivity coefficients for layered media. According to this theory, the relative change in apparent resistivity can be expressed as a weighted sum of relative changes across different regions of the observation area (Qian et al., 1985; Qian et al., 1996; Qian et al., 2013; Park and Van, 1991). This approach has been particularly useful in analyzing disturbances caused by changes in shallow subsurface materials (Lu et al., 1999; Lu et al., 2004). However, challenges arise at many stations where disturbances do not result from uniform changes in a single layer but rather from factors affecting multiple layers near electrodes, such as road construction and excavation. These multi-layer disturbances can complicate the application of traditional one-dimensional sensitivity coefficient theories, necessitating more sophisticated modeling techniques to accurately interpret observed data. Experts have employed a series of 40 theoretical horizontal resistivity profiles to investigate these phenomena. These profiles illustrate how factors like sinkhole dimensions, reflection coefficients (k), and lateral distance from the sinkhole center influence apparent resistivity observation (Kenneth and Russell, 1961). Researchers have observed variations in sensitivity coefficients across different regions of observation areas based on this theoretical framework (Xie and Lu, 2015). While these studies offer qualitative analyses of anomalous apparent resistivity changes, refining quantitative modeling methods remains an ongoing endeavor.

This study utilizes observational data from the Hefei seismic station in Anhui Province to explore the anisotropic variations in apparent resistivity measurements. Building on these findings, a three-dimensional influence coefficient model is constructed using the finite element method to quantitatively exclude the data variation amplitude caused by environmental interference in anisotropic changes. The developed method is then validated at the Xingji seismic station in Hebei Province, with the aim of establishing a method for determining the genuine pre-seismic apparent resistivity anisotropy. This research is intended to provide a reference for the apparent resistivity forecasting and station construction efforts in other seismically active regions internationally.

2 Anisotropy of apparent resistivity observation

2.1 Anisotropy theory and examples

In shallow layers of the Earth's surface, two principal stresses typically align horizontally. Under prolonged tectonic stress, the distribution and expansion of microcrack systems are controlled by the maximum principal stress (Crampin et al., 1984). For a uniform medium, when using a symmetric quadrupole array for surface observations, the apparent resistivity is given by (Kraev, 1954; Qian et al., 1996) and can be represented as Equation 1.

$$\rho_a = \left(\frac{\rho_1 \rho_2 \rho_3}{\rho_1 \cos^2\theta + \rho_2 \sin^2\theta} \right)^{\frac{1}{2}} \tag{1}$$

In the Formula ρ_1, ρ_2 and ρ_3 are the resistivities along the three principal electrical axes, and ρ_1 and ρ_2 aligned horizontally. Assuming ρ_1 represents the minimum electrical axis along which the microcrack system predominantly extends, and $\theta \in [0, \pi/2]$ denotes the angle between the observation device and ρ_1, the variation in apparent resistivity with respect to θ is given by (Xie and Lu, 2020a):

$$\frac{d(d\rho_a/\rho_a)}{d\theta} = \frac{1}{2} \frac{\frac{d\rho_1}{\rho_1} - \frac{d\rho_2}{\rho_2}}{\left(\sqrt{\frac{\rho_1}{\rho_2}} \cos^2\theta + \sqrt{\frac{\rho_2}{\rho_1}} \sin^2\theta \right)^2} \sin 2\theta \tag{2}$$

After a microcrack system expands along the ρ_1 direction, ρ_1 experiences the maximum decrease in apparent resistivity. According to Xie and Lu (2020a), the absolute magnitude of apparent resistivity change increases monotonically with θ, which represents the angle perpendicular to ρ_1 showing the greatest decrease in apparent resistivity. This observation is consistent with field experiments conducted by Zhao et al. (1983). Figure 1 represents the results of a field experiment on stress loading and unloading. From Figure 1, it is evident that the apparent resistivity decreases when stress is applied and rebounds when the stress is removed. The greatest decrease occurs in the direction perpendicular to the maximum principal stress, the smallest in the parallel direction, and the oblique direction shows a decrease that lies between the two, exhibiting anisotropic changes related to the orientation of the maximum principal stress.

Subsurface formations often display lateral heterogeneity, which can cause apparent resistivity values to vary across different directions. However, according to finite element numerical analysis, the effect of lateral heterogeneity on anisotropic changes, quantified by the relative change ratio $\Delta\rho_a/\rho_a$, is relatively minor

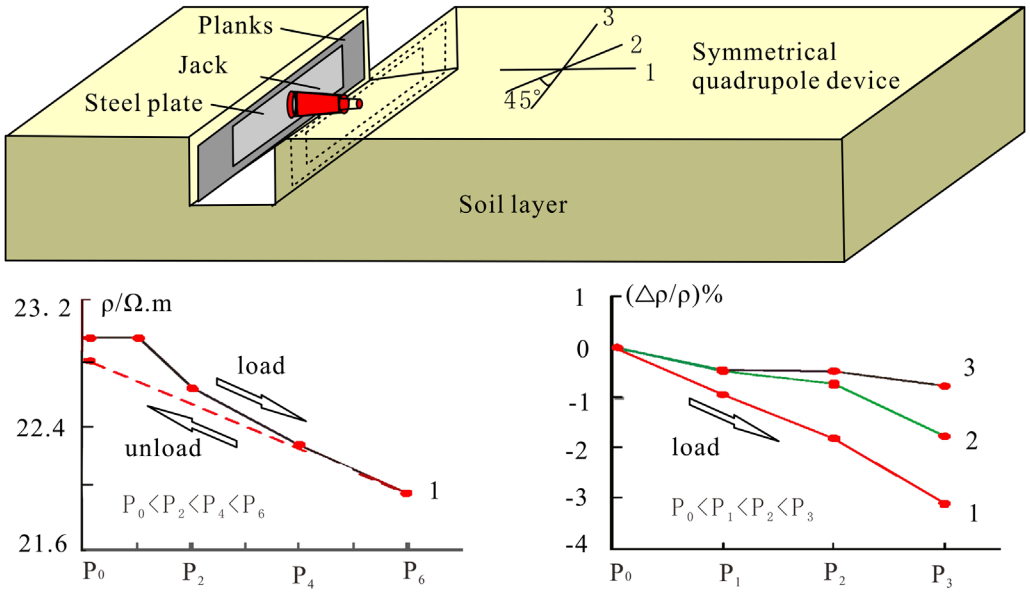

FIGURE 1
Anisotropic apparent resistivity variations in grooved soil under compressive stress (Zhao et al., 1983).

(Xie et al., 2020b). Anomalous fluctuations in apparent resistivity due to anisotropy predominantly result from variations in the resistivity of the medium itself, which are strongly influenced by the orientation of the maximum principal stress. This highlights the critical role of stress orientation in shaping the observed apparent resistivity patterns, emphasizing the directional sensitivity of apparent resistivity measurements in detecting anisotropic changes.

Earthquakes result from long-term accumulation of tectonic stresses, eventually leading to fault instability. Anomalies in apparent resistivity typically occur 1–2 years before major earthquakes. During this period, the subsurface medium undergoes initial closure and deviation of cracks due to prolonged stress accumulation, eventually entering a phase dominated by a new crack system (Crampin et al., 1984). The magnitude of apparent resistivity anomalies varies in different directions relative to the principal stress axis: the greater the angle with the principal stress axis, the greater the anomaly magnitude. Significant anomalies were observed at stations such as Chengdu, Jiangyou, Ganzi, and Wudu before the 2008 Wenchuan *Ms*8.0 earthquake (Du et al., 2017; Zhang et al., 2009; Qian et al., 2013). However, there are differences in the magnitude of data changes among different directional measurements. Table 1 provides information on the apparent resistivity anomaly changes in different directions at various stations before the 2008 Wenchuan earthquake. These stations are located at varying distances from the epicenter, ranging from 30 to 330 km. The duration and magnitude of anomalies in different measurement directions before the earthquake also show significant differences, exhibiting a clear anisotropy.

Apparent resistivity data exhibiting a downward trend that breaks the annual variation is a significant indicator of anomaly. The magnitude of anomalies often varies across different measurement directions, which is called pre-seismic anisotropy. For example, before the *Ms*8.0 Wenchuan earthquake in 2008, the N70°W measurement direction at the Jiangyou station, which is 30 km away from the epicenter, began to show a downward change in August 2006, with a decrease of about 1.5%. The N10°E measurement direction showed no significant changes before the earthquake. On the day of the earthquake, the N70°W and N10°E measurement directions decreased by 3.8% and 5.2% respectively. Post-earthquake, the data recovered and rose (Figures 2A, B).

According to the theory of anisotropy, it's feasible to identify and explain certain pre-seismic anomalous changes. However, contemporary apparent resistivity observations are susceptible to diverse influences, rendering the reasons quite intricate. Some anomalous changes may stem from local environmental alterations. If non-seismic anomalies cannot be accurately discerned, the efficacy of apparent resistivity observations could be compromised. Therefore, effectively identifying various disturbances forms the cornerstone for conducting anisotropy analysis.

2.2 Anisotropic changes at Hefei seismic station

Hefei seismic station is located in Hefei, Anhui Province, situated in a hilly area with micro-topography. The Tanlu Fault Zone traverses the station. The active faults within the Tanlu fault zone in Anhui are predominantly located at the boundary of the faulted basin, extending from south to north along the eastern boundary of the Hefei Basin, the eastern boundary of the Dabie Mountains orogenic belt, and the eastern and western boundaries of the Jiashan Basin (Ni et al., 2022). The epicenters of the 1,673 Hefei *M*5 earthquake and the 1,585 Chaohu $M5^3/4$ earthquake were in close proximity to the station.

The apparent resistivity measurement area is located in Anhui province, featuring a gentle slope from east to west and no

TABLE 1 The apparent resistivity changes before the 2008 Wenchuan earthquakes.

Date	Location	M_S	Station	D/km	Direction	R_C (%)	T/Mon	θ/(°)
2008-05-12	wenchuan	8.0	chengdu	35	N58°E	−6.7	22	61
					N49°W	----	----	12
			jiangyou	30	N70°W	−1.5	22	65
					N10°E	----	----	15
			ganzi	330	N30°E	−5.3	22	83
					N60°W	−4.9	22	7
			wudu	110	N54°W	+2.9	22	41
					N73°W	----	----	22
					N85°E	----	----	0

Notes: D: Epicenter Distance;R_C: magnitude of change; T: The duration of the exception; θ: Angle.

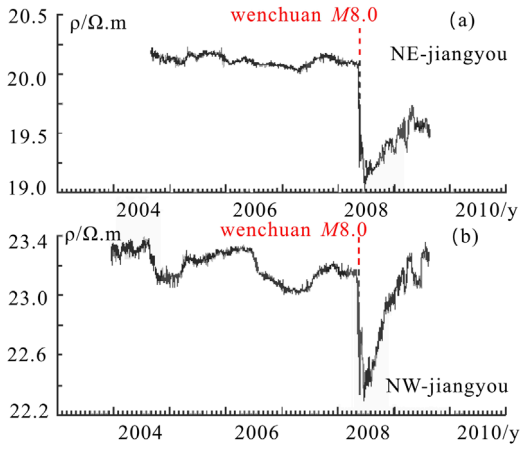

FIGURE 2
Typical trend of apparent resistivity before earthquake. **(A)** The change of N10°E direction data and **(B)** The change of N70°W direction data in Jiangyou station.

significant slope in the north-south direction. The measurement area includes some paddy fields and is free of building facilities and underground pipelines. Apparent resistivity observation is set up with two directions: north-south (NS) and east-west (EW), employing symmetrical four-electrode burial (Figure 3C). The electrode is a 1 m × 1.1 m lead plate, buried at a depth of 2.0 m, with a grounding resistance range of 2–5Ω. The outer circuit consists of single-core copper wire with a plastic skin, supported by overhead cement poles. The distance between the power supply electrodes AB and the measuring electrodes MN is 600 m and 200 m, respectively. When the Chinese fixed station is conducting apparent resistivity observation, the detection range in the depth direction is comparable to the observation electrode distance AB scale, mainly reflecting the changes in the resistivity of the shallow layer medium. The observation electrode distance AB of Hefei station is 600 m, so the apparent resistivity observed by Hefei station is a comprehensive reflection of the medium resistivity from the surface to a depth of 600 m underground.

Based on the distribution of influence coefficients and multi-year observational data, the two directional apparent resistivity observation at the Hefei station have long shown an inverse variation over the years. However, between October 2018 and December 2018, the observation in both directions exhibited a synchronous change, which is a clear anisotropic variation (Figures 3A, B). In Figure 3A, the theoretical observation trend for the NS direction and the actual change curve form an inverse variation, and by comparing with Figure 3B, the change in the NS direction observation while the EW direction remains unchanged, causes the actual curves of the two directions to change from inverse to the same direction, resulting in anisotropic variation. Upon investigating the anomaly, it was found that there is a natural reservoir located between electrode positions B and N in the NS direction of the apparent resistivity observation setup at the station (Figure 3C). This reservoir maintains a stable water level throughout the year. In October 2018, the water level in the reservoir decreased significantly, leading to a reduction in the moisture content in the medium between positions B and N. According to the apparent resistivity calculation formula, a decrease in moisture content should result in an increase in apparent resistivity. However, the observed data showed a decrease instead (Figure 3B). This anomalous decrease in the NS data caused the previously opposite trends in NS and EW data curves to become synchronous starting from October 2018. During this period, there was an anisotropic change observed in the NS and EW data.

It is crucial to conduct a detailed analysis to determine the cause of this change. The anomaly could potentially be attributed to seismic precursor variations caused by anisotropy or environmental disturbances, such as changes in moisture content due to the fluctuating water level in the reservoir. Further investigation and monitoring will be necessary to understand the exact nature of

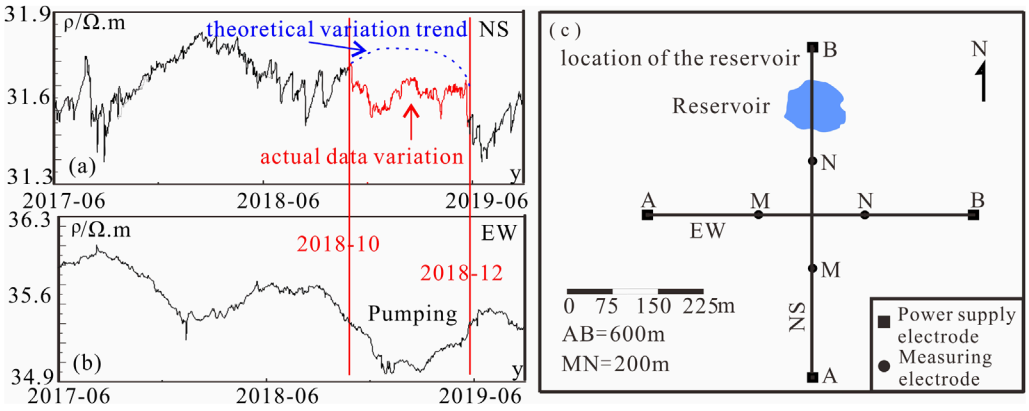

FIGURE 3
The change of apparent resistivity before and after pumping and the position of the reservoir. **(A,B)** the curve between the vertical lines show the changes after pumping water. **(C)** The position of the reservoir.

these anomalous changes in apparent resistivity observation at Hefei station.

3 Model construction

The apparent resistivity of the station in China uses a steady flow source for power supply, and is observed once every hour. One observation collects 10 sets of data, and then the average value is calculated, with the standard deviation of the observation controlled within 1%. Each quarter, the instrument is calibrated with a standard power source and standard resistance to ensure the accuracy of the observed values. The influence coefficient is used to analyze the extent of the impact that the resistivity changes of different positions in the measurement area may have on the observation.

3.1 Influence coefficient analysis

Park and Van (1991) proposed that the influence coefficient is a measure of the relationship between the changes in apparent resistivity and the variations in the medium of the measurement area. When the electrical structure of the measurement area is determined and the observation system is stable, the apparent resistivity can be expressed as a function of the resistivity of the medium in each sub-zone (Lu et al., 2004):

$$d(\ln \rho_a) = \sum_{i=1}^{N} \frac{\partial \ln \rho_a}{\partial \ln \rho_i} d(\ln \rho_i) \tag{3}$$

Since the higher-order terms beyond the first are typically negligible, Equation 3 is a Taylor series approximation that omits second-order and higher terms. Consequently, the relative change in apparent resistivity can be articulated as a weighted sum of the relative changes in resistivity of each layer and it can be represented as Equation 4.

$$\frac{\Delta \rho_a}{\rho_a} = \sum_{i=1}^{N} B_i \frac{\Delta \rho_i}{\rho_i} \tag{4}$$

Based on the layered horizontal structure of the apparent resistivity measurement area, the influence coefficients B for a symmetric quadrupole arrangement can be calculated using the potential distribution analytical expression and the resistivity filter algorithm (O'Neill and Merrick, 1984; Yao, 1989). The coefficient B is defined as:

$$B_i = \frac{\partial \ln \rho_a}{\partial \ln \rho_i} = \frac{\rho_i}{\rho_a} \frac{\partial \rho_a}{\partial \rho_i} \tag{5}$$

$$\sum_{i=1}^{N} B_i = 1 \tag{6}$$

3.2 Steady current fieldfinite element method

The one-dimensional influence coefficient is for horizontally layered stratification, treating each layer as a whole and analyzing the impact of changes in this whole on apparent resistivity observations. It is suitable for situations that can be equivalently transformed into changes of a whole layer, such as rainfall, temperature, and water level variations. However, the one-dimensional influence coefficient cannot be used to analyze the impact of localized changes in the medium on observations. Therefore, numerical simulation methods are needed to further subdivide the one-dimensional influence coefficients into three-dimensional influence coefficients.

Calculating three-dimensional influence coefficients requires the use of numerical simulation methods. There are many numerical simulation methods currently available, such as the finite element method, finite difference method, boundary element method, and other techniques. These methods for computing steady-state electrical current fields are now highly developed. Finite element methods are particularly adept at discretizing irregular geometries effectively. Considering the irregularly shaped reservoir within the observation area at Hefei Station, the finite element method for steady-state electrical current fields proves suitable for accurately modeling the station's observation conditions.

When employing the Wenner array for observation, the measured apparent resistivity provides a comprehensive reflection of the subsurface resistivity over a defined volume of the measurement area. As the distance from the observation site increases, the impact of the medium on the observed values diminishes. At sufficiently large distances, this influence becomes negligible (Li, 2005). Given an electrode spacing of AB = 600 m for apparent resistivity observations, significant influences on the observations are confined to specific depths within the subsurface. Longitudinally, the site is stratified based on the electrical structure of the area, with the deepest layer extending up to twice the length of AB. Laterally, it extends to six times the length of AB. The three-dimensional influence coefficients of the surrounding medium at the observation site are analyzed using finite element numerical analysis methods.

Currently, apparent resistivity observations are conducted using a steady current source with a supply intensity typically ranging from 1 to 2 A. Therefore, the computation of apparent resistivity observations can be viewed as a steady-state electric current field problem, which can be expressed by Poisson's Equation 7:

$$\nabla(\sigma\nabla V) = -I\delta(x,y,z) \tag{7}$$

Where V is the potential generated by the current source I, σ is the dielectric conductivity, and δ (x, y, z) is the Dirac delta function. At the boundary of the model, steady current field satisfy Dirichlet-Neumann boundary condition and it can be represented as Equation 8.

$$\Gamma = \Gamma_s + \Gamma_v \tag{8}$$

The entire boundary of the finite medium space is Γ. A portion of the boundary has no current flow out (such as the ground surface), satisfying the Neumann boundary condition, denoted as Γ_V. The remaining boundary is denoted as Γ_s, satisfying the Dirichlet boundary condition. Among them some parameters can be represented as Equations 9, 10.

$$V|\Gamma_s = P \tag{9}$$

$$\frac{\partial V}{\partial n}|\Gamma_v = 0 \tag{10}$$

n is the normal direction pointing outward from the boundary of the region The weak solution of Poisson equation of steady current field can be obtained by using the principle of virtual work.

$$\int_\Omega \sigma\left[\frac{\partial V}{\partial x}\frac{\partial \varphi}{\partial x} + \frac{\partial V}{\partial y}\frac{\partial \varphi}{\partial y} + \frac{\partial V}{\partial z}\frac{\partial \varphi}{\partial z}\right] = \int_\Omega I\delta(x,y,z)\varphi d\Omega \tag{11}$$

Ω is the computational domain, φ is an arbitrary virtual displacement function. In horizontally layered media, as described by Equation 11, the electric current field generated by two electrodes exhibits inherent symmetry relative to the surface. This symmetry influences the distribution of influence coefficients, which are symmetric concerning the profiles or measuring lines used in the observation. This symmetry simplifies the analysis, as it allows for systematic characterization of how apparent resistivity changes with depth and lateral position across the measurement area.

In apparent resistivity observations, the Earth's surface naturally satisfies the Neumann boundary condition. At the infinite boundary, one can impose either Dirichlet boundary conditions (V = 0) or Neumann boundary conditions (Coggon, 1971). In practical applications, the model scale is finite by necessity. When the model size is fixed and the electrode spacing increases, computing apparent resistivity values with Dirichlet boundary conditions at infinity tends to underestimate the actual values, whereas using Neumann boundary conditions yields results that overestimate the actual values (Dey and Morrison, 1979; Li and Spitzer, 2005).

To minimize the boundary effects on computed results, one can enlarge the model size while keeping the electrode spacing fixed, although this approach increases computational complexity. Therefore, selecting an appropriate model size is crucial. Scholars have suggested, through finite element numerical analysis of apparent resistivity observations, that the horizontal dimension of the model should be greater than 6 times the electrode spacing (AB), and the model thickness should be greater than 2 times AB to effectively disregard boundary effects (Xie et al., 2014).

3.3 Distribution of three-dimensional influence coefficients and quantitative calculations based on finite element method

The site's medium is subdivided into three-dimensional volumes of specific sizes, forming a model using the finite element numerical analysis method. After discretizing the elements and applying current sources and boundary conditions, numerical solutions are computed for the degrees of freedom (potentials) at the nodes of the elements. Using the solved potential differences, apparent resistivity values and corresponding distributions of influence coefficients are calculated based on device coefficients. The influence coefficient for a specific layer of the medium is determined by summing all influence coefficients from the three-dimensional volumes within that layer and it can be represented as Equation 12.

$$B_i^1 = \sum\nolimits_{j\in \text{layer}i} B_j^3 \tag{12}$$

The specific parameters of the apparent resistivity observation instrument at the Hefei station site are as follows: the electrode spacing for the power supply electrodes AB is 600 m, and for the measuring electrodes MN it is 200 m. The observation device is positioned on the surface of the model, with the horizontal dimensions of the model set at 8 times AB. According to the electrical structure, the model is segmented into three layers, with the bottom layer having a thickness of 2 times AB. The calculation region for the influence coefficients spans around the center of the electrode array, covering a spatial extent of 4,800 m × 4,800 m × 1,200 m (Figure 4).

Given the fixed site conditions and the electrical structure described by Equation 2, each block within the site is independent in terms of its influence coefficients from other blocks. Therefore, this study uniformly divides the analysis region into several cubic units measuring 2 m × 2 m × 2 m. To optimize computational efficiency, the remaining areas gradually expand outward during unit division. During calculations, a current of 2I is applied to electrode A and -2I to electrode B. Each unit within the analysis region is computed using central differences to calculate the partial derivatives, as described in Equation 5. This process yields the respective influence

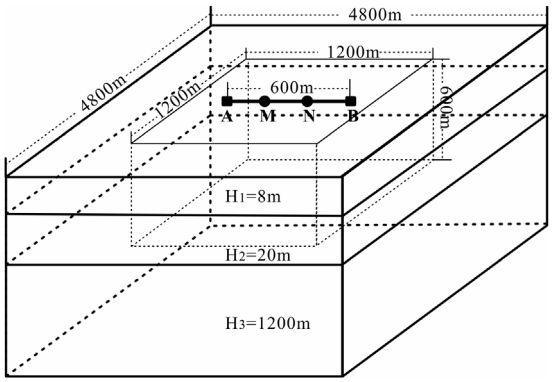

FIGURE 4
Schematic diagram of the finite element numerical analysis model. The model is divided into 3 layers, with the horizontal dimension taken as 8 times AB, and the thickness of the bottom layer taken as 2 times AB.

coefficients for each unit, collectively forming the three-dimensional distribution of influence coefficients across the measurement area.

The three-dimensional distribution of influence coefficients at the site was obtained through the aforementioned calculations (Figure 5). From Figure 5, it can be concluded that the influence coefficients within the site are discontinuous and exhibit significant variability. Analysis of the distribution reveals predominantly positive influence coefficients on the surface. However, an elliptical region of negative coefficients is observed between the measuring electrode and the power supply electrode. Along the vertical line, the coefficients maintain continuity with the surface distribution. Symmetry is evident along both the AB line and the vertical central line, with the absolute values of coefficients increasing proportionally with distance from the electrodes. In regions where coefficients are negative, apparent resistivity changes inversely with resistivity of the site. By investigating the size and intensity of interference factors in areas where the influence coefficient is negative, the aforementioned finite element calculation method can be used to quantitatively calculate the extent of changes caused by the interference. Then, by comparing the actual data changes with the calculated results, it can be determined whether the anomalous data changes are entirely caused by interference.

The three-dimensional distribution of influence coefficients is directly influenced by the positioning of electrodes. Notably, a negative region exists between the power supply electrode and the measuring electrode, a characteristic determined by the device layout rather than guiding the arrangement of the observation system itself. However, understanding the distribution characteristics of these coefficients can aid in selecting measurement areas to avoid potential interference sources based on their locations.

4 The application of the analysis method at Hefei seismic station

4.1 Analysis of influence coefficients in apparent resistivity observations at Hefei seismic station

Based on the theory of influence coefficients, the various parameters of the apparent resistivity observations at Hefei seismic station were substituted into Equations 5, 6 to obtain the one-dimensional influence coefficient model for Hefei Station (Figure 6).

Based on the calculation results from Figure 6, at the Hefei station, the apparent resistivity measurement distance between the electrodes A and B is 600 m, at this time:

In the NS direction it can be represented as Equation 13.

$$\frac{\Delta\rho_a}{\rho_a} = 0.016\frac{\Delta\rho_1}{\rho_1} + 0.417\frac{\Delta\rho_2}{\rho_2} + 0.566\frac{\Delta\rho_3}{\rho_3} \tag{13}$$

In the direction of EW it can be represented as Equation 14.

$$\frac{\Delta\rho_a}{\rho_a} = -0.088\frac{\Delta\rho_1}{\rho_1} + 0.326\frac{\Delta\rho_2}{\rho_2} + 0.763\frac{\Delta\rho_3}{\rho_3} \tag{14}$$

In the analysis of one-dimensional influence coefficients, the influence coefficient of the surface medium in the NS direction remains positive within the calculation range where the electrode distance AB/2 < 1,000 m. Conversely, in the EW direction, the influence coefficient of the surface medium is negative within the range where the electrode distance is between 190 m and 1,000 m. During the rainy season, the one-dimensional influence coefficient analysis indicates that apparent resistivity observation decreases in the NS direction, while it increases in the EW direction.

Based on the one-dimensional influence coefficients, the coefficients for the surface and sub-surface layers in the NS direction are positive. The pumping of water from the reservoir can be understood as a decrease in water level between the NS directions. The pumping operation is equivalent to the water in the reservoir area turning into air. At this time, the apparent resistivity of the reservoir should increase, but the apparent resistivity data decreases instead, causing a deviation between the theoretical and actual values. Therefore, in October 2018, when the reservoir between the power supply electrode B and the measuring electrode N was pumped, this resulted in a change in the local medium's resistivity in the measurement area, which is not a change in the entire layer, and at this time, it no longer meets the analysis conditions of the one-dimensional influence coefficient.

4.2 Quantitative calculations

Since the results obtained from the traditional one-dimensional influence coefficient analysis have deviated, according to the method described in Section 3.3, a finite element analysis method is applied to calculate the three-dimensional influence coefficients, thereby obtaining the distribution of the three-dimensional influence coefficients for the NS direction apparent resistivity site. Based on electrical sounding data, the finite element analysis method was employed to compute the three-dimensional influence coefficients, resulting in a distribution for the NS direction apparent resistivity site, as illustrated in Figure 5. The reservoir lies entirely within the negative influence coefficient region between the power supply electrode B and the measuring electrode N. This indicates that the increase in the reservoir's resistivity leads to a decrease in observed values, aligning with actual observations. The size of the reservoir is approximately 30 m * 30 m * 25 m. Using the constructed three-dimensional finite element model, the impact of water pumping on the apparent resistivity values of the NS direction is quantitatively calculated (Table 2). Through the calculations in Table 2, the

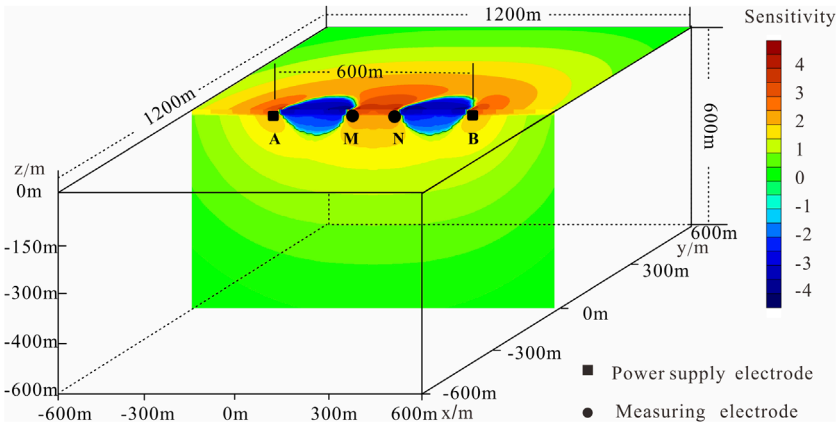

FIGURE 5
The distribution of three-dimensional influence coefficients of apparent resistivity observation area The influence coefficients are non-continuously distributed, with two approximately elliptical areas of negative influence coefficients between the measuring and power supply electrodes in both horizontal and vertical directions, while the coefficients in the other areas are positive. The influence coefficients (in absolute value) are the greatest near the electrodes and decrease rapidly in the areas far from the measurement line. Additionally, the influence coefficients exhibit symmetry in the direction perpendicular to the measurement line.

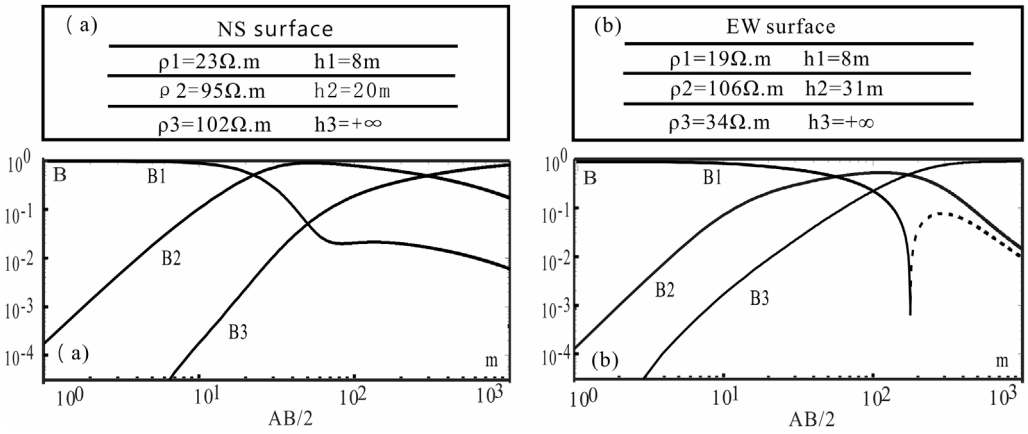

FIGURE 6
Horizontal layered model and its one-dimensional influence coefficient of Hefei station. The layered structure and one-dimensional influence Coefficient of the observation site are inversed according to the electric sounding curve, where **(A)** is in NS direction and **(B)** is in EW direction. B1 is the first coefficient, and so on.

TABLE 2 **Observed values and quantitative calculated values before and after water pumping in 2018.**

Measuring direction	Observed value before pumping (m)	Observed value after pumping (m)	Calculated value before pumping (m)	Calculated value after pumping (m)	Observed value change rate (%)	Calculated value change rate (%)
NS	31.78Ω	31.56Ω	31.82Ω	31.59Ω	0.692	0.723

calculated values match the observed values and the magnitude of change, which indicates that the anomalous variation in the apparent resistivity observation at the Hefei station in 2018 was caused by water pumping, rather than anisotropic variation. Future efforts can utilize finite element quantitative calculations to refine estimates of impact magnitude more precisely.

Following the pumping of the reservoir, the water level gradually recovered through natural replenishment, including rainfall. As air within the reservoir was replaced by water, the resistivity of the reservoir decreased. Considering the negative characteristics of the three-dimensional influence coefficients, the observed apparent resistivity should have continued to increase, consistent with actual

observations. Hence, the apparent resistivity anomalies observed at Hefei Station are attributed to environmental changes rather than anisotropy.

5 Discussion and conclusion

5.1 Discussion

Since 1966, China has been using apparent resistivity observations to forecast strong aftershocks of the Xingtai earthquake. This was followed by the *Ms*7.8 Tangshan earthquake in 1976, the *Ms*7.2 Songpan-Pingwu earthquake in 1976, and the *Ms*7.6 Lancang-Gengma earthquake in 1988. Before these earthquakes, significant anomalies in apparent resistivity were recorded, and retrospective studies have shown that these anomalies typically exhibit anisotropic characteristics before earthquakes. Before the occurrence of major earthquakes, anisotropic changes in apparent resistivity are observed at stations near the epicenter, which is consistent with experimental results (Zhao et al., 1995; Qian et al., 1996; Du et al., 2007) and has been confirmed by many earthquake cases. For example, before the *Ms*8.0 Wenchuan earthquake in 2008, it was known that the Chengdu and Jiangyou stations were about 35 Km and 30 Km away from the main rupture zone, respectively. According to the existing segmentation source mechanism solution of the main shock, the main compressive stress direction near the Chengdu station is N51°W, and near the Jiangyou station is N5°W (Zhang et al., 2009). The observation direction of the Chengdu station at N58°E forms an angle of 71° with the main compressive stress axis, with the maximum decrease before the earthquake being about 7%; the observation direction at N49°W is nearly parallel to the main compressive stress axis, and no decrease was observed before the earthquake. The observation direction of the Jiangyou station at N70°W forms an angle of 65° with the main compressive stress axis, with a decrease of about 1.5% before the earthquake, while the observation direction at N10°E is roughly parallel to the main compressive stress axis, showing no significant anomalous decrease before the earthquake (Lu et al., 2016; Xie et al., 2018).

At the same time, interferences encountered in apparent resistivity observations may also exhibit anisotropic changes. Since both interferences and pre-seismic stress changes can cause anomalous data changes, it is essential to first exclude interferences when data anomalies occur. Common interferences include metal pipelines within the measurement area, subway operation interference, and rainfall interference, among which rainfall interference affects the entire observation area and usually does not produce anisotropic changes. However, subway operation interference and metal pipeline interference within the measurement area can usually cause anisotropic changes in apparent resistivity observations.

This article analyzes the anisotropic anomalies in the apparent resistivity observations at the Hefei seismic station from October to December 2018 and establishes steps for analyzing anisotropic anomalies before earthquakes. First, determine the type and magnitude of the anomaly, then investigate existing sources of interference, and finally, conduct qualitative analysis and quantitative calculation. Through the above steps of model construction, interference can be excluded, thereby establishing a method for analyzing anisotropy in apparent resistivity before earthquakes. If the values are still anomalous after quantitative calculation to remove the effects of interference, it can be determined as anisotropic changes before the earthquake. The above analysis method still has guiding significance for anisotropic analysis of apparent resistivity at other stations.

For example, the Xingji seismic station in Hebei Province is located in the central-eastern part of Hebei Province, with two ground apparent resistivity measurement items of N30°E and N60°W, with a power supply electrode distance of 2 km and a measuring electrode distance of 0.5 km. There is a reservoir between the B electrode and the N electrode of the N60°W direction, which rises with the increase of rainfall in summer and falls in winter (Figure 7A). The precipitation in the area where the station is located is consistent over the years, and the seasonal change of the water level of the reservoir is also consistent. According to the influence coefficient analysis, the rise of the water level of the reservoir will cause an increase in the N60°W observation, so the seasonal change of the water level of the reservoir is an important influencing factor for the "high in summer and low in winter" trend of the N60°W observation (Figure 7C).

In March 2022, the apparent resistivity observation of the N60°W direction at the Xingji seismic station showed a high-value change, breaking through the theoretical trend, while the observation of the N30°E direction was not significantly changed, forming anisotropic changes in the two directions (Figures 7B, C). After the data change, the observation system was checked for no faults. During the patrol of the observation environment, it was found that a steel structure factory building was newly built between the B electrode and the N electrode of the N60°W direction during this period. According to the models and methods in the text, the factory building is located in the area where the influence coefficient of the N60°W direction is negative and the influence coefficient of the N30°E direction is positive. Since the newly built factory building is closer to the N60°W direction, it has a greater impact on this direction, showing a significant increase in the N60°W observation while the N30°E observation remains basically unchanged. By calculating with the finite element method, the newly built steel structure factory building can cause the N60°W observation to rise by 0.07 Ω.m, so this anomaly is caused by the newly built factory building, not a pre-seismic anomaly. After the completion of the steel structure factory building, it has always existed, so the overall data of the N60°W direction is 0.07 Ω.m higher than before the construction of the factory building, and it will not return to the level before the construction of the factory building.

Currently, in addition to China conducting large-scale apparent resistivity observations, other countries that use apparent resistivity observations for earthquake prediction include the United States, Japan, Greece, and so on. However, international research on apparent resistivity anisotropy mostly focuses on the mechanisms by which anisotropy is generated (Sævik et al., 2014; Thongyoy et al., 2023). China has rich experience and successful cases in using apparent resistivity anisotropy for earthquake prediction (Du, 2010; Xu et al., 2014). At the same time, environmental interference such as subway operations near the observation area, metal pipeline networks, and water level changes are universally present in practice, and traditional one-dimensional influence coefficient analysis can no longer meet the needs. Thus,

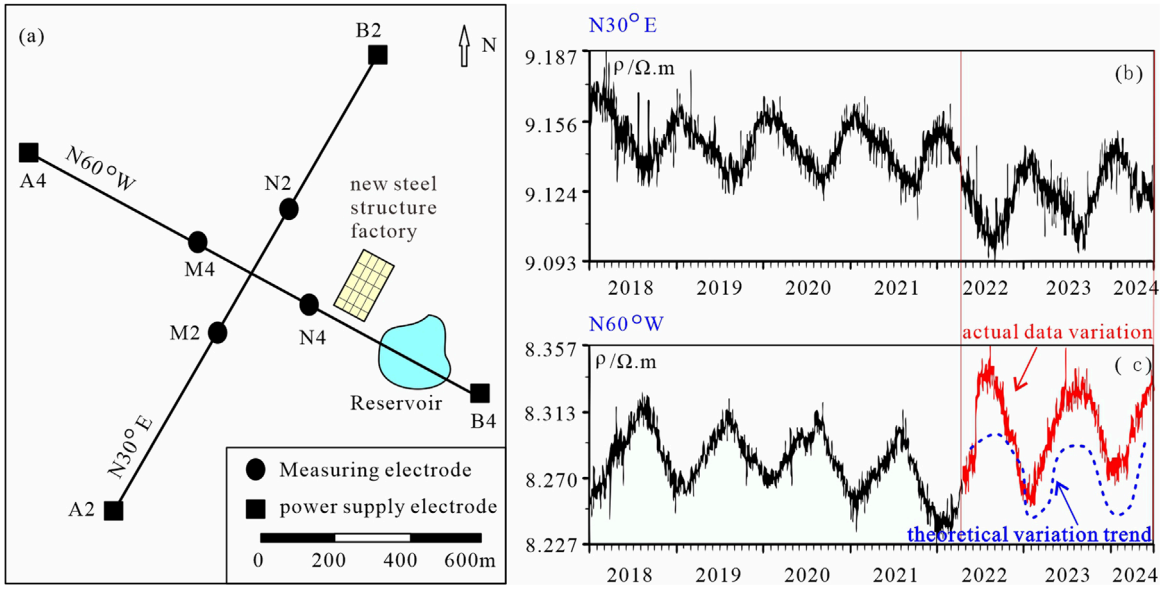

FIGURE 7
Apparent resistivity site conditions and historical data curves of Xingji seismic station from January 2018 to April 2024. **(A)** The layout of the external circuit site, the location of the reservoir, and the factory building. **(B,C)** illustrate the data variation trends for the N30°E and N60°W directions, respectively. The red curves represent the actual data variation, while the blue curves represent the theoretical variation trend.

this study provides a reference for professionals in other regions internationally to use changes in apparent resistivity anisotropy for earthquake prediction. When using anisotropic apparent resistivity observation for forecasting work, it is important to identify the types of interference mentioned in the text and quantitatively remove interference factors. Additionally, it is recommended that when building apparent resistivity stations in seismic areas for earthquake prediction, efforts should be made to avoid areas with large local influence coefficients to ensure that pre-seismic anomaly data is truly reliable.

5.2 Conclusion

Based on the review of the theoretical development and application of apparent resistivity anisotropy, taking the observation of the Hefei seismic station in Anhui Province as an example, a model is constructed using the finite element method to establish a method for determining the pre-seismic apparent resistivity anisotropy. The observation from the Xingji Seismic Station in Hebei Province is used for verification, and the study concludes the following:

(1) Anomalous changes in anisotropic apparent resistivity observations do not necessarily indicate the occurrence of an earthquake; they could also be caused by interference within the observation site, including subway operations, reservoirs, metal pipelines, etc. Therefore, after an anomaly occurs, it is necessary to first investigate these sources of interference.

(2) Through calculation and analysis using the finite element method, on the two-dimensional surface plane of the apparent resistivity observation site, most areas have a positive influence coefficient. However, there are two roughly elliptical areas with a negative influence coefficient between the measuring and power supply electrodes. In three-dimensional space, there is a continuous area between the power supply and measuring electrodes that corresponds to the negative influence coefficient area on the surface. The distribution of the influence coefficient shows obvious symmetry, with the axis of symmetry being the midline of the electrode connection line, and the influence coefficient (in absolute value) is inversely proportional to the distance from the electrodes.

(3) Using the method in this paper, the water level changes in the reservoir within the observation area of the Hefei seismic station in Anhui Province can cause about 0.7% change in the NS direction observation, and the construction of the steel structure factory building in the direction of N60°W at the Xingji seismic station can cause a change of 0.07 Ω.m in the apparent resistivity observation. If the anomaly exceeds this amplitude, it should be considered as a pre-seismic anisotropic anomaly for earthquake prediction.

(4) This study can provide a reference for forecasters in other seismically active regions to quantitatively remove environmental interference factors in anisotropic anomalies. After an anomaly occurs, first investigate instrument faults, external line faults, environmental interference, and other aspects to identify the source of interference, and then quantitatively calculate the data change caused by the interference source to determine whether the data anomaly is entirely caused by interference. It is also recommended that when building apparent resistivity stations in seismic areas for earthquake prediction, efforts should be made to avoid areas with large local influence coefficients to ensure that pre-seismic anomaly data is truly reliable.

Data availability statement

The original contributions presented in the study are included in the article/supplementary material, further inquiries can be directed to the corresponding author.

Author contributions

YL: Writing–original draft, Writing–review and editing. LJ: Writing–review and editing. CJ: Conceptualization, Writing–original draft. HD: Conceptualization, Writing–review and editing. CM: Data curation, Writing–original draft. JW: Data curation, Writing–original draft. MW: Conceptualization, Writing–review and editing.

Funding

The author(s) declare that financial support was received for the research, authorship, and/or publication of this article. China-Asean Earthquake Disaster Monitoring and Defense Capability Improvement Project (No. 123999101), third batch of Fengyun-3 meteorological satellite projects (No. FY-3(03)-AS-11.10-ZT) Anhui Provincial Key Research and Development Project (2022m07020002, 2022m07020005), Spark Program of Earthquake Sciences (XH23021YB), Three combined Project (3JH-202402004), The Seismic Pattern and Impact of the Tan-Lu Fault Zone in the Feidong-Lujiang section research project.

Conflict of interest

Author JW was employed by Geovis Environment Technology Co., Ltd.

The remaining authors declare that the research was conducted in the absence of any commercial or financial relationships that could be construed as a potential conflict of interest.

Publisher's note

References

Bachrach, R. (2011). Elastic and resistivity anisotropy of shale during compaction and diagenesis: joint effective medium modeling and field observations. *Geophysics* 76 (6), E175–E186. doi:10.1190/geo2010-0381.1

Coggon, J. H. (1971). Electromagnetic and electrical modeling by the finite element method. *Geophysics* 36, 132–155. doi:10.1190/1.1440151

Crampin, S., Evan, R., and Atkins, B. K. (1984). Earthquake prediction: a new physical basis. *Geophys. J. R. Astronomical Soc.* 76, 147–156. doi:10.1111/j.1365-246x.1984.tb05016.x

Dey, A., and Morrison, H. F. (1979). Resistivity modeling for arbitrarily shaped three-dimensional structures. *Geophysics* 44 (4), 753–780. doi:10.1190/1.1440975

Du, X.-b. (2010). Two types of changes in apparent resistivity in earthquake prediction. *Sci. China* 40 (10), 1321–1330.

Du, X.-b., Li, N., Ye, Q., Ma, Z.-h., and Yan, R. (2007). A possible reason for the anisotropic changes in apparent resistivity near the focal region of strong earthquake. *Chin. J. Geophys.* 50 (6), 1802–1810. doi:10.3321/j.issn:0001-5733.2007.06.021

Du, X.-b., Sun, J.-s., and Chen, J.-y. (2017). Data processing method of Earth resistivity in earthquake prediction. *Acta Seismo Sin.* 39 (4), 531–548. doi:10.11939/jass.2017.04.008

Ellis, M. H., Sinha, M. C., Minshull, T. A., Sothcott, J., and Best, A. I. (2010). An anisotropic model for the electrical resistivity of two-phase geologic materials. *Geophysics* 75 (6), E161–E170. doi:10.1190/1.3483875

Kemeny, J. M. (1991). A model for non-linear rock deformation under compression due to sub-critical crack growth. *Int. J. Rock Mech. Min. Sci. Geomech. Abstr.* 28 (6), 459–467. doi:10.1016/0148-9062(91)91121-7

Kenneth, L. C., and Russell, L. G. (1961). Theoretical horizontal resistivity profiles over hemispherical sinks. *Geophysics* 9 (3), 342–354. doi:10.1190/1.1438877

Kraev, A. (1954). in *Geoelectrical principles*, Z. Ke-qian, C. Pei-guang, and Z. Zhi-cheng (Beijing: Geological Publishing House).

Li, J.-M. (2005). *Geoelectric field and electrical prospecting*. Beijing: Geology Press, 174–187.

Li, Y. G., and Spitzer, K. (2005). Finite element resistivity modelling for three-dimensional structures with arbitrary anisotropy. *Phys. Earth Planet. Interiors* 150, 15–27. doi:10.1016/j.pepi.2004.08.014

Lu, J., Qian, F.-y., and Zhao, Y.-l. (1999). Sensitivity analysis of the Schlumberger monitoring array: application to changes of resistivity prior to the 1976 earthquake in Tangshan, China. *Tectonophysics* 307 (3-4), 397–405. doi:10.1016/s0040-1951(99)00101-8

Lu, J., Xie, T., Li, M., Wang, Y., Ren, Y., Gao, S., et al. (2016). Monitoring shallow resistivity changes prior to the 12 May 2008 *M*8.0 Wenchuan earthquake on the Longmen Shan tectonic zone, China. *Tectonophysics* 675, 244–257. doi:10.1016/j.tecto.2016.03.006

Lu, J., Xue, S.-z., Qian, F.-y., Zhao, Y., Guan, H., Mao, X., et al. (2004). Unexpected changes in resistivity monitoring for earthquakes of the Longmen Shan in Sichuan, China, with a fixed Schlumberger sounding array. *Phys. Earth Planet. Interiors* 145 (1-4), 87–97. doi:10.1016/j.pepi.2004.02.009

Ni, H.-y., Zheng, H.-g., Zhao, N., Deng, B., Miao, P., Huang, X.-l., et al. (2022). Application of ambient noise tomography with a dense linear array in prospecting active faults in the Mingguang city. *Chin. J. Geophys.* 65 (7), 2518–2531. doi:10.6038/cjg2022P0947

North, L. J., and Best, A. I. (2014). Anomalous electrical resistivity anisotropy in clean reservoir sandstones. *Geophys. Prospect.* 62 (6), 1315–1326. doi:10.1111/1365-2478.12183

O'Neill, D. J., and Merrick, N. P. (1984). A digital linear filter for resistivity sounding with a generalized electrode array. *Geophys Prospect* 32 (1), 105–123. doi:10.1111/j.1365-2478.1984.tb00720.x

Park, S. K., and Van, G. P. (1991). Inversion of pole-pole data for 3-D resistivity structure beneath arrays of electrodes. *Geophysics* 56 (7), 951–960. doi:10.1190/1.1443128

Qian, F.-y., Zhao, Y.-l., and Huang, Y.-n. (1996). Georesistivity anisotropy parameters calculation method and earthquake precursor example. *Acta Seismol. Sin.* 18 (4), 480–488.

Qian, J.-d., Chen, Y.-f., and Jin, A.-z. (1985). *Application of Earth resistivity method in earthquake prediction*. Beijing: Seismological Press.

Qian, J.-d., Ma, Q.-z., and Li, S. (2013). Further study on the anomalies in apparent resistivity in the NE configuration at Chengdu station associated with Wenchuan M_S8.0 earthquake. *Acta Seismol. Sin.* 35 (1), 4–17. doi:10.3969/j.issn.0253-3782.2013.01.002

Sævik, P. N., Jakobsen, M., Lien, M., and Berre, I. (2014). Anisotropic effective conductivity in fractured rocks by explicit effective medium methods. *Geophys. Prospect.* 62 (6), 1297–1314. doi:10.1111/1365-2478.12173

Thongyoy, W., Siripunvaraporn, W., Rung-Arunwan, T., and Amatyakul, P. (2023). The influence of anisotropic electrical resistivity on surface magnetotelluric responses

and the design of two new anisotropic inversions. *Earth, Planets Space* 75 (1), 12. doi:10.1186/s40623-023-01763-1

Xie, T., Liu, J., Lu, J., Li, M., Yao, L., Wang, Y.-l., et al. (2018). Retrospective analysis on electromagnetic anomalies observed by ground fixed station before the 2008 Wenchuan *M*s8.0 earthquake. *Chin. J. Geophys.* 61 (5), 1922–1937. doi:10.6038/cjg2018M0147

Xie, T., and Lu, J. (2015). Three-dimensional influence coefficient of Earth resistivity and its application. *Seismol. Geol.* 37 (4), 1125–1135. doi:10.3969/j.issn.0253-4967.2015.04.015

Xie, T., and Lu, J. (2020a). Apparent resistivity anisotropic variations in cracked medium. *Chin. J. Geophys* 63 (4), 1675–1694.

Xie, T., Wang, H.-q., Liu, L.-b., and Lu, J. (2014). Inverse annual variations of apparent resistivity at Siping earthquake station by using finite method. *Prog. Geophys.* 29 (2), 588–594. doi:10.6038/pg20140215

Xie, T., Ye, Q., and Lu, J. (2020b). Electrical resistivity of three-phase cracked rock soil medium and its anisotropic changes caused by crack changes. *Geomat. Nat. Haz. Risk* 11 (1), 1599–1618. doi:10.1080/19475705.2020.1801527

Xu, X.-q., Gao, C.-z., and Wang, L. (2014). Study on long-term observation data of Earth resistivity at baochang station, inner Mongolia. *J. Earthq. Eng.* 36 (2), 405–412. doi:10.3969/j.issn.1000-0844.2014.02.0405

Yao, W.-b. (1989). *Introduction to numerical computation and interpretation of electrical sounding*. Beijing: Seismological Press, 85–94.

Zhang, X.-m., Li, M., and Guan, H.-p. (2009). Analysis of Earth resistivity anomalies before the wenchuan county *M*8.0 earthquake. *Earthquake* 29 (1), 108–115. doi:10.3969/j.issn.1000-3274.2009.01.014

Zhang, Y., Xu, L.-s., and Chen, Y.-t. (2009). Spatio-temporal variation of the source mechanism of the 2008 great Wenchuan earthquake. *Chin. J. Geophys.* 52 (2), 379–389.

Zhao, Y.-l., Li, Z.-n., and Qian, F.-y. (1995). Comprehensive criteria for the transition from the middle-term to the short-term and impending anomalies of geoelectric precursors. *Earthquake* 4, 308–314.

Zhao, Y.-l., Qian, F.-y., Yang, X.-c., and Liu, J.-y. (1983). Experiments *in situ* of electrical resistivity changes. *Acta Seismo Sin.* 5 (2), 217–225.

frontiers | Frontiers in Earth Science

TYPE Original Research
PUBLISHED 18 September 2024
DOI 10.3389/feart.2024.1439493

OPEN ACCESS

EDITED BY
Giovanni Martinelli,
National Institute of Geophysics and Volcanology, Section of Palermo, Italy

REVIEWED BY
Jia Cheng,
China University of Geosciences, China
Xiaocheng Zhou,
China Earthquake Administration, China
Mita Uthaman,
Indian Institute of Technology Kharagpur, India
Arnab Roy,
University of Idaho, United States

*CORRESPONDENCE
Junshan Xu,
junshanxu@ninhm.ac.cn
Xiangfang Zeng,
zengxf@whigg.ac.cn

RECEIVED 28 May 2024
ACCEPTED 03 September 2024
PUBLISHED 18 September 2024

CITATION
Xu J and Zeng X (2024) Stress modeling for the upper and lower crust along the Anninghe, Xianshuihe, and Longmenshan Faults in southeastern Tibetan plateau. *Front. Earth Sci.* 12:1439493. doi: 10.3389/feart.2024.1439493

Stress modeling for the upper and lower crust along the Anninghe, Xianshuihe, and Longmenshan Faults in southeastern Tibetan plateau

Junshan Xu[1]* and Xiangfang Zeng[2]*

[1]Key Laboratory of Crustal Dynamics, National Institute of Natural Hazards, Ministry of Emergency Management of China, Beijing, China, [2]State Key Laboratory of Geodesy and Earth's Dynamics, Innovation Academy for Precision Measurement Science and Technology, Chinese Academy of Sciences, Wuhan, China

Earthquake occurrence depth in the crust is related to stress, temperature, and brittle–ductile transition, which is also near the transition depth of the upper to lower crust. The composition variation between the upper and lower crust causes remarkable changes of rheological properties and variation in stress distribution. Clarifying the detailed stress distribution in the upper and lower crust is crucial for understanding the brittle–ductile transition and the stress environment of the seismogenic zone. The Southeastern Tibetan Plateau (SETP), with wide spread of active strike–slip faults and clustered earthquakes, provides a natural field for investigating the relationships between crustal stresses, deformation behaviors, and earthquake mechanics. By considering the rheological properties of granite and anorthite, this paper established stress models with different boundary depths (15, 20 and 25 km) between the upper and lower crust along the Anninghe, Xianshuihe, and Longmenshan Faults in the SETP with a horizontal strain of 6×10^{-4} extracted from *in situ* stress data. The stress model with different geothermal gradients and a boundary depth of 20 km between the upper and lower crust suggests two distinct types of the brittle–ductile transition below these three faults. Simultaneously, the stress model can account for the continuity of earthquake depth distribution below the Longmenshan Fault and the seismic gap below the Anninghe and Xianshuihe Faults. The continuity of earthquake depth distribution or seismic gap below these three faults can be explained by their different geothermal gradients. These findings provide new insights for understanding the stress environment of the seismogenic zone in the SETP. Our model reveals the relationships between differential stress, seismicity, brittle–ductile transition, and boundary depth of the upper and lower crust in the continental crust, and connects the multiple observations from geophysics and geology. Furthermore, our model provides insights for studying multiple processes in the continental crust, such as crustal deformation, fault slip, and earthquake occurring.

KEYWORDS

brittle-ductile transition, stress modeling, earthquake depth, Anninghe Fault, Xianshuihe Fault, Longmenshan Fault

1 Introduction

Brittle–ductile transition in the crust is related to not only the change of deformation behaviors due to temperature increase but also the variations of stress, seismicity, and even the transition from the upper to lower crust (Maggi et al., 2000; Jackson, 2002; Scholz, 2002; Bürgmann and Dresen, 2008). Usually, the boundary of the upper to lower crust (denoted as UL boundary hereinafter) corresponds to the compositional decrease in SiO_2 content from 67 wt% to less than 64 wt% (Rudnick and Gao, 2003; Hacker et al., 2015), which suggests the increase in feldspars and pyroxenes and the change of stress sustainability (Bürgmann and Dresen, 2008; Xu and Zeng, 2022) due to the substantially different rheological properties of rocks or minerals (Gleason and Tullis, 1995; Rybacki and Dresen, 2000; Chen et al., 2021; Fukuda et al., 2022; Masuti et al., 2023). Therefore, determining the UL boundary is crucial to understanding the stress distribution in the crust (related to brittle–ductile transition) and the stress environment of the seismogenic zone (related to earthquake depth). The southeastern Tibetan Plateau (SETP) is the eastward extrusion zone of the India–Asia collision, exhibiting strong tectonic movement and continuous crustal deformation (Li et al., 2019; Wang and Shen, 2020). Active strike–slip faults (such as the Xianshuihe, Anninghe, and Longmenshan Faults, Figure 1) with clustered earthquakes provide a natural field for investigating the relationships between crustal stress, brittle–ductile transition, and earthquake depth (Royden et al., 1997; Royden et al., 2008; Clark and Royden, 2000; An et al., 2001; Tapponnier et al., 2001; Meade, 2007; Huang et al., 2009; Zhang, 2008).

Detailed distribution of crustal stress at different depths can directly reflect the behaviors of the deformation and mechanics of the earthquake (Scholz, 2002); however, only the stress variation (stress drop) before and after the earthquake can be obtained by seismic methods. Stresses in the deep crust are mainly controlled by three aspects (Zang and Stephansson, 2010): (1) gravity, which causes vertical stress; (2) horizontal tectonic strain, which causes horizontal stress; (3) rheological deformation and fault friction strength, which diminish and constrain differential stress. Vertical stress is easy to obtain based on overburden rocks. Horizontal tectonic stress can mostly be acquired through analyzing and extrapolating *in situ* stress data measured at shallow depth because conducting stress measurement at depth larger than 1 km is extremely difficult. Until now, conducting stress measurements is nearly impossible at the depth (> 10 km) of the seismogenic zone where stress magnitude may be hundreds of megapascals (Hanks and Raleigh, 1980; Zang and Stephansson, 2010). The *in situ* stress data used in this study were only conducted within 1 km depth, and they are currently the deepest measurement data in the SETP. Directly extrapolating the measured stress at shallow depth into deep depth usually causes large errors because analyzing the stress data needs to exclude the effects from multiple factors such as topography and geologic structure (Brown and Hoek, 1978; Haimson, 1978; Zoback, 1992; Sheorey, 1994; Fairhurst, 2003; Sen and Sadagah, 2002; Zang and Stephansson, 2010; Heidbach et al., 2019). Hence, in this paper, a method was developed through extracting the horizontal strain from measured stress data to calculate the stress at deep depth. The elastic strain caused by horizontal deformation can be assumed constant in the whole elastic crust (Blanton and Olson, 1999). The present *in situ* stress data contain the information of the elastic strain in elastic crust because they are mainly due to the tectonic horizontal deformation. Therefore, the extracted horizontal elastic strain from *in situ* stress data at shallow depth can be used to calculate stresses at deep depth. Furthermore, the effects of rheological deformation on differential stress is controlled by rock rheological properties and temperature. The geothermal gradients for each fault and the UL boundary depth (related to rock composition variation) also need to be considered. Thus, all the stress components (such as horizontal stress, differential stress, and shear and normal stress in a fault plane) at different depths can be obtained. Stresses on fault and slip possibility of fault can also be discussed.

In this study, we analyzed *in situ* stress data measured in five boreholes in the SETP (Figure 1), extracted the corresponding tectonic strain based on the biaxial stress model (Savage et al., 1992), and calculated stresses for both the upper and lower crust along the strike of fault planes by considering the composition change between the upper and lower crust and the rheological properties of rocks. Results suggest that stress distribution for the upper and lower crust with a UL boundary depth of 20 km in the SETP and different geothermal gradients can account for the geophysical, geological, and laboratory observations (such as the earthquake depth distribution, velocity structures, electrical conductivity structures, geothermal gradient, SiO_2 content, and rock rheological properties).

2 Methods

2.1 Overview of methods

First, the maximum horizontal strain of tectonic deformation was extracted from *in situ* stress data. Second, based on the obtained horizontal strain, the horizontal, vertical, and differential stresses for the upper and lower crust were calculated by considering the constrains of rock rheological properties and geothermal gradients along three faults (Anninghe, Xianshuihe, and Longmenshan Faults). Third, the ratio of shear stress to normal stress, which is useful for analyzing the occurring of earthquake and slip, was obtained. Finally, the detailed distribution of differential stress and ratio of shear stress to normal stress along each fault at different depths in the upper and lower crust were determined.

2.2 Extraction of maximum horizontal strain ε_H

In this study, the stresses in the deep crust were calculated using a method based on the horizontal strain, which is extracted from the *in situ* stress data measured in boreholes. The relationship between horizontal strains and stresses was calculated using Equation 1 (Savage et al., 1992; Sheorey, 1994):

$$\begin{aligned} S_H &= \frac{E}{1-\nu^2}(\varepsilon_H + \nu\varepsilon_h) + \frac{\nu}{1-\nu}S_V \\ S_h &= \frac{E}{1-\nu^2}(\varepsilon_h + \nu\varepsilon_H) + \frac{\nu}{1-\nu}S_V \end{aligned} \quad (1)$$

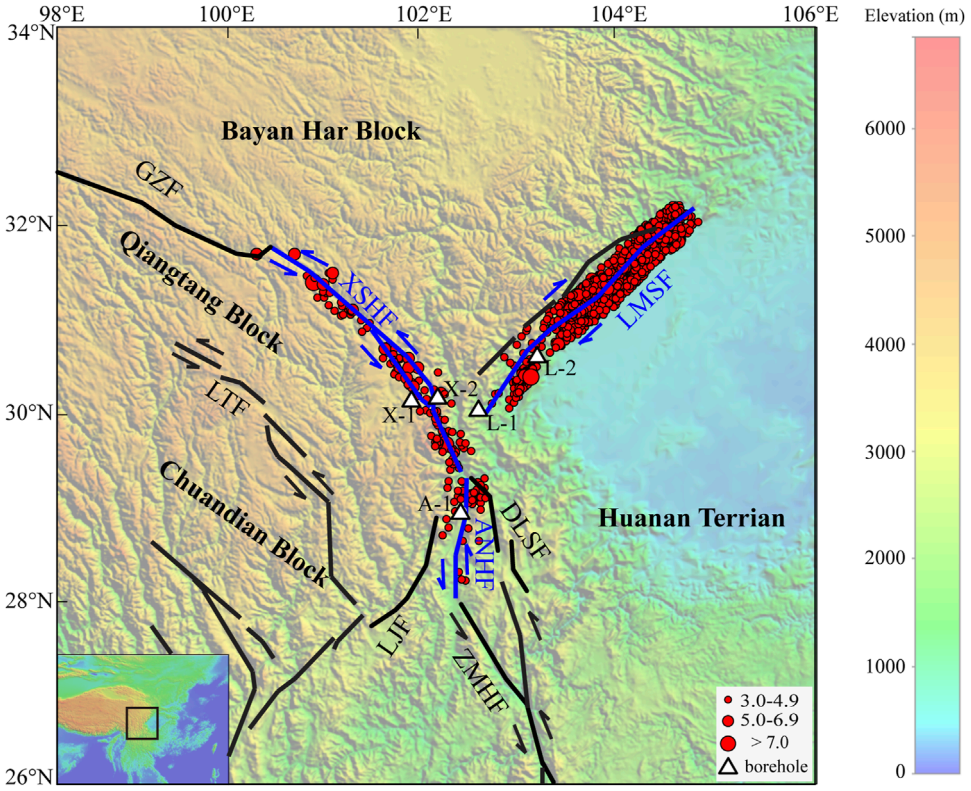

FIGURE 1
Tectonic map and borehole locations. Purple triangles indicate the locations of *in situ* stress measurement boreholes and purple characters are their names. The blue solid lines indicate the faults of Anninghe (ANHF), Xianshuihe (XSHF), and Longmenshan (LMSF). The black solid lines indicate the following faults: LTF, Litang Fault; GZF, Ganzi Fault; LJF, Lijiang Fault; DLSF, Dalianshan Fault; and ZMHF, Zemuhe Fault. Events with $Ms \geq 3.0$ within a distance of 20 km along ANHF, XSHF, and LMSF in the period 1971.1–2022.3 are used (also in the following figures), which are download from China National Seismic Data Center (https://data.earthquake.cn/gcywfl/index.html).

where S_H and S_h are the maximum and minimum horizontal stresses, respectively; ε_H and ε_h are the maximum and minimum horizontal strains, respectively; ν is the Poisson's ratio; E is the Young's modulus; and S_V is the vertical stress. Given that the SETP is located in the strong and continuous crustal deformation area of the India–Asia collision zone (Li et al., 2019; Wang and Shen, 2020), the relationship between ε_H and ε_h is supposed to obey a simple compressive form $\varepsilon_h = \nu\varepsilon_H$ and ε_H is supposed to be vertically uniform in the elastic crust (Blanton and Olson, 1999). Thus, the magnitude of horizontal stresses S_H and S_h can be calculated using Equation 2:

$$\begin{aligned} S_H &= \frac{1+\nu^2}{1-\nu^2}E\varepsilon_H + \frac{\nu}{1-\nu}S_V \\ S_h &= \frac{2\nu}{1-\nu^2}E\varepsilon_H + \frac{\nu}{1-\nu}S_V \end{aligned} \tag{2}$$

S_H and S_h values were obtained within a depth range of 300–1,400 m by hydraulic fracturing method from five boreholes located in the SETP as shown in Figure 1 (Ren et al., 2021; Li et al., 2022). All stress data were measured from granite, whose mechanical parameters (E and ν) usually exhibit a similar trend at the effective pressure range of 5–30 MPa (Nur and Simons, 1969; Blake et al., 2019). S_V can be estimated based on the lithostatic state with a density of 2.65 g/cm^3 (Ren et al., 2021). Therefore, ε_H can be calculated using Equation 2.

2.3 Calculation of horizontal stresses S_H and S_h and differential stress σ_D

From the extracted value of ε_H, the values of S_H and S_h in different depths were calculated using Equation 2. Then differential stress σ_D was calculated according to the difference between S_H–S_h in the shallow depth (S_H>S_V) and S_V–S_h in the deep part (S_V>S_H). Simultaneously, in the deep crust, σ_D is also constrained by the rock creep due to high temperatures, obeying the power law equation shown as Equation 3.

$$\frac{d\varepsilon_v}{dt} = A{\sigma_D}^n \exp\left(-\frac{Q}{RT}\right) \tag{3}$$

where $\frac{d\varepsilon_v}{dt}$ is the viscous strain rate, A is a constant, σ_D is the differential stress, n is the stress exponent, Q is the activation energy, R is the molar gas constant, and T is the absolute temperature. The temperatures at different depths were calculated based on the geothermal gradient obtained by Wang et al. (2018), in which they first estimated the Curie-point depths using the centroid spectral approach based on 3D fractal magnetization model (Tanaka et al., 1999; Li et al., 2017) and then calculated the crustal temperature structures using 1D steady thermal conduction equation. In accordance with previous studies (Wang and Shen, 2020; Sun et al., 2021), a strain rate of 1×10^{-14} s^{-1} was used as

the brittle–ductile transition boundary. Granite (we use the data of granitoid in Rutter et al. (2006), which is consistent with the composition of the upper crust, ~67% SiO_2 content) was taken as the composition of the upper crust, and 80% granite–20% anorthite (~64% SiO_2 content) was set for the lower crust to accommodate the compositional transition from the upper to the lower crust that corresponds to the decrease in SiO_2 content from 67 wt% to no more than 64 wt% due to the increase in feldspars and pyroxenes (e.g., Hacker et al., 2015). Three different depths of UL boundary, namely, 15, 20, and 25 km, were considered to analyze the stress distribution in the upper and lower crust. The rheological parameter of granite is as follows: A is $10^{-12.2}$ s^{-1}, n is 1.8, and Q is 220 *kJ/mol* (Rutter et al., 2006). For anorthite, A is $10^{-12.7}$ s^{-1}, n is 3.0, and Q is 648 *kJ/mol* (Rybacki and Dresen, 2000). For the composition of 80% granite–20% anorthite, A is $10^{-12.3}$ s^{-1}, n is 2.0, and Q is 289 *kJ/mol* according to the multiphase flow law shown as Equation 4 (Tullis et al., 1991; Ji and Zhao, 1993).

$$\begin{cases} n = 10^{(f_1 \log n_1 + f_2 \log n_2)} \\ Q = \dfrac{Q_2(n-n_1) - Q_1(n-n_2)}{n_2 - n_1} \\ A = 10^{[\log A_2(n-n_1) - \log A_2(n-n_2)]} \end{cases} \quad (4)$$

where f_1 = 0.8 and f_2 = 0.2 are the compositional ratios of granite and anorthite, respectively. Q_1, Q_2, n_1, n_2, A_1, and A_2 are the corresponding parameters of power law equations for granite and anorthite, respectively.

2.4 Calculation of the ratio of shear stress to normal stress (τ/σ_n)

According to the Coulomb–Mohr criterion ($\tau = \mu\sigma_n + cohn$, where τ is the shear stress, μ is the static friction coefficient, σ_n is the normal stress on the fault plane, and *cohn* is the cohesion), the τ/σ_n ratio can be roughly taken as the potential friction coefficient μ because the cohesive strength of a fault is relatively unimportant compared with the stress magnitude at deep depth (Zoback et al., 2003; Zang and Stephansson, 2010). Usually, the measured value of S_H is larger than that of S_V at very shallow depth, and S_V becomes larger than S_H with increasing depth (Sheorey, 1994; Yang et al., 2012). Therefore, with S_H, S_h, and S_V as the three principal stresses, they correspond to σ_1, σ_2, and σ_3 in the shallow depth, respectively, and σ_2, σ_3, and σ_1 in the deep part, respectively. The τ and σ_n on the fault plane were the calculated according to the angle of plane strike and dip. The strikes for the Anninghe, Xianshuihe, and Longmenshan Faults are 0°, 130°, and 45°, respectively (Xu et al., 2003). The dip angles for all of them were set to be 90°. The principal stress was set to be NW30° for the Anninghe Fault and E–W for the Xianshuihe and Longmenshan Faults according to the *in situ* stress measurement and focal mechanism results (Chen et al., 2012; Yang et al., 2021). For the part in the deep crust where the rheological deformation rate is higher than 10^{-14} s, τ/σ_n was set to be 1.0, indicating that the friction strength cannot sustain the value of τ and fault slip may occur. Pore pressure P_0, a critical parameter for slip in the actual crust, was also considered and set to be equal to the hydrostatic pressure (Hubbert and Rubey, 1959; Zoback and Townend, 2001).

3 Results

Figure 2 shows the results of calculated and measured maximum horizontal stresses S_H for the five boreholes. The obtained maximum horizontal strain ε_H for borehole A-1 (located in the Anninghe Fault area) is 3–6 × 10^{-4}; those for X-1 and X-2 (located in the Xianshuihe Fault area) are 4–6 × 10^{-4} and 6–6.5 × 10^{-4}, respectively, and those for L-1 and L-2 (located in the Longmenshan Fault area) are both 5–7 × 10^{-4}. Although the measured stress shows variation at the very shallow depth, the ε_H in the relatively deep (>900 m) part of these boreholes is close to 6 × 10^{-4} (Chen et al., 2012; Ren et al., 2021; Li et al., 2022). The minimal difference in ε_H among the different boreholes suggests that the accumulated strain in the SETP is similar. This finding demonstrates that horizontal strain is a suitable parameter to describe the magnitude of deformation caused by tectonic movement.

The distributions of calculated differential stress σ_D with different depths of UL boundary and focal depth along the Anninghe, Xianshuihe, and Longmenshan Faults are shown in Figure 3, Supplementary Figures S1, S2 (in Supplementary Materials). A low-stress layer can be generated at the bottom of granite layer for all of the three faults with a UL boundary depth of 25 km (Supplementary Figure S1, in Supplementary Materials) but not for all of them with a UL boundary depth of 15 km (Supplementary Figure S2, in Supplementary Materials). When the UL boundary depth is 20 km, a clear low-stress layer is generated below the Anninghe and Xianshuihe Faults, yet it is nearly absent beneath the Longmenshan Fault (Figure 3). The distribution of seismic events demonstrates inconsistency with the stress distribution predicted at a boundary depth of 25 km, where many earthquakes occur in the low-stress layer.

The distributions of τ/σ_n ratio along the three faults are shown in Figure 4 Supplementary Figures S3, S4 (in Supplementary Materials). τ/σ_n exhibits an increasing trend with the depth, and most earthquakes are located in a domain with τ/σ_n of 0.5–0.8 (Figure 4). This finding can be explained by Byerlee's law Byerlee (1978), which states that a slip condition occurs when the friction coefficient μ reaches a critical value of 0.6–0.85. The Byerlee's law describes the friction strength of rocks when brittle deformation is dominant at proper temperatures. The composition of 80% granite–20% anorthite has higher strength than pure granite, and exhibits brittle deformation at higher temperatures. Therefore, the Byerlee's law works in the layer of 80% granite–20% anorthite at a deep depth. In addition, the vertical statistical distributions of focal depth for the Anninghe and Xianshuihe Faults show a decrease at 16–20 km (seismic gap in Figure 5) and an increase below 20 km, especially for magnitude Ms≥4.0. No similar phenomenon is observed for the Longmenshan Fault (Figure 5). The numbers of earthquakes with magnitude Ms≥4.0 below all the three faults tend to zero at a depth larger than 22 km, which may be caused by the low differential stress or high ratio of τ/σ_n. These phenomena are analogous to the corresponding distribution of differential stress against depth for the results with a UL boundary depth of 20 km instead of 15 km. Thus, the decreased number of seismic events at 16–20 km depth below the Anninghe and Xianshuihe Faults can be explained by the low differential stress due to granite rheological behavior. The increased number at 20 km depth and the near

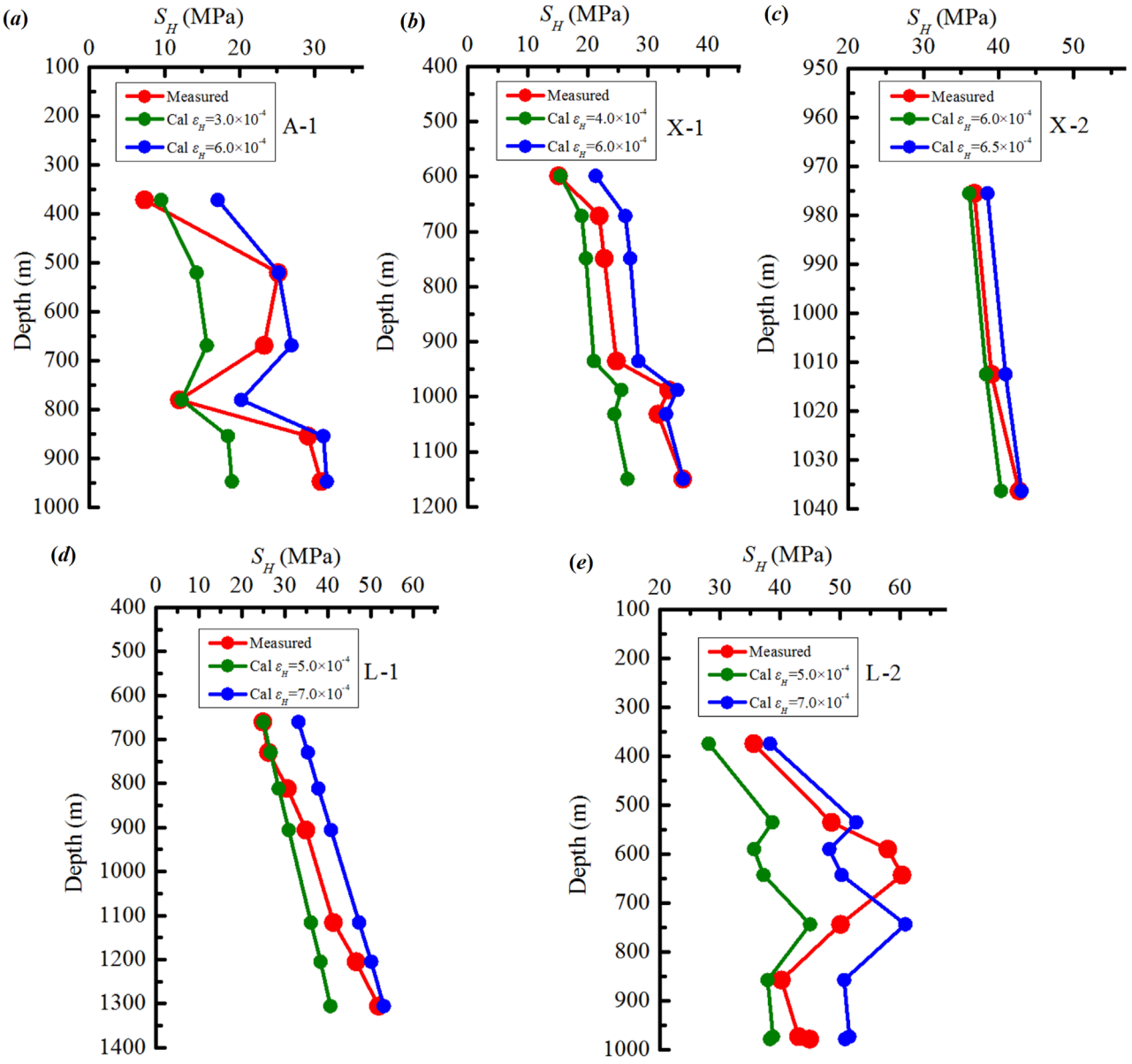

FIGURE 2
Measured and calculated data of the *in situ* stress of S_H. Measured and calculated data of S_H in boreholes A-1 **(A)**, X-1 **(B)**, X-2 **(C)**, L-1 **(D)**, and L-2 **(E)**. The measured stress data for borehole X-1, X-2 and L-1 are from Ren et al. (2021). Those for borehole L-2 and A-1 are from Li et al. (2022) and the present study, respectively.

disappearance at below 22 km are attributed to the existence of the layer of 80% granite–20% anorthite. The granite rheological layer below the Longmenshan Fault is not evident. This phenomenon is probably due to its relatively lower geothermal gradient (~17°C/km) than the Anninghe (~21°C/km) and Xianshuihe (~19°C/km) Faults, which are obtained by averaging the results of Wang et al. (2018) along these three faults. The relatively high geothermal gradient in the Anninghe and Xianshuihe Faults compared with that of the Longmenshan Fault is also demonstrated by observations of geothermal water (Tian et al., 2021). The geothermal gradient results in Wang et al. (2018) cannot exhibit local details because of low resolution but provide larger scale results within the SETP. The local measured geothermal gradients may differ from our data or change largely even along the same fault (e.g., Liu et al., 2017; Cheng et al., 2022; Ullah et al., 2022).

The decrease in differential stress below or above 20 km corresponds to the brittle–ductile transition. The depth of the brittle–ductile transition is similar to the depth of the UL boundary but is also influenced by the UL boundary because the anorthite in the lower crust increases the sustainability of differential stress. Therefore, the brittle–ductile transition can cause low seismicity due to dissipated differential stress, whereas the transition between the upper to lower crust may increase seismicity due to increased differential stress.

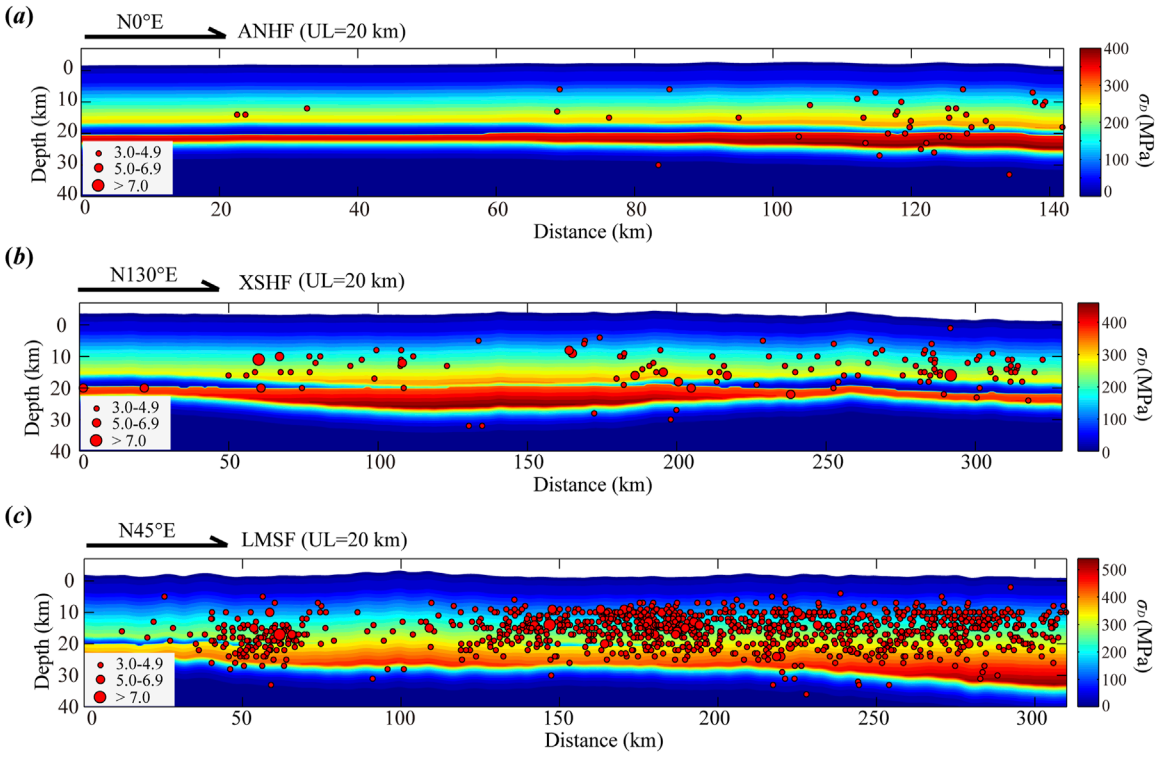

FIGURE 3
Distribution of differential stress (σ_D) and the focal depth along the faults with a UL boundary depth of 20 km (UL = 20 km). **(A)** Anninghe Fault (ANHF), **(B)** Xianshuihe Fault (XSHF), and **(C)** Longmenshan Fault (LMSF).

4 Discussion

4.1 UL boundary, brittle–ductile transition, and differential stress in the SETP

The consistency between our stress model and the vertical distribution of focal depth suggests that the depth of the UL boundary in the SETP is approximately 20 km (Figure 3). In particular, the low-stress layers at depth 16–20 km along the XSHF and ANHF have few seismic events. Most seismic events are located in high stress areas, which are below, above, and around these low-stress areas. In consideration of the 5 km average height of India–Asia collision, the 20 km depth of the upper crust is also comparable with the model of CRUST1.0, which shows a 26.2 km thickness of the upper crust for the India–Asia collision zone (Laske et al., 2013; Hacker et al., 2015). Our stress model in the deep part is essentially sensitive to geothermal gradient, which is extracted from the magnetic anomalies (Wang et al., 2018) and also verified by the measured results in boreholes LMS-2 (15°C/km, Li et al., 2022) and ANH (24°C/km, measured in this study). Errors of focal depths, which may reach to 5 km even after relocation (Liu et al., 2023), influence the judgment of UL boundary. Therefore, earthquakes $Ms < 3.0$ were excluded in this study. The low-stress layer in our model at a depth range of 16–20 km below the Anninghe and Xianshuihe Faults probably corresponds to low electrical conductivity as observed by magnetotelluric imaging (Zhao et al., 2008) and a decrease in velocity structures (Wang et al., 2007). At a depth below 16 km, the low strength of granite can be deformed easily, supporting the possible crustal channel flow suggested by the low electrical conductivity (Zhao et al., 2008; Wan et al., 2010) and tomography (Bao et al., 2015). The velocity structures below the Xianshuihe Fault show a decreased value from 6.10 km/s to 5.85 km/s at the depth of approximately 16 km but without a decrease below the Longmenshan Fault (Wang et al., 2007). The increase in velocity (from 5.85 km/s to 6.25 km/s) at a depth of approximately 20 km is probably caused by the increased content of pyroxenes or feldspars (e.g., anorthite in our model), which can sustain a larger differential stress under a relatively higher temperature than granite. Though constrained by the resolution, the velocity structures along the three faults (Supplementary Figures S5, S6, in Supplementary Materials) interpolated from the high-resolution community velocity model V2.0 of southwest China (Liu et al., 2023) also suggest that the low-velocity layers are identifiable below the Anninghe and Xianshuihe Faults but almost disappear below the Longmenshan Fault.

The low-stress layer in our model below the Anninghe Fault suggests a different type of brittle–ductile transition from that below the Longmenshan Fault, whereas both types partially exist below the Xianshuihe Fault. Figure 6 shows schematic plots of differential stress against depth. In Figure 6A, the brittle–ductile transition can be generated in the granite and 80% granite–20% anorthite layers (Type A: double-layer brittle–ductile transition), whereas in Figure 6B, it only appears in the 80% granite–20%

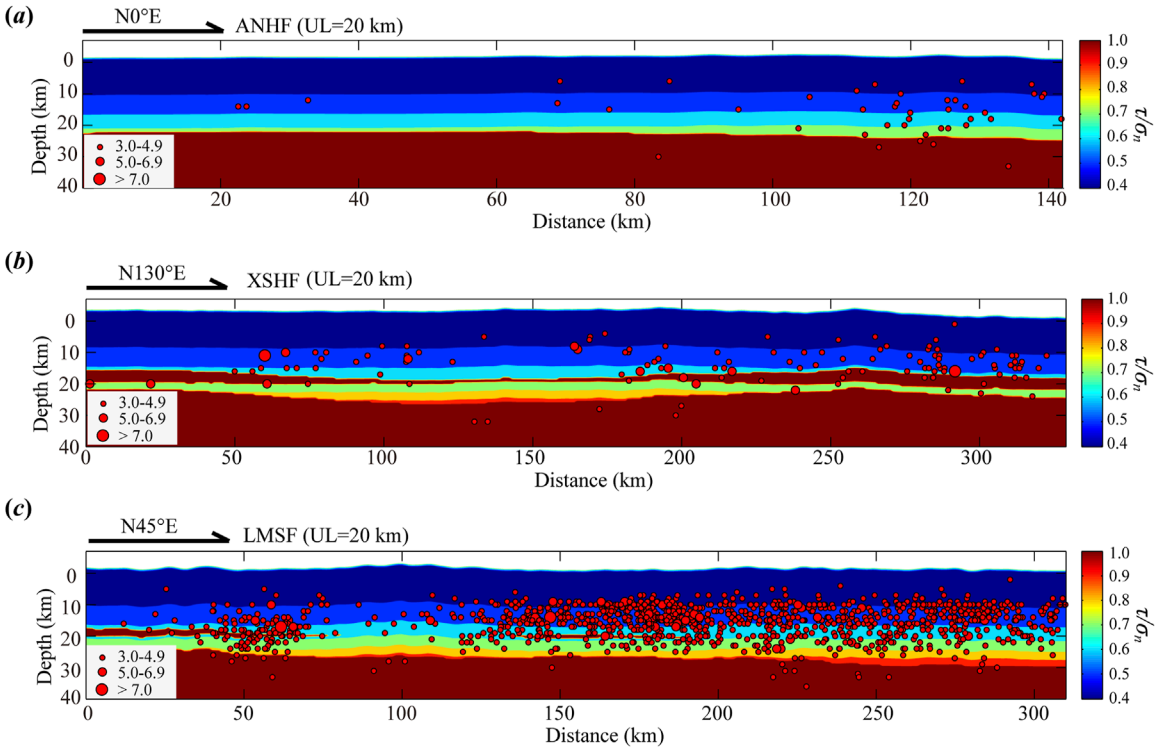

FIGURE 4
Distribution of the ratio between shear and normal stresses (τ/σ_n) and the focal depth along the faults with a UL boundary depth of 20 km (UL = 20 km). **(A)** Anninghe Fault (ANHF), **(B)** Xianshuihe Fault (XSHF), **(C)** Longmenshan Fault (LMSF).

anorthite layer (Type B: single-layer brittle–ductile transition). Here in the SETP as part of India–Asia collision zone, the crustal thickness of the crust is in a range of 55–60 km (Hu et al., 2011; Wang et al., 2017); therefore, the depth of the UL boundary can also influence the brittle–ductile transition. Comparing the stress results between Figure 3 and Supplementary Figure S1 reveals that if the depth of the UL boundary changes from 20 km to 15 km, the brittle–ductile transition below the Anninghe and Xianshuihe Faults can switch from Type A to Type B. The decrease in differential stress corresponds to the brittle–ductile transition and causes the decrease of seismicity (Figure 3). However, the seismicity decrease is not totally caused by the brittle–ductile transition in the deep crust because a high τ/σ_n ratio may facilitate fault slip (or free slip) without seismicity. This outcome is verified by comparing Figures 3, 4, where the locations with highest differential stress at around 25 km depth and high τ/σ_n ratio exhibit low seismicity. The brittle–ductile transition is essentially the reduction in differential stress, different from the transition between the upper and lower crust. The composition variations in the transition between upper and lower crust influence the differential stress, thereby the styles of brittle–ductile transition (Rudnick and Gao, 2003; Bürgmann and Dresen, 2008; Hacker et al., 2015). Furthermore, the brittle–ductile transition is complex because the experimental results of rock deformation suggest this transition is generally affected by deformation mechanism, water content, and even grain size of rocks (Zhou et al., 2017; Chen et al., 2021; Fukuda et al., 2022; Masuti et al., 2023).

Differential stress is a basis of the maximum shear stress and associated with the stress drop of earthquake (Aki and Richards, 1980). The stress values in our model shown in Figure 3 Supplementary Figures S1, S2 mainly exhibit a potential stress possibility, indicating the ability of rocks to withstand differential stress. The true values of stress is locally sensitive to many factors, such as the angle between fault strike and principal stress and pore pressure. The differential stress in the deep crust depends on the strength of rocks and the friction strength of faults, which is controlled by the intrinsic frictional strength of faulted rock and the pore pressure at different depths (Hubbert and Rubey, 1959). Therefore, the differential stress in the part with τ/σ_n ratio smaller than 0.6 (mainly in the upper crust) can be sustained with no slip occurring, exhibiting the elastic properties constrained by tectonic movement. The differential stress in the part with τ/σ_n ratio larger than 0.6 (mainly in the lower crust) suggests that the friction property plays an important role. The τ/σ_n ratio decreases with the increasing strain and is also affected by the angle between strike and maximum stress direction. If slip occurs, then the actual stress magnitude in the lower crust is no more than that of the upper crust. Whether pore pressure can develop in the lower crust remains controversial. Observations from deep boreholes at several locations worldwide indicate that hydrostatic pore pressures persist to depths as deep as 12 km in the upper crust (Zoback and Townend, 2001). The stress value in the lower crust with a composition of 80% granite–20% anorthite is consistent with that

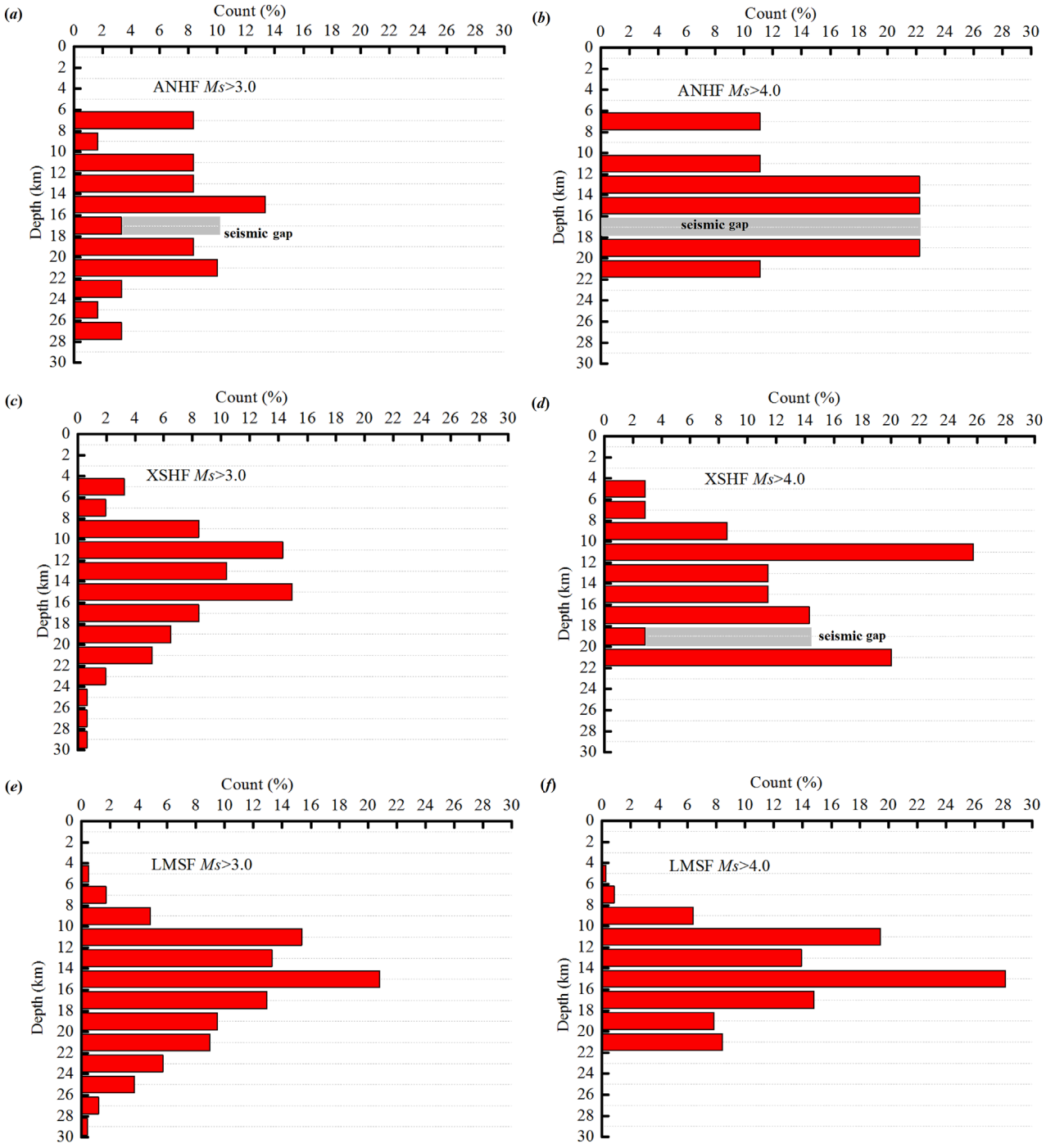

FIGURE 5
Statistical focal distribution against depth. Statistical focal distribution of seismic events in ANHF $M_S \geq 3.0$ **(A)** and $M_S \geq 4.0$ **(B)**, XSHF $M_S \geq 3.0$ **(C)** and $M_S \geq 4.0$ **(D)**, and LMSF $M_S \geq 3.0$ **(E)** and $M_S \geq 4.0$ **(F)**. The earthquake distribution against depth with an interval of 2 km along the three faults were analyzed and compared with the stress distribution. The events with $Ms \geq 3.0$ and $Ms \geq 4.0$ away from the fault plane within 20 km were used. All the events were from the period 1971.1–2022.3 and the China National Seismic Data Center with a website: https://data.earthquake.cn/gcywfl/index.html.

in the lower crust with SiO_2 content of no more than 64 wt% (Hacker et al., 2015). If the bottom of the lower crust has 53 wt% SiO_2 content (Hacker et al., 2015), then the corresponding group with composition of granite50%–anorthite50% sustains larger differential stress in deeper depths than that of 80% granite–20% anorthite. Different compositions in the lower crust may influence the stress magnitude according to the flow equations (Bürgmann and Dresen, 2008). The increase in feldspar and pyroxene promotes stress and strength in the lower crust, providing shear stress for seismogenic processes.

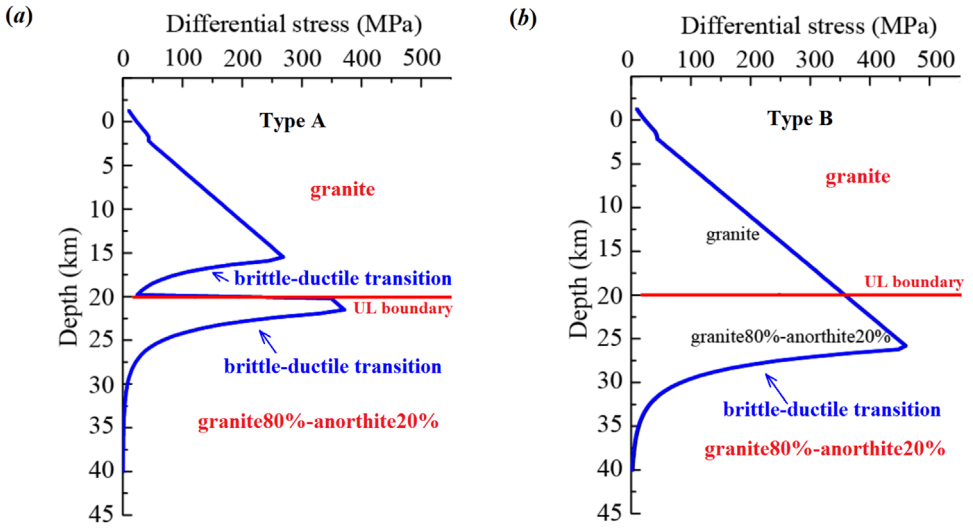

FIGURE 6
Schematic plots of differential stress against depth. **(A)** Typical curve of differential stress below the Anninghe Fault with a 20 km depth of the UL boundary. **(B)** Typical curve of differential stress below the Longmenshan Fault with a 20 km depth of the UL boundary.

It is pointed out that the calculation of differential stress constrained by rock creep is concentrated on in this study, and the plastic strength of faults and rocks was not considered. Actually, the areas with a high τ/σ_n ratio suggest the possible locations for plastic deformation caused by slip of faults or fracture of rocks, and the plastic deformation impacts the overall strength calculations through diminishing differential stress in a more transient way compared with rock creep. In addition, our model provides the stress estimation in the deep crust in accordance with the current absolute strain revealed by *in situ* stress data, and the variation in strain within a short term cannot be detected by the resolution of stress measurements. The calculated differential stress constrained by the strain rate of the rock creep equation reveals the upper limits of differential stress because the deviatoric strain rate was also not considered in this study.

4.2 Strain–stress accumulation and seismic activity

The maximum horizontal strain ε_H indicates the local accumulation of absolute strain caused by tectonic movement, providing the basic stress accumulation for seismogenic processes. Although the Anninghe and Xianshuihe Faults are a lateral strike slip fault and the Longmenshan Fault mainly shows compression shortening (Wang et al., 2008; Zhang, 2008), the similar strain magnitude for these three faults suggests that the local strain is in a relatively stable and balanced state in the SETP. The derived horizontal strain is assumed constant at different depth in the elastic crust in this study, and the values of strain are obtained based on stress data from 1 km depth borehole. It is still possible that the horizontal strain increases with depth. However, the increment may not be larger than 1×10^{-4} according to the nearly stable modulus of granite at higher pressures (deep depth). A high amount of accumulated strain generates large shear stress and the contribution of 1×10^{-4} strain to horizontal stress is estimated at 10 MPa (with a modulus of 100 GPa). Simultaneously, if the strain increase is caused by continuous deformation, considering a strain variation of 10^{-7} per year (Wang and Shen, 2020), the increase in strain by a magnitude of 1×10^{-4} requires approximately 1,000 years. Given the stress drop and earthquake recurrence interval, a strain of 1×10^{-4} is equivalent to the strain consumed by several earthquakes with magnitude larger than 5.0 (Allmann and Shearer, 2009; Li and Shibazaki, 2014). A similar seismic activity should be observed among these three faults according to the elastic storage energy. However, the seismicity of the Anninghe Fault is much lower than those of the other two faults. One of the reasons may be their different geothermal gradients that influence the mechanical behaviors in their deep parts. The high geothermal gradients in the Anninghe Fault (Wang et al., 2018) expands the low-stress layer in the upper crust near the UL boundary, exhibiting the easy condition for aseismic slip (Xu and Zeng, 2022). Hence, the Anninghe Fault is similar to a deformation channel by the slip of fault (Zhang, 2008), where low-stress layer exists from the upper crust, generating a decoupled upper and lower crust and leading to a low seismicity. In the Xianshuihe Fault, the low-stress layer in the upper crust is only partial distributed and stress can still accumulate in the upper and lower crust, resulting in relatively high seismicity. The low geothermal gradient in the Longmenshan Fault prevents the generation of low-stress layer in 16–18 km depth of the upper crust. Therefore, the strong upper and lower crust below the Longmenshan Fault makes it difficult for slip occurring and earthquakes with long recurrence interval and large magnitude generate easily. This finding is similar to the results of the strain rate from GPS inversion, that is, a dilatation state is observed in the west of the Anninghe Fault and a contraction state is recorded in the Longmenshan and Xianshuihe Faults (Wang and Shen, 2020). Furthermore, in the Anninghe Fault, a seismic gap appears at a depth around 8 km (Figure 5). However, determining whether it is seismic gap is difficult because of the small

number of seismic events, and the stress model cannot display this low-stress layer due to present data. Although the mechanism of seismogenesis is controlled by many other factors, the depth of the lower crust combined with the geothermal gradient plays a vital role in determining the stress distribution and understanding the mechanism of earthquake genesis. Finally, the present results mainly exhibit the overall stress differences between these three faults. The resolution of the geothermal gradients used in this study is at a scale of approximately 10 km. The details in some sections of these three faults may not display very well, especially for the southeast section of Xianshuihe Fault, which shows complexity of velocity, geothermal gradient, and stress environment (Li et al., 2015; 2023; Liu et al., 2023; 2017; Liang et al., 2023; Sun et al., 2023; Sun et al., 2021; Cheng et al., 2022; Zhu et al., 2024). More detailed works are needed in the future for stress investigation on the local sections of these three faults.

4.3 Implications in general continental crust

In this paper, our results are obtained in the area of the SETP, but they also provide insights for studying multiple processes (such as crustal deformation, fault slip, and earthquake occurrence) in the continental crust around the world. First, our model demonstrates a new method to investigate the detailed stress distribution in the continental crust. Our approach calculates the detailed stress distribution at different depths and explains multiple observations from geophysics, geology, and laboratory. Second, our results clearly demonstrate the relationships between differential stress, brittle–ductile transition, seismicity, and UL boundary. The decrease in differential stress corresponds to the brittle–ductile transition, which is caused by rheological deformation due to temperature. The brittle–ductile transition causes the decrease in seismicity. Though the brittle–ductile transition occurs near the UL boundary, they are caused by different mechanisms. The UL boundary cannot be determined by the decrease in seismicity. The increase in pyroxenes or feldspar at the UL boundary causes the increase in differential stress. Therefore, the brittle–ductile transition can cause low seismicity due to dissipation of differential stress, whereas the UL boundary may cause the increase in seismicity due to the increase in differential stress. Different areas show distinct characteristics in depth distribution of earthquakes (Maggi et al., 2000). Our findings can help further understand the stress environment of the seismogenic zone in the continental crust around the world, such as the North America (Mogistrale, 2002), the Central and East Asia (Sloan et al., 2011; Dong et al., 2018), and the East African (Albaric et al., 2009; Craig et al., 2011).

5 Conclusion

The crustal stress model with different depths (15, 20, and 25 km) of the UL boundary below the Anninghe, Xianshuihe, and Longmenshan Faults in the SETP are built based on *in situ* stress data and rock rheological properties. The results suggest that the 20 km depth of the UL boundary and the different geothermal gradients in the SETP can account for most geophysical and geological observations, such as composition, *in situ* stress, electric conductivity, and velocity structures. The differential stress distribution against depth reveals a different type of brittle–ductile transition (double-layer) below the Anninghe Fault from that (single-layer) below the Longmenshan Fault, whereas it shows both types below the Xianshuihe Fault, agreeing with their focal depth distributions. This observation can be explained by geothermal gradient differences among these three faults. The stress model provides new insights for understanding the stress environment of the seismogenic zone in the SETP. The relatively wider low-stress layer in the bottom of the upper crust easily dissipates the stress to prevent the generation of large earthquakes in the Anninghe Fault compared with that in the Xianshuihe Fault, whereas the low-stress layer only appears in the lower crust below the Longmenshan Fault, suggesting a special upper crust that facilitates stress accumulation. Our model further clarifies the relationships between differential stress, seismicity, brittle–ductile transition, and boundary depth of the upper and lower continental crust. By combining with geothermal gradients, the composition variation between the upper and lower crust can strongly cause the change of differential stress, thereby affecting the brittle–ductile transition and depth distribution of earthquakes. Furthermore, our results demonstrate that multiple observations from geophysics, geology, and laboratory can verify one another and provide a more detailed understanding for the environment of the seismogenic zone in the continental crust.

Data availability statement

The raw data supporting the conclusions of this article will be made available by the authors, without undue reservation.

Author contributions

JX: Data curation, Formal Analysis, Funding acquisition, Methodology, Writing–original draft, Writing–review and editing. XZ: Funding acquisition, Writing–original draft, Writing–review and editing.

Funding

The author(s) declare that financial support was received for the research, authorship, and/or publication of this article. This work was supported by the National Natural Science Foundation of China (Grant No. U2239203 and 41941016).

Acknowledgments

The authors would like to thank Dr. Jianxin Wang for part of *in-situ* stress data and Dr. Jian Wang for the geothermal data. This manuscript was much improved by thoughtful reviews of Prof. Valerio Acocella and four reviewers.

Conflict of interest

The authors declare that the research was conducted in the absence of any commercial or financial relationships that could be construed as a potential conflict of interest.

Publisher's note

All claims expressed in this article are solely those of the authors and do not necessarily represent those of their affiliated organizations, or those of the publisher, the editors and the reviewers. Any product that may be evaluated in this article, or claim that may be made by its manufacturer, is not guaranteed or endorsed by the publisher.

Supplementary material

The Supplementary Material for this article can be found online at: https://www.frontiersin.org/articles/10.3389/feart.2024.1439493/full#supplementary-material

References

Aki, K., and Richards, P. G. (1980). *Quantitative seismology-theory and methods*. San Francisco: W.H. Freeman and Company.

Albaric, J., Déverchère, J., Petit, C., Perrot, J., and Gall, B. L. (2009). Crustal rheology and depth distribution of earthquakes: insights from the central and southern East African Rift System. *Tectonophysics* 468, 28–41. doi:10.1016/j.tecto.2008.05.021

Allmann, B. P., and Shearer, P. M. (2009). Global variations of stress drop for moderate to large earthquakes. *J. Geophys. Res. Solid Earth* 114, B01310. doi:10.1029/2008JB005821

An, Z., Kutzbach, J. E., Prell, W. L., and Porter, S. C. (2001). Evolution of Asian monsoons and phased uplift of the Himalaya–Tibetan plateau since Late Miocene times. *Nature* 411, 62–66. doi:10.1038/35075035

Bao, X., Sun, X., Xu, M., Eaton, D. W., Song, X., Wang, L., et al. (2015). Two crustal low-velocity channels beneath SE Tibet revealed by joint inversion of Rayleigh wave dispersion and receiver functions. *Earth Planet. Sci. Lett.* 415, 16–24. doi:10.1016/j.epsl.2015.01.020

Blake, O. O., Faulkner, D. R., and Tatham, D. J. (2019). The role of fractures, effective pressure and loading on the difference between the static and dynamic Poisson's ratio and Young's modulus of Westerly granite. *Int. J. Rock Mech. Min. Sci.* 116, 87–98. doi:10.1016/j.ijrmms.2019.03.001

Blanton, T. L., and Olson, J. E. (1999). Stress magnitudes from logs: effects of tectonic strains and temperature. *SPE Reserv. Eval. and Eng.* 2, 62–68. doi:10.2118/54653-pa

Brown, E. T., and Hoek, E. (1978). Trends in relationships between measured *in-situ* stresses and depth. *Int. J. Rock Mech. Min. Sci. and Geomechanics Abstr.* 15, 211–215. doi:10.1016/0148-9062(78)91227-5

Bürgmann, R., and Dresen, G. (2008). Rheology of the lower crust and upper mantle: evidence from rock mechanics, geodesy, and field observations. *Annu. Rev. Earth Planet. Sci.* 36, 531–567. doi:10.1146/annurev.earth.36.031207.124326

Byerlee, J. (1978). Friction of rocks. *Pure Appl. Geophys.* 116, 615–626. doi:10.1007/BF00876528

Chen, J., Jin, Z., Liu, W., Wang, Y., and Zhang, J. (2021). Rheology of dry K-feldspar aggregates at high temperature and high pressure: an experimental study. *Tectonophysics* 817, 229072. doi:10.1016/j.tecto.2021.229072

Chen, Q., Feng, C., Meng, W., Qin, X., and An, Q. (2012). Analysis of *in situ* stress measurements at the northeastern section of the Longmenshan fault zone after the 5.12 Wenchuan earthquake. *Chin. J. Geophys. Chin. Ed.* 55, 3923–3932. doi:10.6038/j.issn.0001-5733.2012.12.005

Cheng, Y., Pang, Z., Kong, Y., Chen, X., and Wang, J. (2022). Imaging the heat source of the kangding high-temperature geothermal system on the Xianshuihe fault by magnetotelluric survey. *Geotermics* 102, 102386. doi:10.1016/j.geothermics.2022.102386

Clark, M. K., and Royden, L. H. (2000). Topographic ooze: building the eastern margin of Tibet by lower crustal flow. *Geology* 28, 703–706. doi:10.1130/0091-7613(2000)028<0703:tobtem>2.3.co;2

Craig, T. J., Jackson, J. A., Priestley, K., and McKenzie, D. (2011). Earthquake distribution patterns in Africa: their relationship to variations in lithospheric and geological structure, and their rheological implications. *Geophys. J. Int.* 185, 403–434. doi:10.1111/j.1365-246X.2011.04950.x

Dong, Y., Ni, S., Yuen, D. A., and Li, Z. (2018). Crustal rheology from focal depths in the North China Basin. *Earth Planet. Sci. Lett.* 497, 123–138. doi:10.1016/j.epsl.2018.06.018

Fairhurst, C. (2003). Stress estimation in rock: a brief history and review. *Intern. J. Rock Mech. Min. Sci.* 40, 957–973. doi:10.1016/j.ijrmms.2003.07.002

Fukuda, J., Muto, J., Koizumi, S., Sawa, S., and Nagahama, H. (2022). Enhancement of ductile deformation in polycrystalline anorthite due to the addition of water. *J. Struct. Geol.* 156, 104547. doi:10.1016/j.jsg.2022.104547

Gleason, G. C., and Tullis, J. (1995). A flow law for dislocation creep of quartz aggregates determined with the molten salt cell. *Tectonophysics.* 247, 1–23. doi:10.1016/0040-1951(95)00011-B

Hacker, B. R., Kelemen, P. B., and Behn, M. D. (2015). Continental lower crust. *Annu. Rev. Earth Planet. Sci.* 43, 167–205. doi:10.1146/annurev-earth-050212-124117

Haimson, B. C. (1978). The hydrofracturing stress measuring method and recent field results. *Int. J. Rock Mech. Min. Sci. and Geomechanics Abstr.* 15, 167–178. doi:10.1016/0148-9062(78)91223-8

Hanks, T. C., and Raleigh, C. B. (1980). The conference on magnitude of deviatoric stresses in the Earth's crust and uppermost mantle. *J. Geophys. Res. Solid Earth* 85, 6083–6085. doi:10.1029/JB085iB11p06083

Heidbach, O., Rajabi, M., Reiter, K., and Ziegler, M. (2019). "World stress map," in *In Encyclopedia of petroleum geoscience* (Germany: Springer), 1–8.

Hu, J., Xu, X., Yang, H., Wen, L., and Li, G. (2011). S receiver function analysis of the crustal and lithospheric structures beneath eastern Tibet. *Earth Planet. Sci. Lett.* 306, 77–85. doi:10.1016/j.epsl.2011.03.034

Huang, R., Wang, Z., Pei, S., and Wang, Y. (2009). Crustal ductile flow and its contribution to tectonic stress in Southwest China. *Tectonophysics* 473, 476–489. doi:10.1016/j.tecto.2009.04.001

Hubbert, M. K., and Rubey, W. W. (1959). Role of fluid pressure in mechanics of overthrust faulting: I. Mechanics of fluid-filled porous solids and its application to overthrust faulting. *GSA Bull.* 70, 115–166. doi:10.1130/0016-7606(1959)70[115:ROFPIM]2.0

Jackson, J. A. (2002). Faulting, flow, and strength of the continental lithosphere. *Int. Geol. Rev.* 11, 39–61. doi:10.2747/0020-6814.44.1.39

Ji, S., and Zhao, P. (1993). Flow laws of multiphase rocks calculated from experimental data on the constituent phases. *Earth Planet. Sci. Lett.* 117, 181–187. doi:10.1016/0012-821X(93)90125-S

Laske, G., Masters, G., Ma, Z., and Pasyanos, M. E. (2013). Update on CRUST1.0 - a 1-degree global model of earth's crust. *Geophys. Res. Abstr.* 15, EGU2013–2658.

Li, B., Xie, F., Huang, J., Xu, X., Guo, Q., Zhang, G., et al. (2022). *In situ* stress state and seismic hazard in the Dayi seismic gap of the Longmenshan thrust belt. *Sci. China Earth Sci.* 65, 1388–1398. doi:10.1007/s11430-021-9915-4

Li, C. F., Wang, J., Lin, J., and Wang, T. (2017). Thermal evolution of the North Atlantic lithosphere: new constraints from magnetic anomaly inversion with a fractal magnetization model. *Geochem. Geophys. Geosystems* 14, 5078–5105. doi:10.1002/2013GC004896

Li, D., Ding, Z., Wu, P., Zheng, C., Ye, Q., and Liang, M. (2015). The deep seismogenic environment of the southeastern section of the Xianshuihe fault zone and the 2014 Kangding *Ms* 6.3 earthquake. *Chin. J. Geophys. Chin. Ed.* 58, 1941–1953. doi:10.6038/cjg20150610

Li, X., and Shibazaki, B. (2014). 3D modeling of earthquake cycles of the Xianshuihe fault, southwestern China. *J. Asian Earth Sci.* 96, 205–212. doi:10.1016/j.jseaes.2014.08.040

Li, Y., Liu, M., Li, Y., and Chen, L. (2019). Active crustal deformation in southeastern Tibetan plateau: the kinematics and dynamics. *Earth Planet. Sci. Lett.* 523, 115708. doi:10.1016/j.epsl.2019.07.010

Li, Y., Tian, J., Li, X., Li, S., Wang, Q., and Gao, Y. (2023). Deep tectonic pattern of the luding *ms* 6.8 earthquake on 5th september 2022 in sichuan province, China. *Chin. J. Geophys. Chin. Ed.* 66, 1385–1396. doi:10.6038/cjg2023Q0742

Liang, J., Yu, Y., Shi, Z., Li, Z., Huang, Y., Song, H., et al. (2023). Geothermal springs with high δ13CCO2-DIC along the Xianshuihe fault, Western Sichuan, China: a geochemical signature of enhanced deep tectonic activity. *J. Hydrology* 623, 129760. doi:10.1016/j.jhydrol.2023.129760

Liu, Q., Shi, Y., Wei, D., Han, P., Chen, S., Liu, P., et al. (2017). Near-surface geothermal gradient observation and geothermal analyses in the Xianshuihe fault zone, eastern Tibetan Plateau. *Acta Geol. Sinica-English Ed.* 91, 414–428. doi:10.1111/1755-6724.13108

Liu, Y., Yu, Z., Zhang, Z., Yao, H., Wang, W., Zhang, H., et al. (2023). The high-resolution community velocity model V2.0 of southwest China, constructed by joint body and surface wave tomography of data recorded at temporary dense arrays. *Sci. China Earth Sci.* 66, 2368–2385. doi:10.1007/s11430-022-1161-7

Maggi, A., Jackson, J. A., McKenzie, D., and Priestley, K. (2000). Earthquake focal depths, effective elastic thickness, and the strength of the continental lithosphere. *Geology* 28, 495–498. doi:10.1130/0091-7613(2000)028<0495:efdeet>2.3.co;2

Masuti, S., Muto, J., and Rybacki, E. (2023). Transient creep of quartz and granulite at high temperature under wet conditions. *J. Geophys. Res. Solid Earth* 128, e2023JB027762. doi:10.1029/2023JB027762

Meade, B. J. (2007). Present-day kinematics at the India-Asia collision zone. *Geology* 35, 81–84. doi:10.1130/G22924A.1

Mogistrale, H. (2002). Relative contributions of crustal temperature and composition to controlling the depth of earthquakes in Southern California. *Geophys. Res. Lett.* 29, 87. doi:10.1029/2001GL014375

Nur, A., and Simmons, G. (1969). The effect of saturation on velocity in low porosity rocks. *Earth Planet. Sci. Lett.* 7, 183–193. doi:10.1016/0012-821X(69)90035-1

Ren, Y., Wang, D., Li, T., Ran, X., Liu, Z., and Zhang, J. (2021). *In-situ* geostress characteristics and engineering effect in Ya'an-Xinduqiao section of Sichuan-Tibet Railway. *Chin. J. Rock Mech. Eng.* 40, 65–76. doi:10.13722/j.cnki.jrme.2020.0537

Royden, L. H., Burchfiel, B. C., King, R. W., Wang, E., Chen, Z. L., Shen, F., et al. (1997). Surface deformation and lower crustal flow in eastern Tibet. *Science* 276, 788–790. doi:10.1126/science.276.5313.788

Royden, L. H., Burchfiel, B. C., and van der Hilst, R. D. (2008). The geological evolution of the Tibetan Plateau. *Science* 321, 1054–1058. doi:10.1126/science.1155371

Rudnick, R. L., and Gao, S. (2003). Composition of the continental crust. *Treatise Geochem. 2nd Ed.* 3, 1–64. doi:10.1016/B0-08-043751-6/03016-4

Rutter, E. H., Brodie, K. H., and Irving, D. H. (2006). Flow of synthetic, wet, partially molten "granite" under undrained conditions: an experimental study. *J. Geophys. Res. Solid Earth* 111, B06407. doi:10.1029/2005JB004257

Rybacki, E., and Dresen, G. (2000). Dislocation and diffusion creep of synthetic anorthite aggregates. *J. Geophys. Res. Solid Earth* 105, 26017–26036. doi:10.1029/2000JB900223

Savage, W. Z., Swolfs, H. S., and Amadei, B. (1992). On the state of stress in the near-surface of the Earth's crust. *Pure Appl. Geophys.* 138, 207–228. doi:10.1007/BF00878896

Scholz, C. H. (2002). *The mechanics of earthquakes and faulting*. Cambridge: Cambridge University Press.

Sen, Z., and Sadagah, B. H. (2002). Probabilistic horizontal stress ratios in rock. *Math. Geol.* 34, 845–855. doi:10.1023/A:1020928727867

Sheorey, P. R. (1994). A theory for *in situ* stresses in isotropic and transverseley isotropic rock. *Intern. J. Rock Mech. Min. Sci. and Geomechanics Abstr.* 31, 23–34. doi:10.1016/0148-9062(94)92312-4

Sloan, R. A., Jackson, J. A., McKenzie, D., and Priestley, K. (2011). Earthquake depth distributions in central Asia, and their relations with lithosphere thickness, shortening and extension. *Geophys. J. Int.* 185, 1–29. doi:10.1111/j.1365-246X.2010.04882.x

Sun, L., Zhao, Z., Pan, J., Liang, F., Zhang, L., and Zhang, J. (2021). The stress and strain state of Yalahe fault in the Kangding segment of the Xianshuihe fault zone and its seismogenic environment. *Acta Petrol. Sin.* 37, 3225–3240. doi:10.18654/1000-0569/2021.10.15

Sun, Y., Li, H., Fan, T., and Li, B. (2023). Effect of rheological heterogeneities on the lithospheric deformation of the Tibetan Plateau and neighbouring regions. *Front. Earth Sci.* 11, 1153744. doi:10.3389/feart.2023.1153744

Tanaka, A., Okubo, Y., and Matsubayashi, O. (1999). Curie point depth based on spectrum analysis of the magnetic anomaly data in East and Southeast Asia. *Tectonophysics* 306, 461–470. doi:10.1016/S0040-1951(99)00072-4

Tapponnier, P., Xu, Z. Q., Roger, F., Meyer, B., Arnaud, N., Wittlinger, G., et al. (2001). Oblique stepwise rise and growth of the Tibet Plateau. *Science* 294, 1671–1677. doi:10.1126/science.105978

Tian, J., Pang, Z., Liao, D., and Zhou, X. (2021). Fluid geochemistry and its implications on the role of deep faults in the genesis of high temperature systems in the eastern edge of the Qinghai Tibet Plateau. *Appl. Geochem.* 131, 105036. doi:10.1016/j.apgeochem.2021.105036

Tullis, T. E., Horowitz, F. G., and Tullis, J. (1991). Flow laws of polyphase aggregates from end-member flow laws. *J. Geophys. Res. Solid Earth* 96, 8081–8096. doi:10.1029/90JB02491

Ullah, J., Luo, M., Ashraf, U., Pan, H., Anees, A., Li, D., et al. (2022). Evaluation of the geothermal parameters to decipher the thermal structure of the upper crust of the Longmenshan fault zone derived from borehole data. *Geothermics* 98, 102268. doi:10.1016/j.geothermics.2021.102268

Wan, Z. S., Zhao, G. Z., Tang, J., Chen, X. B., Wang, L. F., Xiao, Q. B., et al. (2010). The electrical structure of the crust along Mianning-Yibin profile in the eastern edge of Tibetan plateau and its tectonic implications. *Chin. J. Geophys. Chin. Ed.* 53, 585–594. doi:10.3969/j.issn.0001-5733.2010.03.012

Wang, C., Han, W., Wu, J., Lou, H., and Chan, W. W. (2007). Crustal structure beneath the eastern margin of the Tibetan Plateau and its tectonic implications. *J. Geophys. Res. Solid Earth* 112, B07307. doi:10.1029/2005JB003873

Wang, J., Zhang, G. W., Li, C. F., and Liang, S. S. (2018). Correlating seismicity to Curie-point depths in the eastern margin of the Tibetan Plateau. *Chin. J. Geophys. Chin. Ed.* 61, 1840–1852. doi:10.6038/cjg2018M0130

Wang, M., Shen, Z., Gan, W., Liao, H., Li, T., Ren, J., et al. (2008). GPS monitoring of temporal deformation of the Xianshuihe fault. *Sci. China Earth Sci.* 51, 1259–1266. doi:10.1007/s11430-008-0095-3

Wang, M., and Shen, Z. K. (2020). Present-day crustal deformation of continental China derived from GPS and its tectonic implications. *J. Geophys. Res. Solid Earth* 125, e2019JB018774. doi:10.1029/2019JB018774

Wang, W., Wu, J., Fang, L., Lai, G., and Cai, Y. (2017). Crustal thickness and Poisson's ratio in southwest China based on data from dense seismic arrays. *J. Geophys. Res. Solid Earth* 122, 7219–7235. doi:10.1002/2017JB013978

Xu, J., and Zeng, X. (2022). Tectonic stress redistribution induced by geothermal gradient difference: numerical modeling of stress around the Anninghe seismic gap in the southeastern Tibetan plateau. *Pure Appl. Geophys.* 179, 3713–3726. doi:10.1007/s00024-022-03162-1

Xu, X., Wen, X., Zheng, R., Ma, W., Song, F., and Yu, G. (2003). Pattern of latest tectonic motion and its dynamics for active blocks in Sichuan-Yunnan region, China. *Sci. China Earth Sci.* 46, 210–226. doi:10.1360/03dz0017

Yang, S., Yao, R., Cui, X., Chen, Q., and Huang, L. (2012). Analysis of the characteristics of measured stress in Chinese mainland and its active blocks and North–South seismic belt. *Chin. J. Geophys. Chin. Ed.* 55, 4207–4217. doi:10.6038/j.issn.0001–5733.2012.12.032

Yang, Y., Zhang, X., Hua, Q., Su, L., Feng, C., Qiu, Y., et al. (2021). Segmentation characteristics of the Longmenshan fault–Constrained from dense focal mechanism data. *Chin. J. Geophys. Chin. Ed.* 64, 1181–1205. doi:10.6038/cjg2021O0286

Zang, A., and Stephansson, O. (2010). *Stress field of the Earth's crust*. London: Springer.

Zhang, P. Z. (2008). Present-day tectonic deformation, strain partitioning and deep dynamics in the western Sichuan, eastern Tibetan Plateau. *Sci. China Earch Sci.* 38, 1041–1056. doi:10.1360/zd2008-38-9-1041

Zhao, G., Chen, X., Wang, L., Wang, J., Tang, J., Wan, Z., et al. (2008). Evidence of crustal 'channel flow' in eastern margin of Tibet plateau from MT measurements. *Chin. Sci. Bullettin* 52, 1887–1893. doi:10.1360/csb2008-53-3-345

Zhou, Y., Zhang, H., Yao, W., Dang, J., and He, C. (2017). An experimental study on creep of partially molten granulite under high temperature and wet conditions. *J. Asian Earth Sci.* 139, 15–29. doi:10.1016/j.jseaes.2016.10.011

Zhu, Y., Diao, F., Chen, F., Wang, Y., Shao, Z., Wang, R., et al. (2024). Probing the interseismic locking state of the Xianshuihe fault based on a viscoelastic deformation model. *Sci. China Earth Sci.* 67, 134–145. doi:10.1007/s11430-022-1152-2

Zoback, M. D., Barton, C. A., Brudy, M., Castillo, D. A., Finkbeiner, T., Grollimund, B. R., et al. (2003). Determination of stress orientation and magnitude in deep wells. *Int. J. Rock Mech. Min. Sci.* 40, 1049–1076. doi:10.1016/j.ijrmms.2003.07.001

Zoback, M. D., and Townend, J. (2001). Implications of hydrostatic pore pressures and high crustal strength for the deformation of intraplate lithosphere. *Tectonophysics* 336, 19–30. doi:10.1016/S0040-1951(01)00091-9

Zoback, M. L. (1992). First-and second-order patterns of stress in the lithosphere: the world stress map project. *J. Geophys. Res. Solid Earth* 97, 11703–11728. doi:10.1029/92JB00132

frontiers | Frontiers in Earth Science

TYPE Review
PUBLISHED 18 October 2024
DOI 10.3389/feart.2024.1488690

OPEN ACCESS

EDITED BY
Fuqiong Huang,
China Earthquake Networks Center, China

REVIEWED BY
Giovanni Martinelli,
National Institute of Geophysics and Volcanology, Italy
Guodong Zheng,
China University of Geosciences Wuhan, China

*CORRESPONDENCE
Hongbiao Gu,
hongbiaosw@126.com

RECEIVED 30 August 2024
ACCEPTED 08 October 2024
PUBLISHED 18 October 2024

CITATION
Li J, Liu Z, Chen Z, Gao Y, Hao Y and Gu H (2024) The role of gas emissions (He, Rn, and CO_2) from fault zones in understanding fault and seismic activity.
Front. Earth Sci. 12:1488690.
doi: 10.3389/feart.2024.1488690

The role of gas emissions (He, Rn, and CO_2) from fault zones in understanding fault and seismic activity

Jiye Li[1], Zhaofei Liu[2], Zhi Chen[2], Yan Gao[1], Yongmei Hao[1] and Hongbiao Gu[3]*

[1]Heilongjiang Earthquake Agency, Heilongjiang, China, [2]CEA Key Laboratory of Earthquake Prediction (Institute of Earthquake Forecasting), China Earthquake Administration, Beijing, China, [3]College of Transportation Engineering, Nanjing Tech University, Nanjing, China

Active fault zones are critical pathways for the migration of deep fluids to the Earth's surface, carrying gases such as He, Rn, and CO_2 that provide evidence for the physical and chemical dynamics of the Earth's interior. This review examines the geochemical characteristics of fault zone gases and their implications for understanding fault activity and seismic events. Fault zones with high activity levels exhibit significant gas release, and variations in soil and hot spring gas concentrations can serve as indicators of seismic activity. Changes in gas concentrations and isotopic ratios, particularly before and after earthquakes, reflect the dynamic interplay between deep-sourced and shallow-sourced fluids. Seismic-induced stress alterations enhance gas release along fault zones, leading to observable anomalies that can aid in earthquake monitoring and prediction. The study underscores the importance of isotope tracing in deciphering fluid sources, migration pathways, and the evolution of fault zones, providing valuable information for assessing tectonic activity and mitigating seismic risks.

KEYWORDS

gas emission, fault zone, fault activity, seismic activity, earthquake forecasting

1 Introduction

Fluids play a crucial role in Earth's system, particularly those migrating along fault zones, which often carry geochemical signatures indicating the physical and chemical evolution of Earth's deep interior. These fluids serve as valuable indicators for studying block movements, earthquake prediction, fault activity assessment, and related fields (Martinelli, 2020; Zhang et al., 2021). Due to the high permeability and porosity of active faults, these zones frequently act as conduits for the migration and release of deep-sourced fluids. This process typically manifests at the surface through elevated soil gas emissions, including radon (Rn), carbon dioxide (CO_2), helium (He), hydrogen (H_2), and methane (CH_4), as well as intense degassing from hot springs and increased geothermal heat flow (Weinlich, 2014; Voltattorni et al., 2015; Singh et al., 2016; Bond et al., 2017).

During fluid migration, stable isotope signatures of non-metallic elements frequently undergo equilibrium or kinetic fractionation. Isotopic analyses, such as $^4He/^{20}Ne$, $^3He/^4He$, and $\delta^{13}C_{CO2}$, can elucidate the origins, migration pathways, circulation processes, formation mechanisms, and evolutionary history of these fluids (Zheng et al., 2013;

Zhang et al., 2021). Furthermore, the chemical composition of fluids and isotopes is highly sensitive to variations in regional tectonic stress. Earthquake-induced stress changes can alter pore pressure and microcrack density, affecting fluid-rock interactions and subsequently modifying the surface emission levels of deep gases (Camarda et al., 2016; Randazzo et al., 2021; Caracausi et al., 2022). Therefore, analyzing the characteristics of fault zone gases and isotope sources provides an effective method for studying fluid migration within fault zones and its relationship to tectonic activity (Faulkner et al., 2010; Tian et al., 2021; Li et al., 2023).

2 Characteristics and sources of fluids in fault zones

2.1 Helium and neon

Helium (He) and neon (Ne) are inert noble gases whose isotopic compositions in various reservoirs make them effective geological tracers for mantle-derived fluids. Among the eight isotopic forms of helium, ^{3}He and ^{4}He are stable, while ^{5}He through ^{10}He are unstable. The ratios ^{4}He/^{20}Ne and ^{3}He/^{4}He are commonly employed to differentiate crustal from mantle-derived fluids (Sano and Wakita, 1985; Shao et al., 2024). The R/Ra ratio, representing He isotopic characteristics, is defined as the ratio of ^{3}He/^{4}He in a sample relative to that in the atmosphere.

In Earth's atmosphere, He is predominantly composed of ^{4}He, which constitutes ~99.99986% of atmospheric He. The concentration of He in the atmosphere is relatively low, at 5.239 ± 0.004 ppm (Walia et al., 2010). The atmospheric ^{3}He/^{4}He (Ra) value is 1.4×10^{-6}, and the ^{4}He/^{20}Ne value is ~0.318 (Sano and Wakita, 1985). Most atmospheric ^{4}He is radiogenic, originating from the α-decay of radioactive isotopes such as ^{238}U, ^{235}U, and ^{232}Th (Figure 1). The He abundance in Earth's crust is estimated at ~ 5.5×10^{-7}%. Crustal He typically exhibits an R/Ra value of ~0.02 and a ^{4}He/^{20}Ne value of 1,000 (Andrews, 1985). Conversely, the ^{3}He isotope, thought to originate from the solar nebula or solar wind radiation present during Earth's formation, has accumulated in the mantle throughout Earth's history. Mantle-derived He generally displays an R/Ra value exceeding 5 (Lupton, 1983), with mid-ocean ridge basalt (MORB) inclusions showing an R/Ra value of 8.0 and a ^{4}He/^{20}Ne value of 1,000 (Graham, 2002). R/Ra values between 5 and 50 are indicative of He from the lower mantle (White, 1957). The highest recorded R/Ra value of 67.2 ± 1.8 was found in olivine from 62 Ma-old lava flows on Baffin Island, suggesting a possible origin from Earth's core (Horton et al., 2023). Due to He's chemical inertness, stable physical properties, and low solubility in water, gases such as N_2 and CO_2, along with groundwater, often act as carriers for He migration (Hong et al., 2010; Walia et al., 2010; Lee et al., 2019). He typically accumulates in sedimentary basins and is released to the surface via faults or fractures (Gao et al., 2024).

2.2 Radon

Radon (Rn) is the only naturally occurring radioactive noble gas, existing in 34 unstable isotopic forms, ranging from ^{215}Rn to ^{242}Rn. In nature, radon is found primarily in three isotopes: ^{219}Rn (with a half-life of 3.96 s), ^{220}Rn (half-life of 55 s), and ^{222}Rn (half-life of 3.82 days) (Audi et al., 2003). Of these, ^{222}Rn is a decay product of ^{226}Ra in the ^{238}U decay chain (Figure 1), with the longest half-life, and its concentration in the atmosphere is typically ranging from 10 to 100 Bq·m^{-3} (Porstendörfer, 1994).

Uranium (U) and radium (Ra), naturally occurring radioactive elements, are widely distributed across the lithosphere, hydrosphere, and atmosphere. Uranium, which has 28 unstable isotopes (^{215}U to ^{242}U), is found in concentrations of ~3×10^{-4}% in the lithosphere and ~1×10^{-4}% in soil. Radium, with 33 unstable isotopes (^{202}Ra to ^{234}Ra), has lithospheric and soil concentrations of ~1×10^{-4}% and ~8×10^{-11}%, respectively (Cheng et al., 2005). The levels of U and Ra in soil or rock directly influence Rn release in soil gas (Pereira et al., 2017). Experimental studies on rock gas emissions have demonstrated that granite, which is rich in U and Ra, releases significantly higher Rn concentrations than limestone or sandstone (King, 1978; El-Arabi et al., 2006). Consequently, regions with extensive granite outcrops typically exhibit elevated Rn levels (Pereira et al., 2017).

Within mineral particles, radium undergoes α-decay, releasing α-particles (^{4}He) and enabling Rn to escape. The fraction of Rn atoms generated from the decay of ^{226}Ra that escape into rock pores is defined as the Rn emanation coefficient (Martinelli et al., 1995; Miklyaev et al., 2020; Phong Thu et al., 2020). Rn recoil can take three paths: 1) remaining within the same particle, 2) passing through a pore and embedding in adjacent particles, or 3) escaping into an open pore (Sakoda et al., 2011). Only Rn escaping into pore space is considered emanated (A, B, E, and F in Figure 2); otherwise, it is non-emanated (C, D, and G). The recoil range of Rn is 77 nm in water and 53 mm in the atmosphere, with the latter being 688 times greater (Sakoda et al., 2011). This difference indicates that rainfall and moisture content can significantly impact Rn diffusion.

Gas transport through porous media often occurs via two primary processes: diffusion and convection. Diffusion, driven by concentration gradients, involves the movement of substances from areas of high concentration to low concentration due to random molecular motion (Flügge and Zimens, 1939). Convection, also known as advection, mass transport, or viscous flow, is driven by pressure gradients (Ciotoli et al., 2007). In natural environments, gas transport typically results from a combination of these two mechanisms.

Due to Rn's relatively large atomic mass and chemical inertness, deep-source gases such as CO_2, N_2, and CH_4 often serve as carrier gases that facilitate its migration to the surface (Yuce et al., 2017). CO_2, the most prevalent component of Earth's interior, frequently acts as the carrier gas for Rn as it migrates along fault zones. Consequently, increased soil gas Rn concentrations are often observed in conjunction with rising CO_2 levels in fault zones (Li et al., 2013). In rock fractures and pores, typically ranging from 10^{-2} to 10^{1} mm in size at depths of several hundred to several thousand meters (Etiope and Martinelli, 2002; Girault and Perrier, 2014), Rn convection velocities can reach up to 10^{0} to 10^{4} m·d^{-1}(Etiope and Martinelli, 2002; Muto et al., 2021). For example, convection velocities of Rn in the Osaka Basin, Baikal Rift, and North Caucasus are estimated at 340 m·d^{-1}, 5.2 m·d^{-1}, and 28 m·d^{-1}, respectively

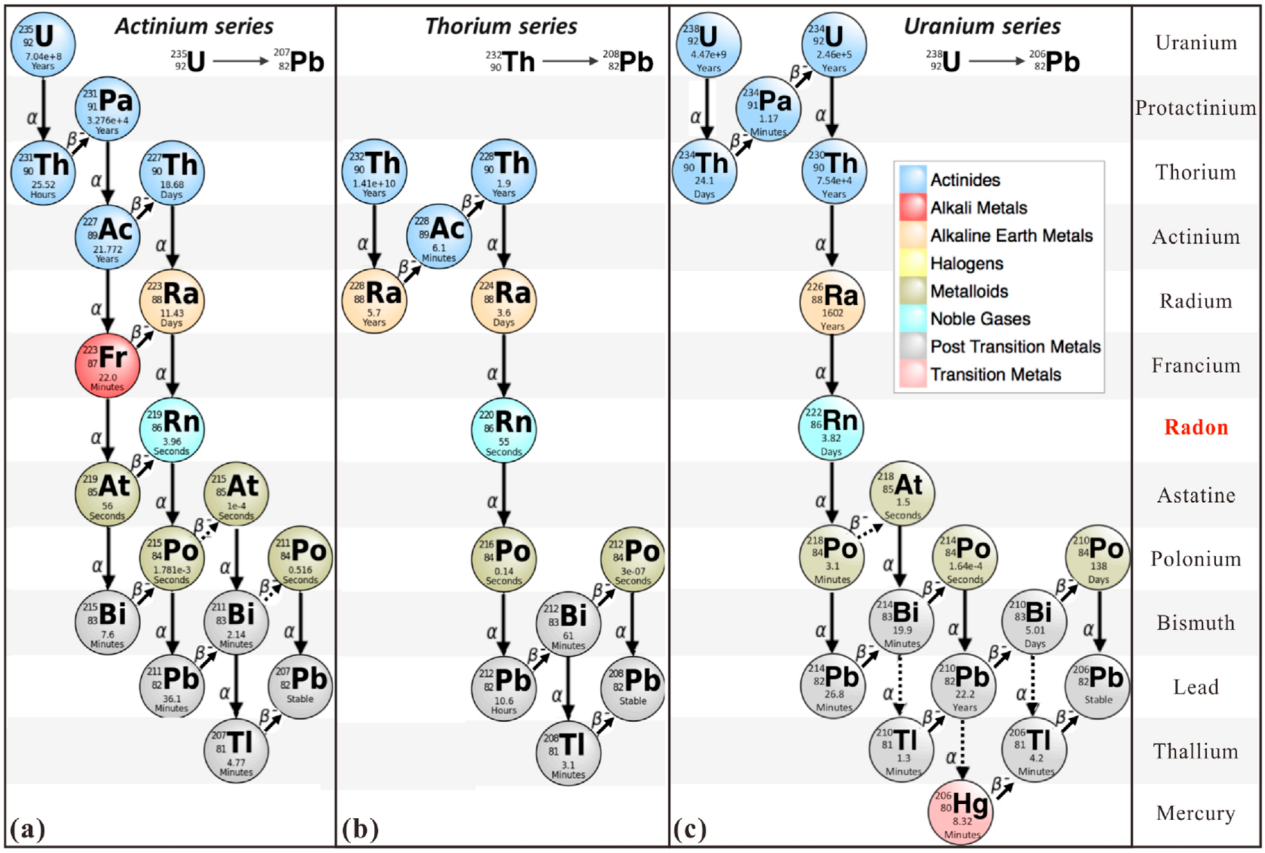

FIGURE 1
The α-decay chains of ^{219}Rn **(A)**, ^{220}Rn **(B)**, and ^{222}Rn **(C)**, adapted from Soddy (1913) and Tan (2016).

(Miklyaev et al., 2020; Muto et al., 2021). When CO_2 acts as the carrier gas, Rn may originate from depths of several hundred to several thousand meters in areas of high permeability (Girault and Perrier, 2014). Moreover, groundwater transport and deposition also contribute to the movement of Rn's parent elements, uranium, and radium (Chen et al., 2018).

2.3 Carbon dioxide

Data from the Mauna Loa Observatory in Hawaii proves that the CO_2 concentration in the atmosphere continues to increase, rising from 315.70 ppm in March 1958 to 422.80 ppm on 5 February 2024 (http://www.co2.earth). CO_2 primarily originates from three sources: the decomposition of organic material, the breakdown of carbonate rocks, and mantle degassing (Barnes et al., 1978). The origin of CO_2 can generally be determined using $\delta^{13}C_{CO2}$ values and CO_2 concentrations, which identify three distinct end-member sources: 1) Deep-source CO_2, derived from magmatic degassing and the decarbonation of carbonate rocks, typically exhibits concentrations near 100% with $\delta^{13}C_{CO2}$ values ~0‰ (Parks et al., 2013); 2) Biogenic CO_2, usually characterized by concentrations of ~4% and $\delta^{13}C_{CO2}$ values ~ −23‰ (Di Martino et al., 2016); and 3) Atmospheric CO_2, currently at 422.80 ppm, with $\delta^{13}C_{CO2}$ values ~ −8‰ (Keeling et al., 2005).

The range of $\delta^{13}C_{CO2}$ from different sources can overlap each other, such as those from Mid-Ocean Ridge Basalts (MORB) and carbonate rocks (Bergfeld et al., 2001). CO_2 also serves as the primary carrier gas for He migration in the crust (Hong et al., 2010; Walia et al., 2010; Lee et al., 2019). Therefore, the He-CO_2 system is often utilized to further deduce the source of CO_2 (Tian et al., 2021; Shao et al., 2024). Analysis of CO_2 origins can be conducted using R/Ra ratios and $\delta^{13}C_{CO2}$ values, which help distinguish between contributions from organic material, carbonate rock metamorphism, and mantle magma degassing (Barnes et al., 1978).

The decomposition of carbonate rocks involves processes such as water-rock interactions, mechanical grinding by faults, thermal metamorphism, and weathering (Rovira and Vallejo, 2008; Tamir et al., 2011). These processes can lead to the release of substantial amounts of CO_2, which then becomes a crustal fluid, potentially contaminating mantle-derived volatiles. Typically, thermal metamorphism of carbonate rocks occurs ~400°C; however, CO_2 release can begin at temperatures above 70°C when water is involved (Pankina G et al., 1979). Extensive fracture networks and fluid interactions can enhance water-rock reactions within the rock, producing significant quantities of CO_2 (Randazzo et al., 2021). Additionally, in regions of significant tectonic uplift, carbon stored in carbonate rocks for millions of years can be released through weathering (Zondervan et al., 2023).

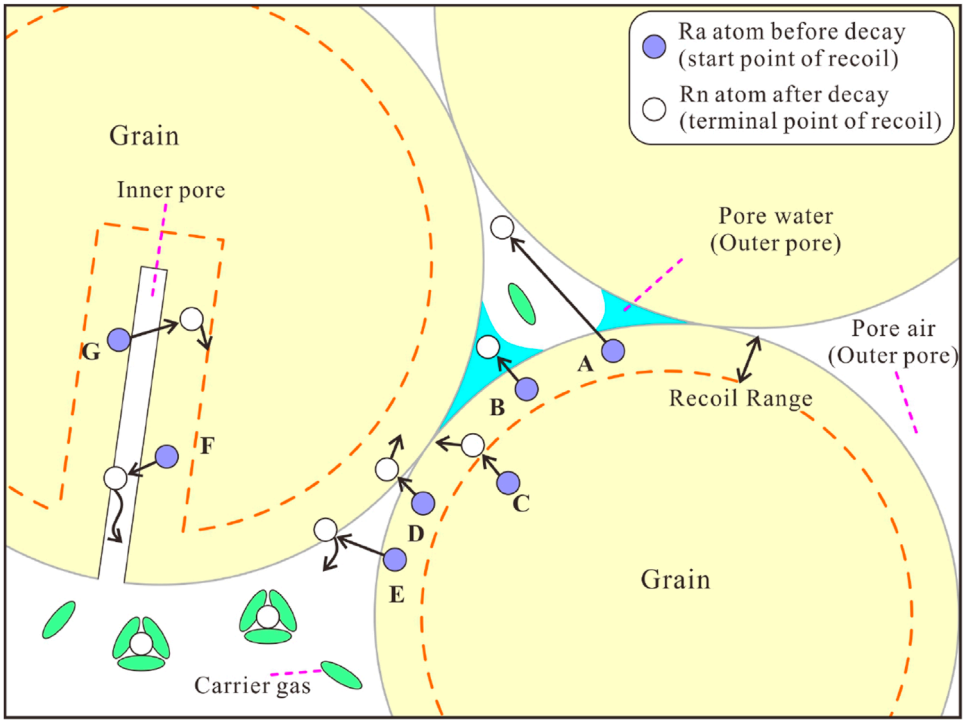

FIGURE 2
A schematic of Rn atom α-recoil, adapted from Sakoda et al. (2011). Arrows indicate diffusion processes, and the carrier gas is illustrative and does not represent actual behavior. **(A, B, E, F)** represent Rn emanated; **(C, D, G)** are non-emanated.

3 Application of fault zone gases in tectonic activity

The Earth is an open system where fluids, especially gaseous components, play a crucial role in material and energy exchange across different layers. Active fault systems, characterized by higher permeability and porosity, facilitate the migration of deep-seated fluids (such as CO_2 and He) toward the surface. These fault systems act as conduits extending to the mantle, allowing mantle-derived fluids to reach the Earth's surface. The geochemical signatures of these fluids provide valuable insights into the physicochemical evolution of the Earth's deep interior (Ciotoli et al., 2007; Yuce et al., 2017; Zhang et al., 2021), which constructed the major direction of gas geochemistry (Zheng et al., 2022). Therefore, in tectonically active regions, analyzing changes in fluid geochemical characteristics has become an essential method for studying block movements, earthquake prediction, revealing hidden faults, evaluating fault activity, and assessing atmospheric contributions (Zheng et al., 2018; Martinelli, 2020; Zhang et al., 2021).

3.1 Relationship between fault zone gases and tectonic activity

The exploration of soil gases, referred to as "geogas", dates back to 1913 (Klusman, 1993). Globally, regions of strong gas release often overlap with tectonic suture zones, volcanic belts, geothermal areas, and seismic zones (Barnes et al., 1978; Tamburello et al., 2018). Regionally, the intensity of fluid release and the geochemical characteristics within fault zones are closely related to fault activity. Significant anomalies in soil gas concentrations (such as Rn, CO_2, He, H_2, and CH_4) have been observed in various fault zones, including the Stivos Fault in Greece (Papastefanou, 2010), the Khlong Marui Fault in Thailand (Bhongsuwan et al., 2011), the Kütahya Simav Fault in Turkey (Manisa et al., 2022), and the Mat Fault in India (Jaishi et al., 2014). Field observations suggest that stronger fault activity correlates with increased soil gas release, making soil gas concentrations a useful metric for assessing fault activity (Seminsky et al., 2013; Capaccioni et al., 2015). Additionally, different fault types (normal, reverse, and strike-slip) exhibit distinct concentrations and flux characteristics (Annunziatellis et al., 2008; Sun et al., 2018). Therefore, tectonic zones with significant gas release are valuable for reconstructing regional geodynamic processes and monitoring subsurface tectonic activity (Faulkner et al., 2010; Tian et al., 2021; Li et al., 2023).

At a global scale, crustal permeability exhibits significant stratification, influenced by both internal and external forces. In the deeper crust, internal processes such as metamorphism and magmatism are dominant, while in the shallow crust, external factors, particularly the hydrologic cycle, play a more crucial role in shaping permeability (Rojstaczer et al., 2008). The difference in permeability of the crust determines the different distribution patterns of fluids underground. Rock deformation experiments indicate that when differential stress exceeds rock shear

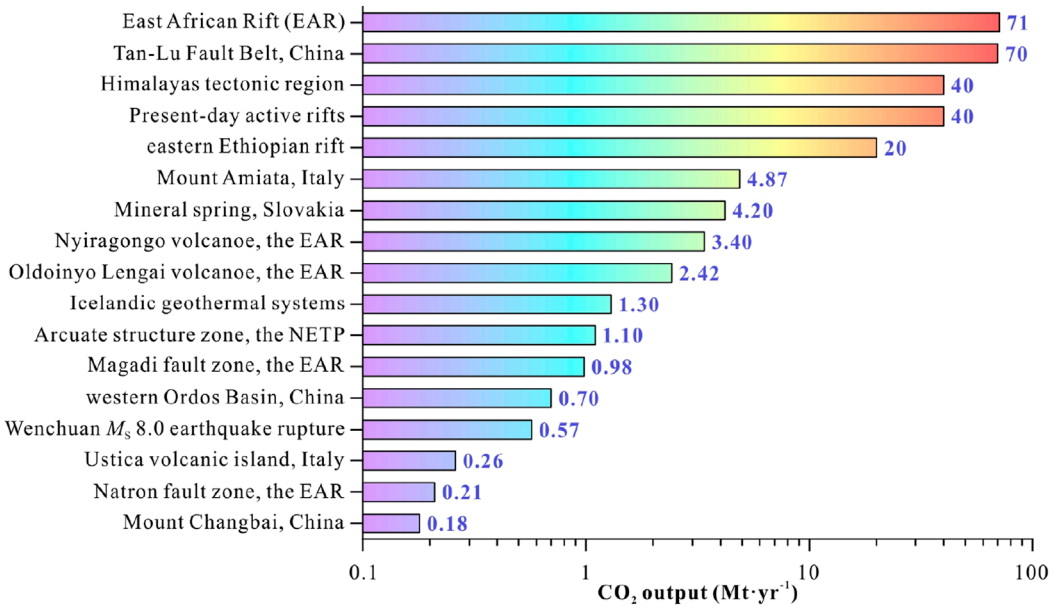

FIGURE 3
Comparison of the CO_2 output in the arcuate structure zone and other regions of the world. Data from: the East African Rift (EAR) (Lee et al., 2016); the Tan-Lu Fault Belt, China (Aulbach et al., 2020); the Himalayas tectonic region (Becker et al., 2008); the present-day active rifts (Brune et al., 2017); the eastern Ethiopian rift (Hunt et al., 2017); the Mount Amiata, Italy (Sbrana et al., 2020); the Mineral spring, Slovakia (Kucharič et al., 2015); the Nyiragongo volcanoe, the East African Rift (Sawyer et al., 2008); the Oldoinyo Lengai volcanoe, the East African Rift (Brantley and Koepenick, 1995); the Icelandic geothermal systems (Ármannsson et al., 2005); the arcuate structure zone, the northeastern Tibetan Plateau (NETP) (Liu et al., 2024); the Magadi fault zone, the East African Rift (Lee et al., 2016); the western Ordos Basin, China (Liu et al., 2023a); the Wenchuan M_S 8.0 earthquake rupture (Zhou et al., 2016); the Ustica volcanic island, Italy (Etiope et al., 1999); the Natron fault zone, the East African Rift (Lee et al., 2016); the Mount Changbai, China (Sun et al., 2021).

strength, pre-existing fractures close, forming new microcracks and pores. Continued stress can link these microcracks into macroscopic fractures, providing new pathways for fluid migration (Tuccimei et al., 2010). Under tectonic stress, the number of microcracks in fault zones increases (Li et al., 2013; Hansberry et al., 2021), accelerating the migration and release of deep gases, which can cause anomalies in gas concentrations and fluxes in shallow soils (Martinelli, 2020; Miklyaev et al., 2020). Research has shown that high sliding rates increase the permeability of sandstone and granite by three orders of magnitude, indicating that high sliding rates can sustain high permeability in fault zones (Tanikawa et al., 2010). Consequently, variations in soil gas release are primarily influenced by changes in fault zone permeability.

Active faults and fractures generally exhibit higher permeability and porosity than surrounding hard rock, resulting in greater deep-sourced gas release in fault zones compared to non-active tectonic areas (Annunziatellis et al., 2008; Giammanco et al., 2009; Weinlich, 2014; Voltattorni et al., 2015; Singh et al., 2016; Bond et al., 2017). In regions outside fault zones with lower permeability, the correlation between Rn and CO_2 concentrations is weak. In contrast, well-connected faults show a stronger positive correlation between Rn and CO_2 (Padrón et al., 2013; Ciotoli et al., 2014). Extensional structures with high permeability are more conducive to deep fluid release than thrust or strike-slip faults, with the scale of extensional faults directly influencing CO_2 emissions (Tamburello et al., 2018). For example, CO_2 emissions from the East African Rift are ~71 $Mt{\cdot}yr^{-1}$ (Lee et al., 2016), from active rifts ~40 $Mt{\cdot}yr^{-1}$ (Brune et al., 2017), and from the eastern Ethiopian Rift ~20 $Mt{\cdot}yr^{-1}$ (Hunt et al., 2017) (Figure 3). Although active faults are key pathways for the release of mantle-derived and crust-derived gases (Caracausi et al., 2022), atmospheric gases can also enter the Earth's interior through high-permeability fractures, with diffusion rates reaching 10 $m{\cdot}d^{-1}$ and maximum depths of 300 m (Arai et al., 2001; Giammanco et al., 2009). Additionally, thick sedimentary layers can obstruct gas migration, influencing atmospheric mixing and the release of deep-sourced gases, while shallow organic gases may mix with rising fluids (Liu, 2006). Therefore, the connectivity of fault zones significantly affects underground gas release, with surface gases reflecting a mix of various sources.

Deep and large active fault zones act as links across different Earth layers. Stable isotopes of deep fluids may undergo equilibrium or kinetic fractionation during geological processes, and fluid isotope tracers can provide important information on fluid sources and migration in active fault zones (Zheng et al., 2013; Zhang et al., 2021). For instance, (Hernández Perez et al., 2003) identified mantle-derived CO_2 in soil gases of the Hakkoda Fault zone in northern Japan, with a contribution of up to 6.7%. Kulongoski et al. (2013) detected high $^3He/^4He$ ratios and CO_2 concentrations in hot spring gases from the San Andreas Fault zone, with mantle-derived He contributing up to 44%. Shao et al. (2024) analyzed hot spring gases in the southern segment of the eastern boundary of the Sichuan-Yunnan rhombic block, finding no intersection between the Red River Fault and

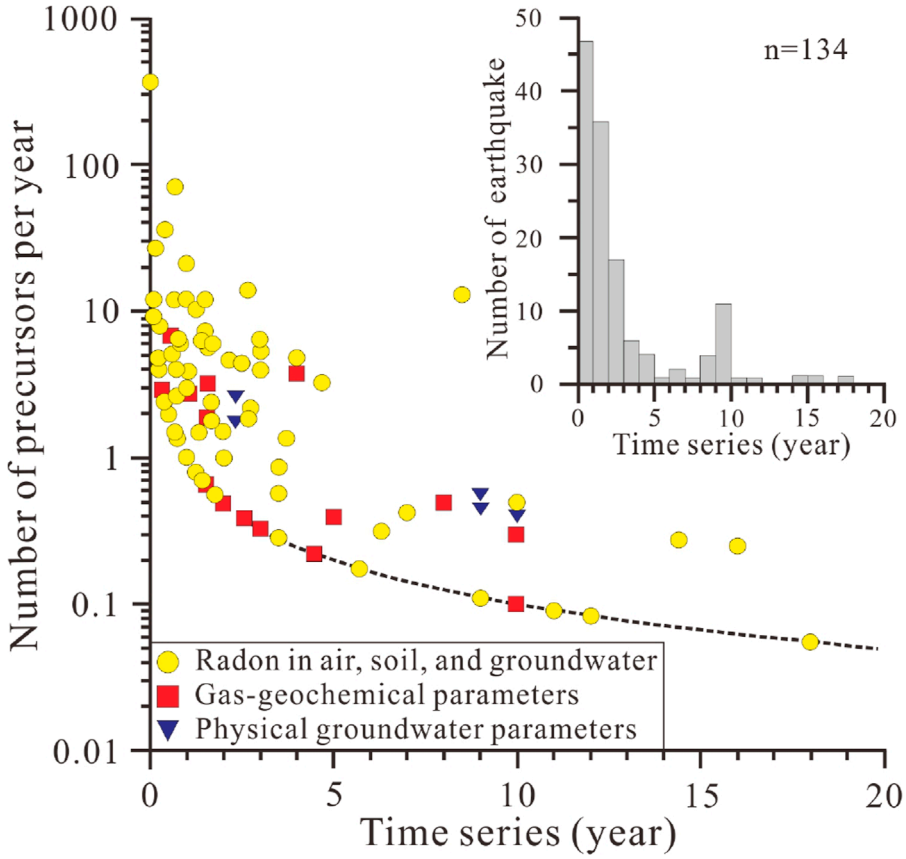

FIGURE 4
Global earthquake precursor statistics from 1967 to 2014, adapted from Woith (2015).

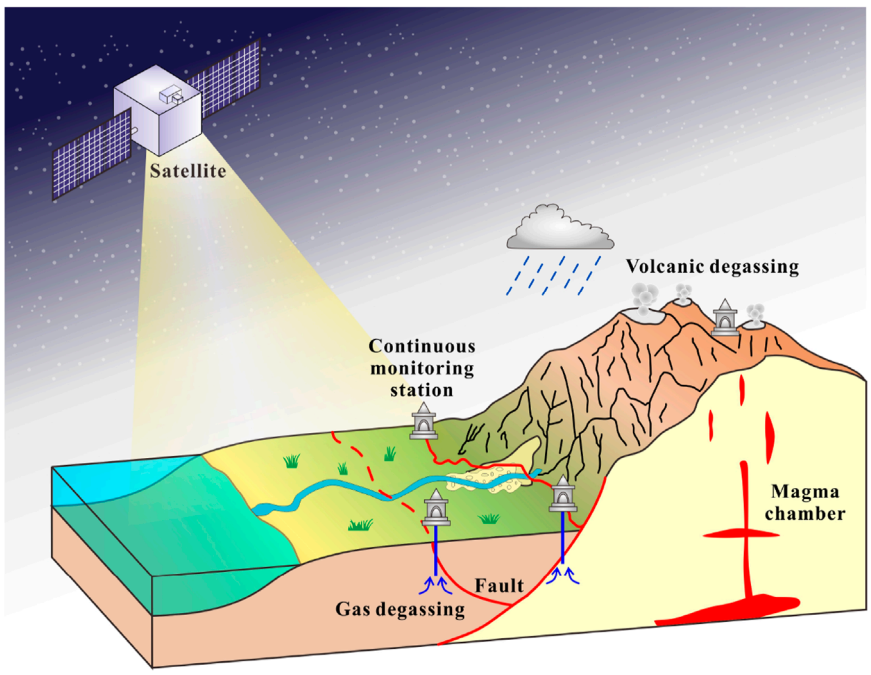

FIGURE 5
Schematic diagram of satellite hyperspectral sensors and continuous monitoring station.

Xiaojiang Fault. Zhang et al. (2021) studied the southeastern margin of the Tibetan Plateau using the He-CO_2-N_2 system in hydrothermal fluids, finding that He isotopes provided evidence for the lateral expansion and localized surface uplift of the Tibetan Plateau. These studies demonstrate that surface-emitted gases and isotopes in hot springs or soil gases are effective indicators of tectonic activity and fluid dynamics.

3.2 Relationship between fault zone gases and seismic activity

Stress changes induced by earthquakes can trigger variations in pore pressure and the number of micro-cracks within fault zones, affecting the interaction between fluids and rocks and altering the release of deep gases at the surface (Camarda et al., 2016; Randazzo et al., 2021; Zhao et al., 2021; Caracausi et al., 2022). These processes can enhance fluid migration along active faults and modify the contribution of different fluid sources to soil gases and hot spring emissions, leading to observable pre-seismic anomalies or post-seismic responses (Martinelli and Dadomo, 2017). Between 1967 and 2014, analysis of 134 global seismic cases revealed that 69% showed anomalies in soil and groundwater Rn, 20% in geochemical parameters of soil and groundwater gases, and 10% in physical groundwater parameters (Woith, 2015) (Figure 4).

Recent studies have increasingly applied geochemical methods for analyzing soil gases to understand seismic activity trends and to develop earthquake monitoring and prediction theories. In tectonically active regions, stress accumulation from seismic activity enhances the release of deep-sourced gases like Rn, CO_2, and He, which accumulate in rock fractures along fault zones (Ciotoli et al., 2014; Yuce et al., 2017; Chen et al., 2015). The correlation between Rn and CO_2 concentrations tends to increase before earthquakes (Fu et al., 2017). The vibroseis truck (Gresse et al., 2016) and active seismic source (Liu et al., 2023b) experiments have demonstrated that seismic waves can boost the release of gases trapped in rock and soil pores. Moreover, low-magnitude earthquakes (M < 4) can release crustal He into the atmosphere, with the He release amount being quantitatively related to the fault zone volume (Caracausi et al., 2022). Periodic monitoring of soil gases in Italy's Emilia region revealed significant increases in CO_2, CH_4, and H_2 concentrations before and after the 2012 Emilia-Romagna earthquake swarm (Sciarra et al., 2017). In Gujarat, India, continuous Rn monitoring successfully detected significant increases in Rn concentrations days to weeks before four earthquakes with magnitudes ranging from 4.0 to 4.1 (Sahoo et al., 2020; Torkar et al., 2010) used soil gas Rn to predict 10 out of 13 earthquake events using an artificial neural network with a backpropagation algorithm. These findings highlight that seismic activity induces the release of deep-sourced gases along fault zones, leading to changes in soil gas concentrations that can serve as indicators for seismic activity and earthquake monitoring.

Hot spring gas geochemistry also shows potential as an indicator of seismic activity. Before the 2008 Tibet M 6.3 earthquake in China, significant anomalies in He and Rn concentrations were observed in hot springs at Bakreswar and Tatta Pani in India (Chaudhuri et al., 2011). Prior to the 1955 Kobe M_W 6.9 earthquake in Japan, Rn release rates in groundwater and atmospheric Rn concentrations significantly increased, correlating with crustal strain fluctuations (Yasuoka et al., 2009). During the 2016 Kumamoto M 7.3 earthquake in Japan, He concentration changes in deep groundwater correlated with volumetric strain changes (Sano et al., 2016). Thus, hot spring gas concentrations can be crucial for earthquake monitoring.

Throughout different stages of earthquake preparation and occurrence, the contribution of deep-sourced and shallow-sourced fluids dynamically evolves. For instance, before and after the 2011 Van M_W 7.2 earthquake in Turkey (Aydın et al., 2015) and the 2013 Lushan M_S 7.0 earthquake in China (Chen et al., 2015), significant increases in $^3He/^4He$ and $\delta^{13}C_{CO2}$ values were observed in hot spring gases in fault zones. As aftershock activity waned, the supply of mantle-derived gases decreased, leading to a decline in $^3He/^4He$ and $\delta^{13}C_{CO2}$ values. Following the 2008 Iwate-Miyagi M 7.2 earthquake in Japan, the ascent of mantle-derived fluids caused a maximum 85% increase in the $^3He/^4He$ value in hot spring gases near the epicenter within a week (Horiguchi and Matsuda, 2008). After 2 M 6.0 earthquakes in the Emilia, Italy in 2012, the $\delta^{13}C_{CO2}$ and $\delta^{13}C_{CH4}$ values of gases released from fault zones in the epicentral area significantly decreased, likely due to the seismic-induced release of shallow biogenic CH_4 and CO_2, overshadowing deep thermogenic gases (Sciarra et al., 2017). These changes in He and C isotopes in hot spring gases near fault zones before and after earthquakes underscore how seismic activity promotes the mixing of gases from various sources, particularly the ascent of mantle-derived fluids.

Atmospheric gas variations induced by seismic activity are integral to understanding the lithosphere-atmosphere coupling mechanism (Veefkind et al., 2012; Jing et al., 2019). Advances in hyperspectral sensors with atmospheric detection capabilities have enabled extensive studies on gas changes associated with seismic and volcanic events (Tramutoli et al., 2013) (Figure 5). Notable anomalies in gases such as CH_4, CO, CO_2 and O_3 have been documented before and after significant earthquakes, such as the 2004 Sumatra-Andaman M_W 9.1 earthquake and the 2005 Sumatra-Nias M_W 8.6 earthquake (Cui et al., 2023), the 2008 Wenchuan M_S 8.0 earthquake and 2013 Lushan M_S 7.0 earthquake in China (Cui et al., 2017), and the 2015 Gorkha M 7.8 earthquake and Dolakha M 7.3 earthquake in Nepal (Jing et al., 2019). Furthermore, a statistical analysis using the Adaboost machine learning algorithm examined infrared and hyperspectral gas parameters among 10 different variables before and after 1,371 global earthquakes of magnitude ≥6 from 2006 to 2013, identifying O_3 and CO_2 as significant contributors to earthquake prediction (Xiong et al., 2021).

4 Conclusion

Active fault zones are vital conduits for deep fluids migrating to the Earth's surface. The gases released (such as CO_2, Rn, and He) contain valuable information about the physical and chemical evolution of the Earth's interior and further reveal fault activity

and seismic events. Isotope tracing is essential for identifying fluid sources, migration pathways, circulation processes, and formation mechanisms.

Gas release in fault zones is closely related to fault activity, and higher fault activity corresponds to higher soil gas release. Different fault types exhibit distinct geochemical fluid characteristics. Fault zones with strong gas release are preferred locations for studying regional geodynamics and monitoring subsurface tectonic activities.

Seismic activity alters stress states, which promotes the release of deep-sourced gases along fault zones and leads to anomalies in concentrations of soil gas and hot spring gas. These anomalies can serve as indicators of seismic activity, providing crucial information for earthquake monitoring. Isotopic changes in hot spring gases before and after earthquakes further demonstrate that seismic activity promotes the mixing of gases from different sources, especially the ascent of crustal or mantle-derived fluids.

In summary, fault zones are crucial for deep fluid migration and as research subjects for monitoring tectonic activity and earthquake prediction. Analyzing fault zone gas geochemistry enhances our understanding of the material cycle and energy exchange processes in the Earth's interior, providing a scientific basis for disaster prevention and mitigation.

Author contributions

JL: Conceptualization, Data curation, Formal Analysis, Funding acquisition, Investigation, Methodology, Project administration, Resources, Software, Supervision, Validation, Visualization, Writing–original draft, Writing–review and editing. ZL: Conceptualization, Data curation, Formal Analysis, Funding acquisition, Investigation, Methodology, Project administration, Resources, Software, Supervision, Validation, Visualization, Writing–original draft, Writing–review and editing. ZC: Writing–original draft, Writing–review and editing. YG: Conceptualization, Data curation, Formal Analysis, Writing–original draft. YH: Conceptualization, Data curation, Formal Analysis, Writing–original draft. HG: Conceptualization, Data curation, Formal Analysis, Funding acquisition, Writing–original draft.

Funding

The author(s) declare that financial support was received for the research, authorship, and/or publication of this article. This work was supported by the National Natural Science Foundation of China (Grant No. 42372282) and the Science for Earthquake Resilience of China Earthquake Administration (Grant No. XH22035).

Conflict of interest

The authors declare that the research was conducted in the absence of any commercial or financial relationships that could be construed as a potential conflict of interest.

Publisher's note

All claims expressed in this article are solely those of the authors and do not necessarily represent those of their affiliated organizations, or those of the publisher, the editors and the reviewers. Any product that may be evaluated in this article, or claim that may be made by its manufacturer, is not guaranteed or endorsed by the publisher.

References

Andrews, J. N. (1985). The isotopic composition of radiogenic helium and its use to study groundwater movement in confined aquifers. *Chem. Geol.* 49 (1), 339–351. doi:10.1016/0009-2541(85)90166-4

Annunziatellis, A., Beaubien, S., Bigi, S., Ciotoli, G., Coltella, M., and Lombardi, S. (2008). Gas migration along fault systems and through the vadose zone in the Latera caldera (central Italy): implications for CO_2 geological storage. *Int. J. Greenh. Gas. Control.* 2 (3), 353–372. doi:10.1016/j.ijggc.2008.02.003

Arai, T., Okusawa, T., and Tsukahara, H. (2001). Behavior of gases in the Nojima Fault Zone revealed from the chemical composition and carbon isotope ratio of gases extracted from DPRI 1800 m drill core. *Isl. Arc.* 10 (3-4), 430–438. doi:10.1111/j.1440-1738.2001.00341.x

Ármannsson, H., Fridriksson, T., and Kristjánsson, B. R. (2005). CO_2 emissions from geothermal power plants and natural geothermal activity in Iceland. *Geothermics* 34 (3), 286–296. doi:10.1016/j.geothermics.2004.11.005

Audi, G., Bersillon, O., Blachot, J., and Wapstra, A. H. (2003). The Nubase evaluation of nuclear and decay properties. *Nucl. Phys. A* 729 (1), 3–128. doi:10.1016/j.nuclphysa.2003.11.001

Aulbach, S., Lin, A. B., Weiss, Y., and Yaxley, G. M. (2020). Wehrlites from continental mantle monitor the passage and degassing of carbonated melts. *Geochem. Perspect. Lett.* 15, 30–34. doi:10.7185/geochemlet.2031

Aydın, H., Hilton, D. R., Güleç, N., and Mutlu, H. (2015). Post-earthquake anomalies in He-CO_2 isotope and relative abundance systematics of thermal waters: the case of the 2011 Van earthquake, eastern Anatolia, Turkey. *Chem. Geol.* 411, 1–11. doi:10.1016/j.chemgeo.2015.06.019

Barnes, I., Irwin, W. P., and White, D. E. (1978). *Global distribution of carbon dioxide discharges, and major zones of seismicity*. Menlo Park: United States: United States Department of the Interior Geological Survey.

Becker, J. A., Bickle, M. J., Galy, A., and Holland, T. J. B. (2008). Himalayan metamorphic CO_2 fluxes: Quantitative constraints from hydrothermal springs. *Earth Planet. Sci. Lett.* 265 (3), 616–629. doi:10.1016/j.epsl.2007.10.046

Bergfeld, D., Goff, F., and Janik, C. J. (2001). Carbon isotope systematics and CO_2 sources in the Geysers-Clear Lake region, northern California, USA. *Geothermics* 30 (2-3), 303–331. doi:10.1016/S0375-6505(00)00051-1

Bhongsuwan, T., Pisapak, P., and Dürrast, H. (2011). Result of alpha track detection of radon in soil gas in the Khlong Marui Fault Zone, Southern Thailand: a possible earthquake precursor. *Wārasān Songkhlā Nakharin* 33 (5), 609–616.

Bond, C. E., Kremer, Y., Johnson, G., Hicks, N., Lister, R., Jones, D. G., et al. (2017). The physical characteristics of a CO_2 seeping fault: the implications of fracture permeability for carbon capture and storage integrity. *Int. J. Greenh. Gas. Control.* 61, 49–60. doi:10.1016/j.ijggc.2017.01.015

Brantley, S. L., and Koepenick, K. W. (1995). Measured carbon dioxide emissions from Oldoinyo Lengai and the skewed distribution of passive volcanic fluxes. *Geology* 23 (10), 933–936. doi:10.1130/0091-7613(1995)023<0933:mcdefo>2.3.co;2

Brune, S., Williams, S. E., and Müller, R. D. (2017). Potential links between continental rifting, CO_2 degassing and climate change through time. *Nat. Geosci.* 10 (12), 941–946. doi:10.1038/s41561-017-0003-6

Camarda, M., De Gregorio, S., Di Martino, R. M. R., and Favara, R. (2016). Temporal and spatial correlations between soil CO_2 flux and crustal stress. *J. Geophys. Res. Solid Earth.* 121 (10), 7071–7085. doi:10.1002/2016JB013297

Capaccioni, B., Tassi, F., Cremonini, S., Sciarra, A., and Vaselli, O. (2015). Ground heating and methane oxidation processes at shallow depth in Terre Calde di Medolla (Italy): Observations and conceptual model. *J. Geophys. Res. Solid Earth.* 120 (5), 3048–3064. doi:10.1002/2014JB011635

Caracausi, A., Buttitta, D., Picozzi, M., Paternoster, M., and Stabile, T. A. (2022). Earthquakes control the impulsive nature of crustal helium degassing to the atmosphere. *Commun. Earth Environ.* 3 (1), 224. doi:10.1038/s43247-022-00549-9

Chaudhuri, H., Bari, W., Iqbal, N., Bhandari, R. K., Ghose, D., Sen, P., et al. (2011). Long range gas-geochemical anomalies of a remote earthquake recorded simultaneously at distant monitoring stations in India. *Geochem. J.* 45 (2), 137–156. doi:10.2343/geochemj.1.0109

Chen, Z., Li, Y., Liu, Z., Wang, J., Zhou, X., and Du, J. (2018). Radon emission from soil gases in the active fault zones in the Capital of China and its environmental effects. *Sci. Rep.* 8 (1), 16772. doi:10.1038/s41598-018-35262-1

Chen, Z., Zhou, X., Du, J., Xie, C., Liu, L., Li, Y., et al. (2015). Hydrochemical characteristics of hot spring waters in the Kangding district related to the Lushan M_S=7.0 earthquake in Sichuan, China. *Nat. Hazards Earth Syst. Sci.* 15 (6), 1149–1156. doi:10.5194/nhess-15-1149-2015

Cheng, Y., Wang, N., and Hou, S. (2005). *Nuclear radiation field and radioactive exploration*. Beijing: Geology Press. (in Chinese).

Ciotoli, G., Bigi, S., Tartarello, C., Sacco, P., Lombardi, S., Ascione, A., et al. (2014). Soil gas distribution in the main coseismic surface rupture zone of the 1980, M_S=6.9, Irpinia earthquake (southern Italy). *J. Geophys. Res. Solid Earth.* 119 (3), 2440–2461. doi:10.1002/2013JB010508

Ciotoli, G., Lombardi, S., and Annunziatellis, A. (2007). Geostatistical analysis of soil gas data in a high seismic intermontane basin: Fucino Plain, central Italy. *J. Geophys. Res. Solid Earth.* 112 (B5), B05407. doi:10.1029/2005JB004044

Cui, Y., Ouzounov, D., Hatzopoulos, N., Sun, K., Zou, Z., and Du, J. (2017). Satellite observation of CH4 and CO anomalies associated with the Wenchuan M_S 8.0 and Lushan M_S 7.0 earthquakes in China. *Chem. Geol.* 469, 185–191. doi:10.1016/j.chemgeo.2017.06.028

Cui, Y., Zheng, C., Jiang, L., Huang, J., Sun, F., Zou, Z., et al. (2023). Variations of multiple gaseous emissions associated with the great Sumatra earthquakes in 2004 and 2005. *Chem. Geol.* 618, 121311. doi:10.1016/j.chemgeo.2023.121311

Di Martino, R. M. R., Capasso, G., and Camarda, M. (2016). Spatial domain analysis of carbon dioxide from soils on Vulcano Island: implications for CO_2 output evaluation. *Chem. Geol.* 444, 59–70. doi:10.1016/j.chemgeo.2016.09.037

El-Arabi, A. M., Abbady, A., Ahmed, N. K., Michel, R., El-Kamel, A. H., and Abbady, A. G. E. (2006). Assessment of radon-222 concentrations and exhalation rates of rocks and building materials. *Indian J. Pure Appl. Phys.* 44 (4), 287–291.

Etiope, G., Beneduce, P., Calcara, M., Favali, P., Frugoni, F., Schiattarella, M., et al. (1999). Structural pattern and CO_2-CH_4 degassing of Ustica island, southern Tyrrhenian basin. *J. Volcanol. Geotherm. Res.* 88 (4), 291–304. doi:10.1016/S0377-0273(99)00010-4

Etiope, G., and Martinelli, G. (2002). Migration of carrier and trace gases in the geosphere: an overview. *Phys. Earth Planet. Inter.* 129 (3), 185–204. doi:10.1016/S0031-9201(01)00292-8

Faulkner, D. R., Jackson, C. A. L., Lunn, R. J., Schlische, R. W., Shipton, Z. K., Wibberley, C. A. J., et al. (2010). A review of recent developments concerning the structure, mechanics and fluid flow properties of fault zones. *J. Struct. Geol.* 32 (11), 1557–1575. doi:10.1016/j.jsg.2010.06.009

Flügge, S., and Zimens, K. E. (1939). Die Bestimmung von Korngrößen und von Diffusionskonstanten aus dem Emaniervermögen. *Z. für Phys. Chem.* 42B, 179–220. doi:10.1515/zpch-1939-4215

Fu, C. C., Yang, T. F., Tsai, M. C., Lee, L. C., Liu, T. K., Walia, V., et al. (2017). Exploring the relationship between soil degassing and seismic activity by continuous radon monitoring in the Longitudinal Valley of eastern Taiwan. *Chem. Geol.* 469, 163–175. doi:10.1016/j.chemgeo.2016.12.042

Gao, Z., Chen, Z., He, H., Liu, Z., Lu, C., Wang, H., et al. (2024). Characteristics and main controlling factors of helium resources in the main petroliferous basins of the North China Craton. *Acta Oceanol. Sin.* 43 (2), 23–33. doi:10.1007/s13131-024-2290-2

Giammanco, S., Immè, G., Mangano, G., Morelli, D., and Neri, M. (2009). Comparison between different methodologies for detecting radon in soil along an active fault: the case of the Pernicana fault system, Mt. Etna (Italy). *Appl. Radiat. Isot.* 67 (1), 178–185. doi:10.1016/j.apradiso.2008.09.007

Girault, F., and Perrier, F. (2014). The Syabru-Bensi hydrothermal system in central Nepal: 2. Modeling and significance of the radon signature. *J. Geophys. Res. Solid Earth.* 119 (5), 4056–4089. doi:10.1002/2013JB010302

Graham, D. W. (2002). Noble gas isotope geochemistry of Mid-Ocean Ridge and ocean island basalts: Characterization of mantle source reservoirs. *Rev. Mineralogy Geochem.* 47 (1), 247–317. doi:10.2138/rmg.2002.47.8

Gresse, M., Vandemeulebrouck, J., Byrdina, S., Chiodini, G., and Bruno, P. P. (2016). Changes in CO_2 diffuse degassing induced by the passing of seismic waves. *J. Volcanol. Geotherm. Res.* 320, 12–18. doi:10.1016/j.jvolgeores.2016.04.019

Hansberry, R. L., King, R. C., Holford, S. P., Hand, M., and Debenham, N. (2021). How wide is a fault damage zone? Using network topology to examine how fault-damage zones overprint regional fracture networks. *J. Struct. Geol.* 146, 104327. doi:10.1016/j.jsg.2021.104327

Hernández Perez, P., Notsu, K., Tsurumi, M., Mori, T., Ohno, M., Shimoike, Y., et al. (2003). Carbon dioxide emissions from soils at Hakkoda, north Japan. *J. Geophys. Res. Solid Earth.* 108 (B4), 1–10. doi:10.1029/2002JB001847

Hong, W., Yang, T. F., Walia, V., Lin, S., Fu, C., Chen, Y., et al. (2010). Nitrogen as the carrier gas for helium emission along an active fault in NW Taiwan. *Appl. Geochem.* 25 (4), 593–601. doi:10.1016/j.apgeochem.2010.01.016

Horiguchi, K., and Matsuda, J. I. (2008). On the change of ^{3}He/^{4}He ratios in hot spring gases after the Iwate-Miyagi Nairiku Earthquake in 2008. *Geochem. J.* 42, e1–e4. doi:10.2343/geochemj.42.e1

Horton, F., Asimow, P. D., Farley, K. A., Curtice, J., Kurz, M. D., Blusztajn, J., et al. (2023). Highest terrestrial ^{3}He/^{4}He credibly from the core. *Nature* 623 (7985), 90–94. doi:10.1038/s41586-023-06590-8

Hunt, J. A., Zafu, A., Mather, T. A., Pyle, D. M., and Barry, P. H. (2017). Spatially variable CO_2 degassing in the main Ethiopian Rift: implications for magma storage, volatile transport, and rift-related emissions. *Geochem. Geophys. Geosyst.* 18 (10), 3714–3737. doi:10.1002/2017GC006975

Jaishi, H. P., Singh, S., Tiwari, R. P., and Tiwari, R. C. (2014). Correlation of radon anomalies with seismic events along Mat fault in Serchhip District, Mizoram, India. *Appl. Radiat. Isot.* 86, 79–84. doi:10.1016/j.apradiso.2013.12.040

Jing, F., Singh, R. P., and Shen, X. (2019). Land – atmosphere – Meteorological coupling associated with the 2015 Gorkha (M 7.8) and Dolakha (M 7.3) Nepal earthquakes. *Geomatics, Nat. Hazards Risk* 10 (1), 1267–1284. doi:10.1080/19475705.2019.1573629

Keeling, C. D., Piper, S. C., Bacastow, R. B., Wahlen, M., Whorf, T. P., Heimann, M., et al. (2005). *Atmospheric CO_2 and $^{13}CO_2$ exchange with the terrestrial biosphere and oceans from 1978 to 2000: observations and carbon cycle implications A History of Atmospheric CO_2 and its Effects on Plants, Animals, and Ecosystems*, 5. New York, United States: Springer New York, 83–113. (Reprinted. doi:10.1007/0-387-27048-5_5

King, C. (1978). Radon emanation on san Andreas Fault. *Nature* 271 (5645), 516–519. doi:10.1038/271516a0

Klusman, R. W. (1993). *Soil gas and related methods for natural resource exploration*. New York, United States: Wiley and Sons.

Kucharič, L. U., Bodiš, D., Panák, D., Liščák, P., and Božíková, J. (2015). A contribution of CO_2 released from mineral springs into overall volume of annual CO_2 emissions in the Slovak Republic. *Environ. Earth Sci.* 73 (1), 231–238. doi:10.1007/s12665-014-3418-z

Kulongoski, J. T., Hilton, D. R., Barry, P. H., Esser, B. K., Hillegonds, D., and Belitz, K. (2013). Volatile fluxes through the Big Bend section of the san Andreas Fault, California: helium and carbon-dioxide systematics. *Chem. Geol.* 339, 92–102. doi:10.1016/j.chemgeo.2012.09.007

Lee, H., Kim, H., Kagoshima, T., Park, J., Takahata, N., and Sano, Y. (2019). Mantle degassing along strike-slip faults in the Southeastern Korean Peninsula. *Sci. Rep.* 9 (1), 15334. doi:10.1038/s41598-019-51719-3

Lee, H., Muirhead, J. D., Fischer, T. P., Ebinger, C. J., Kattenhorn, S. A., Sharp, Z. D., et al. (2016). Massive and prolonged deep carbon emissions associated with continental rifting. *Nat. Geosci.* 9 (2), 145–149. doi:10.1038/ngeo2622

Li, Y., Chen, Z., Sun, A., Liu, Z., Caracausi, A., Martinelli, G., et al. (2023). Geochemical features and seismic imaging of the tectonic zone between the Tibetan Plateau and Ordos Block, central northern China. *Chem. Geol.* 622, 121386. doi:10.1016/j.chemgeo.2023.121386

Li, Y., Du, J., Wang, X., Zhou, X., Xie, C., and Cui, Y. (2013). Spatial variations of soil gas geochemistry in the Tangshan area of northern China. *Terr. Atmos. Ocean. Sci.* 24 (3), 323–332. doi:10.3319/TAO.2012.11.26.01(TT

Liu, J. H. (2006). *Numerical simulation, inversion fitting of radon migration in the overburden above active fault*. China: Jilin University, 1–155. (in Chinese with English abstract).

Liu, L., Chen, Z., Li, Y., Liu, Z., Hu, L., Wang, X., et al. (2023b). Emission of Rn and CO_2 from soil at fault zones caused by seismic waves. *Earth Space Sci.* 10 (6), e2023EA003012. doi:10.1029/2023EA003012

Liu, Z., Chen, Z., Li, Y., Zhao, Z., Sun, A., Li, J., et al. (2024). Crust uplift controls the massive emissions of 222Rn and CO_2 in the Northeastern Tibetan Plateau, China. *Chem. Geol.* 663, 122280. doi:10.1016/j.chemgeo.2024.122280

Liu, Z., Li, Y., Chen, Z., Zhao, Z., Huangfu, R., Zhao, Y., et al. (2023a). Environmental impacts of ^{222}Rn, Hg and CO_2 emissions from the fault zones in the western margin of the Ordos block, China. *Environ. Geochem. Health.* 45 (2), 457–472. doi:10.1007/s10653-022-01350-5

Lupton, J. E. (1983). Terrestrial inert gases; Isotope tracer studies and clues to primordial components in the mantle. *Annu. Rev. Earth Planet. Sci.* 11 (1), 371–414. doi:10.1146/annurev.ea.11.050183.002103

Manisa, K., Erdogan, M., Zedef, V., Bircan, H., and Biçer, A. (2022). Variations of ^{222}Rn concentrations over active fault system in Simav, Kütahya, Western Turkey:

possible causes for soil-gas 222Rn anomalies. *Appl. Radiat. Isot.* 190, 110484. doi:10.1016/j.apradiso.2022.110484

Martinelli, G. (2020). Previous, current, and future trends in research into earthquake precursors in geofluids. *Geosciences* 10 (5), 189. doi:10.3390/geosciences10050189

Martinelli, G., Albarello, D., and Mucciarelli, M. (1995). Radon emissions from mud volcanoes in northern Italy; Possible connection with local seismicity. *Geophys. Res. Lett.* 22 (15), 1989–1992. doi:10.1029/95GL01785

Martinelli, G., and Dadomo, A. (2017). Factors constraining the geographic distribution of earthquake geochemical and fluid-related precursors. *Chem. Geol.* 469, 176–184. doi:10.1016/j.chemgeo.2017.01.006

Miklyaev, P. S., Petrova, T. B., Marennyy, A. M., Shchitov, D. V., Sidyakin, P. A., Murzabekov, M., et al. (2020). High seasonal variations of the radon exhalation from soil surface in the fault zones (Baikal and North Caucasus regions). *J. Environ. Radioact.* 219, 106271. doi:10.1016/j.jenvrad.2020.106271

Muto, J., Yasuoka, Y., Miura, N., Iwata, D., Nagahama, H., Hirano, M., et al. (2021). Preseismic atmospheric radon anomaly associated with 2018 Northern Osaka earthquake. *Sci. Rep.* 11 (1), 7451. doi:10.1038/s41598-021-86777-z

Padrón, E., Padilla, G., Hernández, P. A., Pérez, N. M., Calvo, D., Nolasco, D., et al. (2013). Soil gas geochemistry in relation to eruptive fissures on Timanfaya volcano, Lanzarote Island (Canary Islands, Spain). *J. Volcanol. Geotherm. Res.* 250, 91–99. doi:10.1016/j.jvolgeores.2012.10.013

Pankina G, R., Mekhtieva, L. V., Gurieva, M. S., and Shkutnik, N. E. (1979). Origin of CO_2 in petroleum gases (from the isotopic composition of carbon). *Int. Geol. Rev.* 21 (5), 535–539. doi:10.1080/00206818209467089

Papastefanou, C. (2010). Variation of radon flux along active fault zones in association with earthquake occurrence. *Radiat. Meas.* 45 (8), 943–951. doi:10.1016/j.radmeas.2010.04.015

Parks, M. M., Caliro, S., Chiodini, G., Pyle, D. M., Mather, T. A., Berlo, K., et al. (2013). Distinguishing contributions to diffuse CO_2 emissions in volcanic areas from magmatic degassing and thermal decarbonation using soil gas ^{222}Rn-δ^{13}C systematics: Application to Santorini volcano, Greece. *Earth Planet. Sci. Lett.* 377-378, 180–190. doi:10.1016/j.epsl.2013.06.046

Pereira, A., Lamas, R., Miranda, M., Domingos, F., Neves, L., Ferreira, N., et al. (2017). Estimation of the radon production rate in granite rocks and evaluation of the implications for geogenic radon potential maps: a case study in Central Portugal. *J. Environ. Radioact.* 166, 270–277. doi:10.1016/j.jenvrad.2016.08.022

Phong Thu, H. N., Van Thang, N., and Hao, L. C. (2020). The effects of some soil characteristics on radon emanation and diffusion. *J. Environ. Radioact.* 216, 106189. doi:10.1016/j.jenvrad.2020.106189

Porstendörfer, J. (1994). Properties and behaviour of radon and thoron and their decay products in the air. *J. Aerosol Sci.* 25 (2), 219–263. doi:10.1016/0021-8502(94)90077-9

Randazzo, P., Caracausi, A., Aiuppa, A., Cardellini, C., Chiodini, G., D'Alessandro, W., et al. (2021). Active degassing of deeply sourced fluids in Central Europe: new evidences from a geochemical study in Serbia. *Geochem. Geophys. Geosyst.* 22 (11), e2021GC010017. doi:10.1029/2021GC010017

Rojstaczer, S. A., Ingebritsen, S. E., and Hayba, D. O. (2008). Permeability of continental crust influenced by internal and external forcing. *Geofluids* 8 (2), 128–139. doi:10.1111/j.1468-8123.2008.00211.x

Rovira, P., and Vallejo, V. R. (2008). Changes in δ^{13}C composition of soil carbonates driven by organic matter decomposition in a Mediterranean climate: a field incubation experiment. *Geoderma* 144 (3), 517–534. doi:10.1016/j.geoderma.2008.01.006

Sahoo, S. K., Katlamudi, M., Barman, C., and Lakshmi, G. U. (2020). Identification of earthquake precursors in soil radon-222 data of Kutch, Gujarat, India using empirical mode decomposition based Hilbert Huang Transform. *J. Environ. Radioact.* 222, 106353. doi:10.1016/j.jenvrad.2020.106353

Sakoda, A., Ishimori, Y., and Yamaoka, K. (2011). A comprehensive review of radon emanation measurements for mineral, rock, soil, mill tailing and fly ash. *Appl. Radiat. Isot.* 69 (10), 1422–1435. doi:10.1016/j.apradiso.2011.06.009

Sano, Y., Takahata, N., Kagoshima, T., Shibata, T., Onoue, T., and Zhao, D. (2016). Groundwater helium anomaly reflects strain change during the 2016 Kumamoto earthquake in Southwest Japan. *Sci. Rep.* 6, 37939. doi:10.1038/srep37939

Sano, Y., and Wakita, H. (1985). Geographical distribution of ^{3}He/^{4}He ratios in Japan: implications for arc tectonics and incipient magmatism. *J. Geophys. Res. Solid Earth.* 90 (B10), 8729–8741. doi:10.1029/JB090iB10p08729

Sawyer, G. M., Carn, S. A., Tsanev, V. I., Oppenheimer, C., and Burton, M. (2008). Investigation into magma degassing at Nyiragongo volcano, Democratic Republic of the Congo. *Geochem. Geophys. Geosyst.* 9 (2), Q02017. doi:10.1029/2007GC001829

Sbrana, A., Marianelli, P., Belgiorno, M., Sbrana, M., and Ciani, V. (2020). Natural CO_2 degassing in the Mount Amiata volcanic-geothermal area. *J. Volcanol. Geotherm. Res.* 397, 106852. doi:10.1016/j.jvolgeores.2020.106852

Sciarra, A., Cantucci, B., and Coltorti, M. (2017). Learning from soil gas change and isotopic signatures during 2012 Emilia seismic sequence. *Sci. Rep.* 7 (1), 14187. doi:10.1038/s41598-017-14500-y

Seminsky, K. Z., Demberel, S., Tugarina, M. A., Ganzorig, D., and Bornyakov, S. A. (2013). First estimates of soil radon activity in the fault zones of central Mongolia. *Dokl. Earth Sci.* 448 (1), 21–24. doi:10.1134/S1028334X12110128

Shao, W., Liu, Z., Li, Y., Chen, Z., Lu, C., Zhao, C., et al. (2024). Geochemical characteristics of thermal springs and insights into the intersection between the Xiaojiang Fault and the red River Fault, southeastern Tibet plateau. *Geochem. Geophys. Geosyst.* 25 (3), e2023GC011431. doi:10.1029/2023GC011431

Singh, S., Jaishi, H. P., Tiwari, R. P., and Tiwari, R. C. (2016). A study of variation in soil gas concentration associated with earthquakes near Indo-Burma Subduction zone. *Geoenviron. Disasters* 3 (22), 22–28. doi:10.1186/s40677-016-0055-8

Soddy, F. (1913). "Radioactivity," in *Annual Reports on the Progress of Chemistry* (London: The Chemical Society), 262–288.

Sun, X., Yang, P., Xiang, Y., Si, X., and Liu, D. (2018). Across-fault distributions of radon concentrations in soil gas for different tectonic environments. *Geosci. J.* 22 (2), 227–239. doi:10.1007/s12303-017-0028-2

Sun, Y., Guo, Z., and Fortin, D. (2021). Carbon dioxide emission from monogenetic volcanoes in the Mt. Changbai volcanic field, NE China. *Int. Geol. Rev.* 63 (13-14), 1803–1820. doi:10.1080/00206814.2020.1802782

Tamburello, G., Pondrelli, S., Chiodini, G., and Rouwet, D. (2018). Global-scale control of extensional tectonics on CO_2 earth degassing. *Nat. Commun.* 9 (1), 4608. doi:10.1038/s41467-018-07087-z

Tamir, G., Shenker, M., Heller, H., Bloom, P. R., Fine, P., and Bar-Tal, A. (2011). Can soil carbonate dissolution lead to overestimation of soil respiration? *Soil Sci. Soc. Am. J.* 75 (4), 1414–1422. doi:10.2136/sssaj2010.0396

Tan, C. (2016). Big gaps and short bridges: a model for solving the discontinuity problem. *Answers Res. J.* 9, 149–162.

Tanikawa, W., Sakaguchi, M., Tadai, O., and Hirose, T. (2010). Influence of fault slip rate on shear-induced permeability. *J. Geophys. Res. Solid Earth.* 115 (B07412), 1–18. doi:10.1029/2009JB007013

Tian, J., Pang, Z., Liao, D., and Zhou, X. (2021). Fluid geochemistry and its implications on the role of deep faults in the genesis of high temperature systems in the eastern edge of the Qinghai Tibet Plateau. *Appl. Geochem.* 131, 105036. doi:10.1016/j.apgeochem.2021.105036

Torkar, D., Zmazek, B., Vaupotič, J., and Kobal, I. (2010). Application of artificial neural networks in simulating radon levels in soil gas. *Chem. Geol.* 270, 1–8. doi:10.1016/j.chemgeo.2009.09.017

Tramutoli, V., Aliano, C., Corrado, R., Filizzola, C., Genzano, N., Lisi, M., et al. (2013). On the possible origin of thermal infrared radiation (TIR) anomalies in earthquake-prone areas observed using robust satellite techniques (RST). *Chem. Geol.* 339, 157–168. doi:10.1016/j.chemgeo.2012.10.042

Tuccimei, P., Mollo, S., Vinciguerra, S., Castelluccio, M., and Soligo, M. (2010). Radon and thoron emission from lithophysae-rich tuff under increasing deformation: an experimental study. *Geophys. Res. Lett.* 37 (L05305), 1–5. doi:10.1029/2009GL042134

Veefkind, J. P., Aben, I., McMullan, K., Förster, H., de Vries, J., Otter, G., et al. (2012). TROPOMI on the ESA Sentinel-5 Precursor: a GMES mission for global observations of the atmospheric composition for climate, air quality and ozone layer applications. *Remote Sens. Environ.* 120, 70–83. doi:10.1016/j.rse.2011.09.027

Voltattorni, N., Lombardi, S., and Beaubien, S. E. (2015). Gas migration from two mine districts: the Tolfa (Lazio, Central Italy) and the Neves-Corvo (Baixo Alentejo, Portugal) case studies. *J. Geochem. Explor.* 152, 37–53. doi:10.1016/j.gexplo.2015.01.011

Walia, V., Lin, S. J., Fu, C. C., Yang, T. F., Hong, W., Wen, K., et al. (2010). Soil-gas monitoring: a tool for fault delineation studies along Hsinhua fault (Tainan), southern Taiwan. *Appl. Geochem.* 25 (4), 602–607. doi:10.1016/j.apgeochem.2010.01.017

Weinlich, F. H. (2014). Carbon dioxide controlled earthquake distribution pattern in the NW Bohemian swarm earthquake region, western Eger Rift, Czech Republic - gas migration in the crystalline basement. *Geofluids* 14 (2), 143–159. doi:10.1111/gfl.12058

White, D. E. (1957). Magmatic, connate and metamorphic waters. *Geol. Soc. Am. Bull.* 68 (12), 1659–1682. doi:10.1130/0016-7606(1957)68[1659:mcamw]2.0.co;2

Woith, H. (2015). Radon earthquake precursor: a short review. *Eur. Phys. J. ST, Special Top.* 224 (4), 611–627. doi:10.1140/epjst/e2015-02395-9

Xiong, P., Tong, L., Zhang, K., Shen, X., Battiston, R., Ouzounov, D., et al. (2021). Towards advancing the earthquake forecasting by machine learning of satellite data. *Sci. Total Environ.* 771, 145256. doi:10.1016/j.scitotenv.2021.145256

Yasuoka, Y., Kawada, Y., Nagahama, H., Omori, Y., Ishikawa, T., Tokonami, S., et al. (2009). Preseismic changes in atmospheric radon concentration and crustal strain. *Phys. Chem. Earth.* 34 (6-7), 431–434. doi:10.1016/j.pce.2008.06.005

Yuce, G., Fu, C. C., D'Alessandro, W., Gulbay, A. H., Lai, C. W., Bellomo, S., et al. (2017). Geochemical characteristics of soil radon and carbon dioxide within the Dead Sea Fault and Karasu Fault in the Amik basin (Hatay), Turkey. *Chem. Geol.* 469, 129–146. doi:10.1016/j.chemgeo.2017.01.003

Zhang, M., Guo, Z., Xu, S., Barry, P. H., Sano, Y., Zhang, L., et al. (2021). Linking deeply-sourced volatile emissions to plateau growth dynamics in southeastern Tibetan Plateau. *Nat. Commun.* 12 (1), 4157. doi:10.1038/s41467-021-24415-y

Zhao, Y., Liu, Z., Li, Y., Hu, L., Chen, Z., Sun, F., et al. (2021). A case study of 10 years groundwater radon monitoring along the eastern margin of the Tibetan Plateau and in its adjacent regions: implications for earthquake surveillance. *Appl. Geochem.* 131, 105014. doi:10.1016/j.apgeochem.2021.105014

Zheng, G., Martinelli, G., Wang, Y., Li, S., and Ma, X. (2022). Notes for a history of gas geochemistry. *J. Asian Earth Sci.* 33 (6), 1614–1623. doi:10.1007/s12583-022-1758-2

Zheng, G., Xu, S., Liang, S., Shi, P., and Zhao, J. (2013). Gas emission from the Qingzhu river after the 2008 Wenchuan earthquake, Southwest China. *Chem. Geol.* 339, 187–193. doi:10.1016/j.chemgeo.2012.10.032

Zheng, G., Xu, W., Etiope, G., Ma, X., Liang, S., Fan, Q., et al. (2018). Hydrocarbon seeps in petroliferous basins in China: a first inventory. *J. Asian Earth Sci.* 151, 269–284. doi:10.1016/j.jseaes.2017.10.037

Zhou, X., Chen, Z., and Cui, Y. (2016). Environmental impact of CO_2, Rn, Hg degassing from the rupture zones produced by Wenchuan M_S8.0 earthquake in western Sichuan, China. *Environ. Geochem. Health.* 38 (5), 1067–1082. doi:10.1007/s10653-015-9773-1

Zondervan, J. R., Hilton, R. G., Dellinger, M., Clubb, F. J., Roylands, T., and Ogric, M. (2023). Rock organic carbon oxidation CO_2 release offsets silicate weathering sink. *Nature* 623 (7986), 329–333. doi:10.1038/s41586-023-06581-9

frontiers | Frontiers in Earth Science

TYPE Original Research
PUBLISHED 21 November 2024
DOI 10.3389/feart.2024.1482158

OPEN ACCESS

EDITED BY
Yongsheng Zhou,
China Earthquake Administration, China

REVIEWED BY
Zhengzheng Cao,
Henan Polytechnic University, China
Yifang Chen,
China Earthquake Administration, China

*CORRESPONDENCE
Xuefei Wu,
wuxuefei1212@163.com

RECEIVED 17 August 2024
ACCEPTED 29 October 2024
PUBLISHED 21 November 2024

CITATION
Wu X, Xie Q and Yan J (2024) Research on microseismic source location based on time quality constraints.
Front. Earth Sci. 12:1482158.
doi: 10.3389/feart.2024.1482158

Research on microseismic source location based on time quality constraints

Xuefei Wu[1,2]*, Qian Xie[1,3] and Junsheng Yan[1,3,4]

[1]Xi'an Research Institute, China Coal Technology and Engineering Group Corp., Xi'an, China, [2]College of Energy Science and Engineering, Xi'an University of Science and Technology, Xi'an, China, [3]Xi'an CCTEG Transparent Geology Technology Co., Ltd., Xi'an, China, [4]China Coal Research Institute, Beijing, China

Introduction: To develop a small-scale regional microseismic location model for coal mines and enhance the accuracy of microseismic location at the bottom plate,this article proposes a high-precision location algorithm for 3D-Fast Sweeping Method (3D-FSM) seismic sources under time quality constraints.

Methods: The study investigates the numerical simulation of microseismic location accuracy on coal seam floor, considering various observation systems, arrival time picking errors, and wave velocity discrepancies. The algorithm employs a VGG-16 deep learning network to train and establish a quality control model for P-wave pickup values; Next, utilizing the 3D-FSM framework, it calculate the seismic wave travel time field and applies Fermat's principle for each detection point, as well as the reversible principle of elastic wave propagation path. This allows for the determination of the spatial path and travel time from any potential source point to the detection point. Finally, the algorithm scans each computational node, using the controlled travel time difference to identify the source point corresponding to the smallest spatial node.

Results: The results indicate that the location error of the borehole tunnel observation system is smaller than that of the tunnel observation system. Specifically, with the borehole tunnel observation system, the variance in P-wave arrival time picking is 1 ms, and the wave velocity variance is 20 m/s^2, demonstrating high accuracy.

Discussion: The findings suggest that the 3D-FSM seismic source location algorithm, under quality control, approaches the precision of manual location methods and exhibits high reliability, even when disregarding significant accuracy errors during the quality control location process.

KEYWORDS

microseismic location, observation system, coal seam floor, arrival time picking, deep learning

1 Introduction

Disturbance-induced water hazard during coal seam floor mining represent a significant form of mine water damage. Statistics show that 60% of coal mines in China are at risk of such hazards, making it the country most ffected by coal seam floor water damage worldwide (Yang et al., 2022; Li et al., 2023b). In recent years, China has made substantial strides in evaluating, preventing, and issuing early warnings regarding water hazards

associated with coal seam floors (Zhang et al., 2020; Xue et al., 2023). However, water hazard from the bottom plate still occurs occasionally, posing serious threats to miner safety. Accurate localization of microseismic events on the coal seam floor is crucial for understanding the spatiotemporal development of mining-induced fractures, which is vital for informing strategies to prevent and control water inrushes linked to coal mining activities. Microseismic location technology is widely utilized across various engineering fields to ensure the safety and stability of rock formations. Key applications include deep mineral resource extraction (Mngadi et al., 2019; Pan et al., 2020), excavation of deep-buried tunnel rock masses, maintenance of high and steep slope stability, and location the range of fracturing induced by water pressure (Samsonov et al., 2024; Xiang et al., 2023). In the mining field, micro-seismic location technology addresses a range of issues, including rock burst, mine tremors, roof and floor damage, coal pillar stability, coal and gas outburst, illegal mining activities, and coalbed methane development. The main research directions in microseismic data processing and interpretation focus on arrival time picking (Barthwal and Shcherbakov, 2024; Charles and Maochen, 2018; Qian et al., 2024), microseismic source localization (Cheng et al., 2018; Jiang R. et al., 2021; Sedghizadeh et al., 2023; Zhou et al., 2022), and microseismic source parameter inversion (Li et al., 2023a). Anikiev et al. (2022) used machine learning to analyze the noise and location network sensitivity in the arrival time to obtain the source location, and verified it with the localization of microseismic activity that occurred during actual hydraulic fracturing operations in the Akoma Basin, United States. Cheng et al. (2017) employed micro-seismic location technology to investigate the distribution patterns of micro-seismic events originating from the mining roof rock mass, both vertically and horizontally. He proposed a method to determine displacement angle using micro-seismic data, which was validated in Dongjiahe Coal Mine. Ma et al. (2020) established a microseismic location system in the Dongjiahe coal mine, applying moment tensor theory to deduce the source mechanism of floor micro-seismic anomalies and employing stress inversion method to identify underlying faults. Jiang et al. (2021b) proposed a low-dimensional dual-event joint localization method that simplifies high-dimensional inversion into a set of equations with only six parameters, selecting 2,000 P-wave arrival time combinations from over six sensors. Researchers at the Mining Seismic Acquisition System Institute of Yongshaba Mine in Guizhou Province conducted tests using two composite positions and analyzed data from eight blasting events, confirming the high positioning accuracy of the proposed method. Relative to the scale of coal mines, the depth of coal seam floor mining is relatively small. Numerous theoretical studies and practical location efforts have shown that the layout of observation systems, arrival time picking errors, and velocity model inaccuracies can significantly impact the accuracy of micro-seismic source localization.

In this paper, we propose a high-precision localization algorithm for 3D-FSM seismic sources, developed through an examination of numerical simulation that consider various factors affecting localization accuracy on coal seam floors. Research on the application of micro-seismic location for detecting water hazards at the bottom plate of the 81,307 coal mining face demonstrates that the 3D-FSM seismic source localization algorithm, when subjected to quality control, yields results comparable to manual localization in terms of reliability. However, significant localization accuracy errors may occur without proper consideration of time and quality control.

2 Development of simulation modeling

2.1 Principles of microseismic location

Source location is a fundamental tasks in microseismic monitoring, and the accuracy of this process directly impacts the subsequent analyses. Currently, various methods exist for source location, with the travel time differences method being the most widely adopted (Zhao et al., 2023). As shown in Figure 1, the spatial coordinate of the *i*th detector are represented as (x_i, y_i, z_i), while the coordinates of the microseismic event S are denoted as (x_0, y_0, z_0). The arrival times of these waves in typical microseismic waveforms are highlighted by the green and red vertical lines in Figure 2. In Figure 2A, the microseismic waveform clearly displays both P-wave and S-wave oscillations, with the P-wave propagating rapidly and arriving first, followed by the slower yet more energetic S-wave. Conversely, Figure 2B predominantly shows a pronounced P-wave initiation, while the S-wave is obscured by the P-wave, making identification challenging. In the practical context of coal mine micro-seismic monitoring, the scenario depicted in Figure 2B is quite common, where S-wave initiation is often subtle and difficult to discern. Consequently, coal mine microseismic location typically relies on P-wave travel time differences for source location determinations.

The source location aims to determine the spatial coordinates (x_0, y_0, z_0) of microseismic events along with the time t_0 of which microseismic events occurrence. Given these conditions, the objective function f_t for microseismic source location can be formulated, as shown in Equation 1:

$$f_t = \sum_{i=1}^{n} \left(t_{pi} - \sqrt{(x_0 - x_i)^2 + (y_0 - y_i)^2 + (z_0 - z_i)^2}/v_p - t_0 \right)^2 \quad (1)$$

where n is the effective arrival time, and v_p is the P-wave velocity model.

Without considering errors associated with the velocity model, arrival time picking, and measurement of the location points, the micro-seismic event parameter (x_0, y_0, z_0, t_0) can be substituted into Equation 1. Consequently the objective function f_t achieves a minimum value of 0. Thus, mathematically reframed as the task of finding the minimum value of f_t.

2.2 Numerical simulation experiment on microseismic location accuracy of coal seam floor

2.2.1 Simulation method for microseismic source location accuracy based on d-value theory

Kijko and Sciocatti (1995) conducted comprehensive research on microseismic location theory in order to optimize the spatial arrangement of mining seismic stations. They proposed the D-value theory to enhance microseismic observation systems (Zhao et al., 2022), as shown below.

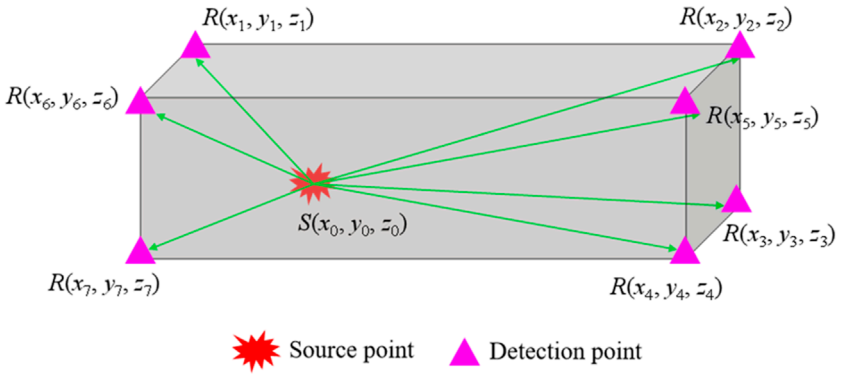

FIGURE 1
Schematic diagram of microseismic source location.

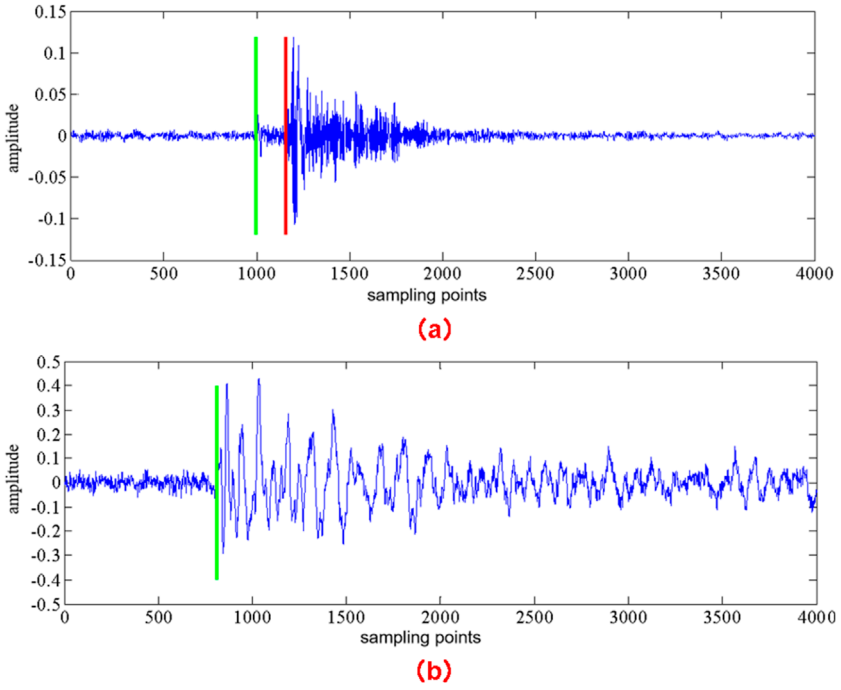

FIGURE 2
Time of P- and S wave of typical microseismic wave signals. **(A)** Both P-wave and S-wave oscillations are evident. **(B)** The situation where the S-wave oscillation is not obvious.

The microseismic arrival time t_i recorded by the ith detector satisfies Equation 2:

$$t_i = t_0 + T(h, s_i) + \varepsilon_i \tag{2}$$

where $h = (x_0, y_0, z_0)$ and $s_i = (x_i, y_i, z_i)$ represent the coordinates of the source and seismic station in the Cartesian coordinate system, ε_i denotes the picking error of the seismic wave recorded by the ith detector, where i=1,…, n, n is the total number of detectors, and $T(h, s_i)$ is the source.

The issue of microseismic location can be reformulated as the following mathematical optimization problems as shown in Equation 3:

$$\Phi(X) = \sum_{i}^{n} |t_i - t_0 - T(h, s_i)|^p \tag{3}$$

where $X = (x_0, y_0, z_0, t_0)$, p is the norm ($p \geq 1$). When p=2, $\Phi(X)$ is the least squares estimate, and when p=1, $\Phi(X)$ is the sum of absolute residual values.

Kijko and M Sciocatti believes that the effectiveness of an observation system should be determined by the covariance matrix of the parameter $X = (x_0, y_0, z_0, t_0)$ to be inverted for microseismic events. Consequently, the optimization problem for microseismic observation systems can be formulated as a mathematical problem,

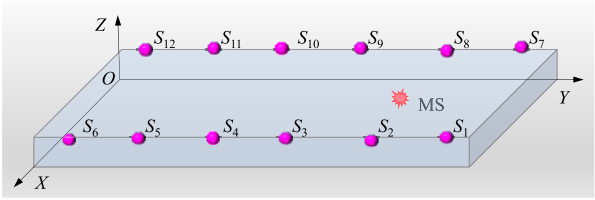

FIGURE 3
Microseismic seismic source location model of floor of roadway observation system.

TABLE 1 Geophone coordinates of roadway observation system.

Detection Point	Coordinate	Notes
S_1	(240, 275, 40)	roadway
S_2	(240, 225, 40)	roadway
S_3	(240, 175, 40)	roadway
S_4	(240, 125, 40)	roadway
S_5	(240, 75, 40)	roadway
S_6	(240, 25, 40)	roadway
S_7	(0, 275, 40)	roadway
S_8	(0, 225, 40)	roadway
S_9	(0, 175, 40)	roadway
S_{10}	(0, 125, 40)	roadway
S_{11}	(0, 75, 40)	roadway
S_{12}	(0, 25, 40)	roadway

as presented in Equation 4:

$$\min f(C_x)\, s \in f(C_x) \tag{4}$$

where C_x is the covariance matrix of the microseismic event parameter X, $S = (S_1, S_2, \ldots, S_n)$ represents the coordinate set of each detection point in the microseismic observation system, and g denotes the spatial domain set of potential source location.

The expression of function $f(\cdot)$ varies depending on the specific problem, with the D-value optimization being the most common approach, aiming to minimize the value of column C_X. John and Draper (1975) provided an in-depth discussion on the selection of D-value criterion parameters. The approximate confidence ellipsoid of the X parameter is represented by Equation 5:

$$\left(X - \hat{X}\right) C_X^{-1} \left(X - \hat{X}\right)^T \leq \text{constant} \tag{5}$$

where $\hat{X}$ is the estimated value of X, constant is the appropriate quantity, and matrix operator T represents transpose.

The steps of the ellipsoid depicted in Equation 5 are proportional to $\sqrt{det\, C_X}$. Therefore, a clear optimization criterion is to minimize

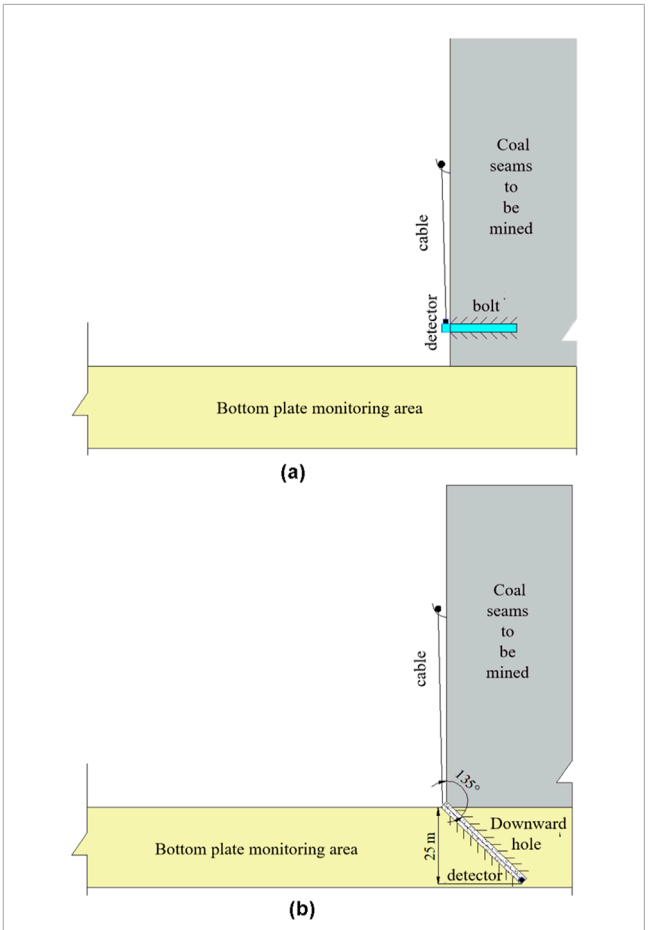

FIGURE 4
Detector layout method. **(A)** Installation of tunnel sensors. **(B)** Installation of bottom plate deep hole detectors.

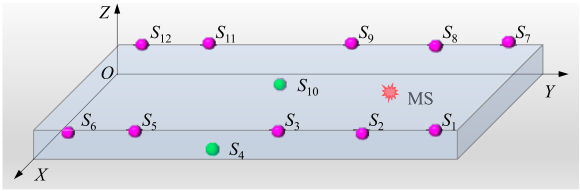

FIGURE 5
Microseismic source location model of the hole-lane observation system.

the ellipsoid shown in Equation 5 by minimizing the source parameter C_X. The microseismic observation system achieves this minimization is referred to as D optimization.

Disregarding error factors such as coordinate measurements of detection points and arrival time picking, the Equation 6 for seismic wave travel time is given by:

$$T_i(H, V_p, X_i) = t_i - t_0 = \frac{\sqrt{(x_i - x_0)^2 + (y_i - y_0)^2 + (z_i - z_0)^2}}{V_p} \tag{6}$$

TABLE 2 Geophone coordinates of the hole-lane observation system.

Detection Point	Coordinate	Notes
S_1	(240, 275, 40)	roadway
S_2	(240, 225, 40)	roadway
S_3	(240, 175, 40)	roadway
S_4	(215, 125, 15)	deep hole
S_5	(240, 75, 40)	roadway
S_6	(240, 25, 40)	roadway
S_7	(0, 275, 40)	roadway
S_8	(0, 225, 40)	roadway
S_9	(0, 175, 40)	roadway
S_{10}	(25, 125, 15)	deep hole
S_{11}	(0, 75, 40)	roadway
S_{12}	(0, 25, 40)	roadway

where t_i is the seismic wave travel time recorded by detector i, $X_i(x_i, y_i, z_i)$ is the spatial coordinate of detector i, i=1, 2, ····, n, $X = (x_0, y_0, z_0, t_0)$ is the parameter (x_0, y_0, z) to be inverted for microseismic events, 0 is the spatial coordinate of the source, t_0 represent the time of the earthquake, and V_p is the P-wave velocity. The seismic wave travel time T_i is a function of (X, V_P, X_i).

The covariance matrix C_X of the source parameter X is presented in Equation 7:

$$C = k\left(A^T A\right)^{-1} \tag{7}$$

where k is a constant and A is a partial differential matrix.

According to the basic properties of the determinant, C_X satisfies the following Equation 8:

$$\det(C_X) = [\det(C_X - 1)] - 1 \tag{8}$$

Therefore, the minimization problem of $\det(C_X)$ is equivalent to the problem of $\det\left(A^T A\right)$. The actual microseismic location problem is much more complex than the D-value optimization theory. Matrix A and the corresponding covariance matrix C_X are functions of the unknown actual source parameter X, which are unsolvable quantities. For this purpose, the partial derivative matrix A is generally calculated at the initial guess value of the actual source parameter X.

If Ω_h is the spatial domain set of all microseismic events, and the probability of microseismic event H_j occurring at location j is $P(Hj)$, then Equation 9 holds:

$$\int \Omega_h p_h(h) dh = 1 \tag{9}$$

Considering the randomness of the source coordinates, the average value within the location range Ω_h Equation 10 can be used to replace $f(C_X)$ in Equation 4.

$$\overline{f(C_X)} = \int_{\Omega_h} p_h(h) f(C_X) dh \tag{10}$$

Considering that the probability of microseismic events occurring at different points in the spatial domain Ω_h varies, the optimal estimation of the microseismic event parameter X is ensured when the observation point s satisfying the following conditions, as shown in Equation 11:

$$\min \int_{\Omega_h} p_h(h) f(C_X) dh \quad s \in \Omega_s \tag{11}$$

In the above derivation process, it is assumed that all n detectors in the microseismic observation system are triggered by one event. For all events, the partial derivative matrix A has the same number of rows, equal to the total number of microseismic detectors n. The fundamental assumption underlying this approach is that the energy emitted by microseismic events must be sufficiently substantial for all detectors to reliably capture the stress waves. To address this stringent assumption, Kijko and Sciocatti (1993) integrated Equation 12 within a certain range of seismic energy:

$$\min \int_{\Omega_h} \int_{E_{\min}}^{E_{\max}} p_h(h) P_E(E) f(C_X) dE dh \quad s \in \Omega_s \tag{12}$$

where $E_{\min}$ and $E_{\max}$ are the minimum and maximum microseismic energies, respectively, and $P_E(E)$ is the probability density distribution function of the energy.

According to the basic theory of seismic wave propagation, both microseismic energy and the covariance matrix C_X are functions of detection distance r. The relationship between microseismic event energy E and detection distance r as shown in Equation 13:

$$E = constr^q \tag{13}$$

where q is approximately equal to 2.

According to Rikitake (1976) derivation of seismic energy distribution, the probability density distribution function $P_r(r)$ for the detectable distance r is given in Equation 14:

$$P(r) = \frac{-bd}{d\left(r_{\max}^{-bq/d} - r r_{\min}^{-bq/d}\right)} r^{-(1+bq/d)} \tag{14}$$

where b is the b value related to magnitude m and the number of events in the Gutenberg Richter equation, and d is the d value in the relationship between seismic energy E and magnitude m shown in Equation 15:

$$\log E = c + dm \tag{15}$$

where d equals 1.5, and the value of b depends on the specific mine, generally ranging from 0.6 to 1.2.

Based on the above factors, the criteria for determining the optimal observation system can be obtained shown in Equation 16:

$$\min \int_{\Omega_h} \int_{r_{\min}}^{r_{\max}} p_h(h) P_r(r) f(C_X) dr dh \quad s \in \Omega_s \tag{16}$$

where $r_{\max}$ is the maximum detection distance, corresponding to the maximum energy release $r_{\max}$ within the energy range. It is important to ensure that $r_{\min} < r_{\max}$ must be ensured.

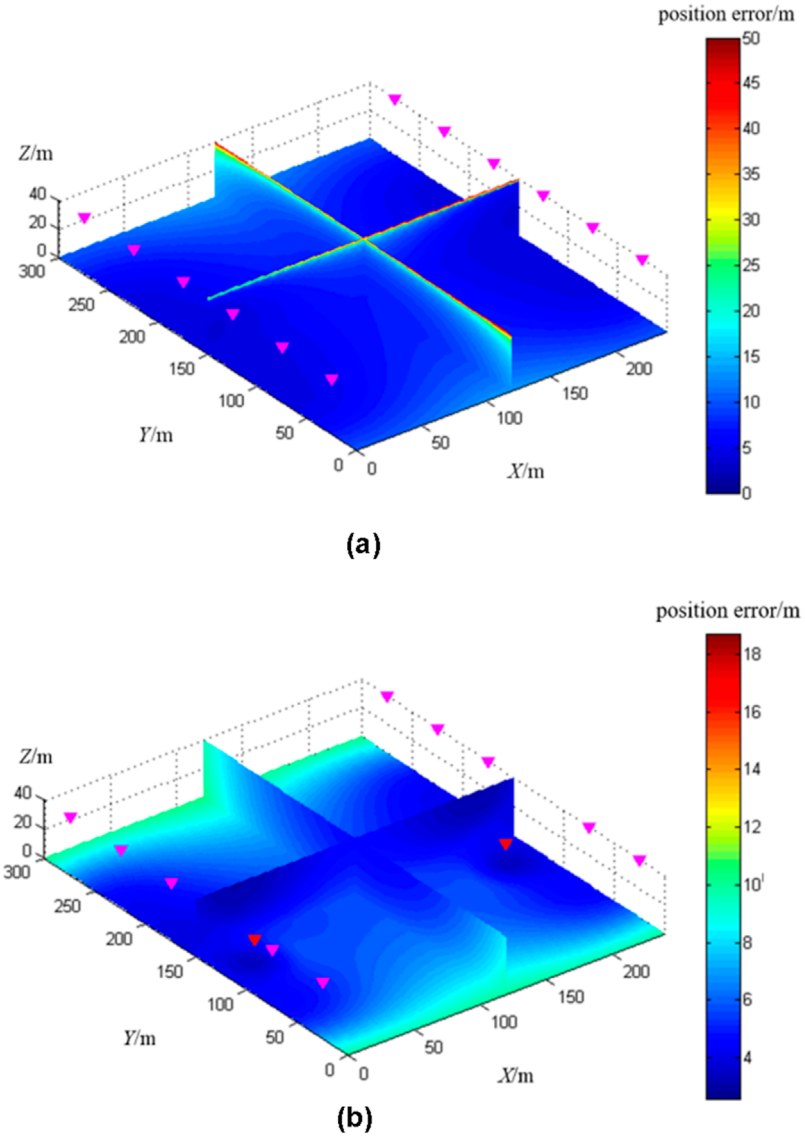

FIGURE 6
Simulation of microseismic location error of coal seam floor under different observation systems. **(A)** Distribution of location errors in the bottom plate seismic source of the tunnel observation system. **(B)** Distribution of bottom plate source location error in hole lane observation system.

The expected standard error diagram of microseismic event parameter C_X is generally used to evaluate the quality of the observation system. This method accounts not only for time error but also for uncertainties in the velocity model. The diagonal elements of matrix C_X represent the variance of the seismic event parameter x_0, y_0, z_0, t_0. The standard error of the epicenter location is defined as the radius of a circle, the area of which is equivalent to the area of the ellipsoid representing the standard error of coordinate x_0, y_0. This standard error of the epicenter location defined in this way is expressed by Equation 17:

$$\sigma_{xy} = \left[\{C_x\}_{22}\{C_x\}_{33} - [\{C_x\}_{23}]^2\right]^{1/4} \tag{17}$$

Due to the eigenvalues $(\lambda_{x0}, \lambda_{y0})$ of the covariance matrix corresponding to the two axes of the ellipse, Equation 17 can be rewritten as Equation 18:

$$\sigma_{xy} = \sqrt{\sqrt{\lambda_{x0}\lambda_{y0}}} \tag{18}$$

Gong et al. (2010) proposed the calculation formula for seismic source error based on Equation 19:

$$\sigma_{xy} = \sqrt[3]{\sqrt{\lambda_{x0}\lambda_{y0}\lambda_{z0}}} \tag{19}$$

where $\lambda_{x0}, \lambda_{y0}, \lambda_{z0}$ corresponds to the X-axis, Y-axis, and Z-axis of the ellipsoid, respectively.

2.2.2 Simulation of source location accuracy under different observation systems

Installing detectors in deep holes within the coal seam floor positions them in the rock layers beneath, bringing them closer

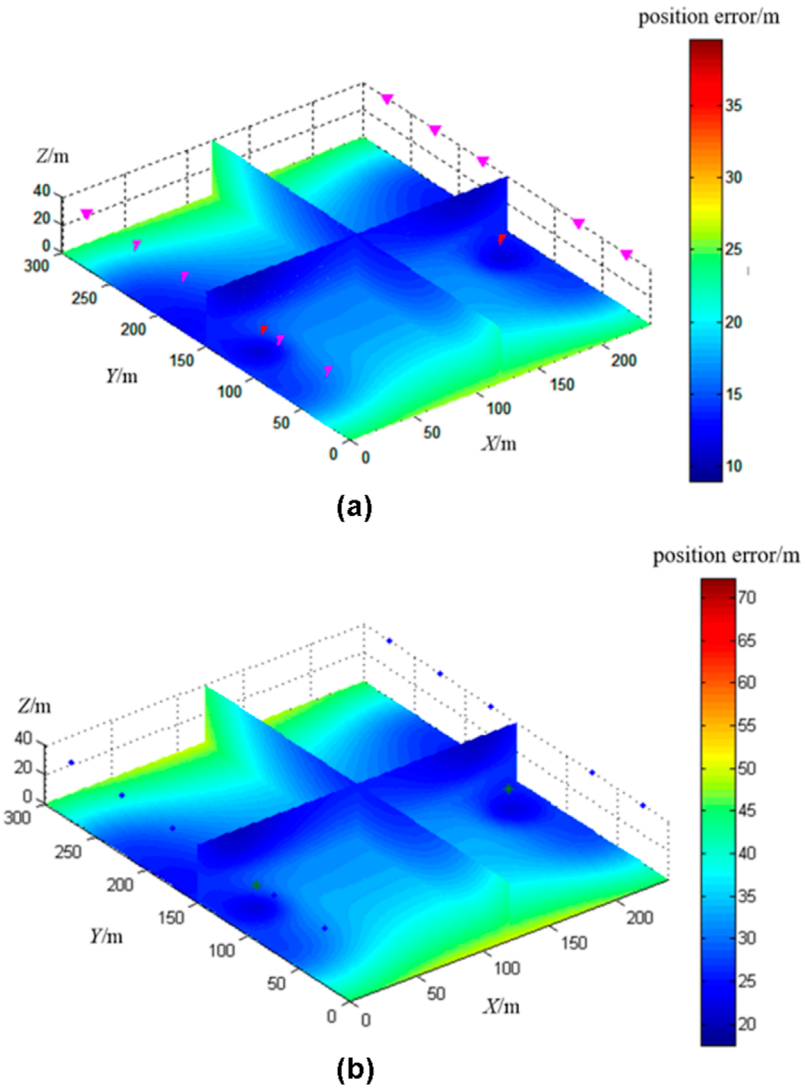

FIGURE 7
Simulation of coal seam floor source location error under different P-pick-up errors. **(A)** P-wave arrival time picking variance 5 m location accuracy. **(B)** P-wave arrival time picking variance 10ms location accuracy.

to the target location area and potential micro-seismic events. Based on the theory of micro-seismic localization theory, this closer proximity is expected to enhance localization accuracy. However, installing detectors in deep boreholes is complex, non-recoverable, and results in high construction costs. To strike a balance between location costs and accuracy, we utilize the D-value optimization criterion to simulate the localization error of micro-seismic events under two observation systems: the bottom-plate-depth hole observation system and the tunnel observation system.

2.2.2.1 Microseismic location of tunnel observation system

A coal seam floor seismic source location model was constructed as illustrated in Figure 3. The model has a Y-axis length of 300 m (representing the location length of the fully mechanized mining face floor), an X-axis width of 240 m (representing the width of the fully mechanized mining face), and a Z-axis height of 40 m (indicating the maximum depth of floor failure). The coordinate distribution of the observation system is shown in Table 1.

2.2.2.2 Microseismic location of the borehole tunnel observation system

To enhance the accuracy of location coal seam floor mining damage, a borehole-tunnel observation system is proposed. This approach strategically optimizes the layout of the microseismic location system. "Lane" refers to the micro-seismic detector installed on the bottom anchor rods of the mine roadway, as illustrated in Figure 4A. "Hole" refers to the micro-seismic detectors placed in the deep boreholes in the floor, where the drilling axis forms a 135° angle with the coal slope of the working face and reaches a vertical depth of 25 m. The detectors are positioned at the bottom of the borehole and sealed with cement mortar, as shown in Figure 4B.

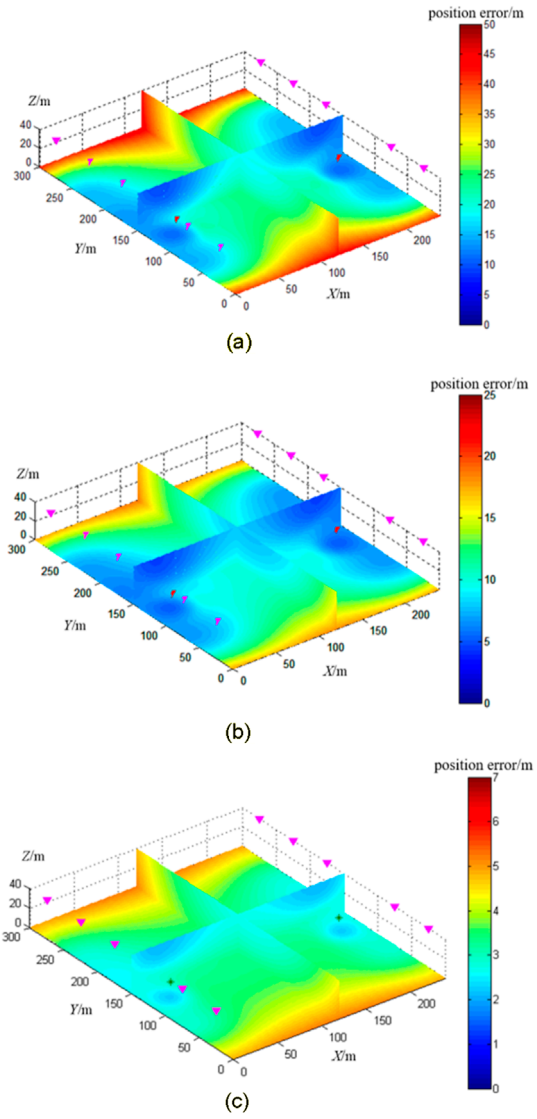

FIGURE 8
Cloud map of focal spatial location accuracy of combined well and hole bottom plate with different wave velocity errors. **(A)** P-wave velocity variance 500 m/s^2. **(B)** P-wave velocity variance 200 m/s^2. **(C)** P-wave velocity variance 20 m/s^2.

A coal seam floor seismic source location model was constructed, as illustrated in Figure 5. The model features a *Y*-axis length of 300 m (representing the location length of the fully mechanized mining face floor), an *X*-axis width of 240 m (representing the width ofx the fully mechanized mining face), and a *Z*-axis height of 40 m (indicating the maximum depth of floor failure). The points S4 and S10 correspond to bottom plate deep holes, and the coordinates of each detection point are provided in Table 2.

2.2.2.3 Location accuracy simulation

The location range for micro-seismic events in coal seam floor mining is defined as {(x, y, z)|0<x<240∩ 0<y<300∩0<z<40}, with an average P-wave velocity of 3,000 m/s, a velocity variance of 100 m/s^2, and an average picking error of 1 m at that time. The grid size is $\delta_x = \delta_y = \delta_z = 2$ m. Using the D-value optimization criterion, the distribution cloud map of micro-seismic event location errors was simulated for both the tunnel micro-seismic observation system and the borehole observation system. The results are shown in Figure 6.

Figure 6 shows that adding deep borehole detector on both sides of the coal mining face significantly enhances the location accuracy of micro-seismic events within the location area. The average location errors of micro-seismic events under the tunnel microseismic observation system and the combined borehole-tunnel observation system are 10.33 m and 5.63 m, respectively.

Based on the experimental results, we selected the borehole-tunnel observation system for microseismic location of the coal seam floor.

2.2.3 Simulation of source location accuracy under different picking errors at different arrival times

Building on the preferred borehole-tunnel observation system, we conducted simulations to assess the spatial localization accuracy of micro-seismic location at the wellbore joint bottom plate. The simulations were performed under three P-wave arrival time picking variances: 1 ms, 5 ms, and 10 ms, while keeping consistent parameters for location range, average P-wave velocity, and P-wave velocity variance. Results for the 1 ms variance are depicted in Figure 6B, and while results for the 5 ms and 10 ms variances are illustrated in Figure 7. With picking variances of 1 ms, 5 ms, and 10 ms, the average micro-seismic location accuracy were 5.63 m, 16.67 m, and 32.04 m, respectively.

The experiment demonstrates that the precision of P-wave arrival time picking has a significant impact on micro-seismic localization accuracy. Enhancing source localization accuracy requires filtering out P-wave arrival time picks with lower precision before determining source location. To address this, this study applies deep learning techniques to identify and eliminate erroneous P-wave arrival time picks, ultimately improving the accuracy of microseismic source localization.

2.2.4 Simulation of source location accuracy under different wave velocity errors

Building on the selected borehole-tunnel observation system, simulation were conducted to assess the spatial location accuracy for micro-seismic location at the wellbore joint bottom plate under three conditions of P-wave velocity variance:500 m/s^2, 200 m/s^2, and 20 m/s^2. The results of these simulations are presented in Figure 8.

According to the simulation results, when the P-wave velocity variance is 500 m/s^2, the source location error in the location area ranges from 10 to 50 m, with an average location accuracy of 21.52 m, which does not meet the accuracy requirements of bottom plate source location. At a P-wave velocity variance of 200 m/s^2, the average source location accuracy in the location area improves to 9.35 m; while a variance of 20 m/s^2 further reduces the average error to 3.33 m. To reliably monitor micro-seismic events on the bottom plate, micro-seismic location at the well hole joint bottom plate must be based on a high-precision velocity model.

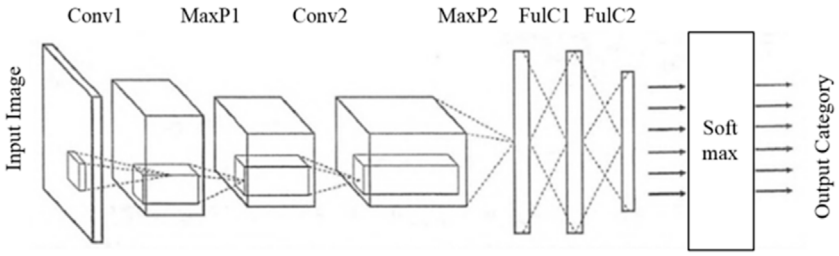

FIGURE 9
Typical convolutional neural network architecture.

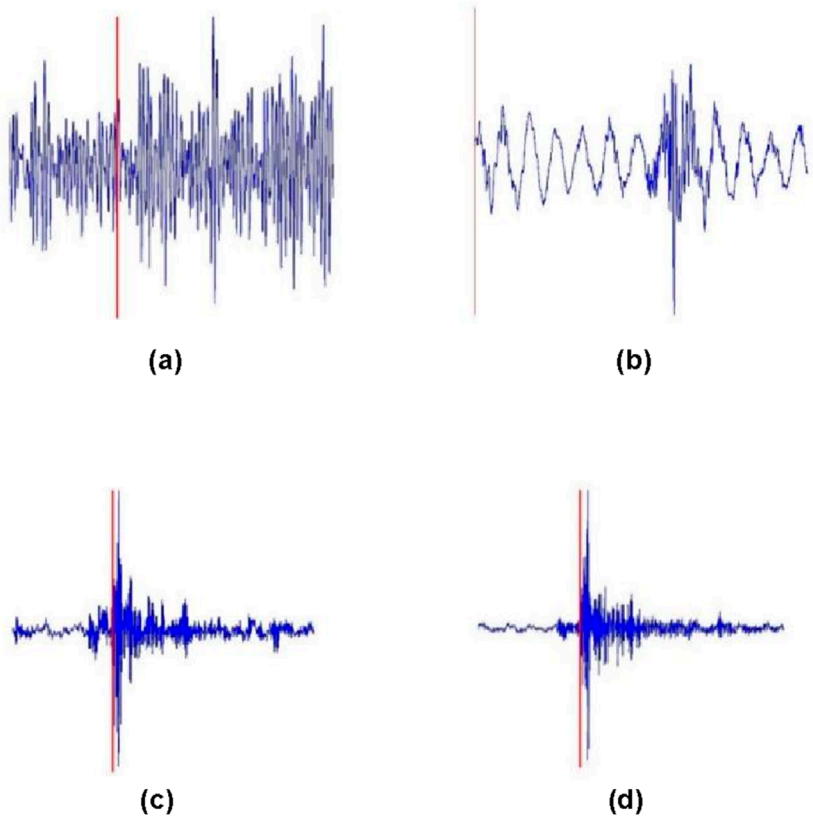

FIGURE 10
Typical error P-wave pickup value.

2.3 Quality control of microseismic pickup values

2.3.1 Convolutional neural network

CNNs are a prominent algorithm in deep learning, specifically a type of feedforward neural network known for its convolutional operations and deep structure. Since 2010, CNNs have achieved significant success in image and video recognition applications, including facial recognition, medical imaging, and autonomous driving. Recently, geophysicists have begun applying deep learning techniques, such as CNNs, in geophysical research. CNN models consist of input layers, multiple convolutional layers, pooling layers, fully connected layers, and output layers. An example architecture of a CNNs architecture is shown in Figure 9. The convolutional layers are responsible for feature extraction, pooling layers reduce image spatial dimensions, and fully connected layers establish connections between adjacent layers, respectively (Huang et al., 2018; Jafari et al., 2023; Viatkin et al., 2021).

2.3.2 P-wave pickup value dataset

The purpose of quality control for P-wave arrival time picks is to use computer intelligence to distinguish between correct and incorrect values. Building large-scale training and

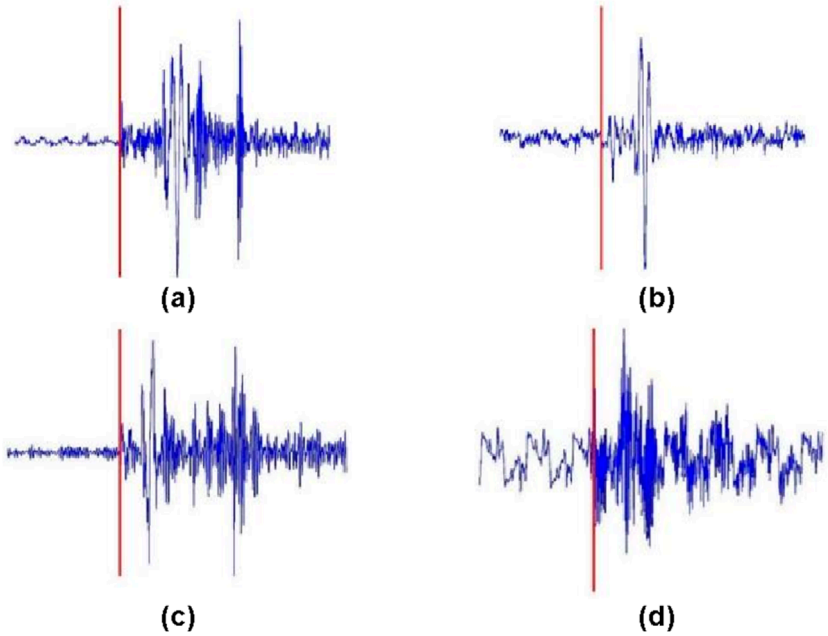

FIGURE 11
Typical high-precision P-wave time pickup value.

TABLE 3 Quality control dataset of P-pickup.

Sample set	Sample set		Total
	Available P-wave pickup values	Unavailable P-wave pickup values	
training set	4,704	4,774	9478
test set	2016	2046	4,062

testing datasets is essential for developing and evaluating models to control P-wave pick quality. Using micro-seismic location waveform data from a certain mine, the AIC algorithm and manual methods were applied to pick the P-wave arrival times of micro-seismic signals. Based on the picking accuracy for each micro-seismic waveform, correct and erroneous P-wave arrival times were identified. The results of automatic picking were saved as images (Figures 10, 11) to serve as input data for the CNNs. Figures 10A, B show typical low signal-to-noise ratio (SNR) signals with P-wave picking errors, commonly due to weak microseismic signals, long propagation distances, or detector failures. Figures 10C, D show incorrect arrival time picks values for medium to high SNR signals, often caused by strong energy of S-wave energy, which conventional algorithms struggle to separate from P-wave arrivals. Figure 11 shows an example of an accurate P-wave arrival time pick with a high SNR.

As shown in Table 3, this study used 13,540 data samples collected from micro-seismic location at the 81,307 working face of a certain mine. The dataset includes 6,720 correct and 6,820 incorrect P-wave picks, with an approximate 1:1 ratio. The dataset was divided training and test sets at a 7:3 ratio, with both correct and incorrect picks proportionately distributed. The training set contains a total of 9,478 samples, comprising 4,704 correct and 4,774 incorrect picks. The test set includes 4,062 samples, with 2,016 correct and 2,046 incorrect P-wave picks.

2.3.3 Training of P-wave pickup value quality control model

To compare the differences in identifying incorrect P-wave pickup values among different convolutional neural network models, this study used four network models to train P-wave pickup value quality control models, including VGG-16, ResNet-50, VGG-SENet, and ResNet-SENet.

This study employs four convolutional neural network models—VGG-16, ResNet-50, VGG-SENet, and ResNet-SENet—to train P-wave pickup quality control models, allowing for a comparative analysis of each model's effectiveness in identifying incorrect P-wave pickup values.

The input P-pickup image is set to a width and height of 128 pixels. During the training process, adjust the learning rate and evaluate the model performance by location val-acc (validation

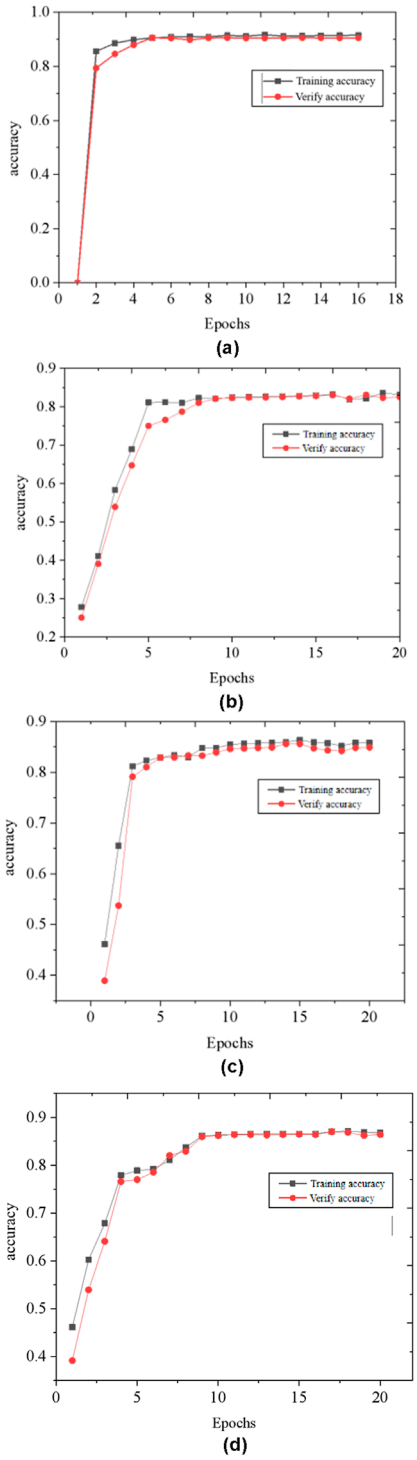

FIGURE 12
Training accuracy curves of VGG-16 ResNet-50 VGG-SENet and ResNet-SENet models. **(A)** VGG-16 accuracy comparison. **(B)** ResNet-50 accuracy comparison. **(C)** VGG-SENet accuracy comparison. **(D)** ResNet-SENet accuracy comparison.

accuracy). The parameters that need to be optimized include patient, factor, and minimum learning rate (*min_lr*). Set the initial patient=2, factor=0.1, and *min_lr*=1e^{-10}. The training accuracy curves of four convolutional neural network models are shown in Figure 12.

The input P-wave pickup images are configured to a resolution of 128x128 pixels. During training, the learning rate is adjusted, and model performance is evaluated by tracking validation accuracy (val-acc). Key parameters to optimize include "patience," "factor," and "minimum learning rate (min_lr)," initially set to 'patience=2′, 'factor=0.1′, and 'min_lr=1e-10`. The training accuracy curves for the four convolutional neural network models are illustrated in Figure 12.

The training results of four CNNs models are shown in Table 4. The accuracy scores for the VGG-16,ResNet-50,VGG-SENet, and ResNet-SENet models are 0.915, 0.821, 0.848, and 0.858, respectively, with corresponding precision scores of 0.905, 0.712, 0.733, and 0.802. Among these, the VGG-16 model achieved the highest accuracy and precision for P-wave pickup quality control. Therefore, this study chose the P-wave pickup quality control model trained on VGG-16.

2.4 A high-precision location algorithm for 3D-FSN seismic sources under time quality constraints

According to simulation assessing the micro-seismic location accuracy of mining-induced fractures at the bottom plate, the accuracy of the velocity model significantly affects the accuracy of the seismic source location. Given that the development depth of these fractures is typically within 30 m, it is essential to base the seismic source location on high-precision velocity models rather than simplified uniform models. Based on the above analysis, this study employs the FSM to locate seismic events at the bottom plate (Chen et al., 2015; Tro et al., 2023). The specific algorithm flowchart is illustrated in Figure 13. The fundamental idea involves first calculating the seismic wave travel time field of each detection point based on 3D-FSM. Next, based on Fermat's principle and the principle of reversible elastic wave propagation, the spatial path and travel time from any potential source point to the detection point are obtained. Finally, each calculation node is scanned, using the travel time difference to identify the spatial node that corresponds to the earliest arrival time as the source point. The 3D-FSM source location algorithm offers advantages such as high computational accuracy, compatibility with complex velocity models, and rapid iteration speed.

Utilizing the principle of seismic wave propagation and source exchange, we calculate the travel time matrix for each grid node within the observation area. This is accomplished by considering each detector in the observation system as a virtual source. By performing pairwise subtraction of these matrices, we derive the travel time difference matrix for each grid point. This information is then compiled into a comprehensive travel time difference database.

Source location involves matching the travel time difference matrix of the source to be inverted with the arrival time difference database. Note that O_{ij} denote the time difference matrix component for the *i*th and *j*th detectors, and *O* represents the time difference matrix of the microseismic event to be inverted. To enhance computational efficiency, we employ the similarity matching search

TABLE 4 Comparison of test results.

Models	Training	Time	Accuracy	Precision	CPUMem
VGG-16	Required	15min	0.915	0.905	3147MiB
ResNet-50	Required	13min	0.821	0.712	7193MiB
VGG-SENet	Required	11min	0.848	0.733	2839MiB
ResNet-SENet	Required	7min	0.858	0.802	2227MiB

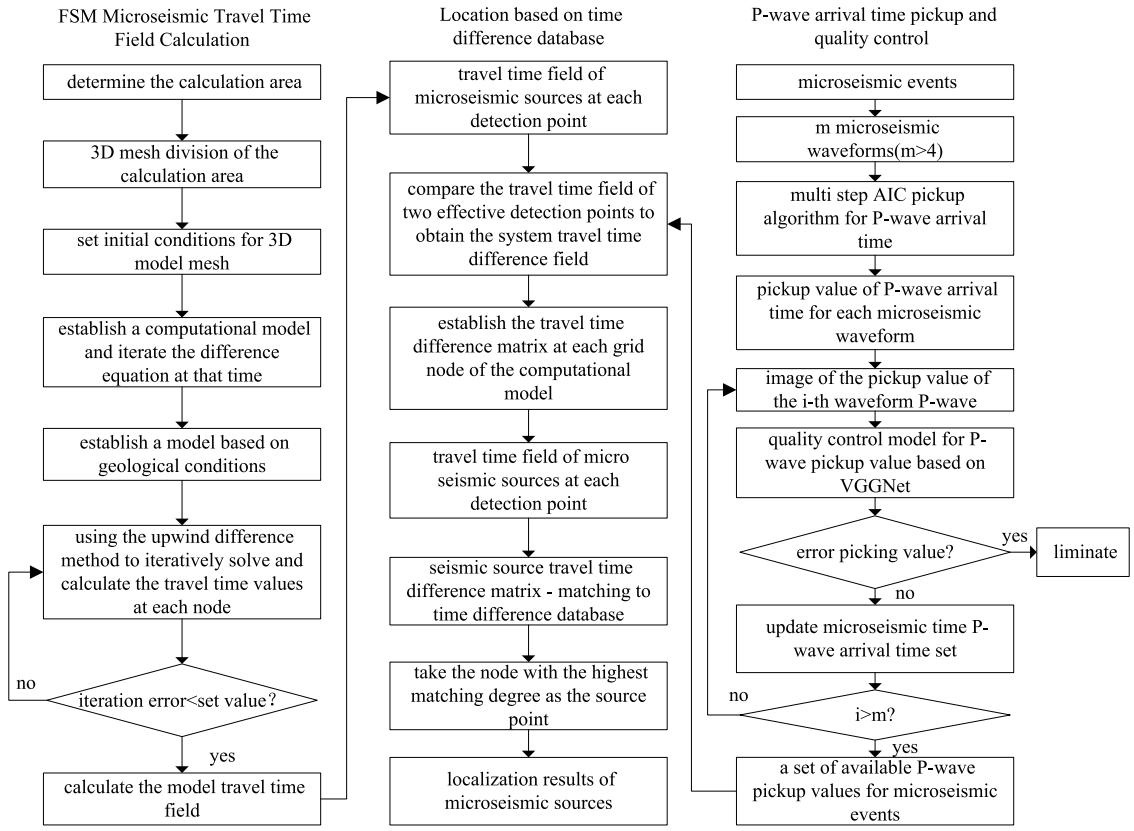

FIGURE 13
High precision source location method of 3D-FSM with P-pickup quality control.

method (Guo Chao, 2019) for matching the event time difference matrix with the time difference database. Specifically, Equation 20 is used to calculate the similarity between the time difference matrix and the event time difference matrix of each grid node in the location area. The geometric centers of the nodes with the smallest similarity values, denoted as δ, are identified as the microseismic sources.

$$\delta = \sum_{\substack{i=1 \\ j=1}}^{n} \left(\left(O_{ij} - N_{ij}^{k} \right) / N_{ij}^{k} \right)^2 (k = 1, 2, \ldots) \tag{20}$$

where N^k is the arrival time difference matrix of the kth node in the arrival time difference database.

3 Research on high-precision location application of microseismic events caused by bottom plate mining

3.1 General situation

The 81,307 fully mechanized mining face in a coal mine in Shanxi province is used to mine 8# coal, with a strike length of 2,491 m and a dip length of 240 m. During the mining period, the west side of the 81,307 working face adjoins the undeveloped 81,308 working face, while the east side borders the fully mined 81,306 working face. The thickness of the coal seam in the 81,307 working face varies from 4.5 to 9.2 m, with an average thickness of 6.8 m, gradually increasing from the cutting eye toward the retreat

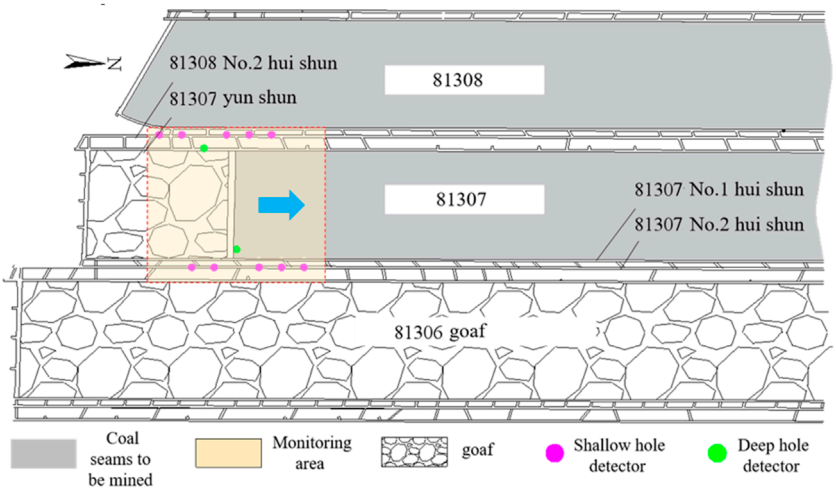

FIGURE 14
Schematic layout of microseismic location system.

channel. The coal dip at an angle of 2°–5°, typically interbedded with an average of 3 layers of gangue, primarily consisting of mudstone. The maximum thickness of a single layer of interbedded gangue reaches 0.9 m. Beneath the 8 # coal seam lies the main 11# coal seam, which is part of the Taiyuan Formation of the Carboniferous-Permian period, with an average thickness of 7.36 m. The Ordovician limestone aquifer below the 11# coal seam serves as the primary aquifer affecting the mining operations. The water level elevation of the Ordovician limestone confined aquifer is +839 m. The average distance from the top interface of the Ordovician aquifer to the 8# coal seam is 112.5 m, while the average distance to the 11# coal seam is 66.7 m. The elevation of the bottom plate of the 81,307 working face is lower than the water head elevation of the Ordovician limestone, presenting a challenge of mining under pressure. The 11# coal seam lies almost entirely beneath the water head of the Ordovician limestone. During the mining process of the 8# coal seam, no structural water transmission phenomena, such as faults, have been observed. However, during the development of the 11# coal seam, multiple small faults were encountered, accompanied by water hazards from the bottom plate of the Ordovician limestone, which poses significant challenges for water prevention and control. At present, the degree of cracks development in the coal seam floor and other related issues remains unclear in the mine. Therefore, microseismic location has been carried out in the 81,307 working face to investigate the evolution of disturbance and damage in the floor rock layer during coal seam mining, thereby providing a scientific basis and experience for the safe mining of the 8# coal seam and the underlying 11# coal seam.

3.2 Layout of microseismic location system for working face

Based on the optimization research results of the micro-seismic observation system, location is conducted using the borehole tunnel observation system. The detectors in the tunnel are positioned on the anchor rods of the coal wall side, with the deep hole axis oriented at a 135° angle to the coal wall of the working face, reaching a vertical depth of 25 m. The detectors are installed at the bottom of the holes and sealed with cement mortar.

The micro-seismic location system for the bottom plate of the 81,307 working face consists of two location stations, located in the 81,308 No.2 return air channel and the 81,307 No.2 return air channel, respectively. The location substation in the 81,308 No.2 return air channel is connected to six sensors, which include five detectors positioned on the coal side of the 81,308 No.2 channel and one deep hole detector located in the 81,307 glue transportation channel. The sensors are spaced horizontally 40–60 m apart. Similarly, the location substation in the 81,308 No.2 return air channel is also connected to six sensors, comprising five detectors on the coal side of the 81,307 No.2 channel and one deep hole detector in the 81,307 No.1 return air channel, with the same horizontal spacing. To monitor the damage to the bottom plate, a rolling method is employed: as the working face advances, the detectors in the rear No. 81,308 and No. 81,307 coal seams are relocated to the unexplored area along the mining direction. The deep hole detectors in the No.81,307 rubber transportation channel and No.1 return air channel remain in place, with new location points established in these two tunnels. The detectors in the tunnels and deep boreholes form a three-dimensional micro-seismic location network that dynamically tracks the development of mining-induced fractures in the coal seam floor, spanning from 150 m behind the mining face to 150 m in front of the working face. Figure 14 illustrates a schematic diagram of the micro-seismic location system as of mid-May 2019.

3.3 Typical microseismic event location

Figure 15 presents the 12 channel signals of the micro-seismic event monitored on 28 June 2019, at 11:41:50. For ease of reference, this event is designated as E20190628-541. With the exception of

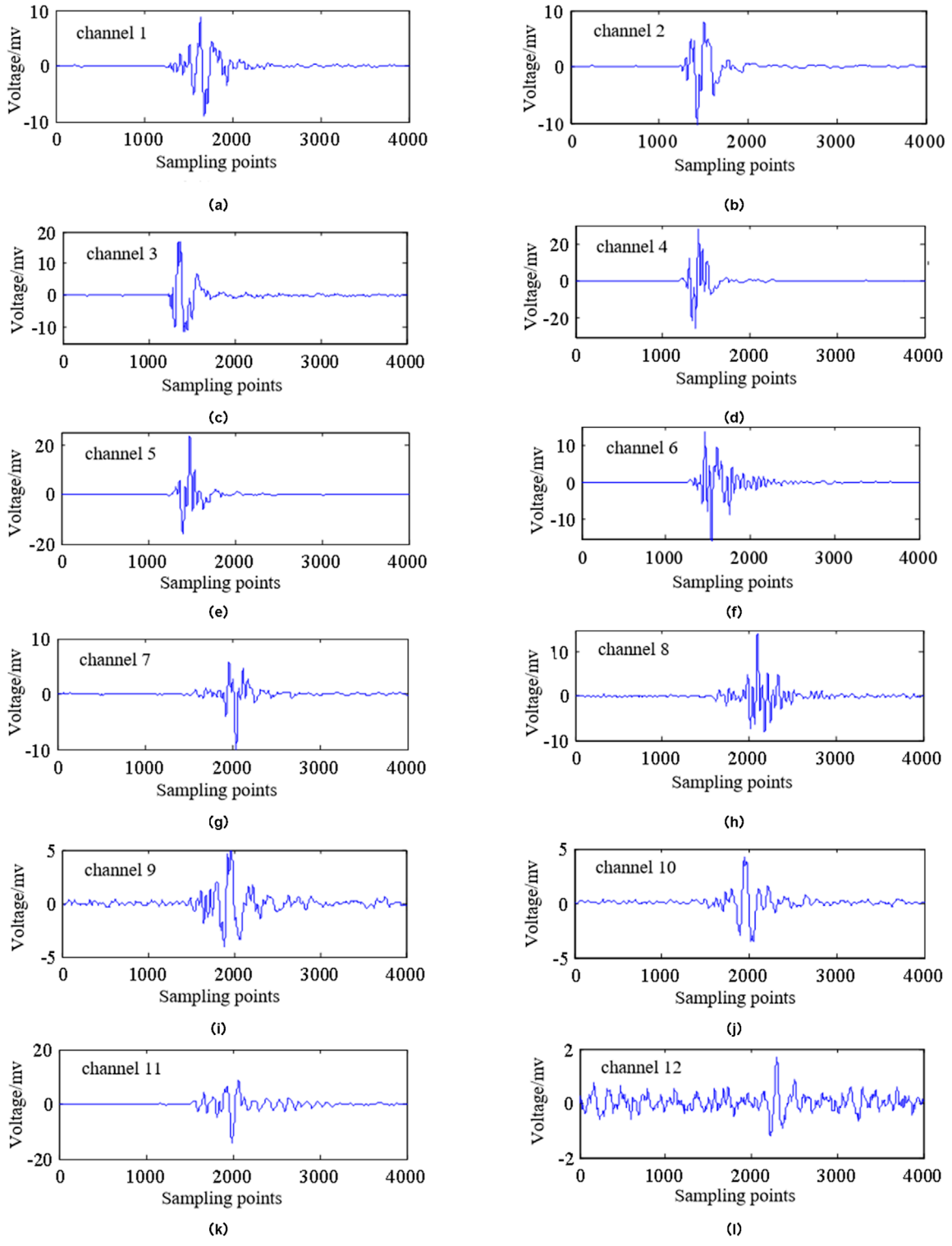

FIGURE 15
Channel waveform of No. E20190628-541 microseismic event.

channel 12, which exhibits a low SNR, the quality of the microseismic signals collected from the other 11 channels is very high, displaying clear oscillations in all P-waves and some S-waves. The VGG-16 pickup value quality control algorithm, derived from previous training, is employed to assess the pickup values of microseismic events. The resulting discrimination vector is {1 1 1 1 1 1 1 1 1 1 1 0}, indicating that the first 11 channel waveforms have valid pickup values, while the 12th pickup value is deemed incorrect and unavailable. The algorithm's discrimination results are accurate.

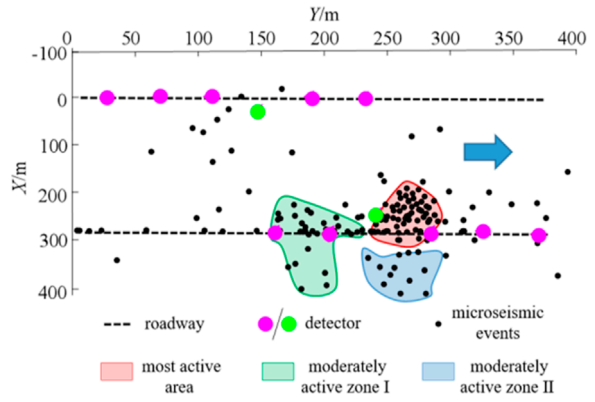

FIGURE 16
X-Y view of microseismic events on the floor.

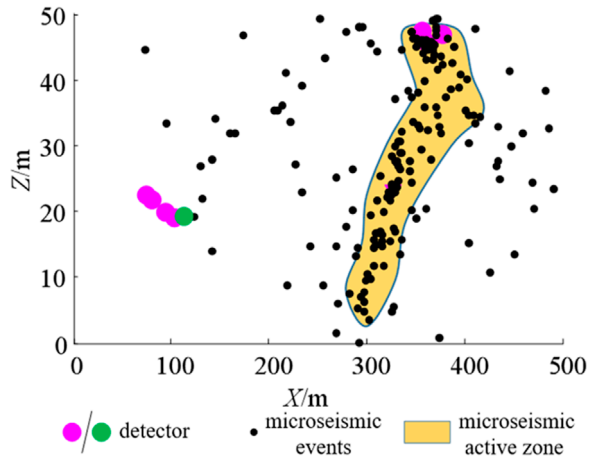

FIGURE 17
X-Z view of microseismic events on the floor.

FIGURE 18
Frequency distribution of microseismic events in front of longwall face.

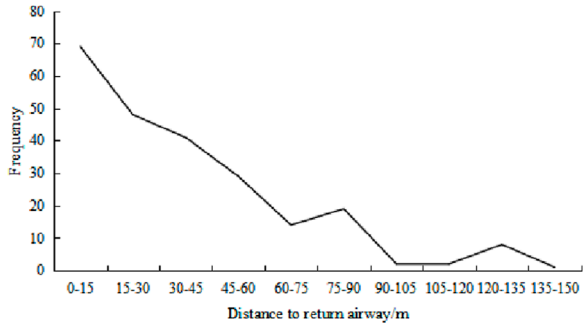

FIGURE 19
Frequency distribution of microseismic events along the trend.

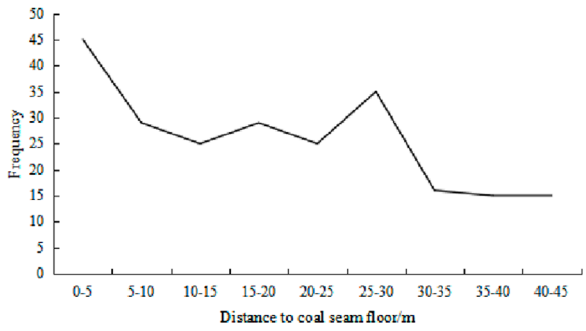

FIGURE 20
Frequency distribution of microseismic events along depth.

Using the aforementioned algorithm for source location, the arrival time of waves 1–11# was processed, resulting in a pickup at P_1=(9334.92, 9938.27, 794.42). For waves 1–12#, the pickup resulted in P_2=(9395.19, 9978.35, 553.48). In contrast, the manually picked arrival time yielded P_3=(9337.32, 9936.29, 793.14). It can be concluded that P_3 is closest to the true source point, while P_1 and are relatively close to P_3. However, P_2 is significantly further from P_3 and lies outside the range of coal mining disturbance, indicating it can be regarded as a location error.

3.4 Spatial distribution pattern of bottom plate microseismic events

From May 2019 to June 2019, the micro-seismic location system recorded a total of 235 strong micro-seismic events from the bottom plate. The XY and XZ views of the distribution of these micro-seismic events are presented in Figures 16, 17, respectively. The XY view reveals that the micro-seismic events are mainly concentrated near the return airway of the 81,307 working face, within an approximate range of 150 m. In the XZ view, it is evident that the micro-seismic events mainly extend to a depth of 32 m below the coal seam floor. The rupture zone is mainly localized on the return airway side of the 81,307 working face, extending toward the middle of the working face at an inclination angle of 16.5°, with a depth of 32 m below the coal seam floor. Conversely, there are fewer

micro-seismic events observed on the floor of the intake airway side of the 81,307 working face. Analysis indicates that the return air roadway of the 81,307 working face is situated near the goal of the 81,308 working face. During the mining process of the 81,307 working face, cracks in the bottom plate of the 81,306 working face rapidly developed due to secondary mining stress, resulting in the concentration of micro-seismic events primarily on one side of the return air roadway.

3.4.1 Characteristics of bottom plate failure along the strike direction

The frequency chart of micro-seismic events in front of the coal wall in the 81,307 working face is shown in Figure 18. Within a range of 0–40 m in front of the coal wall, micro-seismic events account for 55% of the total, with their frequency remaining relatively stable. In the range of 40–70 m, the occurrence of micro-seismic events gradually decrease. Beyond 70 m in front of the coal wall, there is a sharp decline in the number of micro-seismic events.

3.4.2 Characteristics of failure along the inclined bottom plate

The trend chart showing the distance from the bottom plate micro-seismic event to the return airway plane of the 81,307 working face is shown in Figure 19. Micro-seismic events are mainly concentrated within 90 m of the second side of the return airway, accounting for 94% of the events in this area. As the distance from the return airway increases, the number of micro-seismic events decreases sharply.

3.4.3 Characteristics of failure along the depth of the bottom plate

The trend chart depicting the distance from the coal seam floor micro-seismic events to the coal seam floor of the 81,307 working face is shown in Figure 20. The micro-seismic events related to the coal seam floor are primarily concentrated in the area more than 30 m below the coal seam, accounts for 80% of the total events. In contrast, there are significantly fewer micro-seismic events observed in the area further than 30 m below the coal seam floor.

4 Conclusion

With Liu et al. (2022) Compared with the traditional microseismic positioning studied, in order to enhance the localization accuracy of microseismic events in coal seam floor mining, this study employed theoretical analysis and numerical simulation to investigate the impact of various factors on localization precision. These factors include different observation systems, errors in arrival time picking, and inaccuracies in the wave velocity model. Consequently, the study optimized the bottom plate microseismic location observation system and developed a deep learning-based quality control algorithm for the arrival time picking values of microseismic waveforms. Ultimately, a high-precision localization method for 3D-FSM seismic sources under arrival time quality constraints was proposed. Additionally, research was conducted on the application of these methods to bottom plate microseismic events. The main conclusions are as follows:

- A simulation study on the spatial location accuracy of bottom plate microseismic location was conducted using the theory of optimizing the D-value of seismic source location. The optimized hole-tunnel joint micro-seismic observation system was developed, highlighting the importance of eliminating erroneous picking values and utilizing high-precision velocity models for accurate bottom plate microseismic event location.
- A quality control method for P-wave pickup values based on deep learning was proposed, utilizing a VGG-16 network for training. The trained model achieved the highest recognition accuracy, successfully identify 95% of incorrect pickup values.
- A 3D-FSM source location algorithm incorporating quality control was proposed, demonstrating high computational accuracy, suitability for complex velocity models, and fast iteration speed.
- When subjected to quality control, the algorithm produces results comparable to manual localization in terms of reliability. However, without considering time and quality control, significant errors in localization accuracy may occur.
- The next step will be to further investigate and demonstrate the effectiveness of deep learning in data processing for earthquake source localization.

Data availability statement

The original contributions presented in the study are included in the article/supplementary material, further inquiries can be directed to the corresponding author.

Author contributions

XW: Data curation, Funding acquisition, Methodology, Resources, Software, Writing–original draft, Writing–review and editing. QX: Writing–review and editing, Formal Analysis. JY: Software, Writing–review and editing, Resources.

Funding

The author(s) declare that financial support was received for the research, authorship, and/or publication of this article.This paragraph financially supported by the National Key Research and Development Program Tasks of China (2023YFC3008903-02); the National The General Program of the National Natural Science Foundation of China under Grant (42074175); Science and Technology Innovation Fund Project of CCTEGXIAN (2023XAYJS26).

Conflict of interest

Authors XW, QX, and JY were employed by China Coal Technology and Engineering Group Corp. Authors QX and JY were employed by Xi'an CCTEG Transparent Geology Technology Co., Ltd.

Publisher's note

References

Anikiev, D., Waheed, U. B., Staněk, F., Alexandrov, D., Hao, Q., Iqbal, N., et al. (2022). Traveltime-based microseismic event location using artificial neural network. *Front. Earth Sci.* 10, 1046258. doi:10.3389/feart.2022.1046258

Barthwal, H., and Shcherbakov, R. (2024). Unsupervised clustering of mining-induced microseismicity provides insights into source mechanisms. *Int. J. Rock Mech. Min. Sci.* 183, 105905. doi:10.1016/j.ijrmms.2024.105905

Charles, M., and Maochen, G. (2018). Enhancing manual P-phase arrival detection and automatic onset time picking in a noisy microseismic data in underground mines. *Int. J. Min. Sci. Technol.* 28, 691–699. doi:10.1016/j.ijmst.2017.05.024

Chen, W., Chou, C., and Kao, C. (2015). Erratum to: lax–friedrichs multigrid fast sweeping methods for steady state problems for hyperbolic conservation laws. *J. Sci. Comput.* 64, 619. doi:10.1007/s10915-015-0025-4

Cheng, G., Ma, T., Tang, C., Liu, H., and Wang, S. (2017). A zoning model for coal mining - induced strata movement based on microseismic monitoring. *Int. J. Rock Mech. Min. Sci.* 94, 123–138. doi:10.1016/j.ijrmms.2017.03.001

Cheng, J., Song, G., Sun, X., Wen, L., and Li, F. (2018). Research developments and prospects on microseismic source location in mines. *Engineering* 4, 653–660. doi:10.1016/j.eng.2018.08.004

Gong, S.-Y., Dou, L.-M., Cao, A.-Y., He, H., Du, T.-T., and Jiang, H. (2010). Study on optimal configuration of seismological observation network for coal mine. *Chinese Journal of Geophysics* (in Chinese) 53 (2), 457–465. doi:10.3969/j.issn.0001-5733.2010.02.025

Huang, L., Li, J., Hao, H., and Li, X. (2018). Micro-seismic event detection and location in underground mines by using Convolutional Neural Networks (CNN) and deep learning. *Tunn. Undergr. Space Technol.* 81, 265–276. doi:10.1016/j.tust.2018.07.006

Jafari, A., Alesheikh, A., Rezaie, F., Panahi, M., Shahsavar, S., Lee, M., et al. (2023). Enhancing a convolutional neural network model for land subsidence susceptibility mapping using hybrid meta-heuristic algorithms. *Int. J. Coal Geol.* 277, 104350. doi:10.1016/j.coal.2023.104350

Jiang, C., Liu, C., and Shang, X. (2021b). Double event joint location method considering P-wave arrival time system errors. *Soil Dyn. Earthq. Eng.* 149, 106890. doi:10.1016/j.soildyn.2021.106890

Jiang, R., Dai, F., Liu, Y., and Li, A. (2021a). Fast marching method for microseismic source location in cavern-containing rockmass: performance analysis and engineering application. *Engineering* 7, 1023–1034. doi:10.1016/j.eng.2020.10.019

John, R. C. St., and Draper, N. R. (1975). D-optimality for regression designs: a review. *Technometrics* 17 (1), 15–23. doi:10.1080/00401706.1975.10489266

Kijko, A., and Sciocatti, M. (1995). Optimal spatial distribution of seismic stations in mines. *International Journal of Rock Mechanics and Mining Sciences and Geomechanics Abstracts* 32, 607–615. doi:10.1016/0148-9062(94)00052-5

Kijko, A., and Sciocatti, M. (1993). Optimum spatial distribution of seismic stations. In *Guide io Seismic Monitoring in Mines*. Welkom: ISS International.

Li, W., Li, Q., Hu, Q., Qian, Y., Yang, H., Jiang, Z., et al. (2023a). Real-time microseismic evaluation of coalbed methane reservoir stimulation based on improved metaheuristic inversion strategy. *Gas Sci. Eng.* 119, 205151. doi:10.1016/j.jgsce.2023.205151

Liu, H., huang, H., Zhang, P., Li, L., Hou, J., Zhang, L., et al. (2022). Propagation path tracing of hydraulically created fractures based on microseismic monitoring. *Front. Earth Sci.* 10, 952694. doi:10.3389/feart.2022.952694

Li, Z., Ren, T., Black, D., Qiao, M., Abedin, I., Juric, J., et al. (2023b). *In-situ* gas contents of a multi-section coal seam in Sydney basin for coal and gas outburst management. *Int. J. Coal Sci. and Technol.* 10 (62), 62–13. doi:10.1007/s40789-023-00614-4

Ma, K., Sun, X., Tang, C., Yuan, F., Peng, Y., Liu, K., et al. (2020). An early warning method for water inrush in Dongjiahe coal mine based on microseismic moment tensor. *J. Central South Univ.* 27, 3133–3148. doi:10.1007/s11771-020-4534-4

Mngadi, S. B., Durrheim, R. J., Manzi, M. S. D., Ogasawara, H., Yabe, Y., Yilmaz, H., et al. (2019). Integration of underground mapping, petrology, and high-resolution microseismicity analysis to characterise weak geotechnical zones in deep South African gold mines. *Int. J. Rock Mech. Min. Sci.* 114, 79–91. doi:10.1016/j.ijrmms.2018.10.003

Pan, W., Pan, W., Luo, J., Fan, L., Li, S., and Erdenebileg, U. (2020). Slope stability of increasing height and expanding capacity of south dumping site of Hesgoula coal mine: a case study. *Int. J. Coal Sci. and Technol.* 8, 427–440. doi:10.1007/s40789-020-00335-y

Qian, Y., Li, Q., Liang, Y., Hu, Q., Li, W., Li, J., et al. (2024). Evaluation of hydraulic fracturing in coal seam using ground microseismic monitoring and source location. *Rock Mech. Rock Eng.* 57, 679–694. doi:10.1007/s00603-023-03577-9

Rikitake, T. (1976). Recurrence of great earthquakes at subduction zones. *Tectonophysics* 35, 335–362. doi:10.1016/0040-1951(76)90075-5

Samsonov, S. V., Feng, W., Blais-Stevens, A., and Eaton, D. W. (2024). Ground deformation due to natural resource extraction in the Western Canada Sedimentary Basin. *Remote Sens. Appl. Soc. Environ.* 32, 101159. doi:10.1016/j.rsase.2024.101159

Sedghizadeh, M., van den Berghe, M., and Shcherbakov, R. (2023). Statistical and clustering analysis of microseismicity from a Saskatchewan potash mine. *Front. Appl. Math. Stat.* 9, 1126952. doi:10.3389/fams.2023.1126952

Tro, S., Evans, M., Aslam, T., Lazano, E., and Culp, D. (2023). A second-order distributed memory parallel fast sweeping method for the Eikonal equation. *J. Comput. Phys.* 474, 111785. doi:10.1016/j.jcp.2022.111785

Viatkin, D., Garcia-Zapirain, B., Méndez-Zorrilla, A., and Zakharov, M. (2021). Deep learning approach for prediction of critical temperature of superconductor materials described by chemical formulas. *Front. Mater* 8, 714752. doi:10.3389/fmats.2021.714752

Xiang, Z., Zhen, R., Xu, Y., Wang, S., Ao, X., Chen, Z., et al. (2023). A numerical pressure transient model of fractured well with complex fractures of tight gas reservoirs considering gas-water two phase by EDFM. *Geoenergy Sci. Eng.* 231, 212286. doi:10.1016/j.geoen.2023.212286

Xue, Y., Zhu, S., and Qiu, H. (2023). Refinement study on the water-inrush risk of close-distance thin coal seam mining with pressure in the lower coal seam. *Mine Water Environ.* 42, 670–686. doi:10.1007/s10230-023-00965-z

Yang, H., Liu, S., and Yang, C. (2022). Dynamic monitoring of mining destruction on coal seam floor with constrained time-lapse resistivity imaging inversion. *IEEE Access* 10, 84799–84808. doi:10.1109/ACCESS.2022.3197759

Zhang, L., Ge, Z., Lu, Y., Zhou, Z., Xiao, S., and Deng, K. (2020). Tree-type boreholes in coal mines for enhancing permeability and methane drainage: theory and an industrial-scale field trial. *Nat. Resour. Res.* 29, 3197–3213. doi:10.1007/s11053-020-09654-y

Zhao, J., Jiang, Q., Liu, J., Chen, B., Pei, S., and Wang, Z. (2022). Rock fracturing observation based on microseismic location and borehole imaging: *in situ* investigation in a large underground cavern under high geostress. *Tunn. Undergr. Space Technol.* 126, 104549. doi:10.1016/j.tust.2022.104549

Zhao, Y., Yang, T., Hou, J., Jeon, S., Zhang, P., Wang, S., et al. (2023). A new rock fracture reconstruction method under the constraints of microseismic location and focal mechanism. *Int. J. Rock Mech. Min. Sci.* 170, 105493. doi:10.1016/j.ijrmms.2023.105493

Zhou, J., Shen, X., Qiu, Y., Shi, X., and Khandelwal, M. (2022). Cross-correlation stacking-based microseismic source location using three metaheuristic optimization algorithms. *Tunn. Undergr. Space Technol.* 126, 104570. doi:10.1016/j.tust.2022.104570

frontiers | Frontiers in Earth Science

TYPE Original Research
PUBLISHED 27 November 2024
DOI 10.3389/feart.2024.1457240

OPEN ACCESS

EDITED BY
Fuqiong Huang,
China Earthquake Networks Center, China

REVIEWED BY
Jeffrey Todd Freymueller,
Michigan State University, United States
Chen Chieh-Hung,
China University of Geosciences
Wuhan, China

*CORRESPONDENCE
Alexandre Canitano,
canitano@earth.sinica.edu.tw

RECEIVED 30 June 2024
ACCEPTED 12 November 2024
PUBLISHED 27 November 2024

CITATION
Lin H-F, Canitano A and Hsu Y-J (2024) Kinematic GNSS inversion of the large afterslip (M_w 6.4) following the 2019 M_w 6.2 Hualien earthquake (Taiwan).
Front. Earth Sci. 12:1457240.
doi: 10.3389/feart.2024.1457240

Kinematic GNSS inversion of the large afterslip (M_w 6.4) following the 2019 M_w 6.2 Hualien earthquake (Taiwan)

Hsiao-Fan Lin[1,2], Alexandre Canitano[3]* and Ya-Ju Hsu[3]

[1]Université Côte d'Azur, IRD, CNRS, Observatoire de la Côte d'Azur, Géoazur, France, [2]Geological Survey of the Netherlands, Nederlandse Organisatie Voor Toegepast Natuurwetenschappelijk Onderzoek (TNO), Utrecht, Netherlands, [3]Institute of Earth Sciences, Academia Sinica, Taipei, Taiwan

The postseismic deformation following the April 2019 Mw 6.2 Hualien earthquake presents an unique opportunity to investigate the mechanisms by which the northern section of the Longitudinal Valley accommodates lithospheric deformation. We apply a variational Bayesian independent component analysis approach to displacement time-series to infer a 6-month long afterslip. Kinematic inversion shows that displacements are well explained by widespread afterslip (~60 km in the along-strike direction) with limited slip (≤0.1 m) surrounding the coseismic slip area. The total geodetic moment relieved by afterslip (M0 ~ 4.6×10^{18} Nm, i. e., Mw ~ 6.4) is twice as large as the mainshock seismic moment, which represents a rare exception of a moderate magnitude event for which the afterslip moment exceeds that of the seismic moment. Then, combining geodetic and seismological analysis, we infer that afterslip is the dominant mechanism of near-to intermediate-field postseismic deformation and also likely represents the driving force that controls aftershock productivity and the spatiotemporal migration of seismicity. Besides, the fault zone frictional stability parameter a-b of rate-and-state dependent friction (a-b ~ 0.0067–0.02) is comparable with previous estimates in the Longitudinal Valley. Finally, the study demonstrates that the northern Longitudinal Valley region hosts complex seismogenic structures that display a variety of slip behaviors.

KEYWORDS

postseismic activity, kinematic inversion, aftershock activity, rate and state dependent friction, taiwan

1 Introduction

Geodetic measurements have revealed that earthquakes are generally followed by a phase of postseismic relaxation gradually decaying with time. Postseismic deformation, which represents the Earth's response to coseismic stress perturbations, can last hours to years following an earthquake (Fukuda and Johnson, 2021; Zhao et al., 2022). Several mechanisms are commonly involved in postseismic deformation, including afterslip on fault portions surrounding the coseismic rupture (Marone et al., 1991) or on nearby faults (Tang et al., 2023), viscoelastic flow in the lower crust and/or upper mantle (Bürgmann and Dresen, 2008; Fukuda and Johnson, 2021) and poroelastic fluid flow in the shallow crust (Peltzer et al., 1996; McCormack et al., 2020). Postseismic deformation usually contributes significantly more to earthquake moment release than aftershocks (Gualandi et al., 2020)

and afterslip is often considered as the primary force that drives aftershocks (Perfettini and Avouac, 2004; Canitano et al., 2018).

Located at the collisional boundary between the Eurasian plate (EP) and the Philippine Sea plate (PSP), Taiwan is a highly active seismic and tectonic zone. In eastern Taiwan, the Longitudinal Valley (LV) represents the suture of the collision (Barrier and Angelier, 1986), accounting for a third of tectonic plate convergence (Yu and Kuo, 2001). A major part of the oblique plate convergence (geodetic rate ~ 40 mmyr^{-1}) is accommodated by the Longitudinal Valley fault (LVF) (Thomas et al., 2014), which bounds the eastern flank of the LV, and represents the main active fault in eastern Taiwan (Yu and Kuo, 2001). The Central Range fault (CRF) dips westward beneath the western flank of the LV, contributing to the rapid uplift (geological rate of 3–10 mmyr^{-1}) of the Central Range (Shyu et al., 2006). The Hualian region in the northern LV is located in a complex post-collisional environment (Shyu et al., 2016; Lin et al., 2023a) characterized by the transition from the Ryukyu subduction to the collision between the Luzon arc and the Chinese continental margin (Rau et al., 2008) (Figure 1). This complex tectonic setting creates various seismogenic structures associated with destructive earthquakes [e.g., 1951 M_L 7.3 Hualien-Taitung sequence (Chen et al., 2008), 2018 M_w 6.4 Hualien earthquake (Huang and Huang, 2018) or the 2024 M_w 7.4 event (Chang et al., 2024)] and also with frequent seismic swarms (Rau and Liang, 2022; Huang and Wang, 2022).

The 18 April 2019 M_w 6.2 earthquake ruptured a compact asperity (about 15 km × 10 km) located on the intermediate to deep section of a west-dipping blind fault (15–25 km depth) (Jian and Wang, 2022) with maximum coseismic slip of 0.8 m (Lee et al., 2020). Huang and Wang (2022) proposed that this blind fault may represent the northern extension of the CRF, albeit further observations are needed to better characterizing the complex seismotectonics of the northern LV. However, the rare occurrence of a moderately large earthquake in the area presents an unique opportunity to investigate the mechanisms by which the northern LV region accommodates lithospheric deformation. In this study, we invert GNSS displacement time-series to derive a kinematic model for the 6-month long afterslip following the 2019 Hualien event. We then analyze the seismicity and its possible interactions with aseismic fault motion throughout the earthquake postseismic period.

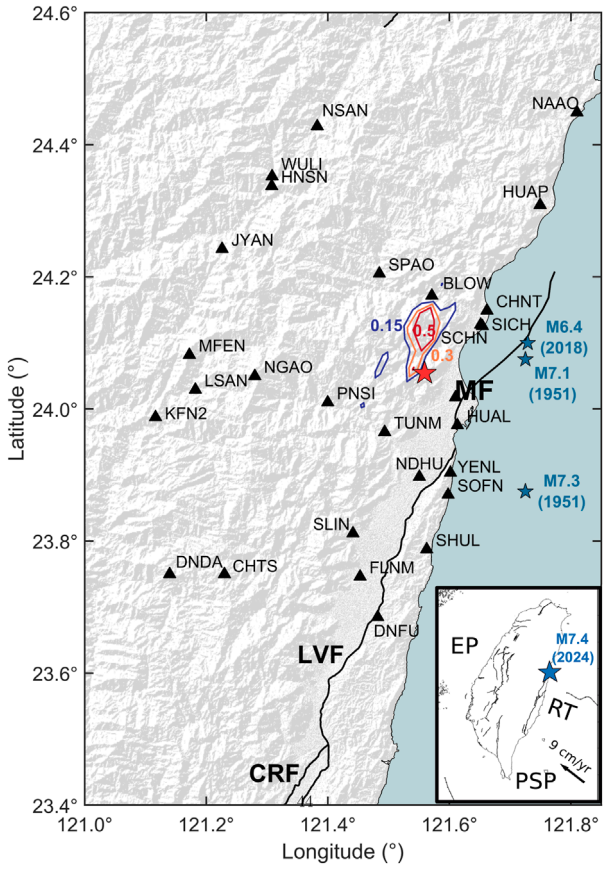

FIGURE 1
Map of eastern Taiwan. The red star shows the epicenter of the 2019 Hualien earthquake and colored contours outline the coseismic slip distribution (with 0.15, 0.30 and 0.50-m intervals) of the Lee et al. (2020) finite-fault source. The blue stars show the epicenters of the large earthquakes ($M_w \geq 6.4$) occurring in the Hualien region from 1951 to 2024. The black triangles represent the GNSS stations used in this study (Inset) Geodynamic framework of Taiwan. The black arrow indicates the relative motion between the Philippine Sea plate (PSP) and the Eurasian plate (EP); (RT): Ryukyu Trench. LVF: Longitudinal Valley fault; CRF: Central Range fault; MF: Milun fault.

2 Instrumentation and data processing

2.1 GNSS displacements

We use the *GAMIT10.42/GLOBK5.16* software packages (Herring et al., 2010) to process the 3-D displacement time-series from 2018 to 2021 for 27 Global Navigation Satellite System (GNSS) stations deployed in the Hualien region (Figure 1). We obtain daily solutions in the ITRF2014 reference frame (Altamini et al., 2016) by utilizing double-differenced carrier phase measurements, and we enhance the regional deformation pattern for Taiwan by incorporating additional stations, including 362 from Taiwan, 8 from the Ryukyu islands and 17 International GNSS Service sites in the Asia-Pacific region. We utilize the following model equation to parametrize the time-dependent displacements (Lin et al., 2023b):

$$x(t) = x_0 + vt + \sum_{i=1}^{n_{eq}} H\left(t - t_{eq}^{(i)}\right) A_{eq}^{(i)} + \sum_{j=1}^{n_{off}} H\left(t - t_{off}^{(j)}\right) A_{off}^{(j)} + A_{yr}\sin(2\pi t) + B_{yr}\cos(2\pi t) + A_{hfyr}\sin(4\pi t) + B_{hfyr}\cos(4\pi t) + \sum_{i=1}^{n_{eq}} H\left(t - t_{eq}^{(i)}\right) A_{post}^{(i)} \times \left(1 - e^{-\frac{t - t_{eq}^{(i)}}{\tau_{post}^{(i)}}}\right)$$

where $x_0 + vt$ is the secular velocity, $A_{eq}^{(i)}$ and $A_{off}^{(j)}$ are the coseismic steps and instrumental offsets starting at time $t_{eq}^{(i)}$ and $t_{off}^{(j)}$ respectively, n_{eq} and n_{off} are the number of detected earthquakes and offsets, A_{yr} and B_{yr} are sine and cosine terms to represent the annual seasonal motion, A_{hfyr} and B_{hfyr} are sine and cosine terms to represent the semi-annual cycle, $A_{post}^{(i)}$ is the maximum amplitude of the postseismic displacement with relaxation time $\tau_{post}^{(i)}$, and H is the Heaviside step function. The H function aims to correct offsets that inevitably contaminate

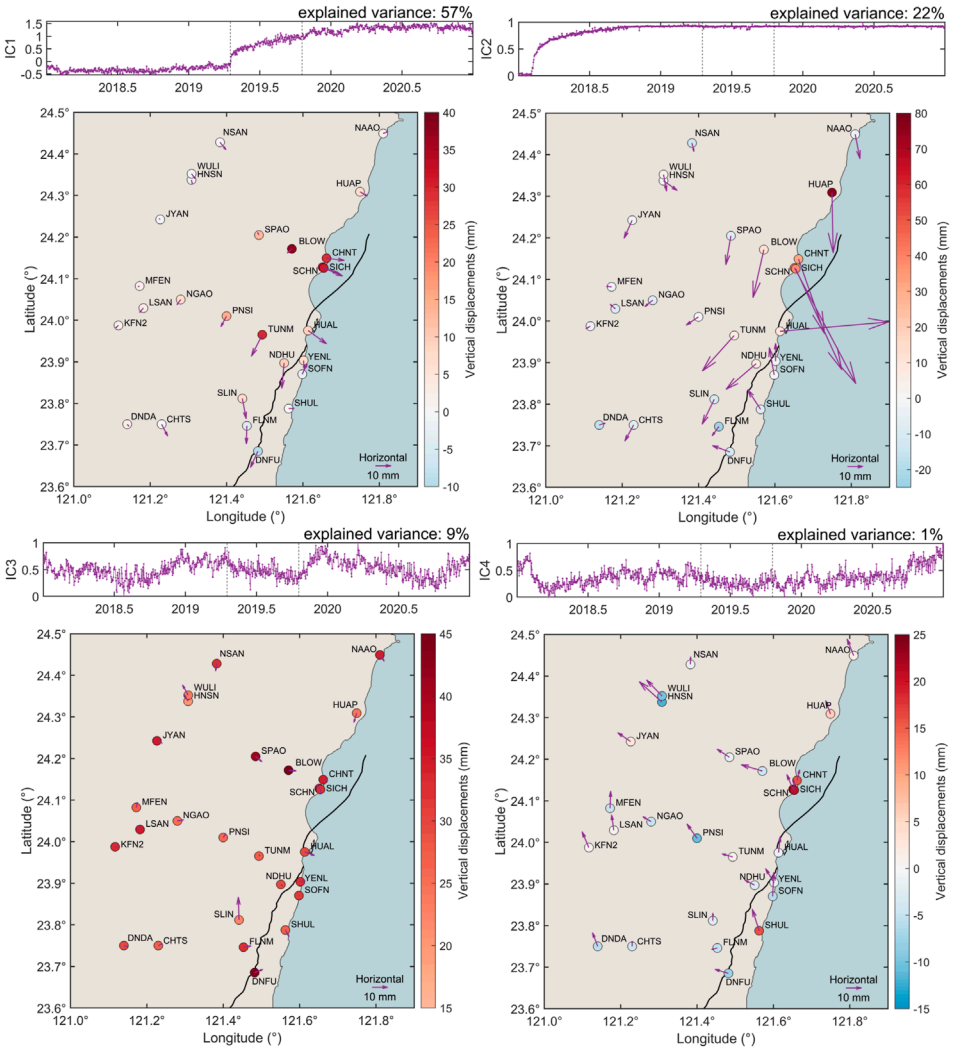

FIGURE 2
Temporal evolution of the four independent components (ICs) over a 3-year period (2018–2021) and related 3-D displacements. The vertical dashed lines denote the occurrence of the 2019 Hualien earthquake and the duration of postseismic deformation (about 6 months), respectively. The afterslip following the 2019 Hualien earthquake is mapped in IC1 component.

GNSS time-series. Offsets can be categorized into actual crustal motions such as earthquakes, or artificial events (e.g., equipment malfunction and change, environmental perturbations) (Williams, 2003). In particular, changes of antennas at GNSS reference stations frequently produce discontinuities in the coordinate time series that are mainly caused by changes of carrier-phase multipath effects and different errors in the antenna phase center corrections (Wanninger, 2009).

To isolate the signals related to postseismic deformation, we input the GNSS time-series detrended and cleaned for tectonic and non-tectonic offsets into a variational Bayesian independent component analysis (vbICA) algorithm (Choudrey and Roberts, 2003) modified to study complex geodetic signals (Gualandi et al., 2016). This method assumes that observations are a combination of a limited number of statistically independent sources, which can be extracted and characterized using their multimodal probability density functions. We extract four independent components (IC) determined by the Automatic Relevance Determination method (Gualandi et al., 2016). The postseismic deformation signal from the 2019 earthquake is mapped in the first independent component IC1 (Figure 2) and explains approximately 60% of the total GNSS data variance. IC2 component denotes the postseismic signal associated with the 2018 M_w 6.4 Hualien event (Zhao et al., 2020) (early to mid-2018), explaining about 20%–25% of the signal variance. Finally, annual (IC3) and multi-annual (IC4) hydrological perturbations (Hsu et al., 2020; Lin et al., 2023b) represent less than 10% of the total GNSS data variance. Figure 3 shows an example of vbICA approach over the 3-year period (2018–2021) that shows the extraction of the 6-month long postseismic displacements (IC1).

2.2 Seismicity

We analyze the seismicity collected by the Central Weather Administration (CWA) of Taiwan during the first 6 months

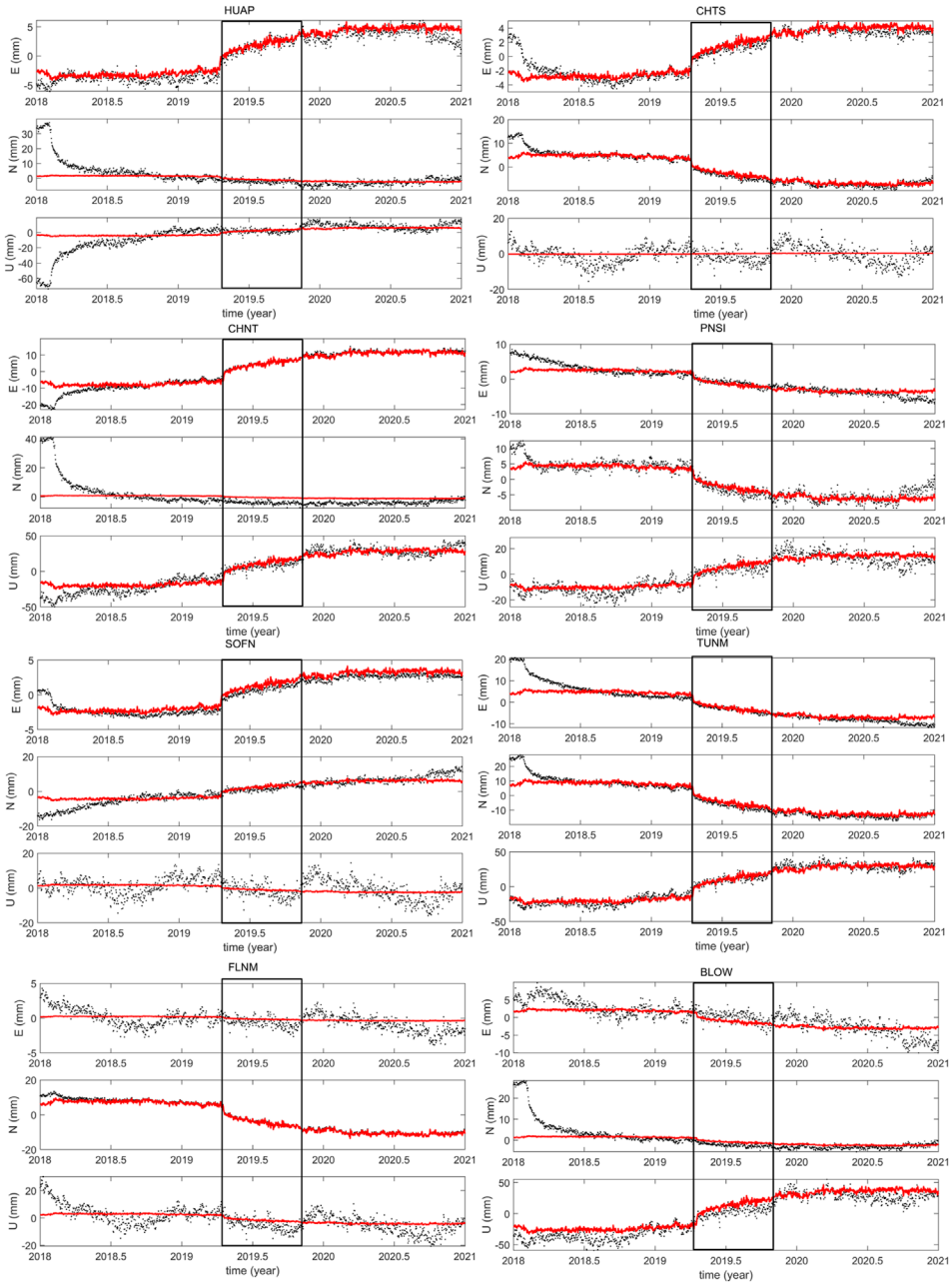

FIGURE 3
Example of analysis in independent component (ICA) over a 3-year period (2018–2021) showing the extraction of the 6-month long postseismic displacements (IC1) (black box) related to the 2019 Hualien earthquake. The black curve denotes the GNSS time-series corrected for a linear trend and large coseismic and instrumental offsets and the red curve shows the IC1 component, respectively.

following the mainshock (until 15 October 2019). We select all events located between the depth of 0–30 km in the region defined by 121.4°E–121.7°E and 23.8°N-24.3°N (2,504 events). We estimate the magnitude of completeness M_c of the aftershock sequence using the maximum curvature approach in the *ZMAP* software (Wiemer, 2001) with a correction factor of 0.1 (Schorlemmer et al., 2005). We find M_c = 1.1 ± 0.1 and estimate parameters a = 4.20 and b = 0.86 ± 0.01 in the Gutenberg-Richter law (Gutenberg and Richter, 1944) through a maximum-likelihood approach (Supplementary Figure S1). We observe that the b-value is slightly larger than previous estimates inferred for the LV (b ~ 0.70–0.80) (Wu et al., 2018).

We observe mainly two patterns of seismicity during the 6 months following the mainshock (Figure 4). First, the main earthquake cluster is concentrated at mid-crustal depth (~ 13–25 km) and events fall both within and at the edge of the regions of moderate to large coseismic slip (0.15–0.5 m). The temporal evolution of seismicity is well explained by an Omori-like decay (Utsu et al., 1995) with parameters: p = 0.67, k =

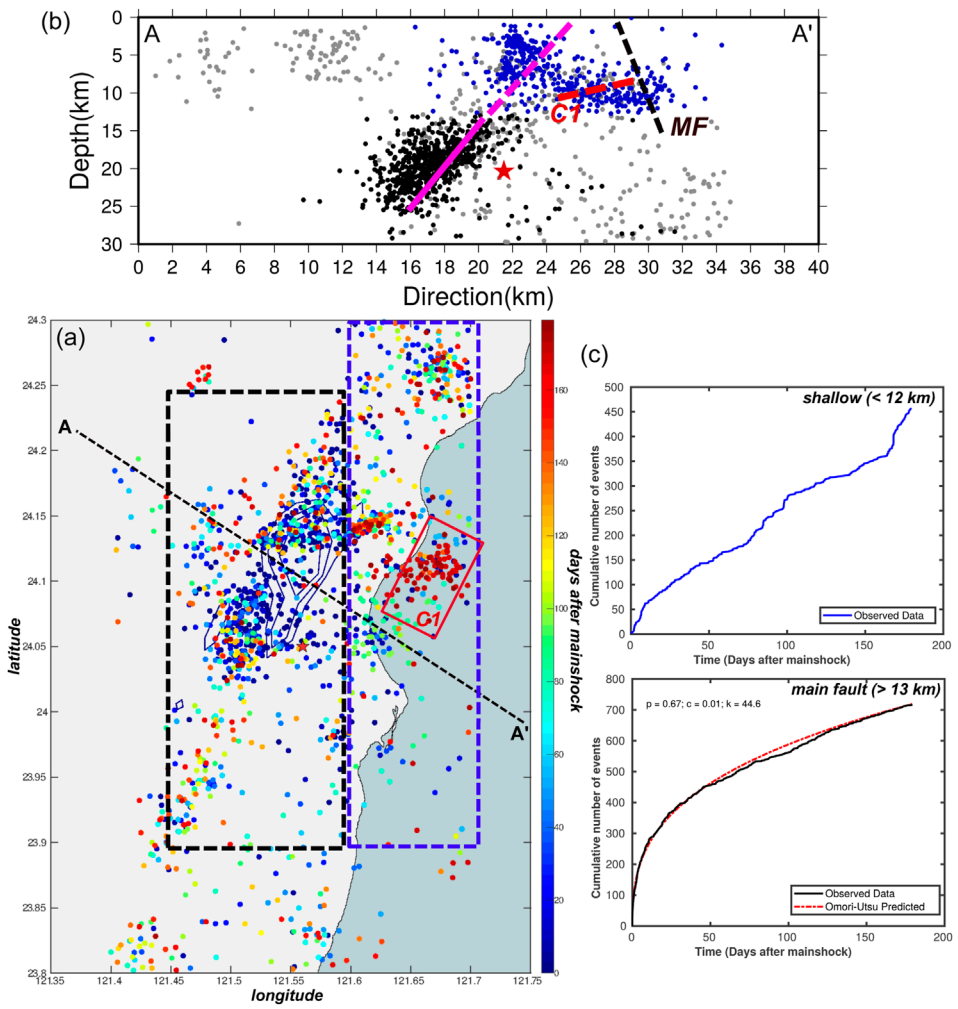

FIGURE 4
(A) Surface projection of the spatiotemporal evolution of the seismicity (with $M_L \geq 1.1$) during the first 6 months following the 2019 Hualien mainshock. The blue contours outline the coseismic slip distribution (see Figure 1). The black dashed line denotes the cross-section in **(B)**. The black and blue dashed boxes represent the events retained to analyze the seismicity in **(B)** and **(C)**. The red plane outlines the west-dipping fault plane C1 associated with earthquake swarms in September-October 2019 [adapted from Jian and Wang (2022)]. The red star shows the mainshock epicenter. **(B)** Cross-section perpendicular to the mainshock fault plane. The black and blue dots show the events that occurred on the mainshock fault plane (depth $\geq$ 13 km) and at shallower depth (depth $<$ 12 km), respectively. Gray dots are events not used in **(C)**. The black dashed line denotes the MF, the purple line is the mainshock fault plane with its possible extension towards the surface denoted as a purple dashed line and the red dashed line denotes C1, respectively. **(C)** Cumulative seismicity (with $M_L \geq 1.1$) calculated for each region over a 6-month period following the mainshock. Cumulative number of events (N) in the mainshock region are approximated with the cumulative Omori-Utsu law ($N(t) = K(c^{1-p} - (t+c)^{1-p})/(p-1)$, where K, c and p are constants and t is time).

44.6, and c = 0.01 days. Second, several events (about 30%) are also located at shallow depth (≤~12 km). A first cluster, which is possibly activated during the entire postseismic period, is located in the NE Hualien region (between 24.2°N to 24.3°N) at the depth of about 2–8 km. The second cluster is located on the eastern side of the rupture region at the depth of 8–12 km and coincides with the activity of a NW-dipping structure in September-October 2019 (cluster C1) (Jian and Wang, 2022). Overall, the cumulative seismicity at shallow depth shows a succession of low earthquake activity followed by impulsive seismic episodes, which is likely characteristic of earthquake swarm activity (Hainzl, 2004).

3 Analysis of the postseismic deformation process

3.1 Forward models of postseismic deformation

In a first step, we perform a forward modeling to approximate the 3-D surface displacements generated by viscoelastic relaxation in the lower crust and by poroelastic rebound. We use the finite-fault coseismic model from Lee et al. (2020) as the initial stress perturbation. Although being usually the dominant mechanism of deformation in the long run (Bürgmann and Dresen, 2008),

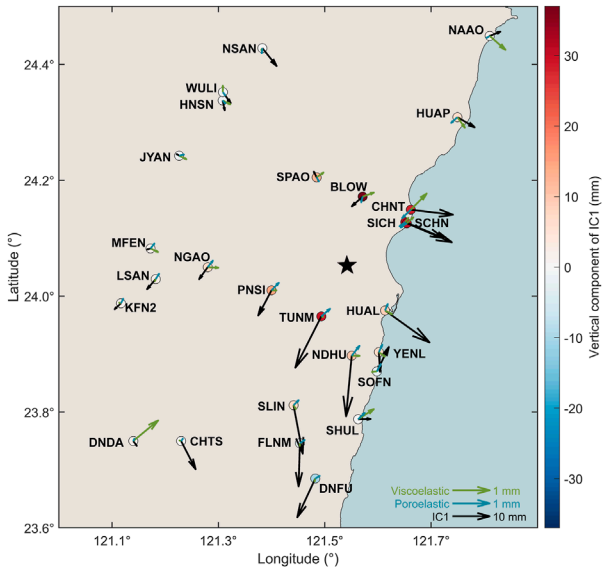

FIGURE 5
Forward modeling approximating the surface displacements generated by viscoelastic relaxation in the lower crust (green vector) and by poroelastic rebound (blue vector) during the first 6 months following the mainshock. The black vectors show the displacements related to IC1 component (Figure 2) and the black star denotes the mainshock epicenter. Viscoelastic relaxation and poroelastic rebound show no appreciable contribution to postseismic deformation (maximum displacements ≤1 mm).

viscoelastic deformation can also accompany moderate-magnitude events (typically M_w ~ 6.0–6.5) (Bruhat et al., 2011; Mandler et al., 2021). We utilize the Relax software (Barbot and Fialko, 2010a; Barbot and Fialko 2010b) to estimate the contribution of viscoelastic relaxation to postseismic deformation signals. We use a Maxwell model with an effective viscosity of 10^{18} Pa.s and a rigidity of 30 GPa to characterize the viscoelastic behavior of the lower crust below the CR at depths greater than 20 km (Huang et al., 2015; Tang et al., 2019) during the first 6 months following the mainshock. We model poroelastic flow by subtracting the elastic coseismic solution for the undrained condition (Poisson ratio of 0.25) to the solution for the drained condition (Poisson ratio of 0.31) (Freed et al., 2017; Li et al., 2021). We observe that poroelastic rebound and viscoelastic relaxation make very little contribution to the postseismic deformation (maximum horizontal displacements ≤1 mm) (Figure 5), therefore we assume that afterslip represents the dominant mechanism of postseismic slip following the Hualien event. Consequently, we do not correct the GNSS displacements for viscoelastic and poroelastic deformation for the kinematic afterslip inversion (Table 1).

3.2 Kinematic afterslip inversion

To obtain a realistic afterslip model, we discretize the mainshock fault plane into 240 subfaults with dimensions of 5 km × 4 km. We fix the fault geometry (strike = 205°, dip = 56°) following the Lee et al. (2020) model but we allow for a variable rake on each subfault to account for possible slip complexity. We perform a weighted linear slip inversion incorporating a smoothness constraint and zero-slip boundary conditions (Lin et al., 2023b) in which we add a zero-slip asperity constraint (Zhao et al., 2022). The latter condition precludes that velocity-weakening regions that exhibit the largest coseismic slip (≥0.5 m) would continue to rapidly slide throughout the postseismic period (Johnson et al., 2012). We solve for the slip on each subfault by minimizing the following cost function $\phi(s)$:

$$\phi(s) = \| \sum_{d}^{-1/2} (d - Gs) \|^2 + \alpha \|Bs\|^2 + \beta \|Ls\|^2 + \gamma \|A W_s s\|^2$$

where Σ_d is the data covariance matrix, d is the matrix of GNSS displacements (Table 1), G is the Green's function following Okada (1992), s is the slip vector on each subfault, B represents the zero slip boundary condition, and L is the 9-point stencil finite difference Laplacian. α and β are the weighting factors for boundary and smoothing constraints, respectively, A represents the zero slip asperity condition with weight W_s proportional to the amount of coseismic slip on each subfault and γ is the related weighting factor. We define the weighted misfit m_G between the corrected GNSS displacements and the modeled afterslip displacements following Lin et al. (2023b):

$$m_G = \sqrt{\frac{r^T W r}{Tr(W)/3}}$$

where r is the vector of residual displacements between GNSS observations and models, W is the weight matrix, and $Tr(.)$ is the matrix trace. We estimate the optimal smoothing factor ($\beta = 181$) by minimizing the leave-one-out cross-validation mean squared error (Matthews and Segall, 1993) (Supplementary Figure S2A).

Our preferred model (m_G = 6.0 mm, see Supplementary Figure S2B) exhibits a dominant thrust-faulting mechanism with a left-lateral component, which is compatible with the coseismic slip direction of the mainshock (Lee et al., 2020) (Figure 6A). The afterslip spreads around the coseismic slip region with relatively limited slip (≤ 0.1 m) and extends about 60 km in the along-strike direction and 40 km in the along-dip direction. The two main peaks of afterslip (~ 0.07–0.09 m) are located at the NE and SW edges of the coseismic slip within a similar depth range as the latter. We also observe afterslip (~0.05–0.07 m) that extends toward the surface in the region located right above the main asperity. We infer a total geodetic moment of 4.6×10^{18} N.m, which represents an equivalent moment magnitude of about 6.4. Then, we assess the effect of coseismic slip and associated stress changes on the occurrence and on the spatial distribution of afterslip by resolving the coseismic shear stress changes onto the mainshock fault plane (Figure 6B). The regions with moderate afterslip (0.04–0.06 m) that surround the coseismic rupture are associated with maximum coseismic shear changes (0.04–0.05 MPa) while the areas with peak afterslip are associated with shear changes of about 0.03 MPa. We observe an overall coherent spatial correlation between afterslip distribution and positive coseismic shear changes, which suggests that coseismic shear stress changes may have played a role in controlling the spatial distribution of afterslip (Zhao et al., 2020; Fukuda and Johnson, 2021).

TABLE 1 GNSS displacements analyzed for the kinematic afterslip inversion.

Station	Lon. (°E)	Lat. (°N)	E (mm)	ϵ_E (mm)	N (mm)	ϵ_N (mm)	Z (mm)	ϵ_Z (mm)
CHTS	121.2300	23.7500	3.52055	0.3609	−6.28924	0.6213	0.31164	0.1623
DNFU	121.4822	23.6851	−4.36337	0.4472	−8.62132	0.8535	−8.83389	0.9333
FLNM	121.4533	23.7463	0.31428	0.0785	−9.64335	0.9516	−3.72925	0.4131
NDHU	121.5508	23.8972	1.37732	0.1566	−13.56111	1.3362	8.99052	0.9080
SLIN	121.4414	23.8118	2.22781	0.2444	−10.79723	1.0708	6.61607	0.7451
TUNM	121.4935	23.9652	−6.31210	0.6300	−11.44353	1.1286	26.43101	2.6334
YENL	121.6018	23.9035	−0.28539	0.0780	−4.41704	0.4365	6.45018	0.6596
CNHT	121.6618	24.1492	−10.24275	1.0110	−1.12445	0.1293	25.36721	2.5025
HNSN	121.3080	24.3377	−0.51742	0.1096	−2.17092	0.2246	−0.84161	0.2405
HUAL	121.6135	23.9753	10.79289	1.0655	−7.13185	0.7065	8.27951	0.8526
HUAP	121.7494	24.3090	4.18179	0.4265	−2.26274	0.2378	5.62176	0.7081
KFN2	121.1168	23.9877	−1.52488	0.1641	−1.30382	0.1347	1.48761	0.2070
LSAN	121.1821	24.0293	−2.10250	0.2224	−2.25115	0.2290	2.50860	0.3063
NGAO	121.2800	24.0500	−2.07548	0.2234	−2.68336	0.2700	6.34886	0.6379
PNSI	121.4000	24.0100	−3.22908	0.3400	−5.59497	0.5540	13.17611	1.3254
SCHN	121.6515	24.1277	9.24827	0.9161	−3.53354	0.3507	27.89040	2.7499
SICH	121.6544	24.1257	10.92829	1.0787	−4.22624	0.4176	27.67777	2.7275
SPAO	121.4848	24.2050	−0.68109	0.1095	1.26727	0.1448	11.56746	1.1677
WULI	121.3084	24.3522	1.91145	0.2145	−2.45274	0.2525	0.04578	0.2406
SHUL	121.5627	23.7876	3.03831	0.3138	0.05761	0.0651	0.53350	0.2881
SOFN	121.5981	23.8702	2.88928	0.2981	5.44437	0.5385	−2.13397	0.2845
BLOW	121.5712	24.1717	−2.59863	0.2785	−2.14021	0.2350	33.09211	3.2973
DNDA	121.1400	23.7500	0.84343	0.1075	−1.05328	0.1122	1.72099	0.2159
NAAO	121.8102	24.4493	2.58221	0.2694	0.91013	0.1118	1.26840	0.2837
NSAN	121.3828	24.4282	3.45371	0.3618	−3.98438	0.4015	0.29160	0.3793
JYAN	121.2263	24.2424	−0.60480	0.0914	0.36428	0.0789	−0.49415	0.1908
MFEN	121.1724	24.0821	−0.82052	0.1099	−0.23821	0.0486	1.49199	0.2021

Note: E, N and Z are the east, north and vertical components of postseismic displacements, respectively; ϵ_E, ϵ_N, and ϵ_Z are the errors in east, north and vertical components, respectively.

4 Dynamics of the aftershock sequence in the mainshock region

We investigate a possible link between aftershock activity in the mainshock region and afterslip by comparing the cumulative seismicity with the afterslip temporal function mapped in the IC1 component. We find that the cumulative number of aftershocks and afterslip follow a similar temporal decay that is relatively well-explained with p-value ~0.67 (Figure 7). To investigate a possible gradual expansion of the aftershock front on the fault plane, as often observed during aftershock migration driven by afterslip (Frank et al., 2017; Perfettini et al., 2018), we consider a rate-strengthening rheology (Dieterich, 1994), and assume that an aftershock is triggered when afterslip reaches a critical level on

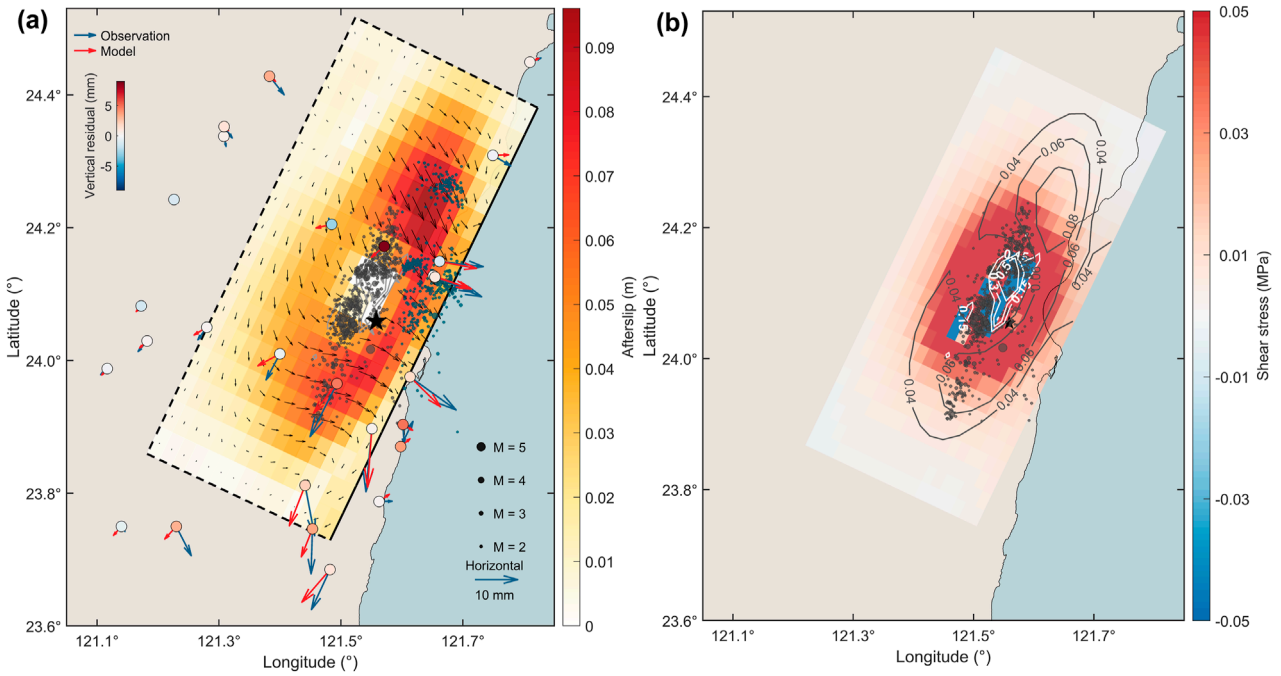

FIGURE 6
(A) Kinematic afterslip distribution over a 6-month period following the 2019 Hualien earthquake resolved on 5 km × 4 km subfaults (β = 181). The black and blue circles show the aftershocks in the mainshock and shallow regions sized by magnitude, respectively (see Figure 4 for detail). The gray contours outline the coseismic slip distribution and the black star denotes the mainshock epicenter. The thick black line depicts the top edge of the fault plane and the dashed lines show its surface projection. **(B)** Coseismic shear stress changes resolved onto the mainshock fault plane. The gray contours outline the afterslip distribution in **(A)** and the white contours denote the coseismic slip distribution.

a nearby creeping patch (Perfettini et al., 2018). The bilateral expansion of the aftershock zone $\Delta A^{+/-}$ along-strike and along-dip since the onset time t_i of the first aftershock can be expressed as (Perfettini et al., 2018; Perfettini et al., 2019):

$$\Delta A^{+/-} = \zeta (a-b)\sigma \frac{A^{+/-}}{\Delta\sigma} \log\left(\frac{t}{t_i}\right) \quad (1)$$

where ζ is a constant of order unity (Frank et al., 2017), $(a-b)\sigma$ is a constitutive parameter, $\Delta\sigma$ is the earthquake stress drop and $A^{+/-}$ are characteristic dimensions of the coseismic rupture ($W^{+/-}$ and $L^{+/-}$ in Figure 7).

We assume $\Delta\sigma$ = 3.3 MPa (Lee et al., 2020), t_i = 98 s and inferred $(a-b)\sigma$ = 1 MPa that best fit our data. This value is consistent with typical values observed for afterslip on continental faults (Perfettini and Avouac, 2004). We observe that the first order features of the bilateral aftershock migration along-strike and along-dip on the fault plane during the first 6 months following the mainshock are well captured by our simple model. We find aftershock migration away from the epicenter with apparent velocity of approximately 5–10 km. day^{-1}, which is in good agreement with estimates typically observed in the case of seismicity driven by aseismic slip (Lohman and McGuire, 2007). Further, we also find an overall coherent spreading of seismicity through the analysis of the event-index (i.e., the order of the occurrence of events) plots for along-strike and along-dip directions, suggesting that subsequent aftershock ruptures are mainly facilitated by aseismic slip rather than by the coseismic slip itself (Fischer and Hainzl, 2021; Cabrera et al., 2022).

Finally, we estimate the effective stress drop $\Delta\sigma_{eff}$ of the aftershock sequence in the mainshock region following Fischer and Hainzl (2017):

$$\Delta\sigma_{eff} = \frac{7}{16}\frac{M_0^{aft}}{R^3}$$

where R is the characteristic radius of the aftershock activated area and M_0^{aft} represents the total seismic moment of the aftershock sequence (M_0^{aft} = 1.25×10^{16} N.m for events with $M_L \geq 1.1$). We infer $\Delta\sigma_{eff}$ varying from 0.0016 MPa to 0.044 MPa for R ranging from 5 km to 15 km. In general, $\Delta\sigma_{eff} <$ ~0.1 MPa is indicative of a low density of asperities with respect to the area covered by the seismicity (Cabrera et al., 2022). Therefore, the relatively low estimated values further support the idea that afterslip represents the dominant mechanism that drives aftershock activity rather than stress transfer in-between sparse asperities (Essing and Poli, 2024).

5 Discussion and conclusions

We analyze GNSS and seismological data to constrain the spatiotemporal evolution of crustal deformation and seismicity throughout the postseismic phase of the 2019 Hualien earthquake. Afterslip often represents the dominant deformation mechanism in the early postseismic phase (Gualandi et al., 2020; Lin et al., 2023b) and we demonstrate that near-source GNSS displacements during the 6 months following the 2019 Hualien earthquake are

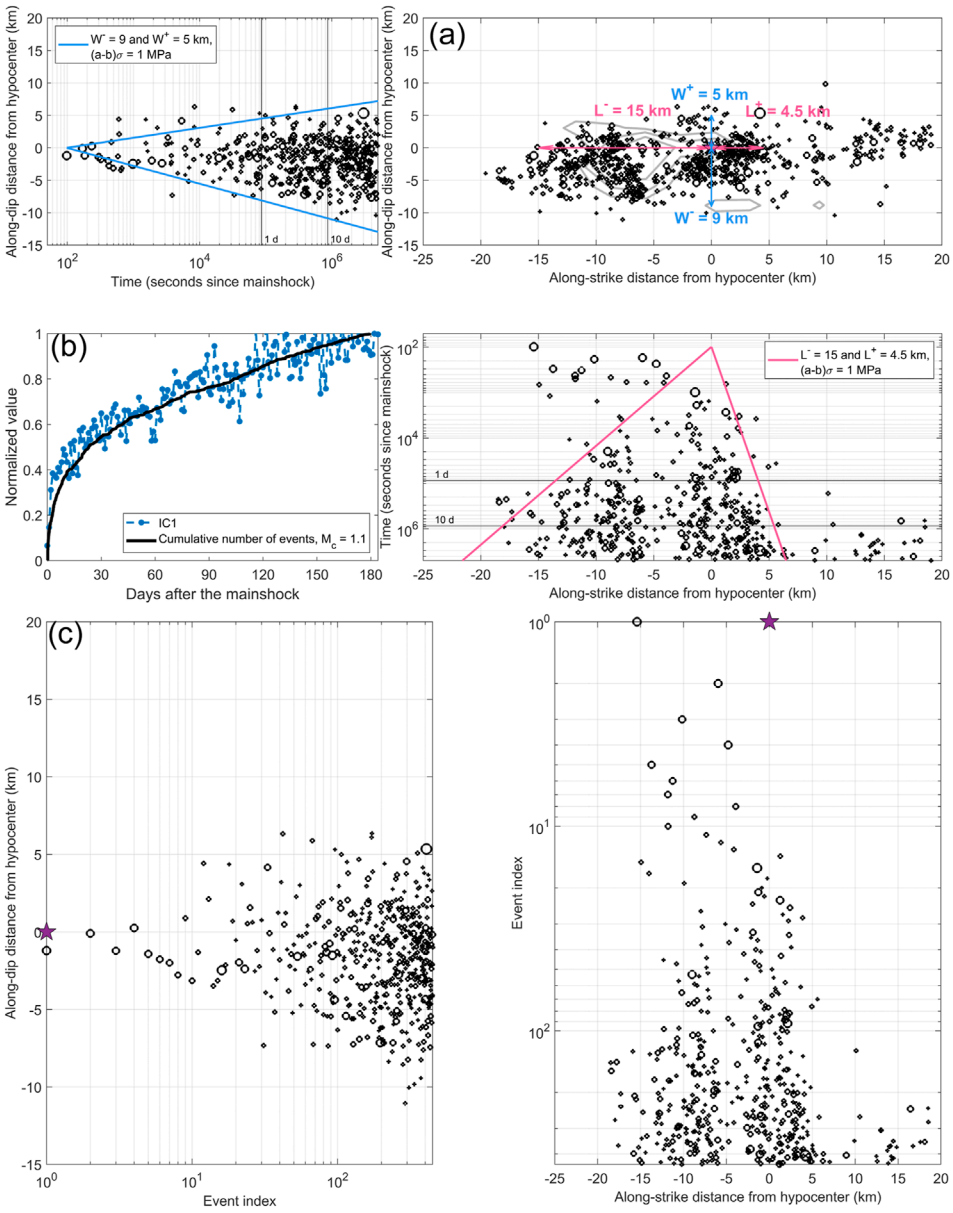

FIGURE 7
(A) Spatiotemporal evolution of the aftershocks along the mainshock fault plane (see Figure 4, black cluster) during the first 6 months following the Hualien earthquake. The pink and blue arrows represent the characteristic dimensions retained for modeling the expansion of the seismicity front along-strike (L^+ = 4.5 km, L^- = 15 km) and along-dip (W^+ = 5 km, W^- = 9 km) away from the centroid (purple star), respectively. The gray contours outline the coseismic slip distribution. The blue and pink lines denote the semilogarithmic bilateral expansion of the aftershock front Equation 1 along dip (left) and along strike (bottom) on the fault plane, respectively. **(B)** Comparison between the cumulative seismicity (with $M_L \geq 1.1$) (black curve) and the temporal evolution of afterslip (IC1 component) (blue dotted dashed line) over a 6-month period. Signals are normalized by their maximum amplitude after 6 months **(C)** Event-index plots computed for the along-dip and along-strike directions away from the hypocenter.

well explained by widespread afterslip located on the mainshock fault plane. While the existence of velocity-strengthening regions, that can sustain afterslip for months or years, were previously evidenced on the southern section of the LVF (Thomas et al., 2014; Canitano et al., 2018) and on the southern and central sections of the CRF (Lin et al., 2023b; Tang et al., 2023), the 2019 Hualien earthquake reveals unambiguously the presence of a large velocity-strengthening zone at shallow to mid-crustal depth in the Hualien region. The afterslip distribution shows a relatively good spatial coherence with coseismic shear stress changes, which suggests that the latter may have helped to promote afterslip (Fukuda and Johnson, 2021). We infer that mid-crustal aftershocks (15–20 km depth) are mainly located in areas of moderate afterslip (~0.03–0.05 m) that directly surround the rupture zone. Besides, the presence of the velocity-strengthening region with moderate afterslip (~0.05–0.07 m) right above the coseismic zone may be compatible with the gap of aftershocks observed at the depth of 10–15 km (see Figure 4). We assess the fault zone frictional

stability parameter $a-b$ in the mainshock region based on the relationship between afterslip and aftershock migration in a rate-and-state regime (Section 4). Considering an effective normal stress at the depth of 20 km ranging from about 50 to 150 MPa in eastern Taiwan (Thomas et al., 2017), we infer $a-b \sim 0.0067$–0.02 that are comparable to estimates in the LV (Thomas et al., 2017) and to laboratory measurements (Marone et al., 1991).

The analysis of seismicity during the first 6 months following the mainshock exhibits two distinct features (Figure 4). The main aftershock cluster is located at mid-crustal depth (~ 13–25 km) in regions associated with moderate to large afterslip (≥ 0.04 m) (Figure 6). We show evidence that the first order features of the bilateral aftershock migration along-strike and along-dip on the fault plane are well captured by a simple model of afterslip migration built on rate-and-state rheology (Perfettini et al., 2019) (Figure 7). Besides, the temporal evolution of seismicity and afterslip are likely correlated, which may further suggest that afterslip represents the driving force behind aftershock productivity (Perfettini and Avouac, 2004; Canitano et al., 2018; Gualandi et al., 2020). We found that the cumulative seismic moment released by aftershocks is only an infinitesimal percent (≤0.03%) of the total geodetic moment relieved by afterslip. Consequently, afterslip represents the prominant driving mechanism of near-to intermediate-field postseismic deformation following the 2019 Hualien event; a pattern typically observed in active regions (Gualandi et al., 2020; Lin et al., 2023b). Nonetheless, Omori-like decays (Utsu et al., 1995) of seismicity and afterslip are well explained with p-value ~0.67, which is slightly lower than the typical estimates ($p = 0.80$–1.04) (Ingleby and Wright, 2017). The Omori-like decay of afterslip with $p < 1$ suggests that additional post-earthquake processes may have contributed to GNSS surface displacements (Morikami and Mitsui, 2020). For instance, Periollat et al. (2022) proposed that early postseismic deformation (minutes to months) with $p < 1$ can result from a transient brittle creep mechanism within an unruptured fault section and its surroundings; a mechanism that is not accounted for in our kinematic model.

We also observe clustered seismic activity at shallow depth (depth ≤ 10 km). The cumulative seismicity pattern shows a succession of low earthquake activity followed by impulsive seismic episodes (Figure 4) that is likely characteristic of earthquake swarm activity (Hainzl, 2004). These events are part of the intense seismic swarm activity in the northern LV that strenghtened following the 2018 M_w 6.4 Hualien earthquake (Jian and Wang, 2022; Huang and Wang, 2022). Here, we infer a first cluster located in the NE Hualien region (between 24.2°N to 24.3°N) at the depth of about 2–8 km. The cluster, which coincides with the region of maximum afterslip (Figure 6A), is activated during the entire postseismic period, likely through sustained aseismic slip at shallow depth. A second cluster, located on the eastern side of the rupture region at the depth of 8–12 km (cluster C1, Figure 4) (Jian and Wang, 2022), is activated in September-October 2019. This cluster, which likely occurred near the end of the postseismic period, coincides with the activity of a NW-dipping structure. Therefore, the afterslip had likely little to no impact on the activation of cluster C1. Overall, the impact of afterslip on shallow seismicity is difficult to assess because of the episodic nature of earthquakes swarms (Soares et al., 2023). The analysis of the interplay between aseismic transient slip and the occurrence of seismic swarms would require further seismological [e.g., repeating earthquakes (Peng et al., 2021)] and geodetic observations [e.g., borehole strainmeter data (Canitano et al., 2021)] and is thus beyond the scope of this study.

Finally, we observe that the geodetic moment of the afterslip ($M_w \sim 6.4$) exceeds that of the seismic moment (M_w 6.2). In general, the afterslip moment of $M_w \geq 6.0$ events rarely exceeds that of the seismic moment (Churchill et al., 2022), with rare exceptions of the 2004 M_w 6.0 Parkfield earthquake (Bruhat et al., 2011) or the 2008 M_w 6.8 Methoni earthquake sequence (Greece) (Howell et al., 2017). However, Hawthorne et al. (2016) suggested that compact ruptures have the potential to generate higher afterslip rates compared to larger, more elongated ruptures because of the relatively larger size of the velocity-strengthening region surrounding the coseismic region that can experience afterslip. For instance, the 2013 M_w 6.3 Ruisui earthquake, which has a rupture elongation about twice larger than the 2019 Hualien event, has generated afterslip with moment that did not exceed 30% of the seismic moment (Lin et al., 2023b). Besides, the unusually large regional ground shaking (> 4 m s^{-2}) for a mainshock of the size of the 2019 earthquake (Lee et al., 2020) may have induced a transient perturbation of the elastic and frictional properties of the fault zone material (Cruz-Atienza et al., 2021) that could have contributed to enhance afterlip. Finally, since high afterslip rates often correlate with fault regions associated with a high level of fluid pressure (Moreno et al., 2014), the elevated pore-fluid pressure observed in the source regions of the 2019 and 2018 Hualien earthquakes (Toyokuni et al., 2021) may have contributed to induce abundant afterslip. Nonetheless, the afterslip moment of the 2018 Hualien earthquake is only a fraction of the seismic moment (about 25%) (Zhao et al., 2020), which further suggests that several factors likely influence afterlip rates in active regions (Churchill et al., 2022).

Data availability statement

The original contributions presented in the study are included in the article/Supplementary Material, further inquiries can be directed to the corresponding author.

Author contributions

H-FL: Conceptualization, Formal Analysis, Investigation, Software, Visualization, Writing–original draft. AC: Conceptualization, Funding acquisition, Project administration, Supervision, Validation, Writing–original draft. Y-JH: Conceptualization, Formal Analysis, Investigation, Software, Visualization, Writing–original draft.

Funding

The author(s) declare that financial support was received for the research, authorship, and/or publication of this article. This research is supported by the Ministry of Science and Technology grant NSTC 113-2116-M-001-009.

Acknowledgments

We are grateful to IES colleagues for collecting and processing the GNSS data. We are thankful to Shiann-Jong Lee for providing

the coseismic slip model and Wen-Tzong Liang for insightful comments. Figures were created by using the Generic Mapping Tools (GMT) (version: GMT 4.5.7, URL link: https://www.generic-mapping-tools.org/download/) (Wessel and Smith, 1998). We are thankful to the Associate Editor Fuqiong Huang and two reviewers for their constructive suggestions and comments allowing to improve the manuscript. This is the contribution of the Institute of Earth Sciences, Academia Sinica, IESAS2423.

Conflict of interest

The authors declare that the research was conducted in the absence of any commercial or financial relationships that could be construed as a potential conflict of interest.

Publisher's note

Supplementary material

The Supplementary Material for this article can be found online at: https://www.frontiersin.org/articles/10.3389/feart.2024.1457240/full#supplementary-material

References

Altamini, Z., Rebischung, P., Metivier, L., and Collilieux, X. (2016). ITRF2014: a new release of the International Terrestrial Reference Frame modeling nonlinear station motions. *J. Geophys. Res. Solid Earth* 121, 6109–6131. doi:10.1002/2016jb013098

Barbot, S., and Fialko, Y. (2010a). Fourier-domain Green's function for an elastic semi-infinite solid under gravity, with applications to earthquake and volcano deformation. *Geophys. J. Int.* 182 (2), 568–582. doi:10.1111/j.1365-246x.2010.04655.x

Barbot, S., and Fialko, Y. (2010b). A unified continuum representation of postseismic relaxation mechanisms: semi-analytic models of afterslip, poroelastic rebound and viscoelastic flow. *Geophys. J. Int.* 182 (3), 1124–1140. doi:10.1111/j.1365-246x.2010.04678.x

Barrier, E., and Angelier, J. (1986). Active collision in eastern taiwan: the coastal range. *Tectonophysics* 125, 39–72. doi:10.1016/0040-1951(86)90006-5

Bruhat, L., Barbot, S., and Avouac, J. P. (2011). Evidence for postseismic deformation of the lower crust following the 2004 M_w6.0 Parkfield earthquake. *J. Geophys. Res.* 116, B08401. doi:10.1029/2010JB008073

Bürgmann, R., and Dresen, G. (2008). Rheology of the lower crust and upper mantle: evidence from rock mechanics, geodesy, and field observations. *Annu. Rev. Earth Planet. Sci.* 36, 531–567. doi:10.1146/annurev.earth.36.031207.124326

Cabrera, L., Poli, P., and Frank, W. B. (2022). Tracking the spatio-temporal evolution of foreshocks preceding the M_w6.1 2009 L'Aquila earthquake. *J. Geophys. Res. Solid Earth* 127. doi:10.1029/2021JB023888

Canitano, A., Godano, M., Hsu, Y. J., Lee, H. M., Linde, A. T., and Sacks, S. (2018). Seismicity controlled by a frictional afterslip during a small magnitude seismic sequence (ML < 5) on the Chihshang Fault, Taiwan. *J. Geophys. Res. Solid Earth* 123 (2), 2003–2018. doi:10.1002/2017jb015128

Canitano, A., Godano, M., and Thomas, M. Y. (2021). Inherited state of stress as a key factor controlling slip and slip mode: inference from the study of a slow slip event in the Longitudinal Valley, Taiwan. *Geophys. Res. Lett.* 48 (3). doi:10.1029/2020GL090278

Chang, J. M., Chao, W. A., Yang, C. M., and Huang, M. W. (2024). Coseismic and subsequent landslides of the 2024 hualien earthquake (M7.2) on April 3 in taiwan. *Landlides* 21, 2591–2595. doi:10.1007/s10346-024-02312-x

Chen, K. H., Toda, S., and Rau, R. J. (2008). A leaping, triggered sequence along a segmented fault: the 1951 M_L 7.3 Hualien-Taitung earthquake sequence in eastern Taiwan. *J. Geophys. Res.* 113. doi:10.1029/2007JB005048

Choudrey, R. A., and Roberts, S. J. (2003). Variational mixture of Bayesian independent component analyzers. *Neural comput* 15 (1), 213–252. doi:10.1162/089976603321043766

Churchill, R. M., Werner, M. J., Biggs, J., and Fagereng, A. (2022). Afterslip moment scaling and variability from a global compilation of estimates. *J. Geophys. Res. Solid Earth* 127, e2021JB023897. doi:10.1029/2021JB023897

Cruz-Atienza, V. M., Tago, J., Villafuerte, C., Wei, M., Garza-Girón, R., Dominguez, L. A., et al. (2021). Short-term interaction between silent and devastating earthquakes in Mexico. *Nat. Commun.* 12, 2171. doi:10.1038/s41467-021-22326-6

Dieterich, J. H. (1994). A constitutive law for rate of earthquake production and its application to earthquake clustering. *J. Geophys. Res.* 99, 2601–2618. doi:10.1029/93jb02581

Essing, D., and Poli, P. (2024). Unraveling earthquake clusters composing the 2014 Alto Tiberina earthquake swarm via unsupervised learning. *J. Geophys. Res. Solid Earth* 129. doi:10.1029/2022JB026237

Fischer, T., and Hainzl, S. (2017). Effective stress drop of earthquake clusters. *Bull. Seismol. Soc. Am.* 107, 2247–2257. doi:10.1785/0120170035

Fischer, T., and Hainzl, S. (2021). The growth of earthquake clusters. *Front. Earth Sci.* 9. doi:10.3389/feart.2021.638336

Frank, W. B., Poli, P., and Perfettini, H. (2017). Mapping the rheology of the Central Chile subduction zone with aftershocks. *Geophys. Res. Lett.* 44, 5374–5382. doi:10.1002/2016gl072288

Freed, A. M., Hashima, A., Becker, T. W., Okaya, D. A., Sato, H., and Hatanaka, Y. (2017). Resolving depth-dependent subduction zone viscosity and afterslip from postseismic displacements following the 2011 Tohoku-oki, Japan earthquake. *Earth Planet. Sci. Lett.* 459, 279–290. doi:10.1016/j.epsl.2016.11.040

Fukuda, J., and Johnson, K. M. (2021). Bayesian inversion for a stress-driven model of afterslip and viscoelastic relaxation: method and application to postseismic deformation following the 2011 M_w 9.0 Tohoku-Oki earthquake. *J. Geophys. Res. Solid Earth* 126. doi:10.1029/2020JB021620

Gualandi, A., Liu, Z., and Rollins, C. (2020). Post-large earthquake seismic activities mediated by aseismic deformation processes. *Earth Planet. Sci. Lett.* 530, 115870. doi:10.1016/j.epsl.2019.115870

Gualandi, A., Serpelloni, E., and Belardinelli, M. E. (2016). Blind source separation problem in GPS time series. *J. Geod.* 90, 323–341. doi:10.1007/s00190-015-0875-4

Gutenberg, R., and Richter, C. F. (1944). Frequency of earthquakes in California. *Bull. Seismol. Soc. Am.* 34, 185–188. doi:10.1785/bssa0340040185

Hainzl, S. (2004). Seismicity patterns of earthquake swarms due to fluid intrusion and stress triggering. *Geophys. J. Int.* 159, 1090–1096. doi:10.1111/j.1365-246x.2004.02463.x

Hawthorne, J. C., Simons, M., and Ampuero, J.-P. (2016). Estimates of aseismic slip associated with small earthquakes near San Juan Bautista, CA. *J. Geophys. Res. Solid Earth* 121, 8254–8275. doi:10.1002/2016jb013120

Herring, T., King, W., and McCluskey, S. M. (2010). *Introduction to GAMIT/GLOBK release 10.4*. Cambridge: Mass. Inst. of Technol.

Howell, A., Palamartchouk, K., Papanikolaou, X., Paradissis, D., Raptakis, C., Copley, A., et al. (2017). The 2008 Methoni earthquake sequence: the relationship between the earthquake cycle on the subduction interface and coastal uplift in SW Greece. *Geophys. J. Int.* 208, 1592–1610. doi:10.1093/gji/ggw462

Hsu, Y. J., Fu, Y., Bürgmann, R., Hsu, S. Y., Lin, C. C., Tang, C. H., et al. (2020). Assessing seasonal and interannual water storage variations in Taiwan using geodetic and hydrological data. *Earth Planet. Sci. Lett.* 550, 116532. doi:10.1016/j.epsl.2020.116532

Huang, H. H., and Wang, Y. (2022). Seismogenic structure beneath the northern Longitudinal Valley revealed by the 2018-2021 Hualien earthquake sequences and 3-D velocity model. *Terr. Atmos. Ocean. Sci.* 33, 17. doi:10.1007/s44195-022-00017-z

Huang, M. H., and Huang, H. H. (2018). The complexity of the 2018 M_w6.4 Hualien earthquake in east Taiwan. *Geophys. Res. Lett.* 45 (13), 249–313. doi:10.1029/2018gl080821

Huang, T. Y., Gung, Y., Kuo, B. Y., Chiao, L. Y., and Chen, Y. N. (2015). Layered deformation in the Taiwan orogen. *Science* 349, 720–723. doi:10.1126/science.aab1879

Ingleby, T., and Wright, T. (2017). Omori-like decay of postseismic velocities following continental earthquakes. *Geophys. Res. Lett.* 44, 3119–3130. doi:10.1002/2017gl072865

Jian, P. R., and Wang, Y. (2022). Applying unsupervised machine-learning algorithms and MUSIC back-projection to characterize 2018-2022 Hualien earthquake sequence. *Terr. Atmos. Ocean. Sci.* 33, 28. doi:10.1007/s44195-022-00026-y

Johnson, K. M., Fukuda, J., and Segall, P. (2012). Challenging the rate-state asperity model: afterslip following the 2011 M9 Tohoku-oki, Japan, earthquake. *Geophys. Res. Lett.* 39. doi:10.1029/2012GL052901

Lee, S. J., Wong, T. P., Liu, T. Y., Lin, T. C., and Chen, C. T. (2020). Strong ground motion over a large area in northern Taiwan caused by the northward rupture directivity of the 2019 Hualien earthquake. *J. Asian Earth Sci.* 192, 104095. doi:10.1016/j.jseaes.2019.104095

Li, S., Tao, T., Chen, Y., He, P., Gao, F., Qu, X., et al. (2021). Geodetic observation and modeling of the coseismic and postseismic deformation associated with the 2020 M_w6.5 Monte Cristo earthquake. *Earth Space Sci.* 8. doi:10.1029/2021EA001696

Lin, H. F., Gualandi, A., Hsu, Y. F., Hsu, Y. J., Huang, H. H., Lee, H. M., et al. (2023b). Interplay between seismic and aseismic deformation on the central Range fault during the 2013 M_w6.3 Ruisui earthquake (taiwan). *J. Geophys. Res. Solid Earth* 128 (9). doi:10.1029/2023JB026861

Lin, H. F., Hsu, Y. F., and Canitano, A. (2023a). Source modeling of the 2009 Fengpin-Hualien earthquake sequence, Taiwan, inferred from static strain measurements. *Pure Appl. Geophys.* 180, 715–733. doi:10.1007/s00024-022-03068-y

Lohman, R. B., and McGuire, J. J. (2007). Earthquake swarms driven by aseismic creep in the Salton Trough, California. *J. Geophys. Res.* 112, B04405. doi:10.1029/2006JB004596

Mandler, E., Pintori, F., Gualandi, A., Anderlini, L., Serpelloni, E., and Belardinelli, M. E. (2021). Post-seismic deformation related to the 2016 Central Italy seismic sequence from GPS displacement time-series. *J. Geophys. Res. Solid Earth* 126, e2021JB022200. doi:10.1029/2021JB022200

Marone, C. J., Scholz, C. H., and Bilham, R. (1991). On the mechanics of earthquake afterslip. *J. Geophys. Res.* 96, 8441–8452. doi:10.1029/91jb00275

Matthews, M. V., and Segall, P. (1993). Estimation of depth-dependent fault slip from measured surface deformation with application to the 1906 San Francisco earthquake. *J. Geophys. Res.* 98 (12), 12153–12163. doi:10.1029/93jb00440

McCormack, K., Hesse, M. A., Dixon, T., and Malservisi, R. (2020). Modeling the contribution of poroelastic deformation to postseismic geodetic signals. *Geophys. Res. Lett.* 47. doi:10.1029/2020GL086945

Moreno, M., Haberland, C., Oncken, O., Rietbrock, A., Angiboust, S., and Heidbach, O. (2014). Locking of the Chile subduction zone controlled by fluid pressure before the 2010 earthquake. *Nat. Geosci.* 7, 292–296. doi:10.1038/NGEO2102

Morikami, S., and Mitsui, Y. (2020). Omori-like slow decay ($p < 1$) of postseismic displacement rates following the 2011 Tohoku megathrust earthquake. *Earth Planets Space* 72, 37. doi:10.1186/s40623-020-01162-w

Okada, Y. (1992). Internal deformation due to shear and tensile faults in a half-space. *Bull. Seism. Soc. Am.* 82 (2), 1018–1040. doi:10.1785/bssa0820021018

Peltzer, G., Rosen, P., Rogez, F., and Hudnut, K. (1996). Postseismic rebound in fault step-overs caused by pore fluid flow. *Science* 273 (5279), 1202–1204. doi:10.1126/science.273.5279.1202

Peng, W., Marsan, D., Chen, K. H., and Pathier, E. (2021). Earthquake swarms in Taiwan: a composite declustering method for detection and their spatial characteristics. *Earth Planet. Sci. Lett.* 574, 117160. doi:10.1016/j.epsl.2021.117160

Perfettini, H., and Avouac, J. P. (2004). Postseismic relaxation driven by brittle creep: a possible mechanism to reconcile geodetic measurements and the decay rate of aftershocks, application to the Chi-Chi earthquake, Taiwan. *J. Geophys. Res.* 109. doi:10.1029/2003JB002488

Perfettini, H., Frank, W. B., Marsan, D., and Bouchon, M. (2018). A model of aftershock migration driven by afterslip. *Geophys. Res. Lett.* 45, 2283–2293. doi:10.1002/2017gl076287

Perfettini, H., Frank, W. B., Marsan, D., and Bouchon, M. (2019). Updip and along-strike aftershock migration model driven by afterslip: application to the 2011 Tohoku-Oki aftershock sequence. *J. Geophys. Res. Solid Earth* 124 (3), 2653–2669. doi:10.1029/2018jb016490

Periollat, A., Radiguet, M., Weiss, J., Twardzik, C., Amitrano, D., Cotte, N., et al. (2022). Transient brittle creep mechanism explains early postseismic phase of the 2011 Tohoku-Oki megathrust earthquake: observations by high-rate GPS solutions. *J. Geophys. Res. Solid Earth.* 127. doi:10.1029/2022JB024005

Rau, R. J., Ching, K. E., Hu, J. C., and Lee, J.-C. (2008). Crustal deformation and block kinematics in transition from collision to subduction: global positioning system measurements in northern Taiwan, 1995–2005. *J. Geophys. Res.* 113, B09404. doi:10.1029/2007jb005414

Rau, R. J., and Liang, W. T. (2022). Introduction to the special issue on the Hualien earthquake swarms. *Terr. Atmos. Ocean. Sci.* 33, 27. doi:10.1007/s44195-022-00028-w

Schorlemmer, D., Wiemer, S., and Wyss, M. (2005). Variations in earthquake-size distribution across different stress regimes. *Nature* 437, 539–542. doi:10.1038/nature04094

Shyu, J. B. H., Chen, C. F., and Wu, Y. M. (2016). Seismotectonic characteristics of the northernmost Longitudinal Valley, eastern Taiwan: structural development of a vanishing suture. *Tectonophysics* 692, 295–308. doi:10.1016/j.tecto.2015.12.026

Shyu, J. B. H., Sieh, K., Chen, Y. G., and Chung, L. H. (2006). Geomorphic analysis of the Central Range fault, the second major active structure of the Longitudinal Valley suture, eastern Taiwan. *Geol. Soc. Am. Bull.* 118, 1447–1462. doi:10.1130/b25905.1

Soares, A., Custodio, S., Cesca, S., Silva, R., Vuan, A., and Mendes, V. B. (2023). The february 2018 seismic swarm in sao miguel, azores. *Front. Earth Sci.* 11. doi:10.3389/feart.2023.1144151

Tang, C. H., Hsu, Y. J., Barbot, S., Moore, J. D. P., and Chang, W. L. (2019). Lower-crustal rheology and thermal gradient in the Taiwan orogenic belt illuminated by the 1999 Chi-Chi earthquake. *Sci. Adv.* 5 (2), eaav3287. doi:10.1126/sciadv.aav3287

Tang, C. H., Lin, Y., Tung, H., Wang, Y., Lee, S. J., Hsu, Y. J., et al. (2023). Nearby fault interaction within the double-vergence suture in eastern Taiwan during the 2022 Chihshang earthquake sequence. *Commun. Earth Environ.* 4, 333. doi:10.1038/s43247-023-00994-0

Thomas, M. Y., Avouac, J. P., Champenois, J., Lee, J. C., and Kuo, L. C. (2014). Spatiotemporal evolution of seismic and aseismic slip on the Longitudinal Valley fault, taiwan. *J. Geophys. Res.* 119 (6), 5114–5139. doi:10.1002/2013jb010603

Thomas, M. Y., Avouac, J. P., and Lapusta, N. (2017). Rate-and-state friction properties of the Longitudinal Valley Fault from kinematic and dynamic modeling of seismic and aseismic slip. *J. Geophys. Res.* 122 (4), 3115–3137. doi:10.1002/2016jb013615

Toyokuni, G., Zhao, D., and Chen, K. H. (2021). Structural control on the 2018 and 2019 hualien earthquakes in taiwan. *Phys. Earth Planet. Inter.* 312, 106673. doi:10.1016/j.pepi.2021.106673

Utsu, T., Ogata, Y., Matsu'ura, R. S., Matsu'ura, (1995). The centenary of the Omori formula for a decay law of aftershock activity. *J. Phys. Earth* 43, 1–33. doi:10.4294/jpe1952.43.1

Wanninger, L. (2009). Correction of apparent position shifts caused by GNSS antenna changes. *GPS Solutions* 13, 133–139. doi:10.1007/s10291-008-0106-z

Wessel, P., and Smith, W. H. F. (1998). New, improved version of generic mapping tools released. *Eos Trans. AGU* 79, 579. doi:10.1029/98EO00426

Wiemer, S. (2001). A software package to analyze seismicity: ZMAP. *Seismol. Res. Lett.* 72 (3), 373–382. doi:10.1785/gssrl.72.3.373

Williams, S. D. P. (2003). Offsets in global positioning system time series. *J. Geophys. Res.* 108. doi:10.1029/2002JB002156

Wu, Y. M., Chen, S. K., Huang, T. C., Huang, H. H., Chao, W. A., and Koulakov, I. (2018). Relationship between earthquake *b*-values and crustal stresses in a young orogenic belt. *Geophys. Res. Lett.* 45, 1832–1837. doi:10.1002/2017gl076694

Yu, S. B., and Kuo, L. C. (2001). Present-day crustal motion along the Longitudinal Valley fault, eastern taiwan. *Tectonophysics* 333, 199–217. doi:10.1016/s0040-1951(00)00275-4

Zhao, B., Bürgmann, R., Wang, D., Zhang, J., Yu, J., and Li, Q. (2022). Aseismic slip and recent ruptures of persistent asperities along the Alaska-Aleutian subduction zone. *Nat. Comm.* 13, 3098. doi:10.1038/s41467-022-30883-7

Zhao, D., Qu, C., Shan, X., Bürgmann, R., Gong, W., Tung, H., et al. (2020). Multifault complex rupture and afterslip associated with the 2018M_w6.4 Hualien earthquake in northeastern Taiwan. *Geophys. J. Int.* 224, 416–434. doi:10.1093/gji/ggaa474

frontiers | Frontiers in Earth Science

TYPE Original Research
PUBLISHED 06 January 2025
DOI 10.3389/feart.2024.1474630

OPEN ACCESS

EDITED BY
Giovanni Martinelli,
National Institute of Geophysics and Volcanology, Section of Palermo, Italy

REVIEWED BY
Jiao Tian,
China Earthquake Administration, China
Xiaocheng Zhou,
China Earthquake Administration, China

*CORRESPONDENCE
Mingbo Yang,
yangmb2008@163.com
Guiping Liu,
liuguiping@bjseis.gov.cn
Yuxuan Chen,
cyx630@163.com

RECEIVED 02 August 2024
ACCEPTED 24 October 2024
PUBLISHED 06 January 2025

CITATION
Yang M, Liu G, Chen Y, Hua P, Hu L, Wang Z, Wang S, Sun X, Zhou Y, Zhang H, Feng G, Gao X and Zhang Y (2025) Short-term seismic precursor anomalies in hydrogen concentration at fault gas stations along the Northern Margin Fault of the Yanqing Basin of Beijing, China.
Front. Earth Sci. 12:1474630.
doi: 10.3389/feart.2024.1474630

Short-term seismic precursor anomalies in hydrogen concentration at fault gas stations along the Northern Margin Fault of the Yanqing Basin of Beijing, China

Mingbo Yang[1]*, Guiping Liu[1]*, Yuxuan Chen[1]*, Peixue Hua[1], Leyin Hu[1], Zhiguo Wang[1], Shanshan Wang[2], Xiaoru Sun[1], Yonggang Zhou[3], Haichun Zhang[1], Gang Feng[1], Xiang Gao[1] and Yuqi Zhang[4]

[1]Beijing Earthquake Agency, Beijing, China, [2]Beijing Municipal Commission of Planning and Natural Resources, Beijing, China, [3]The Bureau of seismology of Yanqing District of Beijing, Beijing, China, [4]The Bureau of seismology of Haidian District of Beijing, Beijing, China

The Northern Margin Fault of the Yanqing Basin (NMYB Fault) is an important active fault at the intersection of the Zhangjiakou–Bohai (Zhang-Bo) Belt and the Shanxi Belt in North China. The Yanqing Basin, controlled by the NMYB Fault, is rich in escaping gas from hot springs, and previous investigations have indicated that the Yanqing Basin is located in the peak area of upwelling deep fluids from the mantle source material within the Zhang-Bo Belt. Hence, the site is suitable for geochemical gas precursor observations; to facilitate this, five new fault soil gas continuous stations were built on different segments of the NMYB Fault to carry out observations of fault gas (H_2 and CO_2) concentrations. The five new stations were approximately 50–60 m deep in the bedrock to monitor the release of gas from the depths of the fault. This was the first time that such geochemical station arrays were deployed in the same fault zone at a high density and depth. The results of the deep-hole observations of fault gas within the Yanqing Fault zone show that the time series of the hydrogen (H_2) escape gas concentration has a close relationship with recent seismic activities, reflecting different physical processes of YFBF fault activity. The H_2 concentration at the observatory was more sensitive to the stress-loading response of the NMYB Fault system.

KEYWORDS

Zhangjiakou–Bohai tectonic zone, gas geochemistry, helium isotope, Yanqing–Huailai basin, earthquake prediction

10.3389/feart.2024.1474630

1 Introduction

Earthquake precursor mechanisms are difficult to understand, which has hindered the development of earthquake prediction (Donald, 1988; Cicerone et al., 2009; Gherardi et al., 2017). The high uncertainty and low predictability of the earthquake forecasting process also make earthquakes one of the most serious natural hazards, often leading to instantaneous loss of life and property (Gupta, 2001; Wen et al., 2008). In recent years, especially in China, Japan, Italy, and the United States, anomalously high concentrations of hydrogen, carbon dioxide, helium, radon, and methane (H_2, CO_2, He, Rn, and CH_4, respectively) in fault and hot spring gases have been extensively studied in seismically active faults in search of a probable earthquake precursor (King, 1986; Sugisaki and Sugiura, 1986; Nagamine, 1994; Cicerone et al., 2009; Babuska et al., 2016; Weinlich et al., 2016; Fischer et al., 2017; Huang et al., 2017; Yang et al., 2022). Temporal anomalous changes in gas concentrations, which could last from a few hours to a few days, have been observed at some monitoring stations before and after some large earthquakes, the epicenters of which were hundreds of kilometers away. The anomalous mechanisms are usually associated with chemical and physical changes occurring in active faults before and after the earthquakes, such as enhanced/decreased water–rock interactions, crustal stresses/strains, and permeability changes (Sugisaki et al., 1983; Sugisaki et al., 1996; Cicerone et al., 2009; Umeda et al., 2013; Weinlich et al., 2016; Chen and Liu, 2023).

The Yanqing Basin is rich in escaping gas from hot springs, making it an ideal site for fault gas monitoring. Previous investigations and studies of the samples of escaping gas from geothermal hot spring wells in the Yanqing North Fault of Beijing [Northern Margin Fault of the Yanqing Basin (NMYB Fault)] had been carried out. The results show that (Table 1) the hot spring escaping gas in the Yanqing Basin controlled by the Yanqing North Fault was rich in helium, and helium isotope ratios were richer, varying from 0.65 to 2.93 Ra. The mantle-sourced He averages 21.95% (maximum: 35.4%), indicating that the Yanqing Basin is located in the area of the upwelling deep fluids. The very good correspondence between the release of mantle-sourced gases and regional seismic activities indicates that the Yanqing Basin is a sensitive area for seismic geochemical observations and also an important active fault at the intersection of the Zhangjiakou–Bohai (Zhang-Bo) Seismic Belt and the Shanxi Seismic Belt of North China.

Therefore, in this paper, six new gas geochemical stations at high density along the NMYB Fault distribution were constructed (Figure 1) as pilots for applied research on gas geochemistry on active faults for an earthquake precursor. The research objectives of the paper include 1) monitoring the H_2 concentration changes in the NMYB Fault before and after the earthquake; 2) analyzing hydrogen concentration characterization of short-term anomalies; and 3) investigating the mechanism of the gas precursor of earthquakes at the NMYB Fault.

2 Geological background

Beijing is the capital of China with a large population, and it is located at the intersection of the North China Plain and

TABLE 1 Chemical composition and helium and carbon isotope data of hot spring gas in geothermal wells along the Zhangjiakou–Bohai Fault Zone (cited by Yang et al., 2022).

Date	Temperature (°C)	He (10-6)	H_2 (10-6)	CO_2 (%)	CH_4 (%)	N_2 (%)	O_2 (%)	$^3He/^4He$ (R/Ra)	$^3He/^4He$ (Rc/Ra)	$^4He/^{20}Ne$	He mantle-derived %	$\delta^{13}C_{CO2}$ ‰	$\delta^{13}C_{Ch4}$ ‰
22/10/2020	60	683	2.4	0.63	0.1	99.37	0.14	2.86	2.93	8.3	0.354	-14.3	0
26/10/2020	44	1851	5	0.23	0.14	98.98	0.29	1.38	1.382	68	0.174	-17.1	-35.5
26/10/2020	65	996	0	0.11	–	96.49	–	2.33	2.342	35	0.295	-14.2	—
16/11/2020	33	700	0	2.7	1	96.06	0	1.85	1.86	29	0.233	-16.2	-71.3
23/11/2021	44	180	0	0.027	13.8	85	0.06	1.49	1.5	21	0.19	-10.2	-74.2
23/11/2021	38	200	320	0	0.48	97.91	0.05	0.65	0.66	17	0.071	-10	-51.2

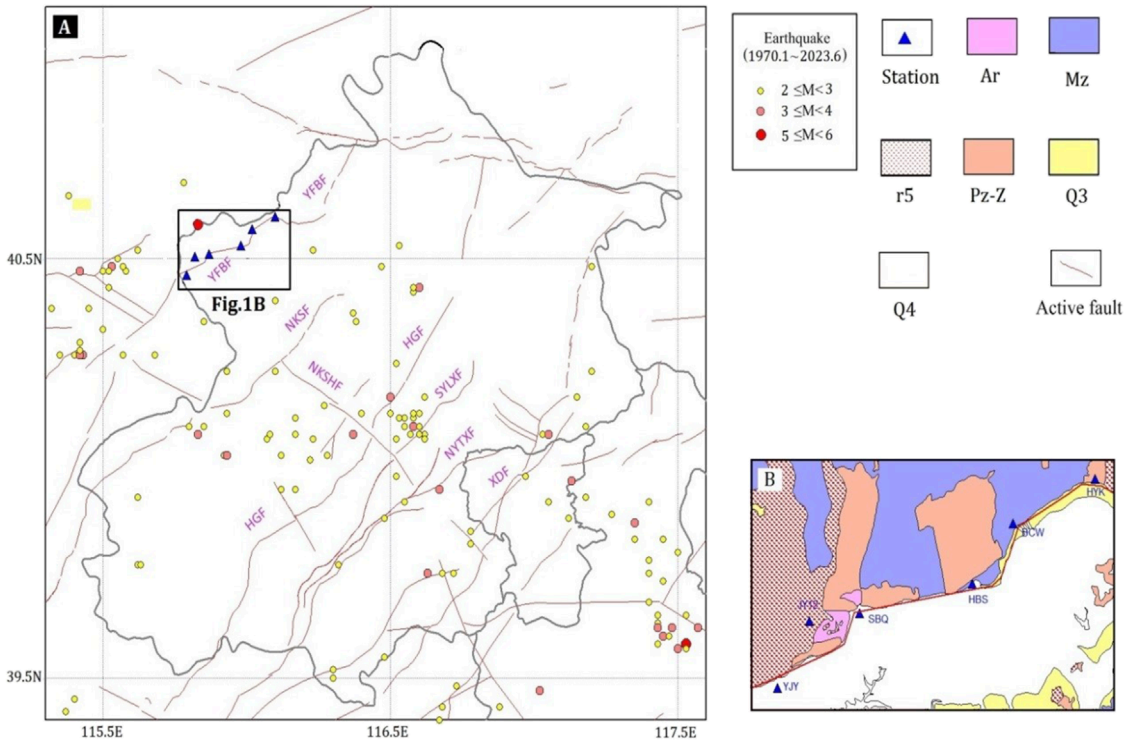

FIGURE 1
Distribution of gas geochemical stations at the Northern Margin Fault of the Yanqing Basin (NMYB Fault). **(A)** Locations of gas stations in the historic earthquake distribution map of Beijing. **(B)** Locations of gas stations in the geological map of the study area.

the Zhang-Bo seismic belt. North China has experienced frequent strong earthquakes over the last few decades (Chen and Liu, 2023; Luo et al., 2024), such as the Xingtai M7.2 earthquake in 1966, Bohai M7.4 earthquake in 1969, Haicheng M7.3 earthquake in 1975, Tangshan M7.8 earthquake in 1976, and Zhangbei M6.2 earthquake in 1998. The Zhang-Bo seismic belt is a group of NW-W orderly active fault zones, starting from the northern margin of the Taihang Mountains in the west and entering the Bohai Sea in the east. It is an important NW seismic activity zone with frequent seismic activity in North China (Yang et al., 2022). Hence, there is a potential risk of damaging earthquakes in Beijing in the following years.

The Yanqing–Huailai (Yan-Huai) sediment basin is in the northwest region of Beijing, where the junction area of the Zhang-Bo seismic belt and Yanshan Mountains is located (Figure 1). Geologically, the basin boundary is mainly controlled by the pre-Cenozoic NNE-oriented positive-tilted and sliding fault groups. The faults continued to be active until the Late Quaternary (Fang et al., 1993). In terms of the overall structure of the basin, the NMYB Fault is the main active fault that controlled the formation and development of this shovel-type fault basin (Yu and Xu, 2004).

Bedrock is exposed in the study area from old to new, based on the stratigraphy of the area (Figure 1), including Archean Gneiss, Meso-Proterozoic carbonate, Mesozoic igneous rock, and Quaternary sediment. Most of the bedrock exposed in the fault zone consists mainly of Cretaceous and Jurassic coarse–facies felsic breccia tuffs, hornblende coarse andesite, gray–green andesite breccia mafic rocks, and volcanic rocks such as granite, which are in angular unconformable contact with the underlying tuffaceous dolomites of the Wumishan Formation in the Jixian System (Calymmian).

The existing geochemical methods from hot springs and gas stations in the Yanqing Basin have many typical earthquake precursor cases. For example, a large number of hot springs and gas anomalies were observed at several underground fluid-monitoring sites in the Yanqing Basin (Che et al., 1999) before the Datong earthquake (19 October 1989), Baotou West earthquake (3 May 1996), and Zhangbei earthquake (10 January 1998), which also suggested that the Yanqing Basin is a typical sensitive area for seismic gas precursors.

3 Methods

3.1 Gas sampling in the study area

Gas samples were collected from the hot springs and five deep soil holes from the NMYB Fault on 23 December 2022 (see Table 2). The gas samples were immediately sent to the Key Laboratory of the Institute of Earthquake Forecasting, China Earthquake Administration. Measurements of the samples were finished within 30 days. The compositions of the gas samples were analyzed using an Agilent 490 Gas Chromatograph, which measured H_2, He, CO_2, N_2, O_2, and CH_4. The measurement accuracy was estimated as follows: the relative standard deviation

TABLE 2 Chemical composition of deep soil gas from the Yanqing Basin.

	He (ppm)	H_2 (ppm)	O_2 (%)	N_2 (%)	CH_4 (%)	CO_2 (%)	Rn (bq/m3)
HYK	12.42	2.09	19.66	79.23	0.112	1.001	8000
YJY	11.72	467.5	17.82	80.96	0.11	1.06	150
HBS	13.65	6.09	18.63	80.1	0	1.3	100
BCW	16	2.9	19.47	80.53	0	0	2000
SBQ	12.97	12.66	18.66	81.12	0	1.2	6200

was <0.5% when the content was 1%–100%, and the relative standard deviation was <1% when the content was 0.01%–1% (Zhou et al., 2015; Zhou et al., 2020). Helium and neon isotopes were measured using the Noblesse noble gas isotope mass spectrometer. When the R-value in helium isotope measurement was above 1×10^{-7}, the test error was ±10%, and the measurement data error was at 1×10^{-8}–1×10^{-7} were ±15% (Cao et al., 2018). The results were normalized to standard atmospheric values. The carbon isotope ratio was analyzed using the DeltaPlusXL mass spectrometer (Thermo Finnigan, United States), consisting of an HP 6890 Gas Chromatograph, a combustion/conversion furnace, and an interface connecting to the DeltaPlusXP mass spectrometer. The stable carbon isotope composition was expressed by $\delta^{13}C$; the accuracy of $^{13}C/^{12}C$ was 0.6‰ (Li et al., 2014).

3.2 Gas concentrations at gas geochemical stations

Based on the above concentration characteristics of the soil gas measurement, five new continuous gas monitoring stations were built along the NMYB Fault (Figure 1); these stations aim to monitor the continuous changes in fault gases (H_2 and CO_2), analyze the spatial differences of the gas characteristics in different fault segments, and observe their changes over time. Furthermore, the five gas stations can monitor the stress adjustments and seismicity of the Beijing area. The five geochemical monitoring sites along the Northern Margin Fault form high-density gas geochemical networks for automatic and continuous gas sampling and observation (Figure 1 shows the distribution of the stations).

In the past, traditional soil/fault gas observations were subject to many disturbing factors, mainly the shallow depth of gas extraction and its susceptibility to biogenic gases and atmospheric disturbances. In order to minimize the influence of these surface factors, the quality of monitoring was improved, the influence of gases produced by biogenic layers and humus in the soil was avoided as much as possible, and the seasonal interference of the ground temperature was avoided. Fault gas fixed monitoring sites were constructed this time, reaching approximately 50–60 m deep into the bedrock. The depth was well beyond the variable temperate zone of the region (the region's variable temperature zone is generally in the range of 20 m).

Hot spring well stations and faulted soil gas stations make the monitoring of additional tectonic activity possible. The monitoring environment is very stable. There is no industrial or mining activity around the monitoring stations. Instead, the fault gas is introduced at a depth of 50–60 m below ground level using sieve-perforated gas collection cylinders. Both hot spring and fault gases are accumulated (Figure 2) and introduced using polytetrafluoroethylene (PTFE) tubes (length: 33–55 m, outer diameter: 3 cm, and inner diameter: 2 cm). Hydrogen concentrations were monitored every 2 h using an ATG-6118H autoanalyzer in the range of 0.01–1,000 ppm with an accuracy of ±5%, and CO_2 concentrations were monitored every 2 h using an ATG-C600 CO_2 continuous monitor in the measurement range of 0%–60% with a resolution of 0.001%. Both instruments were calibrated and maintained by the instrument manufacturing company (Wen et al., 2018; NOA Certification, 2019). All gas piping was well sealed from the effects of weather, air, and temperature, as well as external humidity and rainfall. The data obtained from this system were transmitted in real time via 5G.

The gas background values of the new deep-bore fault gas wells in the NMYB Fault correlate with the historical earthquakes. According to the curves of the background H_2 observation values of the stations when the station was being constructed (Figure 3), it could be seen that the background values of the hydrogen concentration in the area between Yaojiaying (YJY) and Huangbaisi (HBS), where more historical earthquakes had occurred, were higher. In addition, the historical earthquakes of Baicaowa (BCW) and Huangyukou (HYK), located in the northeast of the rupture, were also fewer, and their H_2 concentration background values were low at the same time (Sugisaki and Sugiura, 1986; Cheng et al., 1995).

4 Results

4.1 Gas chemical composition in stations

Gases (isotopic ratios of CO_2, He, Ne, and other gas compositions) collected from Yanqing soil gas wells from 1 January 2023 to 31 January 2024 are shown in Table 2. The N_2 concentration of the gas samples was ≥79 vol%. Helium and H_2 concentrations in the gases were relatively low (≤500 ppm). O_2 concentrations in most fugitive gas samples were less than 20%. Methane concentrations were below 3%. Most CO_2 concentrations were below 5%.

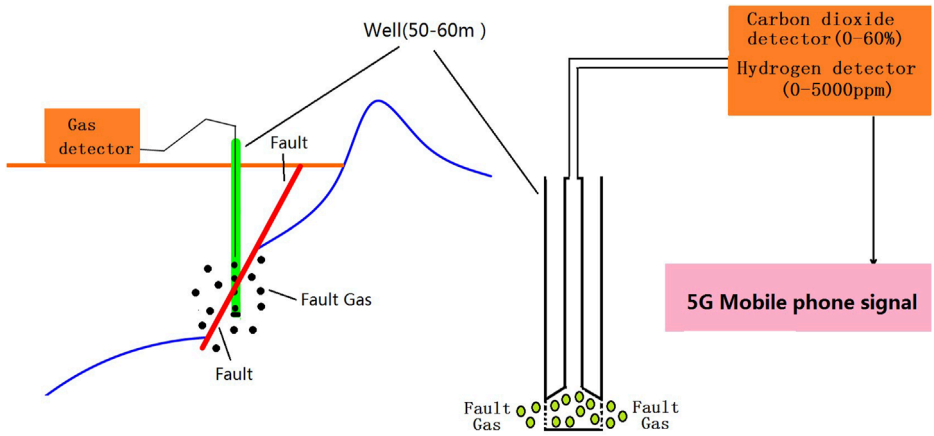

FIGURE 2
Schematic diagram of H_2 and CO_2 concentration monitoring stations.

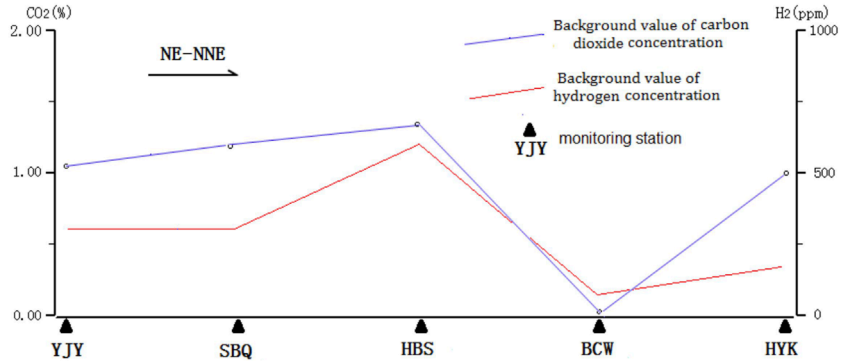

FIGURE 3
Monitoring values of the five H_2 and CO_2 concentrations were sent to a laboratory in Beijing through cellphone signals.

4.2 Concentration of H_2 in stations

4.2.1 Time-series variation in H_2 concentration at the Huangbaisi (HBS) station

From 1 January 2023 to 31 January 2024, there were 4,752 datasets on H_2 concentrations (Table 3), which ranged from 0.01 to 501 ppm, with an average of 97 ppm. The anomaly threshold is 170 ppm (Table 3; Figure 4A) according to the Q–Q plot, which is a method of determining the relationship between background and anomalous geochemical data based on the cumulative probability plot delineation of the data threshold (Sinclair, 1991; Zhou et al., 2021). In order to analyze the effect of humidity on the observed values, the correlation coefficient between hydrogen and humidity was calculated to be −0.127 for the 1 January 2023 value of 31 January 2024 at HBS, indicating a very low correlation (see Figure 4B).

4.2.2 Time-series variation in H_2 at the Shangbanquan (SBQ) station

From 1 January 2023 to 31 January 2024, there were 4,752 datasets on H_2 concentrations (Table 3), which ranged from 0.01 to 40 ppm, with an average of 10 ppm. The anomaly threshold was 15 ppm (Table 3; Figure 5A) according to the Q–Q plot. In order to analyze the effect of humidity on the observed values, from 1 January 2023 to 31 January 2024, the correlation coefficient between hydrogen and humidity was calculated to be 0.069 at SBQ, which is also a low correlation (see Figure 5B).

4.2.3 Time-series variation in H_2 at the Huangyukou (HYK) station

From 1 January 2023 to 31 January 2024, there were 4,752 datasets on H_2 concentrations (Table 3), which ranged from 0.01 to 40 ppm, with an average of 9.7 ppm. The anomaly threshold of 16 ppm (Table 3; Figure 6A) was determined by a Q–Q plot. In order to analyze the effect of humidity on the observed values, the correlation coefficient between hydrogen and humidity was calculated to be 0.44 for the 1 January 2023 value of 31 January 2024 at SBQ, which is also a low correlation (see Figure 6B).

5 Discussion

5.1 Sources of H_2

The source of H_2 is most likely attributable to (A) H_2 produced by water–rock reactions. Abiotic H_2 is produced

TABLE 3 Summary of H_2 concentrations at three geochemical stations along the NMYB Fault.

Station name	Number of concentration datasets	Concentration range of H_2 (ppm)	Concentration average (ppm)	Abnormal threshold (ppm)	Correlation coefficient with humidity (r^2 value)
HBS	4,752	1–501	97	170	0.016
SBQ	4,752	1–40	10	15	0.005
HYK	4,752	1–70	9.7	16	0.19

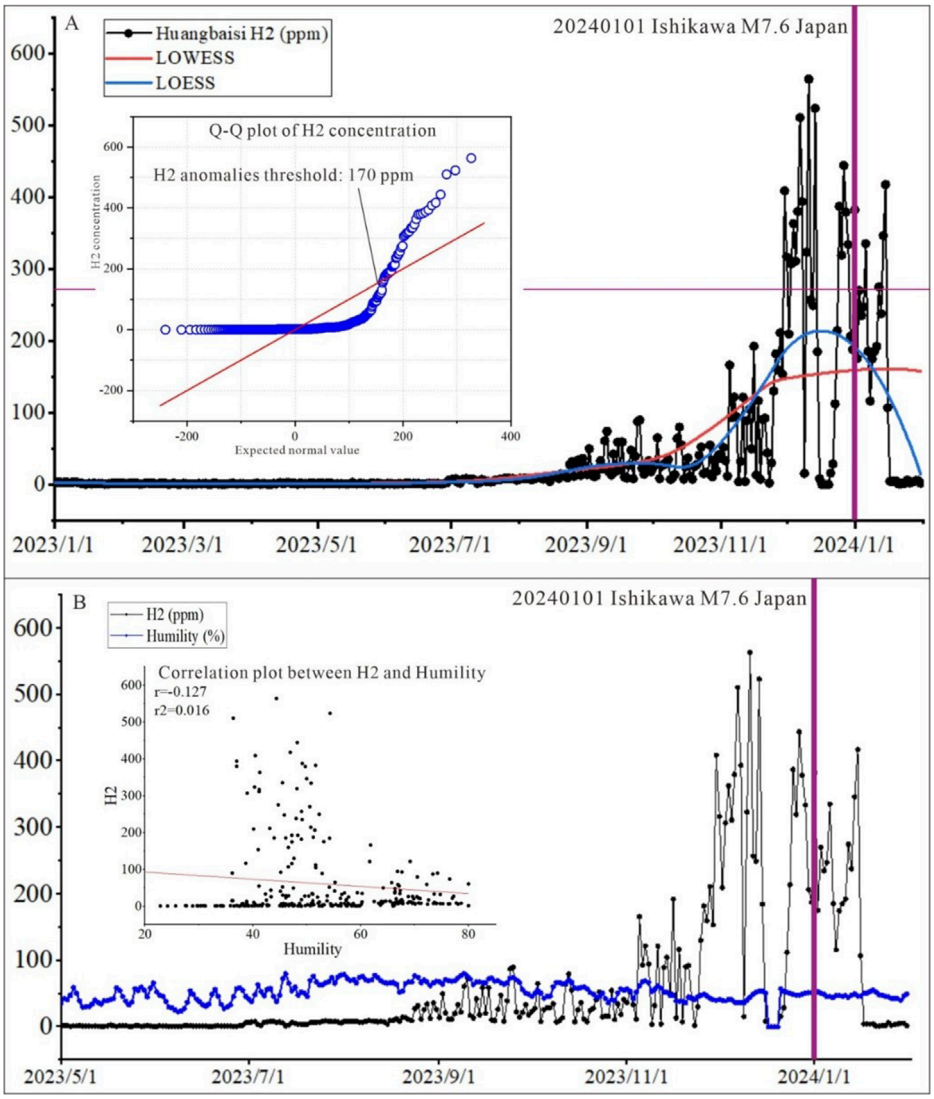

FIGURE 4
(A) Q–Q plot of H_2 concentration at HBS. **(B)** Correlation between H_2 concentration and humidity.

under near-surface conditions when water reacts with ultramafic rocks or serpentinization and migrates from deeper reservoirs (Lollar et al., 2014; Parnell and Blamey, 2017; Irfan et al., 2019; Wang et al., 2019; Wang et al., 2020); (B) water interaction with the newly exposed rock surface (Hirose et al., 2011); and (C) mixing with large amounts of microbial H_2 produced by bioactivity and organic matter decomposition (Prinzhofer et al., 2019; Myagkiy et al., 2020).

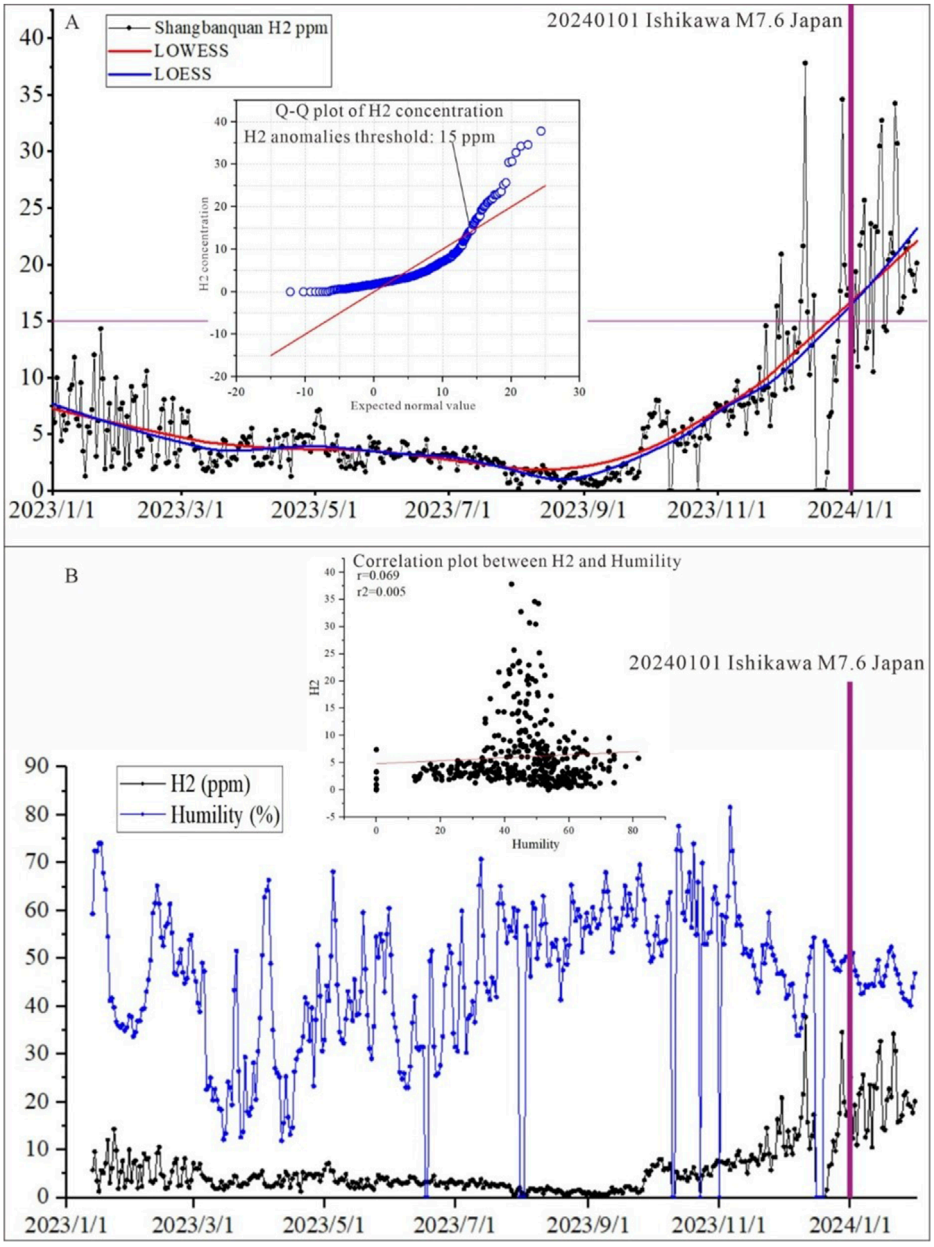

FIGURE 5
(A) Q–Q plot of H_2 concentration at SBQ. **(B)** Correlation between H_2 concentration and humidity.

Laboratory experimental data showed that tectonic stress caused by the reaction of broken minerals and groundwater can produce H_2. The observed significant increase in H_2 in the high concentration of anomalies before and after many large earthquakes suggests that there is a close relationship between the changes in the concentration of H_2 and the earthquakes (Sugiyaki et al., 1983; Zhou et al., 2021). A background investigation on soil was carried out by Li et al. (2014) and Chen et al. (2022) over a larger area including the study area. The results show that there are low-velocity bodies in the upper crust of the eastern part of the Yanqing–Huailai Basin (including the Yanqing Basin), with strong tectonic activity. The investigated gases, including Hg and He, mainly originate from the deeper part of the fault zones, contributing more to the soil gas. H_2 also originates from the deeper part but was influenced by the redox environment in the soil deposits, which results in a wide range of variations in the H_2 content (Li et al., 2014).

5.2 Time-series variation characteristics and anomalies of H_2 before earthquakes

Prior to earthquakes from 1 January 2023 to 1 January 2024, there were significant short-term (120–720 h) seismic precursor anomalies in the H_2 concentration of fault escape gases at HYK, HBS, and SBQ (Figure 7). Earthquakes occur when stress increases

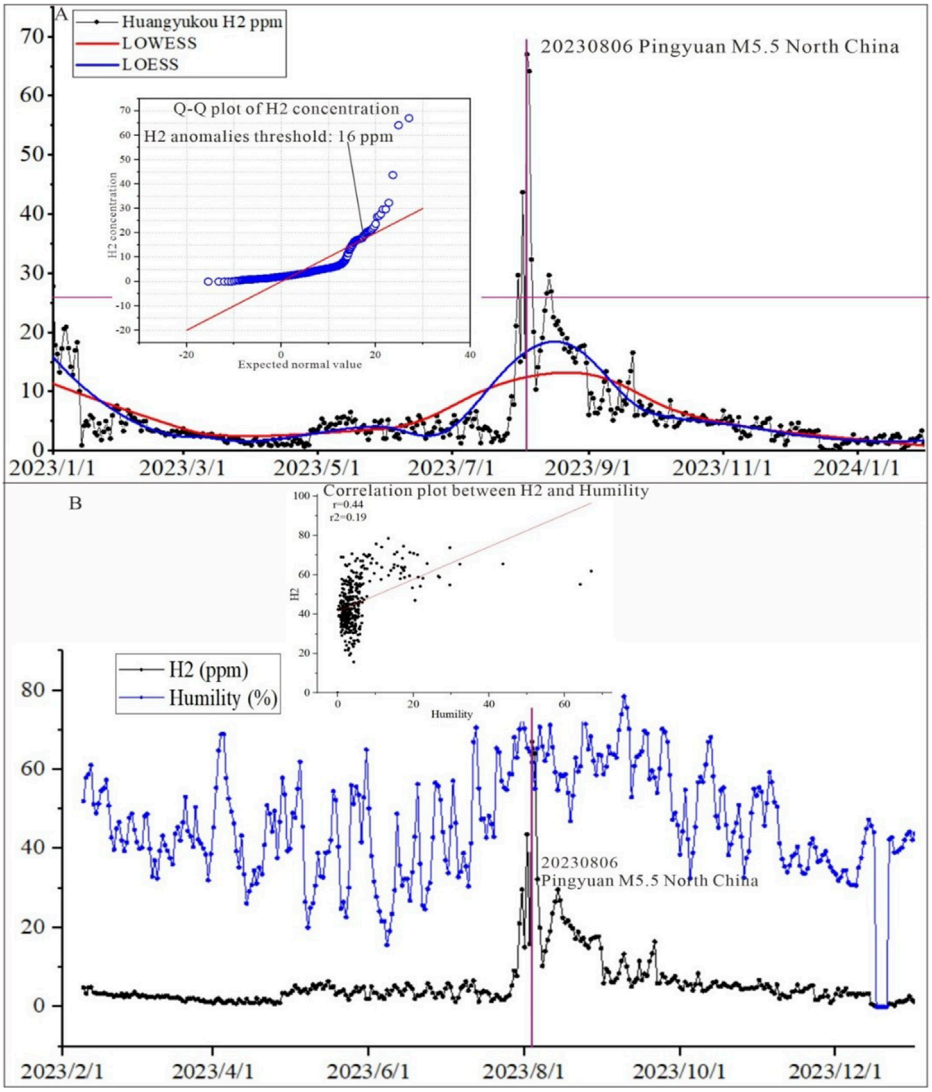

FIGURE 6
(A) Q–Q plot of H_2 concentration at HYK. **(B)** Correlation between H_2 concentration and humidity.

to a state of sub-instability stress on faults (Ma, 2016). The hydrogen concentration in the escaping gas is very sensitive to the increase in stress, which may enhance the openness of microfractures in the fractures along the Northern Margin of the Yanqing Basin.

The anomaly information was reported to the Beijing Earthquake Agency prior to the 5 August 2023 Shandong Pingyuan M5.5 and 1 January 2024 Japan M7.3 earthquakes.

Prior to these two earthquakes, there were significant and persistent precursor anomalies in the H_2 concentrations of soil gas in each of the HYK, HBS, and SBQ stations. When the stress increases to a state of sub-instable stress on the faults, the faults misalign to produce earthquakes (Ma, 2016), so the mechanism of precursor anomalies may have been caused by the sustained stress increase prior to the natural seismic events.

The hydrological response to earthquakes depends on the earthquake's magnitude and epicenter (Wang and Manga, 2010; Cox et al., 2015). Therefore, systematic identification of short-term seismic precursor anomalies based on multiple earthquakes using certain criteria is difficult. By drawing on and analyzing the collection of many natural earthquake cases in the same region, the equation of geochemical gas precursor anomalies in relation to magnitude and distance from the epicenter can be summarized, and some criteria can be provided.

5.2.1 H_2 concentration at HYK

Before the 5 August 2023 Pingyuan County M5.5 earthquake in Dezhou city of Shandong Province of China, the H_2 concentration anomaly increased at Huangyukou (Figure 7), which appeared 5 days before the earthquake and ended before the earthquake. Details were as follows: it began to rise abruptly on July 30, reaching a first peak of 65.65 ppm on the July 31, a second peak of 91.56 ppm at 11:40 on August 2, and a third peak of 174.6 ppm at 00:40 on August 5, and then, it returned to a low point of 19.568 ppm at 18:40 on August 5. The M5.5 earthquake in Shandong Pingyuan occurred at

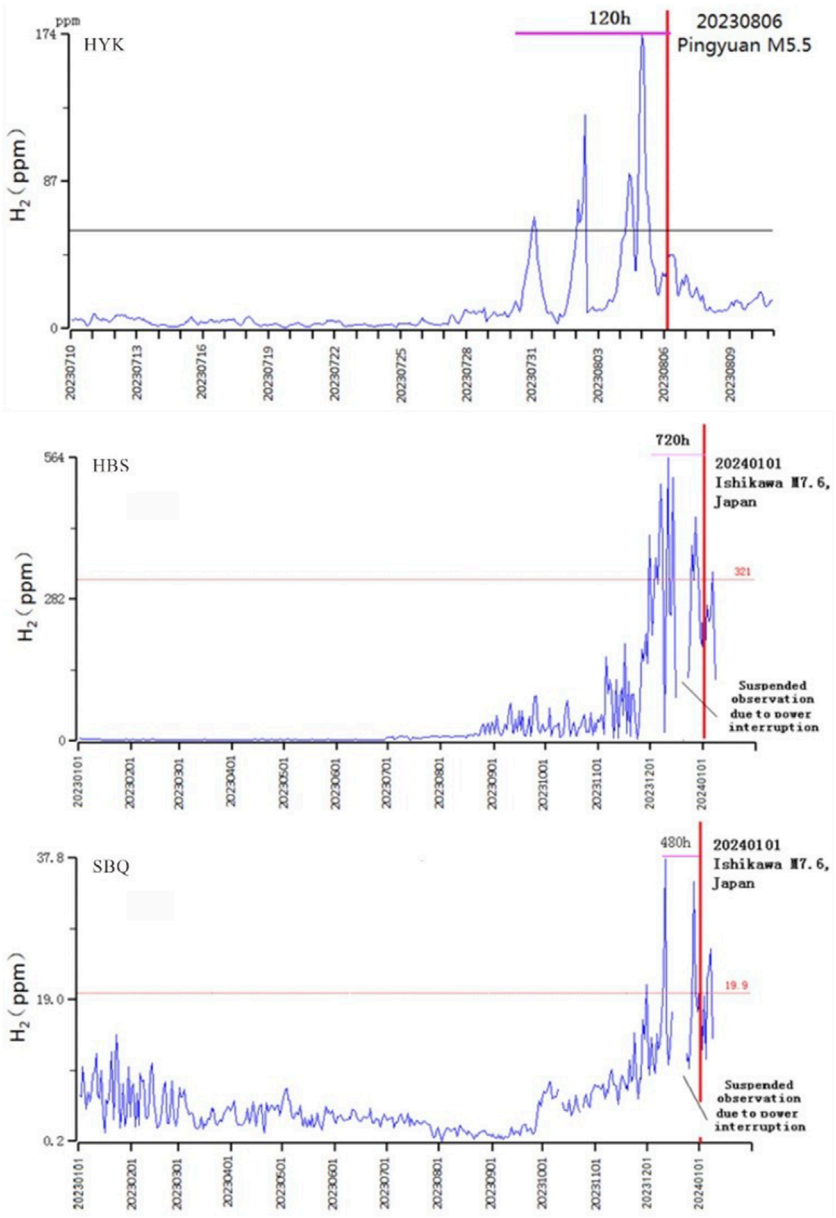

FIGURE 7
H_2 concentration anomalies prior to earthquakes at HYK, HBS, and SBQ.

02:33 on August 6 and returned to normal at 18:40 on August 7 (Figure 7; Table 4).

5.2.2 H_2 concentration at HBS and SBQ

Before the 1 January 2024 M7.6 earthquake in Ishikawa, Japan, there were significant short-term anomalies in the hydrogen concentration in HBS and SBQ (occurring 30 days and 20 days before the earthquake, respectively, and the anomalies decreased significantly after the earthquake), and the parameters of the precursor anomalies for the earthquakes are shown in Figure 7; Table 4.

Analyzing the H_2 anomaly magnitude, it was found that the H_2 anomaly magnitude at HYK before Shandong Pingyuan M5.5 was larger than that at SBQ and HBS before the Japan M7.6 earthquake. The anomaly amplitude before the Shandong Pingyuan M5.5 earthquake was as high as seven times, while the anomaly amplitudes before the Japan M7.6 earthquake were four and five times, respectively (Figure 7). From another point of view, it indicates that the loading effect of the stress field of the earthquakes with far epicentral distance has a significantly weaker relation with the earthquakes within the North China region.

10.3389/feart.2024.1474630

TABLE 4 Seismic precursor parameters of three geochemical stations on the NMYB Fault.

Time	Earthquake magnitude	Location	Epicentral distance of HYK	Epicentral distance of HBS	Epicentral distance of SBQ	Latitude	Longitude	Focal depth	Abnormal duration
August 6, 2023 at 14:33	M5.5	Pingyuan, China	380 km	——	——	37.16°N	116.34	10 km	5 days
January 01, 2024 at 15:10	M7.4	Nengdeng, Japan	——	——	1,890 km	37.55°N	137.49°E	59 km	24 days
January 01, 2024 at 15:10	M7.4	Nengdeng, Japan	——	1890 km	——	37.55°N	137.49°E	59 km	30 days

5.3 Simulation of gas concentration migration in faults

Chen et al. (2022) investigated the relationship between the gas release characteristics of the major active fault zones within the North China Craton and the regional tectonic framework. The results show that in the Zhang-Bo tectonic belt, the release of soil gas Rn and CO_2 and the contribution of crustal or mantle sources in the escaping gas from hot springs are significantly higher than in other tectonic zones in the region. A comprehensive analysis combining the results of the shear strain rate field, GPS horizontal velocity field, and S-wave velocity imaging reveals that the region was characterized by strong tectonic activities, and the development of nascent fractures may be widespread in the subsurface, and mantle-source fluids may be present in the subsurface of the Zhang-Bo tectonic belt for 20–40 km. It was also found that the peak region of helium from the mantle source material in the Zhang-Bo belt in the Yanqing Basin region showed increased deep fluid upwelling.

The NMYB Fault is located in the northern part of the central orogenic belt of the North China Craton, which consists of two east–west grade blocks of the North China Craton collided and spliced in the Paleoproterozoic (Liu and Zhao, 2012). After experiencing many geologic effects, a large number of faults were developed under the stresses of Cenozoic tensile-slip, and basin–mountain coupling tectonics were formed in the adjacent basins blocked by the mountain system (Xu et al., 1998), and the Yanqing Basin is one of them (Yang et al., 2022).

Subduction of the paleo-Pacific plate sheet is the geodynamic mechanism leading to the thinning and destruction of the lithospheric mantle of the North China Craton (Zhu et al., 2017). The destruction of the North China Craton occurred mainly in the area east of the Taihang Mountains in North China, resulting in the intrusion of magma, earthquakes, and volcanism in the area, including the Zhang-Bo belt, which are closely related to the geologic activities. The Yanhuai Basin, located in the Zhang-Bo Belt, is one of the areas with the potential danger of strong earthquakes in the eastern part of mainland China. The mechanism of earthquake occurrence in the Yanhuai Basin and basin–mountain interaction, the monitoring and prediction of future strong earthquakes, and other scientific and applied issues have also been attracting the attention of earthquake scientists.

Hence, in the broader context of tectonically active and fracture development in the Zhang-Bo belt region, combined with gas observation anomalies in this region, a model was designed to explain the anomalies. The model assumes that the NMYB Fault is a gas source system capable of responding to external stress loading and that during the anomalous time period, there was stress loading from the periphery of the fault, and anomalous gas rises, along with increases in the H_2 concentration, were observed at the observatory stations (see Figure 8).

This can be explained by the fact that in the fracture system, the hydrogen concentration in the escaping gas is very sensitive to the increase in stress, which has the potential to enhance the openness of the microfracture under the Yanqing Fracture, leading to an increase in the concentration of the gas originating from the depth.

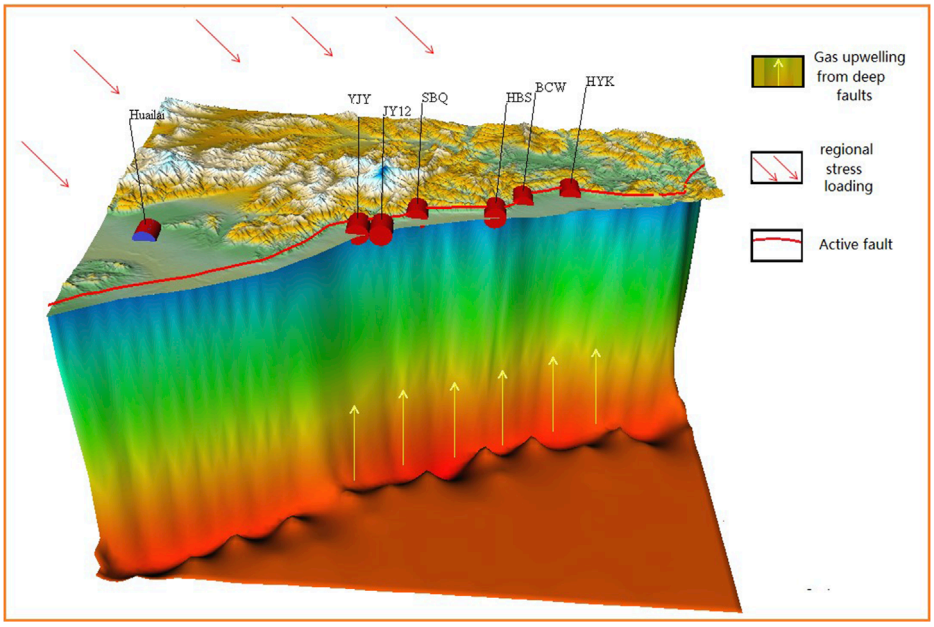

FIGURE 8
Modeling of the stress loading and gas transportation process in the fracture at the Northern Margin of the Yanqing Basin.

At the same time, during stress loading, hydrogen released from rock fragmentation and hydrogen generated by water–rock chemistry at the active fault site make hydrogen more concentrated near the active fault, so some hydrogen anomalies can be observed at the location of the active fault at the surface.

6 Conclusion

1. The high-density geochemical observatory stations near the fractures at the Northern Margin of the Yanqing Basin are a preferable site for pilot research on gas geochemistry in active faults.
2. The time series of H_2 concentration observations exhibit complex temporal patterns, reflecting a wide range of different physical processes. Observatories located along the rupture showed significant short-term hydrogen concentration anomalies (5–30 days) prior to the earthquake, which may be related to regional stress loading.
3. The use of high-precision automatic continuous monitoring stations to observe hydrogen concentration and other concentrations (CO_2, He, radon, water temperature, and ion concentrations) at active rupture locations can be analyzed to determine the physical process of rupture zone activity; the next step is to combine and synthesize the time series and spatial characteristics of hydrogen concentrations and multiple fault gases from observation stations in the same rupture zone. This approach could be a valuable tool for further unraveling the mechanism of earthquakes and predicting earthquakes.

Data availability statement

The original contributions presented in the study are included in the article/supplementary material; further inquiries can be directed to the corresponding authors.

Author contributions

MY: conceptualization, funding acquisition, investigation, methodology, writing–original draft, and writing–review and editing. GL: conceptualization, funding acquisition, supervision, and writing–review and editing. YC: methodology, visualization, and writing–review and editing. PH: investigation and writing–review and editing. LH: writing–review and editing. ZW: writing–review and editing. SW: investigation and writing–review and editing. XS: writing–review and editing. YoZ: writing–review and editing. HZ: methodology, investigation, writing–review and editing. GF: methodology, investigation, writing–review and editing. XG: methodology, investigation, writing–review and editing. YZ: formal analysis, writing–review and editing.

Funding

The author(s) declare that financial support was received for the research, authorship, and/or publication of this article. This work was supported by the surface technology project of the Beijing Earthquake Agency (No. BJMS-2024005).

Acknowledgments

The authors thank the editors and reviewers for valuable constructive comments on this manuscript that greatly enhanced the clarity and improved this work.

Conflict of interest

The authors declare that the research was conducted in the absence of any commercial or financial relationships that could be construed as a potential conflict of interest.

Publisher's note

All claims expressed in this article are solely those of the authors and do not necessarily represent those of their affiliated organizations, or those of the publisher, the editors, and the reviewers. Any product that may be evaluated in this article, or claim that may be made by its manufacturer, is not guaranteed or endorsed by the publisher.

References

Babuska, V., Ruzek, B., and Dolejs, D. (2016). Origin of earthquakes warms in the western Bohemian Massif:Is the mantle CO2 degassing, followed by the Cheb Basin subsidence, an essential driving force? *Tectonophysics* 668–669, 42–51. doi:10.1016/j.tecto.2015.12.008

Cao, C. H., Zhang, M. J., Tang, Q. Y., Yang, Y., Lv, Z. G., Zhang, T. W., et al. (2018). Noble gas isotopic variations and geological implication of Longmaxi shale gas in Sichuan Basin, China. *China. Mar. Petrol. Geol.* 89, 38–46. doi:10.1016/j.marpetgeo.2017.01.022

Che, Y. T., Yu, J. Z., Liu, W. Z., and Yi, L. X. (1999). Analysis of groundwater anomaly field and its causes in the Zhangbei-Shangyi earthquake (in Chinese). *Acta Seismol. Sin.* 1999 (3), 194–201.

Chen, Y. X., and Liu, J. B. (2023). Groundwater trace element changes were probably induced by the ML3.3 earthquake in Chaoyang district, Beijing. *Front. Earth Sci.* 11. doi:10.3389/feart.2023.1260559

Chen, Z., Ying, Li, Liu, Z., He, H., Martinelli, G., Lu, C., et al. (2022). Geochemical and geophysical effects of tectonic activity in faulted areas of the North China Craton. *Chem. Geol.* 609, 121048. doi:10.1016/j.chemgeo.2022.121048

Cheng, S. P., Fang, Z. J., Yang, G. Z., and Yang, Z. (1995). On segmentation of the fault zone along the North Margin of Yanqing Basin and earthquake prediction. *Seismol. Geol.* 17 (3), 231–240. doi:10.1007/978-3-642-31445-2_7

Cicerone, R. D., Ebel, J. E., and Britton, J. (2009). A systematic compilation ofearthquake precursors. *Tectonophysics* 476 (3–4), 371–396. doi:10.1016/j.tecto.2009.06.008

Cox, S. C., Menzies, C. D., Sutherland, R., Denys, P. H., Chamberlain, C., and Teagle, D. A. H. (2015). Changes in hot spring temperature and hydrogeology of the Alpine Fault hanging wall, New Zealand, induced by distal South Island earthquakes. *Geofluids* 15, 216–239. doi:10.1111/gfl.12093

Donald, T. (1988). Geochemical precursors to seismic activity. *Pure Appl. Geophys126* 126 (2-4), 241–266. doi:10.1007/bf00878998

Fang, Z. J., Cheng, S. P., and Ran, Y. K. (1993). Yan-Huai basin-ridge structure and some features of late quanternary fracture movement (in Chinese). *Prog. Geophys.* (04), 265–266.

Fischer, T., Matyska, C., and Heinicke, J. (2017). Earthquake-enhanced permeability-evidence from carbon dioxide release following the ML 3.5 earthquake in West Bohemia. *Earth Planet Sci. Lett.* 460, 60–67. doi:10.1016/j.epsl.2016.12.001

Gherardi, F., Pierotti, L., and Vista, A. D. (2017). Water-rock interactions in a siteinvestigated for geochemical precursors of earthquakes: the pieve foscianaspring (Italy). *Earth Planet Sci. Lett.* 17, 360–363. doi:10.1016/j.proeps.2016.12.091

Gupta, H. K. (2001). Short-term earthquake forecasting may be feasible at Koyna, India. *Tectonophysics* 338 (3–4), 353–357. doi:10.1016/s0040-1951(01)00083-x

Hirose, T., Kawagucci, S., and Suzuki, K. (2011). Mechanoradical H2 generation during simulated faulting: Implications for an earthquake-driven subsurface biosphere. *Geophys. Res. Lett.* 38, L17303. doi:10.1029/2011.gl048850

Huang, F., Li, M., Ma, Y., Han, Y., Tian, L., Yan, W., et al. (2017). Studies on earthquake precursors in China: A review for recent 50 years. *Geod. Geodyn.* 8 (1), 1–12. doi:10.1016/j.geog.2016.12.002

Irfan, M., Zhou, L., Bai, Y., Yuan, S., Liang, T. T., Liu, Y. F., et al. (2019). Insights into the hydrogen generation from water-iron rock reactions at low temperature and the key limiting factors in the process. *Int. J. Hydrogen Energy* 44 (33), 18007–18018. doi:10.1016/j.ijhydene.2019.05.086

King, C. Y. (1986). Gas geochemistry applied to earthquake prediction: anoverview. *J. Geophys. Res.* 91, 12269–12281. doi:10.1029/jb091ib12p12269

Li, Z. P., Wang, X. B., Li, L. W., Zhang, M. J., Tao, M. X., Xing, L. T., et al. (2014). Development of new method of δ13C measurement for trace hydrocarbons in natural gas using solid phase micro-extraction coupled to gas chromatography isotope ratio mass spectrometry. *J. Chromatogr. A* 1372, 228–235. doi:10.1016/j.chroma.2014.10.089

Liu, C. H., Liu, F. L., and Zhao, G. C. (2012). The Paleoproterozoic basin evolution in the Trans-North China Orogen, North China Craton. *Acta Petrol. Sin.* 28 (9), 2770–2784.

Lollar, B. S., Onstott, T. C., Lacrampe-Couloume, G., and Ballentine, C. J. (2014). The contribution of the Precambrian continental lithosphere to global H2 production. *Nature* 516, 379–382. doi:10.1038/nature14017

Luo, Z., Yang, M., Zhou, X., Liu, G., Liang, J., Liu, Z., et al. (2024). Evaluation of Various Forms of Geothermal Energy Release in the Beijing Region, China. *Water* 16, 622. doi:10.3390/w16040622

Ma, J. (2016). On whether earthquake precursors help for prediction do exist. *Chin. Sci. Bull.* 61, 409–414. doi:10.1360/n972015-01239

Myagkiy, A., Brunet, F., Popov, C., Krüger, R., Guimarães, H., Sousa, R. S., et al. (2020). H2 dynamics in the soil of a H2-emitting zone (São Francisco Basin, Brazil): Microbial uptake quantification and reactive transport modelling. *Appl. Geochem.* 112, 104474. doi:10.1016/j.apgeochem.2019.104474

Nagamine, K. (1994). Origin and coseismic behavior of mineral spring gas atByakko, Japan, studied by automated gas chromatographic analyses. *Chem. Geol.* 114 (1–2), 3–17. doi:10.1016/0009-2541(94)90038-8

NOA certification (2019). Validity of the certificate:2019/7/25~2020/7/25. Available at: http://cx.cnca.cn/CertECloud/result/skipResultList.

Parnell, J., and Blamey, N. (2017). Global hydrogen reservoirs in basement and basins. *Geochem. Trans.* 18, 2. doi:10.1186/s12932-017-0041-4

Prinzhofer, A., Moretti, I., Françolin, J., Pacheco, C., D'Agostino, A., Werly, J., et al. (2019). Natural hydrogen continuous emission from sedimentary basins: The example of a Brazilian H2-emitting structure. *Int. J. Hydrogen Energy* 44 (12), 5676–5685. doi:10.1016/j.ijhydene.2019.01.119

Sinclair, A. J. (1991). A fundamental approach to threshold estimation in exploration geochemistry: Probability plots revisited. *J. Geochem. Explor.* 41 (1-2), 1–22. doi:10.1016/0375-6742(91)90071-2

Sugisaki, R., Ido, M., Takeda, H., Isobe, Y., Hayashi, Y., Nakamura, N., et al. (1983). Origin of hydrogen and carbon dioxide in fault gases and its relation to fault activity. *J. Geol.* 91 (3), 239–258. doi:10.1086/628769

Sugisaki, R., Ito, T., Nagamine, K., and Kawabe, I. (1996). Gas geochemical changes at mineral springs associated with the 1995 southern Hyogo earthquake (M = 7.2), Japan. *Earth Planet Sci. Lett.* 139 (1-2), 239–249. doi:10.1016/0012-821x(96)00007-6

Sugisaki, R., and Sugiura, T. (1986). Gas anomalies at three mineral springs and afumarole before an inland earthquake, central Japan. *J. Geophys. Res.* 91 (B12), 12296–12304. doi:10.1029/jb091ib12p12296

Umeda, K., Asamori, K., and Kusano, T. (2013). Release of mantle and crustalhelium from a fault following an inland earthquake. *Appl. Geochem.* 37, 134–141. doi:10.1016/j.apgeochem.2013.07.018

Wang, C. Y., and Manga, M. (2010). Hydrologic responses to earthquakes and a general metric. *Geofluids* 10, 206–216. doi:10.1111/j.1468-8123.2009.00270.x

Wang, J., Watanabe, N., Okamoto, A., Nakamura, K., and Komai, T. (2019). Acceleration of hydrogen production during water-olivine-CO2 reactions via high-temperature-facilitated Fe(II) release. *Int. J. Hydrogen Energy* 44 (23), 11514–11524. doi:10.1016/j.ijhydene.2019.03.119

Wang, J., Watanabe, N., Okamoto, A., Nakamura, K., and Komai, T. (2020). Characteristics of hydrogen production with carbon storage by CO2-rich hydrothermal

alteration of olivine in the presence of Mg–Al spinel. *Int.J. Hydrogen Energy* 45 (24), 13163–13175. doi:10.1016/j.ijhydene.2020.03.032

Weinlich, F. H., Gazdová, R., Teschner, M., and Poggenburg, J. (2016). The ˇOctober 2008 Nový Kostel earthquake swarm and its gas geochemicalprecursor. *Geofluids* 16 (5), 826–840. doi:10.1111/gfl.12187

Wen, L., He, L., Feng, E., Lian, K., Chen, Q., Zhang, L., et al. (2018). Calibration,Performance Testing and Their Results of the Automatic Trace Hydrogen Analyzer ATG-6118H. *Earthq. Res. China* 34 (3), 571–579.

Wen, X., Ma, S., Xu, X., and He, Y. (2008). Historical pattern and behavior ofearthquake ruptures along the eastern boundary of the Sichuan-Yunnanfaulted-block, southwestern China. *Phys. Earth Planet* 168 (1-2), 16–36. doi:10.1016/j.pepi.2008.04.013

Xu, J., Song, C., and Chu, Q. (1998). Preliminary study on the seismotectonic characteristics of the Zhangjiakou Penglai fault zone. *Seismol. Geol.* 20 (2), 146–154. doi:10.1088/0256-307X/16/9/027

Yang, M. B., Liu, G. P., Liu, Z., Ma, J. C., Li, L. W., Wang, Z. G., et al. (2022). Geochemical characteristics of geothermal and hot spring gases in Beijing and Zhangjiakou Bohai fault zone. *Front. Earth Sci.* 10, 933066. doi:10.3389/feart.2022.933066

Yu, G. H., and Xu, X. W. (2004). Study on relationship between deep and shallow Structures along north boundary fault of yanqing-fanshan basin (in Chinese). *Acta Seismol. Sin.* 26 (1), 68–76.

Zhou, X., Wang, W., Chen, Z., Yi, L., Liu, L., Xie, C., et al. (2015). Hot spring gasgeochemistry in western Sichuan Province, China after the Wenchuan Ms 8.0earthquake. *Terr. Atmos. Ocean. Sci.* 26 (4), 361–373. doi:10.3319/tao.2015.01.05.01(tt

Zhou, X., Wang, W., Li, L., Hou, J., Xing, L., Li, Z., et al. (2020). Geochemicalfeatures of hot spring gases in the Jinshajiang-Red River fault zone,Southeast Tibetan Plateau. *Acta Petrol. Sin.* 36 (7), 2197–2214. doi:10.18654/1000-0569/2020.07.18

Zhou, X., Yan, Y., Fang, W., Wang, W., and Shi Hand Li, P. (2021). Short-Term Seismic Precursor Anomalies of Hydrogen Concentration in Luojishan Hot SpringBubbling Gas, Eastern Tibetan Plateau. *Front. Earth Sci.* 8, 586279. doi:10.3389/feart.2020.586279

Zhu, R. X., Zhang, H. F., Zhu, G., Meng, Q. R., Fan, H. R., Yang, J. H., et al. (2017). Craton destruction and related resources. *Int. J. Earth Sci-Geol Rundsch* 106, 2233–2257. doi:10.1007/s00531-016-1441-x

frontiers | Frontiers in Earth Science

TYPE Methods
PUBLISHED 19 February 2025
DOI 10.3389/feart.2025.1541346

OPEN ACCESS

EDITED BY
Fuqiong Huang,
China Earthquake Networks Center, China

REVIEWED BY
Davide Fronzi,
Marche Polytechnic University, Italy
Chen Yuxuan,
Beijing Earthquake Agency, China

*CORRESPONDENCE
Mingqian Li,
18253791266@163.com

RECEIVED 07 December 2024
ACCEPTED 03 February 2025
PUBLISHED 19 February 2025

CITATION
Zhang W, Li M, Yang Y, Rui X, Lu M and Lan S (2025) Implications of groundwater level changes before near field earthquakes and its influencing factors - several earthquakes in the vicinity of the Longmenshan-Anninghe fault as an example.
Front. Earth Sci. 13:1541346.
doi: 10.3389/feart.2025.1541346

Implications of groundwater level changes before near field earthquakes and its influencing factors - several earthquakes in the vicinity of the Longmenshan-Anninghe fault as an example

Wenxu Zhang[1], Mingqian Li[1]*, Yao Yang[2], Xuelian Rui[2], Minggui Lu[3] and Shuangshuang Lan[4]

[1]School of Ecology and Environment, Institute of Disaster Prevention, Beijing, China, [2]Sichuan Earthquake Bureau, Chengdu, Sichuan, China, [3]College of Transportation Engineering, Nanjing Tech University, Nanjing, China, [4]College of Architecture and Civil Engineering, Beijing University of Technology, Beijing, China

Characteristics of groundwater level changes may be correlated with subsequent earthquake events. However, the relationship and its determining factors remain unclear. This study examines eight wells situated near the Longmenshan-Anninghe fault zone, which exhibit significant disparities in changes of groundwater level. We quantified these changes by Molchan diagram and investigated factors that may affect it using correlation assessments. The results indicate groundwater levels changes that are more responsive to static stresses and tidal forces also have a high correlation with subsequent earthquake events. Specific leakage, a hydraulic parameter, also effects the correlation between groundwater levels and subsequent earthquakes. Spatial distribution of epicenters may also contribute to differences in this correlation, while aquifer confinement appears to have minimal effect. We used a random forest regression to calculate the comprehensive contribution of these factors to the correlation between groundwater levels and subsequent earthquakes. Notably, epicenter locations showcase the utmost sensitivity to this correlation. These findings can help us understand the complex mechanisms of water level changes before earthquakes and provide insights into the optimal locations for monitoring boreholes.

KEYWORDS

groundwater level changes, before earthquakes, near field, aquifer properties, correlation analysis, sensitivity analysis

1 Introduction

As an active element capable of responding positively to crustal stresses, hydrological changes in groundwater due to seismic effects have been widely documented

(Barberio et al., 2020; Del Gaudio et al., 2024; Granin et al., 2018; Hattori and Han, 2018; Pulinets et al., 2018; Zhang et al., 2023), with pre-earthquake anomalies in groundwater levels being a consistent observation. For instance, the 1975 Haicheng earthquake in China was successfully predicted due to anomalies detected at numerous hydrological monitoring sites (Wang et al., 2006). Similarly, prior to the 1985 California Ms6.1 earthquake, two wells in close proximity exhibited a remarkable 3-cm rise in groundwater level (Roeloffs et al., 1997). In the case of the 1999 Ms7.7 Taiwan Chi-Chi earthquake, anomalous downward changes in water level were detected in several monitoring wells located on a nearby alluvial fan within a 200-day period (Chen et al., 2015). Through retrospective analysis, it was detected that groundwater level changes before multiple earthquakes in the Kamchatka Peninsula were highly correlated with subsequent earthquakes (Kopylova and Boldina, 2020). Additionally, Prior to the 2008 Wenchuan Ms8.0 earthquake in China, an increase in high-frequency anomalies was observed in the water level of wells near the Longmenshan Fracture (Sun et al., 2016). Yan et al. (2018) found a significant increase in anomalies at three times the rupture scale in the 5 months preceding the Wenchuan Ms8.0 earthquake. These studies underscore the potential of groundwater level anomalies as the means for earthquake prediction.

While numerous pre-earthquake water level anomalies have been observed in monitoring wells, the earthquake prediction utilizing water level changes remains largely challenging. The primary obstacle is the complex formation mechanism of groundwater level precursors, which is not yet fully understood. Furthermore, a comprehensive quantitative framework to account for various factors influencing groundwater levels during seismic events is often lacking. The direct establishment of a one-to-one connection between groundwater level changes and the occurrence of earthquakes is elusive, thereby placing limitations on the reliability of using groundwater level changes as sole indicator of earthquake occurrence.

Since earthquake precursors are difficult to capture, and it is difficult to find a one-to-one correspondence between tectonic stress and groundwater level precursors. Mathematical-statistical methods, such as the Molchan diagram method (Molchan, 1990), have become increasingly accepted in the probabilistic prediction of earthquakes. These methods analyze the statistical relationship between seismic event triggers and the corresponding changes in observed groundwater levels. Their purpose is identifying mathematical relationships that can approximate the underlying connection between these two phenomena. Molchan (1990) introduced the use of loss functions to predict arbitrary points, while Zechar and Jordan (2008) enhanced Molchan's method, enabling comprehensive probabilistic prediction of three elements of earthquakes. Sun et al. (2017) employed the Molchan diagram method to analyze hydrological data, thereby quantitatively assessing the ability reflecting earthquake of groundwater level through the utilization of water temperature anomalies as a discriminating factor. Lai et al. (2021) employed the Molchan diagram method to assess the short- and medium-term predictive capabilities of subsurface fluid dynamics by incorporating the correlation between groundwater level and temperature data. These studies highlight that the Molchan method can effectively filter out groundwater level changes from a large amount of data and can indicate the correlation between groundwater level changes and subsequent earthquakes.

At present, there is still a lack of success in accurately predicting earthquakes, but models such as statistics and machine learning can help us mine potential information from a large amount of observational data and past events to aid in understanding the complex process of groundwater level changes. Therefore, we select the Molchan method to quantify the characteristics of groundwater level changes before earthquakes, and further determines the factors that control groundwater level changes through wavelet analysis, leaky aquifer model and random forest regression.

This study seeks to quantitatively evaluate potential factors that exert influence on characteristics of groundwater level changes before earthquakes in eight wells located in Longmenshan-Anninghe faults zone. Based on observed groundwater level data, we focus on the correlation between groundwater level changes characteristics and aquifer confinement, hydraulic parameters, earthquake epicenter orientation, response to tidal effect and seismic static stresses. Additionally, sensitivity analysis was conducted to identify the dominant factors that influence groundwater level changes characteristics. This approach can systematically reveal the reasons behind the variability in forecasting accuracy observed across different monitoring wells. Limited by the lack of theoretical research, this paper initially reveals the drivers of groundwater level changes before earthquakes by using a combination of Molchan Diagram, Wavelet Coherence Analysis, and Random Forest Regression. Additionally, it will offer guidance for future monitoring of seismic fluid activities.

2 Background to the study

2.1 Backgrounds

The Longmenshan Fault, positioned critically between the Tibetan Plateau and the Sichuan Basin, extends impressively over a length exceeding 500 km and spans approximately 70 km in width, featuring a northeast-southwest strike (Figure 1). The fault zone is subject to continuous compression from the Tibetan Plateau in the northwest, resulting in highly active geological activity (Zhang, 2008). Throughout the Late Quaternary period, the fault zone's activity has exhibited a gradual intensification from north to south. The fault zone is developed within a metamorphic heterogeneous rock body, characterized by high rupture intensity, thereby facilitating energy accumulation and predisposing the area to the occurrence of powerful earthquakes. Since the 1960s, "Y"-shaped fault zone (F1, F2, and F3 in Figure 1) has experienced a total of seven earthquakes with magnitudes of 7.0 or greater in Sichuan Province, establishing it as the most active region for strong earthquakes in western mainland China (Bai et al., 2019). The 2008 Wenchuan Ms8.0 earthquake has generated large ruptures of up to 300 km in length beneath the surface, occurring within an exceptionally brief time frame. The central rupture zone has been observed to span approximately 240 km (Zhang et al., 2008).

Emerging from the southernmost segment of the Longmenshan fault zone, the Anninghe fault constitutes an additional region

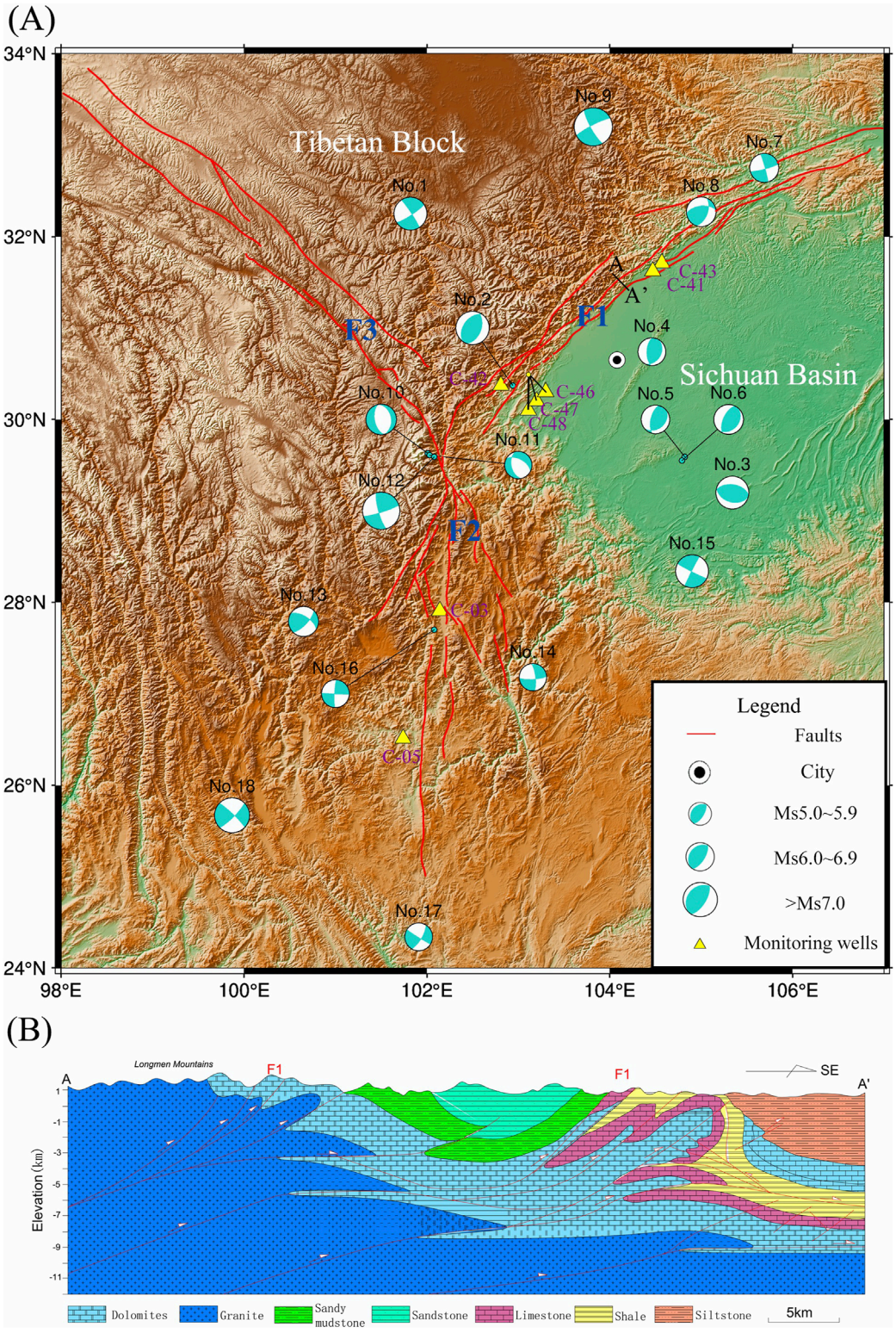

FIGURE 1
Locations of 8 wells and the 18 earthquakes. **(A)** The "beach balls" show the focal mechanism for earthquakes. Red lines show the faults, F1 is the Longmenshan Fault, F2 is the Anninghe Fault, and F3 is the Xianshuihe Fault. The yellow triangles indicate the monitoring wells. **(B)** The geological sections across F1 are shown at A-A'.

prone to frequent seismic activity. This fault, extending in a north-south direction, is predominantly characterized by sinistral strike-slip faults. It spans approximately 170 km in length and exhibits a complex hierarchical structure (Yi et al., 2004). Occupying a pivotal role, the Anninghe fault has been the site of a series of earthquakes (He and Ikeda, 2007).

2.2 Selections of monitoring wells and earthquakes

Following the statistical relationship between magnitude and distance as detailed in the "China Seismic Code," the study selected earthquakes at a certain distance from the monitoring wells, near the Longmenshan-Anninghe Faults (98–107°N, 24–34°E). Specifically, earthquakes of magnitude Ms5.0-6.0 were chosen within a 250 km seismic distance from the wells, earthquakes of magnitude Ms6.0-7.0 within 300 km and those of Ms7.0 or higher within 500 km (Table 1). This provides reasonable assurance that all monitoring wells will be within the range of seismic static strain (Shi et al., 2013). The earthquake time frame selection criteria are based on recent earthquake occurrences (2017–2023) and the inclusion of a wide range of magnitudes, particularly focusing on earthquakes above magnitude 5 and 6 to ensure methodological compatibility. Moreover, the groundwater level time series is selected within the same 2017-2023 timeframe to correspond with the seismic events under investigation. The surface wave magnitude (Ms) was chosen as the magnitude type for this paper, which was determined by measuring Rayleigh wave amplitudes at periods of approximately 20 s. Unlike Local magnitude (ML), which is calibrated for regional distances (<600 km) and specific to local crustal structures. Moment magnitude (Mw), based on the seismic moment tensor solution, provides the most complete physical description of earthquake size by considering fault parameters. However, Ms remains the standard scale in China, particularly effective for shallow earthquakes (depth <70 km) and historical catalog comparisons. A total of eight groundwater monitoring wells, depicted in Figure 1, were chosen for this study to ensure a better correspondence with the earthquakes. Some wellbore and stratigraphical are shown in Figure 2. Monitoring wells were deployed by the China Earthquake Administration (CEA) and were equipped with LN-3 and ZKGD3000-N groundwater level detectors, recording at a frequency of one measurement per minute, 1 mm resolution and 0.2% F.S. The original groundwater level curves and the difference curves are illustrated in Figure 3. Difference curves are calculated using first-order differences, which helps in highlighting changes in the rate of change of ground water level. The key information regarding the monitoring wells and their related features are outlined in Table 2.

3 Methods

3.1 Molchan diagram test

The Molchan diagram method offers a quantitative approach to assess the correspondence between groundwater level changes and subsequent events (Molchan, 1990; Zechar and Jordan, 2008). It involves establishing various differential thresholds to calculate the Abnormal time period occupancy rate τ and the Miss rate ν can be calculated. These values are then plotted as τ-ν step lines within the Molchan diagram, also known as the Molchan test line. The position of the step lines determines the strength of the correlation between groundwater level changes and subsequent earthquakes (Molchan, 1990; Zechar and Jordan, 2008). Molchan diagram requires the assessment of probability *Gain* and significance, and the equations involved and the significance of the parameters are as follows (Zechar and Jordan, 2008):

$$Gain = \frac{h}{\tau} = \frac{1-\nu}{\tau} \tag{1}$$

$$B(h|N,\tau) = C_h^N \tau^h (1-\tau)^{N-h} \tag{2}$$

where h is the number of hits: the number of earthquakes that successfully landed in the alarm region; ν is the miss rate: The ratio of earthquakes not falling within the alarm region to the total number of earthquakes; τ is the abnormal time period occupancy rate: the ratio of the anomalous time horizon of the groundwater level to the total; B is the cumulative binomial distribution, which is used to test for statistical significance; and N is the number of random hits. *Gain* is determined by the combination of ν and τ, and the length of the time period does not affect the results. The closer the Molchan test line is to the line of greater probability gain, the better its overall prediction. For convenience, we define the normalized area to the right of the Molchan test line as the pre-response index (PRI), that is, the potential of groundwater level to reflect subsequent earthquakes. The PRI range is 0–1, and the closer it is to 1, the stronger the correlation between groundwater level changes and subsequent events. The PRI value changes with the position of the Molchan test line (Sun et al., 2017).

In this study, a criterion is established to differentiate between high and low PRI. This criterion is based on setting a threshold value that reflects the absolute magnitude of differential values. Differences that exceed the threshold value are identified as anomalous. The alarm area will be set within a certain period of time after anomalous. An earthquake is deemed to have been successfully hit if it occurs both within the alarm area. Conversely, a hit is regarded as unsuccessful if the earthquake happens outside of the alarm area. To facilitate understanding, let's consider the example of well C-48 for a 94-day period from 1 July 2018, to 1 October 2018 (Figure 4). We will set the alarm area as 10 days.

a) When the threshold line is set to 0.5, only the value of July 3 is determined to be anomalous. At this time, according to Equations 1, 2, $\tau = (1 + 10)/94 = 0.12$. The 7th earthquake does not fall within the alarm area, thereby $\nu = 1/1 = 1$.
b) When the threshold line is set to 0.25, there are 7 days of values exceeding the threshold. The last anomaly, which occurs in September 16 after the 10-day alarm area, contains the 7th earthquake, indicating a successful hit. With eliminating duplicate alarm area and anomalous segments, $\tau = (7 + 40 - 12)/94 = 0.37$ and $\nu = 1/1 = 1$.

In use, there is no need to manually select a threshold. The Molchan method automatically traverses the cycle from the differential water values maximum to the minimum value, we can obtain multiple sets of ν and τ corresponding to the different

TABLE 1 Basic information of 18 earthquakes.

Earthquake numbers	Longitude (°)	Latitude (°)	Time	Magnitude (M_s)	Epicenter depth (km)
1	101.82	32.25	6 June 2022	6.0	13
2	102.94	30.37	1 June 2022	6.1	17
3	105.34	29.20	16 September 2021	6.0	10
4	104.46	30.74	3 February 2020	5.1	21
5	104.82	29.59	18 December 2019	5.2	14
6	104.79	29.55	8 September 2019	5.4	10
7	105.69	32.75	12 September 2018	5.3	11
8	105.00	32.27	30 September 2017	5.4	13
9	103.82	33.20	8 August 2017	7.0	20
10	102.01	29.63	26 January 2023	5.6	11
11	102.03	29.61	22 October 2022	5.0	12
12	102.08	29.59	5 September 2022	6.8	16
13	100.65	27.79	2 January 2022	5.5	10
14	103.16	27.18	18 May 2020	5.0	8
15	104.90	28.34	17 June 2019	6.0	16
16	102.08	27.70	31 October 2018	5.1	19
17	101.91	24.34	10 June 2022	5.1	8
18	99.87	25.67	21 May 2021	6.4	8

Data from *China Earthquake Administration Network Center* (https://news.ceic.ac.cn).

thresholds. Molchan diagram takes into account the combined results of all thresholds and avoids subjectivity in identifying anomalies.

3.2 Wavelet coherence analysis

Wavelet coherence analysis quantifies the correlation between groundwater level and theoretical tidal series by measuring their temporal relationship (Grinsted et al., 2004; Song et al., 2023; Yang and McCoy, 2023). It identifies resonance periods through phase-shifted arrows in highlighted regions, revealing the degree of correlation between two time series X and Y:

$$R^2(s) = \frac{\left|S\left(s^{-1}W^{XY}(s)\right)\right|^2}{S\left(s^{-1}|W^x(s)|^2\right) * S\left(s^{-1}|W^y(s)|^2\right)} \quad (3)$$

where W^X and W^Y are discrete wavelet transforms, W^{XY} is the cross wavelet transform of X and Y, S is the smoothing window, and R^2 is the coherence coefficient. R^2 is ranging from 0 to 1, with values close to 1 indicating that groundwater levels and tides vary in a high correlated manner. The wavelet coherence coefficient resembles the correlation coefficient in the traditional sense, and it can be understood as a localized correlation coefficient within the frequency space. Simply enter two time series groundwater level and theoretical tide with the same resolution, and R^2 between them will be calculated according to Equation 3. The code based on MATLAB is already publicly available for download (Grinsted et al., 2004).

3.3 Leaky aquifer model construction

Based on the tidal effect of groundwater level, the Leaky Aquifer Model is used to invert the specific leakage. First, tidal analysis of the water level data facilitates the determination of both observed and theoretical values for various tidal sub-waves' parameters. In this analysis, two key parameters are the amplitude ratio, which is the observed amplitude divided by the theoretical amplitude, and the phase shift, which represents the difference between the observed phase and the theoretical phase. Both parameters are essential for understanding the tidal analysis. By constructing response models for different well-aquifer systems, the phase shift and amplitude can be utilized to invert the hydraulic parameters of the aquifer.

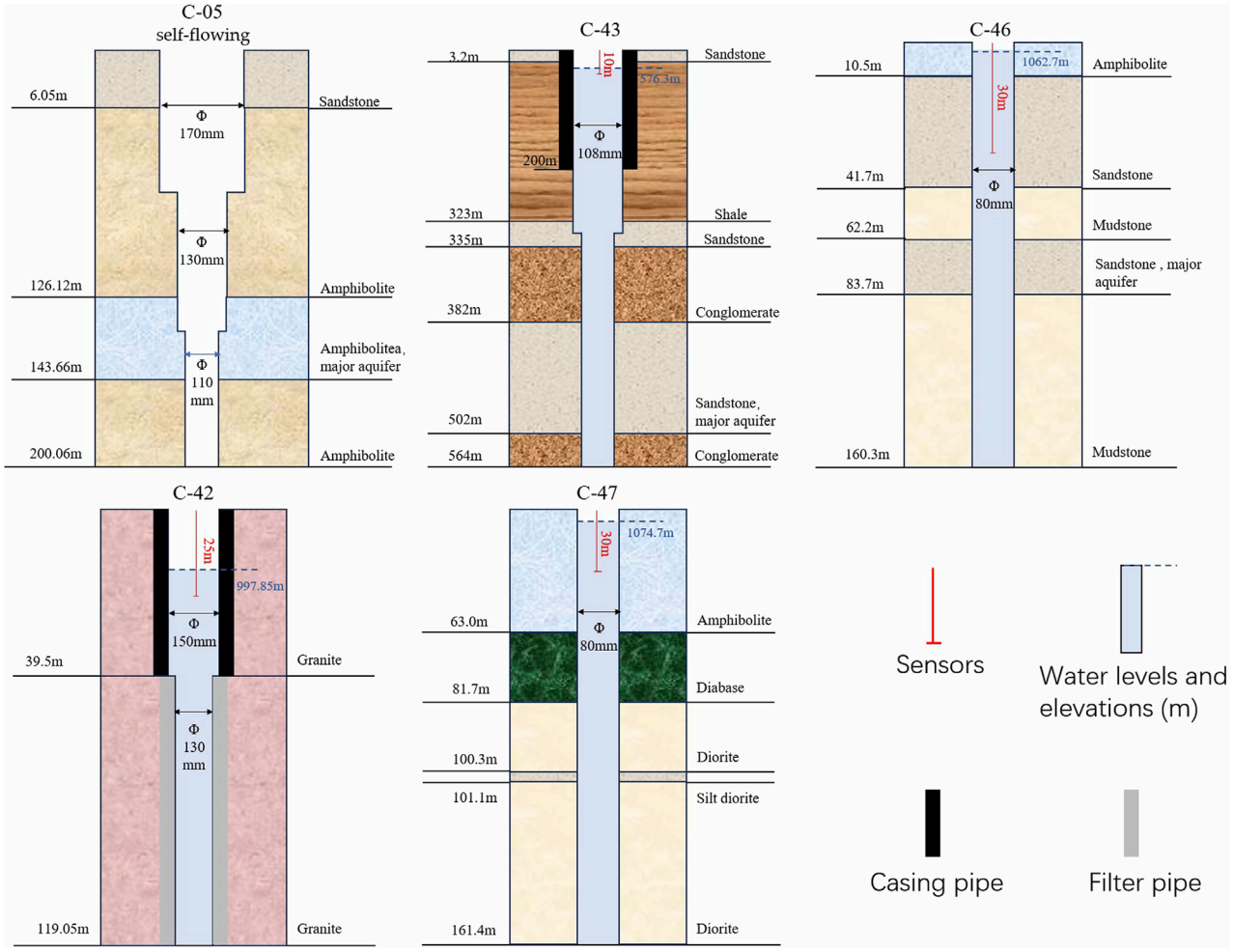

FIGURE 2
Partial wellbores structure and their lithology. The water level is converted from the water pressure measured by the sensor; the depth of the monitoring probe inside the wells refers to the distance from the sensor to the surface.

In situations where the aquifer's water primarily flows horizontally towards the borehole, a negative phase shift is observed. The radial flow model (Cooper et al., 1965; Hsieh et al., 1987) can be employed to invert the permeability coefficient under these conditions. However, in more realistic scenarios where the aquifer interacts with surrounding rocks through hydraulic processes such as leakage, the phase shift tends to exhibit a leading behavior. The leaky aquifer model can be utilized to derive the specific leakage (σ), expressed as $\sigma = k'/b'$, where k' and b' represent the permeability coefficient and thickness of the aquitard (Gu et al., 2024; Wang et al., 2018). Significantly, this model also accounts for scenarios where flow within the aquifer is purely radial ($k' = 0$). The specific leakage (σ) serves as an indicator of the aquitard's vertical water transport capacity. The theoretical equations of leaky aquifer model are as follows:

$$T\left(\frac{\partial^2 h}{\partial r^2}+\frac{1}{r}\frac{\partial h}{\partial r}\right)-\frac{K'}{b'}h=S\left(\frac{\partial h}{\partial t}-\frac{Bk_u}{\rho g}\frac{\partial \varepsilon}{\partial t}\right) \tag{4}$$

where T (m^2/s) and S are the transmissivity and storage coefficient of the aquifer, respectively, r is the lateral distance from the well, k and k' are the permeability coefficients of the aquifer and the aquitard, respectively, b and b' are the thicknesses of the two, and B and K_u are the skempton's coefficient and the undrained bulk modulus, respectively. Equation 4 has the analytical solution as:

$$A = abs\left(\frac{i\omega S}{i\omega S+(k'/b')\xi}\right) \tag{5}$$

$$\eta = \arg\left(\frac{i\omega S}{i\omega S+(k'/b')\xi}\right) \tag{6}$$

Where

$$\xi = 1+\left(\frac{r_c}{r_\omega}\right)^2\frac{i\omega r_\omega K_0(\beta r_\omega)}{2T\beta K_1(\beta r_\omega)} \tag{7}$$

$$\beta = \sqrt{\frac{k'}{Tb'}+\frac{i\omega S}{T}} \tag{8}$$

where A and η are the tidal parameter amplitude and phase shift, respectively, and r_c and r_ω are the case pipe radius and well filter pipe radius, respectively.

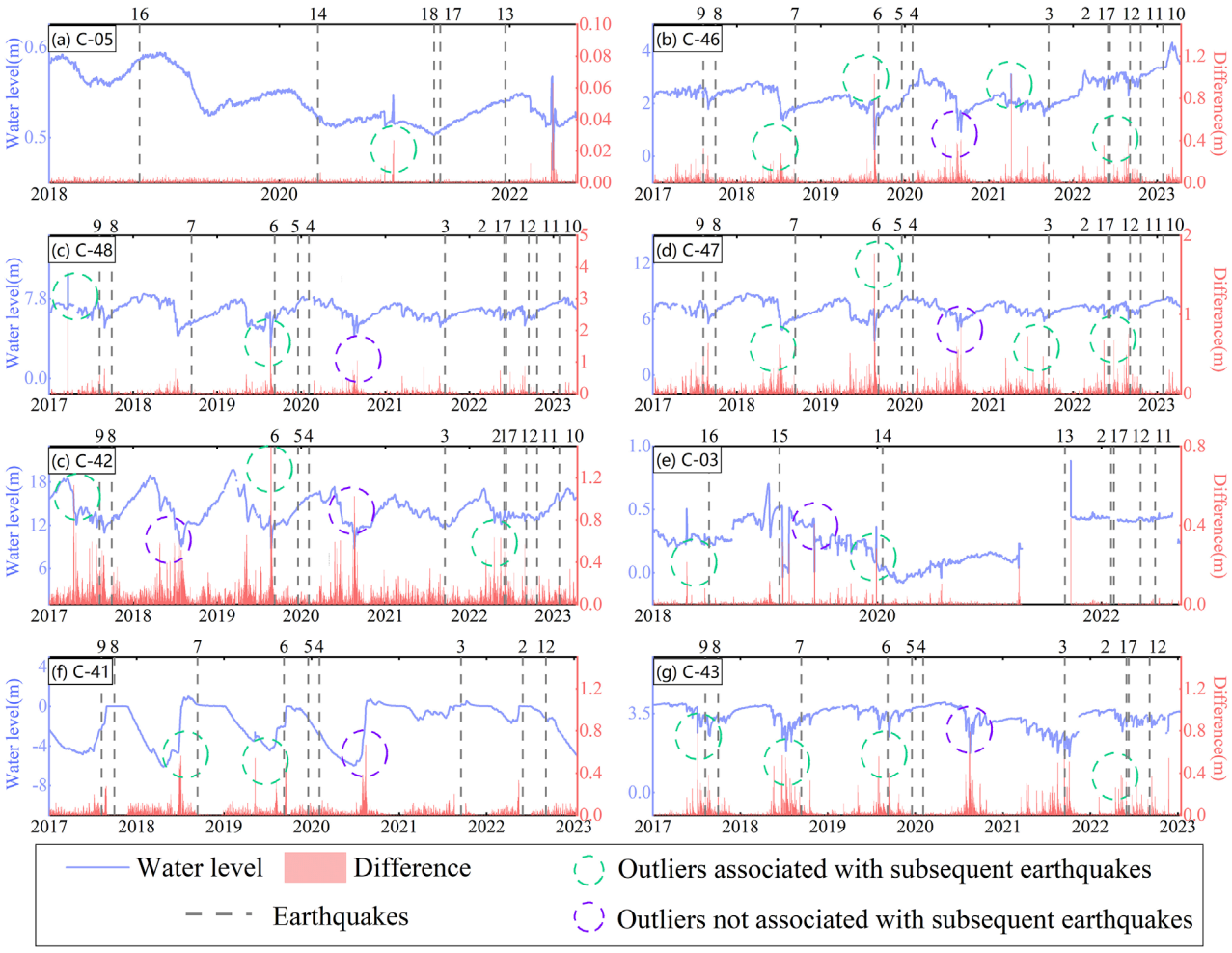

FIGURE 3
Daily water level and differential values of the 8 wells. The blue lines indicate the Water level and the red curve show the differential values. The water level here is the distance between the surface of the water in the well and the surface of the ground, a positive value means that the water level is below the surface and a negative value means that it is above the surface. The black dashed line shows the seismic events that occurred during the study time in Table 1. The differentials represented by the green and purple circles show elevated values that markedly exceed those of their surroundings, which is a suspected anomaly. The key distinction is that the anomalies within the green circles are associated possibly with subsequent earthquakes, whereas the purple circle anomalies are not.

In use, we need to input the known parameters: A, η, r_c, r_ω and Bku, then the specific leakage can be computed by combining Equations 5–8 in MATLAB using open-source code (Zhang et al., 2024).

3.4 Random forest regression

Random forest regression (RFR) was used for sensitivity analysis and was able to quantify the potential contribution of multiple factors to PRI (Borup et al., 2023; Rigatti, 2017). It uses the bootstrap resampling technique to generate a new set of training samples by repeated random sampling of n samples from the original training sample set T. Each independently sampled training sample is used to train a tree, and the n decision trees generated from the sample set are computed in parallel to select the optimal result, which improves the model's generalization ability. The *Gini* index is used to complete the establishment of the regression tree, the smaller the *Gini* index, the better the decision tree division (Breiman, 2001). Assuming that the sample T contains k classes, the *Gini* coefficient can be expressed as:

$$Gini(T) = 1 - \sum_{k=1}^{n} p_k^2 \tag{9}$$

where p_k denotes the probability that the sample belongs to the kth class. The smaller the *Gini* index, the smaller the uncertainty will be and will be more useful for feature testing. After normalizing all the factor series and inputting them into the RFR at the same time as the PRI, the contribution of each type of factor to the PRI will be output. The code is based on MATLAB's own function Treebagger, and the resluts of Equation 9 will automatically calculate (https://ww2.mathworks.cn/help/stats/treebagger.html).

10.3389/feart.2025.1541346

TABLE 2 Basic Information of the 8 wells.

Well name	Major aquifer lithology	Time scale of water level	Depth/m	Tectonical structure	Self-flowing/non-self-flowing	Water temperature (°C)
C-43	Mudstone	January 2017-January 2023	560.0	North-east section of F1	Non-self-flowing	18.80
C-41	Mudstone	January 2017-January 2023	190.0		Self-flowing	20.15
C-42	Granite	January 2017-January 2023	119.5	Southwest section of F1	Non-self-flowing	16.34
C-46	Sandstone	January 2017-January 2023	160.3		Non-self-flowing	13.29
C-47	Sandstone	January 2017-January 2023	161.4		Non-self-flowing	12.96
C-48	Sandstone	January 2017-January 2023	125.6		Non-self-flowing	25.84
C-03	Gabbro	May 2018- January 2023	756.6	Middle section of the F2	Self-flowing	25.75
C-05	Quartz diorite	January 2018-August 2022	200.6	Southern section of the F2	Self-flowing	24.40

Self-flowing means that the water level in the well will automatically flow out of the ground under the action of hydrostatic pressure, while non-self-flowing means that the water level in the well will not flow out of the ground.

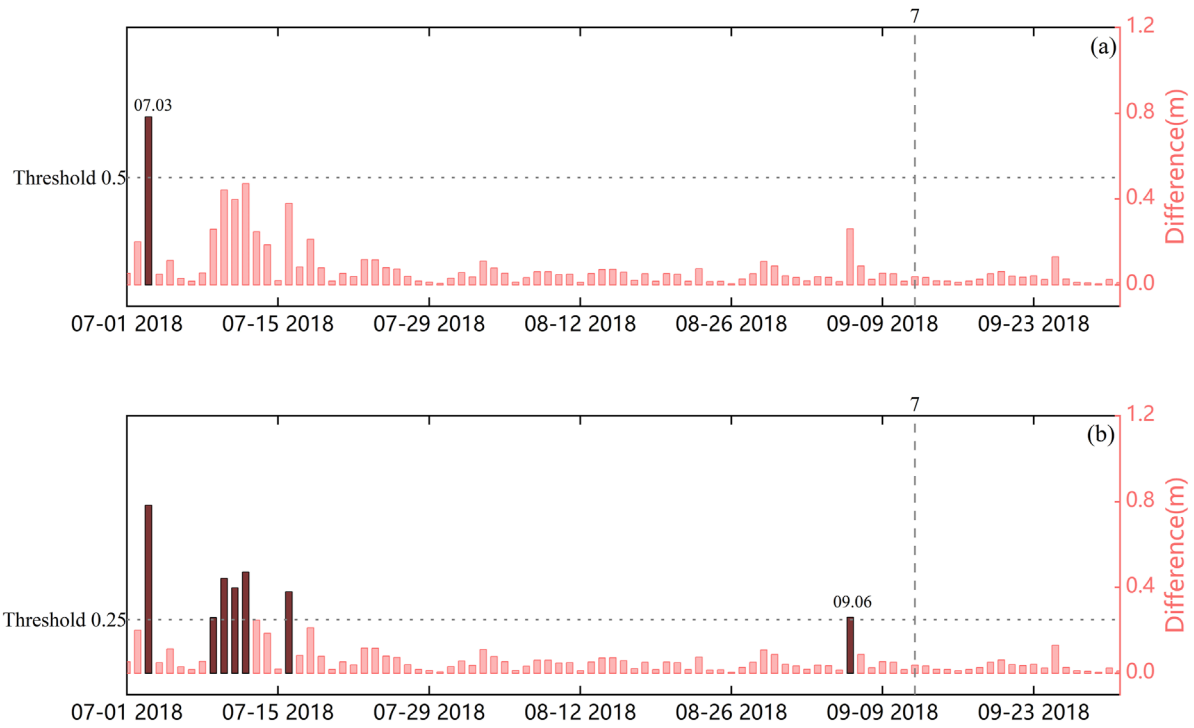

FIGURE 4
Anomaly judgement of water level differential scores at different thresholds. The red columns are water level differential scores for well C-48, studied over the period 1 July 2018 to 1 October 2018, and seismic 7 is indicated by vertical scribing. A horizontal dotted line denoted the thresholds, while the red bar depicted the differences of the groundwater level, and the differential above the threshold line is the black bar, i.e., the anomaly.

4 Results and discussion

4.1 Quantification of groundwater level changes characteristics before earthquakes

Some studies have reported changes in groundwater levels prior to certain earthquakes (Wang and Manga, 2021), but these observations are not universal or consistent. The mechanisms of such changes remain poorly understood, and currently there is no reliable way to use groundwater level variations as earthquake precursors. Therefore, it is necessary to statistically screen valid anomalies from a large number of suspected anomalies and establish the correspondence between groundwater level anomalies and subsequent earthquakes by the Molchan method. Anomalies are defined in this paper as differences exceeding a certain threshold. In the Molchan method, the threshold is adaptively selected (more details see Section 3.1). The premise of the method: a certain number of samples are needed, the samples include groundwater level and seismic data, and the longer the groundwater level series, the better. In the groundwater level time series, we can identify suspected anomalies, but this may not actually be the case (Figure 3). After accumulating a certain number of suspected anomalies, they are then matched with seismic data occurring in the vicinity. The more samples involved in the calculation, the more accurate the statistical results will be, ultimately revealing the correlation between groundwater level changes and subsequent earthquake events.

Figure 3 shows that pre-processing groundwater level data using differential values effectively highlights anomalies in groundwater levels. These anomalies are mainly marked by notably high values that deviate significantly from the surrounding data points, particularly in the period preceding the earthquake event (Differential values in green circles). Wells C-43, C-42, and C-47 exhibit more anomalies prior to the earthquake, potentially providing clearer indications of seismic activity. In contrast, wells C-05, C-03, and C-48 show no significant groundwater level changes, and the remaining two wells display only general fluctuations. However, subjectivity is not a discriminating criterion, and we will use the Molchan diagram to a further test.

Molchan method unifies the characteristics of groundwater level changes before earthquakes, which provides a quantitative indicator that we defined as pre-response index (PRI). PRI represents the area to the right of the Molchan test line, ranging from 0 to 1.The closer it is to 1, the stronger the correlation between groundwater level changes and subsequent events (Lai et al., 2021; Sun et al., 2017). Figure 5 shows the results of the PRI for eight wells under a 30-day alarm region period. The *v-t* test lines for wells C-41, C-47, and C-48 are closer to the *Gain* line of *Gain* = 2, and grey areas are higher and more significant, indicating a relatively higher PRI. The *v-t* test lines for wells C-05 are the lowest, falling well below 0.5, indicating that the PRI is relatively lower.

Furthermore, to enhance the precision and reliability of the Molchan test, an assessment of PRI was conducted across various alarm regions, limited to a maximum of 180 days. Figure 6 presents the PRI of eight monitoring wells within this timeframe. Distinct variations in PRI were observed among the wells. The average PRI over a 6-month period ranged from a minimum of 0.35 to a maximum of 0.71, indicating a considerable disparity. Wells C-41, C-43, and C-47 have a good performance in general (PRI of more than 2/3), while the PRI of wells C-03 and C-05 is relatively low (PRI close to 1/3), C-42, C-46 and C-48 show average performance (between 2/3 and 1/3).

Despite the similarity in tectonic units and the wells' location in fractured media aquifers, as well as the comparable distances between the selected earthquakes and the wells, the groundwater level PRI exhibits noticeable variations. These variations provide a unique opportunity to identify factors that govern groundwater level changes before earthquakes.

4.2 Attribution analysis of groundwater level changes characteristics before earthquakes

The aquifer characteristics, particularly the confinement, play a crucial role in determining the wells' responsiveness to seismic stress. Furthermore, hydraulic parameters significantly influence the magnitude of water level response, thereby affecting the characteristics of groundwater level changes. Tidal effect and seismic static stresses induce certain disturbances within the aquifer and can be considered as "typical representatives" of aquifer response to external stresses. Groundwater levels that exhibit favorable responses to both types of stresses are more likely to demonstrate satisfactory correlations with subsequent earthquakes. Additionally, the distribution of epicenters in relation to the stress propagation path may also influence PRI, serving as an important factor that warrants consideration. In this section, we selected the degree of tidal action experienced by the wells, the co-seismic response magnitude, the hydraulic properties of the aquifer, and the orientation of the epicenter as factors to correlate with PRI. This comprehensive analysis aims to shed light on the factors contributing to the difference of PRI among the monitored wells. The PRI serves as a reliable indicator of the correlation between groundwater level changes and subsequent earthquake events.

This analysis involved multiple steps. First, we evaluated the co-seismic and tidal response coefficients by basic statistics and wavelet coherence analysis, since the role of tides is potentially significant and needs to be treated in the frequency domain to highlight the correlation between the time series. In addition, spectral analysis and leaky aquifer model were utilized to assess the aquifer confinement and hydraulic parameter, both of which are suitable for dealing with periodic signals similar to tidal action. Based on these evaluations, a comparative analysis was performed to assess whether the conditions were responsible for the observed differences in PRI. Secondly, we quantitatively analyzed the impact of the epicenter's distribution location on the PRI of the wells' water levels. This analysis aimed to identify any correlations between the spatial distribution of seismic events and the PRI. Lastly, we employed the RFR method to integrate the analyzed factors with the sensitivity analysis of the factors controlling the differences in PRI. This is because it is suitable for multiple series to be analyzed simultaneously with strong robust-ness. This combined analysis aimed to identify the factors that are more likely to contribute to the variations in PRI. Ultimately, our goal was to identify the key factors that significantly impact the variations in PRI.

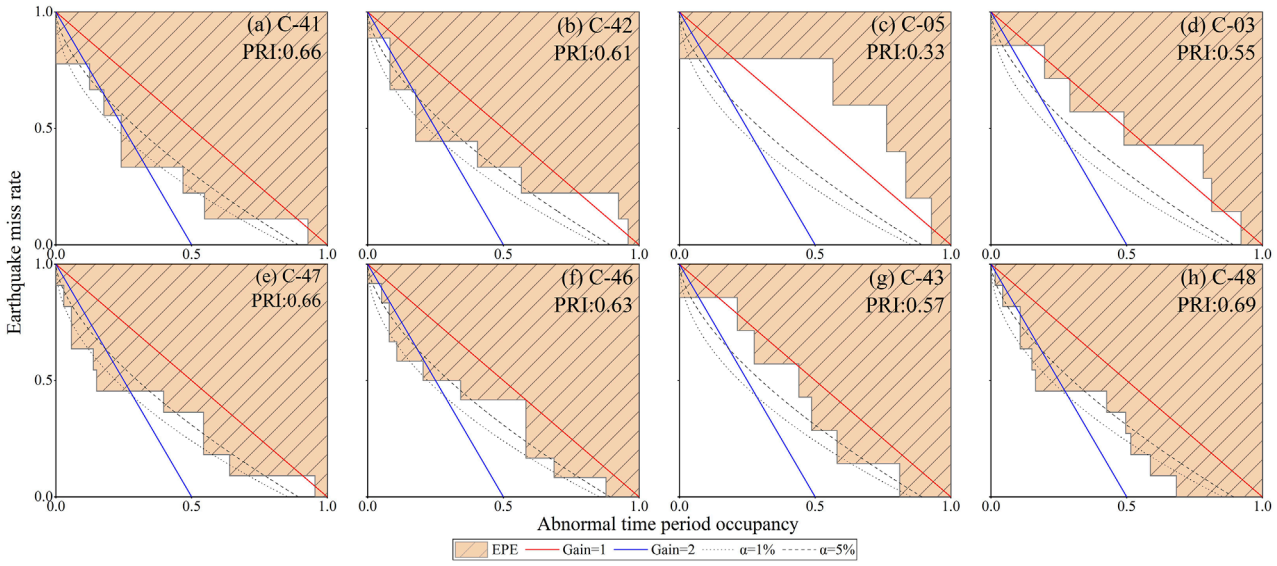

FIGURE 5
Results of the Molchan test for 8 wells over a 30-day alarm region. The red lines and blue lines show the *Gain* value. The dashed lines indicate the significance level. Shaded area points to the PRI.

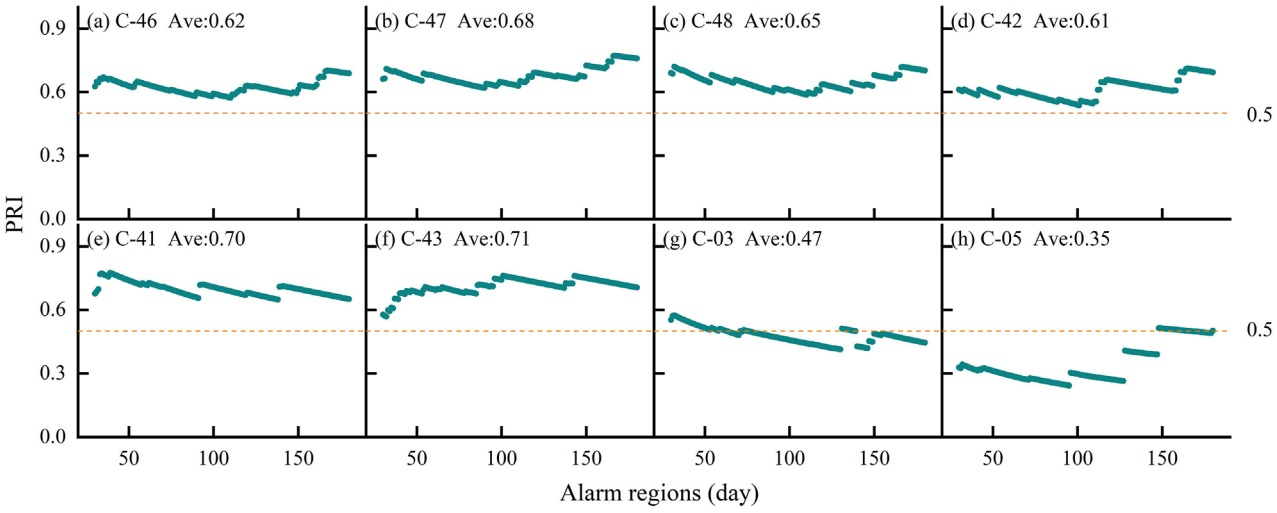

FIGURE 6
PRI of groundwater levels in 8 wells across different alarm regions (ranging from 1 month to 6 months). The green dots indicate the PRI under different alarm regions. The yellow dotted line denotes the median of PRI.

4.2.1 Influence of co-seismic response and tidal effect

Tidal forces, being a distinct form of crustal stress, often generate long-lasting cyclic variations in well water level. A frequently observed phenomenon is that earthquakes may semi-permanently alter the character of the tidal response (Shi and Wang, 2014; Shi and Wang, 2015). Similarly, seismic events exert static stresses that induce temporary alterations in well water level (Wang and Chia, 2008). Wells that exhibit heightened sensitivity to these common external stresses are expected to display more pronounced responses before earthquakes.

To determine the extent of tidal influence, we quantified the ratio of the time during which water levels were affected by tides to the overall duration of the study period. The relevant rate can be obtained by inputting a tidal sequence and a groundwater level sequence with the same time span and calculating them using Equation 3 The results were presented using the wavelet coherence method, as shown in Figure 7A. Additionally, the degree of co-seismic response was evaluated by calculating the co-seismic response rate Figure 7B, based on the earthquake data from Table 1. This analysis allows us to gauge the wells' sensitivity to seismic events (Table 3).

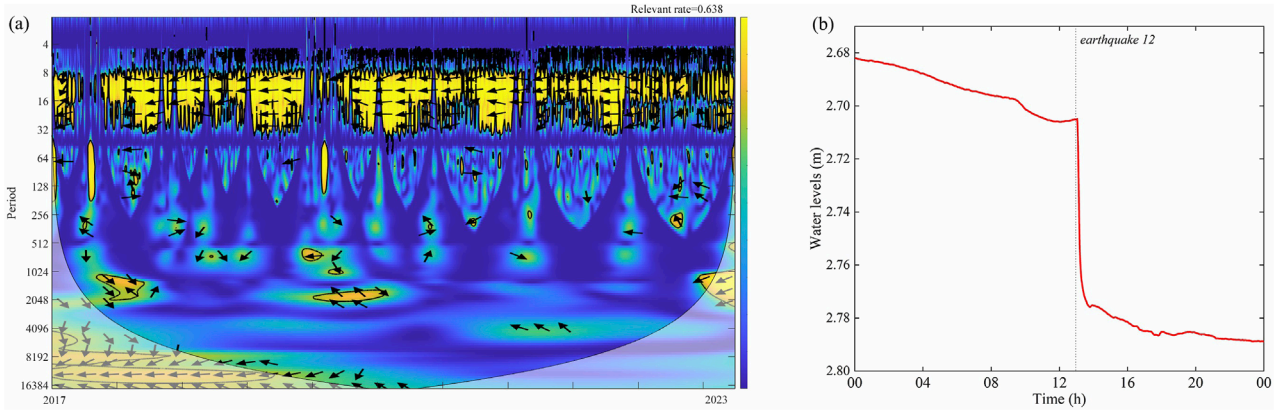

FIGURE 7
Tidal and co-seismic responses of water levels **(A)** Wavelet coherence analysis between water levels and tidal effects. The vertical coordinate of the graph represents the period (h), while the horizontal coordinate represents the time (year) Highly correlated regions are highlighted in yellow and those surrounded by a thick black line represent those that passed the Monte Carlo test at a significance level of 5%. Arrows to the right of the graph represent a same-direction alignment, and arrows to the left represents an opposite-direction alignment, and arrows pointing vertically down represents the lead of 90°. **(B)** co-seismic water level changes. If the water level changes rapidly within a short period of time after an earthquake, it is considered to have a co-seismic effect.

TABLE 3 Sensitivity of groundwater level in monitoring wells to co-seismic response and tidal effect.

Wells	Co-seismic response rates	Tidal relevant rates
C-43	0.571	0.634
C-41	0.67	0.467
C-42	0.56	0.416
C-46	0.67	0.298
C-47	0.364	0.638
C-48	0.273	0.08
C-03	0.143	0.356
C-05	0	0.405

Considering that the Molchan diagram method utilized in this study is based on daily average water level data, the impact of co-seismic events and the persistence of solid tides on PRI are likely to be minimal. Consequently, the statistical results presented in Table 3 are likely to accurately reflect the actual situation. Wells C-41, C-47, and C-43 consistently exhibit superior performance across all stress factors, while wells that perform poorly under one or both stresses tend to have lower PRI. To further investigate the relationship between the degree of stress influence and PRI, a multivariate regression analysis was conducted. The PRI (P) was treated as the dependent variable, while the degree of co-seismic response (C) and the degree of tidal response (T) were considered as independent variables, presupposed to be independent of each other. The resulting binary regression equation derived from this analysis is as follows: $P = 0.411C + 0.462T + 0.205$. The regression model highlights that higher degrees of co-seismic and tidal responses in the groundwater level are associated with higher PRI. However, it is worth noting that well C-48 deviates from this relationship, possibly due to its location within the fault fracture zone which is more sensitive and vulnerable than the hydraulic properties away from the fault damage zone (Yan et al., 2016; Zhang et al., 2021). This model underscores the notion that wells exhibiting heightened sensitivity to external stresses are more likely to demonstrate superior PRI.

4.2.2 Influence of aquifer confinement

Confined aquifers are generally recognized for their heightened responsiveness to crustal strains, while unconfined aquifers are considered to be less susceptible to strain-induced changes. Leveraging this characteristic, the analysis of groundwater level data in terms of tidal response can serve as a means to distinguish aquifer confinement. The presence of tidal components in the water levels can exhibit inconsistencies that are constrained by the level of well confinement (Bredehoeft, 1967). The groundwater level includes five principal tidal constituents: M2, O1, S2, N2, and K1. These components, with periods close to 12 h and 24 h, account for 95% of the total tidal potential. By analyzing their individual energies, we can infer the degree of confinement of the aquifer (Hu et al., 2024).

We performed a spectral analysis of groundwater levels. To focus on the target frequencies, we excluded those below 0.5 cycles per day (cpd) and frequencies above 2.5 cpd, thereby eliminating the trend term of the water level data. The discrimination of confinement was based on the fact that aquifers with all tidal components and dominated by the M2 component indicate. a certain degree of confinement. In contrast, aquifers with minimal confinement did not contain O1, M2 and N2 (Rahi and Halihan, 2013).

Applying the aforementioned criterion for discrimination, we observed that well C-48 lacks any discernible component waves in its water level, indicating weak confinement characteristics. Similarly,

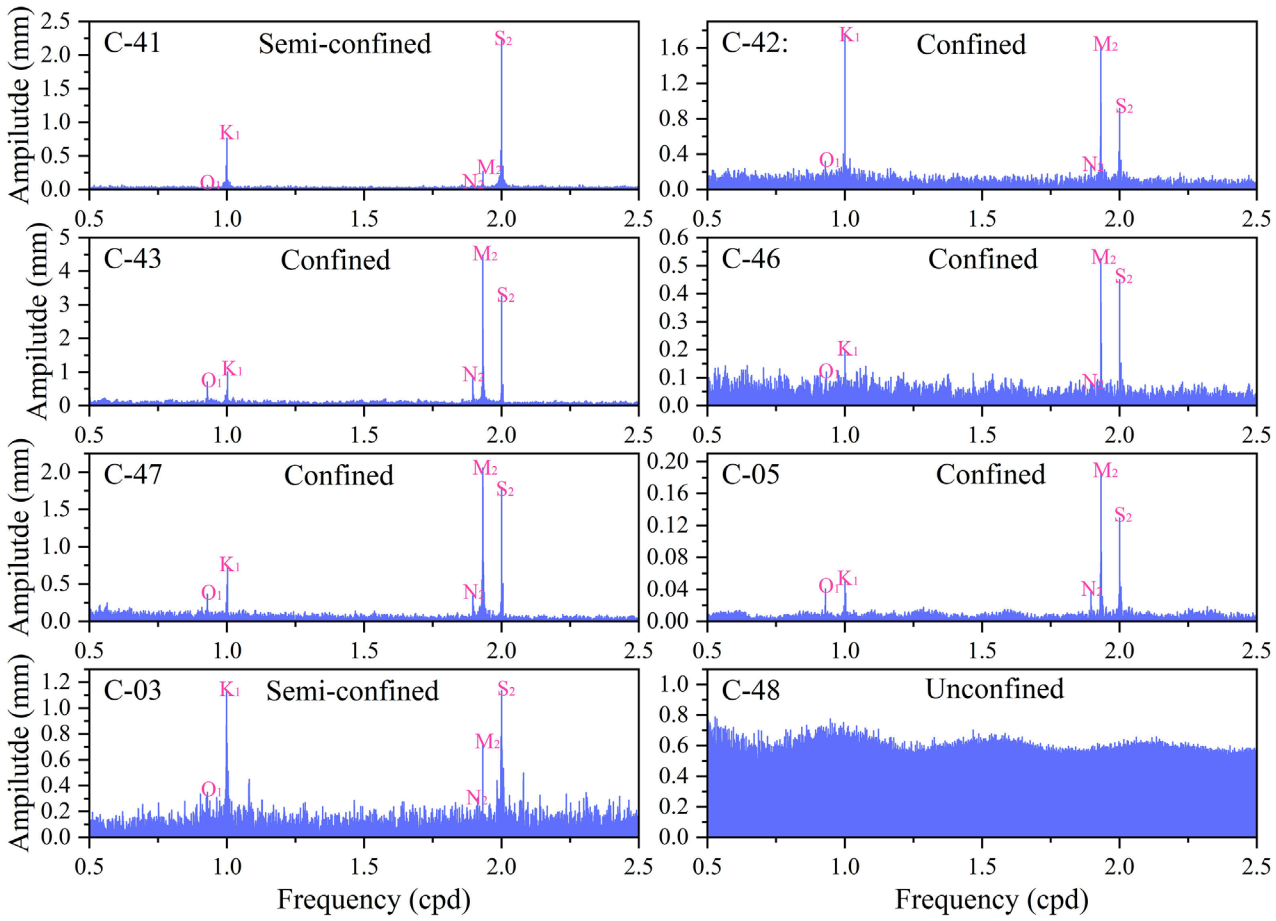

FIGURE 8
Fast Fourier spectral analysis of water level in 8 Wells. Five main tidal constituents are marked by red.

wells C-03 and C-41 exhibit signs of inadequate confinement, as they lack the prominent M2 wave. In contrast, the remaining five wells C-05, C-42, C-43, C-46, C-47 display the highest amplitude for the M2 wave and encompass the presence of other tidal components, which suggests a relatively robust system constraint and a certain degree of aquifer confinement (Figure 8).

The correlation analysis conducted between aquifer confinement and PRI reveals unexpected findings. Well C-48, characterized by very poor aquifer confinement, surprisingly exhibits a moderate PRI of 0.65. On the other hand, well C-05, which demonstrates a minimum PRI of 0.35, is deemed to possess good confinement. We also adopted a similar strategy to Hu et al. (2024) by dividing confined, semi-confined, and unconfined into 1, 0.5, and 0 to facilitate PRI comparisons, but still did not find a significant correlation. These results indicate that aquifer confinement may not be the dominant factor influencing changes of groundwater level before earthquakes. Instead, the relationship between confinement and PRI appears to exhibit a certain level of randomness on a smaller scale.

4.2.3 Influence of hydraulic parameters

To determine the hydraulic parameters, we first performed tidal analysis on the water level data using the Baytap08 software (Tamura et al., 1991). The software is now publicly available for download (https://igppweb.ucsd.edu/~agnew/Baytap/baytap.html). We only need to import the groundwater level series and time series to automatically calculate the relevant tidal parameters. The analysis used a 30-day window and a 15-day step size (Zhang et al., 2021; Zhang et al., 2024). To ensure accuracy, data with significant errors were excluded (Figure 9). The focus was on M2 wave component, which is less affected by baroclinic interference and exhibits a more pronounced amplitude.

Typically, the aquifer's water is assumed to undergo radial flow, resulting in an expected lag in the phase shift of the water level during tidal analysis. However, the wells selected for this study exhibited a phase ahead during their monitoring periods. This observation suggests that the water level dynamics are influenced not only by radial flow within the aquifer but also by other factors, such as aquifer leakage. In such cases, hydrodynamic exchange with neighboring aquifers in the vertical direction can induce a positive change in the phase shift (Hsieh et al., 1987; Wang et al., 2018). As an illustrative example, well C-46 exhibits a noticeable positive phase shift. This particular well comprises two aquifers characterized by sandstone as the predominant lithology, providing favorable conditions for aquifer leakage (Figure 2). This alignment with theoretical lends support to the observed phase shift. Similarly, well

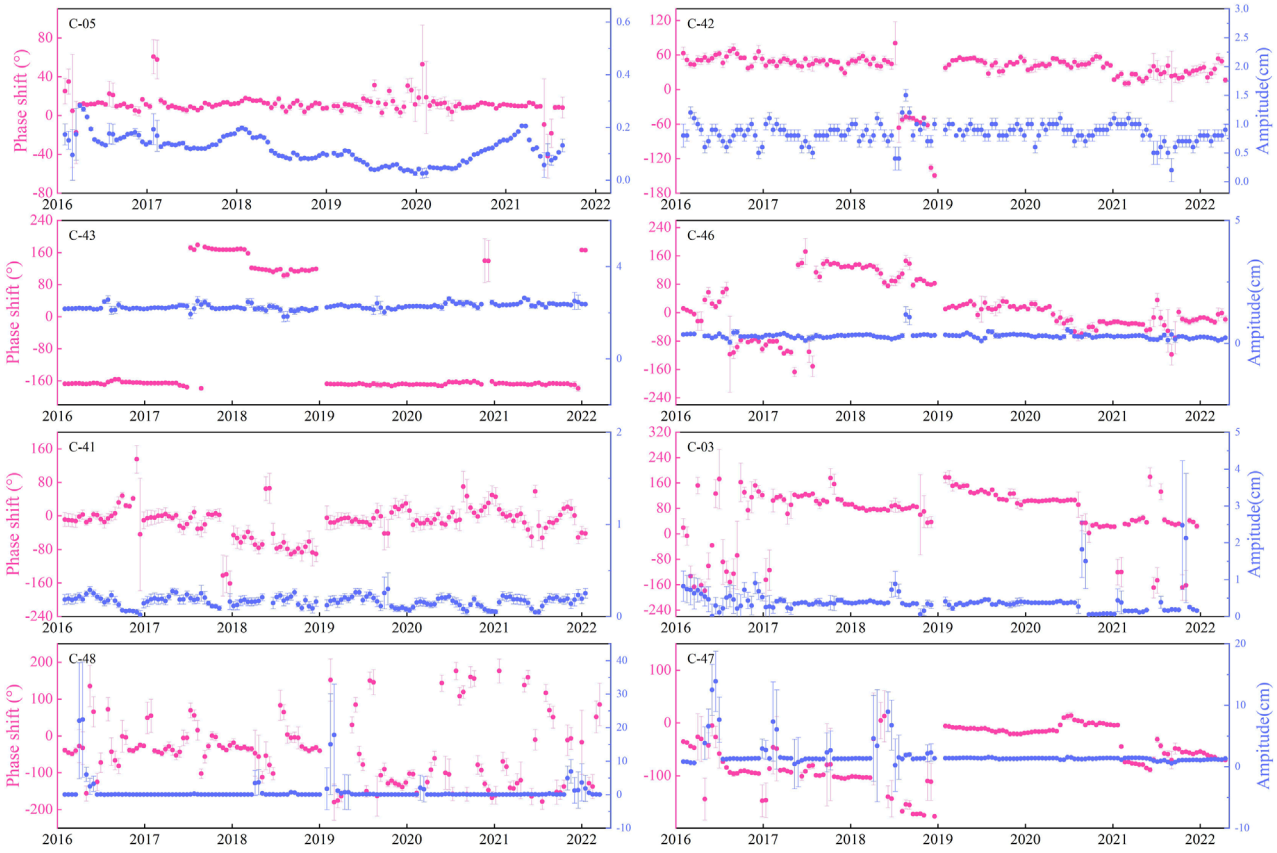

FIGURE 9
Phase shift and amplitude of M2 calculated using Baytap08 for water level in 8 wells.

C-05 contains a main aquifer with an overburden aquifer, allowing for geological conditions conducive to leakage, thus aligning with the observed phase shift behavior. By employing appropriate models, these configurations enable the calculation of specific leakage. The distinct variations in phase and amplitude of the water level among wells can be attributed to varying hydraulic parameters. Differences in hydraulic parameters may, in turn, further contribute to divergent levels of PRI.

In summary, there is a suitable condition to calculate the specific leakage using the leaky aquifer model. The phase shift and amplitude ratios obtained from the tidal analysis served as inputs for the model. By employing a 15-day time step, the specific leakages were calculated, providing a comprehensive set of coefficient values for each well throughout the study period. The calculations were visualized in Figure 10, with the long blue bars representing the magnitude of PRI. Bars offer a clear indication of the PRI across the analyzed time frame. A significant correlation is observed between a decrease in PRI and an increase in specific leakage (R^2 = *0.91*). Wells C-43 and C-47, characterized by higher PRI, exhibit relatively smoother specific leakage, converging towards zero. Conversely, the specific leakage values of well C-05 present a notable degree of deviation and dispersion, displaying a broad range of magnitudes. Meanwhile, wells C-42 and C-46 demonstrate a moderately transitional pattern in their specific leakage values, inversely related to their respective PRI. This observed pattern suggests that the specific leakage, as a contributing factor influencing the changes in water volume within the aquifer, plays a crucial role in modulating the sensitivity of the groundwater level to strain. Consequently, this variability in specific leakage contributes to fluctuations in the PRI. Furthermore, previous studies have highlighted the relationship between increased vertical permeability of aquifers and a subsequent rise in local groundwater level and flow rates (Rutter et al., 2016; Wang et al., 2016). The result further supports the notion that discrepancies in hydraulic parameter magnitudes within aquifers, particularly specific leakage, exert a substantial influence on the PRI of water levels in wells. Specific leakage variations may serve as key determinants in the overall PRI of water levels.

4.2.4 Influence of the epicenter location distribution

Extensive investigations have demonstrated distinct hydrological responses associated with various earthquake parameters, including magnitude, epicenter distance, and seismic energy density (Lai et al., 2016; Weaver et al., 2019). In this subsection, we focus on exploring whether the distribution of epicenter influences the observed disparities in water level PRI.

The Longmenshan-Anninghe fault zone lies between the Tibetan Plateau and the Sichuan Basin, with the 8 selected wells positioned at the intersection of these two geological features. The

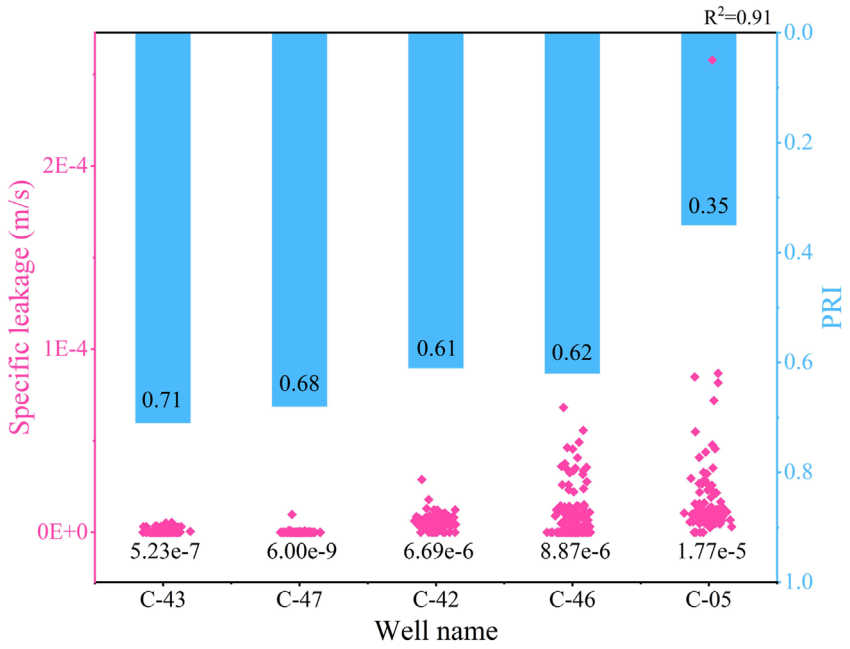

FIGURE 10
Comparison of well specific leakage and PRI. The long blue bar indicates PRI; the red scatter points denote all specific leakage for different wells at the study timeline, with the mean of specific leakage displayed below. R^2 = 0.91 refers to the correlation between specific leakage and PRI.

TABLE 4 Assessment of PRI across different epicenter distributions.

Well	PRI	
	Earthquakes occurring at the target faults	Earthquakes occurring at the other faults
C-42	0.61	0.47
C-41	0.62	0.58
C-43	0.68	0.57
C-46	0.64	0.58
C-47	0.66	0.57
C-48	0.65	0.54
C-03	0.45	0.56
C-05	0.56	0.4

seismic activity in this vicinity is influenced by the active ruptures occurring in the broader regional context. Thus, the assessment of water level PRI focuses on earthquakes listed in Table 1, categorized based on whether the epicenters align with the Longmenshan-Anninghe fault (as detailed in Table 4). Specifically, the analysis includes earthquakes numbered 2, 7, 8, 10, 11, 12, and 16, which are associated with the target rupture zone.

The application of the Molchan test reveals notable disparities in water level among the examined wells, highlighting superior PRI for earthquakes occurring along the target rupture zone. This observed phenomenon may be attributed to the influence of shear stress. Wells exhibiting favorable PRI are positioned between extensive fracture zones and lie within dominant propagation paths of the earthquakes (Brodsky et al., 2020; Freed, 2005). Consequently, wells are subjected to increased tectonic stresses, which may enhance their PRI. Moreover, laboratory studies on rock have shown that stress loading and unloading can significantly alter the permeability of fractured rocks (Ishibashi et al., 2018; Olsson and Barton, 2001). It is likely that the stress changes associated with seismic events interact with the geological structures, thereby affecting the permeability properties of the surrounding rocks. Consequently, variations in PRI can be attributed to the specific distribution patterns of earthquakes

TABLE 5 Sensitivity calculations of factors influencing PRI by RFR.

Aquifer confinement	Hydraulic parameters	Tidal effects	Co-seismic responses	Distribution of the earthquakes
0.450	0.853	0.716	0.690	1.028

and their corresponding impact on the hydrogeological properties around the wells.

4.3 Sensitivity analysis of multiple influencing factors

Hydraulic parameters and seismic distribution can significantly affect the PRI of water level, and the degree of water level response to stress can also reflect the PRI, while the confinement of the aquifer in wells may not have a significant effect on the PRI. In order to identify the relative influence of various factors on the PRI of water level, the sensitivity analysis of these four types of factors was conducted using the RFR. This method effectively integrates both quantitative and qualitative results, and is easy to be combined with the previous analysis. Here, weights in confinement to unconfinement are given as 1, 0.5 and 0, and other relevant factors need to be normalized as well. Then by inputting the series corresponding to each type of factor and PRI, RFR can automatically generate results.

Table 5 presents the weight proportions obtained from the RFR. Among the selected factors, distribution of the earthquakes stands out as the predominant control, exerting a substantial influence on the discrepancies observed in PRI. The hydraulic parameters also contribute to the variations in water level PRI, but with a weightage that is only slightly lower than the distribution of the earthquakes. In contrast, the degree of water level response to external stress (Tidal effects and Co-seismic responses) and the confinement conditions of the aquifer exhibits comparatively weaker impacts on PRI, as indicated by their lower weightages, indicating their relatively lesser significance in determining the PRI of water level.

In our selected cluster of wells, C-46, C-42, and C-48 exhibiting moderate PRI in comparison to the remaining wells. These three wells are situated at the intersection of the Longmenshan-Anninghe faults, thus are significantly affected by the distribution of earthquakes because seismic signals are more likely to propagate near the rupture zone, but our screening conditions for seismic events are not oriented. If earthquakes do not occur near the target faults, potential earthquake precursor information is just as easily lost.

Furthermore, differences between wells C-41, C-43, and C-47, characterized by high PRI, and wells C-05 and C-03, identified as having poor PRI, can largely be attributed to the differences in hydraulic parameters of the aquifer, since most of which are located far from faults intersections. The specific leakages differ by 2–3 orders of magnitude, as confirmed in the previous section.

The sensitivity of water level to external stresses (Tidal effects and Co-seismic responses) also offers some insights into PRI, although it is as a secondary criterion. In this regard, the contrasting performance of excellently responding well C-43 compared to wells C-05 and C-03 underscores the potential influence of stress sensitivity on PRI, and can be a useful reflection of the overall expected performance of the well. In our selected wells, the aquifer confinement on PRI shows some randomness, and it may show correlation on a larger scale, so our results conclude that confinement is not enough of a key cue for high or low PRI.

Furthermore, additional factors such as well depth, borehole radius, and the height of the water column within the well should be considered, as they may potentially contribute to variations in PRI. However, their impact on water level PRI is relatively minor. For instance, the slight differences in PRI between wells C-41 and C-43, which have having similar PRI, or among wells C-46, C-48, and C-42, where the difference in PRI varies only slightly within a range of 0.05, illustrate the limited impact of these factors. Although these factors can be relevant in certain scenarios, their overall contribution to altering water level PRI remains secondary in comparison to the dominant factors previously discussed. Hence, the factors affecting the disparities in PRI, ranked in descending order of sensitivity, encompass 1) distribution of the earthquakes in relation to well locations, 2) hydraulic parameters and 3) the sensitivity of water level to external stress responses.

5 Conclusion

We used the Molchan diagram method to quantitatively represent the characteristics of groundwater level changes before an earthquake using pre-response index (PRI). The closer the PRI is to 1, the higher the correlation between water level changes and subsequent events. Over the semi-annual alarm regions, it was observed that wells C-41, C-43, and C-47 exhibited high PRI, while wells C-03 and C-05 displayed low PRI. Meanwhile, the PRI of wells C-42, C-46, and C-48 were found to be of moderate magnitude. Correlation analysis and RFR methods identify the factors influencing the PRI: distribution of the earthquakes in relation to well locations, hydraulic parameters and the sensitivity of water level to external stress responses. In the well water levels studied, we suggest that differences in the distribution of the earthquakes in relation to well locations most favor the variation in PRI. Conversely, the confinement conditions of the aquifer were found to have an insignificant impact on PRI.

Our study data are mainly based on calculations of extensions over observed water levels, additional data used in the article for correlation and sensitivity analyses can be used to derive more precise values from field measurements or expeditions: e.g., hydraulic parameters, confinement, etc. This would be a better balance of accuracy and hopefully further contrast with our study.

Data availability statement

The original contributions presented in the study are included in the article/supplementary material, further inquiries can be directed to the corresponding author.

Author contributions

WZ: Conceptualization, Methodology, Software, Visualization, Writing–original draft. ML: Conceptualization, Funding acquisition, Supervision, Validation, Writing–review and editing. YY: Investigation, Resources, Supervision, Writing–review and editing. XR: Investigation, Resources, Writing–review and editing. ML: Data curation, Visualization, Writing–review and editing. SL: Methodology, Supervision, Writing–review and editing.

Funding

The author(s) declare that financial support was received for the research, authorship, and/or publication of this article. This research was funded by National Natural Science Foundation of China (grant number 42372282), Beijing Natural Science Foundation (grant number 8222003) and National Natural Science Foundation of China (grant number 41877205).

Conflict of interest

The authors declare that the research was conducted in the absence of any commercial or financial relationships that could be construed as a potential conflict of interest.

Generative AI statement

The author(s) declare that no Generative AI was used in the creation of this manuscript.

Publisher's note

All claims expressed in this article are solely those of the authors and do not necessarily represent those of their affiliated organizations, or those of the publisher, the editors and the reviewers. Any product that may be evaluated in this article, or claim that may be made by its manufacturer, is not guaranteed or endorsed by the publisher.

References

Bai, Y., Huayong, N., and Hua, G. (2019). Advances in research on the geohazard effect of active faults on the southeastern margin of the Tibetan Plateau. *J. Geomechanics* 25 (6), 1116–1128. doi:10.12090/j.issn.1006-6616.2019.25.06.095

Barberio, M. D., Gori, F., Barbieri, M., Billi, A., Caracausi, A., De Luca, G., et al. (2020). New observations in Central Italy of groundwater responses to the worldwide seismicity. *Sci. Rep.* 10 (1), 17850. doi:10.1038/s41598-020-74991-0

Borup, D., Christensen, B. J., Mühlbach, N. S., and Nielsen, M. S. (2023). Targeting predictors in random forest regression. *Int. J. Forecast.* 39 (2), 841–868. doi:10.1016/j.ijforecast.2022.02.010

Bredehoeft, J. D. (1967). Response of well-aquifer systems to Earth tides. *J. Geophys. Res.* 72 (12), 3075–3087. doi:10.1029/JZ072i012p03075

Breiman, L. (2001). Random forests. *Mach. Learn.* 45, 5–32. doi:10.1023/a:1010933404324

Brodsky, E. E., Mori, J. J., Anderson, L., Chester, F. M., Conin, M., Dunham, E. M., et al. (2020). The state of stress on the fault before, during, and after a major earthquake. *Annu. Rev. Earth Planet. Sci.* 48, 49–74. doi:10.1146/annurev-earth-053018-060507

Chen, C.-H., Tang, C.-C., Cheng, K.-C., Wang, C. H., Wen, S., Lin, C. H., et al. (2015). Groundwater–strain coupling before the 1999 Mw 7.6 Taiwan Chi-Chi earthquake. *J. Hydrology* 524, 378–384. doi:10.1016/j.jhydrol.2015.03.006

Cooper, H. H., Jr, Bredehoeft, J. D., Papadopulos, I. S., and Bennett, R. R. (1965). The response of well-aquifer systems to seismic waves. *J. Geophys. Res.* 70 (16), 3915–3926. doi:10.1029/JZ070i016p03915

Del Gaudio, E., Stevenazzi, S., Onorati, G., and Ducci, D. (2024). Changes in geochemical and isotopic contents in groundwater before seismic events in Ischia Island (Italy). *Chemosphere* 349, 140935. doi:10.1016/j.chemosphere.2023.140935

Freed, A. M. (2005). Earthquake triggering by static, dynamic, and postseismic stress transfer. *Annu. Rev. Earth Planet. Sci.* 33, 335–367. doi:10.1146/annurev.earth.33.092203.122505

Granin, N. G., Radziminovich, N. A., De Batist, M., Makarov, M. M., Chechelnitcky, V. V., Blinov, V. V., et al. (2018). Lake Baikal's response to remote earthquakes: lake-level fluctuations and near-bottom water layer temperature change. *Mar. Petroleum Geol.* 89, 604–614. doi:10.1016/j.marpetgeo.2017.10.024

Grinsted, A., Moore, J. C., and Jevrejeva, S. (2004). Application of the cross wavelet transform and wavelet coherence to geophysical time series. *Nonlinear Process. Geophys.* 11 (5/6), 561–566. doi:10.5194/npg-11-561-2004

Gu, H., Xu, Y., Lan, S., Yue, M., Wang, M., and Sauter, M. (2024). Spatial variation of aquifer permeability in the North China Plain from large magnitude earthquake signals. *Pure Appl. Geophys.* 181, 1845–1858. doi:10.1007/s00024-024-03511-2

Hattori, K., and Han, P. (2018). "Statistical analysis and assessment of ultralow frequency magnetic signals in Japan as potential earthquake precursors," in *Pre-earthquake processes: a multidisciplinary approach to earthquake prediction studies*, 229–240. doi:10.1002/9781119156949.ch13

He, H., and Ikeda, Y. (2007). Faulting on the anninghe fault zone, southwest China in late quaternary and its movement model. *Acta Seismol. Sin.* 29 (5), 571–583. doi:10.1007/s11589-007-0571-4

Hsieh, P. A., Bredehoeft, J. D., and Farr, J. M. (1987). Determination of aquifer transmissivity from Earth tide analysis. *Water Resour. Res.* 23 (10), 1824–1832. doi:10.1029/WR023i010p01824

Hu, C., Liao, X., Shi, Y., Liu, C., Yan, R., Lian, X., et al. (2024). Comprehensive quantitative determination of aquifer confinement based on tidal response of well water level and its application in North China. *Sci. Rep.* 14 (1), 9464. doi:10.1038/s41598-024-59909-4

Ishibashi, T., Elsworth, D., Fang, Y., Riviere, J., Madara, B., Asanuma, H., et al. (2018). Friction-stability-permeability evolution of a fracture in granite. *Water Resour. Res.* 54 (12), 9901–9918. doi:10.1029/2018WR022598

Kopylova, G., and Boldina, S. (2020). Hydrogeological earthquake precursors: a case study from the Kamchatka peninsula. *Front. Earth Sci.* 8, 576017. doi:10.3389/feart.2020.576017

Lai, G., Jiang, C., Han, L., Sheng, S., and Ma, Y. (2016). Co-seismic water level changes in response to multiple large earthquakes at the LGH well in Sichuan, China. *Tectonophysics* 679, 211–217. doi:10.1016/j.tecto.2016.04.047

Lai, G., Jiang, C., Wang, W., Han, L., and Deng, S. (2021). Correlation between the water temperature and water level data at the Lijiang well in Yunnan, China, and its implication for local earthquake prediction. *Eur. Phys. J. Special Top.* 230 (1), 275–285. doi:10.1140/epjst/e2020-000255-3

Molchan, G. (1990). Strategies in strong earthquake prediction. *Phys. Earth Planet. Interiors* 61 (1-2), 84–98. doi:10.1016/0031-9201(90)90097-H

Olsson, R., and Barton, N. (2001). An improved model for hydromechanical coupling during shearing of rock joints. *Int. J. rock Mech. Min. Sci.* 38 (3), 317–329. doi:10.1016/S1365-1609(00)00079-4

Pulinets, S., Ouzounov, D., Karelin, A., and Davidenko, D. (2018). "Lithosphere-atmosphere-ionosphere-magnetosphere coupling-A concept for pre-earthquake signals generation," in *Pre-earthquake processes: a multidisciplinary approach to earthquake prediction studies*. Editors D. Ouzounov, S. Pulinets, K. Hattori, and P. Taylor, 234, 79–98.

Rahi, K. A., and Halihan, T. (2013). Identifying aquifer type in fractured rock aquifers using harmonic analysis. *Ground Water* 51 (1), 76–82. doi:10.1111/j.1745-6584.2012.00925.x

Rigatti, S. J. (2017). Random forest. *J. Insur. Med.* 47 (1), 31–39. doi:10.17849/insm-47-01-31-39.1

Roeloffs, E., Quilty, E., and Scholtz, C. H. (1997). Case 21: water level and strain changes preceding and following the August 4, 1985 Kettleman Hills, California, earthquake. *Pure Appl. Geophys.* 149 (1), 21–60. doi:10.1007/bf00945160

Rutter, H., Cox, S., Dudley Ward, N., and Weir, J. J. (2016). Aquifer permeability change caused by a near-field earthquake, C anterbury, N ew Z ealand. *Water Resour. Res.* 52 (11), 8861–8878. doi:10.1002/2015WR018524

Shi, Z., and Wang, G. (2014). Hydrological response to multiple large distant earthquakes in the Mile well, China. *J. Geophys. Res. Earth Surf.* 119 (11), 2448–2459. doi:10.1002/2014jf003184

Shi, Z., and Wang, G. (2015). Sustained groundwater level changes and permeability variation in a fault zone following the 12 May 2008, Mw 7.9 Wenchuan earthquake. *Hydrol. Process.* 29 (12), 2659–2667. doi:10.1002/hyp.10387

Shi, Z., Wang, G., and Liu, C. (2013). Co-seismic groundwater level changes induced by the May 12, 2008 Wenchuan earthquake in the near field. *Pure Appl. Geophys.* 170, 1773–1783. doi:10.1007/s00024-012-0606-1

Song, C., Chen, X., and Xia, W. (2023). Improving the understanding of the influencing factors on sea level based on wavelet coherence and partial wavelet coherence. *J. Oceanol. Limnol.* 41 (5), 1643–1659. doi:10.1007/s00343-022-2102-5

Sun, X., Xiang, Y., Shi, Z., and Wang, B. (2017). Preseismic changes of water temperature in the yushu well, western China. *Pure Appl. Geophys.* 175 (7), 2445–2458. doi:10.1007/s00024-017-1579-x

Sun, X.-L., Wang, G.-C., and Yan, R. (2016). Extracting high-frequency anomaly information from fluid observational data: a case study of the Wenchuan Ms8.0 earthquake of 2008. *Chin. J. Geophys.* 59 (5). doi:10.6038/cjg20160512

Tamura, Y., Sato, T., Ooe, M., and Ishiguro, M. (1991). A procedure for tidal analysis with a Bayesian information criterion. *Geophys. J. Int.* 104 (3), 507–516. doi:10.1111/j.1365-246x.1991.tb05697.x

Wang, C. y., and Chia, Y. (2008). Mechanism of water level changes during earthquakes: near field versus intermediate field. *Geophys. Res. Lett.* 35 (12). doi:10.1029/2008gl034227

Wang, C. Y., Doan, M. L., Xue, L., and Barbour, A. J. (2018). Tidal response of groundwater in a leaky aquifer—application to Oklahoma. *Water Resour. Res.* 54 (10), 8019–8033. doi:10.1029/2018wr022793

Wang, C. Y., Liao, X., Wang, L. P., and Manga, M. (2016). Large earthquakes create vertical permeability by breaching aquitards. *Water Resour. Res.* 52 (8), 5923–5937. doi:10.1002/2016WR018893

Wang, C.-Y., and Manga, M. (2021). *Water and earthquakes*. Springer Nature.

Wang, K., Chen, Q.-F., Sun, S., and Wang, A. (2006). Predicting the 1975 Haicheng earthquake. *Bull. Seismol. Soc. Am.* 96 (3), 757–795. doi:10.1785/0120050191

Weaver, K., Doan, M. L., Cox, S., Townend, J., and Holden, C. (2019). Tidal behavior and water-level changes in gravel aquifers in response to multiple earthquakes: a case study from New Zealand. *Water Resour. Res.* 55 (2), 1263–1278. doi:10.1029/2018wr022784

Yan, R., Tian, L., Wang, G., Zhong, J., Liu, J., and Zhou, Z. (2018). Review and statistically characteristic analysis of underground fluid anomalies prior to the 2008 Wenchuan Ms8.0 earthquake. *Chin. J. Geophys.* 61 (5), 1907–1921. doi:10.6038/cjg2018M0162

Yan, R., Wang, G., and Shi, Z. (2016). Sensitivity of hydraulic properties to dynamic strain within a fault damage zone. *J. Hydrology* 543, 721–728. doi:10.1016/j.jhydrol.2016.10.043

Yang, G., and McCoy, K. (2023). Modeling groundwater-level responses to multiple stresses using transfer-function models and wavelet analysis in a coastal aquifer system. *J. Hydrology* 627, 130426. doi:10.1016/j.jhydrol.2023.130426

Yi, G., Xueze, W., Jun, F., and Wang, S. w. (2004). Assessing current faulting behaviors and seismic risk of the Anninghe-Zemuhe fault zone from seismicity parameters. *Acta Seismol. Sin.* 17, 322–333. doi:10.1007/s11589-004-0054-9

Zechar, J. D., and Jordan, T. H. (2008). Testing alarm-based earthquake predictions. *Geophys. J. Int.* 172 (2), 715–724. doi:10.1111/j.1365-246X.2007.03676.x

Zhang, H., Shi, Z., Wang, G., Yan, X., Liu, C., Sun, X., et al. (2021). Different sensitivities of earthquake-induced water level and hydrogeological property variations in two aquifer systems. *Water Resour. Res.* 57 (5), e2020WR028217. doi:10.1029/2020WR028217

Zhang, P.-Z. (2008). The tectonic deformation,strain distribution and deep dynamic processes in the eastern margin of the Tibetan Plateau. *Sci. China Ser. D-Earth Sci. Chin.* 38 (9), 1041–1056. doi:10.3321/j.issn:1006-9267.2008.09.001

Zhang, P.-Z., Xu, X.-W., Wen, X.-Z., and Ran, Y.-K. (2008). Slip rates and recurrence intervals of the Longmen Shan active fault zone and tectonic implications for the mechanism of the May 12 Wenchuan earthquake, 2008, Sichuan, China. *Chin. J. Geophys.* 51 (4), 1066–1073 doi:10.3321/j.issn:0001-5733.2008.04.015

Zhang, S., Shi, Z., Wang, G., Zhang, Z., and Guo, H. (2023). The origin of hydrological responses following earthquakes in a confined aquifer: insight from water level, flow rate, and temperature observations. *Hydrology Earth Syst. Sci.* 27 (2), 401–415. doi:10.5194/hess-27-401-2023

Zhang, Y., Manga, M., Fu, L. Y., Zhang, H., Huang, T., Yang, Q., et al. (2024). Long-and short-term effects of seismic waves and coseismic pressure changes on fractured aquifers. *J. Geophys. Res. Solid Earth* 129 (3), e2023JB027970. doi:10.1029/2023jb027970

frontiers | Frontiers in Earth Science

TYPE Original Research
PUBLISHED 09 April 2025
DOI 10.3389/feart.2025.1553967

OPEN ACCESS

EDITED BY
Nicola Alessandro Pino,
University of Camerino, Italy

REVIEWED BY
Ameha Atnafu Muluneh,
University of Bremen, Germany
Hom Nath Gharti,
Queen's University, Canada
Leah Langer,
Tel Aviv University, Israel

*CORRESPONDENCE
Caibo Hu,
hucb@ucas.ac.cn
Huai Zhang,
hzhang@ucas.ac.cn

RECEIVED 31 December 2024
ACCEPTED 28 March 2025
PUBLISHED 09 April 2025

CITATION
Chen Y, Hu C, Shi M and Zhang H (2025) InSAR-constrained parallel elastic finite element models for fault coseismic dislocation inversion: a case study of the 2016 M_W 5.9 Menyuan earthquake.
Front. Earth Sci. 13:1553967.
doi: 10.3389/feart.2025.1553967

InSAR-constrained parallel elastic finite element models for fault coseismic dislocation inversion: a case study of the 2016 M_W 5.9 Menyuan earthquake

Yuhang Chen [1], Caibo Hu[1]*, Mingqian Shi[1] and Huai Zhang[1,2]*

[1]National Key Laboratory of Earth System Numerical Modeling and Application, College of Earth and Planetary Sciences, University of Chinese Academy of Sciences, Beijing, China, [2]Beijing Yanshan Earth Critical Zone National Research Station, University of Chinese Academy of Sciences, Beijing, China

The study of fault coseismic dislocation distribution is crucial for understanding fault stress release, fault sliding behavior, and surface deformation during seismic events. This knowledge is essential for engineering design and disaster prevention. Traditional seismic dislocation theories, which assume a uniform elastic semi-infinite space, fail to account for topographic relief, medium inhomogeneity in the seismic source area. In contrast, parallel elastic finite element models effectively address these complexities by accommodating geometric, material, and boundary condition variations, offering high spatial resolution and efficient computation. In this paper, we introduce a novel fault coseismic dislocation inversion method based on parallel elastic finite element simulations. We conduct inversion tests using several idealized fault models to validate our approach. Applying this method to the 2016 M_W 5.9 Menyuan earthquake, we successfully invert the coseismic dislocation distributions. Our results align with previous studies and show excellent agreement with InSAR coseismic observations, thereby confirming the method's validity. Ideal model tests demonstrate that a 10% Young's modulus contrast across fault interfaces significantly affects coseismic dislocation inversion. Topographic relief exhibits limited influence on the coseismic dislocation inversion of the 2016 Menyuan M_W 5.9 earthquake. The distinct mechanical responses of material heterogeneity and topographic effects require separate quantification, confirming our method's viability for coseismic dislocation inversion in actual large earthquakes.

KEYWORDS

fault coseismic dislocation inversion, parallel elastic finite element model, the 2016 MW 5.9 Menyuan earthquake, checkerboard test, damped least square method

1 Introduction

The inversion of coseismic dislocation in seismic faults is a key area of interest in earthquake science, playing a critical role in understanding the rupture process, surface deformation during earthquakes, and the characterization of seismic source parameters.

This knowledge is essential for effective earthquake prevention and disaster mitigation. Accurately capturing the inhomogeneity and geometric complexity of the Earth's medium is crucial for realistic modeling of seismogenic faults. Therefore, there is a need to develop a numerical simulation-based method for coseismic dislocation inversion that reflects these complexities.

Medium inhomogeneity and geometrical complexity exert distinct influences on both numerical Green's function computation and coseismic fault dislocation inversion processes. Some studies employing finite-element codes to generate Green's functions have demonstrated that topography has a relatively small effect, reducing seismic potency by approximately 5% compared with a flat model for a shallow slow slip events offshore of the North Island of New Zealand (Williams and Wallace, 2018). But the impact of topography could be highly significant for steep slopes, particularly in regions with significant topographic relief (>500 m) (Moreno et al., 2012; Ragon and Simons, 2021). The incorporation of material heterogeneity derived from a New Zealand-wide seismic velocity model reveals substantial amplification effects, with seismic potency enhancements exceeding 58% (Williams and Wallace, 2018). The effects of 3D crustal heterogeneity (Masterlark, 2003; Ragon and Simons, 2021), basin media heterogeneity, and structural tectonics (Langer et al., 2023) on coseismic dislocation inversion are very different and unique, which indicates that independent and individualized case studies are required and cannot be generalized. Additionally, investigations employing 3D spherical finite element models to invert the coseismic slip distribution of the 2010 M_W 8.8 Maule earthquake along the Nazca-South America plate boundary revealed non-negligible Earth curvature effects when rupture lengths approach 500 km (Moreno et al., 2012). A representative study is the coseismic dislocation inversion of the 2015 Gorkha, Nepal earthquake, which simultaneously accounted for the influences of topography and material heterogeneity (Wang and Fialko, 2018; Langer et al., 2019). Some scholars employed the Gamra finite-difference framework (Landry and Barbot, 2016) to construct elastostatic Green's functions linking subsurface deformation to surface displacements, utilizing adaptive meshing and Immersed Interface Method adaptations (Leveque and Li, 1994) to resolve fault-slip singularities, constraining the Sierra Madre-Puente Hills-Compton thrust system's long-term slip rate (3–4 mm/yr) and current partial locking in upper sections consistent with interseismic strain accumulation (Rollins et al., 2018).

A high-resolution 3D finite element model (FEM) constrained by coseismic GNSS, Sentinel-1 DInSAR, and pixel offset data is implemented for sequential fault slip inversion of the 2019 Ridgecrest earthquake sequence complex fault surface ruptures. The optimal solution is derived through heterogeneous FEM modeling and fused geodetic datasets combining pixel offsets, interferograms, and GNSS measurements (Barba-Sevilla et al., 2022). Some scholars employed idealized (M1A-M1D) and regional (GEONET, M2A-M2H) kinematic finite-source models to quantify grid-size effects on slip distributions and resolves the 2011 M_W 9.0 Tohoku-oki slip distribution through Bayesian-optimized finite-element modeling integrating terrestrial and seafloor geodetic data, demonstrating enhanced capacity to reconcile near-trench slip deficits while addressing grid-dependent resolution limits in coseismic inversions (Kim et al., 2024). The 2008 M_W 7.9 Wenchuan earthquake source is inverted through integration of strong-motion waveforms, geodetic offsets, and 3D synthetic ground motions. A multi-time-window approach is implemented with static/dynamic Green's functions derived from finite-element modeling, incorporating reciprocity principles and strain tensor formulations. The rupture process is systematically constrained by combined utilization of complex fault geometry, GPS/strong-motion datasets, and 3D heterogeneous structure (Ramirez-Guzman and Hartzell, 2020).

Coseismic dislocation inversion is a powerful technique for accurately mapping fault dislocation distributions during earthquakes, thus elucidating fault rupture mechanisms and sliding processes. For instance, the inversion of slip distribution for the 2011 M_W 9.0 Tohoku earthquake, using GPS and InSAR data, highlighted the extensive rupture area and provided crucial insights into tsunami generation (Ozawa et al., 2011). Similarly, GPS and InSAR data have been used to invert the coseismic fault dislocations and associated surface deformation for the 2008 M_W 7.9 Wenchuan earthquake and the 2015 M_W 7.8 Gorkha earthquake (Wan et al., 2017; Duan et al., 2020; Hong and Liu, 2021; Shi et al., 2023). These studies are of significant theoretical importance for understanding earthquake rupture propagation and source mechanisms, including strike-slip, thrust, and normal faulting.

Coseismic dislocation inversion is instrumental in studying the triggering effects of earthquakes. Large earthquakes can trigger seismic events on adjacent faults through the mechanism of coseismic stress transfer. By analyzing coseismic slip and its impact on nearby faults, we can gain deeper insights into the mechanisms behind earthquake swarms and the formation of earthquake sequences (King et al., 1994; Stein, 1999; Freed, 2005).

Currently, the inversion of coseismic dislocations for seismogenic faults predominantly relies on the Okada analytical model of elastic uniform semi-infinite space (Okada, 1992; Niu et al., 2016; Li and Barnhart, 2020). This model is favored for its simplicity and the high accuracy and efficiency of its Green's function calculations. However, a limitation of this approach is its inability to account for medium heterogeneity, particularly lateral inhomogeneities on either side of the fault, and the complex geometry of surface undulations. These constraints systematically bias both forward models and inverse solutions, particularly in regions with significant topographic relief (>500 m) or strong material heterogeneity (Masterlark, 2003; Moreno et al., 2012; Williams and Wallace, 2018; Ragon and Simons, 2021).

The Green's function for coseismic dislocation inversion of seismic faults can be determined using the analytical solution from Okada's seismic dislocation theory or through numerical methods like finite elements. Observation data typically include coseismic GPS, InSAR, or a combination of both. Based on these inputs, the inversion process commonly employs the least squares method with smooth constraints (Niu et al., 2016; Zuo et al., 2016; Duan et al., 2020).

Some researchers have developed a coseismic dislocation inversion method for originating faults utilizing both far-field seismic and near-field strong-motion waveform data (Zhang et al., 2012; Zhang et al., 2014; Tilmann et al., 2016). Fault dislocation inversion methods comprise several approaches, including the steepest descent method, synoptic dislocation inversion using triangular mesh faults, techniques for updating mesh configurations,

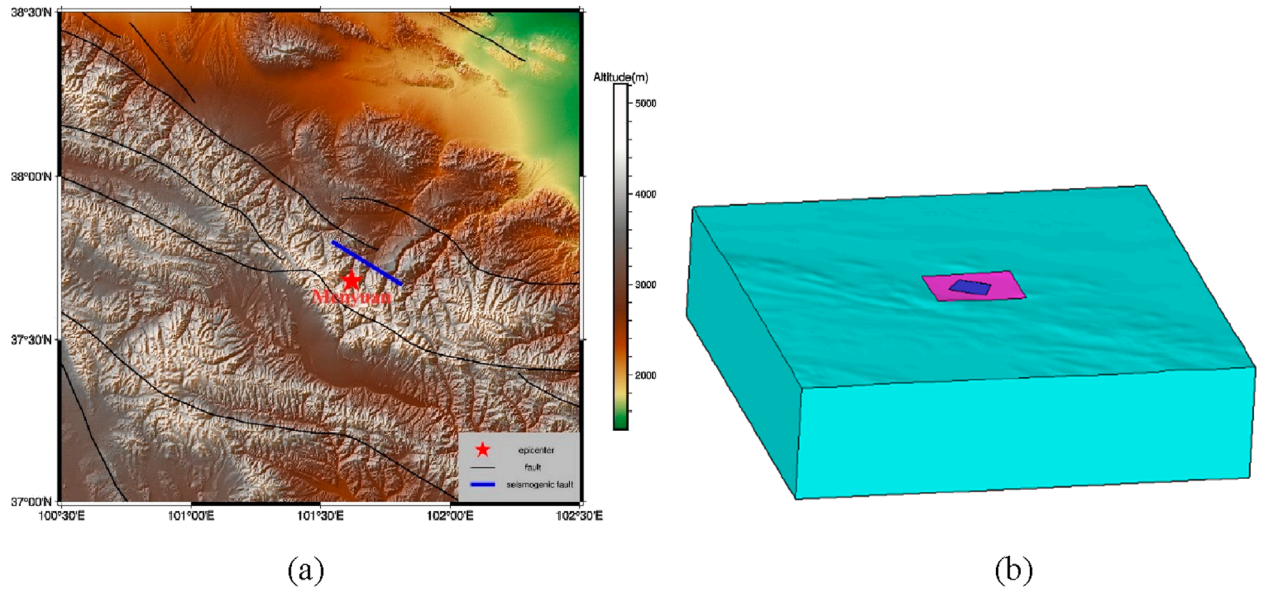

FIGURE 1
Tectonic setting and 3D topography-incorporated finite element model of the 2016 M_W 5.9 Menyuan earthquake. **(a)** Tectonic setting (modified from Luo and Wang, 2022); **(b)** 3D topography-incorporated finite element model.

and methods employing Bayesian probabilistic models to invert fault geometric parameters.

The Earth's medium exhibits significant inhomogeneities, particularly lateral ones, with considerable differences in material parameters on either side of an earthquake-generating fault. For instance, the 2008 Wenchuan earthquake along the Longmenshan Fault demonstrated significant lateral variations, with topographic relief differences exceeding 4,000 m (Shi et al., 2023). Okada's ideal model does not account for such lateral inhomogeneities and topographic variations, as well as the undulations of major structural surfaces within the Earth's interior. Consequently, the use of numerical simulations for coseismic dislocation inversion of seismogenic faults has become a prominent research focus in earthquake science. This paper introduces a novel method for coseismic dislocation inversion based on finite element numerical simulation. We validate the accuracy of this new inversion method using an ideal model and apply it to analyze the fault coseismic dislocation distribution of the 2016 Menyuan M_W 5.9 earthquake (Figure 1).

2 Methods for fault coseismic dislocation inversion using parallel elastic finite element simulation

2.1 Fundamental equations for fault coseismic dislocation inversion

In this paper, we employ a fault coseismic dislocation inversion method using parallel elastic finite element simulation. The fault is divided into k sub-faults, with the inversion parameters represented as **m**. For the *i*th sub-fault (i = 1, k), the dislocation components along the strike and dip are denoted as m_{is} and m_{id}, respectively. Here, the subscript i refers to the *i*th sub-fault, while s and d indicate the strike and dip components. The ground surface coseismic displacements are measured at n observation points, represented as **d**. At the *j*th observation point, the observed surface displacement components are d_{jx}, d_{jy} and d_{jz}, where j stands for the *j*th observation point (j = 1, n), and x, y, z represent the eastward, northward, and upward directions, respectively. The Green's function for inversion is denoted as **G**. For a unit dislocation of the *i*th sub-fault at the *j*th observation point, the Green's function components are $g_{jx.is}$, $g_{jy.is}$, $g_{jz.is}$, $g_{jx.id}$, $g_{jy.id}$ and $g_{jz.id}$. The indices i, j, x, y, z, d, and s have the same definitions as before.

In coseismic fault dislocation inversion, the relationship between the coseismic surface displacement data **d** and slip parameters **m** is mathematically formulated as (Tikhonov, 1963; Tilmann et al., 2016; Li and Barnhart, 2020):

$$\mathbf{d} = \mathbf{G}\mathbf{m} + \boldsymbol{\varepsilon} \tag{1}$$

where **d** denotes InSAR-derived Line-of-Sight (LOS) deformation measurements or three-component GPS displacement vectors, **G** represents the Green's function coefficient matrix, **m** corresponds to the slip parameters of sub-faults (Strike-slip component, Dip-slip component), and **ε** encapsulates observational uncertainties. The specific expressions for **d**, **m**, **G** are given in Equations 2–4.

$$\boldsymbol{d}_{(3n*1)} = \begin{bmatrix} d_{1x} \\ d_{1y} \\ d_{1z} \\ \cdots \\ d_{nx} \\ d_{ny} \\ d_{nz} \end{bmatrix} \tag{2}$$

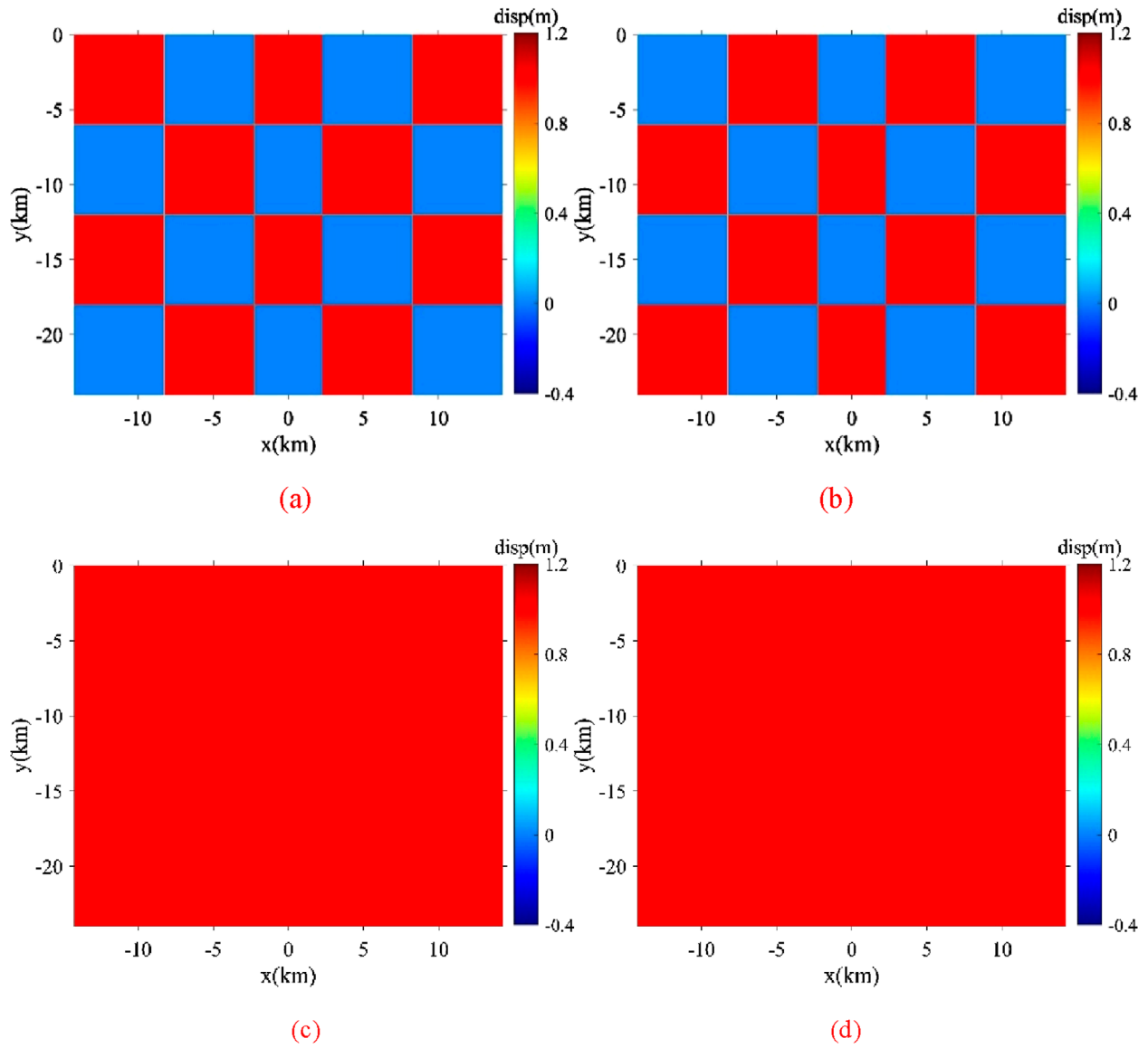

FIGURE 2
Ideal fault coseismic dislocation models: **(a, b)** show the dislocation distribution along the strike and dip for the model of intersecting distributed dislocations; **(c, d)** depict the distribution along the strike and dip for the homogeneous model.

$$\boldsymbol{m}_{(2k*1)} = \begin{bmatrix} m_{1s} \\ m_{1d} \\ \cdots \\ m_{ks} \\ m_{kd} \end{bmatrix} \tag{3}$$

where s and d represent the strike and dip components of dislocation, respectively, and x, y, z indicate the components of surface displacement in the eastward, northward, and upward directions.

The Green's function matrix **G** is:

$$\boldsymbol{G}(3n * 2k) = \begin{bmatrix} g_{1x.1s} & \cdots & g_{1x.ks} & g_{1x.1d} & \cdots & g_{1x.kd} \\ g_{1y.1s} & \cdots & g_{1y.ks} & g_{1y.1d} & \cdots & g_{1y.kd} \\ g_{1z.1s} & \cdots & g_{1z.ks} & g_{1z.1d} & \cdots & g_{1z.kd} \\ \cdots & \cdots & \cdots & \cdots & \cdots & \cdots \\ g_{nx.1s} & \cdots & g_{nx.ks} & g_{nx.1d} & \cdots & g_{nx.kd} \\ g_{ny.1s} & \cdots & g_{ny.ks} & g_{ny.1d} & \cdots & g_{ny.kd} \\ g_{nz.1s} & \cdots & g_{nz.ks} & g_{nz.1d} & \cdots & g_{nz.kd} \end{bmatrix} \tag{4}$$

where subscripts x, y, z, d, and s are the same as above.

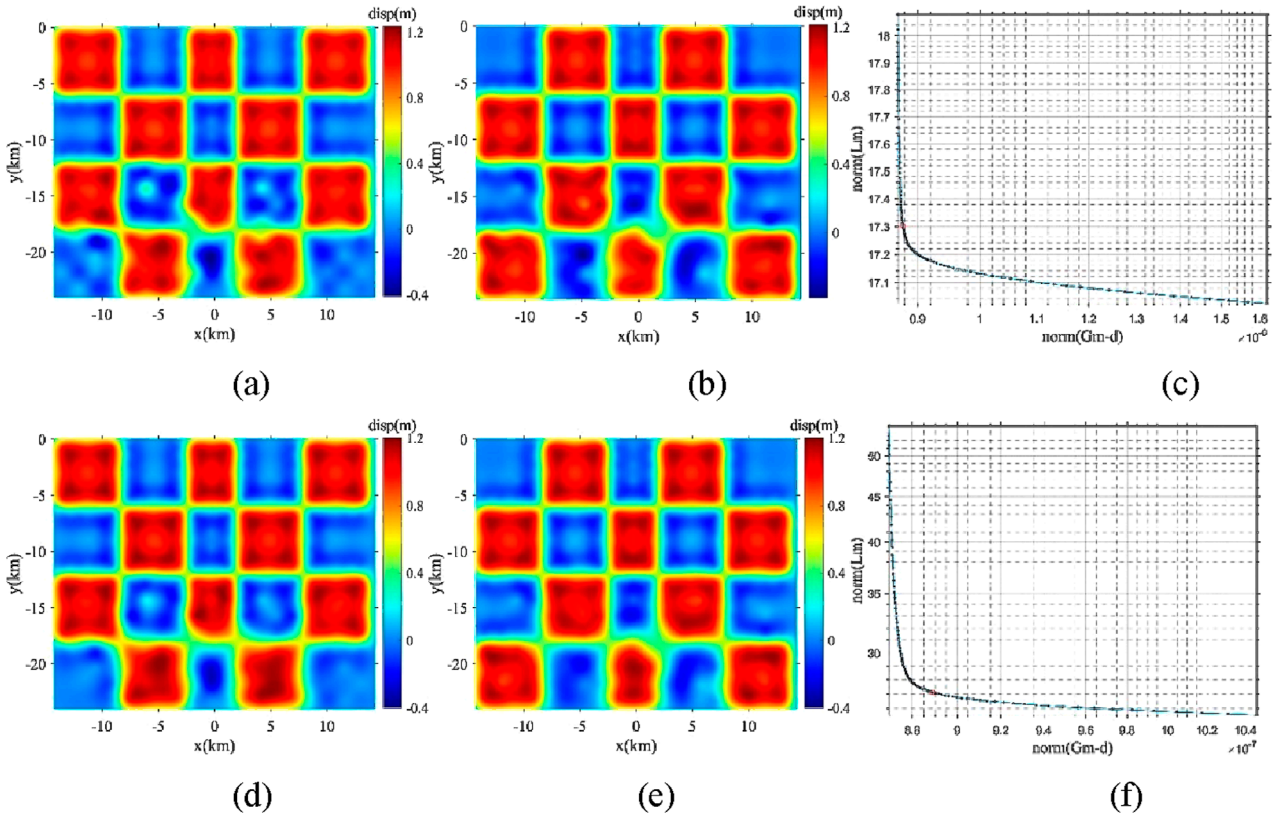

FIGURE 3
Inversion results for the model of intersecting distributed dislocations using a diagonal L-matrix and the 2D Laplace smooth matrix as the L-matrix. **(a–c)** for diagonal L-matrix: inversed coseismic dislocation along strike direction, inversed coseismic dislocation along dip direction and L-Curve, respectively. **(d–f)** for 2D Laplace smooth matrix as the L-matrix.

In practical inversion applications, it is generally required that the degrees of freedom of observation, 3n, exceed those of the inversion parameters, 2 k. This condition is met when the number of observations exceeds the number of inversion parameters, allowing **m** to be calculated using the least squares method:

$$\boldsymbol{m} = \left(\boldsymbol{G}^{\mathrm{T}}\boldsymbol{G}\right)^{-1}\boldsymbol{G}^{\mathrm{T}}\boldsymbol{d} \tag{5}$$

2.2 Calculation of the green's function G

We developed a parallel elastic finite element program to compute coseismic displacements and stresses, considering factors such as topographic relief, medium inhomogeneity, and non-uniform dislocation distributionusingthe split-node technique (Melosh and Raefsky, 1981; Shi et al., 2023). This program allows us to calculate the numerical displacement Green's function for any subfault dislocation at surface observation points, using parameters like fault dislocation, length, width, dip, strike angle, and slip angle. A key feature of this paper is the use of a 3D parallel finite element model to calculate these functions, fully accounting for the effects of topographic relief, medium inhomogeneity, complex fault geometry, and dislocation distribution. This approach enhances the realism of fault dislocation inversion results.

2.3 Regularization method for fault coseismic dislocation inversion

The fault coseismic dislocation distributions obtained by direct inversion using the least squares method Equation 5 are often pathologized by Equation 1 because of the overly strong linear correlation of some rows of the Green's function G matrix. In order to reduce the effect of this pathology, a Tikhonov regularization term is often added to the inversion (Tikhonov, 1963):

$$\begin{bmatrix} \boldsymbol{G} \\ \alpha\boldsymbol{L} \end{bmatrix}\boldsymbol{m} = \begin{bmatrix} \boldsymbol{d} \\ \boldsymbol{0} \end{bmatrix} \tag{6}$$

where α represents the regularization parameter, and **L** is the regularization matrix, which can be selected based on specific requirements. When L is the simplest form, a diagonal matrix **I**, the least squares solution for **m** is calculated as follows:

$$\boldsymbol{m} = \left(\boldsymbol{G}^{\mathrm{T}}\boldsymbol{G} + \alpha^2\mathrm{I}\right)^{-1}\boldsymbol{G}^{\mathrm{T}}\boldsymbol{d} \tag{7}$$

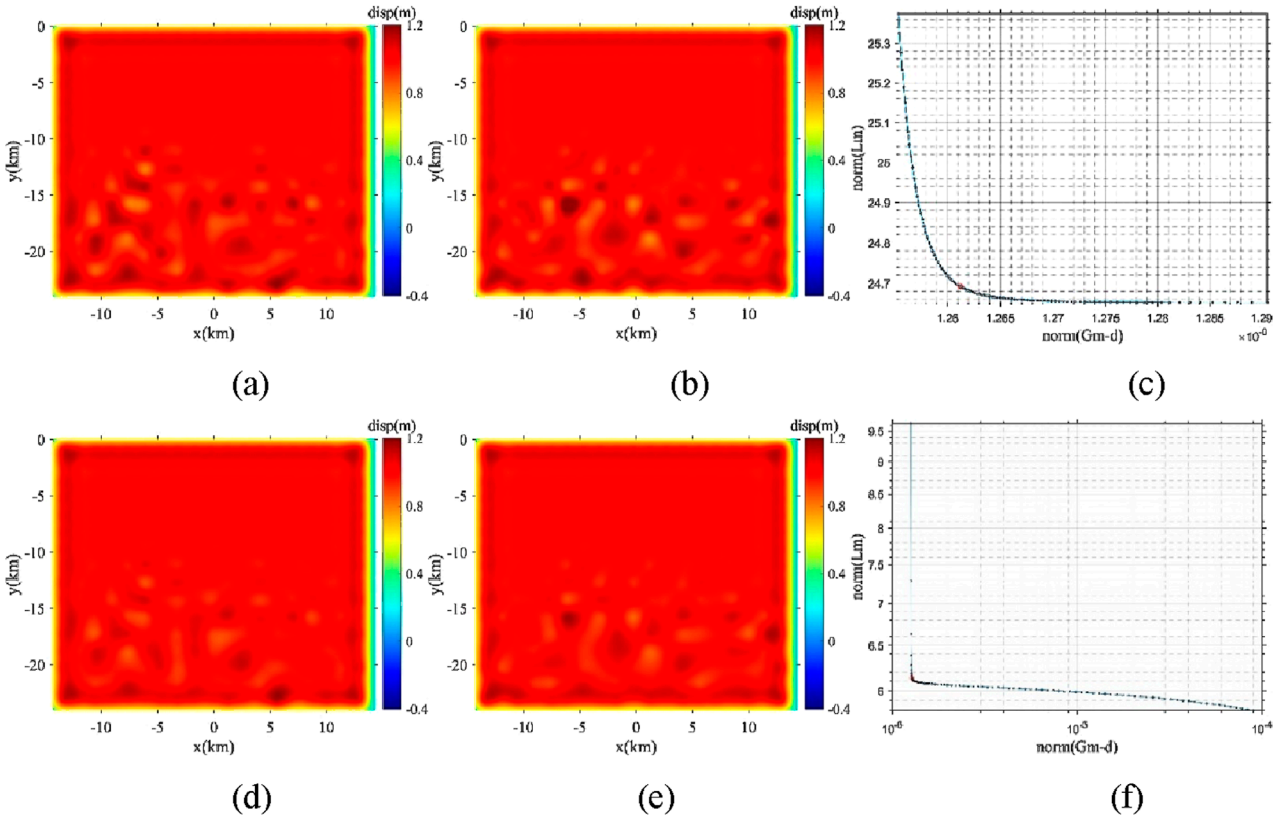

FIGURE 4
Inversion results for the model of uniformly distributed dislocations using a diagonal L-matrix and the 2D Laplace smooth matrix as the L-matrix. **(a–c)** for diagonal L-matrix: inversed coseismic dislocation along strike direction, inversed coseismic dislocation along dip direction and L-Curve, respectively. **(d–f)** for 2D Laplace smooth matrix as the L-matrix.

If the Laplace operator $L = \nabla^2$ is used, the least squares solution for m is calculated as follows:

$$\boldsymbol{m} = \left(\boldsymbol{G}^{\mathrm{T}}\boldsymbol{G} + \alpha^2 \boldsymbol{L}^{\mathrm{T}}\boldsymbol{L}\right)^{-1}\boldsymbol{G}^{\mathrm{T}}\boldsymbol{d} \tag{8}$$

2.4 Determination of regularization parameters

For general linear least-squares problems, there may be infinitely many least-squares solutions. Considering that data contain noise and precisely fitting such noise is meaningless, the Tikhonov regularization linear inversion method is a mathematical technique that stabilizes the inversion process by introducing smoothness constraints. The core principle of this method lies in pursuing the match between model parameters and observed data while enforcing gradual variation of parameter values between adjacent spatial locations, thereby preventing solutions from exhibiting severe oscillations or overfitting noise. Specifically, the system balances data fitting accuracy and model smoothness through an adjustable weighting coefficient (regularization parameter): when the weight is increased, inversion results show high continuity but may lose details; when the weight is reduced, model details become richer but may amplify data errors. This method is particularly suited for scenarios requiring continuous gradual features, such as velocity structure reconstruction in geophysical exploration and earthquake source slip distribution inversion. Its advantages include computational efficiency and solution uniqueness, while its limitation lies in reduced resolution for anomalies with sharp boundaries, potentially causing edge blurring.

How to find the regularization parameter of Equations 6–8 is the key to fault coseismic dislocation inversion. In seismic slip distribution inversion, there are numerous methods used to determine the regularization parameter. Allen (1974) first proposed to use the Generalized Cross Validation (GCV) method to find the regularization parameter (Allen, 1974), which is able to obtain a more ideal regularization parameter (Golub et al., 1979; Fan et al., 2017). In addition, the variance component estimation method was first proposed by Helmert (1907) for determining the posterior variance of the data, which is more effective for fault coseismic dislocation inversion (Xu et al., 2019; Xu et al., 2019; Xu et al., 2019; Fan et al., 2017). Determining the regularization parameter in Equations 6–8 is crucial for fault coseismic dislocation inversion. In seismic slip distribution inversion, various methods exist for this purpose. Allen (1974) first introduced the Generalized Cross Validation (GCV) method to identify an optimal regularization parameter (Golub et al., 1979; Fan et al., 2017).

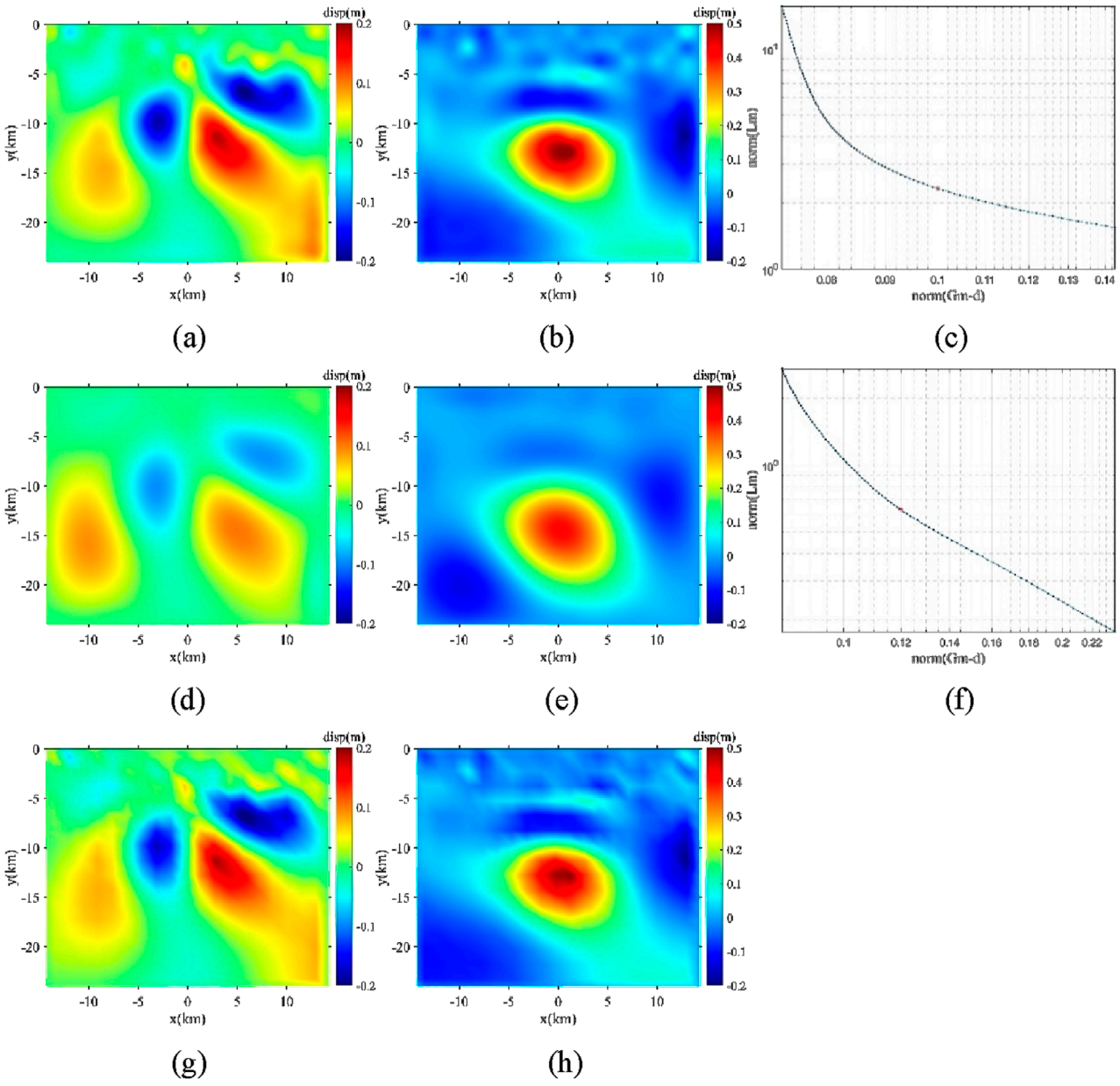

FIGURE 5
Fault dislocation inversion of the 2016 Mengyuan M_W 5.9 earthquakebased on flat-topography FEM model. **(a–c)** for diagonal L-matrix with regularization parameter 0.0331: inversed coseismic dislocation along strike direction, inversed coseismic dislocation along dip direction and L-Curve, respectively. **(d–f)** for 2D Laplace smooth matrix as the L-matrix with regularization parameter 0.1259. **(g–h)** by steepest descent method with 300 iterations.

In fault coseismic slip distribution inversion, the L-curve method is widely used due to its computational simplicity. Introduced by Hansen in 1992, this method effectively addresses the inversion of ill-posed equations (Hansen, 1992). It has been applied in geodetic surveying and is currently used in gravity downward continuation, image smoothing, and slip distribution inversion to determine regularization parameters (Hansen and O'leary, 1993). In this study, the L-curve method is also employed to determine the regularization parameters for fault dislocation inversion.

2.5 Inversion steps

(1) Collect surface coseismic GPS or InSAR observation data **d.**
(2) Divide the seismogenic fault into k subfaults, forming a column vector m with 2 k components.
(3) Use a 3D parallel elastic finite element model to compute the Green's function **G** for the unit dislocation in both the strike and dip components of each subfault at the surface observation points.
(4) Determine the strike and dip dislocations **m** for all subfaults by plotting L-curves using Equations 6–8.

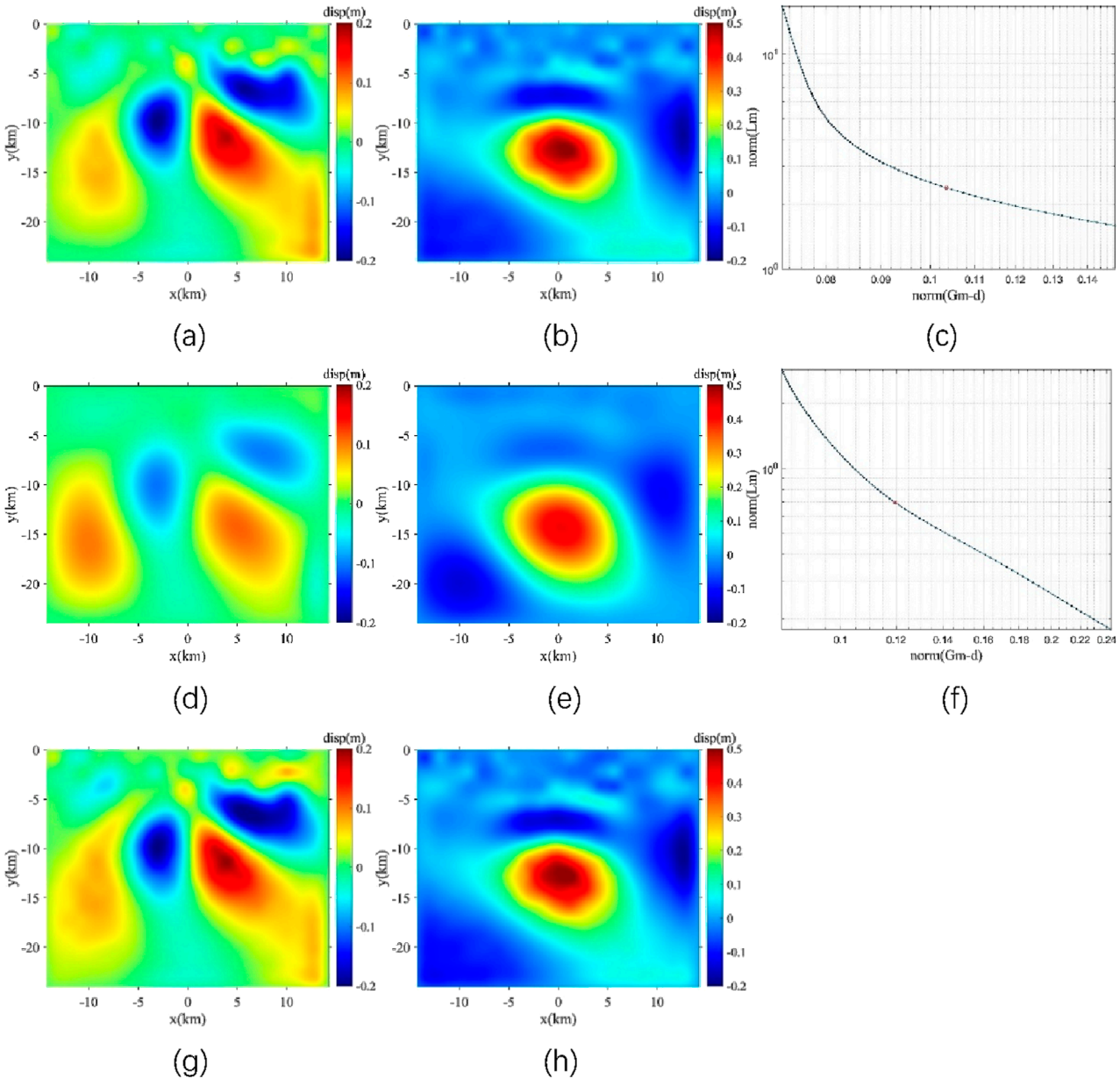

FIGURE 6
Fault dislocation inversion of the 2016 Mengyuan M_W 5.9 earthquake based on undulating-topography FEM model. **(a–c)** for diagonal L-matrix with regularization parameter 0.0331: inversed coseismic dislocation along strike direction, inversed coseismic dislocation along dip direction and L-Curve, respectively. **(d–f)** for 2D Laplace smooth matrix as the L-matrix with regularization parameter 0.1259. **(g–h)** by steepest descent method with 300 iterations.

3 Coseismic dislocation inversion for the 2016 Mengyuan M_W 5.9 earthquake

3.1 The background and coseismic deformation observation of the earthquake

On 12 January 2016, an earthquake of magnitude M_W5.9 occurred under the Lenglongling Mountains in Menyuan County, China (Figure 1). Previous studies have shown that the mechanism of the 2016 M_W5.9 earthquake was purely thrust-slip (e.g., Li et al., 2016; Zhang et al., 2020). A more accurate inversion of the fault coseismic dislocation can better characterize the coseismic rupture process and source mechanism of this earthquake. The raw Sentinel-1 satellite data were obtained from the European Space Agency (ESA) and were processed using Sentinel-1 Interferometry Processor (Jiang et al., 2017; Luo and Wang, 2022). The dates of the SAR images of AT128 and DT33 are 2016/01/13-2016/02/06, 2016/01/18-2016/02/11, both of which contain the onset time of this earthquake, can be used to calculate the surface coseismicity caused by this earthquake.

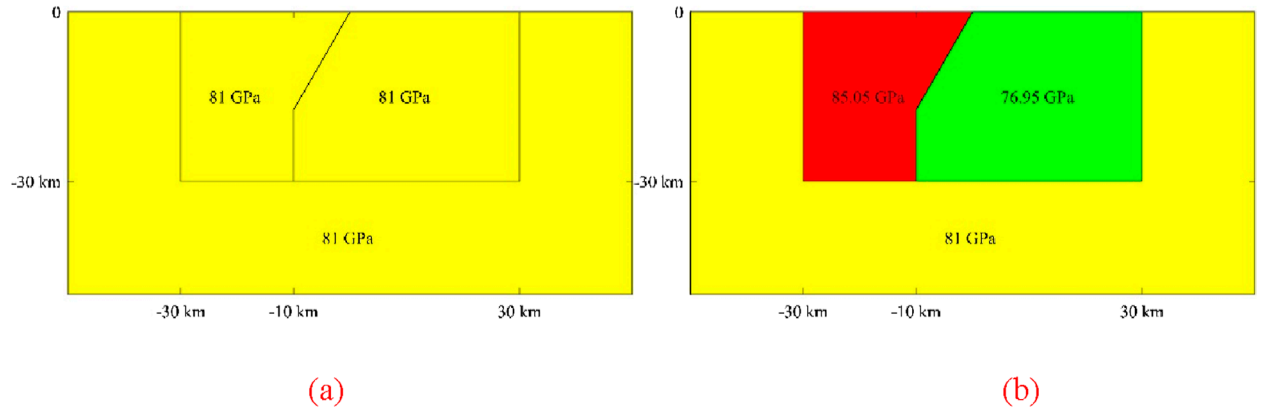

FIGURE 7
Benchmark tests of medium heterogeneity effects on coseismic slip inversion across fault zones **(a)** Homogeneous model (Model1); **(b)** Heterogeneous model (Model 2). The numerical values in GPa represent the Young's modulus of respective regions. All domains maintain a uniform poisson's ratio of 0.25.

Sentinel-1 SAR images were processed using the Sentinel-1 interferometry processor (http://sarimggeodesy.github.io/software) (Jiang et al., 2017). Luo and Wang (2022) obtained the main geometric information of the fault from which the earthquake originated using a Bayesian approach: an optimal model shows the push-slip mechanism on a low-angle, south-dipping fault plane (strike = 122°, dip = 43°) with a length of 28.5 km and a width of 16.5 km. The fault was inverted in a Bayesian framework using geodetic Bayesian inversion software (Bagnardi and Hooper, 2018). The InSAR observation has just recorded the coseismic surface deformation of this earthquake, which provides the most valuable observational data for inverting the distribution of fault coseismic dislocations of this earthquake. This provides the most valuable observation data for the inversion of the fault coseismic dislocation distribution of this earthquake.

3.2 Two checkerboard tests of fault coseismic dislocation inversion

To validate the proposed fault coseismic dislocation inversion method using parallel elastic finite element numerical simulation, we segmented the source fault of the 2016 Mengyuan earthquake into 20 larger subfaults, comprised of 19*16 basic subfaults. We developed two ideal fault coseismic dislocation models and utilized a three-dimensional elastic parallel finite element program to generate theoretical surface observations (Figure 2). This program was also used to calculate the numerical Green's function for unit dislocations in subfault strike and dip, enabling us to evaluate the accuracy of our inversion method.

We performed inversions of two sets of ideal fault coseismic dislocation distributions using two regularization methods. Figures 3A–C presents the results using a diagonal matrix as the L-matrix for intersecting distributed dislocations, while Figures 3D–F uses a two-dimensional Laplacian smooth matrix for the same. Figures 4A–F provide the inversion results for uniformly distributed dislocations using a diagonal matrix or 2D Laplace smooth matrix as the L-matrix, respectively. The inversion results align with the ideal fault coseismic dislocation distributions, validating the accuracy of our proposed inversion method based on parallel elastic finite element simulation.

3.3 Inversion of fault coseismic dislocations for the 2016 Mengyuan M_W 5.9 earthquake using InSAR data (based on flat-topography FEM model)

Based on the two checkerboard tests of fault coseismic dislocation inversion in Section 3.2, we inverted the fault coseismic dislocations of the 2016 Mengyuan M_W 5.9 earthquake using real InSAR data. The data consists of two sets, including ascending and descending tracks (Figure 1). The fault responsible for the earthquake was divided into 19 × 8 subfaults, and the Green's functions for surface coseismic displacements caused by unit dislocations along the strike and dip of each subfault were calculated using a three-dimensional parallel finite element program (Shi et al., 2023). For the parallel elastic finite element model of the 2016 M_W 5.9 earthquake in Mianyang with flat terrain, tetrahedral elements were used, with 1,084,231 nodes, 6,400,464 tetrahedrons, and 60 partitions. We adopted the homogeneous elastic medium with Young's modulus E = 81 GPa, Poisson's ratio ν = 0.25 from previous work (Luo and Wang, 2022). The total computation time for numerical Green's function solutions was 1.54×10^5 s. The parallel computing architecture of the PFELAC 2.2 platform is illustrated by Chen et al. (2025). This architecture ensures efficient parallelization while maintaining computational coherence across distributed processes. Based on the principles of domain decomposition, it adopts a modular programming approach, dividing the main program into a master process and slave processes. Each part consists of functionally distinct components. During computation, when the slave processes invoke solver programs, the master process correspondingly activates

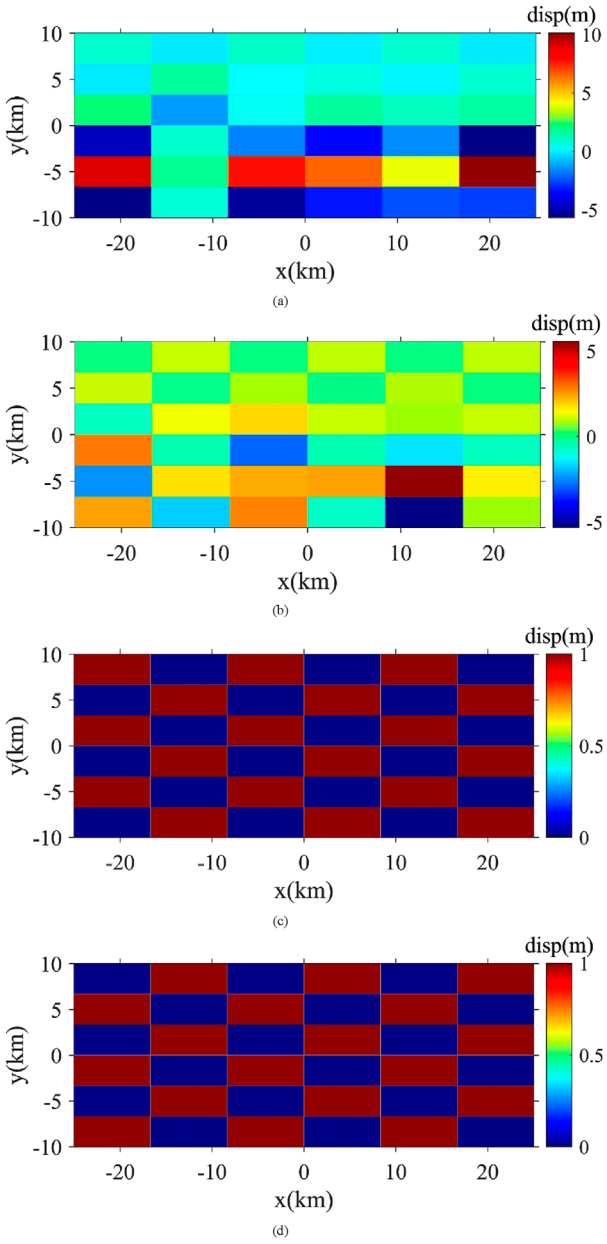

FIGURE 8
Comparison of fault dislocation inversion based on uniformity model 1 and non-uniformity model 2. **(a)** Inversed coseismic dislocation along strike direction by Model 1; **(b)** inversed coseismic dislocation along dip direction by Model 1; **(c)** inversed coseismic dislocation along strike direction by Model 2; **(d)** inversed coseismic dislocation along dip direction by Model 2.

solver interface programs to ensure synchronization across the entire system (Element Computing Technology Co., Ltd, 2018).

We directly employed preprocessed InSAR data from ascending and descending tracks (AT128, DT33), downsampled to 1,951 observation points, as LOS displacement components for coseismic fault dislocation inversion (Luo and Wang, 2022). The InSAR data processing methodology follows Luo and Wang (2022). Optimized InSAR Processing & Fault Slip Inversion Workflow (Luo and Wang, 2022): 1. SAR Data Acquisition: Processed Sentinel-1 ascending (AT128) and descending (DT33) track data covering the 2016 M_W 5.9 Menyuan earthquake using Sentinel-1 Interferometry Processor (Jiang et al., 2017). 2. Coseismic Interferogram Generation: Generated differential interferograms with phase unwrapping via Statistical-cost, Network-flow Algorithm (Chen and Zebker, 2000). 3. Derived near-field surface displacements through pixel-offset tracking (Wang et al., 2014; Wang and Jonsson, 2015). 4. Data Downsampling: Applied quadtree-based downsampling to optimize computational efficiency while preserving deformation signals (Jonsson et al., 2002). 5. Fault Geometry Optimization: Performed Bayesian inversion of uniform-slip rectangular fault models (Free parameters: Strike, dip, length, width, depth, slip magnitude) in homogeneous elastic half-space using Geodetic Bayesian Inversion Software (Bagnardi and Hooper, 2018). 6. Distributed Slip Inversion: Solved slip distribution on optimized fault planes through least-squares inversion with steepest descent regularization (Wang et al., 2011).

Three inversion methods were appliedbased on Flat-topography FEM model: the diagonal matrix as the L-matrix (Figures 5A–C), the Laplace smoothing matrix as the L-matrix (Figures 5D–F), and the steepest descent method (Figures 5G, H). All three methods produced similar coseismic dislocation distributions, which are consistent with previous results (Luo and Wang, 2022), confirming the accuracy and reliability of our inversion methods.

3.4 Inversion of fault coseismic dislocations for the 2016 Mengyuan M_W 5.9 earthquake using InSAR data (based on undulating-topography FEM model)

For the 2016 M_W 5.9 Menyuan earthquake, we have additionally developed a parallel elastic finite element model incorporating actual topographic relief, computed numerical Green's functions considering topographic relief, and inverted the coseismic fault dislocation distribution (Figure 6). We adopted the homogeneous elastic medium with Young's modulus E = 81 GPa, Poisson's ratio ν = 0.25 from previous work (Luo and Wang, 2022). We compared the fault dislocation inversion results between actual and flat topography, as well as the differences in the three-component surface coseismic displacement distributions. The effect of topographic relief on the inversion of fault coseismic dislocations is small and almost negligible for the 2016 Mengyuan earthquake.

4 Discussion

4.1 Advantages and disadvantages of different inversion methods

In the study of coseismic dislocation distribution, several inversion methods are available, each with distinct features. The Least Squares Method (LSM) is foundational, offering computational simplicity and efficiency but is sensitive to noise, risking overfitting (Minato et al., 2020). The Damped Least Squares Method (DLSM) enhances result stability through a damping parameter, though its selection is experience-based (Deo and Walker, 1995). The Smoothed Constrained Least Squares

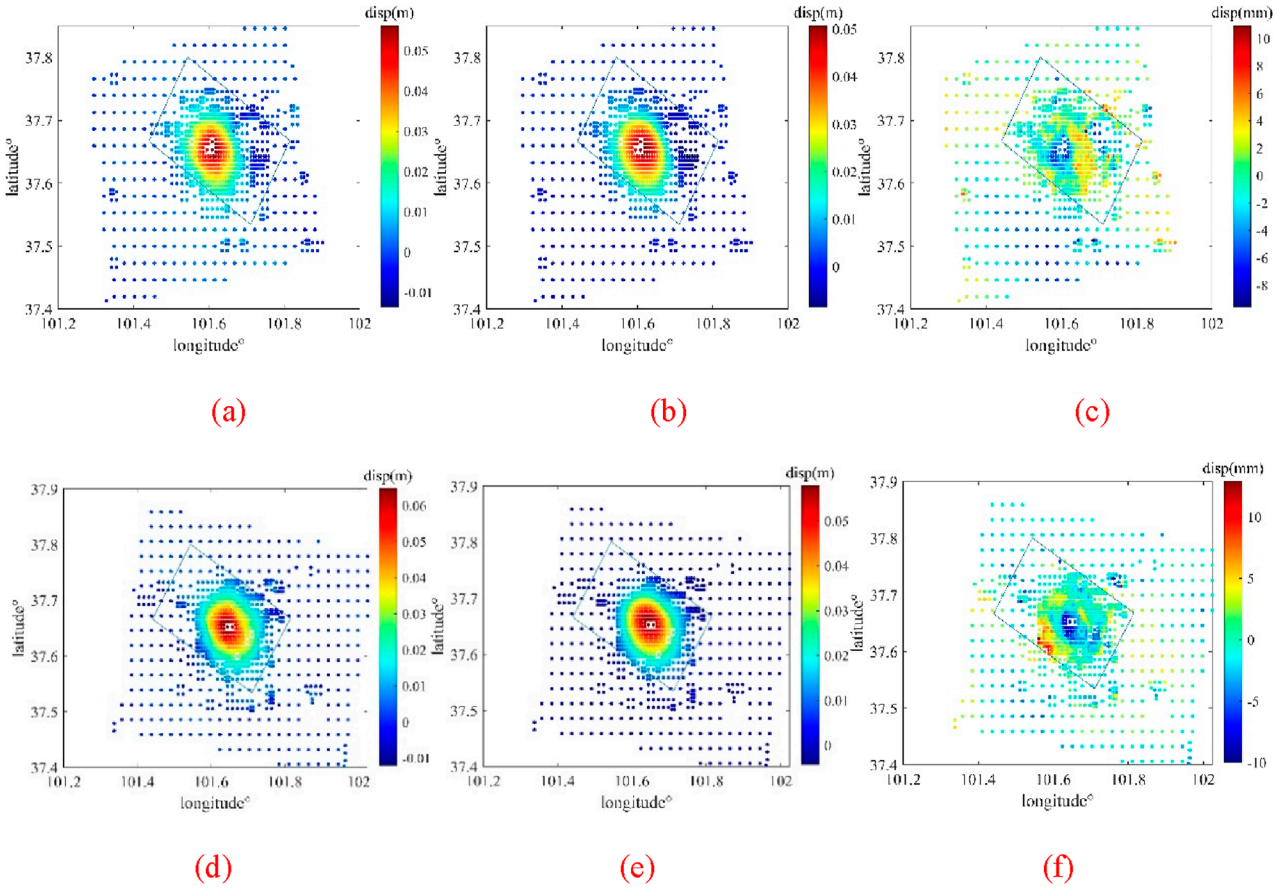

FIGURE 9
InSAR vs flat-topography FEM LOS displacements with residuals: 2016 M_W 5.9 Menyuan earthquake. Surface-projected fault traces are delineated by blue polygons. The root mean square error (RMSE) between finite element simulations and InSAR-derived LOS displacements at 1,951 surface observation points is $2.71071210902590 \times 10^{-3}$ m. **(a)** Ascending LOS displacements (Track AT128) from Sentinel-1A InSAR; **(b)** Predicted ascending LOS displacements by our finite element model; **(c)** Residual ascending LOS displacements (Observed−Modeled); **(d)** Descending LOS displacements (Track DT33) from Sentinel-1A InSAR; **(e)** Predicted descending LOS displacements by our finite element model; **(f)** Residual descending LOS displacements (Observed−Modeled).

(SLSM) method suppresses high-frequency noise with smoothing constraints, ideal for smoother dislocation scenarios, yet may overly smooth and obscure local details (Harris and Segall, 1987).

The Steepest Descent Method (SDM), used in nonlinear inversion, is straightforward and suitable for initial solutions, but is slow in convergence and prone to local optima (Quiroz et al., 2008). The triangular mesh refinement method increases resolution for complex fault geometries, though at a high computational cost (Zuo et al., 2016). Bayesian Inversion (BI) effectively manages uncertainty by integrating prior information with observations, yet its complexity and reliance on model assumptions are significant (Duan et al., 2020).

In summary, the choice of inversion method should be scenario-specific, balancing various factors. This study applies Damped Least Squares (DLSM), Smoothed Least Squares (SLSM), and the Steepest Descent Method (SDM) to the fault coseismic dislocation distribution of the 2016 M_W 5.9 earthquake. The simulated displacements align well with InSAR observations, demonstrating the adaptability of the proposed finite element-based inversion approach.

4.2 Rationale for selecting the finite element model-based inversion method

We employ a parallel elastic finite element model, a numerical framework that extends beyond simple analytical solutions. This approach fully utilizes the unique advantages of finite element methodology, enabling effective integration of real surface undulation and elastic medium inhomogeneity into coseismic deformation modeling for large earthquakes. Through parallel computing technology, we implement large-scale numerical simulations with millions of grid nodes while maintaining mesh resolution and computational accuracy, resulting in strong consistency between simulation outputs and geodetic observations such as InSAR data.

To evaluate the impact of lateral inhomogeneity on fault coseismic dislocation inversion, we compared numerical Green's function solutions using a uniform elasticity model (Model 1) and a lateral inhomogeneous elasticity model (Model 2) (Figure 7). 1) Homogeneous Model (Model 1):Homogeneous elastic medium with Young's modulus E = 81 GPa, Poisson's ratio ν = 0.25 (representative

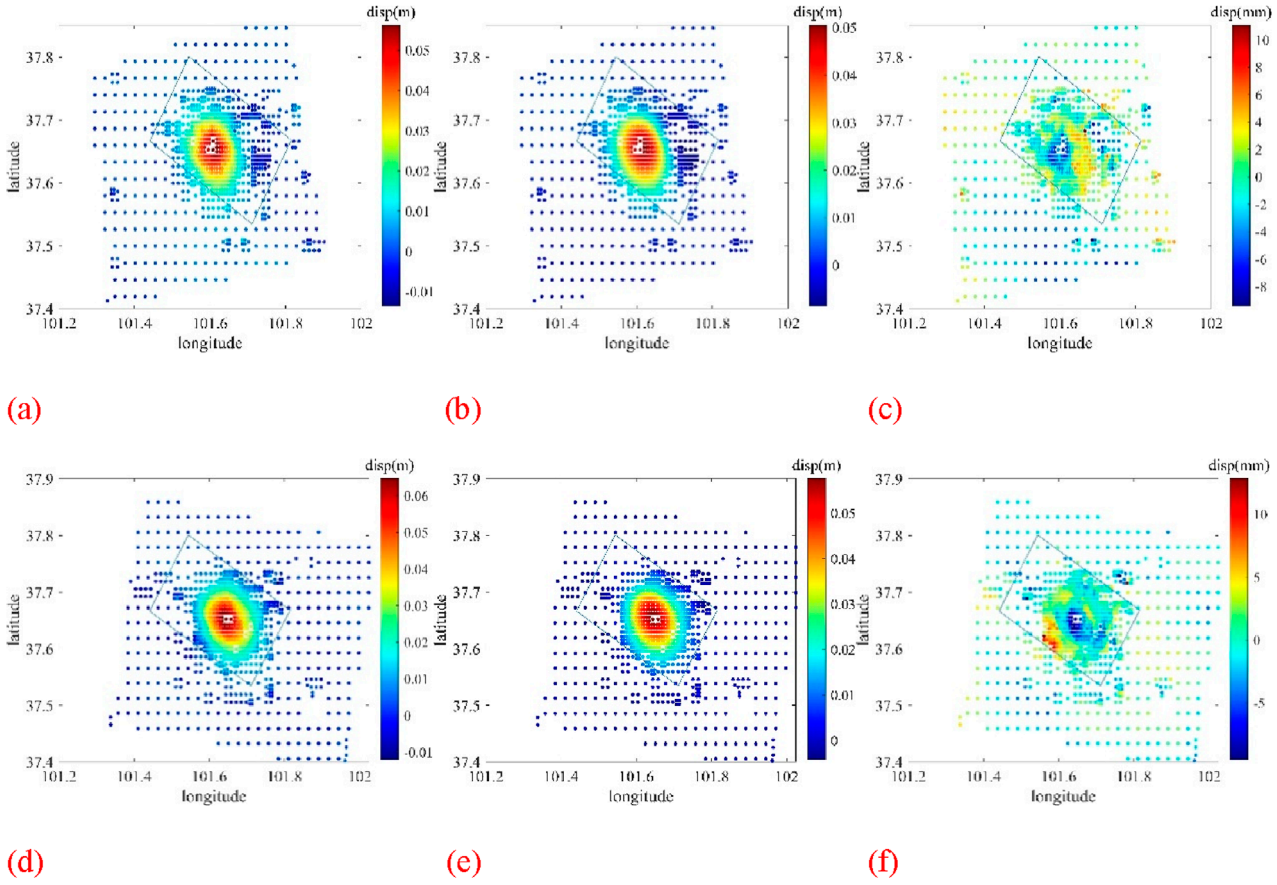

FIGURE 10
InSAR vs undulating-topography FEM LOS displacements with residuals: 2016 M_W 5.9 Menyuan earthquake. Surface-projected fault traces are delineated by blue polygons. The root mean square error (RMSE) between finite element simulations and InSAR-derived LOS displacements at 1,951 surface observation points is 2.70929434322033 × 10^{-3} m. **(a)** Ascending LOS displacements (Track AT128) from Sentinel-1A InSAR; **(b)** Predicted ascending LOS displacements by our finite element model; **(c)** Residual ascending LOS displacements (Observed−Modeled); **(d)** Descending LOS displacements (Track DT33) from Sentinel-1A InSAR; **(e)** Predicted descending LOS displacements by our finite element model; **(f)** Residual descending LOS displacements (Observed−Modeled).

of upper crustal rocks); 2) Heterogeneity Model (Model 2): Laterally stratified structure across fault strike, Hanging wall: E = 85.05 GPa (+5% perturbation), Footwall wall: E = 76.95 GPa (−5% perturbation), Far-field host rock: E = 81 GPa (maintaining continuum consistency), Identical ν = 0.25 throughout.

We applied these models to invert fault coseismic dislocation across a consistent grid of 6 × 6 = 36 subfaults. The seismic displacement data at 100 surface observation points were synthetically generated using Model 2. With these observations fixed, we computed the numerical Green's functions for both Model 1 and Model 2. Figure 8 illustrates the resulting fault coseismic dislocation distributions. The uniform elasticity model (Model 1) shows significant bias, leading to incorrect inversion results. In contrast, the lateral inhomogeneous elasticity model (Model 2) yields highly accurate dislocation distributions, closely matching the predefined fault intersection dislocations. These dual experimental configurations of coseismic fault dislocation inversion utilizing the identical observational dataset demonstrate with clarity that medium heterogeneity exerts substantial influence on the inversion outcomes. To obtain the identical observational dataset, we used an intersecting distributed dislocations with 0 m and 1 m along both the along the strike and dip. This comparison highlights the significant influence of medium inhomogeneity on dislocation inversion, underscoring the effectiveness of using a finite element model-based approach in such analyses.

4.3 The comparison of flat-topography FEM and undulating-topography FEM with InSARobservation

Notably, our comparative analyses of fault displacement components along satellite line-of-sight directions reveal critical insights when evaluating ascending/descending InSAR data from the 2016 M_W 5.9 Menyuan event against finite-element simulations. The displacement patterns and residual distributions (Figure 9: flat-topography FEM model; Figure 10: topography-incorporated FEM model) demonstrate remarkable consistency with the kinematic models proposed by Luo and Wang (2022), particularly in terms of near-field deformation characteristics. This agreement persists

despite our implementation of a topography-incorporated finite element approach - a critical refinement that enhances dislocation inversion precision through explicit consideration of surface elevation gradients. The root mean square error (RMSE) between finite element simulations and InSAR-derived LOS displacements at 1,951 surface observation points is $2.71071210902590 \times 10^{-3}$ m and $2.70929434322033 \times 10^{-3}$ m for flat-topography and topography-incorporated FEM models, respectively. Our analysis demonstrates that topographic variations exert limited influence on coseismic fault dislocation inversion results (≤5% discrepancy), aligning with established methodological frameworks (Williams and Wallace, 2018).

5 Conclusion

In this study, we introduced a novel method for fault coseismic dislocation inversion using parallel elastic finite element numerical simulation. The validity of this approach was confirmed through two checkerboard tests for fault coseismic dislocation inversion, demonstrating its accuracy and reliability. Building on these results, we applied the proposed method to the 2016 M_W 5.9 earthquake to determine the fault coseismic dislocation distribution. The inversion was conducted using three different techniques: Damped Least Squares Method (DLSM), Smoothed Least Squares Method (SLSM), and the Steepest Descent Method (SDM). The resulting surface coseismic displacement distributions closely matched the InSAR observation data, underscoring the method's precision and robustness.

The influences of topographic relief and material heterogeneity on coseismic fault dislocation inversions require separate investigation, as their impact magnitudes and mechanisms may differ substantially. The consistency between inversion results and observational data indicates that our method effectively accounts for surface topography variations and medium inhomogeneity, which are critical factors in accurately modeling fault dislocations. This approach leverages the computational power of parallel processing, enabling efficient handling of complex geophysical models and large datasets, thus demonstrating its potential for widespread application in earthquake science. Ideal model tests show that the 10% difference in Young's modulus between the two sides of the fault has a significanteffect on the coseismic dislocation inversion. For the example of the 2016 Menyuan M_W 5.9 earthquake, topographic relief had a small effect on the coseismic dislocation inversion. In general, the specific effects of medium differences and topographic relief need to be studied individually.

Furthermore, the versatility of the proposed method allows it to adapt to various seismic scenarios, providing a comprehensive tool for researchers and practitioners. By integrating advanced numerical simulation techniques with robust inversion algorithms, this method offers significant improvements over traditional approaches, enhancing our ability to understand and predict seismic events.

In conclusion, the fault coseismic dislocation inversion method based on parallel elastic finite element numerical simulation presents a powerful and adaptable solution for analyzing earthquake-induced displacements. Its ability to incorporate realistic geophysical conditions makes it a valuable asset for advancing seismic research and improving our preparedness for future seismic activities. This work paves the way for further studies to refine and expand the method's capabilities, contributing to the ongoing development of earthquake science and engineering.

Data availability statement

The original contributions presented in the study are included in the article/supplementary material, further inquiries can be directed to the corresponding authors.

Author contributions

YC: Conceptualization, Data curation, Formal Analysis, Investigation, Methodology, Resources, Software, Validation, Visualization, Writing – original draft. CH: Conceptualization, Data curation, Formal Analysis, Funding acquisition, Investigation, Methodology, Project administration, Resources, Software, Supervision, Validation, Visualization, Writing – original draft, Writing – review & editing. MS: Formal Analysis, Investigation, Methodology, Software, Validation, Visualization, Writing – review & editing. HZ: Conceptualization, Funding acquisition, Investigation, Methodology, Project administration, Resources, Software, Supervision, Writing – original draft.

Funding

The author(s) declare that financial support was received for the research and/or publication of this article. This research was financially supported by the National Key Research and Development Program of China (Grant Nos. 2023YFF0804300, 2023YFF0804301) and National Natural Science Foundation of China (Grant Nos. 42374116).

Acknowledgments

We thank Prof. Yaolin Shi (University of Chinese Academy of Sciences), Yongen Cai (Peking University) for their helpful suggestions. This research was financially supported by the National Key Research and Development Program of China (Grant Nos. 2023YFF0804300, 2023YFF0804301) and National Natural Science Foundation of China (Grant Nos. 42374116).

Conflict of interest

The authors declare that the research was conducted in the absence of any commercial or financial relationships that could be construed as a potential conflict of interest.

Generative AI statement

The author(s) declare that no Generative AI was used in the creation of this manuscript.

Publisher's note

References

Allen, D. M. (1974). The relationship between variable selection and data argumentation and a method for prediction. *Technometrics* 16 (1), 125–127. doi:10.2307/1267500

Bagnardi, M., and Hooper, A. (2018). Inversion of surface deformation data for rapid estimates of source parameters and uncertainties: a Bayesian approach. *Geochem. Geophys. Geosystems* 19 (7), 2194–2211. doi:10.1029/2018gc007585

Barba-Sevilla, M., Glasscoe, M. T., Parker, J., Lyzenga, G. A., Willis, M. J., and Tiampo, K. F. (2022). High-resolution finite fault slip inversion of the 2019 Ridgecrest earthquake using 3D finite element modeling. *J. Geophys. Res. Solid Earth* 127, e2022JB024404. doi:10.1029/2022JB024404

Chen, C. W., and Zebker, H. A. (2000). Network approaches to two-dimensional phase unwrapping: Intractability and two new algorithms. *J. Opt. Soc. Am. A* 17 (3), 401–414. doi:10.1364/josaa.17.000401

Chen, Y., Hu, C., and Zhang, H. (2025). Parallel finite element algorithm forlarge elastic deformations: Programdevelopment and validation. *Eng* 6, 48. doi:10.3390/eng6030048

Deo, A. S., and Walker, I. D. (1995). Overview of damped least-squares methods for inverse kinematics of Robot Manipulators. *J. Intelligent Robotic Syst.* 14, 43–68. doi:10.1007/bf01254007

Duan, H., Wu, S., Kang, M., Xie, L., and Chen, L. (2020). Fault slip distribution of the 2015 M_W7.8 Gorkha (Nepal) earthquake estimated from InSAR and GPS measurements. *J. Geodyn.* 139, 101767. doi:10.1016/j.jog.2020.101767

Element Computing Technology Co., Ltd. (2018). *Parallel architecture of FELAC. Element computing technology Co., Ltd.* Tianjin, China, 8–14.

Fan, Q., Xu, C., Yi, L., Liu, Y., Wen, Y., and Yin, Z. (2017). Implication of adaptive smoothness constraint and Helmert variance component estimation in seismic slip inversion. *J. Geodesy* 91 (10), 1163–1177. doi:10.1007/s00190-017-1015-0

Freed, A. M. (2005). Earthquake triggering by static, dynamic, and postseismic stress transfer. *Annu. Rev. Earth Planet. Sci.* 33 (1), 335–367. doi:10.1146/annurev.earth.33.092203.122505

Golub, G. H., Heath, M., and Wahba, G. (1979). Generalized Cross-Validation as a method for choosing a good ridge parameter. *Technometrics* 21 (2), 215–223. doi:10.1080/00401706.1979.10489751

Hansen, P. C. (1992). Analysis of discrete ill-posed problems by Means of the L-Curve. *SIAM Rev.* 34 (4), 561–580. doi:10.1137/1034115

Hansen, P. C., and O'leary, D. P. (1993). The Use of the L-curve in the regularization of discrete ill-posed problems. *SIAM J. Sci. Comput.* 14 (6), 1487–1503. doi:10.1137/0914086

Harris, R. A., and Segall, P. (1987). Detection of a locked zone at depth on the Parkfield, California, segment of the san Andreas fault. *J. Geophys. Res.* 92 (B8), 7945–7962. doi:10.1029/jb092ib08p07945

Harris, R. A., and Segall, P. (1987). Detection of a locked zone at depth on the Parkfield, California, segment of the san Andreas fault. *J. Geophys. Res.* 92 (B8), 7945–7962. doi:10.1029/jb092ib08p07945

Helmert, F. R. (1907). Scientific Books: Die Ausgleichungsrechnung Nach der methode der Kleinsten Quadrate[M]. 26(672): 663–664.

Hong, S., and Liu, M. (2021). Postseismic deformation and afterslip evolution of the 2015 Gorkha earthquake constrained by InSAR and GPS observations. *J. Geophys. Res. Solid Earth* 126, e2020JB020230. doi:10.1029/2020JB020230

Jiang, H., Feng, G., Wang, T., and Burgmann, R. (2017). Toward full exploitation of coherent and incoherent information in Sentinel-1 TOPS data for retrieving surface displacement: application to the 2016 Kumamoto (Japan) earthquake. *Geophys. Res. Lett.* 44, 1758–1767. doi:10.1002/2016gl072253

Jonsson, S. O., Zebker, H., Segall, P., and Falk, A. (2002). Fault slip distribution of the 1999 M_W7.1 Hector Mine, California, earthquake, estimated from satellite radar and GPS measurements. *Bull. Seismol. Soc. Am.* 92 (4), 1377–1389. doi:10.1785/0120000922

Kim, M., So, B., Kim, S., Jo, T., and Chang, S. (2024). Mesh size effect on finite source inversion with 3- D finite-element modelling. *Geophys. J. Int.* 237 (2), 716–728. doi:10.1093/gji/ggae060

King, G. C. P., Stein, R. S., and Lin, J. (1994). Static stress changes and the triggering of earthquakes. *Bull. Seismol. Soc. Amer.* 84, 935–953. doi:10.1785/BSSA0840030935

Landry, W., and Barbot, S. (2016). Gamra: simple meshing for complex earthquakes. *Comput. and Geosciences* 90, 49–63. doi:10.1016/j.cageo.2016.02.014

Langer, L., Beller, S., Hirakawa, E., and Tromp, J. (2023). Impact of sedimentary basins on Green's functions for static slip inversion. *Geophys. J. Int.* 232 (1), 569–580. doi:10.1093/gji/ggac344

Langer, L., Gharti, H. N., and Tromp, J. (2019). Impact of topography and three-dimensional heterogeneity on coseismic deformation. *Geophys. J. Int.* 217 (2), 866–878. doi:10.1093/gji/ggz060

Leveque, R. J., and Li, Z. (1994). The immersed interface method for elliptic equations with discontinuous coefficients and singular sources. *SIAM J. Numer. Analysis* 31 (4), 1019–1044. doi:10.1137/0731054

Li, S. Y., and Barnhart, W. D. (2020). Impacts of topographic relief and crustal heterogeneity on coseismic deformation and inversions for fault geometry and slip: a case study of the 2015 Gorkha earthquake in the central Himalayan arc. *Geochem. Geophys. Geosystems* 21, e2020GC009413. doi:10.1029/2020gc009413

Li, Y., Jiang, W., Zhang, J., and Luo, Y. (2016). Space geodetic observations and modeling of 2016 M_W 5.9 Menyuan earthquake: Implications on seismogenic tectonic motion. *Remote Sens.* 8 (6), 519. doi:10.3390/rs8060519

Luo, H., and Wang, T. (2022). Strainpartitioning on the western Haiyuanfault system revealed by the adjacent 2016 M_W5.9 and 2022 M_W6.7 Menyuan earthquakes. *Geophys. Res. Lett.* 49, e2022GL099348. doi:10.1029/2022GL099348

Masterlark, T. (2003). Finite element model predictions of static deformation from dislocation sources in a subduction zone: Sensitivities to homogeneous, isotropic, Poisson-solid, and half-space assumptions. *J. Geophys. Res.* 108, 2540. doi:10.1029/2002JB002296

Melosh, H. J., and Raefsky, A. (1981). A simple and efficient method for introducing faults into finite element computations. *Bull. Seismol. Soc. Am.* 71 (5), 1391–1400. doi:10.1785/bssa0710051391

Minato, S., Wapenaar, K., and Ghose, R. (2020). Elastic least-squares migration for quantitative reflection imaging of fracture compliances. *Geophysics* 85 (6), 327–342. doi:10.1190/GEO2019-0703.1

Moreno, M., Melnick, D., Rosenau, M., Baez, J., Klotz, J., Oncken, O., et al. (2012). Toward understanding tectonic control on the M_W8.8 2010 Maule Chile earthquake. *Earth Planet. Sci. Lett.* 2012 (3), 152–165. doi:10.1016/j.epsl.2012.01.006

Niu, J., Xu, C., and Fan Q& Yin, Z. (2016). Impact of coseismic deformation fields with different time scales on finite fault modelling in 2010 California Baja Earthquake. *Surv. Rev.* 48 (347), 94–100. doi:10.1179/1752270614y.0000000148

Okada, Y. (1992). Internal deformation due to shear and tensile faults in a half-space. *Bull. Seismol. Soc. Am.*, 82(2):1018–1040. doi:10.1785/bssa0820021018

Ozawa, S., Nishimura, T., Suito, H., Kobayashi, T., Tobita, M., and Imakiire, T. (2011). Coseismic and postseismic slip of the 2011 magnitude-9 Tohoku-Oki earthquake. *Nature* 475 (7356), 373–376. doi:10.1038/nature10227

Quiroz, E. A. P., Quispe, E. M., and Oliveira, P. R. (2008). Steepest descent method with a generalized Armijo search for quasiconvex functions on Riemannian manifolds. *J. Math. Anal. Appl.* 341, 467–477. doi:10.1016/j.jmaa.2007.10.010

Ragon, T., and Simons, M. (2021). Accounting for uncertain 3-D elastic structure in fault slip estimates. *Geophys. J. Int.* 224 (2), 1404–1421. doi:10.1093/gji/ggaa526

Ramirez-Guzman, L., and Hartzell, S. (2020). 3-D joint geodetic and strong-motion finite fault inversion of the 2008 May 12 Wenchuan, China Earthquake. *Geophys. J. Int.* 222 (2), 1390–1404. doi:10.1093/gji/ggaa239

Rollins, C., Avouac, J.-P., Landry, W., Argus, D. F., and Barbot, S. (2018). Interseismic strain accumulation on faults beneath Los Angeles, California. *J. Geophys. Res. Solid Earth* 123, 7126–7150. doi:10.1029/2017JB015387

Shi, M., Meng, S., Hu, C., and Shi, Y. (2023). Crustal heterogeneity effects on coseismic deformation: numerical simulation of the 2008 M_W 7.9 Wenchuan earthquake. *Front. Earth Sci.* 11, 1245677. doi:10.3389/feart.2023.1245677

Stein, R. S. (1999). The role of stress transfer in earthquake occurrence. *Nature* 402 (6762), 605–609. doi:10.1038/45144

Tikhonov, A. N. (1963). Solution of incorrectly formulated problems and the regularization method. *Sov. Math. Dokl.* 4, 1035–1038.

Tilmann, F., Zhang, Y., Moreno, M., Saul, J., Eckelmann, F., Palo, M., et al. (2016). The 2015 Illapel earthquake, central Chile: a type case for a characteristic earthquake? *Geophys. Res. Lett.* 43, 574–583. doi:10.1002/2015GL066963

Wan, Y., Shen, Z.-K., Bürgmann, R., Sun, J., and Wang, M. (2017). Fault geometry and slip distribution of the 2008 M_W 7.9 Wenchuan, China earthquake, inferred from GPS and insar measurements. *Geophys. J. Int.* 208, 748–766. doi:10.1093/gji/ggw421

Wang, K., and Fialko, Y. (2018). Observations and modeling of coseismic and postseismic deformation due to the 2015 M_W7.8 Gorkha (Nepal) earthquake. *J. Geophys. Res. Solid Earth* 123, 761–779. doi:10.1002/2017JB014620

Wang, R., Schurr, B., Milkereit, C., Shao, Z., and Jin, M. (2011). An improved automatic scheme for empirical baseline correction of digitalstrong-motion records. *Bull. Seismol. Soc. Am.* 101 (5), 2029–2044. doi:10.1785/0120110039

Wang, T., and Jonsson, S. (2015). Improved SAR amplitude image offset measurements for deriving three-dimensional coseismic displacements. *IEEE J. Sel. Top. Appl. Earth Observations Remote Sens.* 8 (7), 3271–3278. doi:10.1109/jstars.2014.2387865

Wang, T., Jonsson, S., and Hanssen, R. F. (2014). Improved SAR image coregistration using pixel-offset series. *IEEE Geoscience Remote Sens. Lett.* 11 (9), 1465–1469. doi:10.1109/lgrs.2013.2295429

Williams, C. A., and Wallace, L. M. (2018). The impact of realistic elastic properties on inversions of shallow subduction interface slow slip events using seafloor geodetic data. *Geophys. Res. Lett.* 45, 7462–7470. doi:10.1029/2018GL078042

Xu, G., Xu, C., Wen, Y., and Yin, Z. (2019). Coseismic and postseismic deformation of the 2016 M_W 6.2 Lampa earthquake, southern Peru, constrained by interferometric synthetic aperture radar. *J. Geophys. Res. Solid Earth* 124, 4250–4272. doi:10.1029/2018jb016572

Zhang, Y., Feng, W., Chen, Y., et al. (2012). The 2009 L'Aquila M_W 6.3 earthquake: a new technique to locate the hypocentre in the joint inversion of earthquake rupture process. *Geophys. J. Int.* 191, 1417–1426. doi:10.1111/j.1365-246X.2012.05694.x

Zhang, Y., Shan, X., Zhang, G., Zhong, M., Zhao, Y., Wen, S., et al. (2020). The 2016M_W 5.9 Menyuan earthquake in the Qilian orogen, China: a potentially delayed depth-segmented rupture following from the 1986 M_W6.0 Menyuan earthquake. *Seismol. Res. Lett.* 91 (2A), 758–769. doi:10.1785/0220190168

Zhang, Y., Wang, R., Yun-tai, C. Y., Xu, L., Du, F., Jin, M., et al. (2014). Kinematic rupture model and Hypocenter Relocation of the 2013 M_W 6.6 Lushan earthquake constrained by strong-motion and Teleseismic data. *Seismol. Res. Lett.* 85 (1), 15–22. doi:10.1785/0220130126

Zuo, R. H., Qu, C. Y., Shan, X. J., Zhang, G. H., and Song, X. G. (2016). Coseismic deformation fields and a fault slip model for the M_W7.8 mainshock and M_W7.3 aftershock of the Gorkha-Nepal 2015 earthquake derived from Sentinel-1A SAR interferometry. *Tectonophysics* 686, 158–169. doi:10.1016/j.tecto.2016.07.032

frontiers | Frontiers in Earth Science

TYPE Original Research
PUBLISHED 16 May 2025
DOI 10.3389/feart.2025.1539581

OPEN ACCESS

EDITED BY
Fuqiong Huang,
China Earthquake Networks Center, China

REVIEWED BY
Istvan Bondar,
Seismic Location Services, Portugal
Zhao Bo,
China Earthquake Networks Center, China

*CORRESPONDENCE
Jiashun Yu,
j.yu@cdut.edu.cn

RECEIVED 04 December 2024
ACCEPTED 05 May 2025
PUBLISHED 16 May 2025

CITATION
Yuan J, Ma H, Yu J, Liu Z and Zhang S (2025) An approach for teleseismic location by automatically matching depth phase. *Front. Earth Sci.* 13:1539581. doi: 10.3389/feart.2025.1539581

An approach for teleseismic location by automatically matching depth phase

Jianlong Yuan, Huilian Ma, Jiashun Yu*, Zixuan Liu and Shaojie Zhang

College of Geophysics, Chengdu University of Technology, Chengdu, Sichuan, China

To deal with the low efficiency problem of accurate teleseismic hypocenter location, this paper proposes a fully automatic approach by integrating the advantages of Seismic-Scanning based on Navigated Automatic Phase-picking, which can automatically detect and locate seismic events from continuous waveforms, and the Depth-Scanning Algorithm, which can determine the precise focal depth of local and regional earthquakes by matching depth phases. This approach, named TeleHypo, automatically searches and downloads seismic station data from the Data Management Center of the Incorporated Research Institutions for Seismology according to the original time and centroid location of teleseismic earthquakes reported by the Global Centroid-Moment-Tensor Project. Then, the direct wave was automatic extracted to construct depth-phase templates. All possible depth phases after the direct phase are obtained through a match-filtering method. Finally, high-precision hypocenter depth is determined according to the relationship between the travel time differences of the direct waves and depth phases. TeleHypo can obtain high-precision teleseismic hypocenter parameters automatically through the above process. This approach has been successfully applied to 55 teleseismic events occurred in different global seismogenic regions. It can be used to establish high-quality teleseismic catalogue and depth-phase database.

KEYWORDS

teleseismic location, TeleHypo, depth phase, algorithm, match-filtering

1 Introduction

As an important seismic source parameter, the hypocenter is not only helpful for the analysis of the initial stress state and instability position of the seismogenic region, but also can jointly explain the rupture direction and length with the centroid location (see Figure 1; Smith and Ekström, 1997). It plays a crucial role to focal mechanism inversion and real-time earthquake warning (Shelly et al., 2007; He and Ni, 2017). However, the local geological structure of many remote areas is complex. When seismic network in these areas is sparse or unevenly distributed, there is often a lack of reliable adjacent stations to accurately and automatically locate the hypocenter (Tan et al., 2019; Yuan et al., 2020).

In the absence of a fine near-field velocity model and station data, the hypocenter of an earthquake of large magnitude can be determined using global teleseismic data by travel-time location method. Many authorities (e.g., United States Geological Survey, International Seismological Centre) use this mean for earthquake rapid report and generation of earthquake catalogue. However, with the increase of epicentral distance, the first-arrival travel time becomes insensitive

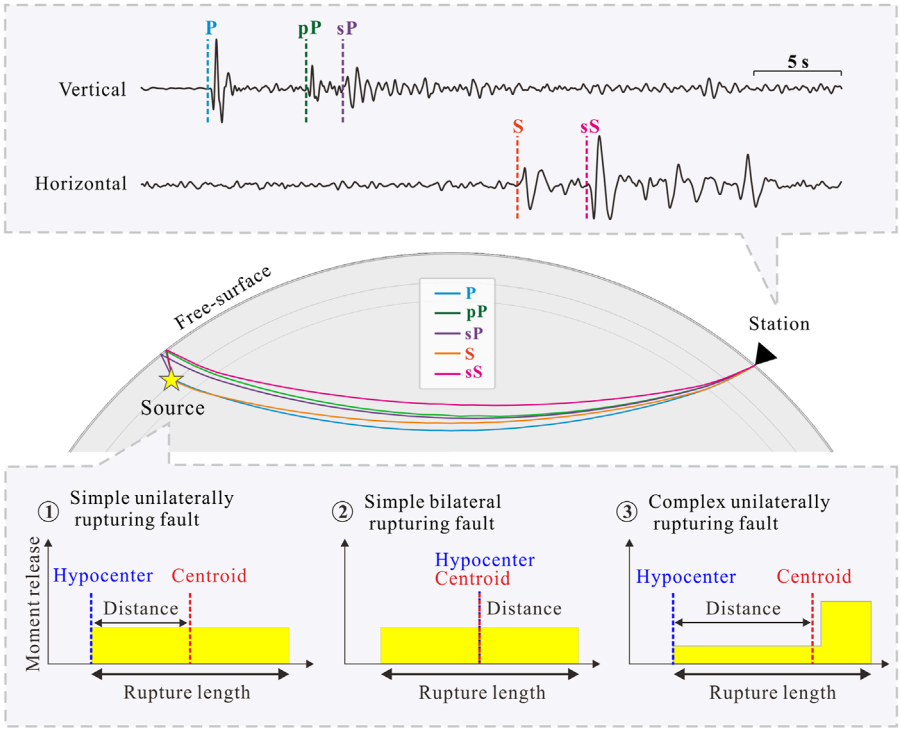

FIGURE 1
Hypocenter and centroid can jointly reveal the direction and length of earthquake rupture (modified from Smith and Ekström (1997).

to source depth. This would lead to a large error in the hypocenter location. That will further make it be unable to reveal the character of rupturing fault by using hypocenter location and the centroid location obtained by the Global Centroid-Moment-Tensor (GCMT) inversion method (see the bottom panel of Figure 1; Dziewonski and Anderson, 1981; Smith and Ekström, 1997).

The travel time difference between direct wave and the depth phases related to the free surface can be used to constrain the hypocenter depth with high accuracy (Kao and Chen, 1991; He et al., 2019; Yuan et al., 2020). However, current methods of improving the location accuracy by using the depth phase of teleseismic earthquakes are still limited by the accuracy and efficiency of depth-phase identification. For example, the International Seismological Centre (ISC) requires manual intervention in the depth-phase confirmation process, which usually takes 2 years to update their catalogue (Engdahl et al., 2020).

To improve the efficiency of depth-phase identification and location, Heyburn and Bowers (2008) proposed a semi-automatic statistical method to identify pP and sP. However, this method may treat the converted wave (S to P) from the Moho surface below the station as pP or sP and consequently results in wrong location. Letort et al. (2015) developed a focal depth location technology that can automatically identify pP and sP, but this method cannot evaluate the depths of earthquakes for the situations that produce only pP or only sP phases. For precise identification of pP, Florez and Prieto (2017) used the station array to carry out velocity spectrum analysis to obtain the accurate travel time difference of pP and P. However, this method assumes that the depth seismic phase identified is always pP, which is often unfortunately not true in practice. To use the travel times of the three depth phases, pP, sP and sS, to solve the hypocenter depth at the same time, Craig (2019) proposed an automated stacking routine using a globally distributed array. However, this semiautomatic technology required analyst input in refining appropriate frequency bands and wavelet window lengths to use, and in inspecting results to check for robustness. To automatically obtain a complete earthquake catalogue, Tan et al. (2019) proposed a fully automatic location method, called Seismicity-Scanning based on Navigated Automatic Phase-picking (S-SNAP). It is successfully applied to the Ridgecrest earthquake sequences in California, United States. But the hypocenter depth of S-SNAP in the case of large epicentral distance carries large uncertainty. To improve focal depth location precision of local and regional earthquakes, Yuan et al. (2020) proposed the Depth-Scanning Algorithm (DSA), which can automatically search all possible depth phases after direct phase to obtain precise hypocenter depth. DSA has been successfully applied to the events from different tectonic settings in Oklahoma, South Carolina, and California. The limitation of DSA is only applicable to constrain the depth location of local/regional earthquake. It also lacks the ability to relocate the epicenter and origin time. If the advantages of S-SNAP and DSA are integrated, a fully automatic precise location method can be developed to suit teleseismic events. In addition, the new method can also avoid the process of artificial intervention in depth-phase identification.

To this end, we combine S-SNAP and DSA to form a new approach, named TeleHypo, for teleseismic hypocenter location.

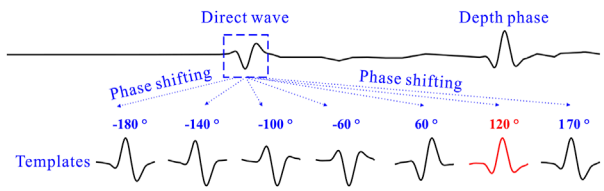

FIGURE 2
Automatic generation of depth phase templates by applying a series of phase shifting, from −180° to 180°, with an interval of 10°, to direct phase (dashed box). The depth phase (text in red in the top waveform) is successfully matched by the template (the waveform segment in red) generated by the direct phase after phase shifting of 120°.

2 Methods

TeleHypo is complished by three steps: Teleseismic data preprocessing, preliminary hypocenter determination, and precise location of hypocenter depth, as introduced below.

2.1 Teleseismic data preprocessing

To obtain station data with a high signal-to-noise ratio (S/N) and avoid dominant location deviation caused by over-dense local network (such as USArray in the United States), a series of specific measures are adopted to preprocess the data:

a) According to the time and centroid location of the teleseismic event reported by GCMT, we select the waveform data of all available stations using a time window within 30 min before and after, separately, the original time and within the epicenter range from 30° to 90°. Then the mean value, linear trend, and instrument response are removed from the waveform data. After that, a 0.25–5.00 Hz band-pass filtering is carried out.

b) Three-component waveforms are rotated to vertical (Z), radial (R), and tangential (T) components. The Z and T components are used for the subsequent locating process of TeleHypo due to the interferences of pS, sea water layer multiple (i.e., pwP), and other seismic phases that often exist in the R component (Craig, 2019). Considering that the amplitudes of pS and pwP within the epicentral distance range of 30°–90° are usually weak, there are no PKP or its branch phases within this range, and SKS and its branch phases usually appear at stations with an epicenter distance of 70° or more. Therefore, three commonly used depth phases (i.e., pP, sP, and sS) with strong amplitudes within this range are used for constraining the depth of the seismic source by TeleHypo.

c) Travel times of the direct waves are calculated using AK135 velocity model (Kennett et al., 1995) according to the centroid and station position. Signal to noise ratio (S/N) is defined as TW2/TW1, where TW1 is the recording from the time window between 40 s and 10 s before the P arrival (Marked purple in Figure 3B), and TW2 is defined as the recording from the 30 s width window directly after the P arrival (Marked green in Figure 3B). The 10 s time-interval before the P arrival is to avoid the direct wave's involvement in TW1 due to velocity model errors. To obtain reliable results, only high-quality data of S/N≥3 are selected for use. These selected high S/N station data will be used for the following hypocenter determination.

2.2 Preliminary hypocenter determination

The technique used for preliminary hypocenter location of TeleHypo is modified from S-SNAP published by Tan et al. (2019). S-SNAP can automatically detect seismic events from continuous waveforms and determine the original time, magnitude, and spatial location of earthquakes. In the locating process, S-SNAP first scans the continuous waveform using the SSA method (Kao and Shan, 2004) to obtain the possible onset time and location of the event; Then, waveform segments containing the direct waves are intercepted and used to automatically pick up the first arrival time of P and S through the kurtosis function (Baillard et al., 2014). These first arrival times are used to improve the location accuracy of the original time and spatial location of the earthquake via the MAXI method (Font et al., 2004). Finally, the results obtained by MAXI are used as a preliminary solution.

It must be pointed out that there are two reasons for using S-SNAP in this paper. Firstly, we need to use S-SNAP to relocate the epicenter based on GCMT. Secondly, this will provide a teleseismic relocation algorithm to more researchers, facilitating their own location works and improving the convenience of scientific research.

It should also be pointed out that for earthquakes of large magnitudes, the centroid and hypocenter may not necessarily be at the same spatial location (see Figure 1). TeleHypo uses S-SNAP to determine the hypocenter (i.e., the starting point of the source rupture), which may not be approximated by the centroid provided by GCMT. In addition, for the station data with an epicenter distance range of 30°–90°, S-SNAP locates the epicenter mainly through the plane wave information of each station. Therefore, we believe that the epicenter location of S-SNAP is robust, which also indicates that when the station is far away from the hypocenter of the earthquake, the accuracy of depth obtained by S-SNAP is often poor because the ray path of direct phase is insensitive to source depth. To overcome this defect, we conjunct the DSA method of Yuan et al. (2020) to improve the hypocenter depth location for teleseismic events.

2.3 Precise location of hypocenter depth

Depth-phase templates are calculated by transforming the direct phase obtained in the first step (Section 2.1) into frequency domain, applying phase shift to the direct phase spectra, and transforming back into the time domain (as shown in Figure 2). With these templates, we carry out matching filter (Shelly et al., 2007) to find out all possible depth phases in the Z/R/T waveforms. Then the arrival time difference between each possible depth phase and direct wave is calculated and treated as observed data. These

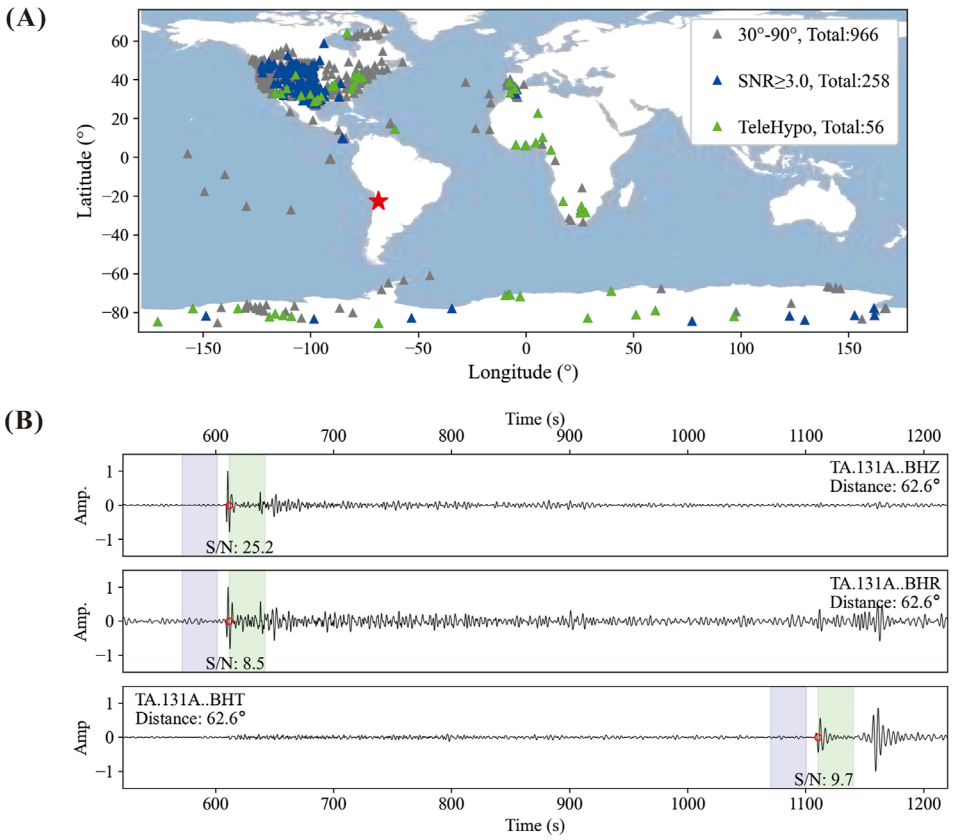

FIGURE 3
The Chile earthquake (4 March 2010, 22:39:29, Mw 6.3, the red star in **(A)**), all available stations (the gray, blue and green triangles in **(A)**), stations with S/N≥3 (the blue triangles in **(A)**), and high S/N stations (the green triangles in **(A)**) used by TeleHypo. **(B)** shows the three-component waveform of station TA.131A with an epicenter distance of 62.6°. The S/N is defined as the ratio of the maximum absolute amplitude values of the waveforms shown in the purple and green windows. The red opened circle is the theoretical travel time of direct wave calculated based on GCMT and AK135 velocity model.

observed data will be compared with the theoretical ones, which is calculated by using the widely used TauP program (Krischer et al., 2015) with a series of given hypothetical source depths.

For each presumed source depth, we count the number of matches and calculate the differential time residuals between the arrival times of the predicted depth phases and the observed with respect to the direct phase. This process is repeated for a range of assumed source depths at an increment of 1 km. Then, the same process is repeated for all available stations. After all stations are scanned for possible depth phases, we sum the total number of phase matches for each assumed focal depth and calculate the corresponding differential arrival time residual. Focal depths with the number of matches exceeding ≥90% of the largest number of matches are taken as preliminary candidates. Among them, the hypothetical depth with the smallest total of travel time difference among these candidates is selected as the high-precision hypocenter depth solution. Finally, the theoretical depth phases (i.e., pP, sP, and sS) calculated by Taup corresponding to this depth solution are used to calibrate the observed depth-phase candidates that meet the matching conditions.

3 Application to teleseismic data

3.1 The 4 March 2010 Mw 6.3 Chile earthquake

The Mw 6.3 Chile earthquake occurred on 4 March 2010 at 22:39:29, at 22.360°N and 68.690°W, with a centroid depth of 118.7 km (the red star in Figure 3A).

There are 966 stations (the gray, blue, and green triangles in Figure 3A) within the range of 30°–90° epicentral distance, and the 60 min width time window beginning 30 min before and ending 30 min after the earthquake original time provided by the GCMT. The waveform data of these stations were processed using the first step of TeleHypo. We kept the wavefield information within the frequency band of 0.25–5.0 Hz (Figure 3B). Next, the theoretical travel times of direct waves (P and S) were calculated according to the GCMT centroid and the position of each station (red circle in Figure 3B). The ratio of the largest absolute amplitudes of the waveforms (the purple and green windows in Figure 3B) is defined as the signal-to-noise ratio (S/N). To avoid systematic biases caused by nonuniform distribution of station-density, we divided stations into 36 regions at an azimuth

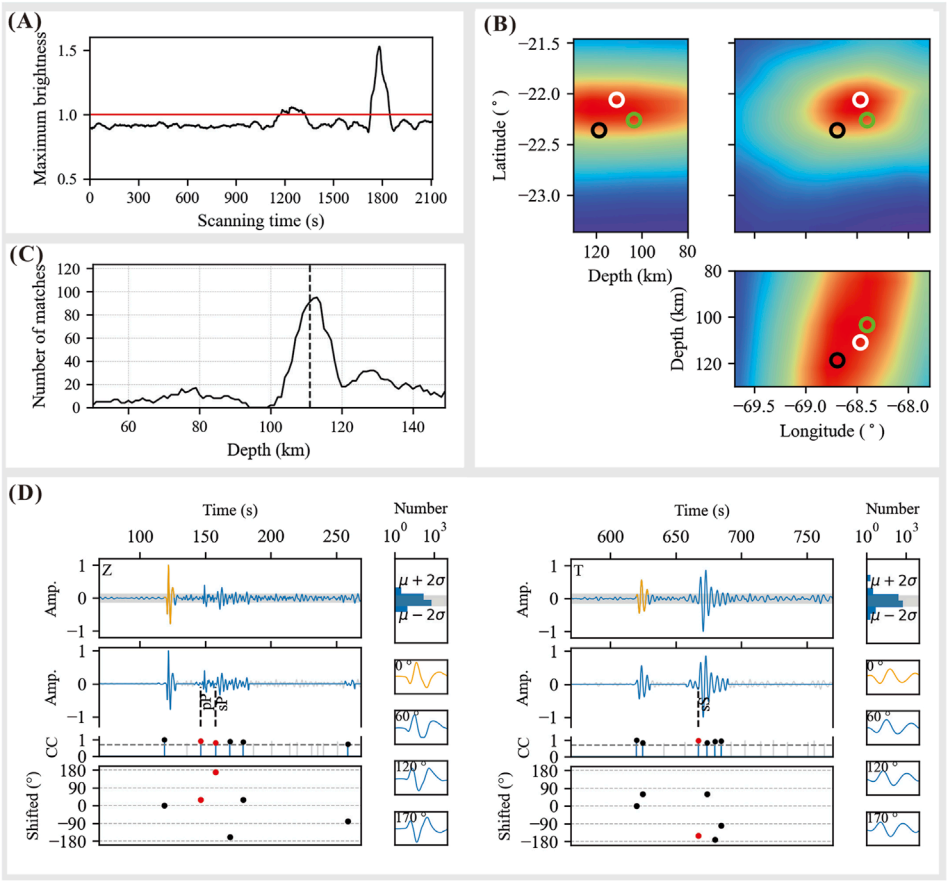

FIGURE 4
Stacked energy as a function of scanning time step obtained by TeleHypo (the black line in **(A)**) and threshold value used to determine possible earthquake events (red line in **(A)**). **(B)** shows the location solutions of TeleHypo (the white circles), ISC-EHB (the green circles) and GCMT (the black circles). **(C)** shows the hypocenter depth (vertical dotted line) obtained by TeleHypo through depth phase constraint. **(D)** shows the depth phase matching on the Z and T components of station TA.131A.

interval of 10°, and selected only the top 5 high S/N stations from each region. We finally selected 56 high S/N stations (the green triangle in Figure 3A) for the following precise hypocenter location.

TeleHypo uses the centroid position of GCMT as a reference to search for hypocenter location. The search range for the hypocenter location is 22.36± 1°N and 68.69± 1°W, with a latitude and longitude interval of 0.1°. The depth scanning range is within the centroid depth ±50 km, with a depth interval of 1 km. We extracted waveform segments from each station using a sliding window of 50 s with a step size of 1 s. The sum (called E) of squares of the waveform amplitudes within the sliding time window is calculated as a function of scanning time step (Figure 4A). Then, we searched for the P- and S-wave arrival times for possible events with E exceeding threshold of 1 (the red line in Figure 4A). Using the MAXI method (Font et al., 2004), the earthquake origin time of 4 March 2010, 22:39:26 and hypocenter location of 22.060°N, 68.465°W were located (the white circle in the upper right panel of Figure 4B). Finally, depth phases were matched with the templates at each assumed depth for each station below the hypocenter location. The scanning depth at 111 km with the highest number of successful matches is token as the hypocenter depth (the vertical dashed line in Figure 4C), along with the corresponding matched depth phases (Figure 4D).

Comparing the solution obtained by TeleHypo (22.060°N, 68.465°W, 111 km, see the white circle in Figure 4B) with that of ISC-EHB (22.261°N, 68.400°W, 103.4 km, see the green circle in Figure 4B), we found that the two methods differ by about 0.201°N, 0.065°W in the epicenter location and 7.6 km in the source depth. The good agreement between the TeleHypo and ISC-EHB in this application example demonstrates the practicality of our method.

3.2 Teleseismic events from different global seismogenic regions

To further test the practicality of TeleHypo for global teleseismic events, we applied TeleHypo to 54 moderate-to-strong teleseismic events occurring in different seismogenic regions of the world (the open circles in Figure 5A). The source parameters of these earthquakes were obtained from the GCMT earthquake catalog, with magnitudes ranging from Mw 5.5 to 7.5, and centroid depths ranging from 20 to 200 km.

10.3389/feart.2025.1539581

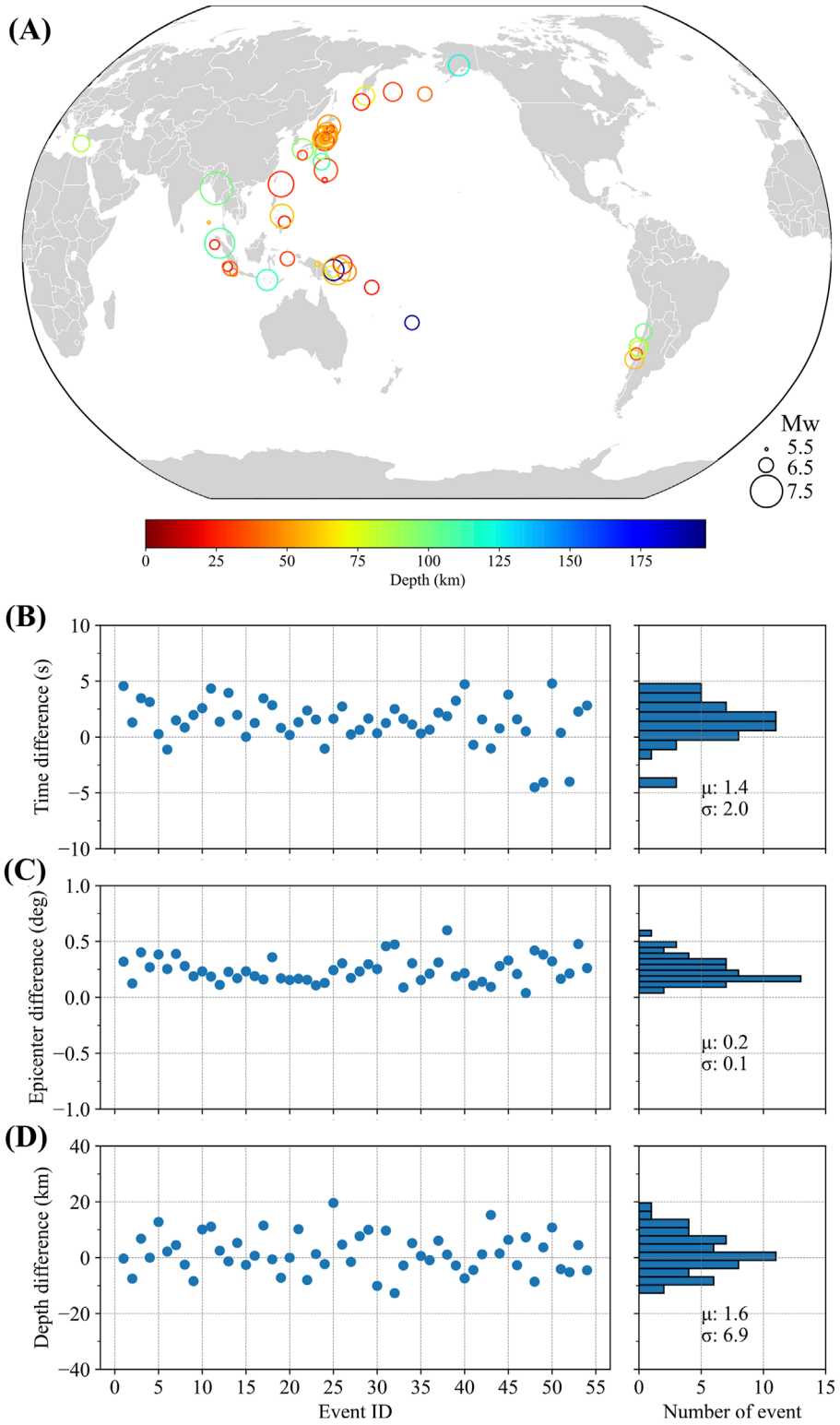

FIGURE 5
The map of 54 global teleseismic events **(A)**. **(B–D)** respectively, show the differences of original time, epicenter distance, and depth between TeleHypo and ISC-EHB. μ and σ represent the mean and standard deviation respectively.

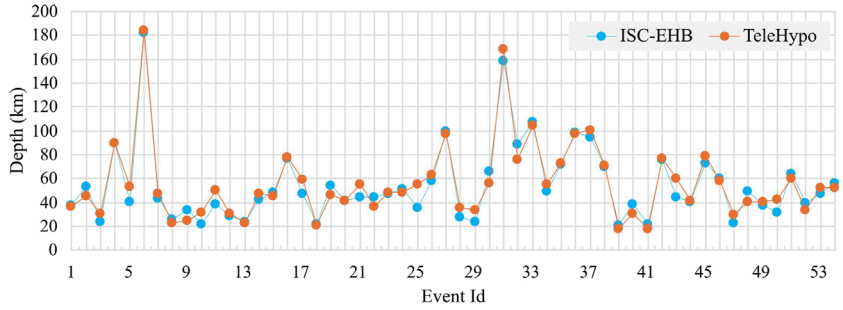

FIGURE 6
Depth distributions between ISC-EHB (The blue dotted line) and TeleHypo (The orange dotted line).

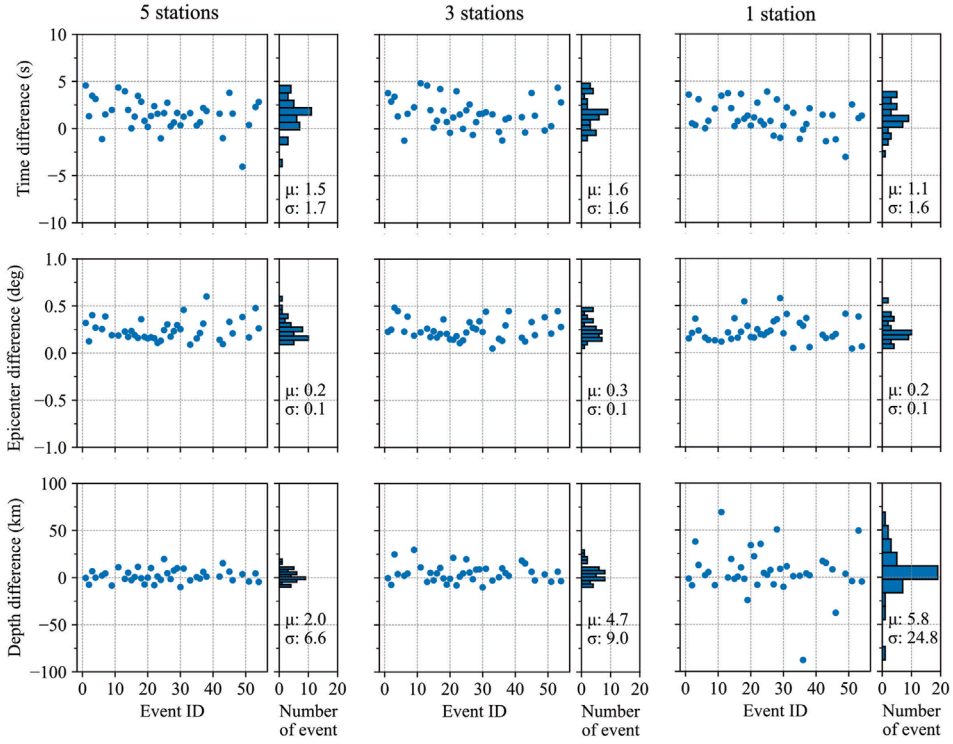

FIGURE 7
Hypocenter parameters located by TeleHypo using 5 (left column), 3 (middle column) and 1 (right column) high-quality stations, separately, from each azimuth area. The three rows of panels from top to bottom are the original time, epicenter distance, and hypocenter depth differences between TeleHypo and ISC-EHB, respectively. μ and σ represent the mean and standard deviation, respectively.

We used TeleHypo with the same parameters as the previous example of the Chile earthquake to locate the hypocenters of these teleseismic events. The location results obtained by TeleHypo are compared with those of the ISC-EHB (see details in Supplementary Table S1 in the appendix). It is showed that the differences of the original time (Figure 5B), epicenter distance (Figure 5C), and hypocenter depth (Figure 5D) between the two methods were 1.4 ± 2.0 s, 0.2 ± 0.1°, and 1.6 ± 6.9 km, respectively. The depth distributions obtained by ISC-EHB (The blue dotted line in Figure 6) and TeleHypo (The orange dotted line in Figure 6) has good agreement. These high precision results demonstrate that TeleHypo has good applicability to teleseismic events occurring in different regions of the world.

4 Discussion

4.1 Impact of the number of stations

To test the influence of the number of stations used on the location accuracy of TeleHypo, we conducted experiments on the Chile earthquake case in Section 3.1 by using 1, 3, and 5 stations with high S/N, separately, selected from each azimuthal area. We

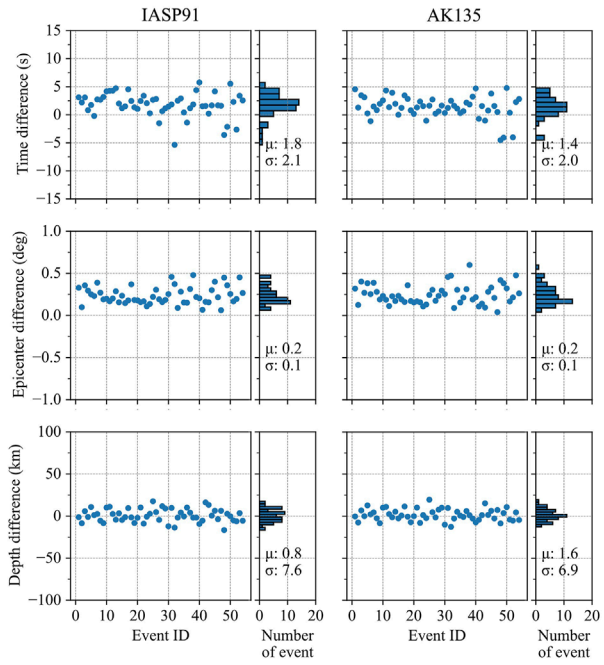

FIGURE 8
Hypocenter parameters located by TeleHypo using the IASP91 (left column) and AK135 (right column) velocity models. The layout is the same as Figure 7.

also conducted similar experiments on 54 global earthquakes in Section 3.2. The difference of origin time, epicentral location, and hypocenter depth between TeleHypo and ISC-EHB catalog were calculated. The statistical results showed that when we use only one station from each azimuthal area, the difference in origin time, epicentral location, and hypocenter depth are 1.1 ± 1.6 s, 0.2 ± 0.1°, and 5.8 ± 24.8 km, respectively (the right column of Figure 7). When three stations from each azimuthal area are used, the differences are 1.6 ± 1.6 s, 0.3 ± 0.1°, and 4.7 ± 9.0 km, respectively (the middle column of Figure 7). When the number of stations in each azimuthal sector reached 5, the differences are 1.5 ± 1.7 s, 0.2 ± 0.1°, and 2.0 ± 6.6 km, respectively (the left column of Figure 7). It indicates that using number of 5 stations with high S/N selected from each azimuthal area is suitable for TeleHypo.

It should be pointed out that the selection of stations for TeleHypo is centered around the epicenter of CGMT. The coverage is divided into 36 regions at intervals of 10° in azimuth. A maximum of 5 high S/N stations are selected from each region. Since the number of high S/N stations in some azimuthal areas can be less than 5, the total number of high S/N stations in all azimuth areas is usually less than 180, which also means that the number of depth phases with high quality will be less than 180. Section 4.4 below presents the statistical results of the number of high S/N stations and depth phases available for each of the five shallow earthquakes (see Figure 10). It indicates that TeleHypo does not necessarily need to use 180 depth phases to obtain accurate source depths.

4.2 The impact of velocity model

TeleHypo needs to use velocity model to calculate the travel times of direct waves and depth phases during location. To test the influence of different velocity models on the location of TeleHypo, we selected the IASP91 (Kennett and Engdahl, 1991) (see their Table 2) and AK135 (Kennett et al., 1995) (see their Table 3) velocity models for testing. The P-wave velocities of these two velocity models are almost the same. However, there are slight differences in their S-wave velocities, especially in the velocities above mantle where the S-wave velocity difference can reach 0.1 km/s. This difference can affect the travel time of S-waves and their associated free surface reflection phases (such as sP and sS), resulting in source location differences using these two velocity models.

We used the IASP91 velocity model to reconducted the locating experiments in Section 3.2. Other experimental parameters are the same as Section 3.2. When IASP91 is used, the differences between TeleHypo and ISC-EHB in origin time, epicentral location, and hypocenter depth are 1.8 ± 2.1 s, 0.2 ± 0.1°, and 0.8 ± 7.6 km, respectively (the left column of Figure 8). When AK135 is used, those differences are 1.4 ± 2.0 s, 0.2 ± 0.1°, and 1.6 ± 6.9 km, respectively (the right column of Figure 8). It suggests that IASP91 is more suitable for TeleHypo to locate the hypocenter depth.

4.3 Seismic phase database

In addition to providing hypocenter parameters, TeleHypo can also provide the arrival times and be used to extract waveform of direct waves and depth phases (as shown in Figure 9), which is useful for building database for direct waves and depth phases of global earthquakes. The direct waves (P and S) and depth phases (pP, sP, and sS) for all teleseismic events in this paper were automatically picked by TeleHypo. There were, in total, 1245 P, 1245 S, 566 pP, 453 sP, and 456 sS phases. Since artificial intelligence nowadays still depends on good training data, TeleHypo can be used to provide a large number of training dataset and labels for artificial intelligence in teleseismic phase identification.

4.4 Applicability of TeleHypo to shallow earthquakes

Among the 55 teleseismic events used in this paper (see the Supplementary Table S1 in the appendix), there are 5 shallow earthquakes with focal depths less than 30 km. The number of high S/N stations for these five events is 54, 73, 38, 67, and 25, separately. From each of these stations, TeleHypo successfully identified 32 (59.3%), 25 (34.2%), 13 (34.2%), 28 (41.8%), and 8 (32.0%) pP/sP phases, and 35 (64.8%), 20 (27.4%), 9 (23.7%), 18 (26.9%), and 7 (28.0%) sS seismic phases, respectively. Statistics show that TeleHypo has an average successful identification rate of 40.3% for pP/sP and 34.2% for sS. The depth solutions of TeleHypo (The orange histograms in Figure 10) for these 5 shallow earthquakes are consistent with that of ISC-EHB (The blue histograms in Figure 10), with an average depth difference of 2.32 km. This suggests that it is possible to use TeleHypo to locate shallow earthquakes occurring

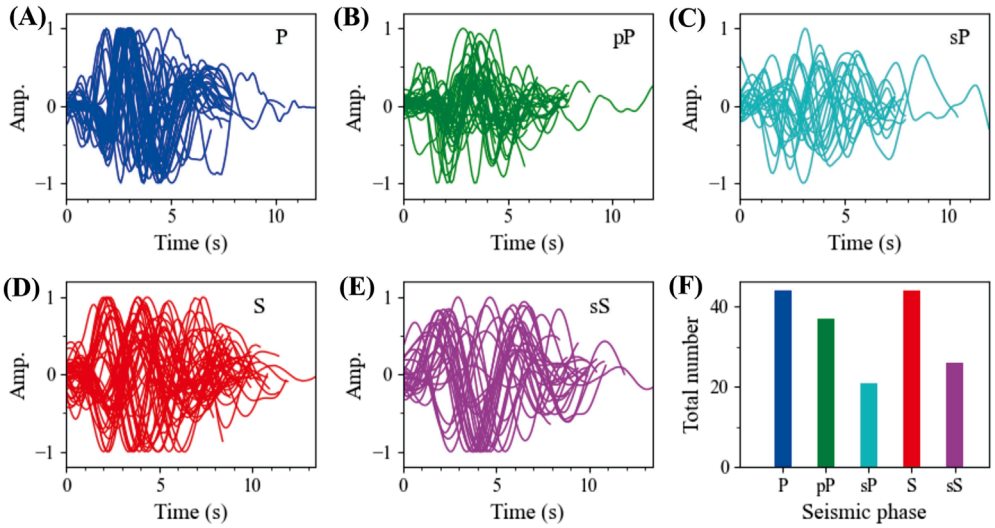

FIGURE 9
The direct waves **(A,D)**, depth phases **(B,C,E)**, and the number of these seismic phases **(F)** picked by TeleHypo from the high S/N stations of the Chile earthquake in Section 3.1.

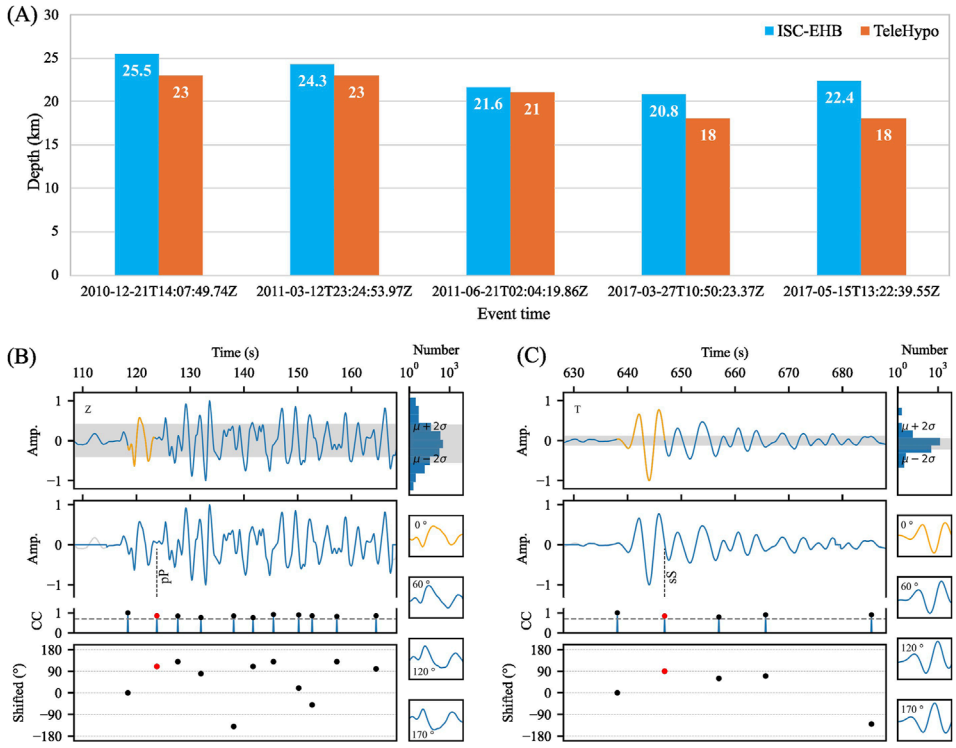

FIGURE 10
The depth solutions for 5 shallow earthquakes located by ISC-EHB (The blue histograms in **(A)**) and TeleHypo (The orange histograms in **(A)**). TeleHypo obtained pP **(B)** and sS **(C)** depth phases by matching the data from station N4.P46A of the fourth earthquake event (2017-03-27T10:50:23.37Z) in **(A)**.

within the crust (e.g., source depth <30 km) if the direct waves and depth phases can be separately identified.

To investigate the depth phase identification of TeleHypo for shallow events, we analyzed the depth phase matching process of the event of 2017-03-27T10:50:23.37Z in Figure 10. The Z-component record of station N4.P46A of the event (Figure 10B) shows obvious direct P-waves (The orange waveform in Figure 10B). We obtained the pP phase through template matching (The red dot and dashed line in Figure 10B). As the source depth of this event was only 18 km, the pP phase followed closely behind the direct P-wave. The direct

S-wave (The orange waveform in Figure 10C) and sS phase (The red dot and dashed line in Figure 10C) in the T-component record also exhibit similar characteristics. This means that shallow earthquakes with a focal depth of 18 km are approaching the depth location limit of TeleHypo. If the source is too shallow, there may be interference between the direct waves and depth phases, leading to waveform distortion and potentially causing TeleHypo to fail. In addition, when the direct wave or depth phase is not obvious, TeleHypo may also fail due to the inability to match the correct phase.

5 Conclusion

In this paper, we propose a new approach, TeleHypo, for automatic teleseismic precise location by integrating the advantages of two near-regional earthquake location methods, i.e., S-SNAP and DSA. During the location process, TeleHypo firstly selects high S/N and reasonably distributed stations. Then it performs preliminary scanning for the earthquake hypocenter using the data from these selected stations, and finally achieves precise hypocenter location by automatically matching depth phases. We tested the correctness of TeleHypo using an earthquake example occurred in Chile, and then further validated the applicability and practicality of this method through 54 global teleseismic events. The location capability of TeleHypo under different numbers of stations and velocity models are analyzed. The results show that TeleHypo has a good robust performance. Besides, the high-quality phase samples picked by TeleHypo can serve research on the identification of depth phases for artificial intelligence, and focal mechanism- or velocity-inversion for different seismogenic regions worldwide.

Data availability statement

The raw data supporting the conclusions of this article will be made available by the authors, without undue reservation.

Author contributions

JLY: Funding acquisition, Writing – original draft, Writing – review and editing. HM: Writing – review and editing, Software, Validation. JSY: Funding acquisition, Writing – review and editing. ZL: Data curation, Writing – review and editing. SZ: Data curation, Writing – review and editing.

References

Baillard, C., Crawford, W. C., Ballu, V., Hibert, C., and Mangeney, A. (2014). An automatic kurtosis-based p-and s-phase picker designed for local seismic networks. *Bull. Seismol. Soc. Am.* 104, 394–409. doi:10.1785/0120120347

Beyreuther, M., Barsch, R., Krischer, L., Megies, T., Behr, Y., and Wassermann, J. (2010). Obspy: a python toolbox for seismology. *Seismol. Res. Lett.* 81, 530–533. doi:10.1785/gssrl.81.3.530

Craig, T. (2019). Accurate depth determination for moderate-magnitude earthquakes using global teleseismic data. *J. Geophys. Res. Solid Earth* 124, 1759–1780. doi:10.1029/2018jb016902

Dziewonski, A. M., and Anderson, D. L. (1981). Preliminary reference earth model. *Phys. earth Planet. interiors* 25, 297–356. doi:10.1016/0031-9201(81)90046-7

Engdahl, E. R., Di Giacomo, D., Sakarya, B., Gkarlaouni, C. G., Harris, J., and Storchak, D. A. (2020). Isc-ehb 1964–2016, an improved data set for studies

Funding

The author(s) declare that financial support was received for the research and/or publication of this article. This research is supported by the Sichuan Science and Technology Program, China (2025ZNSFSC0314 to J Yuan and 2025HJPJ0007 to J Yu).

Acknowledgments

We thank Chenqi Tian for helping downloading and testing teleseismic data. Waveform data used in this study were downloaded from the Data Management Center of the Incorporated Research Institutions for Seismology(last accessed 1 November 2024). The Obspy and Matplotlib software packages are used in data processing and generating figures, respectively (Beyreuther et al., 2010; Hunter, 2007).

Conflict of interest

The authors declare that the research was conducted in the absence of any commercial or financial relationships that could be construed as a potential conflict of interest.

Generative AI statement

The author(s) declare that no Generative AI was used in the creation of this manuscript.

Publisher's note

Supplementary material

The Supplementary Material for this article can be found online at: https://www.frontiersin.org/articles/10.3389/feart.2025.1539581/full#supplementary-material

of earth structure and global seismicity. *Earth Space Sci.* 7, e2019EA000897. doi:10.1029/2019ea000897

Florez, M. A., and Prieto, G. A. (2017). Precise relative earthquake depth determination using array processing techniques. *J. Geophys. Res. Solid Earth* 122, 4559–4571. doi:10.1002/2017jb014132

Font, Y., Kao, H., Lallemand, S., Liu, C.-S., and Chiao, L.-Y. (2004). Hypocentre determination offshore of eastern taiwan using the maximum intersection method. *Geophys. J. Int.* 158, 655–675. doi:10.1111/j.1365-246x.2004.02317.x

He, X., and Ni, S. (2017). Rapid rupture directivity determination of moderate dip-slip earthquakes with teleseismic body waves assuming reduced finite source approximation. *J. Geophys. Res. Solid Earth* 122, 5344–5368. doi:10.1002/2016jb013924

He, X., Zhang, P., Ni, S., and Zheng, W. (2019). Resolving focal depth in sparse network with local depth phase spl: a case study for the 2011 mineral, Virginia, earthquake sequence. *Bull. Seismol. Soc. Am.* 109, 745–755. doi:10.1785/0120180221

Heyburn, R., and Bowers, D. (2008). Earthquake depth estimation using the f trace and associated probability. *Bull. Seismol. Soc. Am.* 98, 18–35. doi:10.1785/0120070008

Hunter, J. D. (2007). Matplotlib: a 2d graphics environment. *Comput. Sci. and Eng.* 9, 90–95. doi:10.1109/mcse.2007.55

Kao, H., and Chen, W.-P. (1991). Earthquakes along the ryukyu-kyushu arc: strain segmentation, lateral compression, and the thermomechanical state of the plate interface. *J. Geophys. Res. Solid Earth* 96, 21443–21485. doi:10.1029/91jb02164

Kao, H., and Shan, S.-J. (2004). The source-scanning algorithm: mapping the distribution of seismic sources in time and space. *Geophys. J. Int.* 157, 589–594. doi:10.1111/j.1365-246x.2004.02276.x

Kennett, B., and Engdahl, E. (1991). Traveltimes for global earthquake location and phase identification. *Geophys. J. Int.* 105, 429–465. doi:10.1111/j.1365-246x.1991.tb06724.x

Kennett, B. L., Engdahl, E., and Buland, R. (1995). Constraints on seismic velocities in the earth from traveltimes. *Geophys. J. Int.* 122, 108–124. doi:10.1111/j.1365-246x.1995.tb03540.x

Krischer, L., Megies, T., Barsch, R., Beyreuther, M., Lecocq, T., Caudron, C., et al. (2015). Obspy: a bridge for seismology into the scientific python ecosystem. *Comput. Sci. and Discov.* 8, 014003. doi:10.1088/1749-4699/8/1/014003

Letort, J., Guilbert, J., Cotton, F., Bondár, I., Cano, Y., and Vergoz, J. (2015). A new, improved and fully automatic method for teleseismic depth estimation of moderate earthquakes ($4.5 < m < 5.5$): application to the guerrero subduction zone (Mexico). *Geophys. J. Int.* 201, 1834–1848. doi:10.1093/gji/ggv093

Shelly, D. R., Beroza, G. C., and Ide, S. (2007). Non-volcanic tremor and low-frequency earthquake swarms. *Nature* 446, 305–307. doi:10.1038/nature05666

Smith, G. P., and Ekström, G. (1997). Interpretation of earthquake epicenter and cmt centroid locations, in terms of rupture length and direction. *Phys. earth Planet. interiors* 102, 123–132. doi:10.1016/s0031-9201(96)03246-3

Tan, F., Kao, H., Nissen, E., and Eaton, D. (2019). Seismicity-scanning based on navigated automatic phase-picking. *J. Geophys. Res. Solid Earth* 124, 3802–3818. doi:10.1029/2018jb017050

Yuan, J., Kao, H., and Yu, J. (2020). Depth-scanning algorithm: accurate, automatic, and efficient determination of focal depths for local and regional earthquakes. *J. Geophys. Res. Solid Earth* 125, e2020JB019430. doi:10.1029/2020jb019430

frontiers | Frontiers in Earth Science

TYPE Original Research
PUBLISHED 23 October 2025
DOI 10.3389/feart.2025.1537480

OPEN ACCESS

EDITED BY
Yongsheng Zhou,
Institute of Geology, China Earthquake Administration, China

REVIEWED BY
Mihaela Kouteva-Guentcheva,
University of Architecture, Civil Engineering and Geodesy, Bulgaria
Seth Carpenter,
University of Kentucky, United States

*CORRESPONDENCE
Jiashun Yu,
j.yu@cdut.edu.cn

RECEIVED 30 November 2024
ACCEPTED 30 September 2025
PUBLISHED 23 October 2025

CITATION
Zhou Q, Yu J, Han C, Yuan J, Fu X, Yu K, Hou X and Fan X (2025) Study on the extremely large seismic ground motion amplification on weak-motion seismograms from the Gongquan valley.
Front. Earth Sci. 13:1537480.
doi: 10.3389/feart.2025.1537480

Study on the extremely large seismic ground motion amplification on weak-motion seismograms from the Gongquan valley

Qiang Zhou[1], Jiashun Yu[1]*, Chao Han[2], Jianlong Yuan[1], Xiaobo Fu[3], Kun Yu[4], Xiaoping Hou[1] and Xinran Fan[1]

[1]College of Geophysics, Chengdu University of Technology, Chengdu, Sichuan, China, [2]Academy of Urban Safety and Emergency Management of Chengdu, Chengdu, Sichuan, China, [3]Research and Development Center, BGP Inc., CNPC, Zhuozhou, Hebei, China, [4]Guangxi Geological Survey Institute, Nanning, Guangxi, China

The Ms 6.0 Changning Earthquake in 2019 caused severe damage to Gongquan Town, Sichuan. Our on-site investigation of seismic damage found that the three-dimensional topography and geological conditions of the town may have exacerbated the earthquake's amplification effects. Research on the amplification effects of seismic ground motion will be of help to understand the local seismic damage mechanisms and provide a scientific basis for disaster prevention and reduction in the region. To this end, we deployed a seismic array in Gongquan Town to observe seismic activities and analyze the amplification effects in the area. The research results, from weak-motion seismograms of aftershocks, indicate that there is a significant seismic ground motion amplification in Gongquan Town, with an average amplification factor of 11 over the frequency range of 5–7 Hz. Additionally, the amplification varied widely among different sites in different earthquakes, with Site G09 experiencing an amplification as high as 26 times of Site G06 during one of the earthquakes. Simulation studies suggest that the extreme amplification at G09 is not caused by the soil layers directly beneath the site. Further analysis found that the extreme amplification at this site is closely related to the orientation of the seismic source, with earthquakes north-northeast to G09 more likely to cause extreme seismic motion amplification at the site. The large peak amplification at G09 of weak motion data is likely to be significantly reduced in a large earthquake due to nonlinearity. However, the phenomenon reminds us to pay special attention to the risk of significant damage caused by the combined effects of extreme amplification in future earthquake defense efforts.

KEYWORDS

changning earthquake, ground motion, extreme amplification, site effect, azimuthal characteristics

1 Introduction

On 17 June 2019, at 22:55, a magnitude 6.0 earthquake occurred in Changning, Sichuan, with the epicenter located at 28.34°N, 104.90°E, and a focal at 16 km. The earthquake caused serious casualties and damage to buildings. Gongquan Town is about 12 km from the epicenter and was significantly affected (Ren et al., 2021; Hu et al., 2023; Yang et al., 2023).

Historical earthquakes show that this area is prone to seismic activity. A series of moderate earthquakes occurred, including the Ms 4.9 earthquake in Junlian on 28 January 2017, the Ms 4.9 earthquake in Gongxian on 4 May 2017, the Ms 5.7 earthquake in Xingwen on 16 December 2018, the Ms 5.3 earthquake in Gongxian on 3 January 2019, and the Ms 6.0 earthquake in Changning on 17 June 2019 (Liang et al., 2017; Yi et al., 2020; Hu et al., 2021). The locations of the earthquakes are shown in Figure 1. After the 2019 Changning earthquake, there were 96 aftershocks of magnitude 3.0 and above, among which, there were 4 earthquakes of magnitude 4.5 and above, making it one of most active seismic area in the Sichuan Basin. With densely packed buildings, many old houses, and a high population density, Gongquan Town is prone to destructive earthquake. So far, there is no research on the seismic response in Gongquan Town. The seismic site effects in earthquake damage to the town remains unknown. Therefore, it is of importance to carry out a study of the seismic ground motion characteristics in the Gongquan area for earthquake mitigation purpose.

Seismic ground motion amplification is a factor playing an important role in earthquake disasters (Li and Huang, 2009). Particularly, when the main frequency of the seismic motion overlaps with the natural frequency of a building, it can cause resonance, exacerbating the destructive effects of the earthquake (Çelebi et al., 2018). We know that local surface geological conditions can lead to seismic motion amplification. During the Ms 8.0 Wenchuan Earthquake of 12 May 2008, high-intensity anomalies occurred in the alluvial plain of the Liusha River, Hanyuan, which is far from the epicenter (Li et al., 2016). Local irregular terrain of valley areas can also cause seismic motion amplification and result in severe earthquake damage (Gao et al., 2021). The impacts of this amplification effect were seen in the 6.6 magnitude earthquake near San Francisco in 1971 and the 6.7 magnitude Northridge Earthquake in Southern California in 1994 (Trifunac and Hudson, 1971; Sepúlveda et al., 2005). The Gongquan Town is located in the valley traversed by the Changning River, with

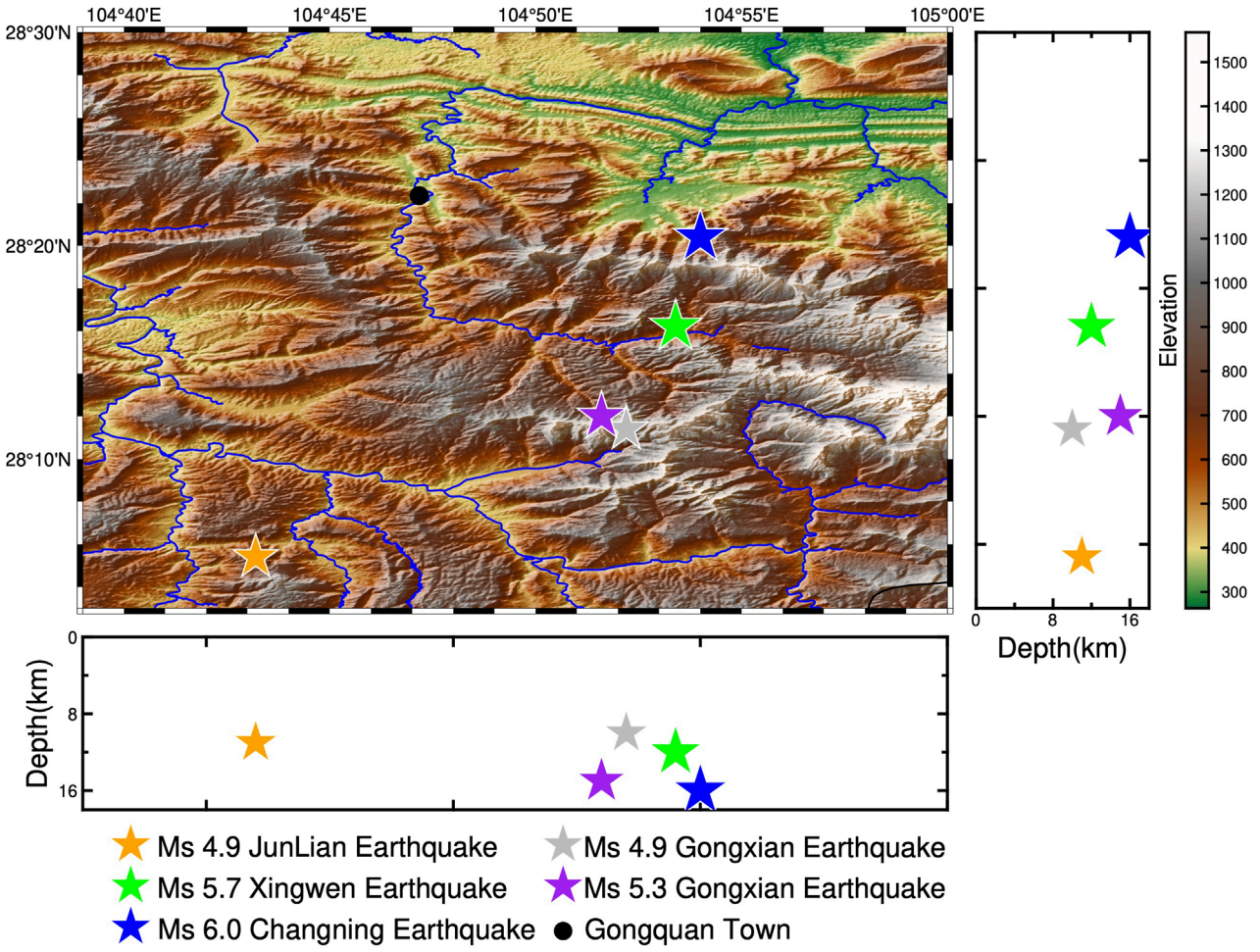

FIGURE 1
Historic earthquakes (pentagrams) occurred in the Gongquan (black solid circle) area in the last 8 years.

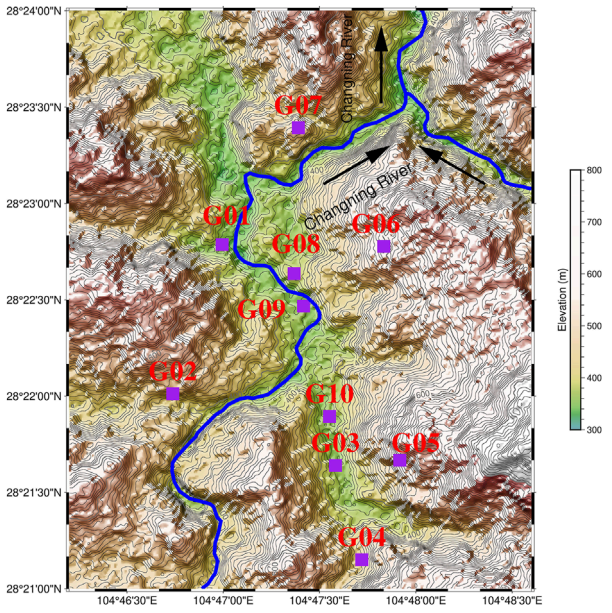

FIGURE 2
Topography of Gongquan valley and the seismic observation stations. The blue curve represents the river; the purple box represents the seismic observation station.

its lower areas consisting of Quaternary floodplain deposits and steep mountain sides revealing rock formations, where elevation differences can reach 500 m (Figure 2), creating conditions for various causes of seismic motion amplification effects. Therefore, studying the characteristics of seismic motion amplification in Gongquan Town is of significant guiding importance for earthquake disaster prevention, regional disaster reduction, and relief efforts.

2 Data

2.1 Observations

We decided to deploy an observation array in the Gongquan Town to study the characteristics of seismic ground motion response in the area. Based on the damage caused by the Changning Earthquake and in-situ geological investigation, 10 observation sites at locations such as riverbanks and hillsides were selected for the array, which make a full coverage for Gongquan Town (Figure 2). The observation equipment used for the observation is the QS-05A portable digital seismometer, with a frequency range of 5 s to 150 Hz.

The array conducted continuous observations from September 17 to 19, 2019 (UTC+8), with the specific operating times of each station detailed in Table 1.

2.2 Data processing

A total of 38 earthquake events were identified from the continuous recordings from the observation array. Referring to the earthquake catalog published by the China National Earthquake Network, the epicenter range of these earthquakes is determined to be 28.20°N to 28.48°N/104.67°E to 104.75°E. Most earthquakes extend along the Changning anticline, with magnitudes ranging from M 0.4 to 2.9 and focal depths from 1 to 15 km. The distribution of the epicenters of the events is specifically shown in Figure 3, and the parameters of each earthquake are detailed in Table 2. Figure 4 shows the three-component waveform of Event 34.

2.3 Ground motion

The ground motion amplification at a site is usually influenced by the surface topography and underground geological conditions. The horizontal amplitude of seismic ground motion is generally larger than the vertical amplitude, and the shear wave ground motion amplification at a site is primarily relevant for seismic mitigation. Therefore, when observing the particle motion trajectories of different seismic events at various observation sites, we focus primarily on the horizontal particle motion trajectories. To demonstrate the horizontal ground motion patterns in area, we plot the horizontal particle motion trajectories of 4 events in Figure 5 to show the characteristics of ground motion at each site. As can be seen that there is significant difference in the magnitude of the horizontal particle vibration amplitude at different sites, which reflects the site effects on seismic ground motion. It is particularly noteworthy that Site G06, located on the hillside east of Gongquan, consistently exhibits smaller horizontal vibration amplitudes compared to other stations over all the events.

2.4 Data selection

We use the Reference Site Spectral Ratio (RSSR) method by Borcherdt (1970) to analyze the seismic ground motion amplification in the Gongquan area. The application of RSSR is predicated on the assumption that the seismic wave amplitude on the ground surface at the reference site is a good approximation of that at the bedrock beneath the study site. In general, seismic data from a reference site may also be influenced by its own site effects due to weathering (Yu and Haines, 2003). However, as long as the weathering layer is thin, so that its effects are on frequencies higher than those of interest to earthquake disaster prevention, the reference site effects is insignificant on the effective frequency range of RSSR characterization for the purpose.

When the observation array was designed, the Reference Site G06 was chosen as reference as it is on the exposed Silurian Supergroup (S3) calcareous siltstone, with a calcareous matrix in the rock, exhibiting thin horizontal layering. Later seismic observation showed that the particle vibration amplitude at G06 was relatively small (See the sixth row in Figure 5), proving that our choice of the reference site at the time was reasonable.

To minimize the impact of the path term, we first excluded earthquakes that were less than 3.1 km from G06, to ensure that the distance between a study site and the reference site does not exceed the hypocentral distance, so that the path effects can be negligible (Steidl et al., 1996). In addition, we specifically analyzed factors such as distances between stations and the rupture radius of each earthquake.

TABLE 1 Information of the earthquake stations.

Site	Lat(°)	Lon(°)	Eelevation(m)	Start (UTC+8)	End (UTC+8)	Notes
G01	28.380°N	104.783°E	428 m	20190918 02:35:36	20190919 02:46:50	Hillside
G02	28.367°N	104.779°E	578 m	20190918 03:28:36	20190919 02:12:34	Hillside
G03	28.361°N	104.793°E	414 m	20190917 08:59:45	20190919 05:47:18	Hillside
G04	28.353°N	104.795°E	395 m	20190917 07:48:38	20190919 03:09:33	Hillside
G05	28.361°N	104.799°E	392 m	20190918 06:36:54	20190919 03:27:35	Hillside
G06	28.380°N	104.797°E	520 m	20190918 04:26:08	20190919 04:27:41	Hillside
G07	28.390°N	104.790°E	426 m	20190918 01:53:38	20190919 01:43:41	Hillside
G08	28.378°N	104.790°E	379 m	20190917 05:59:03	20190919 05:32:38	Floodplain
G09	28.374°N	104.790°E	351 m	20190917 06:28:36	20190919 03:43:15	Floodplain
G10	28.365°N	104.793°E	347 m	20190917 07:03:12	20190919 03:51:12	Floodplain

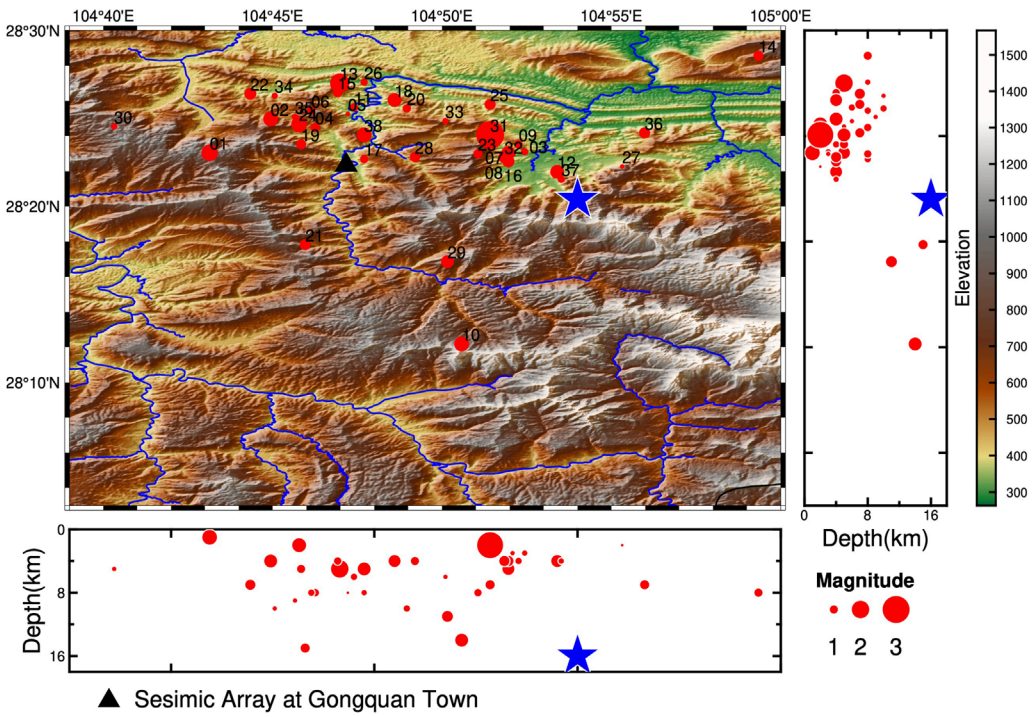

FIGURE 3
Locations of the earthquakes (red solid circle) recorded by the array. The blue pentagram marks the location of the main shock of the Changning Earthquake.

According to Kanamori and Anderson (1975), based on the disc rupture model, the source rupture radius r can be determined by Equation 1, as follows

$$r = \left(\frac{7M_o}{16\Delta\sigma} \right)^{1/3} \quad (1)$$

where M_o is the seismic moment, and $\Delta\sigma$ is the stress drop. According to the spatiotemporal distribution characteristics of earthquake source parameters in the Changning area, Sichuan (Zuo and Zhao, 2021), the seismic moment M_o can be determined by Equation 2, based on the empirical relationship between seismic moment and magnitude

$$\log M_o = 0.94M_L + 10.15 \quad (2)$$

According to Wang (2022), who analyzed the seismic events in the southern Sichuan Basin before and after the Changning earthquake, the stress drop in the study area is between 0.5 and

TABLE 2 catalog of selected events with $SNR \geq 3$

No	Date (dd/mm/yyyy)	Origin time (hr:min:sec)	Epicenter location		Focal depth (km)	Mag.	Epicenter distance† (km)	Stations receiving seismic events									
			Lat.	Lon.				G01	G02	G03	G04	G05	G06	G07	G08	G09	G10
1	9/17/2019	6:29:10	28.38	104.72	1	1.7	7.4								*	*	
2	9/17/2019	9:56:55	28.42	107.75	4	1.5	6.5			*	*				*	*	*
3	9/17/2019	11:30:57	28.39	104.87	3	0.7	8.0			*	*				*	*	*
4	9/17/2019	11:49:06	28.41	104.77	8	0.9	4.5			*	*				*	*	*
5	9/17/2019	11:57:22	28.42	104.79	8	0.4	5.4			*					*	*	
6	9/17/2019	12:11:21	28.42	104.77	8	0.8	6.1			*					*	*	*
7	9/17/2019	12:15:46	28.38	104.87	5	1.4	7.2			*	*				*	*	*
8	9/17/2019	12:49:23	28.38	104.87	3	0.6	7.4			*	*				*	*	*
9	9/17/2019	13:37:05	28.39	104.87	4	0.8	7.9			*	*				*		*
10	9/17/2019	16:29:38	28.2	104.84	14	1.5	19.4			*	*				*	*	*
11	9/17/2019	17:36:58	28.43	104.79	6	0.8	6.0			*	*				*	*	*
12	9/17/2019	18:20:01	28.37	104.89	4	1.4	9.5			*	*				*	*	*
13	9/17/2019	18:59:32	28.45	104.78	5	2	8.6			*	*				*	*	*
14	9/17/2019	19:14:53	28.48	104.99	8	1	22.3			*							
15	9/17/2019	20:59:28	28.44	104.78	4	0.9	7.6			*	*				*	*	*
16	9/17/2019	21:10:31	28.38	104.87	4	1.2	7.1			*	*				*	*	*
17	9/17/2019	21:32:13	28.39	104.8	8	0.8	0.6			*	*				*	*	*
18	9/17/2019	23:58:34	28.34	104.81	4	1.4	7.0			*	*				*	*	*
19	9/18/2019	2:37:02	28.39	104.76	5	1	3.6			*	*			*	*	*	*
20	9/18/2019	5:03:27	28.43	104.82	10	0.8	6.3	*	*	*	*		*	*		*	*
21	9/18/2019	5:53:16	28.3	104.77	15	1.1	8.8	*	*	*	*		*	*	*	*	*

(Continued on the following page)

10.3389/feart.2025.1537480

TABLE 2 (*Continued*) The catalog of selected events with $SNR \geq 3$

No	Date (dd/mm/yyyy)	Origin time (hr:min:sec)	Epicenter location		Focal depth	Mag.	Epicenter distance† (km)	Stations receiving seismic events									
			Lat.	Lon.				G01	G02	G03	G04	G05	G06	G07	G08	G09	G10
22	9/18/2019	5:59:17	28.4	104.74	7	1.2	9.1	*	*	*	*		*	*	*		*
23	9/18/2019	7:42:56	29.52	104.62	8	0.8	5.8	*	*	*	*	*	*	*	*	*	*
24	9/18/2019	10:00:39	28.41	104.76	2	1.6	5.2	*	*	*	*	*	*	*	*	*	*
25	9/18/2019	10:10:19	28.43	104.86	7	1.1	8.9	*	*	*	*	*	*	*			*
26	9/18/2019	12:41:05	28.45	104.8	8	0.7	8.7	*	*	*	*	*	*	*		*	*
27	9/18/2019	13:20:44	28.37	104.92	2	0.4	12.6		*	*	*	*	*	*		*	
28	9/18/2019	14:16:01	28.38	104.82	4	1	2.7	*	*	*	*	*	*	*	*	*	*
29	9/18/2019	16:18:12	28.28	104.84	11	1.3	11.0	*	*	*	*	*	*	*	*		*
30	9/18/2019	17:25:32	28.41	104.67	5	0.6	12.5	*	*	*	*	*	*	*	*	*	*
31	9/18/2019	18:36:08	28.41	104.86	2	2.9	7.0	*	*	*	*	*	*	*	*	*	*
32	9/18/2019	20:35:56	28.38	104.86	4	1.2	7.0	*	*	*	*	*	*	*	*	*	*
33	9/18/2019	21:13:12	28.41	104.84	6	0.6	6.1	*	*	*	*	*	*	*	*		*
34	9/18/2019	22:33:41	28.44	104.75	10	0.6	8.3	*	*	*	*	*	*	*	*	*	*
35	9/19/2019	2:14:47	28.42	104.76	9	0.6	5.9	*		*	*	*	*				
36	9/19/2019	2:20:33	28.4	104.93	7	1.1	14.1	*		*	*	*	*			*	
37	9/19/2019	2:44:30	28.36	104.89	4	0.7	9.8	*		*		*	*			*	*
38	9/19/2019	5:08:18	28.4	104.8	5	1.5	3.1			*					*		

*indicates that the event was recorded by the station; †refers to the distance between G06 and the epicenter.

10.3389/feart.2025.1537480

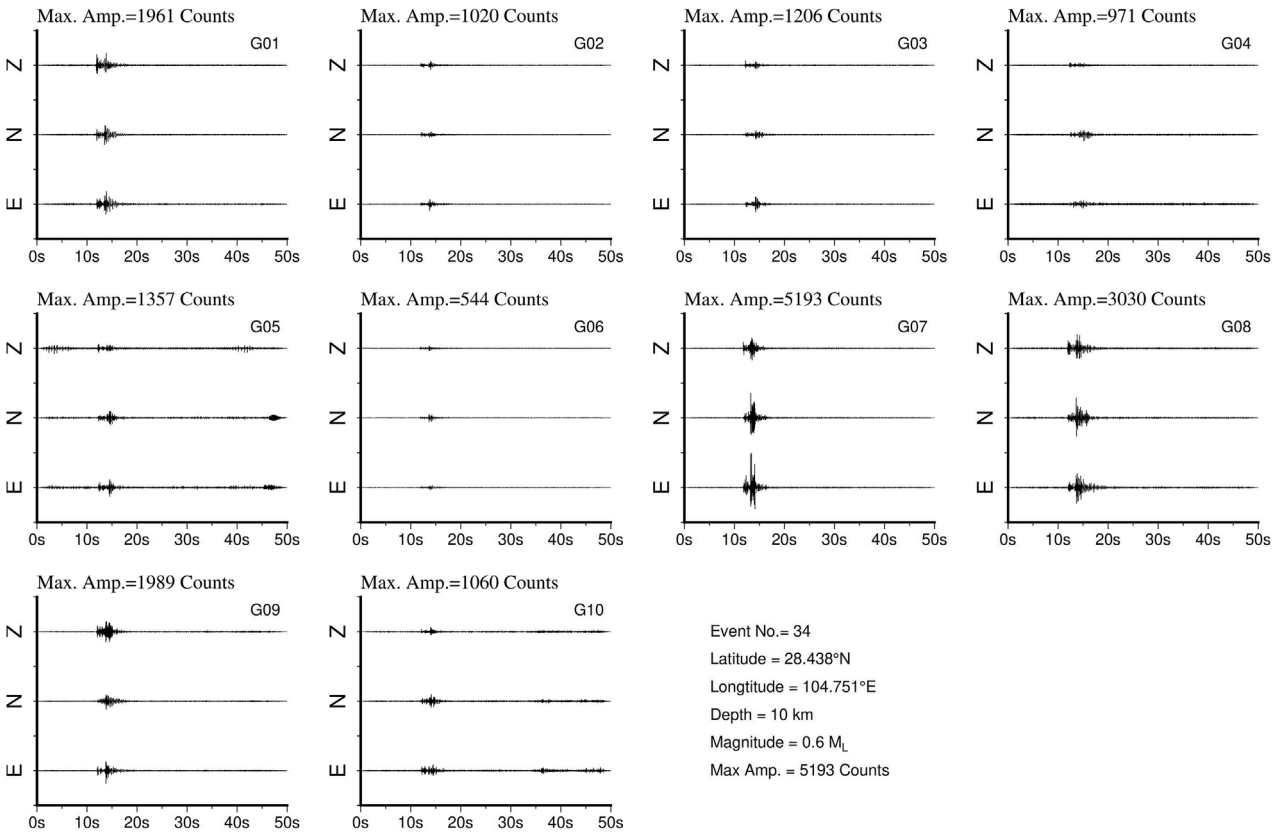

FIGURE 4
Waveform records of Event 34 recorded by the observation network. The seismic motion amplitudes at each station are normalized using the maximum amplitude recorded at station G07. The amplitude labels at the top of each subplot indicate the maximum amplitude among the three components for each site.

30 MPa. By substituting the local magnitudes of each earthquake (see Table 2), it can be calculated that the rupture radius of all earthquakes is less than 80 m, which is much smaller than the epicentral distance. Based on the point source assumption conditions by Aki and Richards (2002), these earthquakes can all be treated as point sources. Therefore, in our subsequent analysis, we do not need to exclude observed earthquake events due to the rupture surface being too large.

In addition, we conducted a signal-to-noise ratio (SNR) analysis on the observed seismic data. We used data before the event as background noise, and extracted effective event signal data to calculate the SNR for each station from each seismic event. Finally, we selected the seismic data with a SNR higher than 3 (Table 2) for subsequent analysis of the seismic ground motion amplification effects.

3 Amplifications

3.1 Spectral ratios

We use the formula of Yu and Haines (2003), as shown in Equation 3, to calculate the amplification effect of seismic motion in the horizontal direction:

$$R_{ij}^{H}(f) = \frac{H_{ij}(f)}{H_{rj}(f)} \tag{3}$$

where H is the horizontal component of the seismic motion defined by Equation 4,

$$H_{ij} = \sqrt{\frac{E_{ij}^{2}(f) + N_{ij}^{2}(f)}{2}} \tag{4}$$

where $E_{ij}(f)$ and $N_{ij}(f)$ represent the Fourier amplitude spectrum functions of the east and north component, respectively, of seismic motion at Site i from Event j, with f standing for frequency.

To eliminate the impact of random factors on the seismic amplification effect analysis (Borcherdt and Glassmoyer, 1992), we performed mean and variance statistical analysis on the spectral ratio functions using Equations 5, 6:

$$\overline{R}_{i}^{H}(f) = \frac{1}{N_i}\sum_{i}^{N_i} R_{ij}^{H}(f) \tag{5}$$

$$\sigma_{i}^{H}(f) = \sqrt{\frac{1}{N_i}\sum_{i}^{N_i}\left[R_{ij}^{H}(f) - \overline{R}_{ij}^{H}(f)\right]^{2}} \tag{6}$$

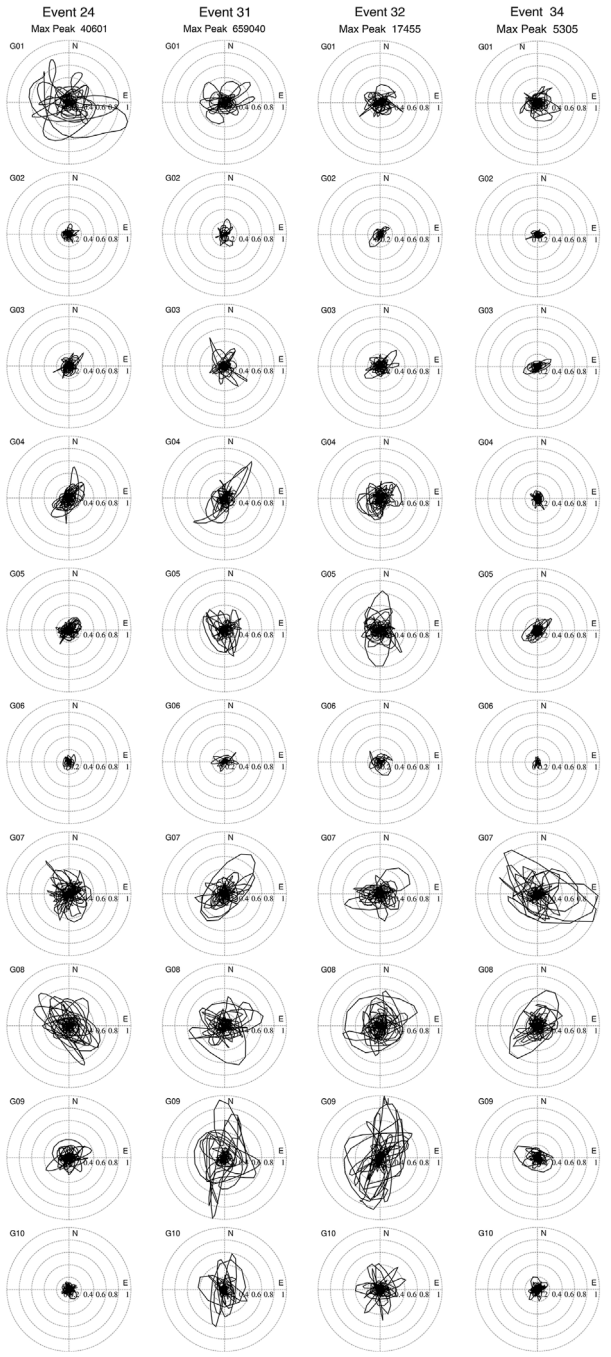

FIGURE 5
Horizontal vibration trajectories at each site in Events 24, 31, 32 and 34 (from the left to the right columns). There is significant difference in the magnitude of the horizontal particle vibration amplitude at different sites, reflecting the site effects on seismic ground motion. It is particularly noteworthy that Site G06 (the sixth row), located on the hillside east of Gongquan, consistently exhibits smaller horizontal vibration amplitudes compared to other stations over all the events.

where $\overline{R}_i^H(f)$ and $\sigma_i^H(f)$ represent the mean and standard deviation of the spectral ratio of the H component from Site i, N_i represents the number of events recorded at Site i.

Using the method introduced above, spectral ratio functions, and means and standard deviations, were calculated for the data selected using the criteria as discussed in Section 2.4. According to the response frequency of the instrumentation, the calculation results have a frequency range greater than 0.2 Hz. On the other hand, considering that most buildings in Gongquan Town are 1-6 stories, we focused on studying the site earthquake amplification effect at frequencies below 12 Hz, with the specific results calculated as shown in Figure 6.

Overall, Site G01 has the lowest dominant frequency of 3 Hz, with an average peak amplification over all the events at 6. Sites G02 and G03 do not show significant seismic amplification. Sites G04, G08, and G09 exhibit significant amplification at 5–6 Hz. Sites G05, G07, and G10 mainly showed amplification at higher frequencies above 7 Hz.

3.2 Spatial patterns

To more intuitively demonstrate the spatial variation of the amplification effect, the spatial distribution of the average seismic amplification over each frequency range at each site are shown in Figure 7, which provides a global overview of the seismic amplification pattern in Gongquan Town. It is evident that site effect in Gongquan is significant, and its impact on the exacerbation of earthquake disasters cannot be overlooked. Furthermore, there are notable differences in seismic amplification characteristics between various sites, which exhibit localized features, indicating that factors such as local topography and near-surface geological conditions greatly influence the distribution of seismic amplification in Gongquan Town.

3.3 Peak amplifications of weak-motion events

Peak amplification and the corresponding frequency, referred to as dominant frequency later, are important parameters for studying seismic ground motion amplification effects. Here, the dominant frequency and peak amplification for each site in each of the weak motion event recorded are shown in Figure 8. We found that dominant frequencies of the sites are concentrated in the range of 5–8 Hz, indicating a relatively stable characteristic. However, there are significant differences in the amplified peak values of seismic motion at different sites.

Figure 8 shows that G09 has peak amplifications ranging from 9 to 26 over the frequency band of 5–6 Hz. Although the peak amplification of 26 is extremely large, it is not exceptional. For example, another large peak amplification of 18 is also found at the same site, and a peak amplification of 25 found at Site G07 on a frequency of around 8 Hz. Actually, an even larger peak amplification of 30 in Lower Hutt, New Zealand, was also reported by Taber and Smith (1992). Therefore, the large amplification at G09 cannot be negligible for future earthquake hazard prevention, as, once it happens, the building structures at the site needs to withstand vibrations 26 times greater than that at the reference site G06. This will inevitably intensify the forces exerted by the earthquake on the building structures. However, it should be pointed

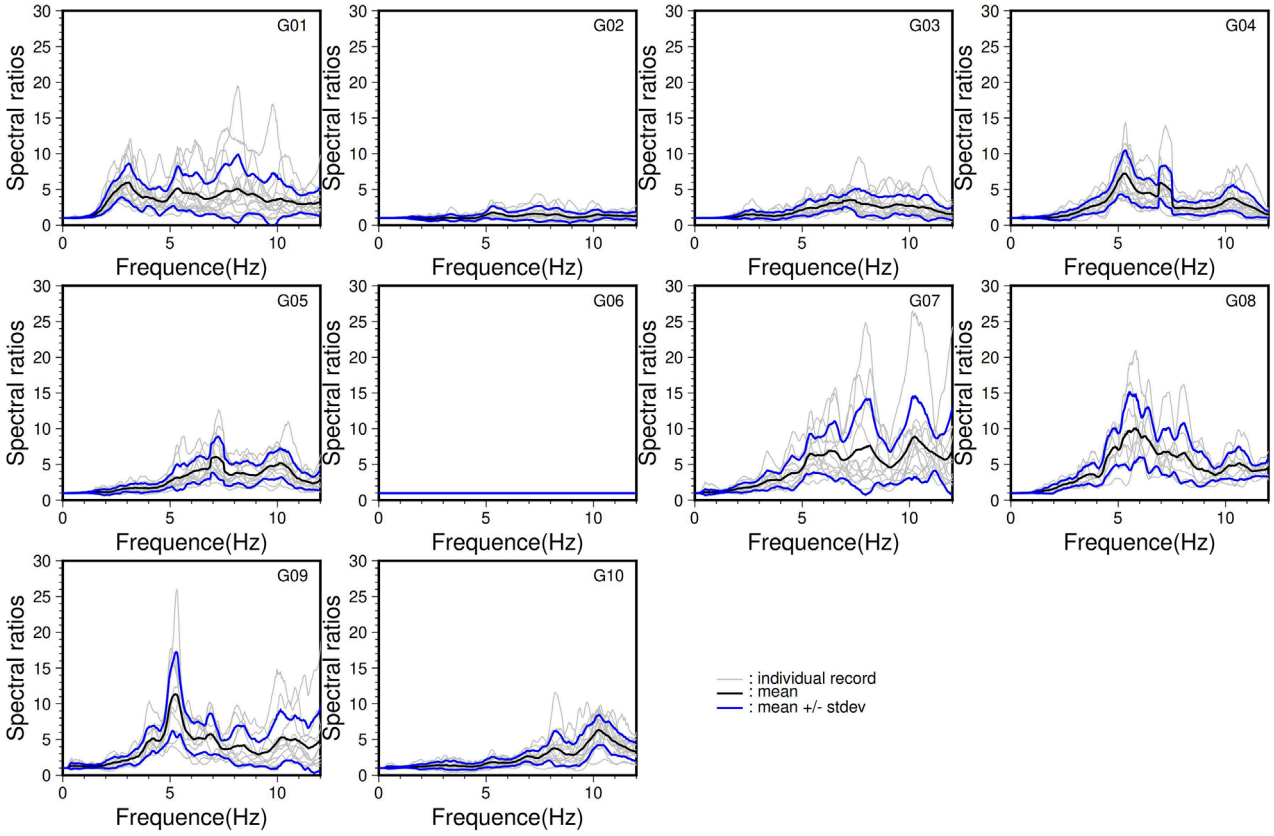

FIGURE 6
Horizontal component spectral ratios from each site. The black solid line represents the mean ratios, while the blue curves above and below the mean represent the mean plus and minus one standard deviation, indicating the range of variation in the seismic response functions.

out that the spectral ratios are determined from weak-motion events. Nonlinearity of soils is likely to reduce ground-motion amplification in a large earthquake (Field et al., 1997).

4 Analysis

4.1 Modelling of amplification due to soil layers

Site G09 is located at a river floodplain. The underground soil layer structure may have an impact on the amplification effect of seismic motion at the site. Therefore, we conducted further analysis and research on this matter.

We conducted ReMi (Louie, 2001) microtremor exploration at Site G09. An acquisition array of 19 three-component short-period seismometers, with a spacing of 5 m, where deployed, and 60 min of three-component continuous noise waveform recordings were collected. After data processing, a surface wave dispersion curve was extracted (Figure 9a), and the underground seismic geological parameter structure of Site G09 was inverted using the method of Wathelet et al. (2008).

In the parameter selection for inversion, we set the range of inversion model parameters to a 10-layer structure based on geological surveys, with an inversion depth range of 1–50 m. These should be able to provide a fully range cover for the possible layered structures and depth variations of the site. The range of P wave velocity was set to 200 to 4,500 m/s, the range of shear wave velocity was set to 100 to 1,500 m/s, the range of Poisson's ratio is set to 0.25 to 0.45, and the density range is set to 1.5 to 2.6 g/cm^3.

The inversion results of the dispersion curve show a structure of four layers (Figure 9b), with the bottom layer being the bedrock. The depths of the interfaces of the three layers of media overlying the bedrock are 2, 9, and 19 m, separately. The shear wave velocities of the media from top to bottom are 186 m/s, 338 m/s, 428 m/s, and 1,010 m/s.

The density of each model layer, from the top to the bottom, are given as 1.9, 2.0, 2.1 and 2.3 g/cm^3, respectively. And the quality factors accounting for damping are determined using the empirical formula of $Q_s = 0.08V_s$ given by Wang et al. (1994). Considering that the shear wave inversion on the low frequency band is not well constrained, there is large uncertainty in the basement velocity of 1,010 m/s from the inversion. From the observation of the outcrops in the study area, the basement of G09 is inferred to be weak weathering sand rock. According to Bourbié (1987), the shear wave velocity of the basement is therefore inferred to be between the range of 850–1,200 m/s. To account for the possible cases due to the error in the basement velocity, we will use 3 different models, separately with a basement velocity of 850, 1,010 and 1,200 m/s, to simulate the possible site response.

10.3389/feart.2025.1537480

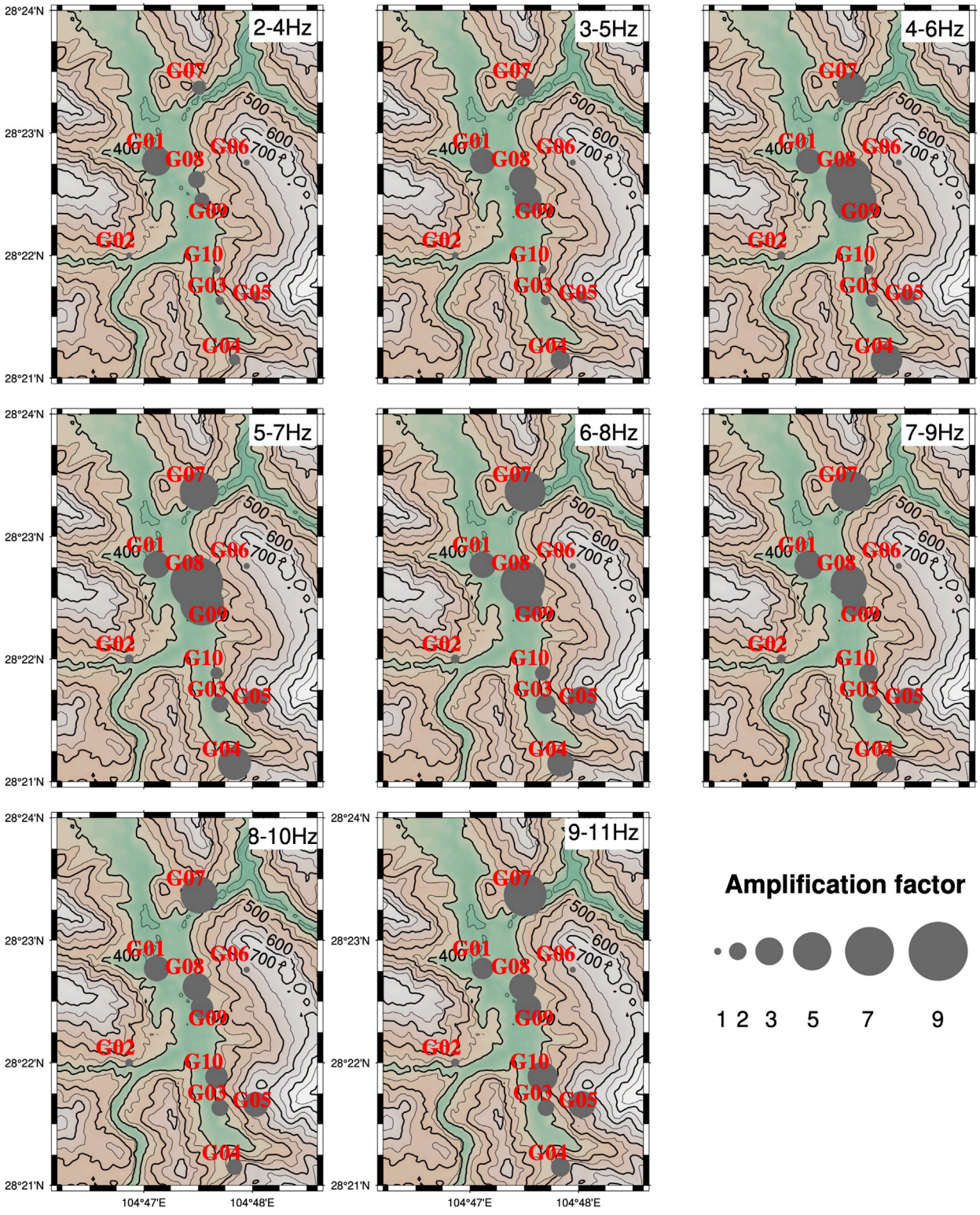

FIGURE 7
Distribution of average amplification factors for seismic ground motions at different frequency bands. The base map depicts the topographic contours of the study area. Gray circles indicate the amplification of seismic ground motions, with the size of the circle indicating the amplification factor.

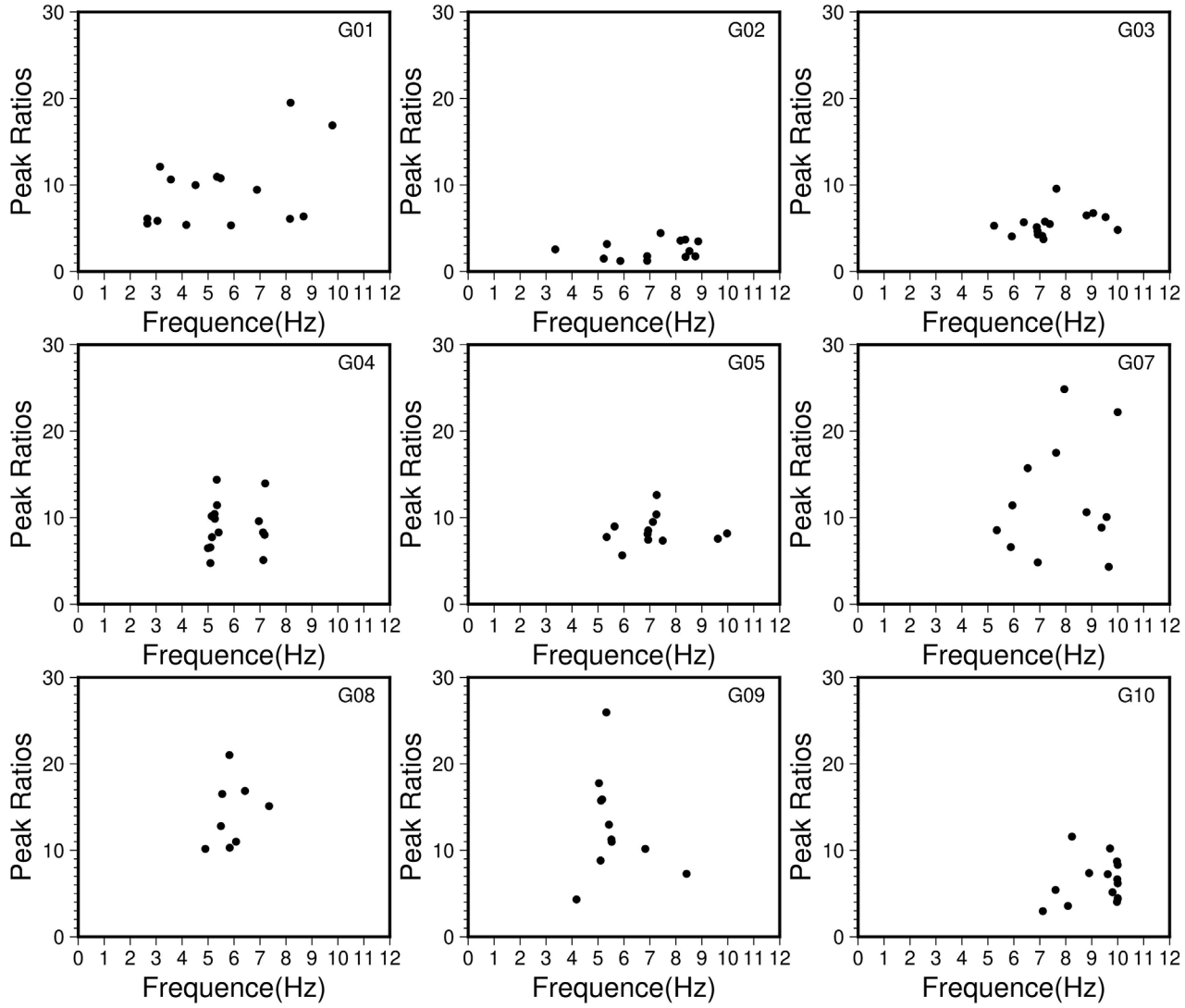

FIGURE 8
The dominant frequency and peak value of seismic amplification at each site. Each dot in the diagram represents the peak value over the frequency band of 0.2–12 Hz.

Based on the structural model given above, a one-dimensional SH wave forward modelling was performed using the method of Yu and He (2003), which is theoretically based on a linear attenuation model.

The modeling results are shown by the red curves in Figure 10. The dominant frequency of site amplification from the modeling is between 5 and 6 Hz, which is very close to the observed dominant frequency. However, the peak amplification from the modelling is only between 2.5 and 3.5 with the basement velocity of the model ranging from 850 to 1,200 *m/s*. This is systematically smaller than the observed results of all earthquakes not only significantly smaller than the observed average amplification peak of 11, but also hugely smaller than the extreme amplification peak of 26. This indicates that the extreme amplification effect observed at site G09 is not solely caused by the one-dimensional layered structure beneath the site, and the mechanism for the seismic amplification effect at site G09 is possibly due to more complex reasons. Considering the topography and geological structure characteristics of Gongquan Town, it may be related to the three-dimensional topography effects.

4.2 Azimuthal characteristics of the extreme peak amplifications

The peak amplification of 26 is from Event 31. We found that the Event 32, which occurred close to the 31st, also triggered a peak amplification of 18 at the site, indicating that the extreme amplification is not a random occurrence. A comparison of the spectral ratios of Events 31 and 32 revealed similarities of the responses of the sites to the events (Figure 11).

Analysis reveals that the two earthquakes, 31 and 32, which caused extreme seismic amplification at G09, are both located to the NNE direction of the site. To understand the orientation distribution characteristics of the extreme seismic amplification

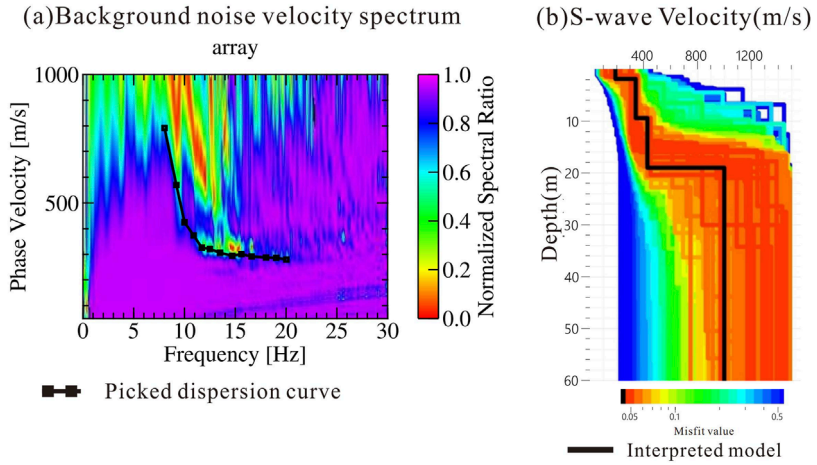

FIGURE 9
Inversion of shear wave velocity structure at Site G09 based on microtremor exploration data. **(a)** The velocity spectra from micro-motion exploration data, and the dispersion curves (black curve) extracted using the passive source ReMi method; **(b)** The shear wave velocity structure obtained from the inversion of the dispersion curve in **(a)**, where the black line represents the best-fitting velocity model.

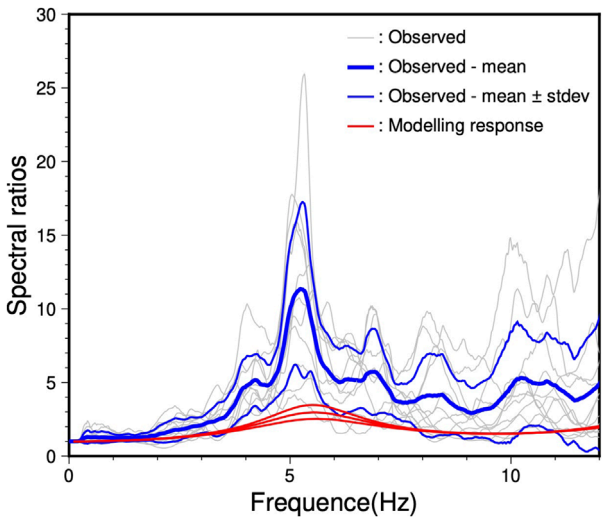

FIGURE 10
Comparison of the spectral ratios of seismic motion at Site G09 with modelling results. The grey curves represent the spectral ratios of the H components observed in various earthquakes. The thick blue curve is the mean spectral ratio, and the thin blue curves are the mean plus and minus one standard deviation. The 3 red curves are the seismic motion amplification functions of S-waves from one-dimensional SH modelling using shear wave velocity of 850 *m/s*, 1,010 *m/s* and 1,200 *m/s*, separately, for the basement of the model.

effect, we conducted statistical analysis of the amplification effects of earthquakes within the 60° to 90° azimuth range against those of other azimuths. The statistical results show that the peak amplification of the earthquakes located within the 60° to 90° azimuth is approximately twice as large as that of earthquakes in other directions (Figure 12), indicating that the extreme amplification effect G09 has a clear directional characteristic.

5 Discussions

The very large ranges of peak RSSRs at most sites, especially G09, and the large ranges in peak frequencies suggest many effects may affect the RSSRs.

As we know that RSSR actually is but a ratio of the ground motion from two different sites. As source observation angle is normally different from one site to another, the source function observed at different sites can be different due to the source radiation patten. Thus, the source term cannot be completely removed from the RSSR results by the ratio cancellation. Similarly, path effect may also not be completely removed by the ratio cancellation due to the path difference of waves propagation from the source to different sites. Therefore, RSSR ratio in general contains not only the site response, but also source and path effects.

The influence of the source and path effects in the RSSR is subject to the site's relation with the hypocentre of the earthquake of interest, including hypocentral distance, azimuth angle, and incident angels of the waves along the propagation paths from the source to the sites. Only when the factors are such that the source and path effects are negligible can the RSSR results be used directly as an interpretation of the site response.

For those events of which the hypocentral distance is not significantly much larger than the distance between the site of interest and the reference site, the source, due to radiation patten difference, and path difference between the sites, can have significant contribution to the RSSR results. In this case, the use of RSSR results as an interpretation of the site response is limited.

However, For Event 31, calculation shows that the hypocentral distance of G09 is 0.7 km longer than G06. In theory, this additional propagation distance would attenuate the wave amplitude to a certain amount for the waves to arrive at Site G09. This means that the RSSR result would underestimate the real amplification at G09, though it is unlikely to be significant as the path length difference is only 0.7 km.

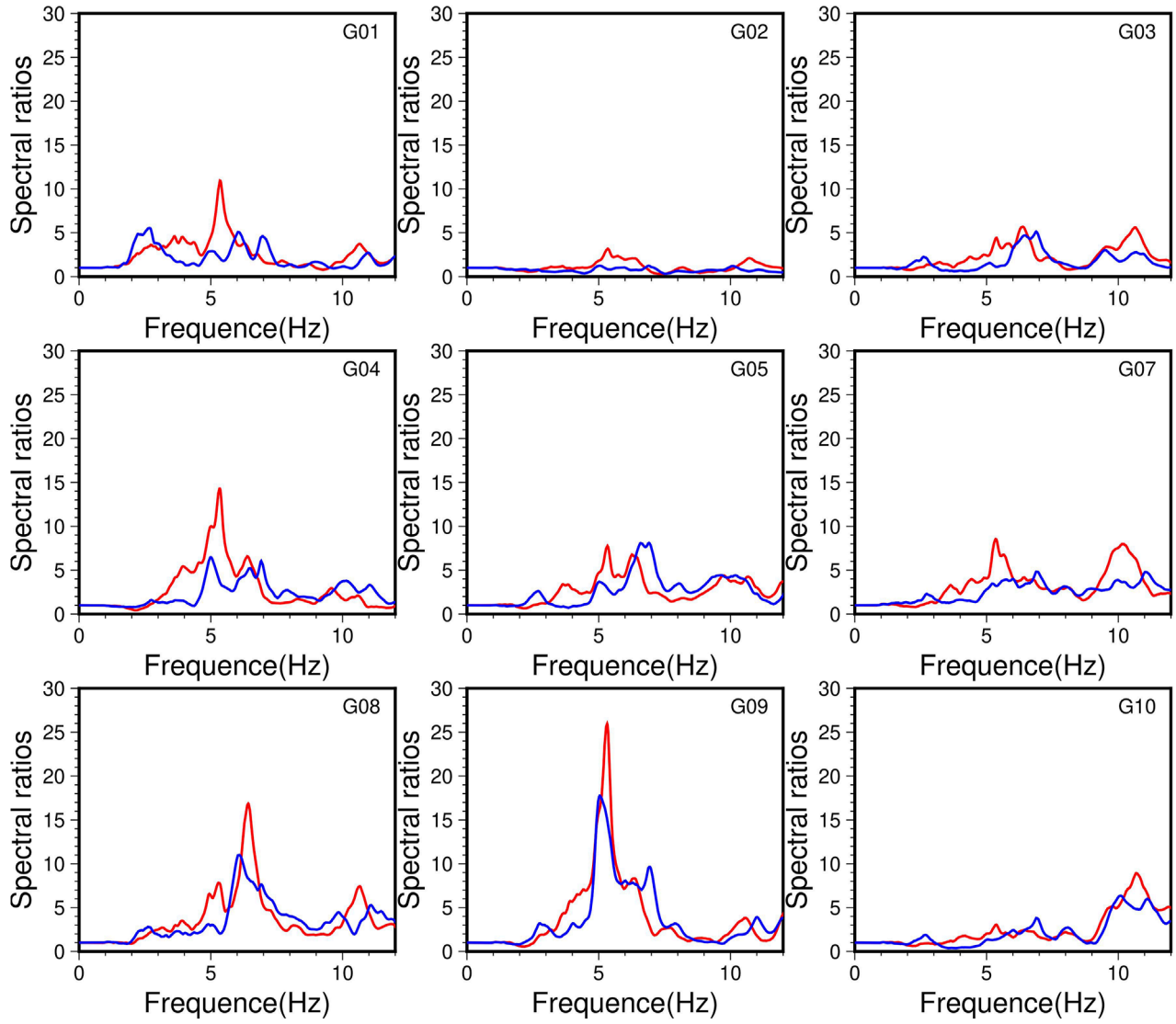

FIGURE 11
Spectral ratios of Events 31 (red) and 32 (blue).

In addition, calculations show that azimuth angle to the epicentre and dip angle to the hypercentre of G09 are 2.2° and 3.6°, respectively, different from those of G06. These small angle differences confine the path difference between G09 and G06 and suggest that the influence of the path on the RSSR for Site G09 should be minor. Similarly, given the small angle differences, the source effects on the RSSR result due to radiation patten of Event 31 should also be minor as well. Therefore, it is reasonable to believe that the RSSR of Site G09 in Event 31 mainly reflects the localized effect at, or around, the site.

The localized effects here may include the wave attenuation along its upward passage through the soil layers beneath the site, the resonance between the free ground surface and the soil basement interface at the site, the three-dimensional resonance of a basin structure in which the site is located, the basin edge effects, the three-dimensional topography effect, and nonlinearity in soil layers, *etc.*

In Section 4.1, we studied the site effects of G09 due to attenuation and resonance by one-dimensional modelling. The results suggest that the remarkable amplification is unlikely to be due to the one-dimensional resonance in the soil layers at the site.

In addition, it is obvious that the geology in the study area does not provide structure conditions for the basin edge seismic resonance to occur at Site G09.

Therefore, the factors to account for the extremely large amplification at Site G09 would possibly be a combination of the azimuth effect of the incident seismic waves to the site, as discussed in Section 4.2, and the effect of the three-dimensional topography.

Finally, it is important to note that the seismic data studied in this paper mainly come from aftershock events. These data are recordings of weak-ground motion. The insights gained reflect only the linear behavior of the sites rather than the nonlinear phenomena during a strong earthquake. Nevertheless, given that the extreme

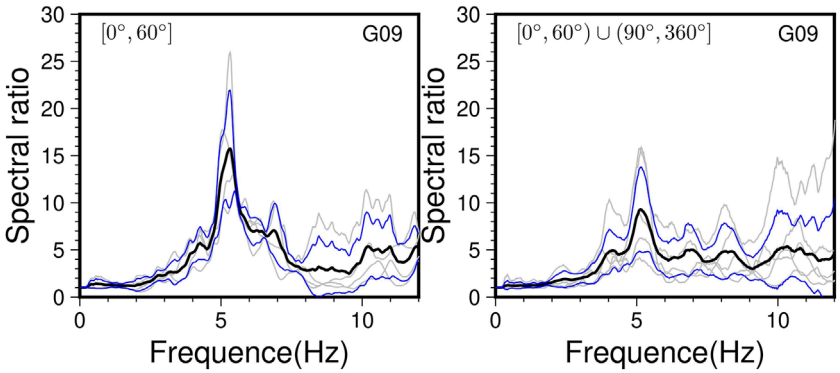

FIGURE 12
Comparison of the H component spectral ratios of earthquakes of different orientations at G09. The black curves represent the means of the spectral ratios, while the blue curves indicate the mean plus or minus one statistical standard deviation. Spectral ratios of earthquakes of azimuths 60° to 90° are shown on the left panel. Those of the other azimuths, i.e., 0° to 60° and 90°–360°, are shown on the right panel. The average peak amplification for earthquakes in the 60° to 90° azimuth is twice that of other azimuths, demonstrating significant differences in directional amplification characteristics.

amplification effect at the G09 site is so large that this phenomenon should not be ignored.

6 Conclusion

Based on the study of the seismic ground motion amplification effect in the valley of Gongquan Town, we can derive the following understandings.

1. There is a significant ground motion amplification effect in the Gongquan valley, with considerable differences in seismic motion at different observation sites. The reference site G06 shows a distinctly lower seismic motion compared to other sites.
2. The average spectral ratio amplification at each observation site ranges from 1 to 11, demonstrating significantly localized site effects, notable ground motion amplification effect in the Gongquan valley.
3. Site G09 shows an extremely large seismic ground motion amplification phenomenon, with maximum peak values of 26. In addition, the results also reveal that the extreme amplification has an event orientation feature. Earthquakes to NNE direction of the site are likely to cause extreme amplification, to which special attention should be paid in future earthquake resistance and disaster prevention efforts.
4. It is important to note that the seismic data studied in this paper mainly comes from aftershock events which are usually of small magnitudes and the insights gained may not fully reflect the nonlinear phenomena present during strong earthquakes. Nevertheless, given that the extreme amplification effect at the G09 site is so large that this phenomenon should not be ignored.
5. The amplification factors from the one-dimensional simulation on the velocity structure of Site G09 are significantly smaller than the observed results, indicating that the local one-dimensional site effect is unlikely to be the main factor causing the large amplification at the site. The mechanisms responsible for the extreme ground motion amplification effects are complex, possibly related to the three-dimensional topography. Future research on this is desired to reveal the mechanisms behind the extreme seismic ground motion amplification effects.

Data availability statement

The raw data supporting the conclusions of this article will be made available by the authors, without undue reservation.

Author contributions

QZ: Writing – original draft, Visualization. JsY: Funding acquisition, Writing – review and editing. CH: Writing – review and editing. JlY: Funding acquisition, Writing – review and editing. XbF: Data curation, Writing – review and editing. KY: Data curation, Writing – review and editing. XH: Data curation, Writing – review and editing. XrF: Data curation, Writing – review and editing.

Funding

The author(s) declare that financial support was received for the research and/or publication of this article. This research is supported by the Sichuan Science and Technology Program, China (2025HJPJ0007 to J Yu and 2025ZNSFSC0314 to J Yuan).

Acknowledgments

This study utilized seismic event data from the China National Seismic Network. Data processing and figure generation were conducted using Geopsy (Wathelet et al., 2020), Seismic Analysis Code (SAC) v.101.6a (Goldstein et al., 2003) and GMT (Wessel et al., 2013) software packages. The research was supported by the Sichuan

Science and Technology Program, China (2025HJPJ0007 to J Yu, and 2025ZNSFSC0314 to J Yuan).

Conflict of interest

Author XbF was employed by Research and Development Center, BGP Inc.

The remaining authors declare that the research was conducted in the absence of any commercial or financial relationships that could be construed as a potential conflict of interest.

Generative AI statement

The author(s) declare that no Generative AI was used in the creation of this manuscript.

Any alternative text (alt text) provided alongside figures in this article has been generated by Frontiers with the support of artificial intelligence and reasonable efforts have been made to ensure accuracy, including review by the authors wherever possible. If you identify any issues, please contact us.

Publisher's note

All claims expressed in this article are solely those of the authors and do not necessarily represent those of their affiliated organizations, or those of the publisher, the editors and the reviewers. Any product that may be evaluated in this article, or claim that may be made by its manufacturer, is not guaranteed or endorsed by the publisher.

References

Aki, K., and Richards, P. G. (2002). *Quantitative seismology*. W. H. Freeman.

Borcherdt, R. (1970). Effects of local geology on ground motion near San Francisco Bay. *Bull. Seismol. Soc. Am.* 60, 29–61. doi:10.1785/BSSA0600010029

Borcherdt, R., and Glassmoyer, G. M. (1992). On the characteristics of local geology and their influence on ground motions generated by the Loma prieta earthquake in the San Francisco Bay region, California. *Bull. Seismol. Soc. Am.* 82, 603–641. doi:10.1785/bssa0820020603

Bourbié, T. (1987). *Acoustics of porous media*. (Editions Technip).

Çelebi, M., Sahakian, V. J., Melgar, D., and Quintanar, L. (2018). The 19 September 2017 M 7.1 Puebla–Morelos earthquake: Spectral ratios confirm Mexico City zoning. *Bull. Seismol. Soc. Am.* 108, 3289–3299. doi:10.1785/0120180100

Field, E., Johnson, P., Beresnev, I., and Zeng, Y. (1997). Nonlinear ground-motion amplification by sediments during the 1994 northridge earthquake. *Nature* 390, 599–602. doi:10.1038/37586

Gao, Y., Dai, D., and Zhang, N. (2021). Progress and prospect of topographic amplification effects of seismic wave in canyon sites. *J. Disaster Prev. Mitig. Eng.* 41, 734–752. doi:10.13409/j.cnki.jdpme.2021.04.004

Goldstein, P., Dodge, D., Firpo, M., and Minner, L. (2003). Sac2000: signal processing and analysis tools for seismologists and engineers. *Int. Geophys.* 81, 1613–1614. doi:10.1016/S0074-6142(03)80284-X

Hu, X., Cui, X., Zhang, G., Wang, G., Zang, A., Shi, B., et al. (2021). Analysis on the mechanical causes of the complex seismicity in changning area, China. *Chin. J. Geophys.* 64, 1–17. doi:10.6038/cjg2021O0232

Hu, G., Zhang, G., and Liang, S. (2023). Study on the spatial distribution of seismic activity in the changning area, Sichuan Province. *Earthquake Research in China* 39, 883–892. doi:10.3969/j.issn.1001-4683.2023.04.015

Kanamori, H., and Anderson, D. (1975). Theoretical basis of some empirical relations in seismology. *Bulletin of the Seismological Society of America* 65, 1073–1095. doi:10.1785/BSSA0650051073

Li, Y., and Huang, R. (2009). Earthquake damage effects of towns and reconstruction site selection in wenchuan earthquake on May 12, 2008. *Chinese Journal of Rock Mechanics and Engineering* 28, 1370–1376. doi:10.3321/j.issn:1000-6915.2009.07.010

Li, P., Liu, H., Bo, J., Li, X., and Yu, X. (2016). Effects of river valley topography on anomalously high intensity in the hanyuan town during the wenchuan Ms 8.0 earthquake. *Chinese Journal of Geophysics* 59, 174–184. doi:10.6038/cjg20160115

Liang, H., Mao, L., Benfu, X., Zhaoheng, Y., Liu, Y., Yan, J., et al. (2017). Preliminary analysis on the seismic disaster characteristics and the intensity abnormal points of junlian M4.9 earthquakes on 28 January 2017. *Earthquake Research in Sichuan* 3, 10–14. doi:10.13716/j.cnki.1001-8115.2017.03.003

Louie, J. (2001). Faster, better: shear-wave velocity to 100 meters depth from refraction microtremor arrays. *Bulletin of the Seismological Society of America* 91, 347–364. doi:10.1785/0120000098

Ren, J., Li, Z., and Li, X. (2021). Contrastive analysis of the accuracy of rapid assessment of earthquake disaster losses by sichuan changning Ms 6.0 earthquake on June 17, 2019. *Seismological and Geomagnetic Observation and Research* 42, 67–79. doi:10.3969/j.issn.1003-3246.2021.04.009

Sepúlveda, S., Murphy, W., Jibson, R., and Petley, D. (2005). Seismically induced rock slope failures resulting from topographic amplification of strong ground motions: the case of pacoima canyon California. *Engineering Geology* 80, 336–348. doi:10.1016/j.enggeo.2005.07.004

Steidl, J. H., Tumarkin, A. G., and Archuleta, R. J. (1996). What is a reference site? *Bulletin of the Seismological Society of America* 86, 1733–1748. doi:10.1785/bssa0860061733

Taber, J. B. J., and Smith, E. G. C. (1992). Frequency dependent amplification of weak ground motions in porirua and lower hutt, New Zealand. *Bulletin of the N. Z. Society for Earthquake Engineering* 25, 303–331. doi:10.5459/bnzsee.25.4.303-331

Trifunac, M. D., and Hudson, D. E. (1971). Analysis of the pacoima dam accelerogram-San fernando, California, earthquake of 1971. *Bulletin of the Seismological Society of America* 61, 1393–1411. doi:10.1785/BSSA0610051393

Wang, S. (2022). *A study on the characteristics of source parameters in the basin in southern sichuan*. Beijing: China University of Petroleum. Master's thesis.

Wang, Z., Street, R., Woolery, E., and Harris, J. (1994). $_{Qs}$ estimation for unconsolidated sediments using first-arrival *SH* wave critical refractions. *Journal of Geophysical Research Solid Earth* 99, 13543–13551. doi:10.1029/94jb00499

Wathelet, M., Jongmans, D., Ohrnberger, M., and Bonnefoy-Claudet, S. (2008). Array performances for ambient vibrations on a shallow structure and consequences over Vs inversion. *Journal of Seismology* 12, 1–19. doi:10.1007/s10950-007-9067-x

Wathelet, M., Chatelain, J.-L., Cornou, C., Di Giulio, G., Guillier, B., Ohrnberger, M., et al. (2020). Geopsy: a user-friendly open-source tool set for ambient vibration processing. *Seismological Research Letters* 91, 1878–1889. doi:10.1785/0220190360

Wessel, P., Smith, W., Scharroo, R., Luis, J., and Wobbe, F. (2013). Generic mapping tools: improved version released. *Eos, Transactions American Geophysical Union* 94, 409–410. doi:10.1002/2013eo450001

Yang, Y., Bai, W., Dai, J., and Chen, X. (2023). Investigation and analysis of building damage caused by Ms6.0 changning earthquake in Sichuan Province. *Building Structure* 53, 738–743. doi:10.19701/j.jzjg.23S2713

Yi, G., Zhou, L., Zhang, L., Long, F., and Gong, Y. (2020). Predictive efficiency tests of moderate earthquakes with sizes Ms ≥4.5 in low seismicity regions within sichuan basin. *Journal of Seismological Research* 43, 262–269. doi:10.3969/j.issn.1000-0666.2020.02.007

Yu, J., and Haines, J. (2003). The choice of reference sites for seismic ground amplification analyses: case study at parkway, New Zealand. *Bulletin of the Seismological Society of America* 93, 713–723. doi:10.1785/0120010289

Yu, J., and He, Z. (2003). Precise modeling of SH propagation in subsurface multi-layer media. *Journal of Seismological Research* 26, 14–19. doi:10.3969/j.issn.1000-0666.2003.01.003

Zuo, K., and Zhao, C. (2021). The spatial and temporal distribution of source parameters of earthquakes in changning area, Sichuan Province. *Earthquake Research in China* 37, 472–482. doi:10.3969/j.issn.1001-4683.2021.02.019

Frontiers in Earth Science

Investigates the processes operating within the major spheres of our planet

Advances our understanding across the earth sciences, providing a theoretical background for better use of our planet's resources and equipping us to face major environmental challenges.

Discover the latest Research Topics

See more →

Frontiers

Avenue du Tribunal-Fédéral 34
1005 Lausanne, Switzerland
frontiersin.org

Contact us

+41 (0)21 510 17 00
frontiersin.org/about/contact